ΕΘΝΙΚΟ ΜΕΤΣΟΒΙΟ ΠΟΛΥΤΕΧΝΕΙΟ
ΣΧΟΛΗ ΠΟΛΙΤΙΚΩΝ ΜΗΧΑΝΙΚΩΝ
ΤΟΜΕΑΣ ΓΕΩΤΕΧΝΙΚΗΣ

ΔΙΕΡΕΥΝΗΣΗ ΤΗΣ ΜΗ-ΓΡΑΜΜΙΚΗΣ ΣΥΜΠΕΡΙΦΟΡΑΣ ΤΩΝ ΕΔΑΦΙΚΩΝ ΥΛΙΚΩΝ ΜΕ ΠΡΟΣΟΜΟΙΩΣΗ ΤΟΥ ΕΡΠΥΣΜΟΥ

INVESTIGATION OF THE NONLINEAR TIME-DEPENDENT SOIL BEHAVIOR

ΔΙΔΑΚΤΟΡΙΚΗ ΔΙΑΤΡΙΒΗ - DOCTORAL THESIS

Αλέξανδρου Ν. Καλού

Διπλωματούχου Πολιτικού Μηχανικού Ε.Μ.Π.,
M.Sc. Georgia Institute of Technology

ΕΠΙΒΛΕΠΩΝ: Μ. ΚΑΒΒΑΔΑΣ, Αν. Καθηγητής Ε.Μ.Π.

Αθήνα, Απρίλιος 2014

ΕΘΝΙΚΟ ΜΕΤΣΟΒΙΟ ΠΟΛΥΤΕΧΝΕΙΟ
ΣΧΟΛΗ ΠΟΛΙΤΙΚΩΝ ΜΗΧΑΝΙΚΩΝ
ΤΟΜΕΑΣ ΓΕΩΤΕΧΝΙΚΗΣ

ΔΙΕΡΕΥΝΗΣΗ ΤΗΣ ΜΗ-ΓΡΑΜΜΙΚΗΣ ΣΥΜΠΕΡΙΦΟΡΑΣ ΤΩΝ ΕΔΑΦΙΚΩΝ ΥΛΙΚΩΝ ΜΕ ΠΡΟΣΟΜΟΙΩΣΗ ΤΟΥ ΕΡΠΥΣΜΟΥ

INVESTIGATION OF THE NONLINEAR TIME-DEPENDENT SOIL BEHAVIOR

ΔΙΔΑΚΤΟΡΙΚΗ ΔΙΑΤΡΙΒΗ - DOCTORAL THESIS

Αλέξανδρου Ν. Καλού

Διπλωματούχου Πολιτικού Μηχανικού Ε.Μ.Π.,
M.Sc. Georgia Institute of Technology

ΕΠΙΒΛΕΠΩΝ: Μ. ΚΑΒΒΑΔΑΣ, Αν. Καθηγητής Ε.Μ.Π.

Αθήνα, Απρίλιος 2014

ΕΘΝΙΚΟ ΜΕΤΣΟΒΙΟ ΠΟΛΥΤΕΧΝΕΙΟ
ΣΧΟΛΗ ΠΟΛΙΤΙΚΩΝ ΜΗΧΑΝΙΚΩΝ
ΤΟΜΕΑΣ ΓΕΩΤΕΧΝΙΚΗΣ

ΔΙΕΡΕΥΝΗΣΗ ΤΗΣ ΜΗ-ΓΡΑΜΜΙΚΗΣ ΣΥΜΠΕΡΙΦΟΡΑΣ ΤΩΝ ΕΔΑΦΙΚΩΝ ΥΛΙΚΩΝ ΜΕ ΠΡΟΣΟΜΟΙΩΣΗ ΤΟΥ ΕΡΠΥΣΜΟΥ

ΔΙΔΑΚΤΟΡΙΚΗ ΔΙΑΤΡΙΒΗ

Αλέξανδρου Ν. Καλού

Διπλωματούχου Πολιτικού Μηχανικού Ε.Μ.Π.,

M.Sc. Georgia Institute of Technology

Η διατριβή υποβλήθηκε στη Σχολή Πολιτικών Μηχανικών του Εθνικού Μετσόβιου Πολυτεχνείου προς εκπλήρωση των προϋποθέσεων του τίτλου του Διδάκτορος Μηχανικού

ΤΡΙΜΕΛΗΣ ΣΥΜΒΟΥΛΕΥΤΙΚΗ ΕΠΙΤΡΟΠΗ:

1. Μ. ΚΑΒΒΑΔΑΣ, Αν. Καθηγητής Ε.Μ.Π. (Επιβλέπων)
2. Γ. ΜΠΟΥΚΟΒΑΛΑΣ, Καθηγητής Ε.Μ.Π.
3. Ν. ΓΕΡΟΛΥΜΟΣ, Επ. Καθηγητής Ε.Μ.Π.

ΕΠΤΑΜΕΛΗΣ ΕΞΕΤΑΣΤΙΚΗ ΕΠΙΤΡΟΠΗ:

1. Μ. ΚΑΒΒΑΔΑΣ, Αν. Καθηγητής Ε.Μ.Π. (Επιβλέπων)
2. Γ. ΜΠΟΥΚΟΒΑΛΑΣ, Καθηγητής Ε.Μ.Π.
3. Ν. ΓΕΡΟΛΥΜΟΣ, Επ. Καθηγητής Ε.Μ.Π.
4. Γ. ΓΚΑΖΕΤΑΣ, Καθηγητής Ε.Μ.Π.
5. Γ.ΤΣΙΑΜΠΑΟΣ, Καθηγητής Ε.Μ.Π.
6. Μ. ΣΑΚΕΛΛΑΡΙΟΥ, Καθηγητής Ε.Μ.Π.
7. ΑΧ. ΠΑΠΑΔΗΜΗΤΡΙΟΥ,
Επ. Καθηγητής Παν. Θεσσαλίας

Αθήνα, Απρίλιος 2014

NATIONAL TECHNICAL UNIVERSITY OF ATHENS
SCHOOL OF CIVIL ENGINEERING
DEPARTMENT OF GEOTECHNICAL ENGINEERING

INVESTIGATION OF THE NONLINEAR TIME-DEPENDENT SOIL BEHAVIOR

DOCTORAL THESIS

Alexandros N. Kalos

Dpl. Civil Engineer, N.T.U.A.,

M.Sc. Georgia Institute of Technology

The thesis is submitted to the School of Civil Engineering of the National Technical University of Athens in fulfilment of the requirements for the Degree of Doctor of Philosophy

ADVISORY COMMITTEE:

1. M. KAVVADAS,
Associate Professor N.T.U.A. (Supervisor)

2. G. BOUCKOVALAS, Professor N.T.U.A.

3. N. GEROLYMOS,
Assistant Professor N.T.U.A.

EXAMINATION COMMITTEE:

1. M. KAVVADAS,
Associate Professor N.T.U.A. (Supervisor)

2. G. BOUCKOVALAS, Professor N.T.U.A.

3. N. GEROLYMOS,
Assistant Professor N.T.U.A.

4. G. GAZETAS, Professor N.T.U.A.

5. G. TSIAMBAOS, Professor N.T.U.A.

6. M. SAKELLARIOU, Professor N.T.U.A.

7. ACH. PAPADIMITRIOU,
Assistant Professor University of Thessaly

Athens, April 2014

ΕΘΝΙΚΟ ΜΕΤΣΟΒΙΟ ΠΟΛΥΤΕΧΝΕΙΟ
ΣΧΟΛΗ ΠΟΛΙΤΙΚΩΝ ΜΗΧΑΝΙΚΩΝ
ΤΟΜΕΑΣ ΓΕΩΤΕΧΝΙΚΗΣ

ΔΙΕΡΕΥΝΗΣΗ ΤΗΣ ΜΗ-ΓΡΑΜΜΙΚΗΣ ΣΥΜΠΕΡΙΦΟΡΑΣ ΤΩΝ ΕΔΑΦΙΚΩΝ ΥΛΙΚΩΝ ΜΕ ΠΡΟΣΟΜΟΙΩΣΗ ΤΟΥ ΕΡΠΥΣΜΟΥ

ΔΙΔΑΚΤΟΡΙΚΗ ΔΙΑΤΡΙΒΗ

Αλέξανδρου Ν. Καλού

Διπλωματούχου Πολιτικού Μηχανικού Ε.Μ.Π.,

M.Sc. Georgia Institute of Technology

Η διατριβή υποβλήθηκε στη Σχολή Πολιτικών Μηχανικών

του Εθνικού Μετσόβιου Πολυτεχνείου

προς εκπλήρωση των προϋποθέσεων του τίτλου του Διδάκτορος Μηχανικού

ΤΡΙΜΕΛΗΣ ΣΥΜΒΟΥΛΕΥΤΙΚΗ ΕΠΙΤΡΟΠΗ:

1. Μ. ΚΑΒΒΑΔΑΣ, Αν. Καθηγητής Ε.Μ.Π. (Επιβλέπων)
2. Γ. ΜΠΟΥΚΟΒΑΛΑΣ, Καθηγητής Ε.Μ.Π.
3. Ν. ΓΕΡΟΛΥΜΟΣ, Επ. Καθηγητής Ε.Μ.Π.

ΕΠΤΑΜΕΛΗΣ ΕΞΕΤΑΣΤΙΚΗ ΕΠΙΤΡΟΠΗ:

1. Μ. ΚΑΒΒΑΔΑΣ, Αν. Καθηγητής Ε.Μ.Π. (Επιβλέπων)
2. Γ. ΜΠΟΥΚΟΒΑΛΑΣ, Καθηγητής Ε.Μ.Π.
3. Ν. ΓΕΡΟΛΥΜΟΣ, Επ. Καθηγητής Ε.Μ.Π.
4. Γ. ΓΚΑΖΕΤΑΣ, Καθηγητής Ε.Μ.Π.
5. Γ.ΤΣΙΑΜΠΑΟΣ, Καθηγητής Ε.Μ.Π.
6. Μ. ΣΑΚΕΛΛΑΡΙΟΥ, Καθηγητής Ε.Μ.Π.
7. ΑΧ. ΠΑΠΑΔΗΜΗΤΡΙΟΥ, Επ. Καθηγητής Παν. Θεσσαλίας

Αθήνα, Απρίλιος 2014

NATIONAL TECHNICAL UNIVERSITY OF ATHENS
SCHOOL OF CIVIL ENGINEERING
DEPARTMENT OF GEOTECHNICAL ENGINEERING

INVESTIGATION OF THE NONLINEAR TIME-DEPENDENT SOIL BEHAVIOR

DOCTORAL THESIS

Alexandros N. Kalos

Dpl. Civil Engineer, N.T.U.A.,
M.Sc. Georgia Institute of Technology

The thesis is submitted to the School of Civil Engineering of the National Technical University of Athens in fulfilment of the requirements for the Degree of Doctor of Philosophy

ADVISORY COMMITTEE:

1. M. KAVVADAS,
Associate Professor N.T.U.A. (Supervisor)
2. G. BOUCKOVALAS, Professor N.T.U.A.
3. N. GEROLYMOS,
Assistant Professor N.T.U.A.

EXAMINATION COMMITTEE:

1. M. KAVVADAS,
Associate Professor N.T.U.A. (Supervisor)
2. G. BOUCKOVALAS, Professor N.T.U.A.
3. N. GEROLYMOS,
Assistant Professor N.T.U.A.
4. G. GAZETAS, Professor N.T.U.A.
5. G. TSIAMBAOS, Professor N.T.U.A.
6. M. SAKELLARIOU, Professor N.T.U.A.
7. ACH. PAPADIMITRIOU
Assistant Professor University of Thessaly

Athens, April 2014

Προλεγόμενα

«Τους Λαιστρυγόνας και τους Κύκλωπας, τον θυμωμένο Ποσειδώνα μη φοβάσαι, τέτοια στον δρόμο σου ποτέ σου δεν θα βρεις…» λέει ο ποιητής. Ένα ταξίδι στην Ιθάκη δεν τελειώνει χωρίς φουρτούνες και εμπόδια, μα η γεύση της γλυκιά «κι αν πτωχική την βρεις, η Ιθάκη δεν σε γέλασε· έτσι σοφός που έγινες, με τόση πείρα, ήδη θα το κατάλαβες η Ιθάκες τι σημαίνουν». Αυτοί οι στίχοι μου έρχονται στο μυαλό την στιγμή αυτή που καλούμαι να γράψω τις ευχαριστίες. Με αυτό ακριβώς θέλω να ευχαριστήσω τον κ. Μιχάλη Καββαδά, Αναπληρωτή Καθηγητή Ε.Μ.Π. γιατί με δίδαξε να απολαμβάνω το ταξίδι. Ο νόστος θα έρθει μαζί με την σοφία αλλά το ταξίδι και η εμπειρία είναι πραγματικά η ίδια η χαρά. Για αυτό τον λόγο θα ήθελα μέσα από αυτές τις λίγες γραμμές να εκφράσω ένα μεγάλο ευχαριστώ. Είναι εκείνος που πίστεψε σε εμένα. Αυτός που με παρακολουθούσε, με επέβλεπε, άκουγε τους προβληματισμούς μου και με επανέφερε πίσω στην πορεία, κάθε φορά που χανόμουν στα χαώδη μονοπάτια της θεωρητικής αναζήτησης της καταστατικής συμπεριφοράς, με την χαρακτηριστική του έκφραση «object oriented». Οφείλω να τον ευχαριστήσω για την αγάπη του που με τόση χαρά μου μετέδωσε για το αντικείμενο, μα πολύ περισσότερο για τον πρακτικό τρόπο σκέψης που μου μετέδωσε.

Θα ήθελα να ευχαριστήσω θερμά τα μέλη της Τριμελούς Συμβουλευτικής Επιτροπή, τον κ. Γιώργο Μπουκοβάλα, Καθηγητή Ε.Μ.Π. και τον Νίκο Γερόλυμο, Επίκουρο Καθηγητή Ε.Μ.Π., για το ενδιαφέρον τους για την έρευνά μου και την προθυμία τους να συνδράμουν και να βοηθήσουν σε κάθε έκφανση της δουλειάς μου, όποτε και αν τους χρειάστηκα. Θα ήθελα να απευθύνω τις ευχαριστίες μου και προς τα υπόλοιπα μέλη της Επταμελούς Εξεταστικής Επιτροπής, τον κ. Γ. Γκαζέτα, Καθηγητή Ε.Μ.Π., τον κ. Γ. Τσιαμπάο, Καθηγητή Ε.Μ.Π., τον κ. Μ. Σακελλαρίου, Καθηγητή Ε.Μ.Π. και τον κ. Αχ. Παπαδημητρίου, Επίκουρο Καθηγητή στο Πανεπιστήμιο

Θεσσαλίας, για τα σχόλια, τις επισημάνσεις και την συμβολή τους στην τελική διαμόρφωση της διατριβής.

Επιθυμώ από αυτό το βήμα να απευθύνω τις ιδιαίτερες ευχαριστίες μου στον ομότιμο καθηγητή κ. Αν. Αναγνωστόπουλο για την ζωντάνια του, για το ενδιαφέρον του για την έρευνά μου και για την αστείρευτη ανησυχία του για την πρόοδο του τομέα Γεωτεχνικής.

Πραγματικά μου είναι δύσκολο να συγκεντρώσω το μυαλό μου για να απευθύνω τις ευχαριστίες. Υπήρξαν όλα τόσο μοναδικά και όπως όλα τα μοναδικά πράγματα περνούν, φεύγουν και απομένει μια γλυκιά θύμηση στην άκρη του μυαλού… Ξεκινώντας θα ήθελα να ευχαριστήσω τον άνθρωπο τον οποίο δεν μπορώ να φανταστώ μακριά από τον Τομέα Γεωτεχνικής Μηχανικής. Θέλω να ευχαριστήσω τον Διδάκτορα Γιάννη Χαλούλο για την ευχάριστη διάθεσή του, για την μοναδικότητά του και το γεγονός ότι αποτελεί την ψυχή του Τομέα.

Θέλω να ευχαριστήσω τα μέλη της ερευνητικής ομάδας. Άλλωστε το ταξίδι μας συνεχίζεται ακόμα (δεν με ξεφορτωθήκατε, θα σας τρελαίνω ακόμα). Είχα την τιμή και την χαρά να ξεκινήσω την έρευνά μου παράλληλα με τον Υποψήφιο Διδάκτορα Κωνσταντίνο Τζιβάκο. Κάθε φορά που αισθανόμουν κουρασμένος ή αγχωμένος καταλάβαινα ότι δεν ήμουν μόνος στο ταξίδι μα υπήρχαν κι άλλες Ιθάκες να περιμένουν Οδυσσέες. Τον Υποψήφιο Διδάκτορα Παναγιώτη Σιταρένιο οφείλω να τον ευχαριστήσω ξεχωριστά. Πόσες συζητήσεις μήνες επί μηνών πραγματοποιήσαμε για να βρούμε τον μίτο της Αριάδνης, ειλικρινά αδυνατώ να θυμηθώ. Διαφωνίες πολλές μα πάντα καλοπροαίρετες και σε ευχαριστώ. Θέλω να ευχαριστήσω και τους Νέους μας, τον Υποψήφιο Διδάκτορα Δημήτρη Λίτσα και το εκκολαπτόμενο μέλος της ερευνητικής μας ομάδας τον Φίλιππο Χόρτη. Θα ήθελα επιπλέον να ευχαριστήσω την Υποψήφια Διδάκτορα Σμαράγδα Ευθυμίου για τις επισημάνσεις της κατά την διάρκεια της διατριβής μου. Πάντα ανήσυχη, πάντα στο τρέξιμο και πάντα αγχωμένη με ένα χαμόγελο. Αγαπητοί μου συναγωνιστές είχα την τιμή να αποτελώ μέρος της ερευνητική μας ομάδας και σας ευχαριστώ για τους προβληματισμούς σας. Με έκαναν καλύτερο άνθρωπο.

Τα τελευταία χρόνια πέρασα τον περισσότερο χρόνο μου μέσα σε ένα γραφείο του Τομέα Γεωτεχνικής. Ξεκίνησα να το βλέπω σαν δεύτερο σπίτι μου μετά από τόσες ώρες και τόσους υπέροχους ανθρώπους. Οι ανεκτίμητοι φίλοι έκαναν τις ώρες

δουλειάς να μοιάζουν διασκέδαση. Δεν θα σας κλείσω σε μια γενική προσέγγιση γιατί δεν σας αξίζει. Ευχαριστώ θερμά τους Υποψήφιους Διδάκτορες Παύλο Αστερίου (απλά μοναδικός), τον Νέο (Γιάννη Τσιάπα), τον βάζελο (Θανάση Ζαφειράκο), τον ψηλό (Γιώργο Προυντζόπουλο) και τον αλληλένδετο Πέτρο Φορτσάκη, την οθόνη (Μαριάννα Λώλη), την Κική Δημητριάδη (ο πρώτος άνθρωπος που γνώρισα στην σχολή) και την Παναγιώτα Τασιοπούλου (μοναδική!). Ελπίζω να μην ξέχασα κανέναν μα κι αν ξέχασα να ξέρετε πως σας σκέφτομαι…

Άφησα τον τελευταίο αυτό χώρο για τους αδερφικούς μου φίλους και την οικογένειά μου. Με ανέχτηκαν και με στήριξαν πολύ και για αυτό τον λόγο σας ευχαριστώ. Με έναν μαγικό τρόπο ήσασταν πάντα δίπλα μου, μπροστά μου, πάντα εκεί. Δεν θέλω να σας αναφέρω γιατί είσαστε μοναδικοί μέσα μου και δεν επιθυμώ να σας μοιραστώ, μα σας ευχαριστώ!! «Εκτός από την μάνα σου κανείς δεν σε θυμάται» αναφέρει ο Καββαδίας και σαν ποιητής κάτι θα ξέρει παραπάνω… Άλλωστε εμείς μηχανικοί είμαστε.

Η παρούσα έρευνα έχει χρηματοδοτηθεί από τον Ειδικό Λογαριασμό Κονδυλίων Έρευνας (ΕΛΚΕ) του Εθνικού Μετσόβιου Πολυτεχνείου. Θέλω να ευχαριστήσω όλα τα μέλη της Επιτροπής Διαχείρισης του Ειδικού Λογαριασμού για την δυνατότητα χρηματοδότησης τόσο της προσωπικής μου έρευνας όσο και της ερευνητικής δραστηριότητας των υπολοίπων μελών της ακαδημαϊκής κοινότητας μέσω των χορηγούμενων υποτροφιών.

Την άγκυρα φουντάρει στις κουκουναριές
φορτώνει φρέσκο αέρα κι απ' τις δυο μεριές

Είναι από μαύρη πέτρα κι είναι απ' όνειρο
κι έχει λοστρόμο αθώο ναύτη πονηρό

Αλέξανδρος Καλός (Απρίλιος, 2014)

ΕΘΝΙΚΟ ΜΕΤΣΟΒΙΟ ΠΟΛΥΤΕΧΝΕΙΟ
ΣΧΟΛΗ ΠΟΛΙΤΙΚΩΝ ΜΗΧΑΝΙΚΩΝ
ΤΟΜΕΑΣ ΓΕΩΤΕΧΝΙΚΗΣ

Διδακτορική Διατριβή

Διερεύνηση της μη-γραμμικής συμπεριφοράς των εδαφικών υλικών με προσομοίωση του ερπυσμού

Αλέξανδρος Ν. Καλός

ΠΕΡΙΛΗΨΗ

Στην παρούσα διδακτορική διατριβή καταστρώνεται ένα νέο χρονικά εξαρτημένο καταστατικό πλαίσιο συμπεριφοράς. Το καινούριο αυτό πλαίσιο θεμελιώνεται πάνω στις ελαστοπλαστικές αρχές των δομημένων γεωυλικών ενώ παράλληλα ενσωματώνει ένα επιπλέον σύνολο δομητικών (π.χ. βελτιωμένους νόμους αποδόμησης της δομής και κινηματικής κράτυνσης της κλίσης c και της μετάθεσης d μέσω της συσσώρευσης πλαστικών παραμορφώσεων) και χρονικά εξαρτημένων χαρακτηριστικών (π.χ. την απομείωση της περιβάλλουσας αντοχής μέσω της συσσώρευσης ερπυστικών παραμορφώσεων).

Η επιτακτική ανάγκη για την διατύπωση ενός νέου καταστατικού πλαισίου συμπεριφοράς απορρέει από την ανεπάρκεια των υφιστάμενων μεθοδολογιών να προσομοιώσουν τον μηχανισμό της προοδευτικής αστοχίας σε πρανή, στηριζόμενα αποκλειστικά και μόνο σε ελαστοπλαστικά χαρακτηριστικά. Η ουσιώδης ατέλεια των ελαστοπλαστικών προσομοιωμάτων απορρέει από την αδυναμία ελέγχου του μεγέθους των πλαστικών παραμορφώσεων. Συνεπώς, δεν δύνανται να συσσωρευτούν σημαντικές ανελαστικές παραμορφώσεις που να οδηγούν στην ενεργοποίηση του μηχανισμού της προοδευτικής αστοχίας. Η ενσωμάτωση ωστόσο των ερπυστικών χαρακτηριστικών επιτρέπει την δυνατότητα ελέγχου των ανελαστικών παραμορφώσεων μέσω της ερπυστικής συνιστώσας. Αποδεικνύεται ότι είναι ο συνδυασμός των δομητικών και των ερπυστικών χαρακτηριστικών που οδηγεί στην αστοχία.

Το εξιδανικευμένο προσομοίωμα θεμελιώνεται επί της κλασσικής θεωρίας πλαστικότητας των εδαφικών υλικών ολοκληρούμενη εντός του πλαισίου της θεωρίας υπερφόρτισης (Perzyna, 1962 & 1966). Τόσο ο μηχανισμός γήρανσης (που

οδηγεί σε αύξηση της αντοχής λόγω της αύξησης της τάσης προστερεοποίησης) όσο και ο μηχανισμός ερπυστικής αστοχίας (που απορρέει από την απομείωση της περιβάλλουσας αντοχής) ενσωματώνονται επιτυχώς εντός των καταστατικών εξισώσεων. Το εξιδανικευμένο προσομοίωμα αξιολογείται σε αριθμητικές αναλύσεις υλικού σημείου και σε επίπεδο πεπερασμένων στοιχείων καθώς και έναντι εργαστηριακών δοκιμών. Αποδεικνύεται ότι το χρονικά εξαρτημένο καταστατικό πλαίσιο συμπεριφοράς προσομοιώνει επιτυχώς τους μηχανισμούς γήρανσης και ερπυστικής αστοχίας (μέσω της συσσώρευσης ανελαστικών παραμορφώσεων).

Το προτεινόμενο εξιδανικευμένο προσομοίωμα χρησιμοποιήθηκε επιτυχώς στην πρόβλεψη του μηχανισμού προοδευτικής αστοχίας σε ένα πλήρως κορεσμένο πρανές.

NATIONAL TECHNICAL UNIVERSITY OF ATHENS
SCHOOL OF CIVIL ENGINEERING
DEPARTMENT OF GEOTECHNICAL ENGINEERING

Doctoral Thesis

Investigation of the nonlinear time-dependent soil behavior

Alexandros N. Kalos

ABSTRACT

The present dissertation develops a constitutive behavioral framework for structured soils with time-dependent characteristics. The model builds on previously developed models for structured soils (Kavvadas and Amorosi, 2000; Belokas and Kavvadas, 2010) and includes additional structural features (e.g. a strength envelope degradation with plastic strains) and, mainly, a complete set of time-dependent characteristics.

The need for the development of this model was based on finite element analyses of slope stability which indicated that structure degradation effects could not model the onset of slope instability by a mechanism of strength reduction due to plastic strains. This deficiency was attributed to the fact that classical inviscid elastoplasticity for structured soils cannot control the magnitude of plastic strains (and thus cannot generate large-enough plastic strains to cause failure), as plastic strains are imposed by the physical problem.

It was envisioned that additional time-dependent characteristics can solve this problem, as accumulation of "creep" strains could be independently controlled and reach large-enough values to cause failure. Thus, it is the combination of time-dependent characteristics and classical structure degradation which leads to the solution of "delayed" failures is slopes (but also in other geotechnical problems).

The model is founded on the classical theory of elastoplasticity integrated within the overstress theory (Perzyna, 1962 & 1966). Both aging effects (leading to an increase of strength through the increase of the preconsolidation pressure) and creep induced failure (stemming from the strength envelope evolution due to creep strains) are

accounted for within the definition of the governing constitutive equations. The model is evaluated through single point and element based numerical analyses and, mainly, against experimental measurements. It is established that the proposed mechanical framework can simulate accurately the underlying mechanisms associated with creep failure and aging.

The developed model was used in the analysis of slope stability and the above features were successfully modeled by predicting a retrogressive slope instability mechanism triggering failure in a saturated slope.

ΕΘΝΙΚΟ ΜΕΤΣΟΒΙΟ ΠΟΛΥΤΕΧΝΕΙΟ
ΣΧΟΛΗ ΠΟΛΙΤΙΚΩΝ ΜΗΧΑΝΙΚΩΝ
ΤΟΜΕΑΣ ΓΕΩΤΕΧΝΙΚΗΣ

Διδακτορική Διατριβή

Διερεύνηση της μη-γραμμικής συμπεριφοράς των εδαφικών υλικών με προσομοίωση του ερπυσμού

Αλέξανδρος Ν. Καλός

ΕΚΤΕΝΗΣ ΠΕΡΙΛΗΨΗ

I. Περιγραφή του προβλήματος

Η επιστήμη του Πολιτικού Μηχανικού είναι συνυφασμένη με την διερεύνηση και επίλυση σύνθετων προβλημάτων αδιάρρηκτα συνδεδεμένων με τις μηχανικές ιδιότητες και την παρελκόμενη συμπεριφορά του γεωυλικού. Η ανάπτυξη αριθμητικών μεθόδων και κωδίκων (numerical methods and codes), εν τάχει αναφέρουμε την μέθοδο των πεπερασμένων στοιχείων (Finite Element Method), την μέθοδο των πεπερασμένων διαφορών (Finite Difference Method) και την μέθοδο των συνοριακών στοιχείων (Boundary Element Method), έχει ως στόχο την επίλυση πολύπλοκων προβλημάτων. Η διερεύνηση και επίλυση τέτοιων σύνθετων προβλημάτων καθίσταται δυνατή στις ημέρες μας λόγω τις αυξανόμενης υπολογιστικής ισχύος των ηλεκτρονικών υπολογιστών.

Πρωταρχικό συστατικό στην προσομοίωση των αριθμητικών μεθόδων αποτελεί η καταστατική συμπεριφορά των γεωυλικών. Το καταστατικό προσομοίωμα αποτελεί την μαθηματική περιγραφή της μηχανικής συμπεριφοράς του γεωυλικού. Οι καταστατικές σχέσεις ελέγχουν την απόκριση του συστήματος σε κάθε μεταβολή του εξωτερικώς επιβαλλόμενου τασικού πεδίου. Το καταστατικό πλαίσιο μηχανικής συμπεριφοράς τείνει να εντοπίζει στην μακροσκοπική φυσική του προβλήματος παρά εξετάζει την αλληλεπίδραση μεταξύ των κόκκων (ή των πλακιδίων) του εδαφικού ιστού σε μικροσκοπικό επίπεδο.

Πληθώρα καταστατικών ελαστοπλαστικών προσομοιωμάτων έχουν προταθεί (π.χ. Kavvadas and Amorosi, 2000; Belokas and Kavvadas, 2010) στην βιβλιογραφία με

απώτερο σκοπό την περιγραφή της μηχανικής συμπεριφοράς των εδαφικών υλικών ανεξαρτήτως του ρυθμού παραμόρφωσης. Η εργαστηριακή διερεύνηση των εδαφικών υλικών φανερώνουν μια έντονα μη-γραμμική, ανισότροπη συμπεριφορά. Αρκετές φορές ενδέχεται να εμφανίσουν χαλάρωση ή ακόμα και κατάρρευση της δομής του εδαφικού ιστού. Η μηχανική συμπεριφορά των γεωυλικών διερευνήθηκε αρχικά σε εργαστηριακό επίπεδο σε αναμοχλευμένα εδαφικά υλικά (με ποσοστό υγρασίας κοντά στο όριο υδαρότητας). Επιπρόσθετα μηχανικά χαρακτηριστικά προτάθηκαν με σκοπό της βελτίωση της προβλεπόμενης συμπεριφοράς των καταστατικών προσομοιωμάτων, εντοπίζοντας τόσο στην περιγραφή της ανισοτροπίας όσο και στην έντονα ανελαστική συμπεριφορά κατά την διάρκεια ανακυκλικών φορτίσεων.

Αν και η μηχανική των αναζυμωμένων εδαφικών υλικών αποτελεί ορόσημο για την διατύπωση της Θεωρίας Κρίσιμης Κατάστασης (Critical State Theory, Schofield and Wroth, 1968) αδυνατεί να περιγράψει με σαφήνεια την μηχανική συμπεριφορά εδαφικών υλικών στην μορφή που αυτά αντιμετωπίζονται στην φύση (natural soils). Η θεμελιώδης διαφορά συνοψίζεται στην ύπαρξη της δέσης (bonding) που «διαχωρίζει» τα φυσικά από τα αναζυμωμένα υλικά. Η δέση δύναται να προκύψει από αποφόρτιση (stress induced structure), από αποσάθρωση επιφανειακών στρωμάτων, από γήρανση, από τσιμέντωση ή ανάπτυξη θιξοτροπικών δεσμών καθώς και από την δημιουργία δεσμών λόγω διαφαινόμενων χημικών ή βιολογικών διεργασιών επί του εδαφικού ιστού. Συνεπώς, είναι εμφανές ότι η δέση προσδίδει επιπρόσθετα χαρακτηριστικά επί της μηχανικής συμπεριφοράς των γεωυλικών ως αποτέλεσμα των φυσικών διεργασιών σχηματισμού αυτής. Με βάση την ύπαρξη ή απουσία δέσης τα εδαφικά υλικά κατατάσσονται σε δομημένα (structured) και μη-δομημένα (structureless). Πιο πρόσφατα καταστατικά πλαίσια (ελαστοπλαστικής) μηχανικής συμπεριφοράς επιχειρούν να ενσωματώσουν την δέση εντοπίζοντας στην φαινόμενη προφόρτιση (apparent preloading).

Η παρούσα διδακτορική διατριβή ξεκίνησε στο πλαίσιο μιας συντονισμένης προσπάθειας μεταχείρισης των μηχανικών χαρακτηριστικών των δομημένων υλικών με απώτερο σκοπό την προσομοίωση του μηχανισμού προοδευτικής αστοχίας (**Σχήμα 1**- θεωρήθηκε ότι η εκσκαφή του πόδα σε ένα αρχικά ήπιο πρανές θα οδηγούσε στην ενεργοποίηση του μηχανισμού προοδευτικής αστοχίας που θα αναδύετο από τον πόδα ανάστροφα προς την στέψη του πρανούς). Ωστόσο η

θεώρηση της ελαστοπλαστικής μηχανικής συμπεριφοράς με προσομοίωση της δέσης απεδείχθη ανεπαρκής. Η αστοχία φυσικών ή τεχνητών πρανών (ως αποτέλεσμα ανθρωπογενών παρεμβάσεων - **Σχήμα 2**) αποτελεί αντικείμενο διερεύνησης όσον αφορά τόσο την αστοχία καθεαυτή όσο και του ενεργοποιούμενου μηχανισμού. Παραδοσιακές θεωρήσεις οριακής ευστάθειας στηριζόμενες επί της μεθόδου των λωρίδων απαιτούν εξαρχής σημαντική γνώση του μηχανισμού αστοχίας. Από την άλλη μεριά, η εντοπισμένη συσσώρευση πλαστικών παραμορφώσεων και η επακόλουθη μόρφωση όλων των πιθανών μορφών διατμητικής αστοχίας όπως αυτές προβλέπονται από την θεωρία διακλάδωσης (bifurcation theory) δεν είναι δυνατόν να περιγραφούν σε πραγματική κλίμακα (ολόκληρου του πρανούς).

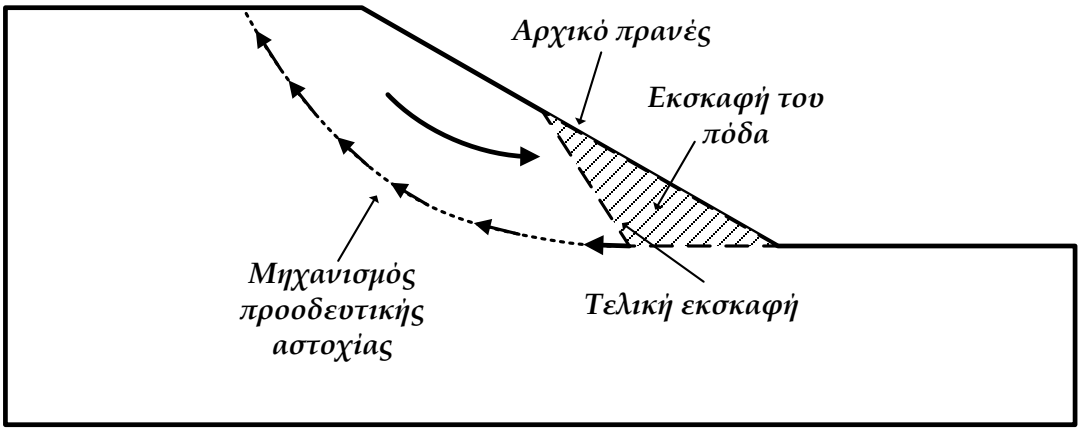

Σχήμα 1: Σχηματική απεικόνιση του μηχανισμού προοδευτικής αστοχίας.

Σχήμα 2: Καταστροφικές συνέπειες της αστοχίας πρανούς σε κατασκευές πολιτικού μηχανικού (California, 2011).

Οι αριθμητικές αναλύσεις επέδειξαν την σαφή αδυναμία του μηχανισμού αποδόμησης της δέσης να ενεργοποιήσει τον μηχανισμό προοδευτικής αστοχίας. Για τον λόγο αυτό επιπρόσθετα μηχανικά χαρακτηριστικά ενσωματώθηκαν στο καταστατικό πλαίσιο μηχανικής συμπεριφοράς. Η περιβάλλουσα αστοχίας συσχετίσθηκε με την συσσώρευση πλαστικών παραμορφώσεων με στόχο την πρόβλεψη σημαντικής χαλάρωσης ακόμα και σε περιπτώσεις που χαρακτηρίζονται από παντελή έλλειψη της δομής. Ωστόσο, τα επιπρόσθετα δομητικά χαρακτηριστικά (όπως διαφαίνονται από την αποδόμηση της περιβάλλουσας αστοχίας λόγω πλαστικών παραμορφώσεων, από τους βελτιωμένους μαθηματικούς νόμους αποδόμησης της δομής κ.α.) διαπιστώθηκε ότι αδυνατούν να οδηγήσουν σε διατμητική αστοχία (ενεργοποιώντας τον μηχανισμό προοδευτικούς αστοχίας στο πρανές).

Η εν λόγω ανεπάρκεια αποδόθηκε στην εγγενή αδυναμία των κλασσικών ελαστοπλαστικών προσομοιωμάτων για δομημένα γεωυλικά να ελέγξουν το μέγεθος των πλαστικών παραμορφώσεων, καθώς οι πλαστικές παραμορφώσεις επιβάλλονται από το φυσικό πρόβλημα. Συνεπώς, κρίθηκε αδύνατο να ενεργοποιηθούν ικανοποιητικά «μεγάλες» πλαστικές παραμορφώσεις για να προκαλέσουν αστοχία. Η θεώρηση της χρονικά εξαρτημένης μηχανικής συμπεριφοράς ωστόσο ενδέχεται να αποτελεί το κλειδί που θα ενεργοποιήσει τον μηχανισμό της προοδευτικής αστοχίας στο πρανές. Η συσσώρευση χρονικώς εξελισσόμενων ανελαστικών παραμορφώσεων, τόσο πλαστικών όσο και ερπυστικών, σε περιοχές έντονες μηχανικής καταπόνησης (κοντά στην αστοχία) φαντάζει ως ένας εναλλακτικός τρόπος ενεργοποίησης της αστοχίας. Κατά αυτόν τον τρόπο αναδεικνύεται η ανάγκη ενός νέου καταστατικού προσομοιώματος που θα χτίζει πάνω στο καλά θεμελιωμένο κατασκεύασμα της μηχανικής συμπεριφοράς των δομημένων γεωυλικών ενώ παράλληλα ενσωματώνει ένα πλήρες σύνολο χρονικά εξαρτημένων μηχανικών χαρακτηριστικών.

II. Σκοπός της διατριβής

Η ενσωμάτωση της ερπυστικής συνιστώσας, με συνεπακόλουθη συσχέτιση του ρυθμού παραμόρφωσης με την μηχανική απόκριση του γεωυλικού, αποτελεί την πεμπτουσία του προσομοιούμενου μηχανισμού που οδηγεί σε αστοχία. Συνεπώς, ο συνδυασμός της μηχανικής συμπεριφοράς των δομημένων εδαφικών υλικών με τα επιπλέον χρονικά εξαρτημένα ερπυστικά χαρακτηριστικά δύναται να προσομοιώσει

την προοδευτική αστοχία σε επίπεδο μηχανισμών . Ο λόγος έγκειται στο γεγονός ότι οι ερπυστικές παραμορφώσεις μπορούν να ελεγχθούν ανεξάρτητα (από τις ελαστικές και πλαστικές συνιστώσες) και να λάβουν μεγάλες τιμές οδηγώντας σε αστοχία. Σημειώνεται ότι ο μηχανισμός της προοδευτικής αστοχίας και συνεπώς τα ερπυστικά χαρακτηριστικά του προτεινόμενου προσομοιώματος δεν περιορίζονται μόνο στα πρανή αλλά μπορούν να τύχουν εφαρμογής σε πολλαπλά προβλήματα του γεωτεχνικού μηχανικού (π.χ. να εξετάσουν την αύξηση της πίεσης επί της τελικής επένδυσης σηράγγων).

Σκοπός της παρούσας διδακτορικής διατριβής αποτελεί η πρόταση ενός νέου καταστατικού προσομοιώματος που ενσωματώνει ένα σύνολο χρονικά εξαρτημένων μηχανικών χαρακτηριστικών σε ένα βελτιωμένο καταστατικό πλαίσιο για δομημένα γεωυλικά (περιλαμβάνοντας βελτιωμένους μηχανισμούς αποδόμησης της δέσης παράλληλα με την απομείωση της περιβάλλουσας αστοχίας τόσο λόγω πλαστικών όσο και ερπυστικών παραμορφώσεων). Το προσομοίωμα αξιολογείται μέσω αριθμητικών αναλύσεων σε πειράματα συμπιεσομέτρου προς διερεύνηση του μηχανισμού γήρανσης συνυφασμένου με την αύξηση της αντοχής (μέσω αύξησης της τάσης προστερεοποίησης) καθώς και σε πειράματα ερπυσμού σε τριαξονική καταπόνηση που ενεργοποιούν τον δευτερογενή ερπυσμό. Ωστόσο, το καταστατικό εξιδανικευμένο προσομοίωμα πρέπει να παρέχει την δυνατότητα πρόβλεψης του τριτογενούς ερπυστικού σταδίου που οδηγεί στην αστοχία σε πειράματα διατμητικής καταπόνησης (π.χ. τριαξονικής καταπόνησης, επίπεδης παραμόρφωσης, απευθείας διάτμησης). Η πρόβλεψη του μηχανισμού προοδευτικής αστοχίας απορρέει από αυτήν την ικανότητα του προσομοιώματος να ενεργοποιεί τον μηχανισμό αστοχίας με τον χρόνο.

Οι άξονες γύρω από τους οποίους εξελίσσεται η παρούσα διδακτορική διατριβή συνοψίζονται παρακάτω:

Άξονας 1: Κατάστρωση του χρονικώς εξαρτημένου καταστατικού πλαισίου μηχανικής συμπεριφοράς. Οι καταστατικές εξισώσεις ενσωματώνουν τις αρχές της θεωρίας της κρίσιμης κατάστασης εντός της θεωρίας υπερφόρτισης (overstress theory) του Perzyna (1962 & 1966). Το καταστατικό πλαίσιο ενσωματώνει πρόσθετα στοιχεία αποδόμησης της δομής (για θεωρούμενα δομημένα γεωυλικά) και

χαρακτηριστικά απομείωσης της περιβάλλουσας αστοχίας αποδιδόμενα στην ανάπτυξη και εξέλιξη των ανελαστικών παραμορφώσεων.

Άξονας 2: Αξιολόγηση του προτεινόμενου ιξωδοελαστοπλαστικού προσομοιώματος μέσω αριθμητικών αναλύσεων και έναντι εργαστηριακών δοκιμών. Το καταστατικό προσομοίωμα αξιολογείται μέσα από σωρεία αριθμητικών αναλύσεων. Οι καταστροφικές συνέπειες της διεκτροπικής ερπυστικής συνιστώσας επί της διατμητικής αντοχής εξετάζεται σε αριθμητικές αναλύσεις ερπυσμού τριαξονικής καταπόνησης, επίπεδης παραμόρφωσης και απευθείας διάτμησης υπό στραγγισμένες συνθήκες (η έννοια του ερπυσμού είναι συνυφασμένη με τις στραγγισμένες συνθήκες αναλογιζόμενοι την απαίτηση για σταθερές ενεργές τάσεις που αποτελεί και τον ορισμό του αμιγούς φαινομένου). Επιπλέον, αναλύσεις πραγματοποιούνται σε συνθήκες συμπιεσομέτρου προσομοιώνοντας τόσο συνθήκες ερπυσμού όσο και τασική χαλάρωση (stress relaxation). Το εξιδανικευμένο καταστατικό προσομοίωμα αξιολογείται έναντι πειραματικών δεδομένων, σε πειράματα ερπυσμού σε συμπιεσομέτρο εξετάζοντας την χρονικά εξαρτημένη μηχανική συμπεριφορά μαλακής αργίλου (τα μηχανικά χαρακτηριστικά της οποίας εμφανίζουν σημαντικές ομοιότητες με τύρφη) καθώς και σε πειράματα που ενεργοποιούν τον μηχανισμό προοδευτικής αστοχίας σε πειράματα ερπυσμού πολλαπλών σταδίων (multi-stage creep tests in the triaxial apparatus) τριαξονικής καταπόνησης σε κάρβουνο.

Άξονας 3: Εφαρμογή του προτεινόμενου ιξωδοελαστοπλαστικού προσομοιώματος στην ευστάθεια πρανών. Το προτεινόμενο εξιδανικευμένο καταστατικό προσομοίωμα χρησιμοποιείται σε αριθμητικές αναλύσεις ευστάθειας πρανών προβλέποντας την συνεχή συσσώρευση ανελαστικών παραμορφώσεων (πλαστικές και ερπυστικές) μέχρις ότου το πρανές αστοχήσει μέσω του μηχανισμού προοδευτικής αστοχίας.

III. Ερευνητική Μεθοδολογία

Η παρούσα διδακτορική διατριβή αποτελείται από δύο σκέλη. Στο πρώτο σκέλος (**Κεφάλαια 2** έως **4**) επιτελείται μια διεξοδική ερευνητική διερεύνηση της χρονικά εξαρτημένης μηχανικής συμπεριφοράς των μηχανικών πλαισίων συμπεριφοράς και των σοφιστευμένων καταστατικών προσομοιωμάτων που ενσωματώνουν στοιχεία ιξωδοπλαστικότητας. Επιπλέον, αναλύεται η κλασσική θεωρία της πλαστικότητας

των εδαφικών υλικών και συνοψίζονται οι βασικές αρχές της θεωρίας κρίσιμης κατάστασης. Ακολουθεί η πρωτότυπη συνεισφορά της διδακτορικής διατριβής στα **Κεφάλαια 5** έως **8** όπου διατυπώνονται οι καταστατικές εξισώσεις μηχανικής συμπεριφοράς με συνυπολογισμό του ρυθμού της παραμόρφωσης και η αξιολόγηση του εξιδανικευμένου προσομοιώματος, όπως αυτό προέκυψε, σε αριθμητικές αναλύσεις και έναντι εργαστηριακών δοκιμών. Τέλος, διερευνάται ο προοδευτικός μηχανισμός αστοχίας σε πρόβλημα ευστάθειας πρανών (**Κεφάλαιο 8**).

ΕΕ 1. Βιβλιογραφική ανασκόπηση

Πληθώρα ερπυστικών προσομοιωμάτων επιχειρούν να προσεγγίσουν τη χρονικά εξαρτημένη μηχανική συμπεριφορά των γεωυλικών. Στα πλαίσια της παρούσας διδακτορικής διατριβής επιχειρείται ο διαχωρισμός των προσομοιωμάτων στις ακόλουθες τρεις κατηγορίες:

- **Εμπειρικά προσομοιώματα**: Αποτελούν απλές εμπειρικές συσχετίσεις που προκύπτουν μέσω προσαρμογής της θεωρούμενης καμπύλης στα πειραματικά δεδομένα, όπως αυτά προκύπτουν από πειράματα ερπυσμού (creep tests), τασικής χαλάρωσης (stress relaxation tests) και πειράματα σταθερού ρυθμού παραμόρφωσης (constant strain rate tests). Οι εμπειρικές συσχετίσεις περιγράφονται από απλές αναλυτικές σχέσεις ή από διαφορικές εξισώσεις ολοκληρούμενες με τον χρόνο. Σημειώνεται ότι οι εμπειρικές συσχετίσεις δύνανται να προσομοιώσουν ικανοποιητικά τόσο την μορφή όσο και το μέγεθος των μηχανικών χαρακτηριστικών (π.χ. τάσεις, ερπυστικές παραμορφώσεις, τον ρυθμό των ερπυστικών παραμορφώσεων κ.α.). Ωστόσο, η εφαρμογή τους είναι περιορισμένη στις συγκεκριμένες συνοριακές συνθήκες φόρτισης και στήριξης για τις οποίες μορφώθηκαν. Οι εμπειρικές συσχετίσεις αυτής της κατηγορίας αποτελούν προσομοιώματα βάσης πάνω στα οποία στηρίζονται πολλά σοφιστευμένα ιξωδοπλαστικά προσομοιώματα στην βιβλιογραφία (όπως και το προτεινόμενο) και χρησιμοποιούνται ως επί των πλείστων για τη βαθμονόμηση αυτών. Οι εμπειρικές συσχετίσεις δύνανται να διαχωριστούν περαιτέρω σε πρωτογενείς (primary) (πχ. ημι-λογαριθμικός ερπυστικός νόμος και παρελκόμενη θεωρία του Bjerrum, 1967, προσομοίωμα Singh-Micthell, 1968, κ.α.) και δευτερογενείς (secondary)

εμπειρικές συσχετίσεις, με την διαφορά ότι οι δευτερεύουσες αποτελούν έναν συνδυασμό δύο ή παραπάνω πρωτογενών προσομοιωμάτων.

Εν τάχει θα αναφερθούμε στις βασικές αρχές του ημι-λογαριθμικού ερπυστικού νόμου και στο προσομοίωμα Singh-Mitchell (1968) που ενσωματώνονται στο προτεινόμενο καταστατικό πλαίσιο συμπεριφοράς. Ο ημι-λογαριθμικός ερπυστικός νόμος προέκυψε από παρατηρήσεις επί της δευτερογενούς συμπίεσης σε δοκίμια συμπιεσομέτρου υποβαλλόμενα σε ερπυσμό. Η χρονικά εξαρτημένη μηχανική συμπεριφορά αποτελεί τον συγκερασμό της ογκομετρικής με την διεκτροπική συνιστώσα. Πειραματικές καταγραφές του ερπυσμού σε συνθήκες συμπιεσομέτρου (**Σχήμα 3**) φανερώνουν την επίδραση της ογκομετρικής ερπυστικής συνιστώσας στην αντοχή μέσω της αύξησης της τάσης προστερεοποίησης. Ο δείκτης δευτερογενούς συμπίεσης C_{ae} (secondary compression index) ορίζεται ακολούθως:

$$C_{ae} = \frac{\Delta e}{\Delta \log(t)} \tag{1}$$

Όπου e ο δείκτης πόρων και t ο χρόνος. Ο δείκτης πόρων δύναται όπως αναδιατυπωθεί ως εξής:

$$e = e_i - C_{ae} \cdot \log\left(\frac{t}{t_0}\right) = e_i - \psi \cdot \ln\left(\frac{t}{t_0}\right) \mid t \geq t_0 \tag{2}$$

Όπου e_i ο αρχικός δείκτης πόρων, t_0 ο χρόνος αναφοράς και ψ ο ισοδύναμος δείκτης δευτερογενούς συμπίεσης στο επίπεδο e-ln$t$ (σημειώνεται ότι $\psi = C_{ae}/\ln 10$). Η επιλογή του χρόνου αναφοράς t_0 αποτελεί σημείο τριβής αρκετών ερευνητών (π.χ. Mesri and Choi, 1985; Bjerrum, 1967; Leroueil et al., 1985; Yin, 1999). Στην παρούσα διδακτορική εργασία θεωρήθηκε ότι ο χρόνος αναφοράς αποτελεί μια εγγενή παράμετρο του γεωυλικού. Συνεκτιμώντας το γεγονός ότι οι μηχανικές ιδιότητες αναφέρονται σε ένα νέο γεωυλικό χωρίς προηγούμενη ιστορία φόρτισης (καθώς αυτή έχει μετασχηματιστεί σε δομή μέσω της μεταβολής της τάσης προστερεοποίησης) ο χρόνος αναφοράς λαμβάνεται ίσος με την αρχή του χρόνου, δηλαδή 1Δt (χρόνος μηδέν δεν υφίσταται παρά μόνον μαθηματικά). Σημειώνεται ότι ο χρόνος αναφοράς t_0

και ο χρόνος που αντιστοιχεί στο τέλος της πρωτογενούς στερεοποίησης t_i συμπίπτουν.

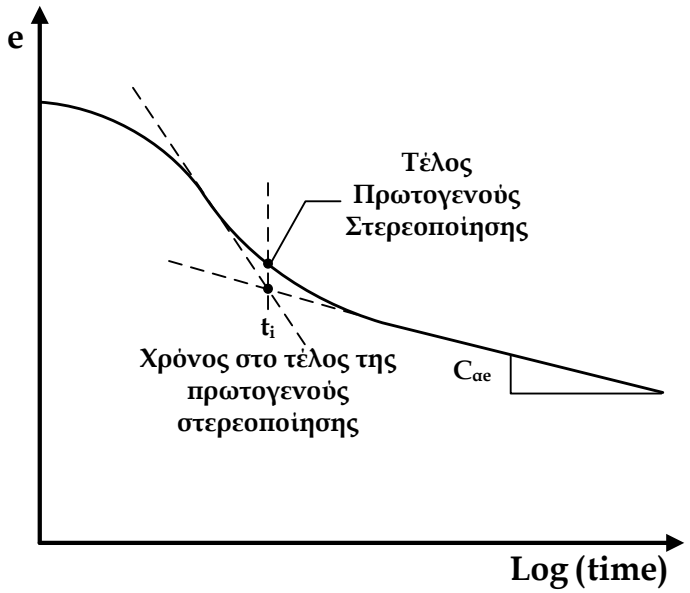

Σχήμα 3: Σχηματική απεικόνιση του δείκτη δευτερογενούς συμπίεσης C_{ae} σε πειράματα συμπιεσομέτρου (σε διάγραμμα του δείκτη πόρων *e* συναρτήσει του λογαρίθμου του χρόνου).

Σημειώνεται ότι ο Bjerrum (1967) εισήγαγε την θεωρία των «χρονικών» καμπύλων (time lines) με σκοπό της περιγραφή της τάσης προστερεοποίησης λόγω γήρανσης του γεωυλικού (**Σχήμα 4**).

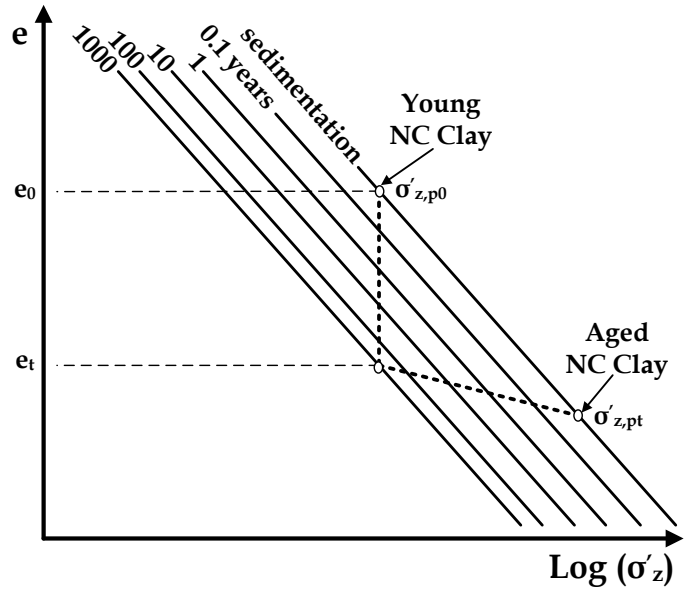

Σχήμα 4: Αύξηση της τάσης προστερεοποίησης λόγω γήρανσης του γεωυλικού (Bjerrum, 1967) (σε διάγραμμα του δείκτη πόρων συναρτήσει του λογαρίθμου της κατακόρυφης ενεργού τάσης).

Είναι εμφανές ότι η ογκομετρική ερπυστική συνιστώσα οδηγεί σε αύξηση της αντοχής μέσω της αύξησης της τάσης προστερεοποίησης. Η διεκτροπική συνιστώσα ωστόσο προβάλλει τα καταστροφικά της αποτελέσματα επί της αντοχής σε ερπυστικά πειράματα τριαξονικής καταπόνησης. Τα ερπυστικά στάδια (πρωτογενής, δευτερογενής και τριτογενής ερπυσμός) σε συνθήκες τριαξονικής καταπόνησης υπό θεώρηση πολλαπλών επιπέδων διατμητικής φόρτισης παρουσιάζονται στο **Σχήμα 5**.

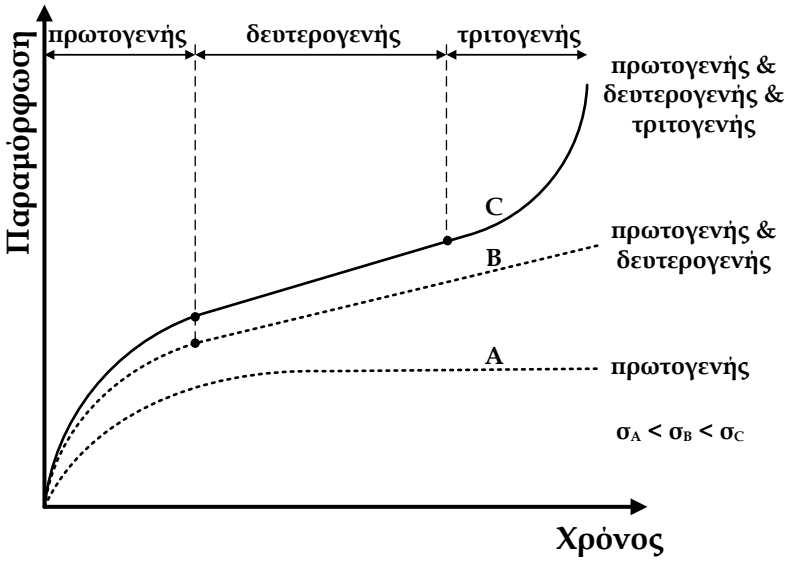

Σχήμα 5: Ερπυστικά στάδια σε πειράματα ερπυσμού υπό τριαξονική καταπόνηση θεωρώντας διαφορετικά επίπεδα φόρτισης.

Οι Singh και Michell (1968) στηριζόμενοι σε πειράματα ερπυσμού στην τριαξονική συσκευή υπό αστράγγιστες συνθήκες διατύπωσαν τον κάτωθεν ερπυστικό νόμο:

$$\dot{\varepsilon} = \frac{\partial \varepsilon}{\partial t} = A \cdot e^{\bar{a} \cdot D} \cdot \left(\frac{t_0}{t} \right)^m \tag{3}$$

Όπου A, m και $\bar{a}$ οι παράμετροι που βαθμονομούνται με βάση τις εργαστηριακές δοκιμές (απαιτούνται 2 πειράματα ερπυσμού σε διαφορετικά επίπεδα φόρτισης). Ο λόγος $D = q / q_{\mathrm{FAIL}}$ εκφράζει τον λόγο της διεκτροπικής τάσης προς την μέγιστη διατμητική τάση (στην αστοχία) στο ίδιο επίπεδο ισότροπης πίεσης. Σημειώνεται ότι η άνωθεν σχέση ισχύει για $0.1 \le D \le 0.6 \div 0.9$ και αναδιατυπώθηκε αργότερα για την καλύτερη προσομοίωση της ερπυστικής συμπεριφοράς για τιμές του λόγου $D < 0.1$:

$$\dot{\varepsilon} = \frac{\partial \varepsilon}{\partial t} = 2 \cdot A \cdot \sinh\left(\overline{a} \cdot D\right) \cdot \left(\frac{t_0}{t}\right)^m \tag{4}$$

Αξίζει να σημειωθεί ότι το καταστατικό ερπυστικό προσομοίωμα Singh-Mitchell επιχειρεί να προσομοιώσει επακριβώς μόνο τον δευτερογενή ερπυσμό σε πειράματα τριαξονικής καταπόνησης και όχι τον πρωτογενή κλάδο (ο τριτογενής ερπυσμός αδυνατεί να προσομοιωθεί από οποιοδήποτε εμπειρικό ή σοφιστευμένο καταστατικό προσομοίωμα).

- **Ρεολογικά Προσομοιώματα**: Τα καταστατικά προσομοιώματα αυτής της κατηγορίας επιχειρούν να προσεγγίσουν μονοαξονικές συνθήκες παραμόρφωσης. Αποτελούν συνήθως συνδυασμό απλών μηχανικών αναλόγων (ελατήρια, αποσβεστήρες, ολισθητήρες) συνδεδεμένα παράλληλα ή/και σε σειρά. Οι μηχανικές θεωρίες ερπυσμού (engineering theories of creep) αποτελούν μια άλλη μορφή ρεολογικών προσομοιωμάτων που επιτρέπει την εισαγωγή του καταστατικού προσομοιώματος υπό μορφή απλής αναλυτικής σχέσης (τυγχάνει εφαρμογής στο σκυρόδεμα και σε μέταλλα). Σημειώνεται ότι τα ρεολογικά προσομοιώματα δύνανται να προσομοιώσουν ικανοποιητικά τόσο την μορφή όσο και το μέγεθος των μηχανικών χαρακτηριστικών. Ωστόσο, η εφαρμογή τους είναι περιορισμένη στις συγκεκριμένες συνοριακές συνθήκες φόρτισης και στήριξης για τις οποίες μορφώθηκαν.
- **Γενικές Θεωρίες Ερπυσμού**: Αποτελούν 3Δ θεωρίες και είναι ο θεμελιώδης λίθος των χρονικά εξαρτημένων πλαισίων συμπεριφοράς. Η διατύπωσή τους στον εξαεδρικό χώρο των τάσεων δεν οριοθετεί κάποιο περιορισμό ως προς την χρήση τους σε μεμονωμένα προβλήματα. Οι βασικοί πυλώνες αποτελούνται από την θεωρία κρατυνόμενης επιφάνειας ροής (Non-Stationary Flow Surface, NSFS) και από την θεωρία υπερφόρτισης του Perzyna (1962 & 1966). Εν τάχει θα αναφερθούμε στην θεωρία υπερφόρτισης καθώς γίνεται χρήση αυτής στην διατύπωση του καταστατικού πλαισίου συμπεριφοράς.

  Η θεωρία υπερφόρτισης στηρίζεται στην θεώρηση ύπαρξης μιας «στατικής» επιφάνειας (static surface) στον γενικευμένο χώρο των τάσεων που διαχωρίζει την ιξωδοπλαστική από την αμιγώς ελαστική συμπεριφορά. Εντατικές καταστάσεις μέσα και επί της επιφάνειας εμφανίζουν ελαστική συμπεριφορά.

Σημειώνεται ότι η «στατική» επιφάνεια έχει την έννοια της περιβάλλουσας αναφοράς εφόσον είναι δυνατόν να κρατύνεται. Η εντατική κατάσταση δύναται να βρεθεί εκτός της «στατικής» επιφάνειας αναφοράς συσσωρεύοντας κατά αυτό τον τρόπο ιξωδοπλαστικές παραμορφώσεις ανάλογες με το μέγεθος της υπερφόρτισης F .

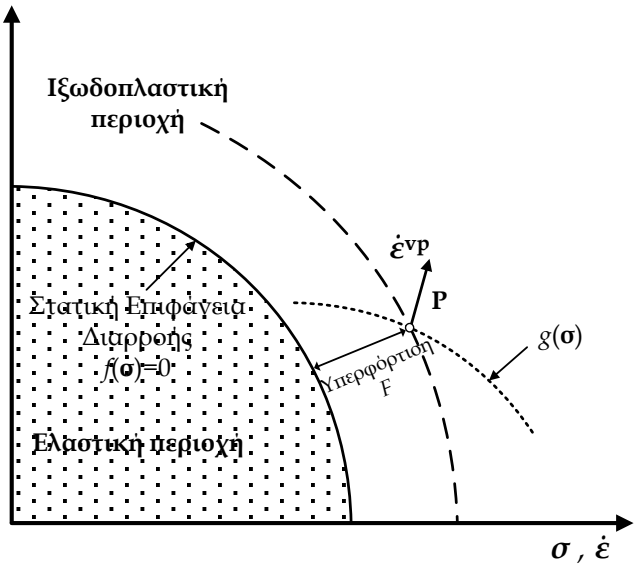

Σχήμα 6: Σχηματική απεικόνιση της θεωρίας υπερφόρτισης του Perzyna (1962 & 1966) (από Debernardi, 2008).

Σύμφωνα με την αρχική θεωρία του ερπυσμού όπως αυτή διατυπώθηκε από τον Perzyna ο τανυστής των παραμορφώσεων εκφράζεται συναρτήσει της ελαστικής και ιξωδοπλαστικής συνιστώσας για απειροστές μεταβολές του τασικού πεδίου ($\dot{\boldsymbol{\varepsilon}} = \dot{\boldsymbol{\varepsilon}}^{e} + \dot{\boldsymbol{\varepsilon}}^{vp}$). Η ιξωδοπλαστική συνιστώσα διατυπώνεται ακολούθως:

$$\dot{\boldsymbol{\varepsilon}}^{vp} = \gamma \cdot \Phi\left(F\right) \cdot \frac{\partial g}{\partial \boldsymbol{\sigma}} \tag{5}$$

Όπου γ η παράμετρος ρευστότητας (ελέγχεται από το ιξώδες), F η υπερφόρτιση, $\Phi\left(F\right)$ εκφράζει τον ιξώδη πυρήνα (viscous nucleus) και g η συνάρτηση του ιξωδοπλαστικού δυναμικού.

Σωρεία καταστατικών προσομοιωμάτων (π.χ. Adachi and Okano, 1974; Boidy, 2002; Debernardi, 2008; Yin et al., 2010) συναντώνται στην διεθνή βιβλιογραφία. Ωστόσο, το σύνολο των προαναφερθέντων προσομοιωμάτων εντοπίζουν ως επί των πλείστων στην προσομοίωση του δευτερογενούς

ερπυσμού ή ακόμα και του πρωτογενούς. Πιο σοφιστευμένα καταστατικά πλαίσια συμπεριφοράς ενσωματώνοντας επιπλέον στοιχεία ανισοτροπίας επιχειρούν να προσεγγίσουν την χρονικά εξαρτημένη συμπεριφορά των εδαφικών υλικών σε συνθήκες συμπιεσομέτρου και τριαξονικής καταπόνησης. Ωστόσο αμελούν εντελώς τον τριτογενή ερπυστικό κλάδο που οδηγεί σε αστοχία υπό συνθήκες έντονης διεκτροπικής καταπόνησης.

Κλείνοντας το κεφάλαιο της βιβλιογραφικής ανασκόπησης συνοψίζεται η κλασσική θεωρία της πλαστικότητας για απειροστές μεταβολές της φόρτισης. Οι βασικές αρχές της θεωρίας κρίσιμης κατάστασης (άπειρες διεκτροπικές παραμορφώσεις υπό σταθερή ισότροπη τάση σκιαγραφούν την κρίσιμη κατάσταση) συνοψίζονται ούτως ώστε να ενσωματωθούν στο προτεινόμενο εξιδανικευμένο ιξωδοελαστοπλαστικό προσομοίωμα. Βασιζόμενοι στην θεώρηση της δομής και ενθυμούμενοι ότι τα εδαφικά υλικά κατατάσσονται σε δομημένα (ύπαρξη δομής) και σε μη-δομημένα (παντελής έλλειψη δομής) γεωυλικά εισαγάγαμε την έννοια της περιβάλλουσας αντοχής δεσμών (structure strength envelope) και την επιφάνεια εγγενούς αντοχής (intrinsic strength envelope) για να υποδηλώσουμε τις οριακές επιφάνειες που περικλείουν όλες τις δομημένες και μη-δομημένες εντατικές καταστάσεις αντίστοιχα. Τέλος, η περιβάλλουσα πλαστικής διαρροής χρησιμοποιείται για την προσομοίωση της απειροστής ελαστικής περιοχής.

ΕΕ 2. Κατάστρωση του προτεινόμενου καταστατικού πλαισίου συμπεριφοράς

Το προτεινόμενο καταστατικό πλαίσιο συμπεριφοράς με εξάρτηση από τον ρυθμό της παραμόρφωσης θεμελιώνεται επί της κλασσικής θεωρίας της πλαστικότητας των εδαφικών υλικών ενώ παράλληλα ενσωματώνει τις θεμελιώδεις αρχές τις θεωρίας υπερφόρτισης (Perzyna, 1962 & 1966). Η καταστατική συμπεριφορά των δομημένων υλικών αποτελεί το μηχανικό πλαίσιο βάσης πάνω στο οποίο ενσωματώνεται ένα σύνολο χρονικά εξαρτημένων χαρακτηριστικών. Το εξιδανικευμένο προσομοίωμα χρησιμοποιεί τις περιβάλλουσες της αντοχής δομής (Structure Strength Envelope, *SSE*), της εγγενούς αντοχής (Intrinsic Strength Envelope) καθώς και την επιφάνεια πλαστικής διαρροής (Plastic Yield Envelope, *PYE*). Η γραφική απεικόνιση του προτεινόμενου εξιδανικευμένου ιξωδοελαστοπλαστικού προσομοιώματος διαφαίνεται στο **Σχήμα 7**. Η σχηματική απεικόνιση πραγματοποιείται στο

υπερεπίπεδο των τάσεων όπου, $\boldsymbol{\sigma}$ ο τανυστής των ενεργών τάσεων 2ας τάξεως, σ η ισότροπη ενεργός τάση και $\boldsymbol{s}$ ο διεκτροπικός τανυστής των τάσεων 2ας τάξεως:

$$\boldsymbol{\sigma} = \sigma \cdot \boldsymbol{I} + \boldsymbol{s} \tag{6}$$

$$\sigma(\equiv p) = \frac{1}{3}(\boldsymbol{\sigma} : \boldsymbol{I}) \tag{7}$$

$$\boldsymbol{s} = \boldsymbol{\sigma} - \sigma \cdot \boldsymbol{I} \tag{8}$$

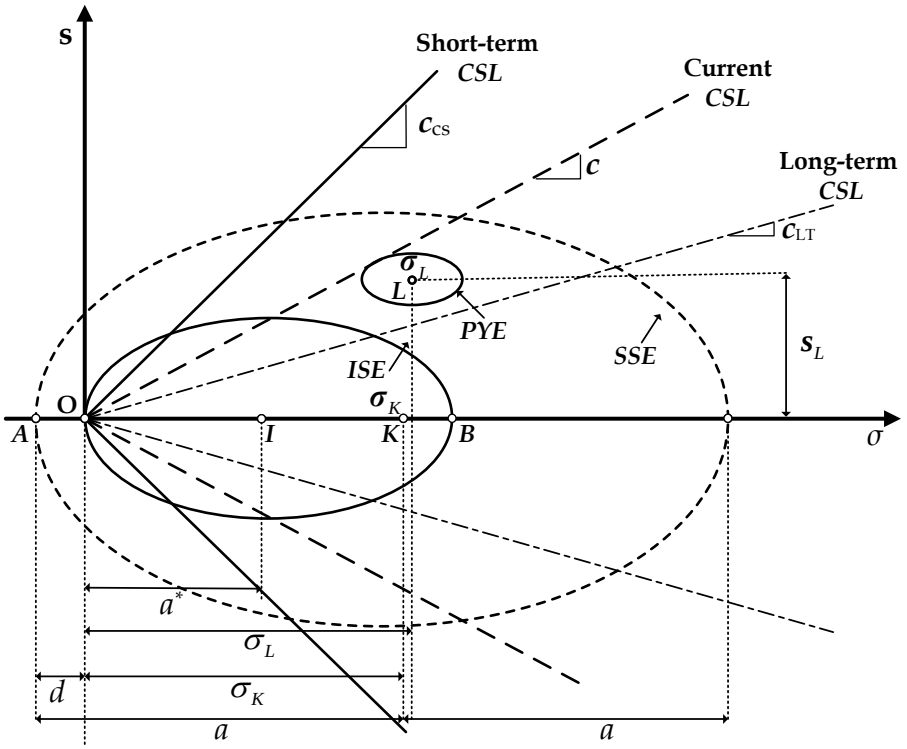

Σχήμα 7: Σχηματική απεικόνιση του προτεινόμενου καταστατικού προσομοιώματος.

Σημειώνεται ότι a είναι το μέγεθος του ημιάξονα της περιβάλλουσας αντοχής δομής, a^* εκφράζει το μέγεθος του ημιάξονα της περιβάλλουσας εγγενούς αντοχής, $\boldsymbol{\sigma}_K$ και $\boldsymbol{\sigma}_L$ εκφράζουν την μετατόπιση των κέντρων της περιβάλλουσας αντοχής δομής και της επιφάνειας πλαστικής διαρροής ως προς την αρχή των αξόνων. Σημειώνεται ότι η περιβάλλουσα αντοχής δομής μετατοπίζεται ορθότροπα (κατά d) επί του ισότροπου άξονα με απώτερο σκοπό την προσομοίωση των εφελκυστικών χαρακτηριστικών που προσδίδει στο δομημένο υλικό η έννοια της δομής. Είναι εμφανές ότι το παρών πλαίσιο καταστατικής συμπεριφοράς δεν προσομοιώνει χαρακτηριστικά πρωτογενούς ανισοτροπίας μιας που η περιβάλλουσα αντοχής

δομής είναι προσανατολισμένη επί του ισότροπου άξονα (χαρακτηριστικό ισότροπου δομημένου γεωυλικού). Τέλος, το σημαντικότερο στοιχείο του προτεινόμενου καταστατικού ιξωδοελαστοπλαστικού προσομοιώματος έγκειται στην απομείωση της περιβάλλουσας αστοχίας σε μια παραμένουσα κατάσταση. Στην περίπτωση που η χρονική εξέλιξη της περιβάλλουσας αστοχίας συσχετίζεται με την ερπυστική παραμόρφωση, η κλίση c (της προβολής της καμπύλης κρίσιμης κατάστασης στο υπερεπίπεδο των τάσεων) εξελίσσεται από την βραχυπρόθεσμη c_{CS} στην μακροπρόθεσμη κατάσταση c_{LT}. Στην υποθετική περίπτωση που η συσσώρευση των πλαστικών διεκτροπικών παραμορφώσεων χρησιμοποιηθεί ως ο κινητήριος μοχλός που ωθεί στην απομείωση της περιβάλλουσας αστοχίας τότε η βραχυπρόθεσμη c_{CS} και η μακροπρόθεσμη κλίση c_{LT} αντικαθίστανται από την αρχική c_{in} και τελική κατάσταση c_{fin} της περιβάλλουσας αστοχίας. Η απομείωση της περιβάλλουσας αστοχίας χρησιμοποιείται για την προσομοίωση σημαντικής χαλαρούμενης συμπεριφοράς ακόμα και σε περιπτώσεις μη δομημένων γεωυλικών.

Κατά όμοιο τρόπο ορίζονται ο τανυστής των παραμορφώσεων $\boldsymbol{\varepsilon}$, η ογκομετρική παραμόρφωση $\varepsilon = \varepsilon_v$ και ο διεκτροπικός τανυστής των παραμορφώσεων $\boldsymbol{e}$:

$$\boldsymbol{\varepsilon} = \frac{1}{3}\varepsilon \cdot \boldsymbol{I} + \boldsymbol{e} \tag{9}$$

$$\varepsilon = \boldsymbol{\varepsilon} : \boldsymbol{I} \tag{10}$$

$$\boldsymbol{e} = \boldsymbol{\varepsilon} - \frac{1}{3}\varepsilon \cdot \boldsymbol{I} \tag{11}$$

Σημειώνεται ότι η θεωρία πλαστικότητας των γεωυλικών χρησιμοποιεί τις απειροστές μεταβολές των τάσεων και των παραμορφώσεων.

Το καταστατικό προσομοίωμα ενσωματώνει την περιβάλλουσα εγγενούς αντοχής και την περιβάλλουσα αντοχής δομής οι συναρτήσεις διαρροής των οποίων ($F^* = 0$ και $F = 0$) δίδονται παρακάτω:

$$F^*\left(\boldsymbol{\sigma}, \alpha^*, c\right) = \frac{1}{c^2} \cdot \boldsymbol{s} : \boldsymbol{s} + \left(\sigma - a^*\right)^2 - \left(a^*\right)^2 = 0 \tag{12}$$

$$F\left(\boldsymbol{\sigma}, a, d, c\right) = \frac{1}{c^2} \cdot \boldsymbol{s} : \boldsymbol{s} + \left(\sigma - a + d\right)^2 - a^2 = 0 \tag{13}$$

Στις άνωθεν συναρτήσεις το εσωτερικό γινόμενο των τανυστών 2ας τάξεως συμβολίζεται ως ":". Το σύμβολο "*" (αστεράκι) χρησιμοποιείται για να δηλώσει τις εγγενείς καταστάσεις (συσχέτιση μόνο με τον δείκτη πόρων και το τασικό πεδίο και όχι από την ιστορία φόρτισης). Τέλος, η εξίσωση που περιγράφει την συνάρτηση διαρροής της περιβάλλουσας πλαστικής διαρροής ορίζεται παρακάτω:

$$f\left(\boldsymbol{\sigma},\boldsymbol{\sigma}_L,\alpha,c\right)=\frac{1}{c^2}\cdot\left(\boldsymbol{s}-\boldsymbol{s}_L\right):\left(\boldsymbol{s}-\boldsymbol{s}_L\right)+\left(\sigma-\sigma_L\right)^2-\left(\xi\cdot a\right)^2=0 \tag{14}$$

Ο λόγος ομοιότητας ξ εξαρτάται από το επιτρεπόμενο μέγεθος του παραμορφωσιακού βήματος (strain increments) που χρησιμοποιείται στην ανάλυση των πεπερασμένων στοιχείων. Εν γένει λαμβάνεται περί του 0.1%÷5%. Η περιβάλλουσα πλαστικής διαρροής διαχωρίζει την ιξωδοελαστική συμπεριφορά (για τασικές καταστάσεις εντός της επιφάνειας πλαστικής διαρροής) από την ιξωδοελαστοπλαστική μηχανική συμπεριφορά (για τασικές καταστάσεις επί της *PYE*). Για να διατυπώσουμε την παραπάνω πρόταση με μαθηματικού όρους, ο τανυστής των παραμορφώσεων δύναται να εκφραστεί ως εξής:

$$d\boldsymbol{\varepsilon}=d\boldsymbol{\varepsilon}^e+d\boldsymbol{\varepsilon}^p+d\boldsymbol{\varepsilon}^v \tag{15}$$

Οι εκθέτες *e*, *p* και *v* υποδηλώνουν την ελαστική, την πλαστική και την χρονικά εξαρτημένη συνιστώσα αντίστοιχα. Η άνωθεν σχέση εκφράζει την απειροστή μεταβολή της παραμόρφωσης συναρτήσει των ελαστικών, πλαστικών και ερπυστικών συνιστωσών αυτής. Καταστάσεις εντός της περιβάλλουσας πλαστικής διαρροής δεν ενεργοποιούν την συσσώρευση πλαστικών παραμορφώσεων. Σημειώνεται ότι η ελαστική συνιστώσα ελέγχεται από την ποροελαστικότητα.

Η ερπυστική συνιστώσα (η απειροστή μεταβολή αυτής $d\boldsymbol{\varepsilon}^v$) δίδεται παρακάτω ως συνάρτηση της ογκομετρικής (μέσω του δείκτη δευτερογενούς συμπίεσης σε πειράματα συμπιεσομέτρου) και της διατμητικής συνιστώσας (ελέγχεται από την θεώρηση της εμπειρικής συσχέτισης των Singh-Mitchell, 1968, προσομοιώνει τον δευτερογενή ερπυσμό σε πειράματα τριαξονικής καταπόνησης):

$$d\boldsymbol{\varepsilon}^v=\dot{\boldsymbol{\varepsilon}}^v\cdot dt=\left[\left(\frac{1}{3}\cdot\dot{\varepsilon}^v\right)\cdot\boldsymbol{I}+\frac{\sqrt{6}}{2}\cdot\dot{\varepsilon}_q^v\cdot\frac{\boldsymbol{s}_f}{\sqrt{\boldsymbol{s}_f:\boldsymbol{s}_f}}\right]\cdot dt \tag{16}$$

Όπου $\dot{\varepsilon}^{v}$ ο ρυθμός των ερπυστικών παραμορφώσεων (τανυστής 2ας τάξεως), $\dot{\varepsilon}^{v}$ ο ρυθμός συσσώρευσης της ογκομετρικής ερπυστικής συνιστώσας και $\dot{\varepsilon}_q^{v}$ το μέτρο του ρυθμού των διεκτροπικών ερπυστικών παραμορφώσεων. Σημειώνεται ότι ενώ η ογκομετρική ερπυστική παραμόρφωση είναι έκδηλη τόσο εντός της περιβάλλουσας πλαστικής διαρροής όσο και επί αυτής, η διεκτροπική ερπυστική συνιστώσα ενεργοποιείται μόνο όταν η τασική κατάσταση έγκειται επί της επιφάνειας διαρροής (για τον λόγο αυτό ο διεκτροπικός τανυστής 2ας τάξεως δηλώνεται ως $\boldsymbol{s}_f$ στην άνωθεν σχέση). Όσον αφορά τους ρυθμούς των ογκομετρικών και διεκτροπικών ερπυστικών παραμορφώσεων αυτοί υπολογίζονται ως παρακάτω:

$$\dot{\varepsilon}^{v} = \frac{\psi}{(1+e)\cdot t_0}\cdot \exp\left[-\frac{(1+e)}{\psi}\cdot \varepsilon^{v}\right] \mid t \geq t_0 \tag{17}$$

$$\dot{\varepsilon}_q^{v} = \frac{2\cdot A\cdot \sinh\left(\overline{a}\cdot D\right)}{\left[1+\frac{(1-m)}{2\cdot A\cdot \sinh\left(\overline{a}\cdot D\right)\cdot t_0}\cdot \varepsilon_q^{v}\right]^{\frac{m}{1-m}}} \mid t \geq t_0 \wedge (\boldsymbol{s}:\boldsymbol{s}) \neq 0 \wedge m \neq 1 \tag{18}$$

$$\dot{\varepsilon}_q^{v} = \frac{2\cdot A\cdot \sinh\left(\overline{a}\cdot D\right)}{\exp\left[\frac{1}{2\cdot A\cdot \sinh\left(\overline{a}\cdot D\right)\cdot t_0}\cdot \varepsilon_q^{v}\right]} \mid t \geq t_0 \wedge (\boldsymbol{s}:\boldsymbol{s}) \neq 0 \wedge m = 1 \tag{19}$$

Είναι εμφανές ότι οι παραπάνω εξισώσεις ενσωματώνουν τις συσσωρευμένες ογκομετρικές και διεκτροπικές ερπυστικές παραμορφώσεις για τον ορισμό του ρυθμού. Ο λόγος εντοπίζεται στο γεγονός ότι ο εδαφικός ιστός δεν δύναται να αντιληφθεί την έννοια του χρόνου παρά μόνο μέσα από την ανακατανομή των τάσεων και των παραμορφώσεων. Συνεπώς, οι άνωθεν εκφράσεις έχουν προκύψει με απλή απαλοιφή του χρόνου όπως φανερώνεται στο **Κεφάλαιο 5** (σημειώνεται ότι όλα τα μεγέθη έχουν ορισθεί). Ο εκθετικός συντελεστής του εμπειρικού προσομοιώματος Singh-Mitchell λαμβάνει τιμές μικρότερες τις μονάδας σύμφωνα με τους ερευνητές (1968). Σε διαφορετική περίπτωση είναι έκδηλος μόνο ο πρωτογενής ερπυσμός κάτι που αδυνατεί να προσεγγίσει το εμπειρικό προσομοίωμα (σημειώστε ότι το $(1-m)$ είναι στον παρονομαστή εντός ριζικού κάτι που δημιουργεί και αριθμητικό πρόβλημα σε περίπτωση που ο εκθετικός συντελεστής *m* λάβει τιμή μεγαλύτερη της μονάδας).

Ο επαυξητικά γραμμικός νόμος ροής (incrementally linear) ως προς τις μεταβολές της τάσης και της παραμόρφωσης δίδεται στον μετασχηματισμένο χώρο των τάσεων ως εξής:

$$d\boldsymbol{\varepsilon}^{p} = d\Lambda \cdot \boldsymbol{P} \tag{20}$$

Όπου $d\Lambda$ αποτελεί ένα βαθμωτό μέγεθος που εκφράζει το μέτρο των πλαστικών παραμορφώσεων και $\boldsymbol{P}$ είναι ο τανυστής πλαστικού δυναμικού που εκφράζει την διεύθυνση των πλαστικών παραμορφώσεων (και σε ένα βαθμό το μέτρο). Σημειώνεται ότι στην παρούσα μορφή του καταστατικού προσομοιώματος γίνεται η παραδοχή συσχετισμένου νόμου ροής όπου $\boldsymbol{Q} = \boldsymbol{P}$. Ο τανυστής $\boldsymbol{Q}$ ορίζεται ως η κλίση της επιφάνειας διαρροής ως προς την εντατική κατάσταση (και συνεπώς ο τανυστής έγκειται πάντα κάθετα ως προς την περιβάλλουσα πλαστικής διαρροής). Ο τανυστής $\boldsymbol{Q}$ ορίζεται ακολούθως:

$$\boldsymbol{Q} = \frac{1}{3} \cdot Q \cdot \boldsymbol{I} + \boldsymbol{Q}' \tag{21}$$

Όπου:

$$Q \equiv \boldsymbol{Q} : \boldsymbol{I} = \frac{\partial f}{\partial \sigma} = 2 \cdot \left(\sigma - \sigma_{L} \right) \tag{22}$$

$$\boldsymbol{Q}' \equiv \boldsymbol{Q} - \frac{1}{3} \cdot Q \cdot \boldsymbol{I} = \frac{\partial f}{\partial \boldsymbol{s}} = \frac{2}{c^{2}} \cdot \left(\boldsymbol{s} - \boldsymbol{s}_{L} \right) \tag{23}$$

Κατόπιν ορισμού του συσχετισμένου νόμου ροής, ακολουθούν οι προτεινόμενοι νόμοι κράτυνσης του καταστατικού πλαισίου μηχανικής συμπεριφοράς. Το μέγεθος του ημιάξονα της ελλειψοειδούς περιβάλλουσας αντοχής δεσμών a ελέγχεται από ένα νόμο ισότροπης κράτυνσης. Σημειώνεται ότι η μετάθεση της περιβάλλουσας αντοχής δεσμών κατά μήκος του ισότροπου άξονα με σκοπό την προσομοίωση εφελκυστικών αντοχών d, η δευτερογενής ανισοτροπία όπως αυτή ορίζεται από την τασική κατάσταση $\boldsymbol{\sigma}_{L}$ (του κέντρου της περιβάλλουσας πλαστικής διαρροής) καθώς και η κλίση c της περιβάλλουσας αστοχίας αποτελούν παραμέτρους κράτυνσης και ελέγχονται από κινηματικούς νόμους κράτυνσης.

Αναγνωρίζοντας ότι οι ισότροποι νόμοι αποδόμησης των Kavvadas και Amorosi (2000) και Belokas και Kavvadas (2010) αδυνατούν να οδηγήσουν αρκετά συχνά

στην ταύτιση της περιβάλλουσας αντοχής δομής με την περιβάλλουσα εγγενούς αντοχής, ο βελτιωμένος νόμος ισότροπης κράτυνσης εισαγάγει την έννοια της δομής μέσω του λόγου B:

$$a = B \cdot a^* \tag{24}$$

Ο λόγος B λαμβάνει τιμές από B_0 (αντιπροσωπεύοντας την αρχική τιμή) έως B_{res} (παραμένουσα δομή). Σημειώνεται ότι στην περίπτωση που βιολογικές ή χημικές διεργασίες έχουν μετασχηματίσει την μακροσκοπική συμπεριφορά του εδαφικού σκελετού μέσω της ανάπτυξης χημικών και θιξοτροπικών δεσμών η παραμένουσα αντοχή B_{res} λαμβάνει τιμές ελάχιστα μεγαλύτερες της μονάδας (στην περίπτωση που η τελική αποδομημένη κατάσταση μεταπίπτει στην εγγενή τότε το $B_{res} = 1$). Για την βελτίωση του νόμου αποδόμησης το μέγεθος a ορίσθηκε αρχικά συναρτήσει της ολικής πλαστικής ογκομετρικής ε^p και διεκτροπικής πλαστικής παραμόρφωσης ε_q^p ως εξής:

$$a = a^* \cdot \begin{Bmatrix} \left(B_0 - B_{res} + \zeta_v^p \cdot \left|\varepsilon^p\right| + \zeta_q^p \cdot \left|\varepsilon_q^p\right|\right) \cdot \exp\left[-\left(\eta_v^p \cdot \left|\varepsilon^p\right| + \eta_q^p \cdot \left|\varepsilon_q^p\right|\right)\right] \\ +B_{res} \end{Bmatrix} \tag{25}$$

Η άνωθεν σχέση στην προσαυξητική της μορφή διατυπώνεται παρακάτω:

$$da = \frac{\partial a}{\partial \boldsymbol{\varepsilon}^p} : d\boldsymbol{\varepsilon}^p + \frac{\partial a}{\partial t} \cdot dt \tag{26}$$

Όπου:

$$\frac{\partial a}{\partial \boldsymbol{\varepsilon}^p} : d\boldsymbol{\varepsilon}^p = \begin{Bmatrix} \dfrac{1+e}{\lambda - \kappa} \cdot a^* \cdot d\varepsilon^p \cdot \left(\mathrm{PART} \cdot \mathrm{EXPONENT} + B_{res}\right) \\ +a^* \cdot \left(\zeta_v^p \cdot \left|d\varepsilon^p\right| + \zeta_q^p \cdot \left|d\varepsilon_q^p\right|\right) \cdot \mathrm{EXPONENT} \\ -a^* \cdot \left(\mathrm{PART} \cdot \mathrm{EXPONENT}\right) \cdot \left(\eta_v^p \cdot \left|d\varepsilon^p\right| + \eta_q^p \cdot \left|d\varepsilon_q^p\right|\right) \end{Bmatrix} \tag{27}$$

$$\begin{aligned} \mathrm{PART} &= \left(B_0 - B_{res} + \zeta_v^p \cdot \left|\varepsilon^p\right| + \zeta_q^p \cdot \left|\varepsilon_q^p\right|\right) \\ \mathrm{EXPONENT} &= \exp\left[-\left(\eta_v^p \cdot \left|\varepsilon^p\right| + \eta_q^p \cdot \left|\varepsilon_q^p\right|\right)\right] \end{aligned} \tag{28}$$

$$\frac{\partial a}{\partial t}\cdot dt = \frac{\partial a^*}{\partial t}\cdot dt\cdot\left[\left(\text{PART}\cdot\text{EXPONENT}\right)+B_{res}\right] \tag{29}$$

$$\frac{\partial a^*}{\partial t}\cdot dt = -a^*\cdot\frac{1}{\lambda-\kappa}\cdot\frac{\partial e}{\partial t}\cdot dt = \frac{1+e}{\lambda-\kappa}\cdot a^*\cdot\dot{\varepsilon}^v\cdot dt = \frac{1+e}{\lambda-\kappa}\cdot a^*\cdot d\varepsilon^v \tag{30}$$

Στις άνωθεν εξισώσεις είναι εμφανές ότι ο ισότροπος νόμος κράτυνσης ενσωματώνει τις καταστατικές σταθερές η_v^p, η_q^p που ελέγχουν την αποδόμηση της δομής (και τις σταθερές ζ_v^p και ζ_q^p που ελέγχουν την πιο ήπια αποδόμηση της δομής ελέγχοντας την συναρμογή με την καμπύλη εγγενούς συμπίεσης στο επίπεδο v-lnσ που απεικονίζεται στο **Σχήμα 8** - οι σταθερές ζ_v^p και ζ_q^p επιλέγονται περί το 5-10% των αντίστοιχων σταθερών η_v^p και η_q^p). κ είναι η σταθερά της ποροελαστικότητας και λ ο δείκτης παρθενικής συμπίεσης ($\lambda = C_c/\ln 10$).

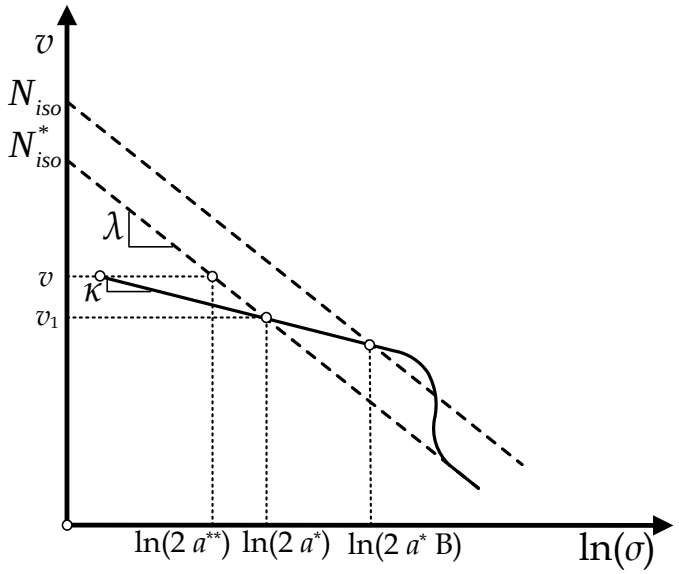

Σχήμα 8: Σχηματική απεικόνιση τασικής όδευσης στο επίπεδο v-lnσ (ειδικού όγκου συναρτήσει του φυσικού λογαρίθμου της ισότροπης τάσης).

Η εξίσωση (30) σκιαγραφεί την επιρροή της ογκομετρικής ερπυστικής συνιστώσας (ορίσθηκε μέσω της εξίσωσης (17)) στην αντοχή μέσω της αύξησης της τάσης προστερεοποίησης. Συνεπώς, το καταστατικό πλαίσιο μηχανικής συμπεριφοράς δύναται να προσομοιώσει τον μηχανισμό γήρανσης όπως αυτός διατυπώθηκε από τον Bjerrum (1967). Ο πλαστικός νόμος κράτυνσης h_a της παραμέτρου κράτυνσης a δίδεται παρακάτω:

$$h_a = \left\{ \begin{array}{l} \dfrac{1+e}{\lambda-\kappa}\cdot a^*\cdot P\cdot\left(\text{PART}\cdot\text{EXPONENT}+B_{res}\right) \\ +a^*\cdot\left(\zeta_v^p\cdot|P|+\zeta_q^p\cdot\sqrt{\dfrac{2}{3}\cdot\left(\boldsymbol{P}':\boldsymbol{P}'\right)}\right)\cdot\text{EXPONENT} \\ -a^*\cdot\left(\text{PART}\cdot\text{EXPONENT}\right)\cdot\left(\eta_v^p\cdot|P|+\eta_q^p\cdot\sqrt{\dfrac{2}{3}\cdot\left(\boldsymbol{P}':\boldsymbol{P}'\right)}\right) \end{array} \right\} \tag{31}$$

Η κλίση της περιβάλλουσας αντοχής c ενσωματώνεται στο καταστατικό πλαίσιο μηχανικής συμπεριφοράς ως παράμετρος κράτυνσης. Η μεταβολή αυτής dc συσχετίζεται με τις διεκτροπικές πλαστικές και ερπυστικές παραμορφώσεις ως παρακάτω:

$$dc = \frac{\partial c}{\partial \boldsymbol{\varepsilon}^p} : d\boldsymbol{\varepsilon}^p + \frac{\partial c}{\partial t}\cdot dt \tag{32}$$

Όπου:

$$\frac{\partial c}{\partial \boldsymbol{\varepsilon}^p} : d\boldsymbol{\varepsilon}^p = -\left(c-c_{LT}\right)\cdot\theta_q^p\cdot\left|d\varepsilon_q^p\right| \tag{33}$$

$$\frac{\partial c}{\partial t}\cdot dt = -\left(c-c_{LT}\right)\cdot a_1^v\cdot\left|d\varepsilon_q^v\right| = -\left(c-c_{LT}\right)\cdot a_1^v\cdot\left|\dot{\varepsilon}_q^v\right|\cdot dt \tag{34}$$

Οι σταθερές θ_q^p και a_1^v ελέγχουν τον ρυθμό απομείωσης της κλίσης c της περιβάλλουσας αστοχίας είτε στην παραμένουσα τιμή αυτής c_{fin} μέσω των πλαστικών διεκτροπικών παραμορφώσεων είτε στην μακροχρόνια τιμή c_{LT} μέσω των διατμητικών ερπυστικών παραμορφώσεων. Η σταθερά a_1^v σημειώνεται ότι αποτελεί τον ακρογωνιαίο λίθο του προτεινόμενου καταστατικού χρονικά εξαρτημένου πλαισίου συμπεριφοράς που οδηγεί σε «ερπυστική» αστοχία (μέσω την συσσώρευσης ανελαστικών παραμορφώσεων τόσο πλαστικών όσο και ερπυστικών). Η προοδευτική αστοχία των πρανών απορρέει από αυτήν ακριβώς την παράμετρο.

Ο πλαστικός νόμος κράτυνσης h_c της παραμέτρου κράτυνσης c υπολογίζεται ως παρακάτω:

$$h_c = \frac{\partial c}{\partial \boldsymbol{\varepsilon}^p} : d\boldsymbol{P} = -\left(c-c_{LT}\right)\cdot\theta_q^p\cdot\sqrt{\frac{2}{3}\cdot\left(\boldsymbol{P}':\boldsymbol{P}'\right)} \tag{35}$$

Η μετάθεση d της περιβάλλουσας αντοχής δομής σε εφελκυστικές τιμές της πίεσης κατά μήκος του ισότροπου άξονα αποτελεί μια επιπλέον παράμετρο κράτυνσης του εξιδανικευμένου ιξωδοελαστοπλαστικού προσομοιώματος. Η μετάθεση d μεταπίπτει σε μηδενικές τιμές με την αποδόμηση της δέσης λόγω συσσωρευόμενων διεκτροπικών ανελαστικών παραμορφώσεων (πλαστικών και ερπυστικών). Η μεταβολή $d(d)$ συσχετίζεται με τις διεκτροπικές πλαστικές και ερπυστικές παραμορφώσεις ως παρακάτω:

$$d(d) = \frac{\partial d}{\partial \boldsymbol{\varepsilon}^p} : d\boldsymbol{\varepsilon}^p + \frac{\partial d}{\partial t} \cdot dt \tag{36}$$

Όπου:

$$\frac{\partial d}{\partial \boldsymbol{\varepsilon}^p} : d\boldsymbol{\varepsilon}^p = -d \cdot \vartheta_q^p \cdot \left| d\varepsilon_q^p \right| \tag{37}$$

$$\frac{\partial d}{\partial t} \cdot dt = -d \cdot a_2^v \cdot \left| d\varepsilon_q^v \right| = -d \cdot a_2^v \cdot \left| \dot{\varepsilon}_q^v \right| \cdot dt \tag{38}$$

Οι σταθερές ϑ_q^p και a_2^v ελέγχουν τον ρυθμό απομείωσης της εφελκυστικής μετάθεσης d της περιβάλλουσας αντοχής δεσμών στο μηδέν μέσω των διεκτροπικών πλαστικών και ερπυστικών παραμορφώσεων αντίστοιχα.

Ο πλαστικός νόμος κράτυνσης h_d της μετάθεσης d υπολογίζεται ως εξής:

$$h_d = \frac{\partial d}{\partial \boldsymbol{\varepsilon}^p} : d\boldsymbol{P} = -d \cdot \vartheta_q^p \cdot \sqrt{\frac{2}{3} \cdot \left(\boldsymbol{P}' : \boldsymbol{P}' \right)} \tag{39}$$

Σημειώνεται ότι η δευτερογενής ανισοτροπία όπως αυτή προβάλλεται μέσα από την τασική κατάσταση του κέντρου της περιβάλλουσας πλαστικής διαρροής $\boldsymbol{\sigma}_L$ ακολουθεί έναν αντίστοιχο νόμο κινηματικής κράτυνσης όμοιο με των Kavvadas και Amorosi (2000).

Όσον αφορά το βαθμωτό μέγεθος $d\Lambda$ που εκφράζει το μέτρο των πλαστικών παραμορφώσεων, αυτό υπολογίζεται από την συνθήκη συμβατότητας για τασικές καταστάσεις επί της περιβάλλουσας αντοχής δομής. Η συνάρτηση παρακάτω αποτελεί την κατακλείδα των μαθηματικών υπολογισμών:

$$d\Lambda = \frac{\boldsymbol{Q} : \boldsymbol{C}^e : \left(d\boldsymbol{\varepsilon} - \dot{\boldsymbol{\varepsilon}}^v \cdot dt \right) + \xi \cdot \left(\frac{\partial F}{\partial a} \cdot \frac{\partial a}{\partial t} + \frac{\partial F}{\partial d} \cdot \frac{\partial d}{\partial t} + \frac{\partial F}{\partial c} \cdot \frac{\partial c}{\partial t} \right) \cdot dt}{H + \boldsymbol{Q} : \boldsymbol{C}^e : \boldsymbol{P}} \tag{40}$$

Η παραπάνω εξίσωση υπολογισμού του βαθμωτού μεγέθους $d\Lambda$ ενσωματώνει τον ελαστικό τανυστή 4ης τάξεως $\boldsymbol{C}^e$ και το πλαστικό μέτρο κράτυνσης H.

Για εντατικές καταστάσεις επί της περιβάλλουσας αντοχής δομής η μαθηματική διατύπωση του πλαστικού μέτρου κράτυνσης κρίνεται απλή και αποδίδεται παρακάτω:

$$H = H_0 = -\xi \cdot \left(\frac{\partial F}{\partial a} \cdot h_a + \frac{\partial F}{\partial d} \cdot h_d + \frac{\partial F}{\partial c} \cdot h_c \right) \tag{41}$$

Οι παράγωγοι της συνάρτησης αντοχής δομής ως προς τις παραμέτρους κράτυνσης υπολογίζονται από τις κάτωθεν σχέσεις:

$$\frac{\partial F}{\partial a} = -2 \cdot \left(\sigma - d \right) \tag{42}$$

$$\frac{\partial F}{\partial d} = 2 \cdot \left(\sigma - a + d \right) \tag{43}$$

$$\frac{\partial F}{\partial c} = -\frac{2}{c} \cdot \left[\frac{1}{c^2} \cdot \left(\boldsymbol{s} : \boldsymbol{s} \right) \right] \tag{44}$$

Για τον υπολογισμό ωστόσο του βαθμωτού μεγέθους $d\Lambda$ σε τασικές καταστάσεις επί της επιφάνειας πλαστικής διαρροής αλλά εντός της περιβάλλουσας αντοχής δομής είναι απαραίτητη η θεώρηση ενός συζυγούς σημείου και η διατύπωση ενός νόμου παρεμβολής (interpolation rule). Η γραφική απεικόνιση της θεώρησης του συζυγούς σημείου *M'* απαντάται στο **Σχήμα 9**. Το συζυγές σημείο υπολογίζεται ως παρακάτω:

$$\boldsymbol{\sigma}_{M'} = \left(a - d \right) \cdot \boldsymbol{I} + \frac{1}{\xi} \cdot \left(\boldsymbol{\sigma} - \boldsymbol{\sigma}_L \right) \tag{45}$$

Ακολουθεί η διατύπωση του νόμου παρεμβολής:

$$H = H_{M'} + \left(\boldsymbol{Q} : \boldsymbol{C}^e : \boldsymbol{P} \right) \cdot \lambda^* \cdot \left[\frac{\frac{1}{c^2} \cdot \left(\boldsymbol{s}_{M'} - \boldsymbol{s} \right) : \left(\boldsymbol{s}_{M'} - \boldsymbol{s} \right) + \left(\sigma_{M'} - \sigma \right)^2}{\frac{1}{c^2} \cdot \left(\boldsymbol{s} - \boldsymbol{s}_0 \right) : \left(\boldsymbol{s} - \boldsymbol{s}_0 \right) + \left(\sigma - \sigma_0 \right)^2} \right]^{\gamma} \tag{46}$$

Η άνωθεν διατύπωση του νόμου παρεμβολής για το πλαστικό μέτρο κράτυνσης ενσωματώνει τα ελλειψοειδή χαρακτηριστικά της περιβάλλουσας εγγενούς αντοχής (και συνεπώς και της αντοχής δομής εφόσον εμφανίζουν παρόμοιο σχήμα). Η τασική κατάσταση $\boldsymbol{\sigma}_0$ συνιστά το τασικό πεδίο την πρώτη στιγμή που συναντάται η πλαστική κατάσταση. Το πλαστικό μέτρο κράτυνσης $H_{M'}$ υπολογίζεται από την σχέση (41) για την τασική κατάσταση όπως αυτή προβλέπεται από την εξίσωση (45). Οι σταθερές λ^* και γ ελέγχουν τον ρυθμό μεταβολής του πλαστικού μέτρου κράτυνσης από $H \to \infty$ (όταν η τασική κατάσταση εισέρχεται για πρώτη φορά στην πλαστική περιοχή) σε $H = H_{M'}$ την στιγμή που η εντατική κατάσταση εντοπίζεται επί της περιβάλλουσας αντοχής δομής.

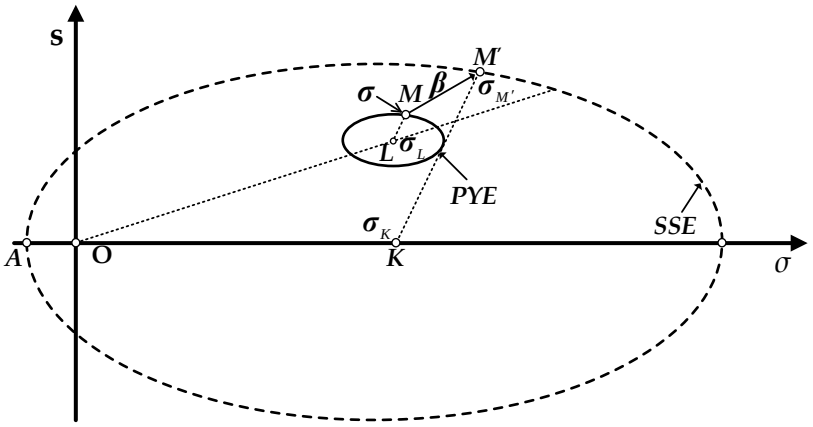

Σχήμα 9: Σχηματική απεικόνιση του συζυγούς σημείου *M′*.

Συνεπώς, το βαθμωτό μέγεθος $d\Lambda$ για τασικές καταστάσεις εντός της επιφάνειας πλαστικής διαρροής και εντός της περιβάλλουσας αντοχής δομής υπολογίζεται ως:

$$d\Lambda = \frac{\boldsymbol{Q} : \boldsymbol{C}^e : \left(d\boldsymbol{\varepsilon} - \dot{\boldsymbol{\varepsilon}}^v \cdot dt \right) + \xi \cdot \left(\frac{\partial F}{\partial a} \cdot \frac{\partial a}{\partial t} + \frac{\partial F}{\partial d} \cdot \frac{\partial d}{\partial t} + \frac{\partial F}{\partial c} \cdot \frac{\partial c}{\partial t} \right) \cdot dt}{H_{M'} + \boldsymbol{Q} : \boldsymbol{C}^e : \boldsymbol{P} \cdot \left\{ 1 + \lambda^* \cdot \left[\frac{\frac{1}{c^2} \cdot \left(\boldsymbol{s}_{M'} - \boldsymbol{s} \right) : \left(\boldsymbol{s}_{M'} - \boldsymbol{s} \right) + \left(\sigma_{M'} - \sigma \right)^2}{\frac{1}{c^2} \cdot \left(\boldsymbol{s} - \boldsymbol{s}_0 \right) : \left(\boldsymbol{s} - \boldsymbol{s}_0 \right) + \left(\sigma - \sigma_0 \right)^2} \right]^{\gamma} \right\}} \tag{47}$$

Η διατύπωση του πλαστικού μέτρου κράτυνσης και του συνεπαγόμενου βαθμωτού μεγέθους $d\Lambda$ αποτελεί σαφή βελτίωση της ελαστοπλαστικής μηχανικής συμπεριφοράς των προσομοιωμάτων Kavvadas και Amorosi (2000) και Belokas και Kavvadas (2010) για έντονα προφορτισμένες τασικές καταστάσεις.

Είναι εμφανές ότι το προτεινόμενο καταστατικό προσομοίωμα θεμελιώνεται πάνω στο μηχανικό πλαίσιο των δομημένων υλικών (και το βελτιώνει) ενώ εισαγάγει επιπλέον δομητικά (π.χ. την απομείωση της περιβάλλουσας αντοχής δομής και της μετάθεσης με την πλαστική παραμόρφωση) και ερπυστικά χαρακτηριστικά.

ΕΕ 3. Αξιολόγηση του προσομοιώματος σε αριθμητικές αναλύσεις

Κατόπιν ολοκλήρωσης της μαθηματικής διατύπωσης του καταστατικού πλαισίου συμπεριφοράς το προτεινόμενο ιξωδοελαστοπλαστικό προσομοίωμα αξιολογείται σε αριθμητικές αναλύσεις υλικού σημείου και σε επίπεδο πεπερασμένων στοιχείων (μέσω εξωτερικής υπορουτίνας UMAT στον κώδικα πεπερασμένων στοιχείων SIMULIA ABAQUS).

Αρχικά εξετάζονται τα ελαστοπλαστικά μηχανικά χαρακτηριστικά του προσομοιώματος. Η αποδόμηση της δομής και η απομείωση της κλίσης c και της εφελκυστικής μετάθεσης d βοηθούν στην πρόβλεψη σημαντικής χαλαρούμενης συμπεριφοράς ακόμα και σε καταστάσεις που χαρακτηρίζονται από παντελή έλλειψη δομής. Επιπλέον, διερευνάται η δυνατότητα ελέγχου της αρχικής (ελαστικής) στιβαρότητας τόσο μέσω του λόγου $2\cdot\left(G/K\right)^{e}$ (που δύναται να συσχετισθεί με τον λόγο του Poisson) όσο και μέσω της σταθεράς της ποροελαστικότητας κ. Η προσομοίωση υποδεικνύει τις αυξημένες δυνατότητες του εξιδανικευμένου προσομοιώματος να ελέγξει και να διαμορφώσει το αρχικό μέτρο στιβαρότητας. Τέλος, διερευνήθηκε η επιρροή των παραμέτρων λ^{*} και γ στην εξέλιξη του πλαστικού μέτρου κράτυνσης μέσω του ελέγχου της στιβαρότητας όταν η εντατική κατάσταση έγκειται επί της επιφάνειας πλαστικής διαρροής. Οι παράμετροι λ^{*} και γ κρίθηκε ότι εμφανίζουν οιονεί αντικρουόμενη συμπεριφορά (αύξηση του λ^{*} και ταυτόχρονη μείωση - όχι ισόποση – του γ οδηγεί σε ακριβώς ίδια μηχανική συμπεριφορά) και συνεπώς προτάθηκε η λήψη του εκθετικού συντελεστή $\gamma=1$ και η βαθμονόμηση μόνο μίας παραμέτρου λ^{*} που εμφανίζει σαφή πλεονεκτήματα.

Αν και το καταστατικό προσομοίωμα παρουσιάζει αρκετές βελτιώσεις έναντι παλαιότερων ελαστοπλαστικών εξιδανικευμένων ομοιωμάτων (π.χ. Kavvadas και Amorosi, 2000; Belokas και Kavvadas, 2010) κρίνεται ότι η βασική συνεισφορά της παρούσας διδακτορικής διατριβής συνοψίζεται στην ενσωμάτωση των ερπυστικών μηχανικών ιδιοτήτων που επιτρέπουν την πρόβλεψη της ερπυστικής αστοχίας. Για

τον λόγο αυτό στην παρούσα εκτενή περίληψη επιλέχθηκε να εντοπιστεί η έρευνα επί αυτού του αντικειμένου. Σε περίπτωση ωστόσο που ο αναγνώστης επιθυμεί να αναγνωρίσει τις ελαστοπλαστικές δυνατότητες του καταστατικού προσομοιώματος καλείται να εισχωρήσει εντός του κυρίου κειμένου.

Ακολούθως διερευνάται η χρονικά εξαρτημένη μηχανική συμπεριφορά όπως αυτή προβλέπεται από το προτεινόμενο εξιδανικευμένο προσομοίωμα. Αξίζει να σημειωθεί ότι η όλη χρονικά συνυφασμένη συμπεριφορά αποτελεί μια συνεχή αντίφαση. Από την μια μεριά ο ογκομετρικός ερπυσμός οδηγεί σε γήρανση με αποτέλεσμα την αύξηση της αντοχής, που απορρέει από την αύξηση της τάσης προστερεοποίησης, ενώ από την άλλη ο διεκτροπικός ερπυσμός οδηγεί σε ερπυστική αστοχία με την απομείωση της κλίσης της περιβάλλουσας αστοχίας μέσω της συσσώρευσης των ανελαστικών παραμορφώσεων. Ο μηχανισμός που υπερτερεί σε κάθε πειραματική δοκιμή καθορίζει και την προβλεπόμενη μηχανική συμπεριφορά.

Παρακάτω εξετάζουμε την μηχανική συμπεριφορά ενός δοκιμίου οι καταστατικές σταθερές προσομοίωσης του οποίου συνοψίζονται στον **Πίνακα 6.18**. Είναι σημαντικό να σημειωθεί ότι επιλέχθηκε να εξετασθεί η χρονικά εξαρτημένη μηχανική συμπεριφορά ελαφρώς υπερστερεοποιημένων γεωυλικών (με OCR<2). Ο λόγος εντοπίζεται στο γεγονός ότι δοκίμια με μεγαλύτερο βαθμό υπερστερεοποίησης εμφανίζουν έντονη πλαστική χαλάρωση και συνεπώς δεν είναι δυνατόν να αποσαφηνιστεί η επίδραση αποκλειστικά και μόνο του μηχανισμού που οδηγεί σε ερπυστική αστοχία.

Δοκίμιο μη-δομημένης αργίλου με δείκτη προφόρτισης OCR=1,25 ($C_c = 0,2$ και $C_r = 0,02$) στερεοποιημένο υπό ισότροπο τασικό πεδίο 80kPa υποβάλλεται σε τριαξονική καταπόνηση (το αρχικό βήμα διαρκεί 1 ημέρα) (η αρχική στερεοποίηση αντιπροσωπεύεται από το σημείο Α). Κατόπιν το δοκίμιο φορτίζεται αξονικά μέχρις ότου η συνολική ενεργή κατακόρυφη τάση αυξηθεί στα 180kPa (από τα 80kPa). Η φόρτιση διαρκεί 0,05 ημέρες έτσι ώστε τα ερπυστικά φαινόμενα κατά την διάρκεια αυτού του βήματος να είναι αμελητέα (το τέλος της φόρτισης αντιπροσωπεύεται από το σημείο Β). Κατόπιν το τασικό πεδίο διατηρήθηκε σταθερό και το δοκίμιο αφέθηκε να έρπει μέχρι την αστοχία (σημείο C). Το **Σχήμα 10** παρουσιάζει την προσομοιούμενη χρονικά εξαρτημένη μηχανική συμπεριφορά του δοκιμίου υποβαλλόμενου σε τριαξονική ερπυστική καταπόνηση για διάφορες τιμές της

σταθεράς a_1^v. Είναι εμφανές ότι η ανάλυση για $a_1^v = 1$ δεν προβλέπει ερπυστική αστοχία εντός του χρονικού πλαισίου των 100 ημερών. Ο λόγος συνοψίζεται στο γεγονός ότι η κλίση της περιβάλλουσας αστοχίας μεταπίπτει στην μακροχρόνια τιμή της με πολύ αργούς ρυθμούς και συνεπώς απαιτείται πολύ περισσότερος χρόνος για να επέλθει η αστοχία.

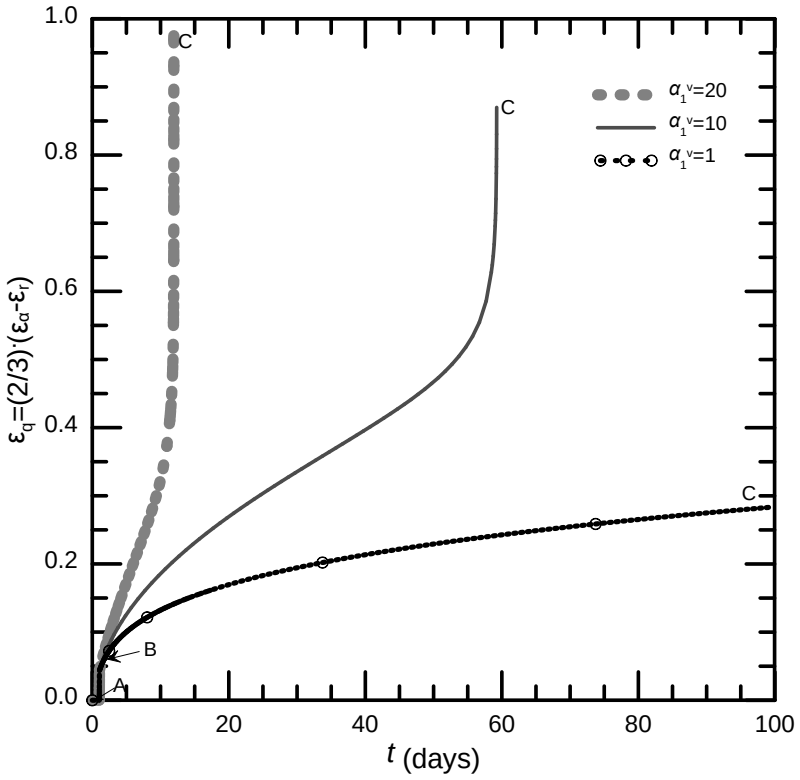

Σχήμα 10: Ερπυστική αστοχία μέσω της απομείωσης της περιβάλλουσας αστοχίας λόγω ερπυστικών παραμορφώσεων σε μη-δομημένο ελαφρώς υπερστερεοποιημένο δοκίμιο υποβαλλόμενο σε ερπυστική τριαξονική καταπόνηση (διατμητική παραμόρφωση ε_q συναρτήσει του χρόνου t σε ημέρες).

Η ερπυστική αστοχία διερευνήθηκε επιπλέον σε αριθμητικές αναλύσεις προσομοίωσης δοκιμής επίπεδης παραμόρφωσης και απευθείας διάτμησης. Στην δοκιμή επίπεδης παραμόρφωσης το ίδιο θεωρούμενο δοκίμιο (στερεοποιημένο σε ισότροπο τασικό πεδίο 80kPa – σημείο A) υποβλήθηκε σε κατακόρυφη συμπίεση μέχρις ότου η κατακόρυφη ενεργή τάση ανέλθει από τα 80kPa στα 355kPa (η επιφόρτιση επιλέχθηκε καταλλήλως ώστε να μεταθέτει την εντατική κατάσταση ανάμεσα στην βραχυχρόνια και την μακροχρόνια περιβάλλουσα αστοχίας). Η διάρκεια της φόρτισης (σημείο B) επιλέχθηκε ίση με 0,05 ημέρες αποσκοπώντας στην αμελητέα συσσώρευση ερπυστικών παραμορφώσεων στο παρόν βήμα. Κατόπιν το

εξωτερικώς επιβαλλόμενο τασικό πεδίο διατηρήθηκε σταθερό και το θεωρούμενο δοκίμιο αφέθηκε να έρπει έως την αστοχία (σημείο C). Το **Σχήμα 11** παρουσιάζει την προσομοιούμενη χρονικά εξαρτημένη μηχανική συμπεριφορά του δοκιμίου υποβαλλόμενο σε ερπυστική καταπόνηση επίπεδης παραμόρφωσης για διάφορες τιμές της σταθεράς a_1^v. Είναι εμφανές ότι η αριθμητική ανάλυση για $a_1^v = 5$ δεν προβλέπει ερπυστική αστοχία εντός του χρονικού πλαισίου των 160 ημερών.

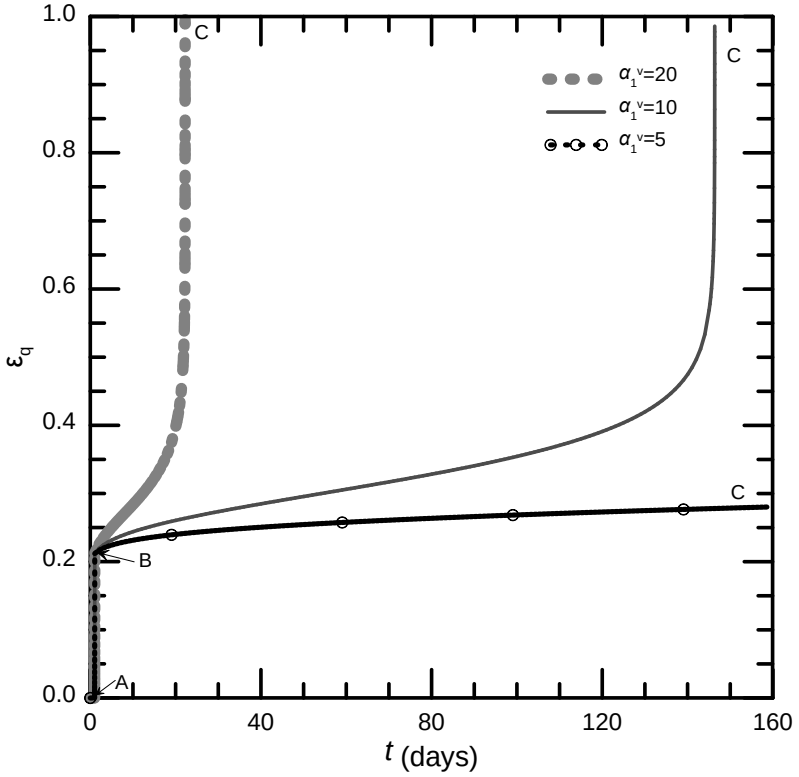

Σχήμα 11: Ερπυστική αστοχία μέσω της απομείωσης της περιβάλλουσας αστοχίας λόγω ερπυστικών παραμορφώσεων σε μη-δομημένο ελαφρώς υπερστερεοποιημένο δοκίμιο υποβαλλόμενο σε ερπυστική δοκιμή επίπεδης παραμόρφωσης (διατμητική παραμόρφωση $\boldsymbol{\varepsilon}_q$ συναρτήσει του χρόνου t σε ημέρες).

Το εξιδανικευμένο ιξωδοελαστοπλαστικό προσομοίωμα εξετάσθηκε επιπλέον ως προς την δυνατότητα πρόβλεψης της ερπυστικής αστοχίας σε δοκιμή απευθείας διάτμησης. Αν και η πειραματική δοκιμή αυτή εκ πρώτης όψεως δεν φαντάζει ως η πλέον κατάλληλη για την διερεύνηση της ερπυστικής αστοχίας, ενεργοποιεί ωστόσο ακριβώς τους ίδιους μηχανισμούς που θα διερευνηθούν αργότερα στην ευστάθεια πρανών και θα οδηγήσουν στην προσομοίωση του μηχανισμού προοδευτικής αστοχίας. Στην δοκιμή απευθείας διάτμησης το ίδιο θεωρούμενο δοκίμιο (στερεοποιημένο σε ισότροπο τασικό πεδίο 80kPa – σημείο A) υποβλήθηκε σε διάτμηση 26kPa στην ελεύθερη άνωθεν επιφάνεια (η κατάντι επιφάνεια έχει

προσομοιωθεί δεσμευμένη ως προς τις μετακινήσεις). Η επιφόρτιση επιλέχθηκε καταλλήλως ώστε να μεταθέτει την εντατική κατάσταση ανάμεσα στην βραχυχρόνια και την μακροχρόνια περιβάλλουσα αστοχίας. Η διάρκεια της φόρτισης (σημείο B) επιλέχθηκε ίση με 0,05 ημέρες αποσκοπώντας στην αμελητέα συσσώρευση ερπυστικών παραμορφώσεων στο παρόν βήμα. Κατόπιν το εξωτερικώς επιβαλλόμενο τασικό πεδίο διατηρήθηκε σταθερό και το θεωρούμενο δοκίμιο αφέθηκε να έρπει έως την αστοχία (σημείο C).

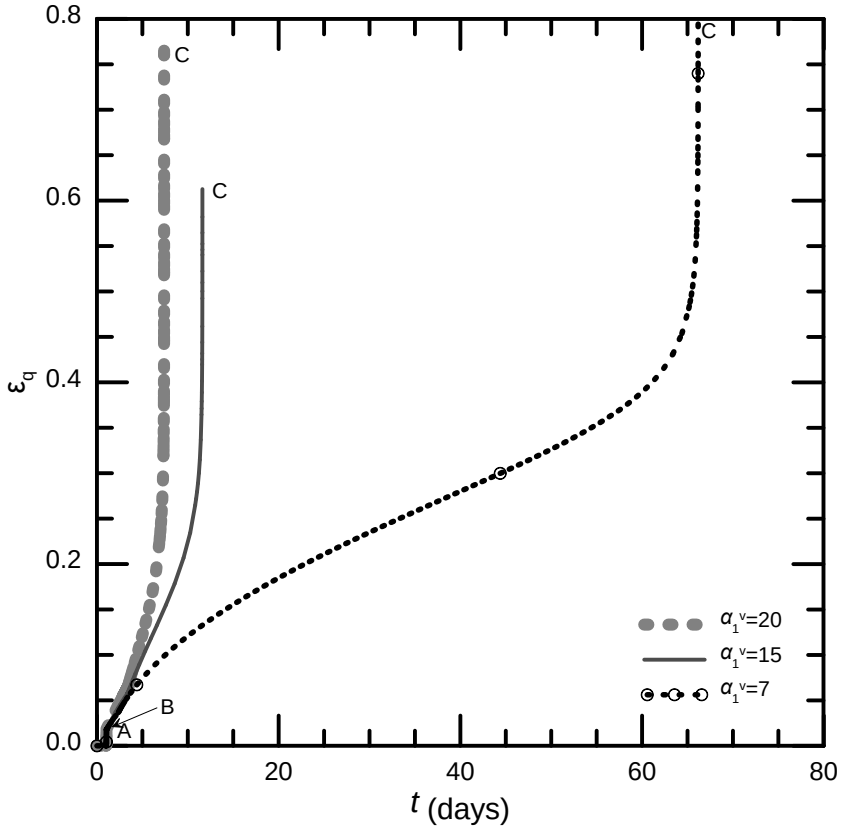

Σχήμα 12: Ερπυστική αστοχία μέσω της απομείωσης της περιβάλλουσας αστοχίας λόγω ερπυστικών παραμορφώσεων σε μη-δομημένο ελαφρώς υπερστερεοποιημένο δοκίμιο υποβαλλόμενο σε δοκιμή ερπυσμού απευθείας διάτμησης (διατμητική παραμόρφωση ε_q συναρτήσει του χρόνου t σε ημέρες).

Το **Σχήμα 12** παρουσιάζει την προσομοιούμενη χρονικά εξαρτημένη μηχανική συμπεριφορά δοκιμίου υποβαλλόμενο σε ερπυστική καταπόνηση επίπεδης παραμόρφωσης για διάφορες τιμές της σταθεράς a_1^v. Είναι εμφανές ότι το καταστατικό προσομοίωμα προβλέπει την ερπυστική αστοχία σε δοκιμές που ενεργοποιούν την διατμητική ερπυστική συνιστώσα. Ωστόσο, απομένει να διερευνηθεί ο μηχανισμός γήρανσης που δεν θα οδηγήσει σε αστοχία αλλά σε αύξηση του συντελεστή πλευρικών ωθήσεων στην μονάδα, μεταθέτοντας την τασική

κατάσταση επί του ισότροπου άξονα. Για τον λόγο αυτό διερευνάται τόσο η μηχανική ερπυστική συμπεριφορά όσο και η εντατική χαλάρωση σε αριθμητικές αναλύσεις προσομοίωσης συνθηκών συμπιεσομέτρου.

Ακολουθεί η διερεύνηση της ερπυστικής συμπεριφοράς σε συνθήκες συμπιεσομέτρου. Στην δοκιμή αυτή το ίδιο θεωρούμενο δοκίμιο (στερεοποιημένο σε ισότροπο τασικό πεδίο 80kPa – σημείο A) υποβλήθηκε σε συμπίεση 3.636kPa (από 80kPa που ήταν αρχικά). Η διάρκεια της φόρτισης (σημείο B) επιλέχθηκε ίση με 0,05 ημέρες αποσκοπώντας στην αμελητέα συσσώρευση ερπυστικών παραμορφώσεων. Κατόπιν το εξωτερικώς επιβαλλόμενο τασικό πεδίο διατηρήθηκε σταθερό και το θεωρούμενο δοκίμιο αφέθηκε να έρπει για 1.000 ημέρες (σημείο C).

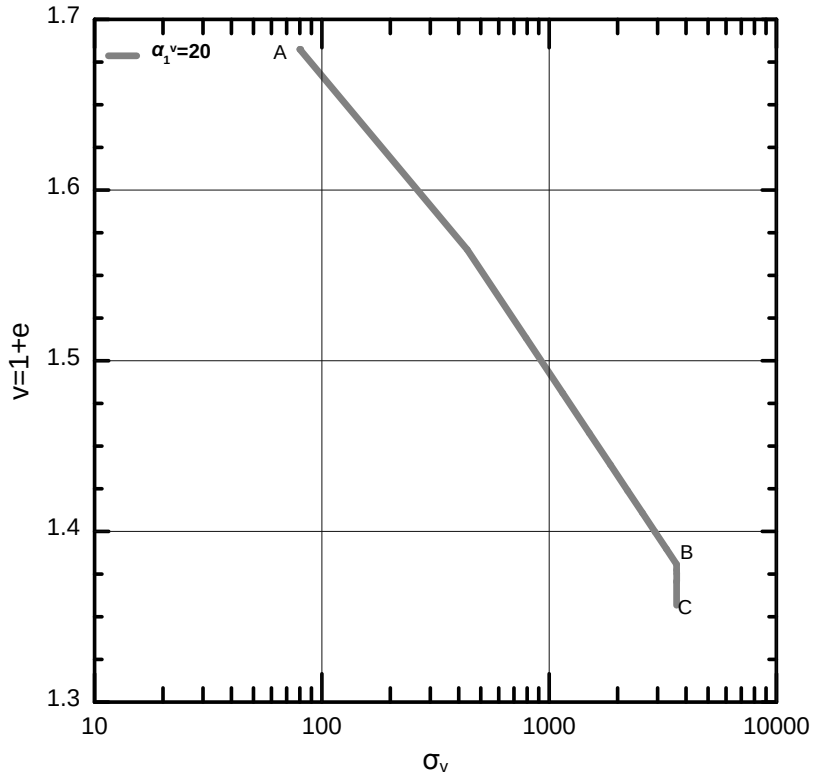

Σχήμα 13: Γραφική απεικόνιση της τασικής διαδρομής στο επίπεδο v-lnσ_v (ειδικού όγκου συναρτήσει του φυσικού λογαρίθμου της εξωτερικά επιβαλλόμενης ενεργού τάσης) σε πείραμα ερπυσμού συμπιεσομέτρου.

Το **Σχήμα 13** παρουσιάζει την επιρροή της ογκομετρικής συνιστώσας στην γήρανση του εδαφικού υλικού και συνεπώς στην διαφαινόμενη αύξηση της τάσης προστερεοποίησης. Είναι εμφανές ότι η εξωτερικά επιβαλλόμενη τάση παραμένει σταθερή κατά την διάρκεια του ερπυσμού ενώ ο δείκτης πόρων μειώνεται, οδηγώντας σε ταυτόχρονη αύξηση της τάσης προστερεοποίησης. Ο μηχανισμός εναρμονίζεται με τις παρατηρήσεις του Bjerrum (1967).

Η αξιολόγηση του καταστατικού προσομοιώματος ολοκληρώνεται με την εξέταση της ερπυστικής συμπεριφοράς σε αριθμητική ανάλυση προσομοίωσης της τασικής χαλάρωσης. Στην δοκιμή αυτή το ίδιο θεωρούμενο δοκίμιο ως παραπάνω (στερεοποιημένο σε ισότροπο τασικό πεδίο 80kPa – σημείο A) υποβλήθηκε σε κατακόρυφη συμπίεση 20% (μέσω επιβαλλόμενων μετακινήσεων). Η διάρκεια της φόρτισης (σημείο B) επιλέχθηκε ίση με μια ημέρα. Κατόπιν ολοκλήρωσης της φόρτισης, οι μετακινήσεις δεσμεύτηκαν και το παραμορφωσιακό πεδίο διατηρήθηκε σταθερό κατά την διάρκεια του ερπυσμού για 1.000 ημέρες (σημείο C).

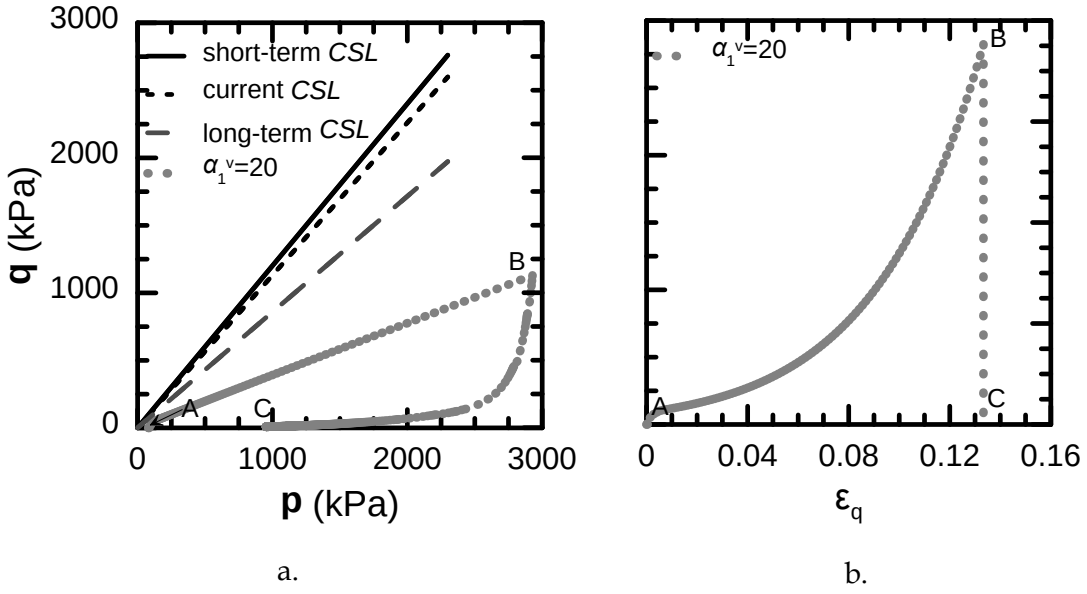

a. b.

Σχήμα 14: Γραφική απεικόνιση της τασικής διαδρομής a. στο επίπεδο *p*-*q* και b. στο επίπεδο *q*-ε_q (διατμητικής τάσης-παραμόρφωσης) σε πείραμα τασικής χαλάρωσης συμπιεσομέτρου.

Το **Σχήμα 14** απεικονίζει τόσο την τασική διαδρομή στο πεδίο των τάσεων όσο και την τασική χαλάρωση που υφίσταται το δοκίμιο στην δοκιμή αυτή (σημειώνεται ότι $p = \sigma$, $q = \sqrt{\frac{3}{2} \cdot \boldsymbol{s} : \boldsymbol{s}}$ και $\varepsilon_q = \sqrt{\frac{2}{3} \cdot \boldsymbol{e} : \boldsymbol{e}}$). Αποδεικνύεται ότι το προτεινόμενο χρονικά εξαρτημένο καταστατικό πλαίσιο μηχανικής συμπεριφοράς προσομοιώνει τους μηχανισμούς που οδηγούν τόσο σε αύξηση της αντοχής όσο και σε ερπυστική αστοχία. Κατόπιν επιχειρείται η αξιολόγηση του εξιδανικευμένου προσομοιώματος έναντι εργαστηριακών δοκιμών.

ΕΕ 4. Αξιολόγηση του προσομοιώματος έναντι εργαστηριακών δοκιμών

Το προτεινόμενο εξιδανικευμένο προσομοίωμα αξιολογήθηκε περαιτέρω έναντι εργαστηριακών δοκιμών. Όσον αφορά την ερπυστική συμπεριφορά σε δοκιμή συμπιεσομέτρου η παρούσα διδακτορική διατριβή εντοπίζει σε πειραματικά αποτελέσματα επί μαλακής αργίλου (που περισσότερο προσεγγίζει την μηχανική και χρονικά εξαρτημένη συμπεριφορά τύρφης – Yin et al., 2010). Ωστόσο, η εκτεταμένη βιβλιογραφική διερεύνηση που διεξήχθη για την εξεύρεση πειραματικών αποτελεσμάτων που ενεργοποιούν την ερπυστική αστοχία επέδειξε μια σαφή έλλειψη πειραμάτων όσον αφορά τις αργίλους. Σημειώνεται ότι η προσομοίωση απαιτείται να προσεγγίζει την στραγγιζόμενη μηχανική συμπεριφορά εντοπίζοντας σε σταθερό ενεργό τασικό πεδίο (που αποτελεί και τον ορισμό του ερπυσμού). Μη στραγγιζόμενες συνθήκες ενεργοποιούν τόσο τον μηχανισμό απομείωσης της περιβάλλουσας αστοχίας λόγω των ερπυστικών παραμορφώσεων όσο και τα γενικότερα ελαστοπλαστικά μηχανικά χαρακτηριστικά του προσομοιώματος. Συνεπώς, δεν είναι δυνατόν να εξαχθούν ασφαλή συμπεράσματα από τέτοια εργαστηριακά δεδομένα αναλογιζόμενοι το γεγονός ότι τα πειράματα κλειστής στράγγισης ωθούν τόσο σε τασική χαλάρωση όσο και σε αστοχία (και συνεπώς δεν είναι εύκολο να απεμπλέξουμε τους μηχανισμούς).

Η βιβλιογραφική διερεύνηση εντόπισε δύο δημοσιεύσεις με την πιο πρόσφατη να χρονολογείται το 1975 (Bishop, 1966; Ter-Stepanian, 1975) που εξετάζουν την ερπυστική αστοχία των αργιλικών εδαφών υπό στραγγισμένες συνθήκες. Ο λόγος εντοπίζεται στην χρονική διάρκεια που απαιτείται για να επέλθει η αστοχία (από 200 έως 1.000 ημέρες). Συνεπώς, δεν κρίνεται εύκολη η διεξαγωγή τέτοιων πειραμάτων στο εργαστήριο, πολύ περισσότερο αν αναλογιστούμε ότι μια σειρά χημικών και βιολογικών διεργασιών μπορεί να οδηγήσει εν τω μεταξύ στον σχηματισμό δομής (π.χ. το στάσιμο νερό μεταξύ των κόκκων μπορεί να οδηγήσει σε βιολογικές διεργασίες που συνδράμουν στην ανάπτυξη δεσμών και συνεπώς δέσης). Για τον λόγο αυτό η ερπυστική αστοχία διερευνήθηκε σε πειραματικά δεδομένα ερπυστικής τριαξονικής καταπόνησης σε κάρβουνο (Debernardi, 2008).

Η δυνατότητα του προσομοιώματος να προβλέψει τον μηχανισμό γήρανσης μέσω πειραμάτων ερπυσμού σε δοκιμή συμπιεσομέτρου διερευνάται παρακάτω. Η διατριβή εντόπισε επί ενός μαλακού αργιλικού υλικού (Yin et al., 2010). Ένα κανονικά στερεοποιημένο δοκίμιο υποβλήθηκε σε συμπίεση ούτως ώστε η

κατακόρυφη τάση να αυξηθεί από 69kPa σε 132kPa. Σημειώνεται ότι ο παρθενικός δείκτης συμπίεσης λήφθηκε ίσος με $\lambda = 0,48$ ενώ η σταθερά της ποροελαστικότητας θεωρήθηκε ίση με $\kappa = 0,038$. Σημειώστε ότι ο λόγος $\lambda/\kappa = 12,63$ κρίνεται εξαιρετικά μεγάλος συγκρινόμενες με βιβλιογραφικές αναφορές. Το **Σχήμα 15** επιδεικνύει την δυνατότητα του προτεινόμενου ιξωδοελαστοπλαστικού προσομοιώματος να προβλέψει την καταγεγραμμένη χρονικά εξαρτημένη μηχανική συμπεριφορά σε δοκιμή ερπυσμού συμπιεσομέτρου.

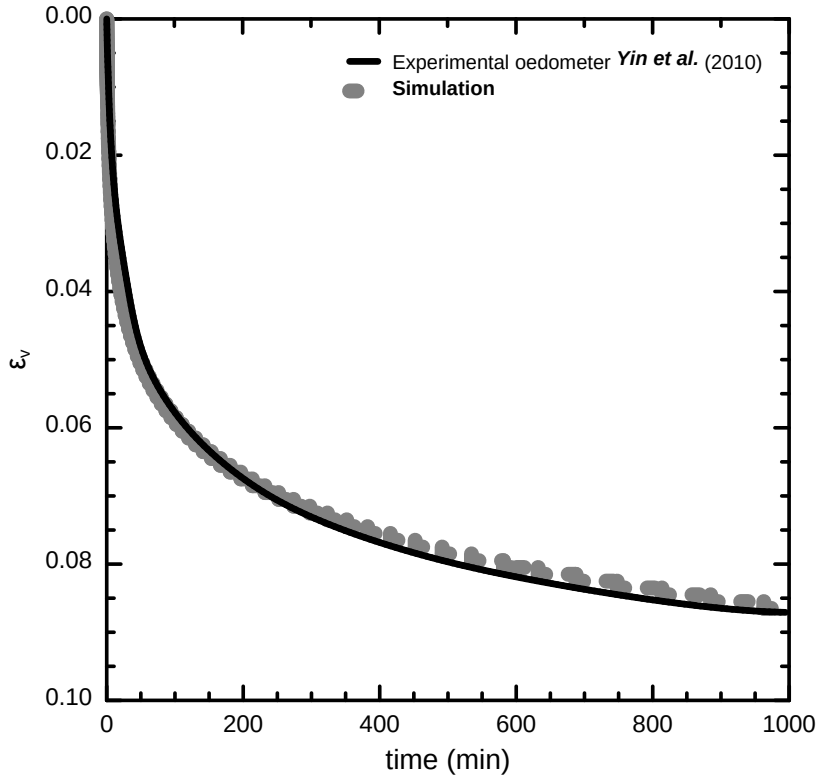

Σχήμα 15: Συγκριτική απεικόνιση της προβλεπόμενης μηχανικής συμπεριφοράς (διακεκομμένη γραμμή) με την πειραματική καταγραφή (συμπαγής μαύρη γραμμή) στο ερπυστικό πείραμα συμπιεσομέτρου των Yin et al. (2010).

Οι εναπομείναντες καταστατικές σταθερές απαντώνται στον **Πίνακα 7.1** του **Κεφαλαίου 7**. Σημειώνεται ότι ο δείκτης δευτερογενούς συμπίεσης θεωρήθηκε ίσος με $\psi = 0,028$. Η τιμή συγκλίνει επί της προτεινόμενης $\psi = 0,026$ των Yin et al. (2010).

Η διερεύνηση της παρούσας πειραματικής δοκιμής δεν πραγματοποιήθηκε τυχαία. Επιλέχθηκε συγκεκριμένα η περίπτωση μια πολύ μαλακής αργίλου (τα χαρακτηριστικά της οποίας ανταποκρίνονται περισσότερο σε τύρφη) κρίνοντας ότι το καταστατικό προσομοίωμα θα επιδείκνυε την χειρότερη δυνατή συμπεριφορά σε ένα τέτοιο υλικό με εξαιρετικά υψηλό ερπυστικό δυναμικό.

Η διεκτροπική ερπυστική συμπεριφορά διερευνήθηκε σε δύο πειράματα πολλαπλών σταδίων του Debernardi (2008) σε κάρβουνο. Παρακάτω συνοψίζεται το πείραμα A17a που οδηγεί σε ερπυστική αστοχία κατά την διάρκεια του τελευταίου σταδίου φόρτισης. Το πείραμα A17b εμφανίζει μειωμένη αξία λόγω μη ενεργοποίησης της ερπυστικής αστοχίας και για τον λόγο αυτό δεν θα αναφερθεί στην παρούσα εκτενή περίληψη. Κατά την εκτέλεση του πειράματος A17a ένα κυλινδρικό δοκίμιο διαμέτρου 50,1mm και ύψους 100mm υποβάλλεται σε διαδοχικά βήματα φόρτισης και ερπυσμού. Αρχικά το δοκίμιο στερεοποιήθηκε σε ισότροπη τάση 20MPa. Μετά από 4 ημέρες ερπυσμού υπό σταθερό τασικό πεδίο μετρήθηκαν αμελητέες ερπυστικές παραμορφώσεις. Κατόπιν το δοκίμιο εντάθηκε μέχρι η μέση τάση να γίνει ίση με p=17.67MPa και η διατμητική q=14MPa. Αυτό συνεπάγεται ότι μεταβάλλεται τόσο η αξονική πίεση όσο και η τάση εγκιβωτισμού. Το δοκίμιο αφέθηκε να έρπει για 16 ημέρες και επαναφορτίσθηκε σε μια μέση τάση εγκιβωτισμού ίση με p=16.67MPa και σε διατμητική τάση q=20MPa. Μετά από 50 ημέρες ερπυσμού μετρήθηκαν ερπυστικές παραμορφώσεις της τάξης του $2*10^{-5}$ (σημειώνεται ότι στο προηγούμενο ερπυστικό βήμα των 16 ημερών η ερπυστική παραμόρφωση ήταν ακόμα μικρότερη). Η φόρτιση συνεχίστηκε μέχρις ότου η μέση πίεση και η ενεργός τάση έλαβαν τιμές p=15.67MPa και q=26MPa αντίστοιχα. Σε αυτό το σημείο οι μετακινήσεις δεσμεύτηκαν και πραγματοποιήθηκε δοκιμή τασικής χαλάρωσης. Μετά από 13 ημέρες η διατμητική τάση μειώθηκε κατά μόνο 1MPa μετατοπίζοντας κατά συνέπεια την τελικά τασική κατάσταση στο σημείο F που αντιστοιχεί σε p=15.33MPa και q=25MPa (η τασική χαλάρωση κρίθηκε αμελητέα από τους ερευνητές, Debernardi, 2008).

Η αριθμητική προσομοίωση που εκπονήθηκε θεωρεί σαν αρχική τασική κατάσταση το σημείο F. Εν συνεχεία η τάση εγκιβωτισμού δεσμεύτηκε στα 7MPa και αυξήθηκε σταδιακά η αξονική πίεση. Η αξονική συμπίεση διακόπτεται στα σημεία G (q=28MPa), H (q=30MPa), I (q=32MPa), J (q=34MPa) και στο σημείο K (q=36MPa) όπου το τασικό πεδίο διατηρείται σταθερό και τα δοκίμια αφήνονται να έρπουν για 3 ημέρες, 3,5 ημέρες, 15 ημέρες, 13 ημέρες και 1,5 ημέρες αντίστοιχα. Σημειώνεται ότι κατά την διάρκεια του τελευταίου βήματος φόρτισης το δοκίμιο αστοχεί σε ερπυσμό. Το **Σχήμα 16** απεικονίζει τόσο την προσομοιούμενη τασική διαδρομή όσο και τις καταγεγραμμένες διεκτροπικές παραμορφώσεις κατά την διάρκεια των ερπυστικών βημάτων (για τα σημεία G, H, I , J).

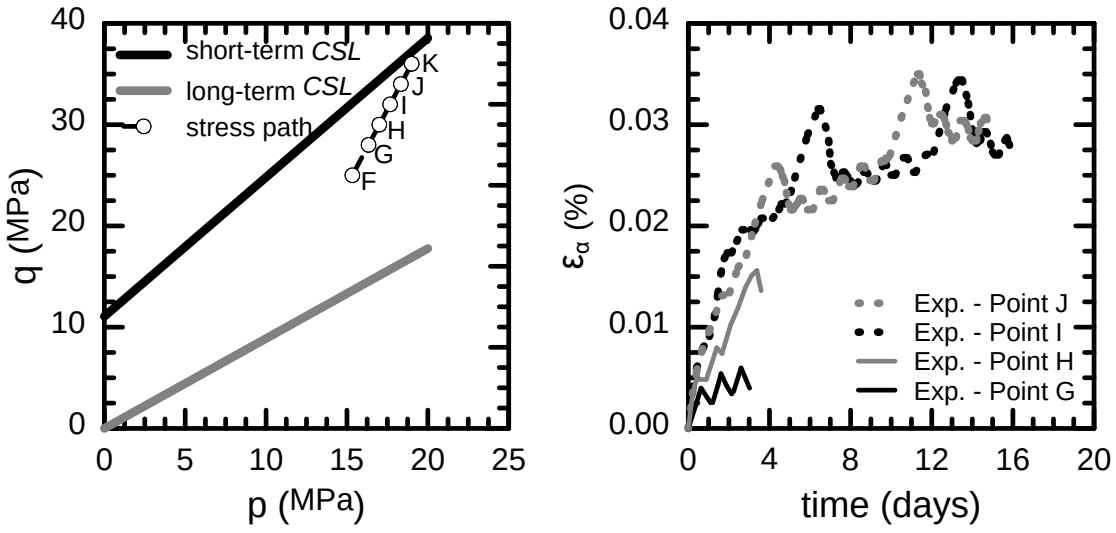

a. b.

Σχήμα 16: Απεικόνιση a. της τασικής διαδρομής στο επίπεδο *p-q* και b. των πειραματικών καταγραφών (Exp.) της αξονικής παραμόρφωσης συναρτήσει του χρόνου, κατά την διάρκεια των ερπυστικών βημάτων για τις τασικές καταστάσεις που αντιστοιχούν στα σημεία G, H, I και J στο πείραμα A17a του Debernardi (2008).

Οι καταγραφές στα σημεία G και H σταμάτησαν μετά από 3 και 3,5 ημέρες αντίστοιχα λόγω προβλημάτων στον τεχνικό εξοπλισμό (Debernardi, 2008). Επιπλέον, κάποιες απότομες μεταβολές των εργαστηριακών δεδομένων αποδόθηκαν σε θερμοκρασιακές μεταβολές στο εργαστήριο (Debernardi, 2008). Οι καταστατικές σταθερές που χρησιμοποιήθηκαν στην προσομοίωση παρατίθενται στον **Πίνακα 1**.

Πίνακας 1: Καταστατικές σταθερές προσομοίωσης του πειράματος A17a (Debernardi, 2008).

B_0	B_{res}	a^* (MPa)	v	c_{in}	c_{fin}	$2\cdot(G/K)^e$	λ	κ
1	1	22.03	1.19	1.099	0.8736	0.923	0.0042	0.00289
λ^*	γ	d_{in} (MPa)	η_v^p	η_q^p	ζ_v^p	ζ_q^p	θ_q^p	ϑ_q^p
5	1	8.05	75	75	0	0	0	0
t_0 (days)	a_1^v	a_2^v	ψ	A	m	$\bar{a}$	DLIMIT	ξ
1	50	2	2.3E-5	4.8E-6	0.994	7	10^{-6}	0.02

Το **Σχήμα 17** απεικονίζει τα συγκριτικά διαγράμματα αξονικής παραμόρφωσης συναρτήσει του χρόνου της προβλεπόμενης καταστατικής συμπεριφοράς και των πειραματικών καταγραφών. Είναι εμφανές ότι για την μικρότερη καταπόνηση στο

σημείο G το καταστατικό προσομοίωμα αδυνατεί να προσεγγίσει ικανοποιητικά τις πειραματικές μετρήσεις. Το γεγονός αυτό αποδίδεται στην εγγενή αδυναμία της εμπειρικής συσχέτισης Singh-Mitchell (1968) να προσεγγίσει τον πρωτογενή ερπυσμό. Ωστόσο σε όλες τις υπόλοιπες περιπτώσεις η καταστατική προσομοίωση προσεγγίζει εξαιρετικά τις εργαστηριακές μετρήσεις.

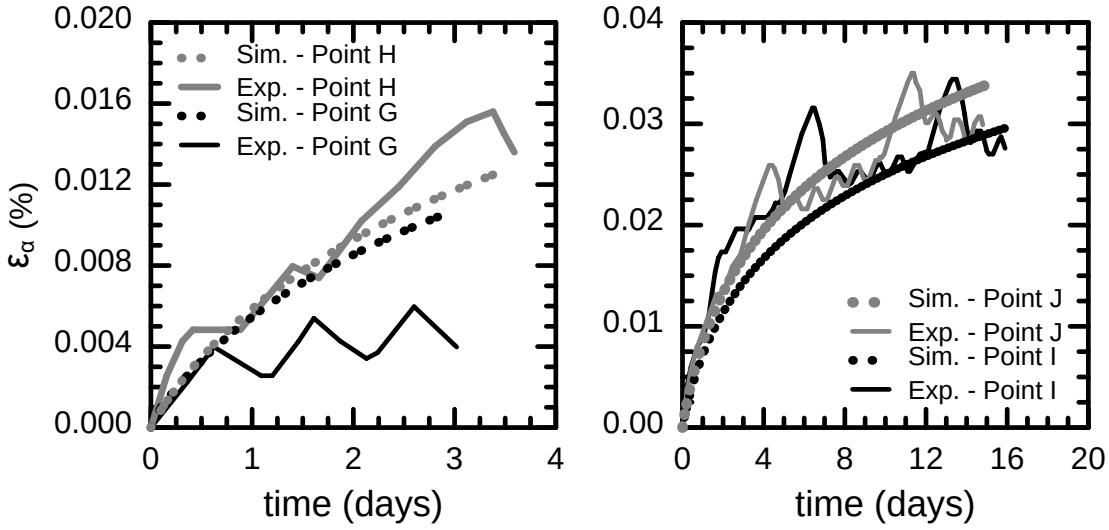

a. b.

Σχήμα 17: Συγκριτική απεικόνιση της αξονικής παραμόρφωσης συναρτήσει του χρόνου a. στα σημεία G και H και b. στα σημεία I και J. Οι πειραματικές καταγραφές δηλώνονται με την ένδειξη «Exp.» και οι προσομοιώσεις με την ένδειξη «Sim.» στο πείραμα A17a του Debernardi (2008).

Τέλος, το **Σχήμα 18** παρουσιάζει την συγκριτική απεικόνιση των πειραματικών καταγραφών και της προβλεπόμενης συμπεριφοράς στο τελευταίο βήμα φόρτισης όπου παρατηρείται και η ερπυστική αστοχία. Είναι εμφανές ότι αν και το προσομοίωμα δείχνει να προσεγγίζει τον μηχανισμό αδυνατεί να προβλέψει τον πρωτογενή ερπυστικό κλάδο κάτι που αποδίδεται στην εγγενή αδυναμία της εμπειρικής συσχέτισης των Singh-Mitchell (1968). Επιπλέον, κρίθηκε αδύνατον να απεμπλέξουμε τον πρωτογενή ερπυστικό κλάδο ώστε να δείξουμε την ανάλογη σύγκριση. Ωστόσο, είναι εμφανές ότι ο προτεινόμενος καταστατικός νόμος ενσωματώνοντας στοιχεία χρονικής εξάρτησης της παραμόρφωσης προσομοιώνει εξαιρετικά σε επίπεδο μηχανισμών την καταγεγραμμένη μηχανική συμπεριφορά.

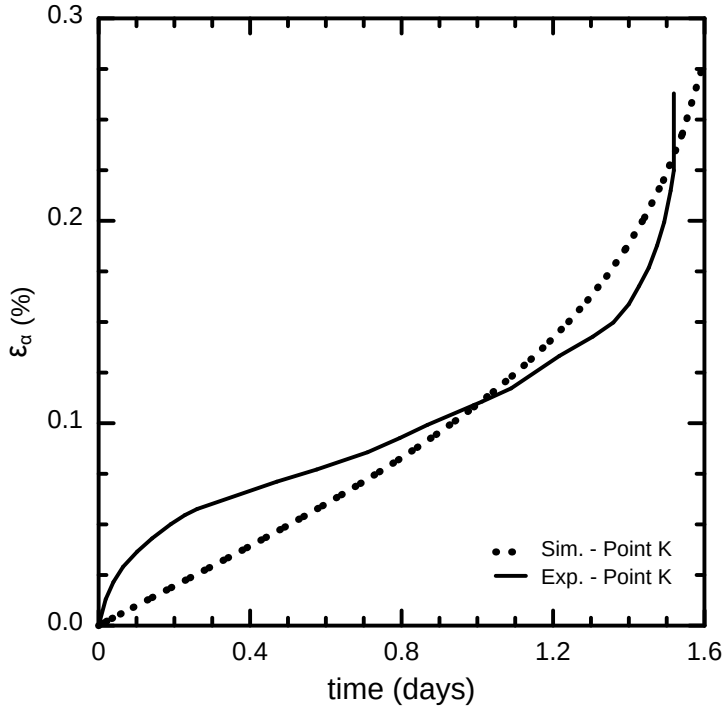

Σχήμα 18: Συγκριτική απεικόνιση της αξονικής παραμόρφωσης συναρτήσει του χρόνου στο σημείο K. Οι πειραματικές καταγραφές δηλώνονται με την ένδειξη «Exp.» και η προσομοίωση με την ένδειξη «Sim.» στο πείραμα A17a του Debernardi (2008). Οι πειραματικές μετρήσεις ενσωματώνουν τον πρωτογενή ερπυστικό κλάδο που αδυνατεί να προβλεφθεί από το εμπειρικό προσομοίωμα Singh-Mitchell.

ΕΕ 5. Εφαρμογή του προσομοιώματος στην ευστάθεια πρανών

Το προτεινόμενο εξιδανικευμένο προσομοίωμα χρησιμοποιήθηκε στην διερεύνηση της ευστάθειας πρανών σε 2Δ αριθμητικές αναλύσεις στον κώδικα πεπερασμένων στοιχείων ABAQUS. Αρχικά εξετάσθηκε η αδυναμία των ελαστοπλαστικών μηχανικών χαρακτηριστικών να οδηγήσουν σε αστοχία. Κρίθηκε ανέφικτο να προσομοιωθεί η προοδευτική αστοχία μέσω των μηχανισμών αποδόμησης της δέσης και απομείωσης της περιβάλλουσας αστοχίας μέσω των πλαστικών παραμορφώσεων. Το γεγονός αυτό αποδόθηκε στην αδυναμία ελέγχου της συσσώρευσης των πλαστικών παραμορφώσεων. Ωστόσο, η χρονική εξέλιξη των ανελαστικών παραμορφώσεων αποτελεί το κλειδί που οδηγεί σε προοδευτική αστοχία.

Θεωρήθηκε ένα πρανές με τα γεωμετρικά χαρακτηριστικά που εμφανίζονται στο **Σχήμα 19**. Τα βήματα εκσκαφής και η αρχική κατάσταση επισημαίνονται στο **Σχήμα 20**. Η αρχική γεωστατική κατάσταση θεωρήθηκε επίπεδη και είχε διάρκεια 1 ημέρας με σκοπό την σύγκλιση του υπολογιζόμενου τασικού πεδίου με τις αρχικές τάσεις. Σημειώνεται ότι σε κάθε βήμα (γεωστατικό ή βήμα εκσκαφής) η επιφάνεια του

υδροφόρου ορίζοντα ταυτίζεται με αυτή του εδάφους. Κατόπιν εφαρμόσθηκε ένα βήμα στερεοποίησης 80 ημερών. Στη συνέχεια πραγματοποιήθηκε η εκσκαφή του αρχικού πρανούς ήπιας κλίσης (περί της 20°). Οι πιέσεις πόρων αποτονώθηκαν κατά την διάρκεια ενός θεωρούμενου βήματος στερεοποίησης 140 ημερών. Το επόμενο βήμα εκσκαφής του πόδα ολοκληρώθηκε σε 0,5 ημέρα και ακολούθησε ένα βήμα στερεοποίησης όπου ενεργοποιήθηκε και ο ερπυσμός.

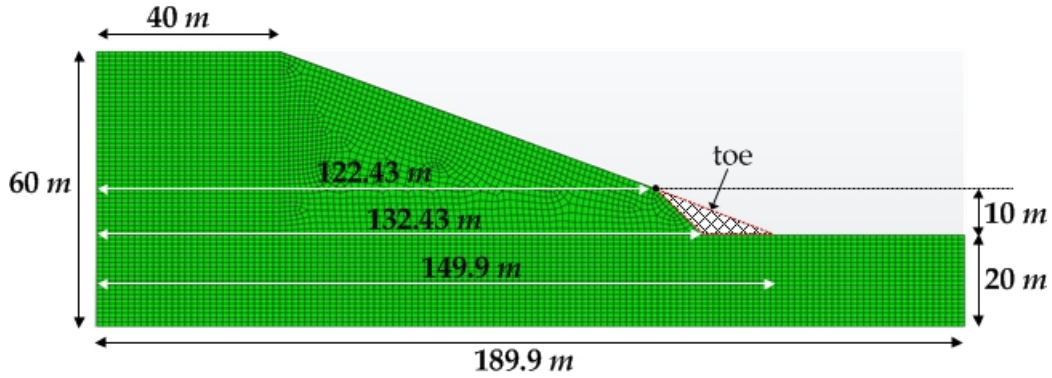

Σχήμα 19: Γεωμετρικά χαρακτηριστικά του θεωρούμενου πρανούς

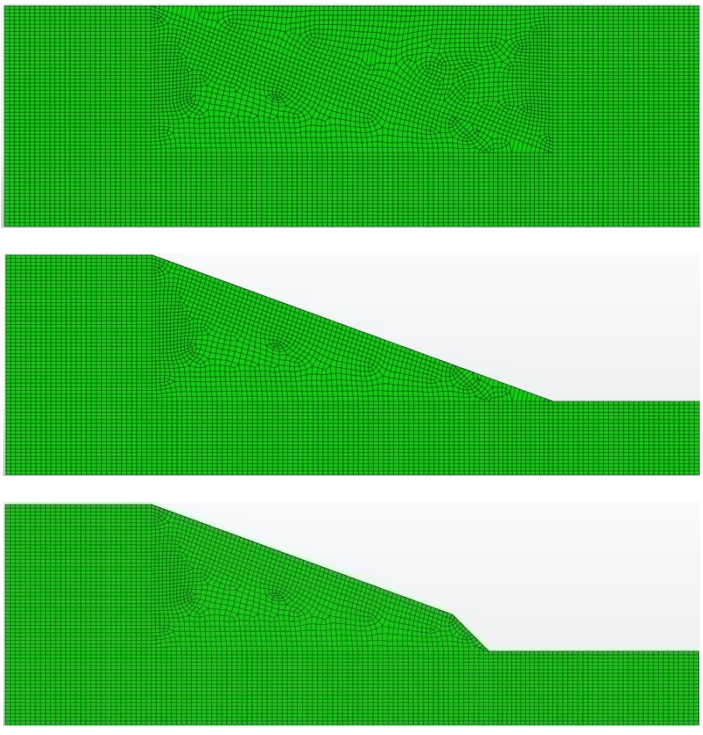

Σχήμα 20: Σχηματική απεικόνιση a. της αρχικής γεωστατικής κατάστασης, b. του αρχικού πρανούς και c. της τελικής εκσκαφής του πόδα.

Αυτό που αναμένεται είναι αφενός να αποτονωθούν αρχικά οι υπερπιέσεις πόρων, και συνεπώς να επέλθει μια «ισοδύναμη σταθεροποιημένη κατάσταση ροής» (ο όρος χρησιμοποιείται για να διατυπώσει την κατάσταση αποτόνωσης των υπερπιέσεων

μιας που η στερεοποίηση αποτελεί μεταβατική κατάσταση ροής), και αφετέρου με την πάροδο του χρόνου το πρανές να συσσωρεύσει ανελαστικές παραμορφώσεις έως ότου αστοχήσει μέσω του μηχανισμού προοδευτικής αστοχίας. Το **Σχήμα 21** συνοψίζει τις πιέσεις πόρων πριν από την εκσκαφή του πόδα μέχρι και την αστοχία. Είναι εμφανές ότι αρνητικές πιέσεις πόρων εντοπίζονται κατά μήκος της επιφάνειας ολίσθησης. Αυτό είναι χαρακτηριστικό των αστράγγιστων συνθηκών που επικρατούν κατά μήκος της επιφάνειας ολίσθησης (και αιτιολογεί την ανάπτυξη αρνητικών υπερπιέσεων πόρων) σε συνδυασμό με τον εξαιρετικά υψηλό βαθμό υπερστερεοποίησης (OCR>>2).

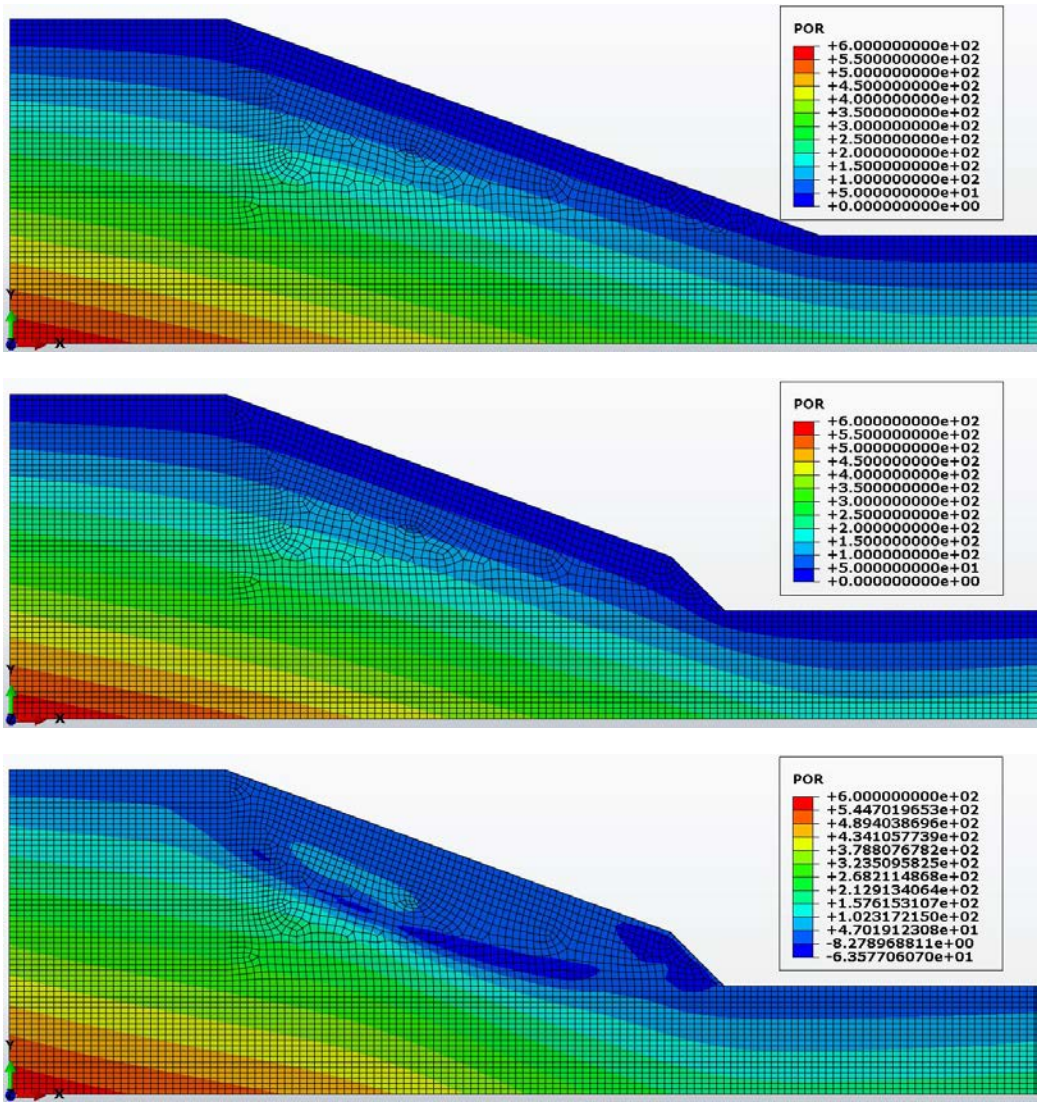

Σχήμα 21: Απεικόνιση των πιέσεων πόρων POR (kPa) a. πριν την εκσκαφή του πόδα, b. αφού έχουν αποτονωθεί οι υπερπιέσεις μετά από 13,13 ημέρες από την εκσκαφή του πόδα («ισοδύναμη σταθεροποιημένη κατάσταση ροής») και c. κατά την αστοχία του πρανούς μετά από 106 ημέρες.

Ακολουθεί η γραφική απεικόνιση της μετακίνησης σε μέτρα στο **Σχήμα 22**. Είναι εμφανές ότι το πρανές δεν αστοχεί μέχρι την στιγμή που επέρχεται η αποτόνωση των υπερπιέσεων πόρων μετά από 13,13 ημέρες. Η μεταβολή των παραμορφώσεων είναι αμελητέα κατά την διάρκεια των 13,13 ημερών και συνεπώς δεν υπάρχει καμία ένδειξη η απόδειξη ότι το πρανές αστοχεί σε αυτή την πρώτη χρονική περίοδο. Συνεπώς, κάποιος μηχανισμός συνδράμει στην αστάθεια του πρανούς όπως αυτή εκδηλώνεται μετά από 106 ημέρες.

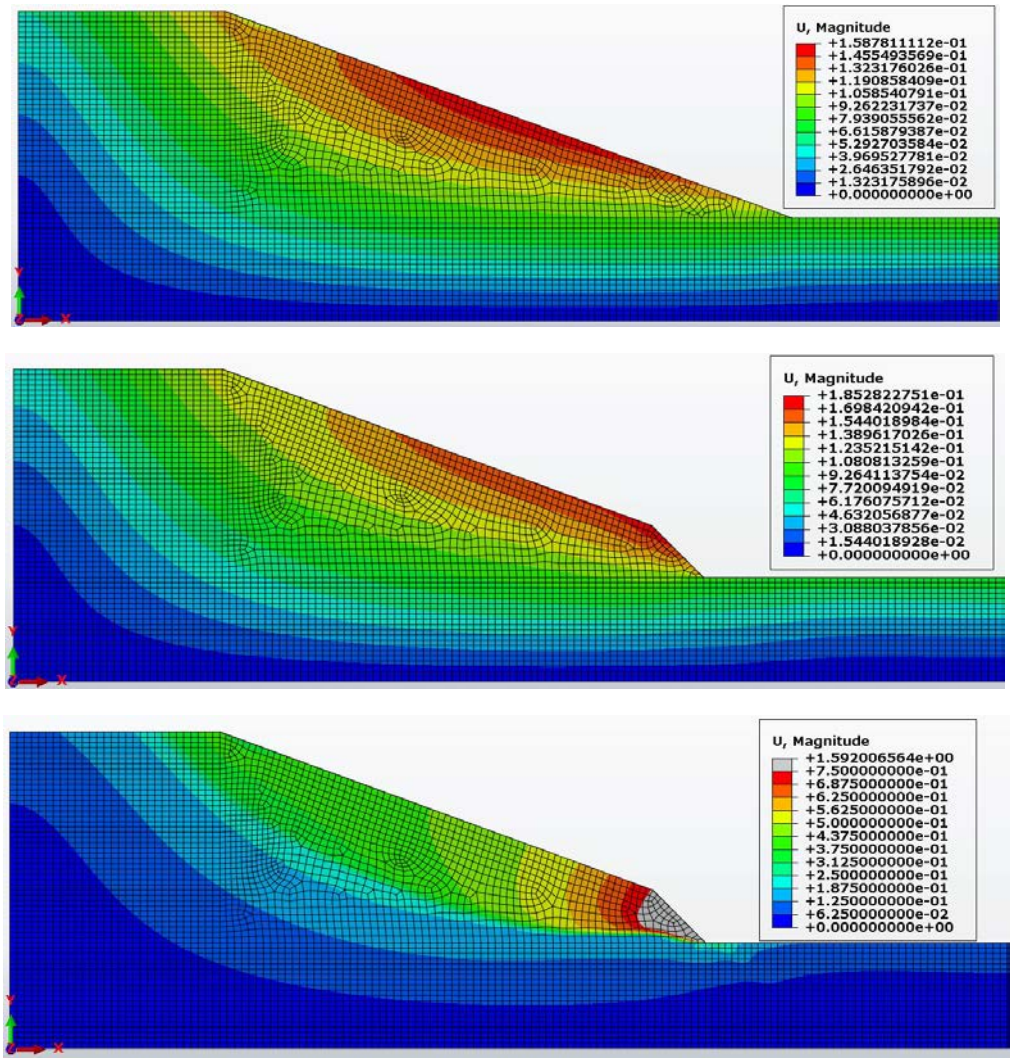

Σχήμα 22: Απεικόνιση της μετακίνησης U (*m*) a. πριν την εκσκαφή του πόδα, b. 13,13 ημέρες από την εκσκαφή του πόδα («ισοδύναμη σταθεροποιημένη κατάσταση ροής») και c. κατά την αστοχία του πρανούς μετά από 106 ημέρες.

Καθίσταται ευκρινές ότι η απομείωση της περιβάλλουσας αστοχίας με την ερπυστική παραμόρφωση ενεργοποιεί τον μηχανισμό της προοδευτικής αστοχίας όπως διαφαίνεται στο **Σχήμα 23**.

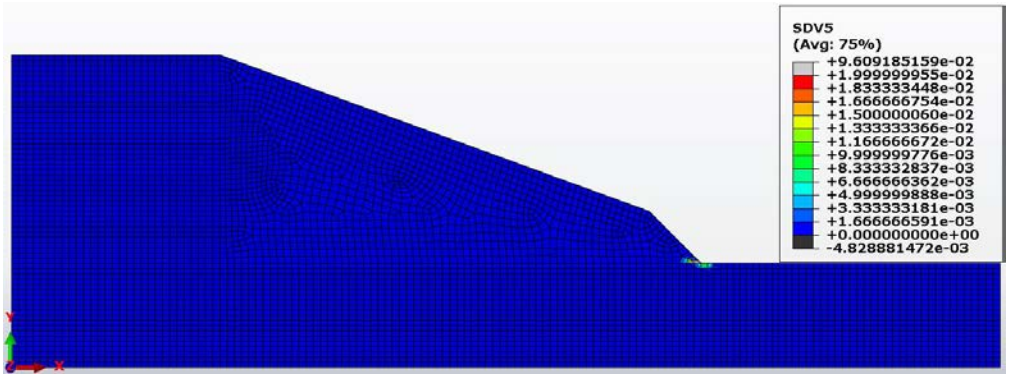

a.

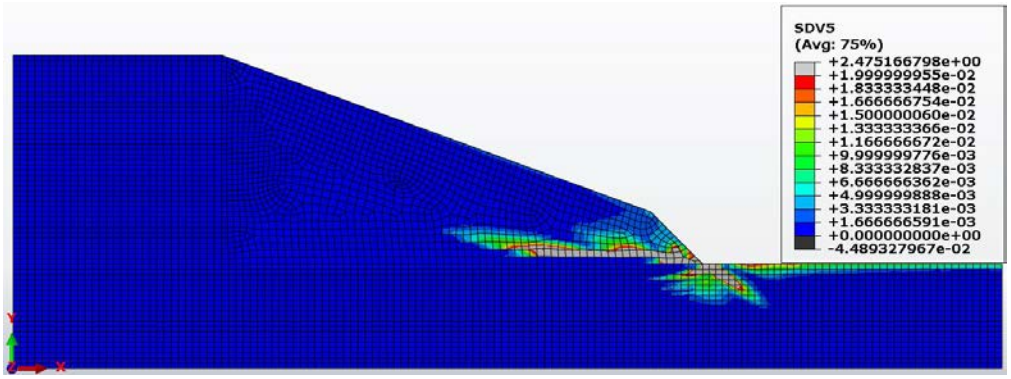

b.

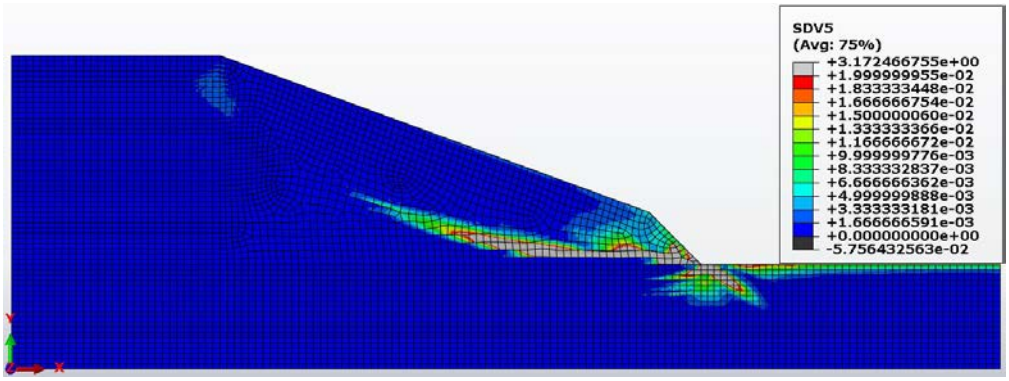

c.

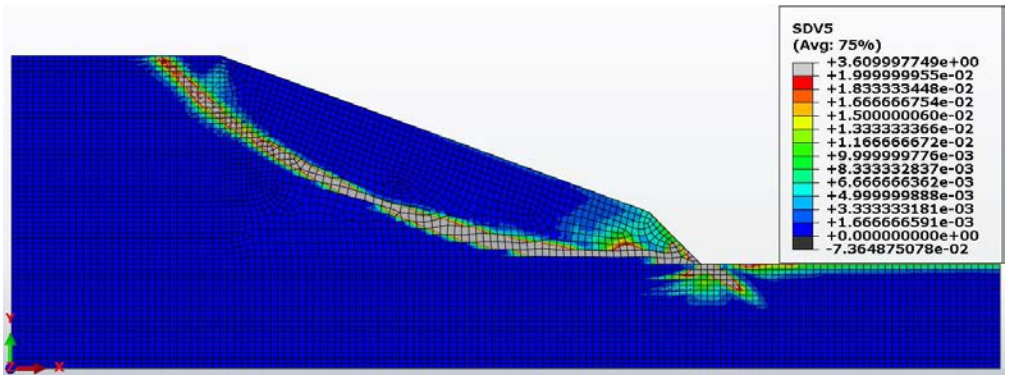

d.

Σχήμα 23: Απεικόνιση του μηχανισμού προοδευτικής αστοχίας μέσα από την χρονική εξέλιξη της διεκτροπικής πλαστικής παραμόρφωσης ε_q^p (SDV5) υπό συνθήκες κορεσμού μετά από a. 13.13 ημέρες, b. 91.56 ημέρες; c. 102 ημέρες και d. στην αστοχία (106 ημέρες) μετά την εκσκαφή του πόδα (η στερεοποίηση και ο ερπυσμός εξελίσσονται ταυτόχρονα).

Ο μηχανισμός προοδευτικής αστοχίας ξεκινάει από τον πόδα και διαδίδεται ανάστροφα προς τα πίσω αναδυόμενος προς την επιφάνεια. Κάποια στιγμή και αφού η επιφάνεια ολίσθησης έχει προσεγγίσει την επιφάνεια του πρανούς (μετά από 96 ημέρες) ενεργοποιείται μια δευτερεύουσα επιφάνεια ολίσθησης που ξεκινάει από την επιφάνεια και διαδίδεται προς τα κάτω για να ενωθεί τελικά με την αρχική μορφώνοντας κατά αυτό τον τρόπο την τελική επιφάνεια αστοχίας.

Στο **Σχήμα 24** απεικονίζεται η χρονική εξέλιξη των μετακινήσεων στον πόδα (toe), στην στέψη (crest) και στο σημείο που ορίζει το αρχικό πρανές με την τελική εκσκαφή (intersection).

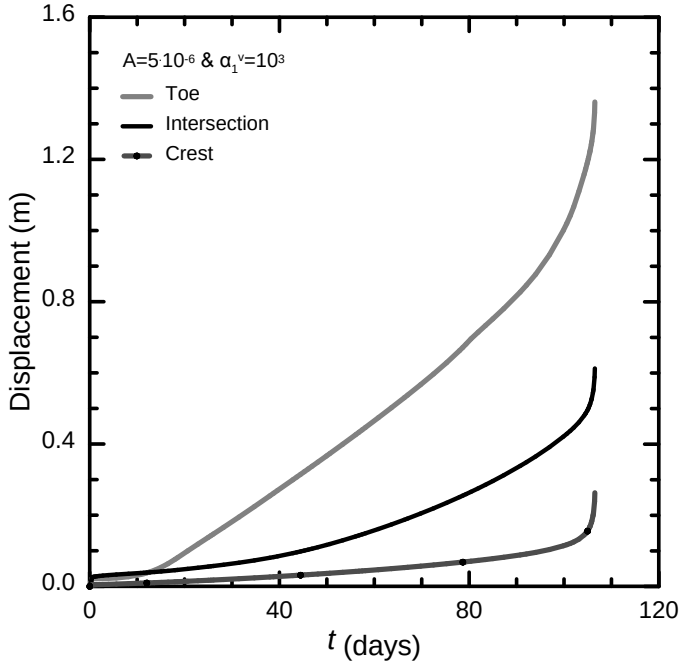

Σχήμα 24: Απεικόνιση της χρονικής εξέλιξης των μετακινήσεων (Displacements) στον πόδα (toe), στην στέψη (crest) και στο σημείο που ορίζει το αρχικό πρανές με την τελική εκσκαφή (intersection).

Ο μηχανισμός της προοδευτικής αστοχίας ενεργοποιήθηκε θέτοντας τις κατάλληλες καταστατικές παραμέτρους στο πρόβλημα. Διερευνήθηκε ωστόσο κατά πόσο η προοδευτική αστοχία οφείλεται στην ύπαρξη του νερού. Τα **Σχήματα 25** και **26** αποδεικνύουν ότι η θεώρηση ξηρού εδάφους και η ενσωμάτωση των ακριβώς ίδιων καταστατικών σταθερών στο πρόβλημα δεν οδηγεί σε αστοχία παρά μόνο σε συσσώρευση πλαστικών παραμορφώσεων στον πόδα με αποτέλεσμα η ανάλυση να σταματάει να συγκλίνει λόγω τοπικής αστοχίας εντοπιζόμενη επί των επιφανειακών στοιχείων αυτού. Συνεπώς, είναι το νερό και η απομείωση της περιβάλλουσας

αστοχίας λόγω των ερπυστικών παραμορφώσεων που ενεργοποιεί τον μηχανισμό της προοδευτικής αστοχίας στα πρανή.

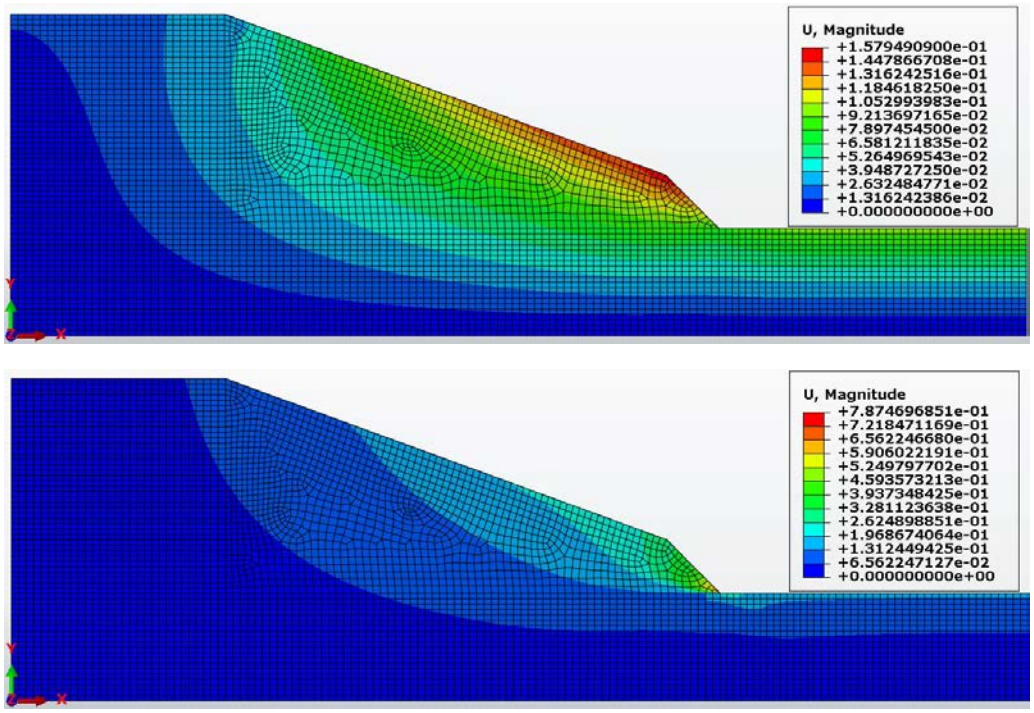

Σχήμα 25: Απεικόνιση της μετακίνησης U (*m*) a. πριν την εκσκαφή του πόδα, b. μετά από 171 ημέρες ερπυσμού. Σημειώνεται ότι η ανάλυση αφορά την περίπτωση ξηρού εδάφους.

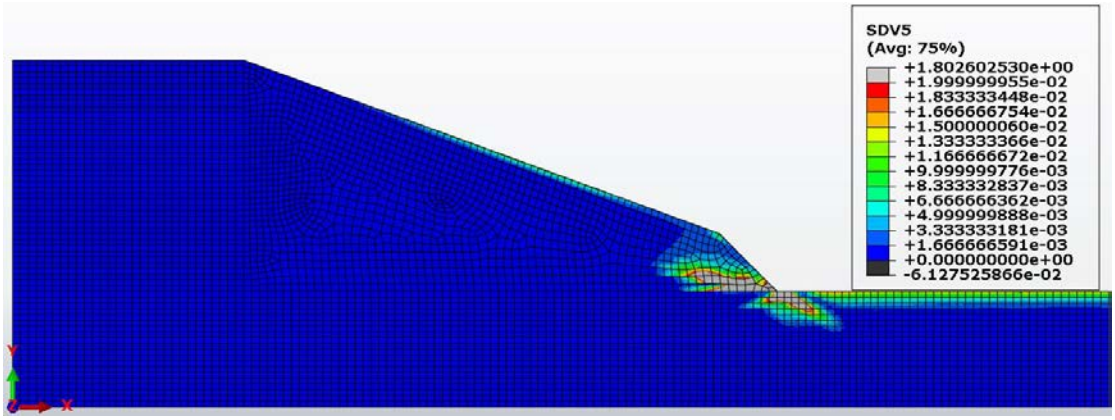

Σχήμα 26: Απεικόνιση της διεκτροπικής πλαστικής παραμόρφωσης ε_q^p (SDV5) υπό συνθήκες ξηρού εδάφους 171 ημέρες μετά την εκσκαφή του πόδα.

IV. Αποτελέσματα, Συμπεράσματα και Προτάσεις

Στην παρούσα διδακτορική διατριβή καταστρώνεται ένα νέο χρονικά εξαρτημένο καταστατικό πλαίσιο συμπεριφοράς. Το καινούριο αυτό πλαίσιο θεμελιώνεται πάνω στις ελαστοπλαστικές αρχές των δομημένων γεωυλικών και παράλληλα ενσωματώνει ένα επιπλέον σύνολο δομητικών (π.χ. βελτιωμένους νόμους αποδόμησης της δομής

και κινηματικής κράτυνσης της κλίσης *c* και της μετάθεσης *d* μέσω της συσσώρευσης πλαστικών παραμορφώσεων) και χρονικά εξαρτημένων χαρακτηριστικών (π.χ. την απομείωση της περιβάλλουσας αστοχίας μέσω της συσσώρευσης ερπυστικών παραμορφώσεων).

Ο σκοπός της διατύπωσης ενός νέου καταστατικού πλαισίου συμπεριφοράς συνοψίζεται στην ανεπάρκεια των υφιστάμενων μεθοδολογιών να προσομοιώσουν τον μηχανισμό της προοδευτικής αστοχίας σε πρανή, στηριζόμενες αποκλειστικά και μόνο σε ελαστοπλαστικά χαρακτηριστικά. Η ουσιώδης ατέλεια των ελαστοπλαστικών προσομοιωμάτων απορρέει από την αδυναμία ελέγχου του μεγέθους των πλαστικών παραμορφώσεων. Συνεπώς, δεν δύνανται να συσσωρευτούν σημαντικές ανελαστικές παραμορφώσεις που να οδηγούν στην ενεργοποίηση του μηχανισμού της προοδευτικής αστοχίας. Η ενσωμάτωση ωστόσο των ερπυστικών χαρακτηριστικών επιτρέπει την δυνατότητα ελέγχου των ανελαστικών παραμορφώσεων μέσω της ερπυστικής συνιστώσας. Συνεπώς, είναι ο συνδυασμός των δομητικών και των ερπυστικών χαρακτηριστικών που οδηγούν στην αστοχία. Το προτεινόμενο εξιδανικευμένο προσομοίωμα χρησιμοποιήθηκε επιτυχώς στην πρόβλεψη του μηχανισμού προοδευτικής αστοχίας σε ένα πλήρως κορεσμένο πρανές.

Τα συμπεράσματα που προέκυψαν από την παρούσα διατριβή συνοψίζονται παρακάτω:

a. Το προτεινόμενο καταστατικό προσομοίωμα θεμελιώνεται πάνω στις καταστατικές αρχές των δομημένων εδαφών και τις βελτιώνει μέσω νέων νόμων κράτυνσης και αποδόμησης της δέσης. Επιπλέον, κινηματικοί νόμοι επιτρέπουν την απομείωση της περιβάλλουσας αστοχίας και της εφελκυστικής μετάθεσης της περιβάλλουσας αντοχής δομής με τις πλαστικές παραμορφώσεις.
b. Το προτεινόμενο καταστατικό προσομοίωμα ενσωματώνει ένα πλήρες σύνολο χρονικά συνυφασμένων μηχανικών χαρακτηριστικών. Η ογκομετρική ερπυστική συνιστώσα προσδίδει αντοχή μέσω της αύξησης της τάσης προστερεοποίησης. Συνεπώς, το πλαίσιο καταστατικής συμπεριφοράς εναρμονίζεται με τις παρατηρήσεις του Bjerrum (1967).
c. Η διεκτροπική συνιστώσα οδηγεί σε ερπυστική αστοχία μέσω της συσσώρευσης ανελαστικών παραμορφώσεων. Σημειώνεται ότι το καταστατικό πλαίσιο συμπεριφοράς θεμελιώνεται πάνω στην εμπειρική

συσχέτιση των Singh-Mitchell (1968) και συνεπώς δύναται να ελέγξει αποκλειστικά τον δευτερογενή ερπυσμό. Ο πρωτογενής ερπυσμός δεν προσομοιώνεται επακριβώς (εντοπίζεται αδυναμία ελέγχου αυτού) στην παρούσα μορφή του καταστατικού πλαισίου συμπεριφοράς. Αυτή η παραδοχή αποτελεί μια εγγενή αδυναμία του ερπυστικού προσομοιώματος Singh-Mitchell. Ο τριτογενής ερπυσμός που οδηγεί στην αστοχία προσομοιώνεται μέσω της απομείωσης της περιβάλλουσας αστοχίας. Το καταστατικό προσομοίωμα αξιολογήθηκε σε αριθμητικές αναλύσεις και έναντι πειραματικών δεδομένων όπου και επέδειξε την ικανότητά του στην σωστή πρόβλεψη των μηχανισμών που οδηγούν στην αστοχία.

d. Το προτεινόμενο ιξωδοελαστοπλαστικό προσομοίωμα χρησιμοποιήθηκε για την διερεύνηση του μηχανισμού αστοχίας των πρανών με την βοήθεια του κώδικα πεπερασμένων στοιχείων ABAQUS (το προσομοίωμα εισήχθη μέσω εξωτερικής υπορουτίνας UMAT). Οι αριθμητικές αναλύσεις επέδειξαν την δυνατότητα προσομοίωσης της προοδευτικής αστοχίας και την αποσαφήνιση του μηχανισμού που οδηγεί σε αυτή.
e. Επιπλέον, κατέστη ευκρινές ότι η προοδευτική αστοχία στα πρανή είναι συνυφασμένη με την ύπαρξη του νερού.

Προτάσεις για μελλοντική έρευνα

Στην παρούσα διδακτορική διατριβή προτείνεται ένα καινούριο χρονικά εξαρτημένο καταστατικό πλαίσιο συμπεριφοράς των δομημένων υλικών. Το πλαίσιο αυτό ενσωματώνει χαρακτηριστικά τα οποία οδηγούν σε σωστή προσομοίωση της ερπυστικής αστοχίας τουλάχιστον σε επίπεδο μηχανισμών.

Προτείνεται η περαιτέρω διερεύνηση και βελτίωση του καταστατικού πλαισίου συμπεριφοράς, που ενσωματώνει την επιρροή του ρυθμού των παραμορφώσεων, τόσο σε επίπεδο καταστατικής προσομοίωσης όσο και ως προς την πρακτική διερεύνηση ενδεχόμενων εφαρμογών.

Ενδεικτικά αναφέρονται οι παρακάτω προτάσεις:

a. Προτείνεται η ενσωμάτωση της πρωτογενούς ανισοτροπίας. Επί της παρούσης η περιβάλλουσα αντοχής δομής είναι προσανατολισμένη επί του ισότροπου άξονα. Ο άξονας της περιβάλλουσας αντοχής δομής συνεπώς θα

πρέπει να εκτραπεί εκ του ισότροπου και να ακολουθήσει ένα κινηματικό νόμο κράτυνσης παρόμοιο με αυτό που προτείνεται από τους Sitarenios et al. (2013). Επιπλέον, προτείνεται η ενσωμάτωση ενός μη-συσχετισμένου νόμου ροής για την πιο ρεαλιστική προσομοίωση των εργαστηριακών καταγραφών.

b. Η σύγκριση του προτεινόμενου εξιδανικευμένου προσομοιώματος επέδειξε την αδυναμία πρόβλεψης του πρωτογενούς ερπυσμού. Συνεπώς, ενδείκνυται η διατύπωση μια νέας απλής εμπειρικής συσχέτισης βασισμένη σε δημοσιευμένα εργαστηριακά δεδομένα και σε ένα νέο σύνολο εργαστηριακών αποτελεσμάτων. Σημειώνεται ότι οι εργαστηριακές δοκιμές απαιτείται να αναφέρονται σε στραγγισμένες συνθήκες κάτι που ενδεχομένως να αποτελεί τροχοπέδη για την ενδελεχή διερεύνηση των αργιλικών εδαφών (εφόσον μπορεί να αστοχούν μετά από 200 ή και 1.000 ημέρες μετά την επιβολή της επιφόρτισης).

c. Αν και ο μηχανισμός της προοδευτικής αστοχίας προσομοιώθηκε και αποσαφηνίστηκε μέσω της παρούσας διδακτορικής διατριβής προτείνεται η ενδελεχής έρευνα γύρω από την αστοχία των πρανών σε επίπεδο διδακτορικής διατριβής. Η έρευνα προτείνεται να αφορά την πρακτική εφαρμογή του καταστατικού πλαισίου συμπεριφοράς με σκοπό ενδεχόμενη πρόταση τεχνικών και μέτρων ανάσχεσης της αστοχίας. Ενδεχομένως κάποιες ανάστροφες αναλύσεις να βοηθήσουν ως προς αυτήν την κατεύθυνση.

d. Μια άλλη πρακτική εφαρμογή αφορά την αύξηση της τάσης εγκιβωτισμού γύρω από την τελική επένδυση σηράγγων. Η ενδεχόμενη αύξηση της πίεσης στην τελική επένδυση ενδεχομένως να ωθήσει σε ρωγμάτωση και αστοχία. Συνεπώς, το καταστατικό προσομοίωμα θα μπορούσε να χρησιμοποιηθεί για να διερευνηθεί η αύξηση της πίεσης στην τελική επένδυση με απώτερο σκοπό την διατύπωση κατευθυντήριων οδηγιών και κανόνων σχεδιασμού.

Η χρονικά-εξαρτημένη μηχανική συμπεριφορά επιτρέπει την χρονική εξέλιξη των ανελαστικών παραμορφώσεων σε περιοχές έντονης καταπόνησης και οδηγεί στην εκδήλωση του μηχανισμού προοδευτικής αστοχίας στα πρανή. Αδυνατεί ωστόσο να προσομοιώσει τους μηχανισμούς αστοχίας που απορρέουν από την κατάρρευση της αντοχής (soil collapse) λόγω μεταβολών της μύζησης. Συνεπώς, το παρών χρονικά εξαρτημένο καταστατικό πλαίσιο συμπεριφοράς απαιτείται να ενσωματώσει τα χαρακτηριστικά των μη-κορεσμένων εδαφικών υλικών στο απώτερο μέλλον.

Table of contents

1

Introduction

1.1 Problem description

The investigation of complex geotechnical problems associated with the mechanical response of the underlying geomaterial summarizes the focal point of geotechnical engineering. The Finite Element and the Finite Difference techniques together with the Boundary element method permit the study of geotechnical problems regardless of the complexity involved. The increasing computational efficiency of modern computing has allowed for a more elaborate simulation of problems incorporating the aforementioned numerical techniques.

Constitutive modeling comprises the foundation pillar where the superstructure of numerical methods is based on. The mathematical description of the undergoing mechanical soil response is controlled through the constitutive models. The governing equations dictate the reaction of the soil fabric to alterations in the applied stress field. The constitutive behavioral framework tends to focus on the macroscopic behavior rather than on the microphysics of the geomaterial.

An ensemble of inviscid elastoplastic formulations (e.g. Kavvadas and Amorosi, 2000; Belokas and Kavvadas, 2010) have been proposed to account for the time-invariant mechanical response of both structured and structureless geomaterials. The objective was to investigate the structure degradation and primary and secondary anisotropy effects. It was falsely assumed that the aforementioned mechanisms would prove the key to the onset of slope instability (**Figure 1.1**). Slope stability of natural or man-made slopes (**Figure 1.2**) has been long examined mostly by employing traditional limit equilibrium analyses founded upon the method of slices, assuming a priori considerable knowledge of the failure mechanism. On the other

hand, plastic strain localization and consequent formation of all possible modes of shear banding described by bifurcation theories cannot be employed on real scale basis.

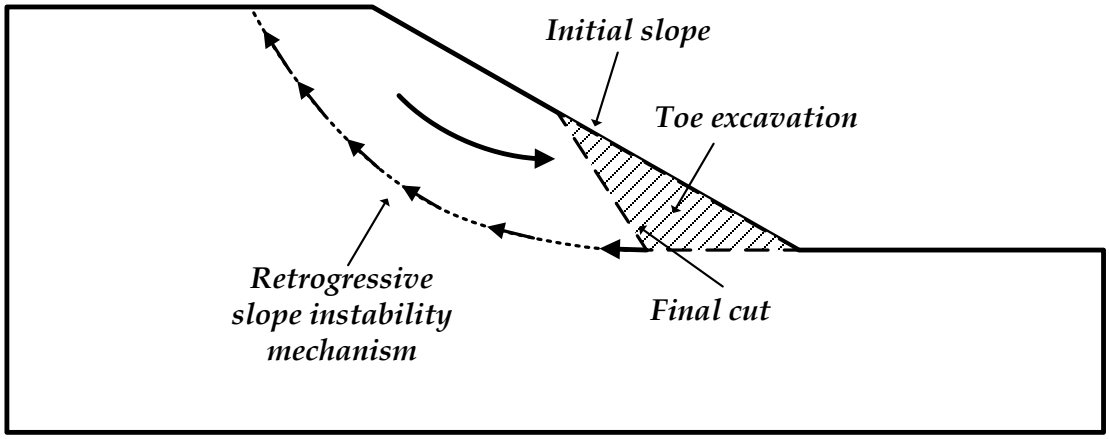

Figure 1.1: Schematic representation of the slope instability problem.

Figure 1.2: Slope instability effects on the infrastructure (California, 2011).

The finite numerical analyses of slope stability indicated that structure degradation effects would not activate the progressive failure mechanism. Hence, additional behavioral features needed to be incorporated to cause failure. In this end, the strength envelope was associated to the plastic strains to introduce significant strain

softening even in the complete absence of structure. However, the additional structural characteristics (e.g. strength envelope degradation with plastic strains, improved structure degradation laws) could not model the onset of retrogressive slope instability by means of a strength envelope reduction due to plastic strains.

This deficiency was attributed to the fact that classical inviscid elastoplastic models for structured soils cannot control the magnitude of plastic strains, as plastic strains are imposed by the physical problem. Thus, it is impossible to generate large-enough plastic strains to cause failure. On the contrary, time-dependent behavior permits the temporal accumulation of inelastic strains, both plastic and viscous, in highly stressed zones. Hence, the necessity arises for a new model that builds on previously developed models for structured soils while at the same time incorporates a complete set of time-dependent characteristics.

1.2 Scope of work

The new idea stems from the fact that the addition of time-dependent characteristics in the sophisticated inviscid elastoplastic formulations can solve this problem, as accumulation of "creep" strains can be independently controlled and reach large-enough values to cause failure. Thus, the combination of time-dependent characteristics and classical structure degradation can lead to the solution of "delayed" failures is slopes (but also in other geotechnical problems).

Hence, the focal point of the current doctoral Thesis is to introduce a new constitutive model that builds on previously developed formulations for structured soils (by accounting for structure degradation and additional structural features, e.g. strength envelope degradation with plastic strains) but at the same time it needs to incorporate an ensemble of time-dependent characteristics. While the model needs to account for the traditional response in oedometer tests exhibiting the strength increase or simulate the stationary (secondary) creep stage in the triaxial apparatus it cannot be bounded to such cases. The model needs to incorporate the capabilities of reproducing the "delayed" failure mechanism in the laboratory shearing tests. The prediction of the retrogressive slope instability mechanism builds on this model characteristic.

The following three steps comprise the pillars around which the current dissertation is founded:

Step 1: Formulation of the mathematical time-dependent behavioral framework integrated in the definition of the new constitutive model. The mathematical formulation incorporates the principles of the overstress postulate proposed by Perzyna (1962 & 1966) while at the same time is founded on the principles of classical elastoplasticity. Structural characteristics emulating structure and strength degradation due to plastic strains are also included within the overlying overstress behavioral framework.

Step 2: Evaluation of the proposed model via a complete set of **numerical analyses**. The deviatoric creep component reveals its devastating effect on soil strength leading ultimately to delayed failure. The statement will be justified through an ensemble of triaxial and shear tests by imposing drained conditions (the assumption of drainage is justified by the very definition of creep postulating drained boundary conditions for the stress state to remain intact). The effect of time dependency is examined in further standard oedometer creep and stress relaxation tests. The proposed model was further **evaluated against experimental measurements**. The sustained strength increase associated with temporal effects was examined in an oedometer test on soft clay (resembling peat). The deleterious effects on soil strength will be revealed through the simulation of a multi-stage shear test in the triaxial apparatus activating the accelerating (another term for tertiary) creep stage on coal, that leads to failure.

Step 3: Application in a slope stability analysis. The developed model will be used in the analysis of slope stability. Analysis shows the aforementioned set of features has been successfully modeled. Thus, the model permits the description of retrogressive failure mechanism in the analyzed slope (**Figure 1.3**).

The proposed time-dependent behavioral framework incorporates the minimum number of constitutive parameters without imposing any limitation in the simulated behavior. The structural characteristics of the proposed model (associated with structure degradation) can be derived easily via experimental measurements similar to Belokas and Kavvadas (2010). As for the set of time-dependent features included in the definition of the governing equations, the secondary compression index and

the Singh-Mitchell (1968) parameters comprise well established quantities in the literature.

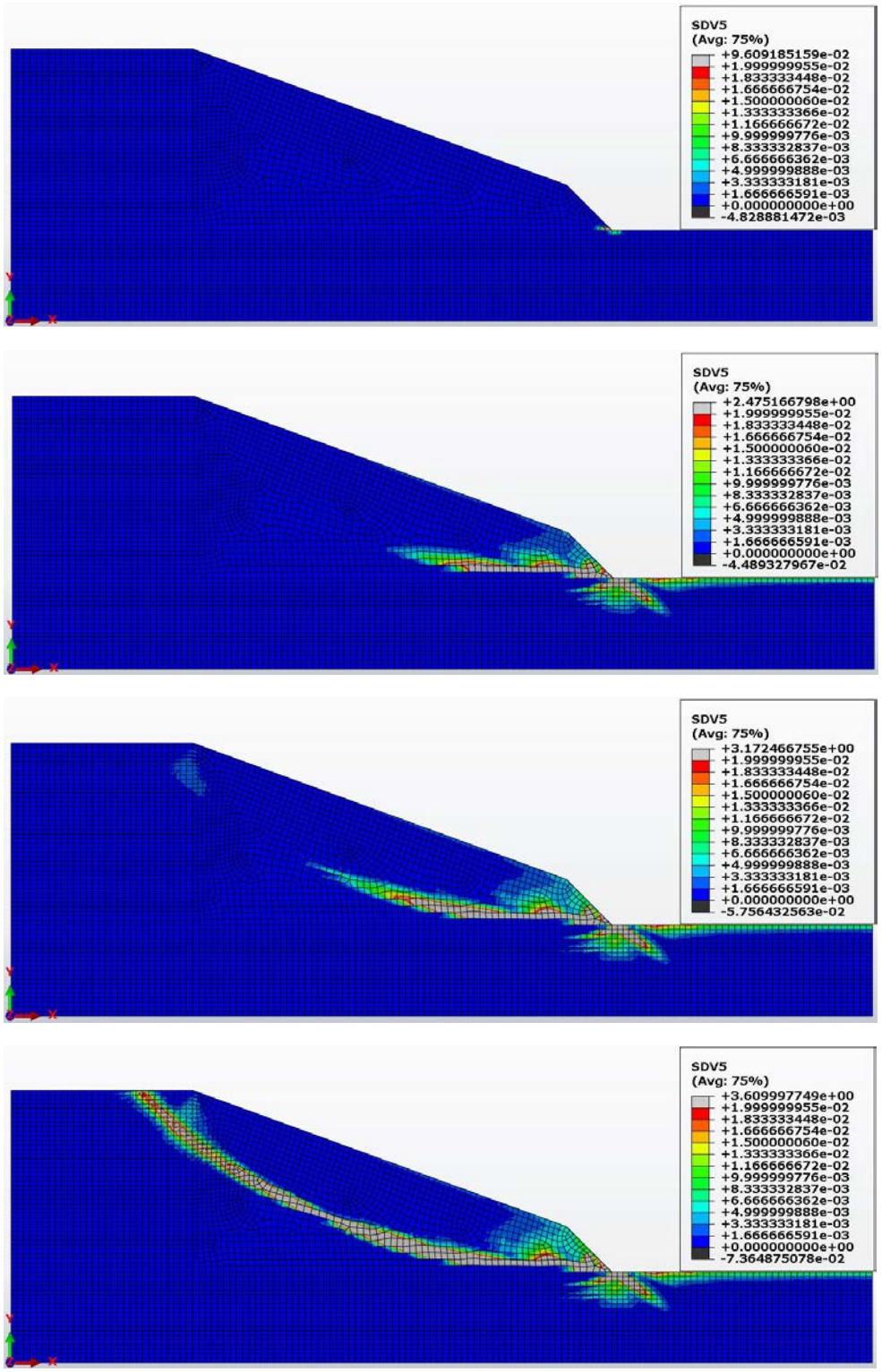

Figure 1.3: Activation of the retrogressive slope instability mechanism portrayed through the evolution of the deviatoric plastic strains ε_q^p (SDV5) at saturated conditions (water) assuming that the strength envelope degrades with time ($t_1<t_2<t_3<t_4$).

The proposed model is composed in FORTRAN to allow for single point testing revealing potential undesired behavioral characteristics. Following the evaluation in single point, the proposed model was incorporated in the Commercial Finite Element Code SIMULIA ABAQUS (via a UMAT subroutine) to allow for a more elaborate evaluation of the time-dependent mechanical response.

The current doctoral Thesis is part of a coordinated effort to construct constitutive models addressing the mechanical response of geomaterials in the National Technical University of Athens, and explore the vast practical implications involved. Relevant research fields address the unsaturated mechanical response of soils leading to soil collapse associated with suction alterations.

1.3 Research Methodology

The dissertation is comprised of two parts. The first section (**Chapters 2** to **4**) focuses on an extensive literature survey of the time-dependent mechanical formulations and associated sophisticated constitutive models and reviews the classical theory of plasticity to highlight the major keypoints. The following section (**Chapters 5** to **8**) addresses the original contribution of the doctoral Thesis. The governing equations are introduced and the proposed model is evaluated against numerical analyses and experimental measurements. Finally, the model is applied in a slope stability problem to investigate the "delayed" characteristics associated with the progressive failure mechanism.

Chapter 2 performs an extensive literature review on the vast load of constitutive formulations associated with the time-dependent characteristics of geomaterials. The constitutive formulations are classified as empirical (primary or secondary semi-empirical) based on the best-fit of experimental measurements (oedometer and triaxial), rheological models (analogical models and integral representation theory) and models founded on the concept of viscoplasticity (are presented extensively in **Chapter 4**). The presented models (with the sole exception of the advanced theories of viscoplasticity) focus solely on the rheological profile of the soil skeleton and neglect alterations in the mechanical behavior associated with consolidation, swelling, structuration/destructuration and saturation. Dynamic effects and temperature dependence elude the focus of the present research and, thus, are not addressed.

Chapter 3 reviews the classical theory of plasticity and highlights the major keypoints. The critical state soil mechanics theory in soils is reviewed and the governing equations of classical elastoplasticity are introduced. Soils are categorized in structured and structureless states and the critical state principle is analyzed. The Intrinsic and Structure Strength envelopes are incorporated to denote the virtual boundaries enclosing all structureless and structured states respectively. Finally, the Plastic Yield Envelope is employed to designate the infinitesimal elastic domain.

Chapter 4 focuses on the most recent advancements in elastoviscoplastic constitutive modeling based on the overstress theory. Some primary constitutive formulations based on overstress are reviewed followed by the most recent state of the art approaches. It is concluded that all approaches focus mainly on the stationary or even the primary creep stage and completely disregard or conveniently ignore the temporal accumulation of inelastic strains, both plastic and viscous, in highly stressed zones which leads to "failure".

Chapter 5 introduces the mathematical framework which builds on previously developed models for structured soils (Kavvadas and Amorosi, 2000; Belokas, 2008) while at the same time includes additional structural characteristics (e.g. a strength envelope degradation with plastic strains) and, mainly, a complete set of time-dependent features. The proposed formulation is founded on the principles of classical elastoplasticity for structured soils integrated within the time-dependent overstress theory (Perzyna, 1962 & 1966). Note that the governing equations are stated in the generalized stress space to allow for direct integration within the numerical code. The proposed expression for the interpolation rule (controlling the plastic hardening modulus) is pressure dependent associated with the phase transformation line projection in the stress hyperplane. The definition addresses the deficiency of Kavvadas and Amorosi (2000) and Belokas (2008) at stress states laying on the dry side. Finally, a hierarchical approach is assumed following the concept by Mroz and Norris (1982), Desai et al. (1986), Pastor et al. (1990) and Gens (1995). Hence, the formulation can degrade into a simple structureless isotropic model lacking all aspects of anisotropy and it can even degenerate into an intrinsic elastoplastic model by further disregarding any undergoing viscous effects.

Chapter 6 evaluates the model through an ensemble of single point and element based (in Finite Element Code SIMULIA ABAQUS) numerical analyses. The scope is to investigate the elastoplastic and time-dependent simulated response. Drained triaxial, plane strain and direct simple shear testing of a slightly overconsolidated structureless soil specimen comprise the case studies to be examined. In such cases, the deviatoric component reveals its catastrophic effect on soil strength thus justifying delayed failure. Drained conditions are assumed to account for pure creep postulating drained boundary conditions for the stress state to remain intact. The effect of time-dependency will be further evaluated in standard oedometer creep and stress relaxation tests. Both experimental setups should result in the lateral pressure coefficient increasing to unity, by activating different mechanisms (of the volumetric and the shear inelastic viscous strain).

In **Chapter 7** the proposed model is further evaluated against experimental measurements both in the oedometer and in the triaxial apparatus. The time-dependent response in an oedometer test is examined in a natural soft clay specimen (resembling peat). It is concluded that the simulated response converged to the experimental observations. Selection of the case study was not random considering that the highest discrepancy would prove at such a soft geomaterial. An extensive literature survey revealed only a limited number of publications addressing the drained time-dependent response of clay in the triaxial apparatus with the last one dating back to 1975 (Bishop, 1966; Ter-Stepanian, 1975). The reason lies with the considerable time period required for the specimen to fail in creep (time to failure may exceed 200 days and even reach 1000 days). Hence, the mechanical response is examined in an experimental study of coal in the triaxial apparatus. Delayed failure is portrayed in a specimen subjected to a high shear stress level undergoing a multi-stage creep test. Regardless of any logical approximations made in the definition of the governing equations, the proposed model performed relatively well in all stages of the experiment (including the tertiary creep stage).

Chapter 8 investigates the practical implications of the model. The proposed model is applied in a 2D slope stability analysis via the finite element method. It was concluded that the time-dependent behavior permits the temporal accumulation of inelastic strains (plastic and creep) in highly stressed zones and thus permits the description of progressive failure in the analyzed slope. The analyses show that the

proposed model has the capabilities to predict delayed failure of a slope by triggering tertiary creep and a retrogressive slope instability mechanism. The failure surface would propagate from the toe backwards and uphill while at same time another slip line originating from the crest would transition downwards to unite with the primal. The slope fails at the time when the two segments unite to form the final slip surface. The progressive failure mechanism is associated inextricably to the presence of water in the slope without which failure is located solely along the toe.

The doctoral Thesis is concluded in **Chapter 9** by reviewing the main keypoints of the doctoral thesis and posing recommendations for future research.

2

Time dependent behavior of soils

2.1 General

Time dependent behavior has been the focal point of scientific research for many decades. Natural soils tend to exhibit transformations in their material fabric associated with time-dependent phenomena. Thus, creep can be defined as the time dependent behavioral trend of a solid material under constant loading conditions. In such sense, the fundamental problem can be summarized in reproducing a general framework emulating the macroscopic behavioral trend.

Numerous approaches have lead to a vast load of constitutive models in the literature associated with the time dependent behavior of soils. Focusing on representing different aspects of the same phenomenon researchers tend to shed light from different views by each focusing on creep, stress relaxation, rate dependence or accumulated effects. The constitutive formulations can be classified as empirical (primary or secondary semi-empirical) models based on the best-fit of experimental measurements (oedometer and triaxial), rheological models (analogical models and integral representation theory) and models founded on the concept viscoplasticity.

The present chapter addresses the necessity of a comprehensive review of the aforementioned models and their basic characteristics, advantages and shortcomings. The models to be presented hereafter (with the sole exception of the advanced theories of viscoplasticity) focus solely on the rheological profile of the soil skeleton and neglect alterations in the mechanical behavior associated with consolidation, swelling, structuration/destructuration and saturation. Dynamic effects and

temperature dependence elude the focus of the present research and thus will not be addressed or summarized.

Next, the constitutive formulations to be presented have been classified as follows:

- **Empirical Models**: Experimental measurements stemming from creep, stress relaxation and constant strain rate tests are employed to derive curve fitting based constitutive relations. The models are usually formulated in an analytical expression or in its differential form. Depending on boundary and loading conditions the aforementioned expressions tend to vary thus leading to their inherent limitation. Such empirical expressions regardless of their shortcomings can be employed as base models in the formulation of advanced viscoplastic constitutive relations or for calibration purposes of those.
- **Rheological Models**: Such formulations tend to describe uniaxial conditions in a rather elegant analytical solution. They are usually comprised of elementary elements (springs, dashpots, sliders) manipulated (in series or in parallel) as to allow for a more accurate replication of the overall time dependent mechanical behavior. The engineering theories of creep present another form of rheological models (addressing the time dependent behavior of concrete and metals) which allows for a more direct introduction of the analytical constitutive equation. Once again, such representations can act as basis for a more elaborate and advanced viscoplastic constitutive model.
- **General Theories**: General three-dimensional theories (usually programmed in finite element or finite difference codes) comprise the keystone of the time dependent behavioral constitutive framework. These formulations are not limited to specific loading or boundary conditions. The most widely employed general theories in the literature are Perzyna's overstress theory and the Non-Stationary Flow Surface (NSFS) theory.

2.2 Empirical Models

The empirical models can be expressed in either simple analytical solutions or in their differential form. The constitutive relations are based on observations on experimental data derived from laboratory (creep, stress relaxation, constant rate) tests. On the downside however, their simplicity is bounded by their inherent

limitation of addressing solely specific boundary and loading conditions. Such models tend to be used as a starting point for the development of more advanced constitutive formulations. Empirical models can be subdivided in primary and secondary.

The primary empirical models are simplified elegant analytical formulations stemming from the curve fitting of experimental measurements. Limited as they are to given boundary and loading conditions, they have the advantage of describing consistently the mechanical behavior at hand. This means that creep, stress relaxation and constant strain rate tests cannot be captured in a single expression.

The secondary semi-empirical formulations are a simple combination of multiple primary models aiming to reconstruct a rather general theory addressing more aspects of the phenomenon.

2.2.1 Primary empirical constitutive formulations

The empirical relations to be analyzed hereafter are:

- **The semi-logarithmic creep law**: The constitutive relation described as semi-logarithmic creep law is based on observations made by careful examination of the secondary compression process in standard oedometer tests (which impose one-dimensional deformation on the soil sample).

  The mechanical behavior associated with creep is a combination of its volumetric and deviatoric component characteristics. Results on oedometer tests tend to reveal the effect of creep on the volumetric component of strain, illustrated in **Figure 2.1**.

  The secondary compression coefficient can thus be defined as follows:

$$C_{ae} = \frac{\Delta e}{\Delta \log(t)} \tag{2.1}$$

  The secondary compression coefficient $C_{a\varepsilon}$ may also be given in terms of the vertical deformation undertaken ε_z. In this case, the logarithmic relation describing the dependence of the vertical displacement on time is defined as:

$$\varepsilon_z = C_{a\varepsilon} \cdot \log\left(1+\frac{t}{t_0}\right) = (1+e_i)\cdot\psi\cdot\ln\left(1+\frac{t}{t_0}\right) \tag{2.2}$$

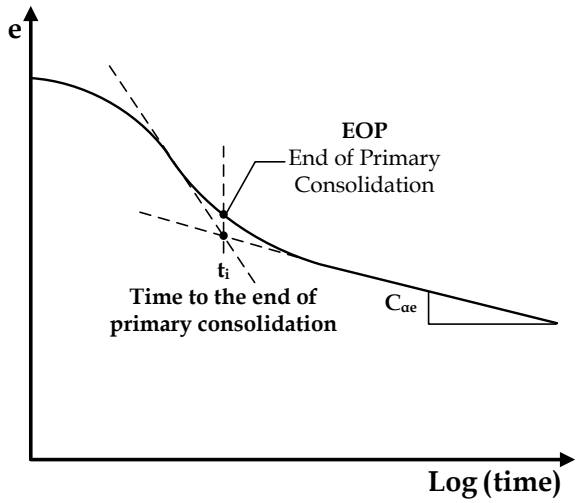

Figure 2.1: Secondary compression coefficient C_{ae} in standard oedometer test**.**

The expression above employs the void ratio at the end of primary consolidation e_i. Parameter ψ is the projection of the secondary compression coefficient $C_{\alpha e}$ in the e-ln$t$ space:

$$\psi = \frac{C_{ae}}{\ln 10} \tag{2.3}$$

The void ratio can be expressed as a function of time as follows:

$$e = e_i - C_{ae} \cdot \log\left(\frac{t}{t_0}\right) = e_i - \psi \cdot \ln\left(\frac{t}{t_0}\right) \mid t \geq t_0 \tag{2.4}$$

One of the major issues arising however is the determination of the reference time t_0. The main concern is the starting point of time at which the volumetric creep strain component begins to accumulate. It is undeniable that creep strains tend to accumulate during primary consolidation thus affecting the dissipation of the excess porewater pressure.

Mesri and Choi (1985) stated that the reference time should be considered as the end of primary consolidation. The aforementioned statement however, raises an issue in clayey soils of whether the reference time should vary with drainage length and soil thickness. According to Mesri and Choi's postulate the creep strains are assumed to be negligible during the state of primary consolidation and are therefore disregarded. Such statement however, fails to consider the case of soft clays and organic materials where the creep potential appears to be dominating the overall mechanical response even during primary consolidation.

Thus, the reference time should be considered solely as an intrinsic parameter characteristic of a given soil, as has been suggested by Leroueil et al. (1985), Bjerrum (1967) and Yin (1999). Thus, t_0 is independent of drainage conditions and thickness of the deposit.

Reference time in such sense possesses another more robust and physical meaning. Regardless of its geological history, it strikes as odd or even ludicrous to assume that one could predict the geotechnical properties of the original deposit much more the exact geological transformations undertaken during the last geological periods. Hence, all physical and mechanical properties extracted from the laboratory tests or in-situ measurements correspond to a rather "newly" formed soil deposit. Regardless of all chemical bonding, biological alterations and mechanical transformations undertaken the soil formation is a snapshot of its geological history revealing information only for the present. Thus, the reference time of such a deposit should be considered as the time of soil extraction. In simple words, the End of Primary Consolidation (EOP) t_i and the reference time t_0 are one and the same and equal to the time measurement employed (1sec, 1min, 1 day, etc). Furthermore, creep tends to accumulate even during the process of primary compression.

- **Bjerrum's approach:** Bjerrum (1967) presented the concept of "time lines" based on results addressing the time dependent behavior of normally and slightly over-consolidated clays incorporating the aforementioned logarithmic creep law by focusing on settlements.

  Based on observations on oedometer creep tests, Bjerrum stated that there is a family of parallel curves in the e - $\log(\sigma'_v)$ diagram corresponding to different duration of applied loads (**Figure 2.2**), the "time lines".

  A careful examination of **Figure 2.2** reveals the importance of the preconsolidation pressure denoted $\sigma'_{z,p}$ in Bjerrum's theory. The value of the preconsolidation pressure depends on the considered time line. Thus, different time lines account for different equilibrium relations holding true after different time periods of sustained loading. Hence, the young NC (Normally Consolidated) clay deposit reveals an active preconsolidation pressure $\sigma'_{z,p0}$ coinciding with the active vertical effective stress $\sigma'_{z,0}$. However, assuming that the vertical effective stress is kept intact throughout a period of

1000 years, the clay medium tends to compress with time, being subjected to secondary compression. The aged NC clay (regardless however if it is no longer being regarded as NC but rather as an overconsolidated clay with an OCR analogous to the time period subjected to secondary compression) reveals a considerably different preconsolidation pressure of $\sigma'_{z,p1}$. In other words, the decrease in void ratio builds up the soil strength, thus increasing the preconsolidation pressure.

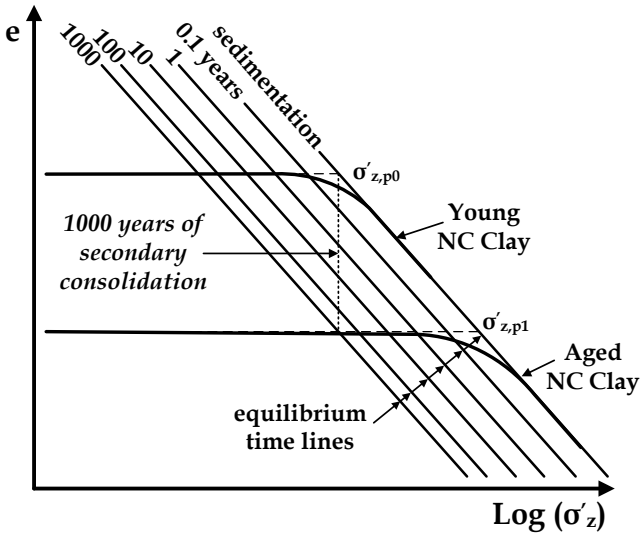

Figure 2.2: Compressibility by accounting for the geological history of a young and aged normally consolidated clay medium after Bjerrum (1967).

The semi-logarithmic creep law was incorporated in Bjerrum's approach by Garlanger (1972) as follows:

$$e = e_0 - C_r \cdot \log\left(\frac{\sigma'_{z,p}}{\sigma'_{z,0}}\right) - C_c \cdot \log\left(\frac{\sigma'_z}{\sigma'_{z,p}}\right) - C_{ae} \cdot \log\left(\frac{t_0 + t}{t}\right) \tag{2.5}$$

In the expression above the void ratio e has been defined as a function of the initial void ratio, e_0, the vertical preconsolidation pressure, $\sigma'_{z,p0}$, the initial vertical effective stress, $\sigma'_{z,0}$, the current effective stress, σ'_z, time t and the reference time t_0.

The ratio of preconsolidation pressure at time t normalized with respect to the initial pressure $\sigma'_{z,p0}$ of the young NC clay reveals the age dependency illustrated in **Figure 2.3** and is given in the following form:

$$\frac{\sigma'_{z,pt}}{\sigma'_{z,p0}} = \left(\frac{t}{t_0}\right)^{\frac{C_{ae}}{C_c - C_r}} \tag{2.6}$$

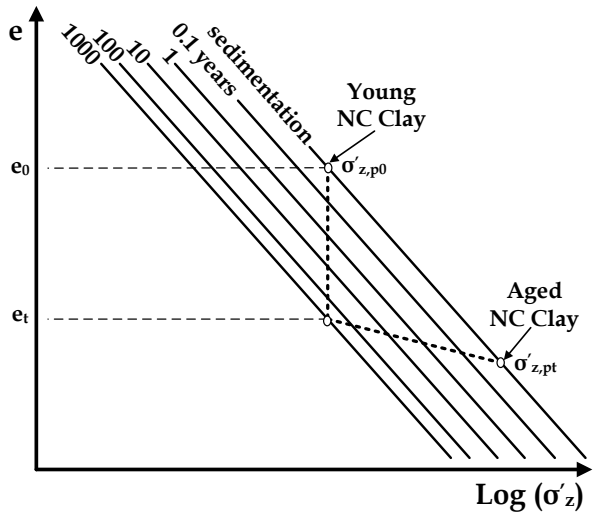

Figure 2.3: Age dependency after Bjerrum (1967).

The ratio $C_{ae}/(C_c-C_r)$, where C_c is the virgin compression index and C_r the recompression index, resembles the parameter m' ($m' = C_{ae}/C_c$) assuming that the recompression index could be neglected. Parameter m' comprises a well established quantity in the literature (Mesri and Godlewski, 1977).

- **The Singh - Mitchell creep model**: Singh and Mitchell (1968) proposed a model based on observations on specimens subjected to undrained triaxial creep. This model describes creep effects in shearing modes and thus it is fundamentally different than the secondary compression model described above.

  Results of shearing in the triaxial apparatus either drained or undrained (regardless whether the stress is not kept constant throughout the process thus not representing pure creep process) tend to produce rather different conceptual mechanical behavior once subjected to different levels of imposed stress, as can be seen in **Figure 2.6**.

  A careful examination of the shear strain - time diagram reveals the undergoing creep stages triggered at different shear stress levels:

  - **primary** or **transient creep:** in this stage the strain rate decreases with time;
  - **secondary** or **stationary creep:** in this stage the strain rate is constant; and
  - **tertiary** or **acceleration creep:** in this stage the strain rate increases with time thus leading to failure attributed to creep.

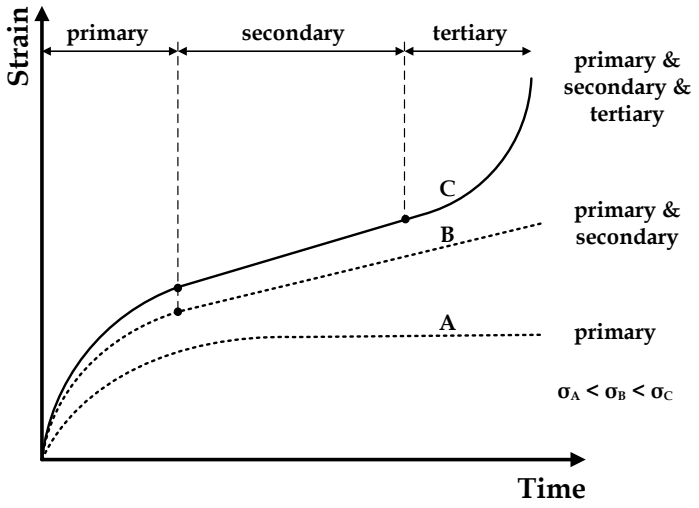

Figure 2.4: Definition of creep stages in shear based on observations on triaxial creep laboratory tests at different stress levels.

The Singh-Mitchell original criterion addresses adequately the stage of secondary creep and at no point can it emulate tertiary creep. The primary creep stage is considered of limited interest but is formulated regardless considering the necessity for a smooth transition towards the stationary strain rate in the analytical formulation below:

$$\dot{\varepsilon} = \frac{\partial \varepsilon}{\partial t} = A \cdot e^{a \cdot D} \cdot \left(\frac{t_0}{t} \right)^m \tag{2.7}$$

In the expression above the deviatoric creep strain rate is expressed as a function of time based on observations from undrained triaxial laboratory measurements, by incorporating three parameters *A*, *m* and *a*. *D* is defined as the ratio $D = q / q_{\text{FAIL}}$, where *q* is a measure of the shear stress and q_{FAIL} the corresponding value at failure (**Figure 2.5**).

Parameter *A* controls the measure of the deviatoric creep strain component by accounting for the chemical composition of the soil and structure (stemming from both bonding and stress history). Parameter *a* portrays the stress intensity effect on creep rate while parameter *m* controls the tempo of strain rate increase with time.

The validity of the aforementioned expression is limited to shear stress intensities ranging from $0.1 \leq D \leq 0.6 \div 0.9$. A careful examination of the expression above (expression (2.7)) reveals a significant shortcoming once the

stress level D drops below 0.1. In this end, Mitchell et al. (1968) published a slight modification of the original formulation (2.7). The modification was proposed rather to extend the validity in regions closer to null values of the shear stress level than to account for higher stress intensity levels that could potentially lead to creep failure (Aristorenas, 1992). Note that the model cannot predict the tertiary creep stage. The revised constitutive relation can be formulated as follows:

$$\dot{\varepsilon} = \frac{\partial \varepsilon}{\partial t} = 2 \cdot A \cdot \sinh\left(a \cdot D\right) \cdot \left(\frac{t_0}{t}\right)^m \tag{2.8}$$

The hyperbolic sinusoidal function may not always provide accurate predictions at low stress levels ($D \leq 0.1$) but has the advantage of providing a smooth transition towards the stationary creep stage and proves invaluable in terms of numerical programming (by eliminating the discontinuity).

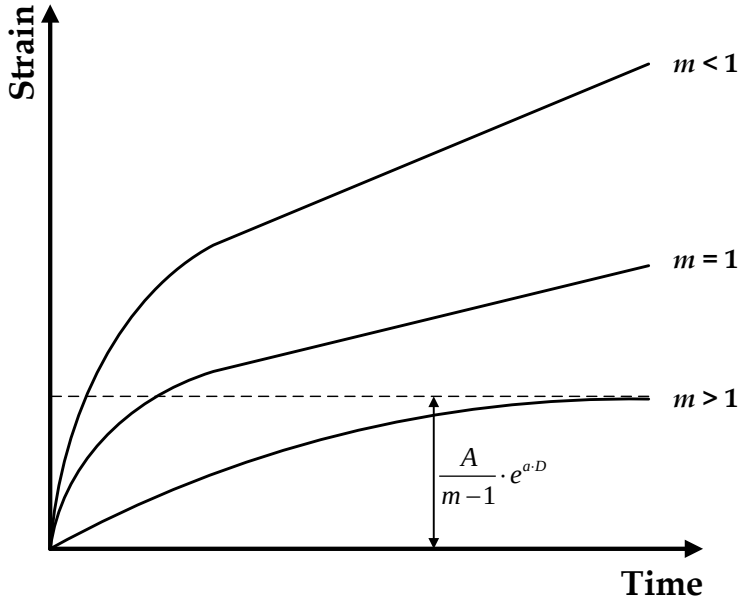

Figure 2.5: Creep strain paths for different values of the exponential factor m predicted by the Sing & Mitchell (1968) constitutive relation.

- **The Lacerda - Houston relaxation model:** The proposed model by Lacerda and Houston (1973) addressed the problem of stress relaxation under shear, based on observations on laboratory tests mainly on clay. The formulation incorporates the well established Singh-Mitchell (1968) parameters.

  Laboratory measurements on N.C. San Francisco bay mud, kaolinite, Monterey sand and Ignacio Valley clay subjected to shear stress relaxation

were employed to clarify several aspects of the time-dependent behavior. It was stated that the normalized deviatoric stress (with respect to its initial value q_0) had the tendency to decay in a linear fashion with respect to the logarithm of time, excluding an initial part where strong nonlinearities tend to be present (**Figure 2.6**).

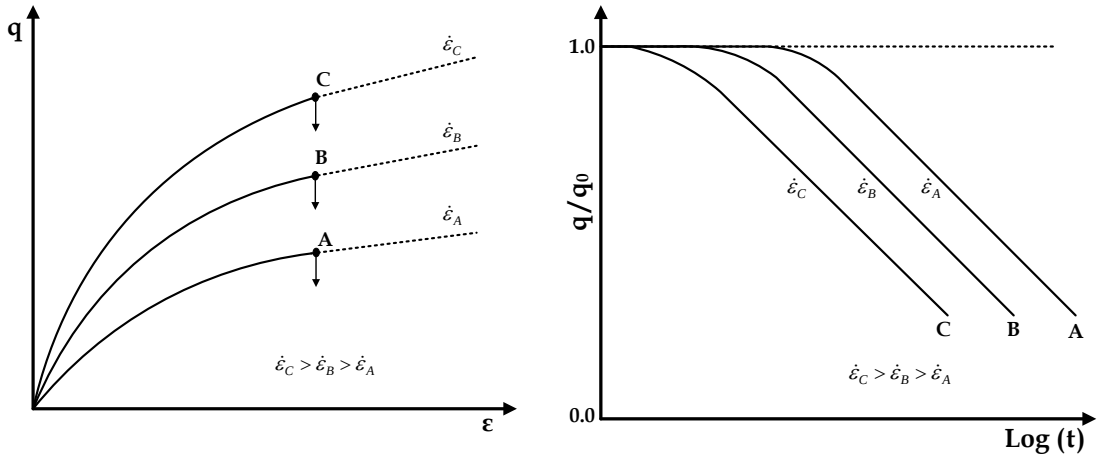

Figure 2.6: Schematic results on clay specimens subjected to stress relaxation: a. stress relaxation diagram at different levels of deviatoric stress and b. corresponding normalized deviatoric stress as a function of the logarithm of time after Lacerda and Houston (1973).

Lacerda and Houston proposed a linear expression connecting the deviatoric stress with the logarithm of time, with a cutoff depending on the reference period t_0:

$$\frac{q}{q_0} = 1 - s \cdot \log\left(\frac{t}{t_0}\right) \;\mid\; t \geq t_0 \tag{2.9}$$

The above expression tends to predict a deviatoric stress decrease for times greater than t_0. Reference time t_0 stands for the time at the initiation of the stress relaxation process and is dependent on the soil characteristics (soil type etc.) and the strain rate. Parameter s depicts the inclination of the stress relaxation line in the q/q_0 versus logarithm of time plot, where q_0 stands for the initial shear stress level imposed and q is the relaxed value of the shear stress. Furthermore, the inclination s can be expressed as a function of the Singh - Mitchell (1968) parameters as follows:

$$s = \frac{2.3 \cdot (1-m)}{a \cdot D_0} \tag{2.10}$$

The expression above holds true for values of the Singh - Mitchell exponential factor $m < 1$ (**Figure 2.5**). D_0 stands for the initial mobilized stress level at $t = t_0$. Lacerda and Houston's model appears to be limited to one-dimensional conditions since it lays on the assumption of the Singh-Mitchell criterion holding true. Furthermore, the expression portrayed in equation (2.10) fails to converge to a final relaxation value thus continuing to degrade gradually to null.

- **The strain rate approach:** Leroueil et al. (1985) assumed a unique relation associating the current effective stress σ'_z to the vertical strain ε_z, assuming that a constant strain rate $\dot{\varepsilon}_z$ is imposed. It was further suggested that the overall mechanical behavior could be described fully by first defining the variation of preconsolidation pressure as a function of the strain rate $(\sigma'_{z,p} = f(\dot{\varepsilon}_z))$ and the effective vertical stress as an expression of the vertical strain ($\sigma'_z = \sigma'_{z,p} \cdot g(\varepsilon_z)$).

  Thus, the strain rate can be defined as a function of the vertical effective stress and the strain rate as follows:

$$\dot{\varepsilon}_z = f^{-1}\left(\frac{\sigma'_z}{g(\varepsilon_z)}\right) \tag{2.11}$$

The graphical representation of the aforementioned expressions is portrayed in **Figure 2.7**.

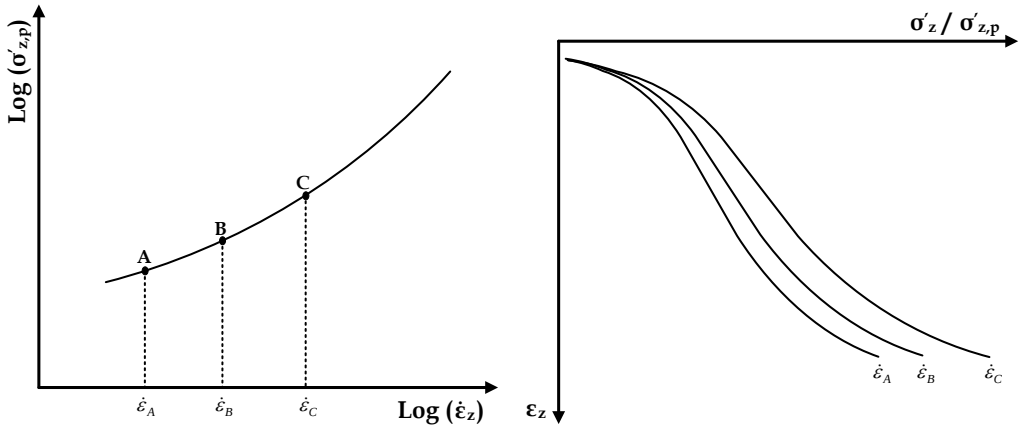

a. b.

Figure 2.7: Stress - strain - strain rate relation based on the Leroueil (1985) approach: a. preconsolidation pressure is expressed as a function of logarithm of strain rate and b. normalized effective vertical stress versus strain curves subjected to various strain rate levels.

The strain rate approach allows for both creep and stress relaxation to be considered within the one-dimensional constitutive framework. Furthermore, the portion of vertical strain employed in the expressions above represents solely the viscoplastic component. Thus, the total strain needs to be deconvolved in an elastic and a viscoplastic component, prior to introducing the aforementioned approach to account for the viscoplastic portion. The formulation addresses solely the mechanical time-dependent response of normally consolidated clays.

2.2.2 Secondary semi-empirical constitutive formulations

The secondary semi-empirical relations are a simple combination of multiple primary models aiming to reconstruct a rather general theory addressing more aspects of creep. The constitutive formulations to be analyzed in this section are:

- **Kavazanjian and Mitchell's concept:** Kavazanjian and Mitchell (1977) proposed a multi-axial stress-strain-time constitutive relation to account for creep.

  The total strain was decomposed in an instantaneous portion and a delayed part, representing creep. The delayed part was further decomposed in a volumetric and a deviatoric component.

  For the volumetric component ε_v the semi-logarithmic creep law was employed:

$$\dot{\varepsilon}_v = \frac{C_{a\varepsilon}}{\ln(10)} \cdot \frac{1}{t} \tag{2.12}$$

  The aforementioned expression incorporates the secondary compression coefficient in terms of the vertical strain.

  As for the deviatoric creep component the Singh-Mitchell constitutive relation was employed. Considering that expression (2.7) refers to the first principal axis ε_1 (in other words the axial strain) the deviatoric strain rate $\dot{\varepsilon}_q$ may be calculated from the axial strain in triaxial conditions as follows:

$$\dot{\varepsilon}_q = \dot{\varepsilon}_1 - \frac{1}{3} \cdot \dot{\varepsilon}_v \tag{2.13}$$

The axial strain rate in triaxial conditions denoted $\dot{\varepsilon}_1$ is portrayed in equation (2.7).

- **Tavena's approach:** Tavenas et al. (1978) proposed a concept in which the creep deformations could be decomposed in a volumetric, ε_v, and a deviatoric component, ε_q, each described by an individual Singh-Mitchell relation given below:

$$\dot{\varepsilon}_v = B \cdot f\left(\sigma'_{ij}\right) \cdot \left(\frac{t_0}{t}\right)^m \tag{2.14}$$

$$\dot{\varepsilon}_q = A \cdot g\left(\sigma'_{ij}\right) \cdot \left(\frac{t_0}{t}\right)^m \tag{2.15}$$

Expressions $f(\sigma'_{ij})$ and $g(\sigma'_{ij})$ are a function of the effective stress σ'_{ij}. Parameters *A* and *B* control the measure of deviatoric and volumetric creep components respectively while *m* governs the rate of the strain rate decrease. In the aforementioned expressions (2.14) and (2.15) the same exponential parameter *m* is incorporated to describe the volumetric and the deviatoric creep components alike. Tavenas et al. further proposed that expressions $f(\sigma'_{ij})$ and $g(\sigma'_{ij})$ are stress functions associated with the yield surface.

Sekiguchi (1984 & 1985) proposed that the ratio of the volumetric over the deviatoric component could be expressed as a new stress function:

$$\frac{\dot{\varepsilon}_v}{\dot{\varepsilon}_q} = \frac{f\left(\sigma'_{ij}\right)}{g\left(\sigma'_{ij}\right)} = h\left(\sigma'_{ij}\right) \tag{2.16}$$

$h(\sigma'_{ij})$ should not be considered as a soil characteristic, but depends on the material properties.

- **Yin and Graham's approach:** Yin and Graham (1996) incorporated Bjerrum's principle and the strain-rate approach in the formulation of a one-dimensional model. In such fashion, the time-dependent behavior of both normally consolidated and overconsolidated clayey soils subjected to a variety of loading and boundary conditions (creep, stress relaxation and constant strain rate tests) can be addressed.

The model is founded upon namely four pillars, visualized in **Figure 2.8**:

a. Equivalent time and time line. Based on the Yin and Graham hypothesis, lines corresponding to the same equivalent time t_e are characterized as time lines. Equivalent time defines the time required to evolve from the reference time line (t_e=0) to the subjected value of strain ε'_z and vertical effective stress σ'_z. For a normal consolidated sample of clay subjected to oedometer testing the equivalent time coincides with the duration of loading increment. On overconsolidated samples however, the equivalent time may be considerably different (higher) depending on the value of the overconsolidation ratio (OCR). Each equivalent time line can be associated uniquely to a single creep strain rate. Thus, the larger strain rates correspond to the minimum equivalent times and vice versa. Equivalent times below the reference time are considered as positive (t_e>0) while the lines laying above it are regarded as negative (t_e<0).
b. Reference time line can be defined as the equivalent time line at which the equivalent time is set to null.
c. Instant time line is the line defined by instantaneous loading response of the soil skeleton. The strains are assumed to lay on the elastic region.
d. Limit time line is the quasi-static boundary when the mechanical behavior appears to be time independent.

The mathematical formulation of the Yin and Graham model is illustrated here below:

$$\dot{\varepsilon}_z = \frac{\kappa}{\nu}\cdot\frac{1}{\sigma'_z}\cdot\dot{\sigma}'_z + \frac{\chi}{\nu\cdot t_0}\cdot\exp\left[-\left(\varepsilon_z-\varepsilon_{z0}\right)\cdot\frac{\nu}{\chi}\right]\cdot\left(\frac{\sigma'_z}{\sigma'_{z0}}\right)^{\frac{\lambda}{\chi}} \tag{2.17}$$

The expression incorporates the initial vertical strain, ε_{z0}, the initial effective vertical stress σ'_{z0}, the projection of the recompression index in the e-ln(σ) space, denoted κ, parameter λ representing the projection of the virgin compression index in the e-ln(σ) space, creep parameter χ and intrinsic time parameter t_0.

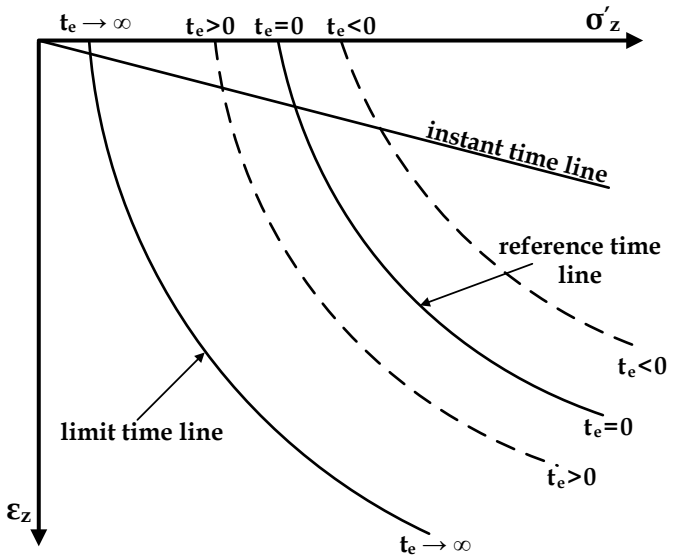

Figure 2.8: Graphical representation of the Yin and Graham (1996) model incorporating the instant time line, reference and limit time lines as well as positive and negative time lines.

2.3 Rheological models

Rheological models were originally developed to describe the time-dependent behavior of metals. Considering that the temperature effect in such materials is of crucial importance attributing to the creep characteristics of the material fabric, it needs to be accounted for within the formulation of the constitutive framework. Historically, rheological models addressing the time-dependent behavior of geomaterials are an extension of the rheological models developed for fluids, gases, metals and even concrete. Although natural soils tend to exhibit significant differences from metals qualitatively they share common rheological properties.

The constitutive behavioral framework of such models is formulated generally to account for one dimensional boundary and loading conditions. The governing equations are expressed in analytical or differential forms and extension to three-dimensional conditions is relatively simple.

Rheological models, despite any lack of finesse, provide an insight to the rheological transformations undergoing throughout the phenomenon and may provide simple and robust mechanisms to capture the macro viscous behavior in its essence.

The rheological behavioral frameworks to be analyzed hereafter may be classified as follows:

- **Analogical and mechanical models**: Such formulations are comprised of simple elementary analogs (springs, dashpots, sliders) manipulated in such a fashion (in series or in parallel) as to allow for an accurate replication of the overall time-dependent mechanical behavior.
- **Integral representation approach**: The integral representation approach is also known as the hereditary principle. This concept is founded on the assumption of a memory function capturing the history dependence of strains (assuming creep behavior is of interest) or stresses (if stress relaxation is assumed).

Furthermore, this section may include phenomenological engineering theories. Such formulations tend to describe the time dependent behavior exhibited in concrete, ice and metals. The constitutive formulations portraying the time dependence are given directly in simple analytical expressions. Phenomenological theories appear to be similar to the empirical relations and can be easily be mistaken for such. They tend however to describe creep characteristics at states below the yield state. The empirical formulations for soils on the other hand need to address the plastic stress states. The phenomenological engineering theories may classified as follows:

a. Total strain approach: The viscous strain ε^c is given as a function of time t and imposed stress σ, $\varepsilon^c = f(\sigma) \cdot g(t)$.
b. Time hardening approach: The viscous strain rate $\dot{\varepsilon}^c$ may be expressed as a function of time t and imposed stress σ, $\dot{\varepsilon}^c = f(\sigma) \cdot g(t)$.
c. Strain hardening approach: The viscous strain rate $\dot{\varepsilon}^c$ is formulated as a function of stress σ and accumulated viscous strain ε^c, $\dot{\varepsilon}^c = f(\sigma) \cdot g(\varepsilon^c)$.

Such formulations tend to describe uniaxial conditions in a rather elegant analytical solution.

2.3.1 Analogical and mechanical constitutive formulations

There is an ensemble of analogical models in the literature. However, they are all comprised of elementary material analogs combined either in series or in parallel. Hookean (visualized by a spring), Saint - Venant's (visualized by a slider) and Newtonian model prove to be the foundation pillars in which all analogical models

are based upon. The aforementioned models may be combined either in series or in parallel depending on the addressed time dependent behavior.

Even though the mechanical analogs tend to be one dimensional, the constitutive equations may be generalized to account for three dimensional conditions of loading or boundary.

Analogical models tend to prove reasonable results for the most boundary and loading conditions they are addressing despite any approximations made in the simulated behavior. Next, the three elementary material models (Newtonian, Hookean, Saint - Venant's) will be analyzed along with some more advanced behavioral analogs such as Maxwell's, Kelvin - Voigt's, Burgers' and Bingham's.

Note that the Hookean spring and the Newtonian dashpot could be manipulated to account for any nonlinearities sustained and the Saint -Ventant's slider may be transformed to account for hardening based on the plasticity theory (Christensen and Wu, 1964; Murayama and Shibata, 1966).

- **Newton's elementary model:** The first elementary model was proposed by Newton (1967) in describing the laws of motion of an ideal viscous fluid and is known as Newtonian fluid. Newton assumed a linear relation between the flow rate and flow resistance. Here follows the mathematical formulation:

$$\sigma^{\eta} = \eta \cdot \frac{\partial \varepsilon^{\eta}}{\partial t} = \eta \cdot \dot{\varepsilon}^{\eta} \tag{2.18}$$

  In the expression above σ^{η} represents the stress (viscous coincides with the total - the superscripts are included solely for visual purposes), η is the coefficient of viscosity either effective or dynamic and $\dot{\varepsilon}^{\eta}$ stands for the viscous strain rate. In rheological behavioral frameworks the Newtonian fluid analog is accustomed to be portrayed as a viscous element (dashpot). The relation between stress and viscous stress rate and the associated mechanical analog are depicted in **Figure 2.9**.

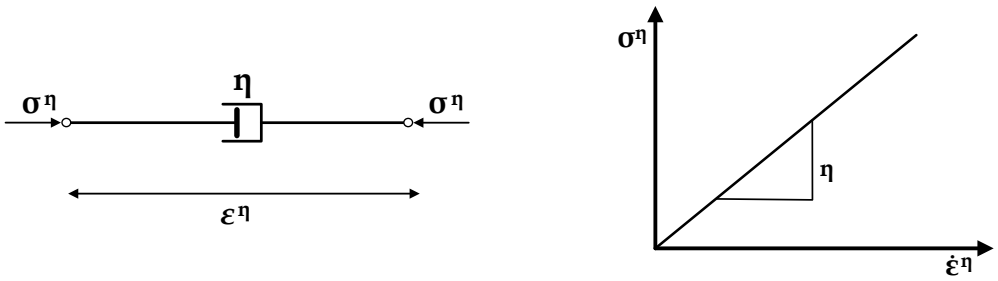

a. b.

Figure 2.9: Newtonian viscous dashpot: a. mechanical analog and b. stress-viscous strain rate schematic diagram.

- **Hookean basic model:** The concept of elasticity is attributed to Hooke. The foundation stone was set in 1660 in a lecture to the Royal society (Hooke et al., 1705). Hooke assumed a linear relation between the stress and strain. Here follows the mathematical formulation:

$$\sigma^e = E \cdot \varepsilon^e \tag{2.19}$$

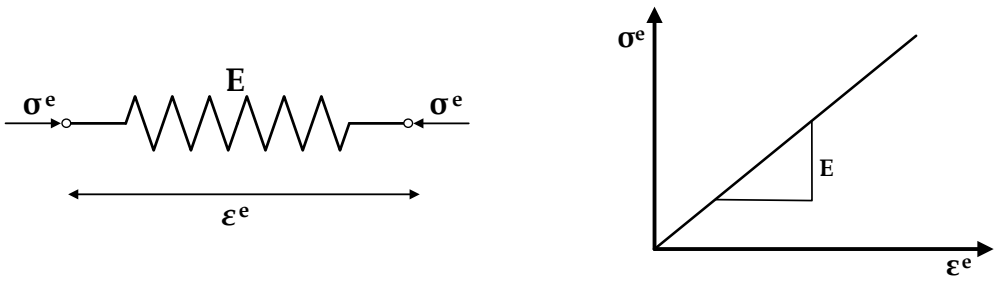

a. b.

Figure 2.10: Hookean elastic spring: a. mechanical analog and b. stress-strain schematic diagram.

In the expression above σ^e represents the elastic stress (elastic stress coincides with the total - the superscripts are included solely for visual purposes), E is the Young's modulus and ε^e stands for the elastic strain. In rheological behavioral frameworks the Hookean analog is portrayed as a spring element. The stress-strain relation and the associated mechanical analog are visualized in **Figure 2.10**.

- **Saint-Venant's plastic model:** Saint-Venant's elementary model is founded on the assumption of an ideal perfectly plastic behavior (Saint-Venant, 1855). The mechanical behavior is similar to that of a rigid body on a

rough horizontal surface subjected to a horizontal force while the interface can be simulated by Coulomb's dry friction law. Once the load exceeds the yield (limit) stress the undergoing deformation tends to infinity. Here follows the mathematical formulation by employing the Macaulay brackets:

$$\left\langle \sigma - \sigma_y \right\rangle = \begin{cases} \sigma - \sigma_y & | \ \sigma \geq \sigma_y \\ 0 & | \ \sigma < \sigma_y \end{cases} \tag{2.20}$$

In the expression above σ_y represents the yield stress. In rheological behavioral frameworks the Saint-Venant's mechanical analog is accustomed to be represented by a slider. The stress-strain relation and the associated mechanical analog are portrayed in **Figure 2.11**.

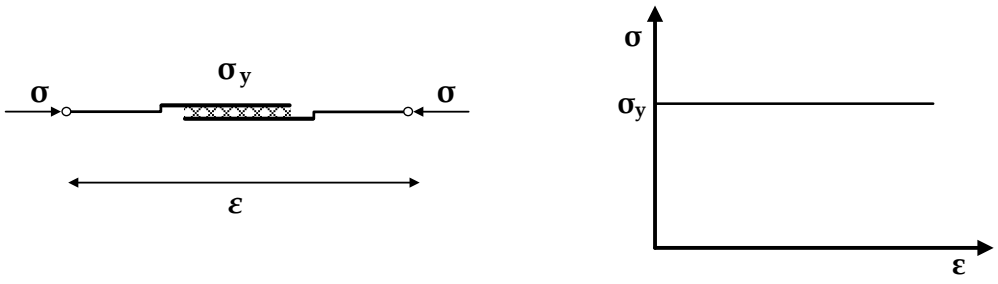

a. b.

Figure 2.11: Saint-Venant's plastic slider: a. mechanical analog and b. stress-strain schematic diagram.

Maxwell's analogical model: The analogical models are simple manipulations of the three elementary material analogs, the Newtonian viscous dashpot, the Hookean elastic spring and the Saint-Venant's plastic slider. Maxwell's viscoelastic model incorporates an elastic spring and a viscous dashpot connected in series (Maxwell, 1868; Havel, 2004; Fortsakis, 2012).Assuming that the system is subjected to some sort of stress, then immediately after the initiation of loading the elastic spring should deform. On the other hand, the viscous dashpot would portray no change in the undergoing strain. With evolving time however, the dashpot should undertake certain pressure by reacting to the imposed pressure. Here follows the mathematical formulation:

$$\varepsilon = \frac{\sigma_0}{E} + \frac{\sigma_0}{\eta} \cdot t \tag{2.21}$$

In the expression above σ_0 represents the imposed stress (either normal or shear), E is the Young's modulus (assuming that shear stress was applied it would have to be replaced with the shear modulus G), η stands for the coefficient of viscosity either effective or dynamic and t is the time. The stress and strain-time relations and associated mechanical analog are summarized in **Figure 2.12**.

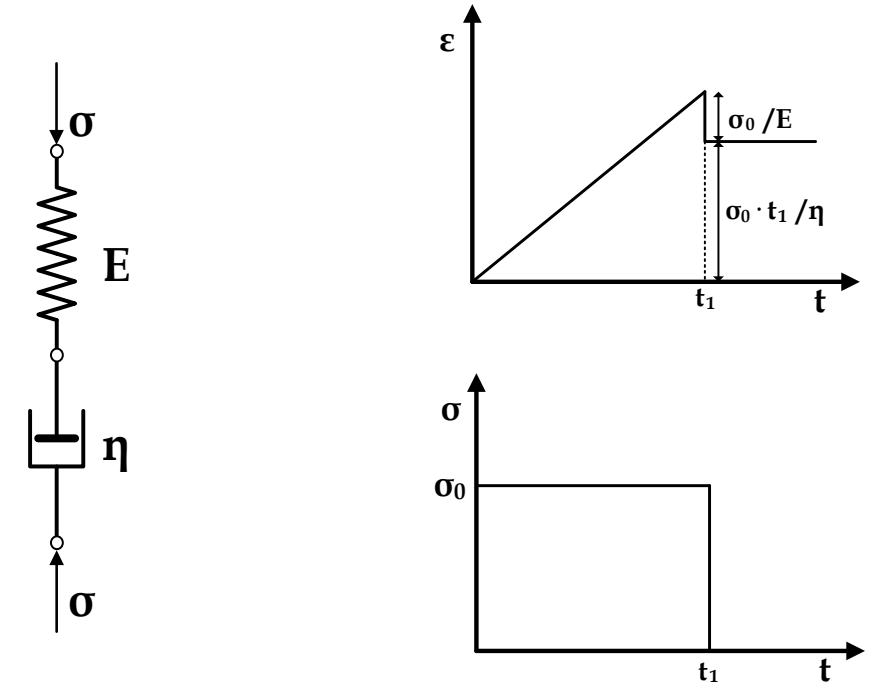

a. b.

Figure 2.12: Maxwell's rheological viscoelastic model: a. mechanical analog and b. stress-strain schematic diagram.

- **Kelvin-Voigt's analogical model:** Kelvin-Voigt's or simply Voigt's viscoelastic solid model incorporates an elastic spring and a viscous dashpot connected in parallel (Kramer, 1996; Fortsakis, 2012) . The elastic spring and the viscous piston may deform in conjunction and at the same extent. In other words there is no instantaneous response to any stress increment undertaken (normal or otherwise). Here follows the mathematical formulation:

$$\varepsilon = \frac{\sigma_0}{E}\left[1-\exp\left(-\frac{E}{\eta}\cdot t\right)\right] \tag{2.22}$$

In the expression above σ_0 represents the imposed stress (either normal or shear), E is the Young's modulus (assuming that shear stress was applied it

would have to be replaced with the shear modulus *G*), η stands for the coefficient of viscosity either effective or dynamic and *t* is the time. The stress and strain diagrams as a function of time and the associated mechanical analog are illustrated in **Figure 2.13**.

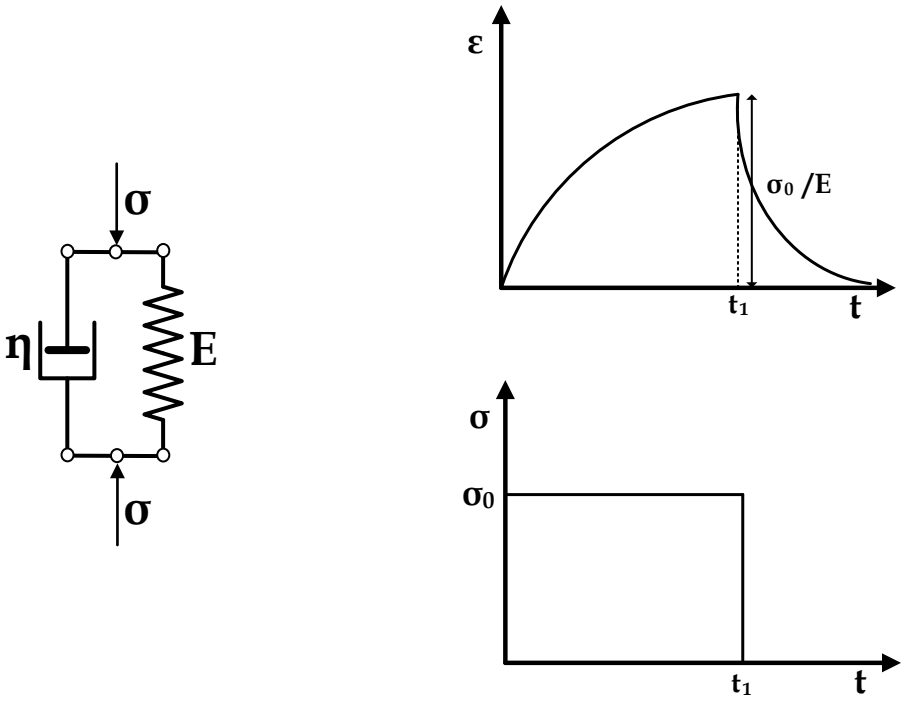

a. b.

Figure 2.13: Kelvin-Voigt's rheological viscoelastic solid model: a. mechanical analog and b. stress-strain schematic diagram.

- **Burgers' analogical formulation:** Burgers' viscoelastic model incorporates a Kelvin-Voigt and a Maxwell model connected in series (Burger, 1948). Here follows the mathematical formulation:

$$\varepsilon = \frac{\sigma_0}{E_2} + \frac{\sigma_0}{E_1}\left[1 - \exp\left(-\frac{E_1}{\eta_1}\cdot t\right)\right] + \frac{\sigma_0}{\eta_2}\cdot t \qquad (2.23)$$

In the expression above σ_0 represents the imposed stress (either normal or shear), E_1 and E_2 are the Young's moduli of the springs (assuming that shear stress was applied they would have to be replaced with the shear moduli *G*), η_1 and η_2 stand for the coefficients of viscosity (effective or dynamic) and *t* is the time. The stress and strain diagrams as a function of time and the associated mechanical analog are depicted here below (**Figure 2.14**).

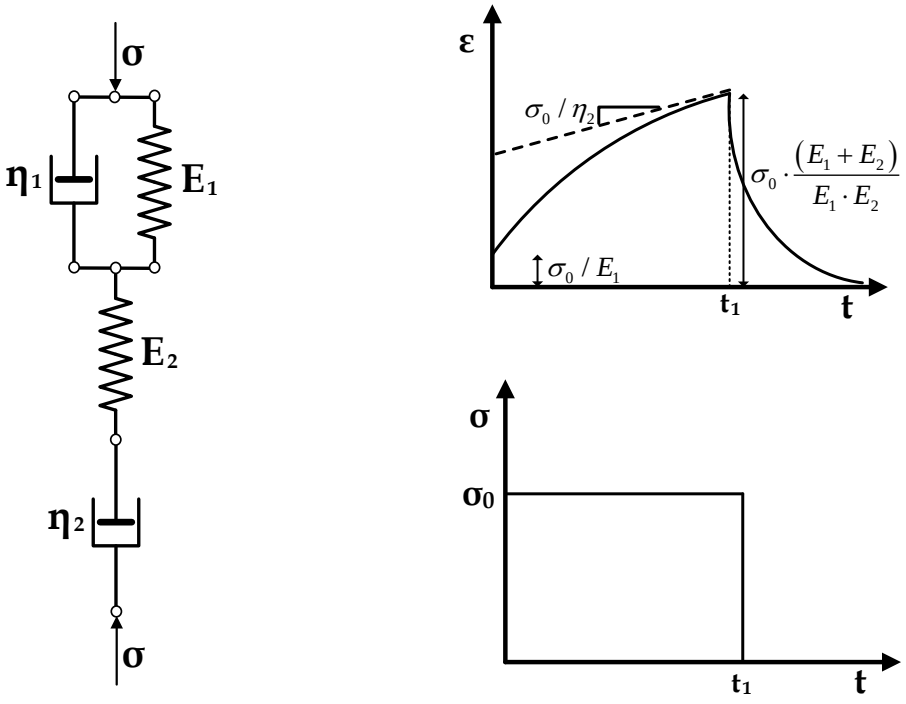

a. b.

Figure 2.14: Burgers' viscoelastic analogical model: a. mechanical analog and b. stress-strain schematic diagram.

- **Bingham's analogical model:** Bingham's viscoplastic rheological model incorporates a Newtonian viscous dashpot and a Saint-Venant's plastic slider connected in parallel (Bingham, 1922). Here follows the mathematical formulation:

$$\sigma = \sigma_y + n_B \cdot \dot{\varepsilon} \tag{2.24}$$

In the expression above σ_y represents the Saint-Venant's yield stress and η_B is the "Bingham viscosity" (another term for "Bingham viscosity" is "Bingham flow coefficient"). The Bingham viscosity is not a physical property of the soil but a parameter computed by curve fitting. The stress as a function of the viscous strain rate plot and the associated mechanical analog are depicted hereafter (**Figure 2.15**).

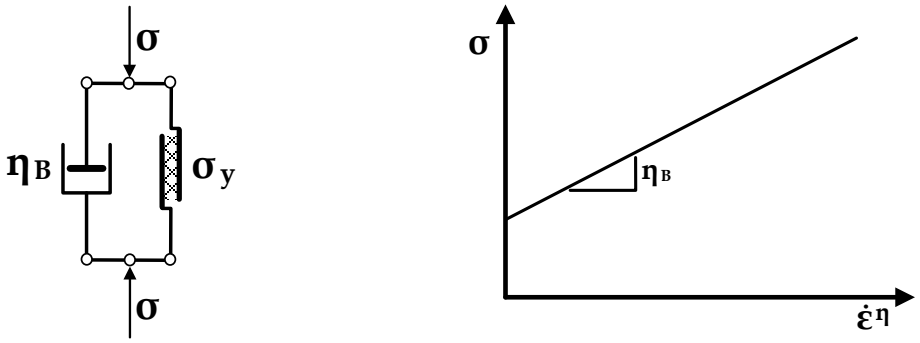

a. b.

Figure 2.15: Bingham's viscoplastic rheological model: a. mechanical analog and b. stress-strain schematic diagram.

2.3.2 Integral representation theory

Integral representation approach is founded on the assumption that the current strain $\varepsilon(t)$ can be computed by integration over the entire loading history (e.g. Murad et al., 2001; Saleeb et al. , 2001; Abuzeid et al., 2010). The integral over all stress changes even the infinitesimal ones on any current time *t* shall provide the overall accumulated strain. Another term for the integral representation approach is hereditary theory. The simplest form of the integral representation theory is based on viscoelasticity, which is nothing more than a generalization of the rheological analog. However, the hereditary approach is possible to incorporate nonlinear behavioral characteristics corresponding to a generalization of the aforementioned rheological engineering theories. The main shortcoming however making it unsuitable for use in soil mechanics application stems from the great number of laboratory measurements required for the calibration. 28 tests (Feda, 1992) are required to describe solely a uniaxial experiment by means of the nonlinear integral representation theory (for the triaxial case are required six times as many).

2.4 General Theories

Numerical analyses are being employed more and more nowadays in geotechnical engineering to investigate complicated mathematical problems. General theories of viscoplasticity represent the governing equations by incorporating principles of plasticity. Such theories are not limited to specific boundary and loading conditions but tend to address potentially all possible stress and strain paths. The time dependent behavioral framework allows for simulation of creep, stress relaxation

and strain rate dependency. More sophisticated models incorporating the principles of this approach may also include aspects of the theory of plasticity (allowing for the plastic component of strain to be defined separately through the theory of plasticity from the elastic and viscoplastic).

The general theories can be classified into three categories:

a. Elastoviscoplastic models based on the Perzyna's overstress theory;
b. Elastoviscoplastic models based on the Non Stationary Flow Surface theory;
c. others.

2.4.1 Perzyna's overstress theory

The overstress theory is attributed to Perzyna (Perzyna, 1962 & 1966; Olszak and Perzyna; 1966). Perzyna in essence combined the classical theory of elastoplasticity with the time-dependent behavior of metals. The new theory developed would be called elastoviscoplasticity and incorporates the elastoplasticity solely as a specific case.

2.4.1.1 Mathematical Formulation

Perzyna's overstress theory was based on experimental measurements and assumes a "static surface" in the effective stress space, comprising the virtual limit separating the elastic from the viscoplastic regime. The static surface is generally different than the employed loading yield surface. The loading yield surface $f(\boldsymbol{\sigma})=0$ is defined by the state of imposed stress and in the general case does not coincide with the strength envelope (neither the intrinsic envelope nor the structure strength envelope to be analyzed in section 3.9).

The state of stress $\boldsymbol{\sigma}$ may cross the static surface at the end of a given loading increment. The aforementioned statement summarizes the essence of Perzyna's overstress theory. By crossing the static surface the stress path oversteps the viscoplastic boundary thus accumulating viscoplastic deformations (**Figure 2.16**).

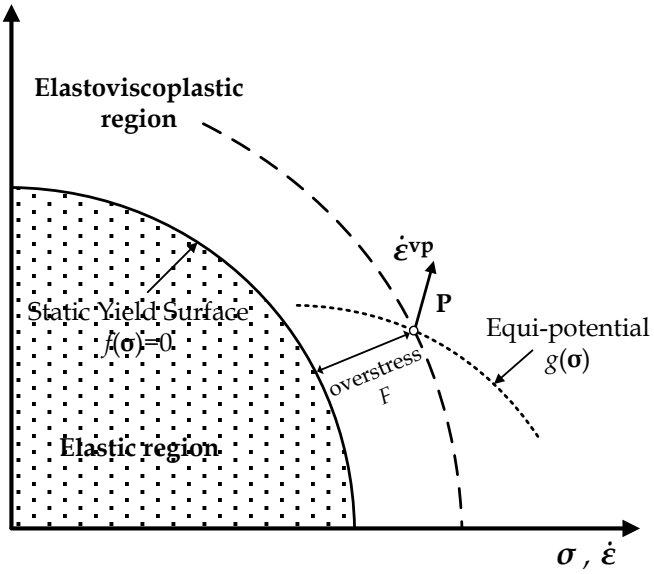

Figure 2.16: Schematic representation of Perzyna's overstress theoretical framework and definition of static yield surface and stress regions (after Debernardi, 2008).

The static yield surface (or yield surface for short) comprises the virtual boundary separating:

- the elastic region inside which the yield function *f* produces negative values, $f(\boldsymbol{\sigma}) < 0$. Within this region the deformations are purely elastic and the constitutive expression describing the overall mechanical behavior can be expressed as follows:

  $$\dot{\boldsymbol{\sigma}} = \boldsymbol{C}^e : \dot{\boldsymbol{\varepsilon}}^e \tag{2.25}$$

  In the expression above superscript *e* is employed to denote the elastic incremental component of strain tensor $\dot{\boldsymbol{\varepsilon}}^e$ and the elastic stiffness matrix $\boldsymbol{C}^e$. The inner product is denoted using the symbol ":".

- the elastoviscoplastic regime laying on the outer bound of the elastic, corresponds to positive values of the yield function $f(\boldsymbol{\sigma}) > 0$. In this case, Perzyna assumed a deconvolution of the strain increment in an elastic and a viscoplastic component portrayed hereafter:

  $$\dot{\boldsymbol{\varepsilon}} = \dot{\boldsymbol{\varepsilon}}^e + \dot{\boldsymbol{\varepsilon}}^{vp} \tag{2.26}$$

  In the expression above the superscripts *e* and *vp* are employed to denote the elastic and viscoplastic components of incremental strain respectively. The

viscoplastic incremental strain tensor employed in equation (2.26) can be computed through the following expression:

$$\dot{\boldsymbol{\varepsilon}}^{vp} = \gamma \cdot \Phi\left(F\right) \cdot \frac{\partial g}{\partial \boldsymbol{\sigma}} \tag{2.27}$$

Where γ is the fluidity parameter influenced (not equal) by the material viscosity, $\Phi\left(F\right)$ represents the viscous nucleus, F is the overstress function, g portrays the viscoplastic potential function and $\boldsymbol{\sigma}$ is the stress tensor.

The overstress function F is a measure of the distance between the stress state and the static yield surface. The viscoplastic potential function g controls the direction of viscoplastic strain rates (and incremental strains). Finally, the overstress function dominates the measure of viscoplastic strain rates through the viscous nucleus.

2.4.1.2 Hardening of the yield surface

In the general case the yield surface is nothing but static. It can evolve throughout time and stress by translating and deforming as a consequence of the accumulated viscoplastic strains. Hardening of the yield surface may be associated with:

a. the measure of deviatoric viscoplastic strains $\varepsilon_q^{vp} = \sqrt{\frac{2}{3} \cdot \left(\boldsymbol{e}^{vp} : \boldsymbol{e}^{vp}\right)}$, where $\boldsymbol{e}^{vp}$ stands for the deviatoric viscoplastic strain tensor ($\boldsymbol{e}^{vp} = \boldsymbol{\varepsilon}^{vp} - \frac{1}{3}\left(\boldsymbol{\varepsilon}^{vp} : \boldsymbol{I}\right)\boldsymbol{I}$) and $\boldsymbol{I}$ is the identity tensor.
b. the viscoplastic work denoted $W^{vp} = \int_0^t \left(\boldsymbol{\sigma} : \dot{\boldsymbol{\varepsilon}}^{vp}\right) d\tau$.

In the original formulation by Perzyna (1962, 1966) the yield function hardening was assumed to be controlled by another two functions namely $\overline{f}\left(\boldsymbol{\sigma}\right)$ and $\kappa\left(\boldsymbol{\varepsilon}\right)$:

$$f\left(\boldsymbol{\sigma}, \boldsymbol{\varepsilon}\right) = \frac{\overline{f}\left(\boldsymbol{\sigma}\right)}{\kappa\left(\boldsymbol{\varepsilon}\right)} - 1 \tag{2.28}$$

2.4.1.3 Definition of viscous nucleus

The viscous nucleus governs the measure of the viscoplastic strain rates thus controlling the time-dependent behavior of a material. In essence, the viscous

nucleus provides null values when the state of stress lays inside the yield surface (no creep). The viscous nucleus needs to meet yet another criterion; it must be a monotonic function of the overstress *F*.

The viscous nucleus may be formulated as follows:

a. in a linear relation $\Phi(F)=\frac{F}{F_0}$, where F_0 is a reference unit.

b. in a power relation $\Phi(F)=\left(\frac{F}{F_0}\right)^n$, where F_0 is a reference unit and n a constitutive parameter. This form is adopted frequently in the fitting of experimental measurements (i.e. Nguyen-Minh, 1986).

c. in an exponential relation $\Phi(F)=A\cdot\left\{\exp\left[\left(\frac{F}{F_0}\right)^n\right]-1\right\}$, where F_0 is a reference unit, A and n are constitutive parameters employed.

2.4.1.4 Constitutive models based on the overstress theory

Some of the most widely known overstress models in the literature are summarized below:

a. Lemaitre's overstress model (Boidy, 2000; Debernardi, 2008);
b. Prager's overstress model (Prager, 1949);
c. Cristescu's overstress model (Jin and Cristescu, 1998);
d. Bodner and Partom's (Bodner and Partom, 1975);
e. Adachi and Okano's overstress model (Adachi and Okano, 1974);
f. Adachi and Oka's overstress model (Adachi and Oka, 1982);
g. Zienkiewicz's overstress model (Zienkiewicz et al., 1974 & 1975);
h. Desai and Zhang's overstress model (Desai and Zhang, 1987);
i. Debernardi's overstress model (Debernardi, 2008; Debernardi and Barla, 2009); and
j. Karstunen's overstress model (Yin et al., 2010; Leoni et al., 2008).

Chapter 4 reviews the main characteristics and highlights the original contribution of the most important of the aforementioned models.

2.4.2 Non-Stationary Flow Surface theory (NSFS)

The Non-Stationary Flow Surface (NSFS) theory was introduced by Naghdi and Murch in 1963. In some ways the NSFS conceptual framework resembles that of classical elastoplasticity and can be regarded as an extension of the theory of plasticity to account for the time-dependent phenomena.

The NSFS theoretical framework differs from the classical elastoplasticity in the sense that the yield surface is not a simple function of the stress state and dependent on time invariable state variables alone. It is allowed to evolve with time. Thus, the yield surface is not regarded as "stationary" (certainly not static since hardening may be incorporated for time independent materials). The NSFS theory assumes a yield function of the following form:

$$f\left(\boldsymbol{\sigma}, \boldsymbol{\varepsilon}^{vp}, w(t)\right) = 0 \tag{2.29}$$

In the above expression above $w(t)$ is a time-dependent function.

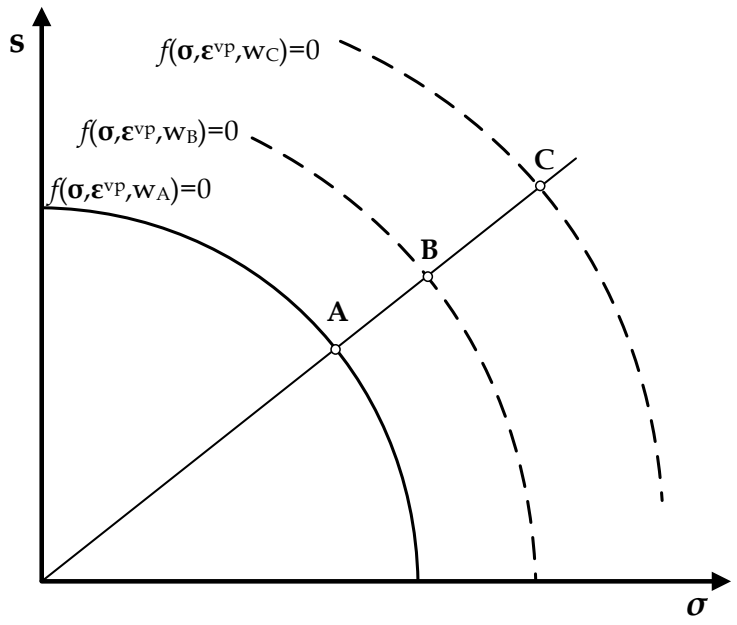

Figure 2.17: NSFS yield surface and stress paths. The elastoviscoplastic behavior simulated by the NSFS theoretical framework even in the case when the viscoplastic strains are kept constant can evolve from point A to C through B or vice versa depending on the simulated behavior by employing function w(t) (i.e. stress relaxation would result in the exact opposite stress path). For an elastoplastic material assuming no change in the plastic strain the stress state would remain exactly the same (i.e. at point A).

One main characteristic of the NSFS theory is that the yield surface is allowed to harden with evolving time even when the viscoplastic strains are kept constant (**Figure 2.17**). This justifies the name of the theory as "non-stationary".

Inside the yield surface the simulated behavior is purely elastic and can be expressed through equation (2.25). The viscoplastic regime is set on the yield surface since no stress state may exceed that. Assuming a loading increment occurs, then the elastoviscoplastic strains tend to accumulate. Similarly to the overstress theory the stress rate tensor may be deconvolved in an elastic and a viscoplastic component by means of equation (2.26).

The viscoplastic strain rate may defined in a way similar to that of elastoplasticity, by employing a potential function *g*:

$$\dot{\boldsymbol{\varepsilon}}^{vp} = \langle \Lambda \rangle \cdot \frac{\partial g}{\partial \boldsymbol{\sigma}} \tag{2.30}$$

The expression above incorporates the non-negative measure of viscoplastic strain denoted Λ inserted in the Macaulay brackets. The Macaulay brackets ensure that the viscoplastic strains accumulate only when the stress state lays on the yield surface. The measure of viscoplastic strain Λ can be determined through the consistency condition (Prager, 1949), similar to the case of classical elastoplasticity:

$$\Lambda = \Lambda_1 + \Lambda_2 = \underbrace{-\frac{\frac{\partial f}{\partial \boldsymbol{\sigma}} : \dot{\boldsymbol{\sigma}}}{\frac{\partial f}{\partial \boldsymbol{\varepsilon}^{vp}} : \frac{\partial g}{\partial \boldsymbol{\sigma}}}}_{\Lambda_1} \underbrace{-\frac{\frac{\partial f}{\partial w} \cdot \dot{w}}{\frac{\partial f}{\partial \boldsymbol{\varepsilon}^{vp}} : \frac{\partial g}{\partial \boldsymbol{\sigma}}}}_{\Lambda_2} = -\frac{\frac{\partial f}{\partial \boldsymbol{\sigma}} : \dot{\boldsymbol{\sigma}} + \frac{\partial f}{\partial w} \cdot \dot{w}}{\frac{\partial f}{\partial \boldsymbol{\varepsilon}^{vp}} : \frac{\partial g}{\partial \boldsymbol{\sigma}}} \tag{2.31}$$

Parameter Λ_1 in the expression above is identical to the measure of plastic strains employed in classical elastoplasticity. Thus, creep and all time-dependent phenomena are included in the definition of Λ_2 multiplier.

The most widely known NSFS models in the literature are depicted below:

a. Matsui and Abe's NSFS model (Matsui and Abe, 1985);
b. Nova's NSFS model (Nova, 1982);
c. Sekiguchi's NSFS model (Sekiguchi, 1984); and
d. Dragon and Mroz's NSFS model (Dragon and Mroz, 1979).

2.4.3 Other Constitutive formulations

In the literature there are an ensemble of models that cannot be classified in any of the aforementioned categories. The most noteworthy formulations are summarized here below:

- The Kaliakin and Dafalias elastoviscoplastic sophisticated model (1990a,b) is probably the most widely known. It incorporates the time dependency and a flow rule similar to that of Perzyna. However, the mathematical formulation tends to introduce an excess of complexity and any real problem application can prove cumbersome.
- The Borja model is comprised of a stress-strain-time relation for cohesive soils addressing the mechanical behavior only in the wet side (Hsieh et al., 1990).
- The subloading surface model by Hashiguchi and Okayasu (2000).
- The Adachi et al. (Adachi et al., 1987; Oka et al., 1994 & 1995) elastoviscoplastic model incorporates memory and internal variables.

2.5 Concluding Remarks

A great number of constitutive formulations have been introduced to account for the time-dependent mechanical behavior of materials. Regardless whether most of the theories originated from material sciences aiming to address metal alloys, steel concrete or ice, they have been extended to account for the viscous behavior of geomaterials. The current chapter addresses the necessity of an extensive survey on the time-dependent constitutive formulations in the literature.

The classification undertaken distinguishes the constitutive formulations in:

a. empirical (primary and secondary semi-empirical) formulations;
b. rheological (analogical models and integral representation theory) models;
c. general theories.

None of the aforementioned constitutive relations however can capture all aspects of the time dependent behavior in situ. Each researcher tends to shed light in the aspect that favors most by neglecting others (creep, stress relaxation, rate dependence or accumulated effects). Hence, it lays on the shoulders of the reader or the designer to adopt the approach that deals best with the loading and boundary conditions at hand.

Aiming to address the time-dependent behavioral response of both structured (resembling stiff soils to weak rocks) and structureless geomaterials (resembling clayey deposits) the main keypoints of the classical elastoplasticity is analyzed next (**Chapter 3**) along with the main characteristics of the aforementioned sophisticated overstress creep models (**Chapter 4**).

3

Plasticity theory for soils

3.1 General

The classical theory of plasticity is used to describe the mechanical elastoplastic behavior of soils. Plasticity theory was originally formulated to account for the inelastic mechanical response of metals and was extended to geomaterials (Drucker et al., 1956). The critical state principles (Roscoe et al., 1963; Schofield and Wroth, 1968) were introduced later, thus leading to a breakthrough in the constitutive formulation of geomaterials, the Cam-Clay model (Roscoe et al., 1963).

Natural media tend to exhibit nonlinear hysteretic mechanical behavior even at low imposed stress levels. Hence, soils tend to portray purely elastic behavior only at extremely low effective stress levels. By exceeding the virtual boundary separating the elastic from the plastic field, the soil fabric tends to yield by accumulating plastic strains. Once the stress state enters the plastic regime then the accumulated strains are no longer retrievable upon removal of the stress increment (the original cause for the plastic deformation).

Aiming to develop a time dependent viscoelastoplastic constitutive framework the foundation stones need to be set sound and solid. For this purpose, the classical theory of plasticity needs to be reviewed and the major keypoints highlighted. All constitutive formulations employing the principles of elastoplasticity are based on the concept of the soil element. Its volume is sufficiently small for the stress distribution to be uniform but at the same time sufficiently large so that the soil may be considered as a continuum medium, rather than a collection of particles. Thus, the constitutive formulations focus on the macroscopic nature of the problem rather than the microphysics of the particulate medium. The overall system behavior is formed

though the ensemble of all soil elements. The classical theory of plasticity in soil mechanics is addressing the mechanical behavior of rate insensitive geomaterials. Thus, following the principles of classical soil mechanics the stress-strain relation may be expressed as a function of the effective stress tensor $\boldsymbol{\sigma}'$ (the dot will be dropped henceforth for simplicity) and the strain tensor denoted $\boldsymbol{\varepsilon}$. All vectors and tensors will be portrayed in bold to distinguish them from the scalar quantities.

3.2 General principles of the incremental plasticity theory for soils

The classical theory of plasticity addressing the mechanical behavior of soils portrays the mathematical framework of the stress-strain relation. The plasticity theory will be described here below in its incremental form. In this sense the increment of strain is comprised of an elastic and an inelastic component, similar to equation (2.26), illustrated hereafter:

$$\dot{\boldsymbol{\varepsilon}} = \dot{\boldsymbol{\varepsilon}}^{e} + \dot{\boldsymbol{\varepsilon}}^{p} \tag{3.1}$$

In the expression above the increment of the total strain tensor $\dot{\boldsymbol{\varepsilon}}$ is formulated as the sum of the elastic strain tensor increment $\dot{\boldsymbol{\varepsilon}}^{e}$ and the plastic strain tensor increment $\dot{\boldsymbol{\varepsilon}}^{p}$. The superscripts *e* and *p* are representative of the elastic and plastic components. The dot symbol is employed solely to denote the incremental nature of the theory rather than the rate dependency since the classical plasticity theory cannot account for the time-dependent behavior of geomaterials.

In the absence of any plastic deformation increment the behavior is classified as elastic and all the incremental strains are reversible upon removal of the infinitesimal stress increment. **Figure 3.1** portrays the elastic and plastic strain components after an unloading cycle. It is noted that the purely elastic region (characterized by the absence of accumulated plastic strains) tends be infinitesimal small (OA part).

This means that at point A the state of stress reaches the yield surface thus entering the plastic regime. Another term employed in the literature to denote the virtual boundary separating the elastic from the inelastic fields is the **Plastic Yield Envelope** (***PYE***) (it will be analyzed in section 3.9 in detail).

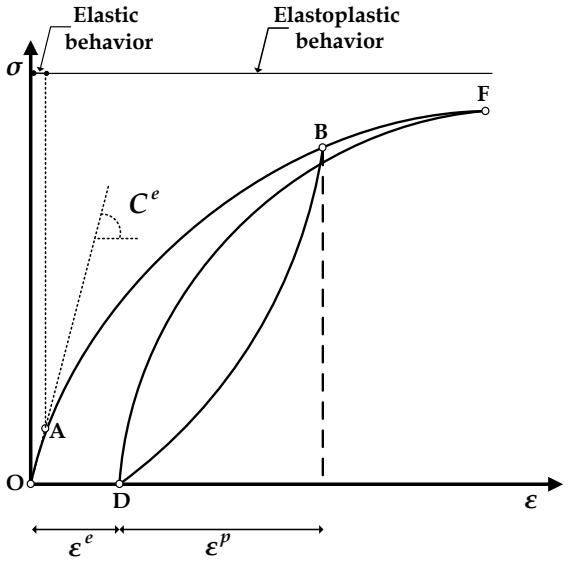

Figure 3.1: Definition of elastic and deviatoric strain components in uniaxial compression.

Furthermore, the concept of the material state employed so extensively includes all aspects influencing and controlling the mechanical response of the soil element. Those aspects may be quantified through the **state variables** controlling:

a. the stress state of the soil element through the stress strain tensor $\boldsymbol{\sigma}$, and are called **stress variables** and
b. the previous history-memory of the soil skeleton and may be described through a series of scalar or even tensorial quantities $\boldsymbol{q}$, called **hardening variables**.

For the material state to change, at least one state variable needs to evolve. Every alteration in the stress or hardening variables, regardless of how small it may be, transforms the material state and shall be called **stressing**. Any change in the hardening variables is called **hardening**. Measures of the accumulated total or plastic strain, the position - size - inclination or shape of *PYE*, the overconsolidation ratio, the porosity, the relative density, the rate of loading are some of the parameters that could potentially be introduced as hardening variables.

In inviscid plasticity, hardening can only be the result of stressing, i.e., there is no hardening without stressing (note: however, there may be stressing without hardening, e.g. in the elastic domain). In viscous plasticity, however, hardening can occur even without stressing or without straining (due to creep/stress relaxation). In inviscid plasticity, stressing usually leads to substantial strain (especially when

loading leads to the accumulation of plastic strains). However, in viscous plasticity, stressing and/or hardening can occur even without a corresponding change in strain.

Loading is defined as any transformation (e.g. change in tractions, other boundary conditions, alterations in temperature or time, in viscous plasticity) that results in alterations in the state variables.

In **rate insensitive (inviscid)** geomaterials, where hardening variables cannot alter without a change in stress, strains can only result from stress changes. Thus, there is a unique relationship between a change in stress and the corresponding change in strain. This means that when a material element (having a state $(\boldsymbol{\sigma}, \boldsymbol{q})$) is subjected to a strain increment $\dot{\boldsymbol{\varepsilon}}$, the resulting changes in stress and hardening variables $(\dot{\boldsymbol{\sigma}}, \dot{\boldsymbol{q}})$ can be uniquely computed. Hence, stressing and hardening can be computed through the theory of plasticity by incorporating the following principles:

- an Elastic Law;
- a Plastic Flow Rule; and
- the Hardening Laws.

In the forthcoming expressions, the stress tensor $\boldsymbol{\sigma} = \sigma \cdot \boldsymbol{I} + \boldsymbol{s}$ shall be portrayed as a function of the volumetric stress (equal to the mean effective stress *p*) σ and the deviatoric stress tensor $\boldsymbol{s}$. The mean effective pressure and deviatoric stress tensor may be formulated as follows:

$$\sigma \left(\equiv p \right) = \frac{1}{3} \left(\boldsymbol{\sigma} : \boldsymbol{I} \right) \tag{3.2}$$

$$\boldsymbol{s} = \boldsymbol{\sigma} - \sigma \cdot \boldsymbol{I} \tag{3.3}$$

The incremental octahedral stress $\dot{\sigma}$ and deviatoric stress tensor $\dot{\boldsymbol{s}}$ may be defined in an exact analogy:

$$\dot{\sigma} \left(\equiv \dot{p} \right) = \frac{1}{3} \left(\dot{\boldsymbol{\sigma}} : \boldsymbol{I} \right) \tag{3.4}$$

$$\dot{\boldsymbol{s}} = \dot{\boldsymbol{\sigma}} - \dot{\sigma} \cdot \boldsymbol{I} \tag{3.5}$$

Furthermore, the strain tensor $\boldsymbol{\varepsilon} = \frac{1}{3}\varepsilon \cdot \boldsymbol{I} + \boldsymbol{e}$ can be decomposed by employing the volumetric strain ε and the strain deviator $\boldsymbol{e}$. The volumetric component of strain and the deviatoric strain tensor may be formulated as follows:

$$\varepsilon = \boldsymbol{\varepsilon} : \boldsymbol{I} \tag{3.6}$$

$$\boldsymbol{e} = \boldsymbol{\varepsilon} - \frac{1}{3}\varepsilon \cdot \boldsymbol{I} \tag{3.7}$$

The incremental expressions of volumetric strain $\dot{\varepsilon}$ and strain deviator $\dot{\boldsymbol{e}}$ can be formulated as follows:

$$\dot{\varepsilon} = \dot{\boldsymbol{\varepsilon}} : \boldsymbol{I} \tag{3.8}$$

$$\dot{\boldsymbol{e}} = \dot{\boldsymbol{\varepsilon}} - \frac{1}{3}\dot{\varepsilon} \cdot \boldsymbol{I} \tag{3.9}$$

The expressions above are given in their tensorial form instead of providing the formulations in the principal stress space. The formulation in tensorial notation is introduced in order to account for a generalized constitutive framework that treats easily all potential stress paths without each time rotating the stress and strain tensors back and forth to the principal stress space. Thus, the constitutive formulations are given straightforward in the generalized stress space comprised of a hyperplane of the octahedral stress σ and the stress deviator $\boldsymbol{s}$.

The constitutive governing equations portray the response of the soil skeleton to infinitesimal alterations in strain. Following Terzaghi's effective stress principle (1936) all quantifiable changes in stress (portrayed in strain and stress resistance) are attributed to alterations in the effective stresses. Hence, all stresses involved are effective. Primes will be dropped for simplicity reasons henceforth.

3.3 Elasticity

The laws of elasticity reviewed here below are addressing the mechanical response of rate insensitive (inviscid) geomaterials. Hence, the effect of certain aspects such as creep or temperature will not be accounted for. A soil element exhibiting linear behavior does not require previous knowledge of the undergoing stress path since there exists a unique mapping from strain to stress and vice-versa. When a loading

increment produces solely elastic strains then the incremental strain tensor is null $\dot{\boldsymbol{\varepsilon}}^p = \mathbf{0}$ and thus no hardening may be introduced through the elastic strains since:

$$\dot{\boldsymbol{\varepsilon}} = \dot{\boldsymbol{\varepsilon}}^e \Rightarrow \dot{\boldsymbol{q}} = \mathbf{0} \tag{3.10}$$

In the literature, there are multiple forms of the elastic law addressing the elastic behavior of geomaterials the most widely employed of which are depicted here below:

- the Cauchy elasticity;
- the hypoelasticity;
- the poroelasticity; and
- the hyperelasticity.

Some of the aforementioned expressions - namely all forms of hypoelasticity, the poroelasticity and some forms of Cauchy elasticity - are not truly elastic (the work along a loading cycle is not null) by thus justifying their characterization as pseudo-elasticities.

In any case the elastic law in its incremental form can be described as follows:

$$\dot{\boldsymbol{\sigma}} = \boldsymbol{C}^e : \dot{\boldsymbol{\varepsilon}}^e \tag{3.11}$$

where $\boldsymbol{C}^e$ is the elastic stiffness matrix, $\dot{\boldsymbol{\sigma}}$ and $\dot{\boldsymbol{\varepsilon}}^e$ are the incremental stress and strain tensors respectively. The stress and strain tensors are 2nd order matrices while the stiffness matrix a 4th order one.

By employing the incremental isotropic and deviatoric components of stress and strain the constitutive formulation (3.11) may be reformed as follows:

$$\dot{\sigma} = K^e \cdot \dot{\varepsilon}^e + \boldsymbol{X}^e : \dot{\boldsymbol{e}}^e \tag{3.12}$$

$$\dot{\boldsymbol{s}} = \boldsymbol{\Psi}^e \cdot \dot{\varepsilon}^e + 2G^e \cdot \dot{\boldsymbol{e}}^e \tag{3.13}$$

In the expression above K^e stands for the elastic bulk modulus, G^e is elastic shear modulus and $\boldsymbol{X}^e$ and $\boldsymbol{\Psi}^e$ are the conjugated stiffness moduli.

In the special case of isotropic elasticity, where there is no association between the isotropic strain and the strain deviator, the constitutive relations can be further simplified (Kavvadas, 1982; Houlsby, 1985) as follows:

$$\dot{\sigma} = K^e \cdot \dot{\varepsilon}^e \tag{3.14}$$

$$\dot{\boldsymbol{s}} = 2G^e \cdot \dot{\boldsymbol{e}}^e \tag{3.15}$$

It is noted that in cases where the stress-strain governing equation is a priori known the incremental form may be computed by simple differentiation of the constitutive equation. Next, we present the major types of elasticity, aside from the hyperelasticity that eludes the purpose of this chapter since it will not be employed in the forthcoming proposed constitutive behavioral framework. Linear elasticity and Cauchy elasticity comprise the simplest forms of elastic law and hence are summarized hereafter. Poroelasticity comprises a special case of elastic law and considering the future implementation in the proposed model in Chapter 5 needs to be reviewed also.

3.3.1 Linear isotropic elasticity

Linear elasticity or Hooke's elastic law was originally proposed by Hooke (1705). The constitutive equation may be formed as depicted in the equation that follows:

$$\boldsymbol{\sigma} = \boldsymbol{C}^e : \boldsymbol{\varepsilon}^e \tag{3.16}$$

In this case, the elastic stiffness matrix $\boldsymbol{C}^e$ is constant. The elastic stiffness tensor portrays the unique transfer function by which the strains may be translated to stresses and vice versa (**Figure 3.2**).

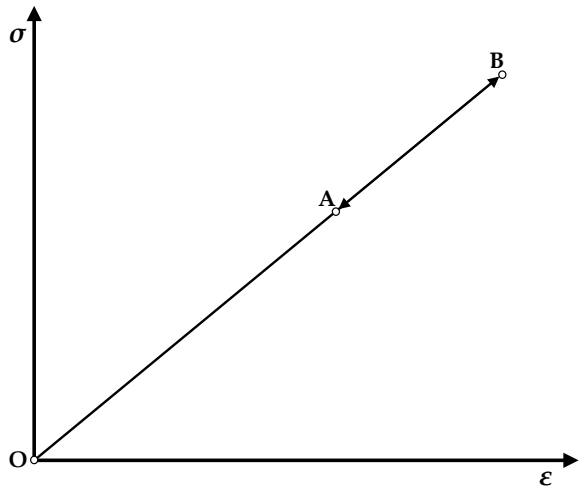

Figure 3.2: Linear elasticity or Hooke's elastic law.

Equation (3.16) in its incremental form may be formulated as expression (3.11).

Assuming that linear elasticity may be defined through the expression (3.14) and (3.15) then the scalar moduli K^e and G^e as well as the tensors $\boldsymbol{X}^e$ and $\boldsymbol{\Psi}^e$ are constant. Special cases of isotropic, orthotropic or cross-anisotropic symmetry denote different forms of linear elasticity. Linear elasticity tends to exhibit limited application to soils and is mainly applied to stiff rocks stressed to yield or failure. However, application to natural media as soils or soft rocks may prove erroneous results and should be avoided.

Isotropic linear elasticity is a 1st order Cauchy elasticity:

$$\boldsymbol{\sigma} = a_1 \cdot \varepsilon \cdot \boldsymbol{I} + a_2 \cdot \boldsymbol{\varepsilon} \tag{3.17}$$

and in its incremental form may be rewritten as follows:

$$\dot{\boldsymbol{\sigma}} = a_1 \cdot \dot{\varepsilon} \cdot \boldsymbol{I} + a_2 \cdot \dot{\boldsymbol{\varepsilon}} \tag{3.18}$$

Where parameter a_1 and a_2 are given as:

$$a_1 = K^e - \frac{2}{3} \cdot G^e \tag{3.19}$$

$$a_1 = 2 \cdot G^e \tag{3.20}$$

By substituting equations (3.19) and (3.20) in (3.18):

$$\dot{\boldsymbol{\sigma}} = \left(K^e - \frac{2}{3} \cdot G^e \right) \cdot \dot{\varepsilon} \cdot \boldsymbol{I} + 2 \cdot G^e \cdot \dot{\boldsymbol{\varepsilon}} = K^e \cdot \dot{\varepsilon} \cdot \boldsymbol{I} + 2 \cdot G^e \cdot \left(\dot{\boldsymbol{\varepsilon}} - \frac{1}{3} \cdot \dot{\varepsilon} \cdot \boldsymbol{I} \right) \Rightarrow$$

$$\dot{\boldsymbol{\sigma}} = K^e \cdot \dot{\varepsilon} \cdot \boldsymbol{I} + 2 \cdot G^e \cdot \dot{\boldsymbol{e}} \tag{3.21}$$

or in terms of the incremental strain tensor:

$$\dot{\boldsymbol{\varepsilon}} = \frac{\dot{\sigma}}{3 \cdot K^e} \cdot \boldsymbol{I} + \frac{\boldsymbol{s}}{2 \cdot G^e} \tag{3.22}$$

In isotropic linear elasticity the bulk and shear moduli may be expressed as functions of the Young's modulus E^e and the Poisson's ratio ν:

$$K^e = \frac{E^e}{3 \cdot (1 - 2 \cdot \nu)} \tag{3.23}$$

$$G^e = 2 \cdot (1 + \nu) \cdot E^e \tag{3.24}$$

3.3.2 Nonlinear elasticity

The mechanical behavior of geomaterials appears to be nonlinear even at extremely low stress levels, even if the strains may be recovered upon removal of the loading increment (Burland, 1989).

It is possible to simulate nonlinear elastic behavior assuming that the stiffness matrix $\boldsymbol{C}^e$ is not constant but can evolve by accounting for alterations in the state variables (i.e. functions of stress or strain). What has also been widely accepted is that the initial elastic modulus is pressure dependent (Wesley, 1990; Allman and Atkinson, 1992; Jardine, 1992; Jamiolkowski et al., 1995; Rampello et al., 1994 & 1997; Kavvadas and Anagnostopoulos, 1998; Kavvadas, 1998; d' Onofrio et al., 1998). Instead of employing a multi-linear approach to overcome the shortcoming of linear approach within the elastic regime it is possible to introduce nonlinear elastic laws. Such realization allows for a continuous evolution of the hardening variables and stiffness moduli. Cauchy elasticity, poroelasticity, hypoelasticity and hyperelasticity are special forms of nonlinear expressions of the elastic law.

3.3.2.1 Cauchy elasticity

In the Cauchy elastic law postulates the existence of a unique relation connecting the stress state with the current strain tensor $\boldsymbol{\varepsilon}$. All polynomial expressions of linear elasticity may be classified as Cauchy elasticities of a given order. The most widely employed expressions of Cauchy elasticity laws are the parabolic or hyperbolic stress-strain relations by Kondner (1963) and Hansen (1963):

$$\boldsymbol{\sigma} = f\left(\boldsymbol{\varepsilon}\right) \tag{3.25}$$

or in terms of strain:

$$\boldsymbol{\varepsilon} = f^{-1}\left(\boldsymbol{\sigma}\right) \tag{3.26}$$

The aforementioned forms of the governing constitutive formulations may be computed through curve fitting of experimental measurements and are thus limited to specific boundary and loading conditions.

The equations above may be expressed in their incremental forms as follows:

$$\dot{\boldsymbol{\sigma}} = \frac{\partial f\left(\boldsymbol{\varepsilon}\right)}{\partial \boldsymbol{\varepsilon}} : \dot{\boldsymbol{\varepsilon}} \tag{3.27}$$

$$\dot{\boldsymbol{\varepsilon}} = \frac{\partial f^{-1}\left(\boldsymbol{\sigma}\right)}{\partial \boldsymbol{\sigma}} : \dot{\boldsymbol{\sigma}} \tag{3.28}$$

However, employing expressions as described through the equations (3.25) and (3.26) (or in their incremental form in (3.27) and (3.28)) is not a necessary condition to ensure truly elastic behavior. It is possible for the work along a full loading cycle to be finite (and therefore not null) and thus the elastic law should be considered as conservative.

3.3.2.2 Poroelasticity

Poroelasticity was originally formulated based on observations on unloading and reloading stress-strain paths subjected to isotropic and uniaxial loading. The governing equation in the v-ln(σ) space is given here below:

$$v = v_0 - \kappa \cdot \ln\left(\frac{\sigma}{\sigma_0}\right) \tag{3.29}$$

where v stands for the current specific volume ($v = 1 + e$), v_0 is the initial specific volume, κ is a constant portraying the inclination in the v-ln(σ) space and σ_0 portrays the initial mean effective stress.

The tangent bulk modulus may be computed through the equation (3.29):

$$\dot{v} = -\kappa \cdot \frac{\partial \ln\left(\frac{\sigma}{\sigma_0}\right)}{\partial \sigma} \cdot \dot{\sigma} = -\kappa \cdot \frac{\dot{\sigma}}{\sigma} \Rightarrow -\dot{\varepsilon}^e \cdot v = -\kappa \cdot \frac{\dot{\sigma}}{\sigma} \Rightarrow \dot{\varepsilon}^e = \kappa \cdot \frac{\dot{\sigma}}{v \cdot \sigma}$$

by considering expression (3.14):

$$K^e = \frac{v}{\kappa} \cdot \sigma \tag{3.30}$$

Hence, the elastic bulk modulus can be expressed as a function of the specific volume and the octahedral stress. Considering that the mean effective stress and void ratio e tends to undergo changes throughout loading the bulk modulus is not constant but is allowed to evolve. The governing equation of poroelasticity tends to predict non-zero values along a full loading cycle and is therefore regarded as conservative. However, it is based on observations on laboratory measurements and has been employed extensively in multiple constitutive formulations founded upon the Cam-Clay (Roscoe et al., 1963) or the Modified Cam-Clay models (Roscoe and Burland, 1968).

Assuming isotropic symmetry of the stiffness matrix, the constitutive equations (3.14) and (3.15) do apply. As for the shear modulus, it may be given by the following expression incorporating the ratio of $\frac{2 \cdot G^e}{K^e}$ as a soil property depending on the Poisson's ratio:

$$G^e = \frac{1}{2} \cdot \left(\frac{2 \cdot G^e}{K^e}\right) \cdot K^e \tag{3.31}$$

3.3.2.3 Hypoelasticity

In the case where hypoelasticity is employed to account for the constitutive elastic behavior the elastic stiffness matrix is defined a priory, thus distinguishing it from all

other expressions of the elastic law. Once again in the case of hypoelasticity the incremental stress-strain relation may be given by means of equation (3.11).

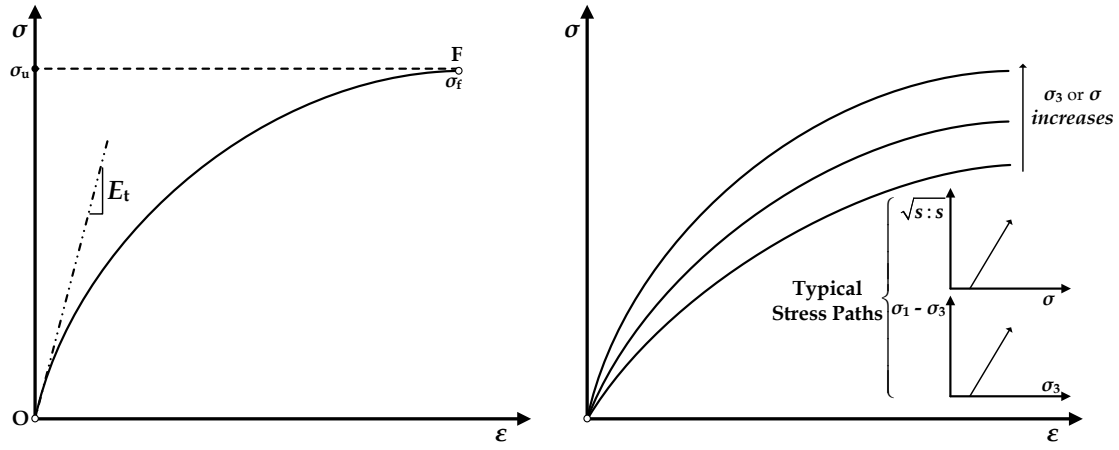

a. b.

Figure 3.3: a**.** Hyperbolic stress-strain hypoelastic law and b. effect of minor principal strain or mean effective stress.

The nonlinear elastic behavior may be introduced assuming a variable elastic stiffness matrix C^e. Thus, it is probable in some cases for the expression of hypoelasticity to prove conservative. Essentially, hypoelasticity is employed to describe monotonic nonlinear hysteretic phenomena through the variable elastic moduli (Desai and Siriwardane, 1984). Such realizations may be portrayed in the tangent Young's modulus by Duncan and Chang (1970) and in the tangent Poisson's ratio by Kulhawy et al. (1969) assuming a hyperbolic stress-strain relationship and by accounting for the effect of lower principle stress σ_3 in the Mohr-Coulomb failure criterion (**Figure 3.3**).

The variable tangent Young's modulus (Duncan and Chang, 1970) and Poisson's ratio (Duncan et al., 1969) formulations are depicted here below:

$$E_t = \left[1 - \frac{R_f \cdot (1-\sin\varphi)\cdot(\sigma_1-\sigma_3)}{2\cdot(c\cdot\cos\varphi+\sigma_3\cdot\sin\varphi)}\right]^2 \cdot K_h \cdot p_a \cdot \left(\frac{\sigma_3}{p_a}\right)^n \tag{3.32}$$

$$v_t = \frac{G - F\cdot\log\left(\frac{\sigma_3}{p_a}\right)}{\left(1-A^2\right)} \tag{3.33}$$

where A may be expressed as follows:

$$A = \frac{\left(\sigma_1 - \sigma_3\right) \cdot d}{K_h \cdot p_a \cdot \left(\frac{\sigma_3}{p_a}\right)^n \cdot \left[1 - \frac{R_f \cdot \left(1 - \sin\varphi\right) \cdot}{2 \cdot \left(c \cdot \cos\varphi + \sigma_3 \cdot \sin\varphi\right)}\right]^2} \tag{3.34}$$

In the aforementioned expressions K_h and n are elastic constants, p_a stands for the atmospheric pressure, $R_f = \frac{\sigma_f}{\sigma_u}$ is the ratio of yield stress over the stress at failure (asymptotic stress), c and φ are the cohesion and friction angle respectively of the Mohr-Coulomb failure criterion. Finally, G, F and d are material constants.

It is also possible to modify the expressions (3.12) and (3.13) by employing the tangential expressions of the elastic stiffness matrices $\boldsymbol{X}_t^e$ and $\boldsymbol{\Psi}_t^e$ (instead of $\boldsymbol{X}^e$ and $\boldsymbol{\Psi}^e$) and the elastic moduli K_t^e and G_t^e (instead of K^e and G^e). In principle, it is rather difficult to account for the interaction-conjugation between volumetric and deviatoric strains. Hence, isotropic symmetry is adopted in reforming the equations (3.14) and (3.15) by accounting for the tangential expressions of the elastic moduli K_t^e and G_t^e:

$$\dot{\sigma} = K_t^e \cdot \dot{\varepsilon}^e \tag{3.35}$$

$$\dot{\boldsymbol{s}} = 2G_t^e \cdot \dot{\boldsymbol{e}}^e \tag{3.36}$$

The tangential expressions of the elastic bulk and shear moduli may be computed as follows:

$$K_t^e = a_0 + a_1 \cdot \sigma + a_2 \cdot \sqrt{\boldsymbol{s} : \boldsymbol{s}} \tag{3.37}$$

$$G_t^e = b_0 + b_1 \cdot \sigma + b_2 \cdot \sqrt{\boldsymbol{s} : \boldsymbol{s}} \tag{3.38}$$

The hypoelastic formulations have been widely employed in their isotropic form mainly due to the pressure dependency imposed on the shear modulus.

Regarding the initial bulk modulus value $K_{\max}$, expressions similar to the ones proposed by Whittle and Kavvadas (1994) may be adopted:

$$K_{\max} = K_0 \cdot p_a \cdot f_K(e) \cdot h_K\left(OCR_p\right) \cdot \left(\frac{p}{p_a}\right)^{m_K} \tag{3.39}$$

where K_0 is a dimensionless parameter, p_a stands for the atmospheric pressure, $f_K(e)$ portrays a function of the void ratio and m_K is a positive exponential parameter employed. Furthermore, $h_K\left(OCR_p\right)$ is a function of the overconsolidation ratio incorporated in the case of cohesive soils.

In a similar fashion the initial value of the shear modulus denoted $G_{\max}$ may be expressed as follows (Rampello et al., 1994 and 1997):

$$G_{\max} = G_0 \cdot p_a \cdot f_G(e) \cdot h_G\left(OCR_p\right) \cdot \left(\frac{p}{p_a}\right)^{m_G} \tag{3.40}$$

where G_0 is a dimensionless parameter, $f_G(e)$ portrays a function of the void ratio and m_G is a positive exponential parameter employed. $h_G\left(OCR_p\right)$ is a function of the overconsolidation ratio incorporated in cohesive soils. The effect of the overconsolidation ratio in cohesionless soils (i.e. sand) inflicted upon the initial values of bulk and shear moduli appears to be negligible (Pestana, 1994; Papadimitriou, 1999).

Hypoelasticity has been incorporated extensively in numerical codes due to its simplicity and elegance. Usually the proposed formulations are easy to calibrate and use. On the downside however, the formulations are potentially conservative and are not directly associated to the laboratory measurements.

3.4 Plastic yield envelope (*PYE*)

The theory of plasticity does not account solely for the elastic strain tensor. It also contains another component that has been so elaborately concealed. The plastic component of strain tensor denoted $\boldsymbol{\varepsilon}^p$ tends to undergo changes once the soil element yields. By entering the plastic regime the mechanical behavior tends to become highly nonlinear and hysteretic. Hence, based on the principles of the classical theory of plasticity the possible states may be classified as follows:

- The **elastic state** comprises the state $(\boldsymbol{\sigma}, \boldsymbol{q})$ at which the incremental stress increment $\dot{\boldsymbol{\sigma}}$ is responsible for the accumulation of elastic strains alone $(\dot{\boldsymbol{\varepsilon}} = \dot{\boldsymbol{\varepsilon}}^e,\ \dot{\boldsymbol{\varepsilon}}^p = \mathbf{0})$. Hence the mechanical behavior tends to portray no hardening $\dot{\boldsymbol{q}} = \mathbf{0}$.
- The **elastoplastic state** is the state $(\boldsymbol{\sigma}, \boldsymbol{q})$ at which the infinitesimal stress increment $\dot{\boldsymbol{\sigma}}$ is responsible for the accumulation of elastic and plastic strains alike $(\dot{\boldsymbol{\varepsilon}} = \dot{\boldsymbol{\varepsilon}}^e + \dot{\boldsymbol{\varepsilon}}^p,\ \dot{\boldsymbol{\varepsilon}}^p \neq \mathbf{0},\ \dot{\boldsymbol{q}} \neq \mathbf{0})$.

The aforementioned states require the introduction of the plastic yield envelope (*PYE*). Assuming that the state of stress lays inside *PYE* the initial state is considered elastic. However, every state laying on the plastic yield surface denotes an elastoplastic state. Hence, *PYE* may be considered as the virtual boundary between the elastic states (inside PYE) and unattainable states laying outside PYE (**Figure 3.4**).

To sum up, every loading increment responsible for reproducing solely elastic straining needs to satisfy one of the following conditions:

- the initial state was elastic;
- the initial state was elastoplastic but the new state lays inside *PYE*; or
- the initial state was indeed elastoplastic but neutral loading was undertaken and regardless whether the new state lays on PYE the loading was imposed vertical to the derivative of PYE with respect to stress. In such case, neutral loading is an elastic stress increment and thus hardening is not undertaken $(\dot{\boldsymbol{\varepsilon}} = \dot{\boldsymbol{\varepsilon}}^e,\ \dot{\boldsymbol{\varepsilon}}^p = \mathbf{0},\ \dot{\boldsymbol{q}} = \mathbf{0})$.

Although it is impossible for the stress state to cross the plastic yield envelope it may be possible for *PYE* to harden. Any alteration in the size, shape and position of *PYE* portrays the effect of hardening and is attributed solely to plastic straining (in the classical inviscid theory of elastoplasticity).

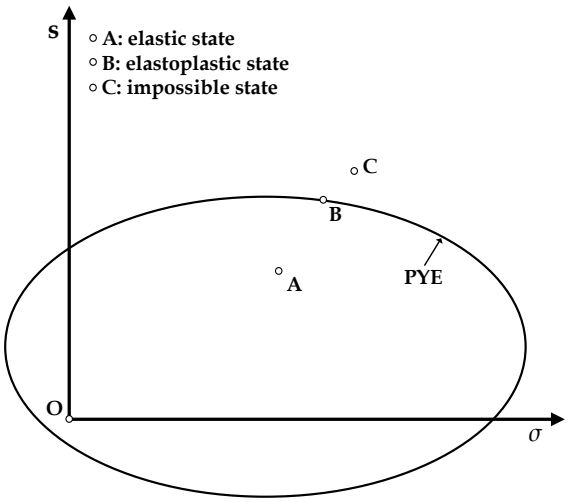

Figure 3.4: Plastic Yield Envelope (*PYE*) and definition of possible states.

The mathematical formulation of the plastic yield envelope is a function of the stress state and hardening variables. Hence, all elastoplastic states laying on *PYE* need to satisfy the expression below:

$$f\left(\boldsymbol{\sigma},\boldsymbol{q}\right)=0 \tag{3.41}$$

The hardening variables denoted $\boldsymbol{q}$ are the ensemble of scalar and potentially tensorial parameters acting as memory variables for the upcoming loading increments through the hardening laws.

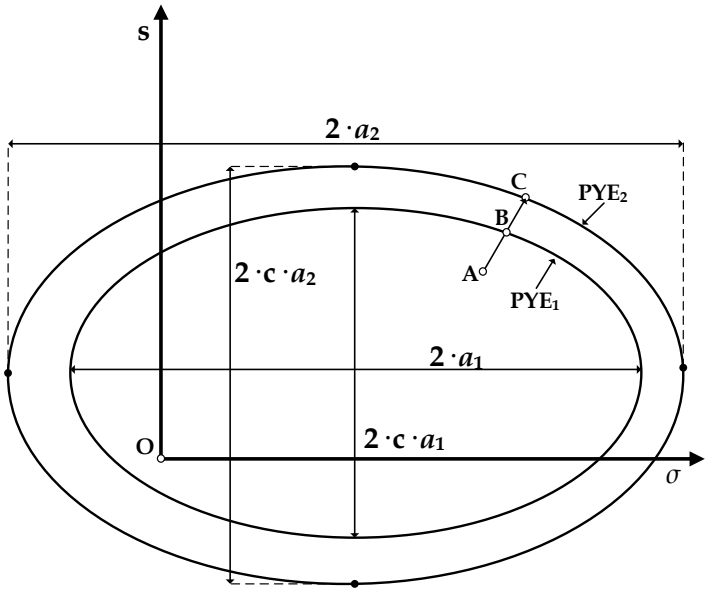

Figure 3.5: Isotropic hardening - changing the size of *PYE*.

The plastic yield function depicted in expression (3.41) produces negative values for states laying inside *PYE* ($f(\boldsymbol{\sigma},\boldsymbol{q})<0$ for elastic states) and positive for the unattainable states laying outside the envelope ($f(\boldsymbol{\sigma},\boldsymbol{q})>0$ for impossible states). Condition (3.41) tends to describe states laying on the boundary that may produce plastic strains and hardening. Hardening may be controlled via either an isotopic (**Figure 3.5**) or some sort of kinematic (**Figure 3.6** and **Figure 3.7**) hardening law. The common denominator however in both cases lies on the fact that hardening occurs only on the plastic path BC and not on AB.

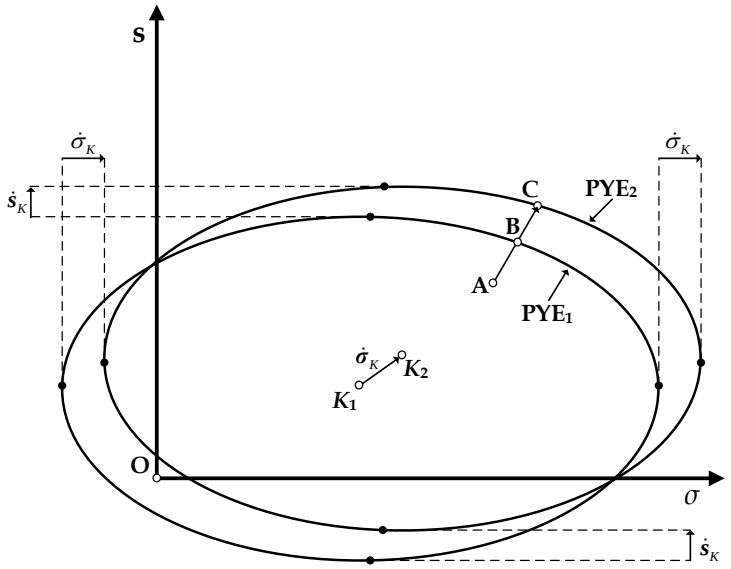

Figure 3.6: Kinematic hardening - translation of *PYE*.

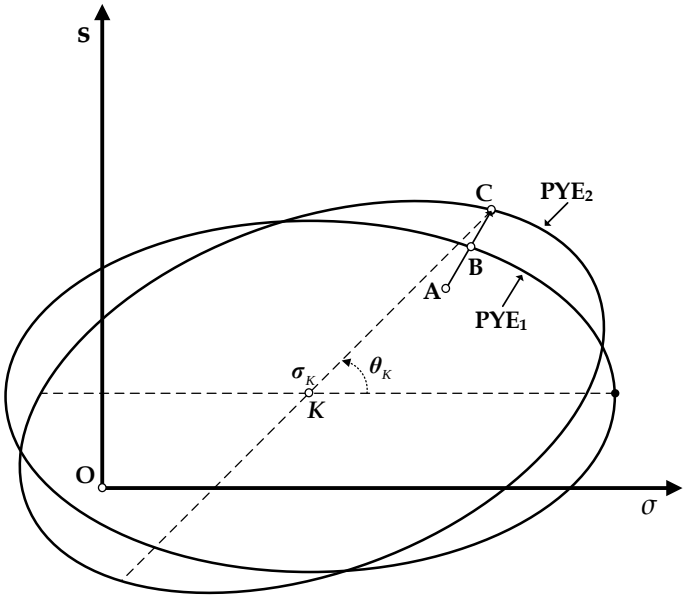

Figure 3.7: Kinematic hardening - rotation of *PYE*.

3.4.1 Criterion for elastoplastic loading and elastic unloading

The mathematical formulation of the yield function may be employed to distinguish the elastic from the elastoplastic states. Hence, on the elastic states (stress point A) the loading state lays inside the plastic yield envelope leading to negative values of $f(\boldsymbol{\sigma},\boldsymbol{q})<0$. Assuming that elastoplastic states (stress point B) are encountered once the loading increment has been subjected, then the yield function is $f(\boldsymbol{\sigma},\boldsymbol{q})=0$. States originating from an elastic state (subjected to a loading increment) that tend to cross *PYE* (stress point C') are simply imaginary and lead to positive values of the yield function $f(\boldsymbol{\sigma},\boldsymbol{q})>0$. Assuming that a stress increment produces such positive values of the yield function then the system portrays an elastic response till point B (Point B lays on *PYE*) followed by an elastoplastic loading increment until point C (**Figure 3.8**).

Assuming an initial elastoplastic state on *PYE* in order to distinguish between elastic unloading and elastoplastic loading we need to employ a criterion incorporating the elastic stressing, holding true for the subjected loading increment, $\dot{\boldsymbol{\sigma}}^e=\boldsymbol{C}^e:\dot{\boldsymbol{\varepsilon}}$ and the gradient of the plastic yield envelope denoted $\boldsymbol{Q}$, where $\boldsymbol{Q}$:

$$\boldsymbol{Q}=\frac{\partial f(\boldsymbol{\sigma},\boldsymbol{q})}{\partial\boldsymbol{\sigma}} \tag{3.42}$$

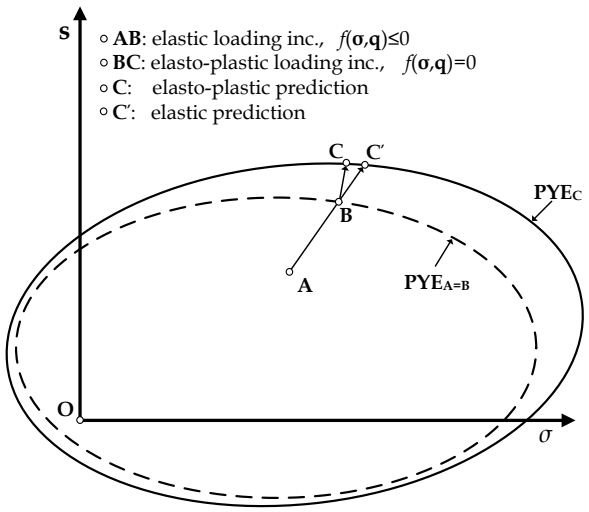

Figure 3.8: Elastic and elastoplastic prediction of the current stress state.

The criterion for plastic loading or elastic unloading concerning plastic states may be described through the inner product $\boldsymbol{Q}:\dot{\boldsymbol{\sigma}}^e=\boldsymbol{Q}:\boldsymbol{C}^e:\dot{\boldsymbol{\varepsilon}}$ assuming convexity of *PYE*.

By assuming convexity of the *PYE* it can be concluded that its gradient is always directed towards the outer normal to the surface. Hence, elastic unloading from an elastoplastic state may only occur when the dot product $\boldsymbol{Q}:\dot{\boldsymbol{\sigma}}^{e}<0$ takes negative values. In this case, there is no hardening and no accumulation of plastic strains $(\dot{\boldsymbol{\varepsilon}}=\dot{\boldsymbol{\varepsilon}}^{e},\ \dot{\boldsymbol{\varepsilon}}^{p}=\mathbf{0},\ \boldsymbol{q}=\mathbf{0})$.

Summarizing, elastic unloading from an initial elastoplastic state laying on the plastic yield envelope should satisfy the following condition:

$$\boldsymbol{Q}:\boldsymbol{C}^{e}:\dot{\boldsymbol{\varepsilon}}<0 \tag{3.43}$$

Considering that stressing is purely elastic and thus $\dot{\boldsymbol{\varepsilon}}=\dot{\boldsymbol{\varepsilon}}^{e},\ \dot{\boldsymbol{\varepsilon}}^{p}=\mathbf{0},\ \boldsymbol{q}=\mathbf{0}$:

$$\boldsymbol{Q}:\boldsymbol{C}^{e}:\dot{\boldsymbol{\varepsilon}}=\boldsymbol{Q}:\boldsymbol{C}^{e}:\dot{\boldsymbol{\varepsilon}}^{e}<0\Rightarrow\boldsymbol{Q}:\dot{\boldsymbol{\sigma}}<0 \tag{3.44}$$

The condition as rewritten in the form (3.44) always accounts for elastic unloading when the elastoplastic state has been attained in the previous increment. However, the expression does not work both ways. Thus, $\boldsymbol{Q}:\dot{\boldsymbol{\sigma}}<0$ does not always mean that elastic unloading is sustained. The condition may also apply to plastic strain softening in which case the size of *PYE* tends to decrease. In every other case originating from an elastoplastic state the stress increment leads to plastic straining and thus the new state lays on *PYE*. In other words:

$$\boldsymbol{Q}:\boldsymbol{C}^{e}:\dot{\boldsymbol{\varepsilon}}\geq 0 \tag{3.45}$$

Here follows the schematic representation of the types of stressing originating from an elastoplastic state (**Figure 3.9**):

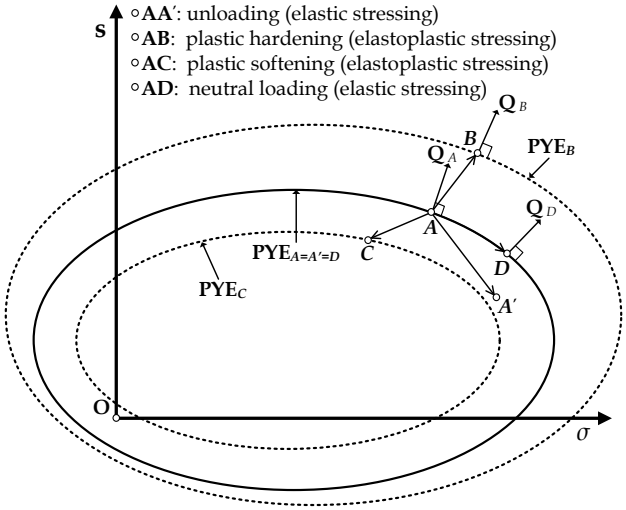

Figure 3.9: Types of stressing originating from an elastoplastic state.

Summarizing, assuming that the state originates on the plastic yield envelope (*PYE*) the following cases of stressing may be considered:

- **Plastic** (**strain**) **hardening** or **elastoplastic loading** (stress path AB in **Figure 3.9** and **Figure 3.10**) represents the case where both of the following conditions hold true, $\boldsymbol{Q}:\boldsymbol{C}^e:\dot{\boldsymbol{\varepsilon}}\geq 0$ and $\boldsymbol{Q}:\dot{\boldsymbol{\sigma}}>0$.
- **Plastic** (**strain**) **softening** (path AC in **Figure 3.9** and **Figure 3.10**) represents the case where both of the following conditions are justified, $\boldsymbol{Q}:\boldsymbol{C}^e:\dot{\boldsymbol{\varepsilon}}\geq 0$ and $\boldsymbol{Q}:\dot{\boldsymbol{\sigma}}<0$.
- **Neutral loading** (path AD in **Figure 3.9** and **Figure 3.10**) represents the case where the following condition is met, $\boldsymbol{Q}:\dot{\boldsymbol{\sigma}}=0$.
- **Elastic unloading** represents the case where both of the following condition hold true $\boldsymbol{Q}:\boldsymbol{C}^e:\dot{\boldsymbol{\varepsilon}}=\boldsymbol{Q}:\boldsymbol{C}^e:\dot{\boldsymbol{\varepsilon}}^e<0\Rightarrow\boldsymbol{Q}:\dot{\boldsymbol{\sigma}}<0$ (path AA in **Figure 3.9** and **Figure 3.10**).

Considering that the plastic yield surface tends to expand or contract depending on the type of hardening sustained, the stress paths depicted in **Figure 3.9** are merely a simple projection of **Figure 3.10** in the stress hyperplane.

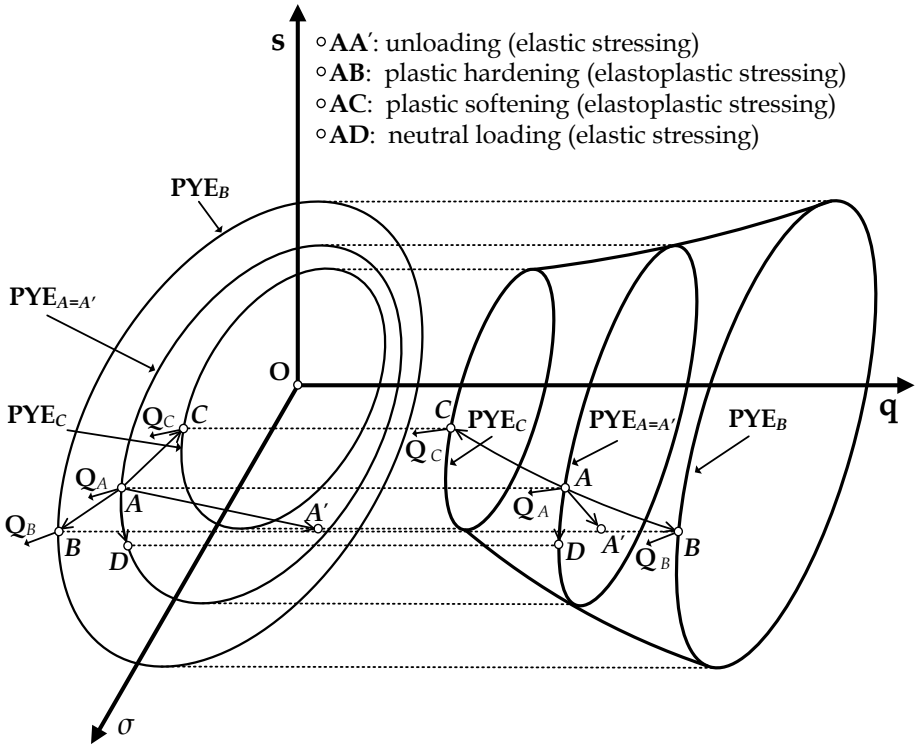

Figure 3.10: Types of stressing originating from a state on *PYE* - effect of plastic strain hardening and softening (after Belokas, 2008).

All the aforementioned criteria for the type of stressing are based on the assumption that the stress state lays on *PYE*. Should the initial state be elastic then application of an infinitesimal stress increment is assumed to be elastic and hence leads to a new elastic state. In such case however, the only criterion to be met lies with the expression $f(\boldsymbol{\sigma},\boldsymbol{q}) \leq 0$. Assuming that the yield function upon application of the elastic increment produces positive values $f(\boldsymbol{\sigma},\boldsymbol{q}) > 0$ then the loading increment needs to be divided accordingly to an elastic part (setting the stress state on *PYE*) and a remaining elastoplastic portion (to account for any plastic strain hardening or softening).

3.5 Plastic flow Rule

The magnitude and direction of plastic strains are described through the plastic flow rule. The incrementally linear form with respect to stress and strain increments can be expressed as follows:

$$\dot{\boldsymbol{\varepsilon}}^{p} = \dot{\Lambda} \cdot \boldsymbol{P} \tag{3.46}$$

In the expression above $\boldsymbol{P}$ is the plastic potential tensor controlling the size (and to some extent the magnitude also) of the plastic strain tensor. Parameter $\dot{\Lambda}$ is a scalar quantity expressing the measure of the plastic strain tensor magnitude. The plastic potential tensor is a second order tensor that can be decomposed in a volumetric and a deviatoric component as follows:

$$P \equiv \boldsymbol{P} : \boldsymbol{I} \tag{3.47}$$

$$\boldsymbol{P}' \equiv \boldsymbol{P} - \frac{1}{3} \cdot P \cdot \boldsymbol{I} \tag{3.48}$$

Thus expression (3.46) may be rewritten as follows by accounting for equations (3.47) and (3.48):

$$\dot{\boldsymbol{\varepsilon}}^p = \frac{1}{3} \cdot \dot{\varepsilon}^p \cdot \boldsymbol{I} + \dot{\boldsymbol{e}}^p = \dot{\Lambda} \cdot \left(\frac{1}{3} \cdot \dot{\varepsilon}^p \cdot \boldsymbol{I} + \dot{\boldsymbol{e}}^p \right) = \dot{\Lambda} \cdot \left(\frac{1}{3} \cdot P \cdot \boldsymbol{I} + \boldsymbol{P}' \right)$$

Hence the volumetric and deviatoric incremental strains may be expressed as:

$$\dot{\varepsilon}^p = \dot{\Lambda} \cdot P \tag{3.49}$$

$$\dot{\boldsymbol{e}}^p = \dot{\Lambda} \cdot \boldsymbol{P}' \tag{3.50}$$

The measure of the plastic strain tensor magnitude $\dot{\Lambda}$ may be expressed as a function of the gradient $\boldsymbol{Q}$ and the stress tensor increment $\dot{\boldsymbol{\sigma}}$:

$$\dot{\Lambda} = \frac{1}{H} \cdot \left(\boldsymbol{Q} : \dot{\boldsymbol{\sigma}} \right) \tag{3.51}$$

The formulation above incorporates the plastic hardening modulus H. By introducing equation (3.51) in (3.46):

$$\dot{\boldsymbol{\varepsilon}}^p = \frac{1}{H} \cdot \left(\boldsymbol{Q} : \dot{\boldsymbol{\sigma}} \right) \cdot \boldsymbol{P} \tag{3.52}$$

The dot product $\boldsymbol{Q} : \dot{\boldsymbol{\sigma}}$ may be expressed by accounting for the volumetric $\left(Q \equiv \boldsymbol{Q} : \boldsymbol{I} \right)$ and the deviatoric $\left(\boldsymbol{Q}' \equiv \boldsymbol{Q} - \frac{1}{3} \cdot Q \cdot \boldsymbol{I} \right)$ components of the gradient $\boldsymbol{Q} = \frac{1}{3} \cdot Q \cdot \boldsymbol{I} + \boldsymbol{Q}'$ (similar to the plastic potential tensor decomposition):

$$\boldsymbol{Q}:\dot{\boldsymbol{\sigma}}=\left(\frac{1}{3}\cdot Q\cdot\boldsymbol{I}+\boldsymbol{Q}'\right):\left(\sigma\cdot\boldsymbol{I}+\boldsymbol{s}'\right)\Leftrightarrow$$

$$\boldsymbol{Q}:\dot{\boldsymbol{\sigma}}=\left(\frac{1}{3}\cdot Q\cdot\boldsymbol{I}\right):\left(\sigma\cdot\boldsymbol{I}\right)+\left(\frac{1}{3}\cdot Q\cdot\boldsymbol{I}\right):\boldsymbol{s}'+\boldsymbol{Q}':\left(\sigma\cdot\boldsymbol{I}\right)+\boldsymbol{Q}':\boldsymbol{s}'\Leftrightarrow$$

$$\boldsymbol{Q}:\dot{\boldsymbol{\sigma}}=Q\cdot\sigma+\boldsymbol{Q}':\boldsymbol{s}' \tag{3.53}$$

It should be noted that the dot product of two unity 2nd order tensors equals three $(\boldsymbol{I}:\boldsymbol{I}=3)$.

Assuming that the plastic hardening modulus in equation (3.52) is null, $H=0$, then expression (3.51) indicates that the magnitude of $\dot{\boldsymbol{\varepsilon}}^{p}$ (denoted $\dot{\Lambda}$) tends to infinity. Consequently, the magnitude of the incremental plastic strain tensor becomes indeterminable. This situation is defined as "failure" and is associated with zero plastic hardening modulus :

$$failure\Leftrightarrow H=0 \tag{3.54}$$

The plastic hardening modulus may be computed through the consistency condition by employing the hardening rules, as will be shown in an upcoming subsection. Scalar measure $\dot{\Lambda}$ on the other hand can be computed by undergoing certain manipulations depicted here below:

$$\dot{\Lambda}=\frac{1}{H}\cdot\boldsymbol{Q}:\dot{\boldsymbol{\sigma}}=\frac{1}{H}\cdot\boldsymbol{Q}:\boldsymbol{C}^{e}:\dot{\boldsymbol{\varepsilon}}^{e}=\frac{1}{H}\cdot\boldsymbol{Q}:\boldsymbol{C}^{e}:\left(\dot{\boldsymbol{\varepsilon}}-\dot{\boldsymbol{\varepsilon}}^{p}\right)=\frac{1}{H}\cdot\boldsymbol{Q}:\boldsymbol{C}^{e}:\left(\dot{\boldsymbol{\varepsilon}}-\dot{\Lambda}\cdot\boldsymbol{P}\right)\Rightarrow$$

$$\dot{\Lambda}=\frac{\boldsymbol{Q}:\boldsymbol{C}^{e}:\dot{\boldsymbol{\varepsilon}}}{H+\boldsymbol{Q}:\boldsymbol{C}^{e}:\boldsymbol{P}} \tag{3.55}$$

The phase transformation state is defined through the isotropic component P of the plastic potential tensor as the state defined by null values of $P=0$. Elastoplastic states laying on the Phase transformation line result in zero sustained isotropic incremental plastic strain $\dot{\varepsilon}^{p}=0$. The phase transformation comprises the boundary between contractive and dilative behavior (and will be further discussed in subsection 3.9). Assuming that the soil fabric undergoes strain softening, by conforming to the conditions $\boldsymbol{Q}:\boldsymbol{C}^{e}:\dot{\boldsymbol{\varepsilon}}\geq 0$ and $\boldsymbol{Q}:\dot{\boldsymbol{\sigma}}<0$, the plastic hardening modulus takes negative values $H<0$. On the other hand, the soil element tends to

exhibit plastic strain hardening, by satisfying simultaneously the conditions $\boldsymbol{Q}:\boldsymbol{C}^e:\dot{\boldsymbol{\varepsilon}}\geq 0$ and $\boldsymbol{Q}:\dot{\boldsymbol{\sigma}}>0$. In other words by considering:

$$\boldsymbol{Q}:\dot{\boldsymbol{\sigma}}=\boldsymbol{Q}:\boldsymbol{C}^e:\dot{\boldsymbol{\varepsilon}}^e=\boldsymbol{Q}:\boldsymbol{C}^e:\left(\dot{\boldsymbol{\varepsilon}}-\dot{\boldsymbol{\varepsilon}}^p\right)=\boldsymbol{Q}:\boldsymbol{C}^e:\left(\dot{\boldsymbol{\varepsilon}}-\dot{\Lambda}\cdot\boldsymbol{P}\right)\Leftrightarrow$$

$$\boldsymbol{Q}:\dot{\boldsymbol{\sigma}}=\boldsymbol{Q}:\boldsymbol{C}^e:\dot{\boldsymbol{\varepsilon}}-\dot{\Lambda}\cdot\boldsymbol{Q}:\boldsymbol{C}^e:\boldsymbol{P}=\boldsymbol{Q}:\boldsymbol{C}^e:\dot{\boldsymbol{\varepsilon}}-\left(\frac{\boldsymbol{Q}:\boldsymbol{C}^e:\dot{\boldsymbol{\varepsilon}}}{H+\boldsymbol{Q}:\boldsymbol{C}^e:\boldsymbol{P}}\right)\cdot\boldsymbol{Q}:\boldsymbol{C}^e:\boldsymbol{P}\Leftrightarrow$$

$$\boldsymbol{Q}:\dot{\boldsymbol{\sigma}}=\left(1-\frac{\boldsymbol{Q}:\boldsymbol{C}^e:\boldsymbol{P}}{H+\boldsymbol{Q}:\boldsymbol{C}^e:\boldsymbol{P}}\right)\cdot\boldsymbol{Q}:\boldsymbol{C}^e:\dot{\boldsymbol{\varepsilon}}$$

it is possible to discriminate between plastic hardening and plastic softening in the case of plastic loading $\boldsymbol{Q}:\boldsymbol{C}^e:\dot{\boldsymbol{\varepsilon}}\geq 0$ by considering the following expressions:

$$\text{plastic hardening}:\ \boldsymbol{Q}:\dot{\boldsymbol{\sigma}}>0\Rightarrow\frac{\boldsymbol{Q}:\boldsymbol{C}^e:\boldsymbol{P}}{H+\boldsymbol{Q}:\boldsymbol{C}^e:\boldsymbol{P}}<1 \tag{3.56}$$

$$\text{plastic softening}:\ \ \boldsymbol{Q}:\dot{\boldsymbol{\sigma}}<0\Rightarrow\frac{\boldsymbol{Q}:\boldsymbol{C}^e:\boldsymbol{P}}{H+\boldsymbol{Q}:\boldsymbol{C}^e:\boldsymbol{P}}>1 \tag{3.57}$$

3.5.1 Plastic potential tensor and stress - dilation association

The direction of the incremental plastic strain tensor is controlled through the plastic potential tensor, by considering equation (3.46). By governing the directionality of the plastic strain however, the plastic strain tensor further controls the plastic dilation *d*:

$$d=\frac{\dot{\varepsilon}_q^p}{\dot{\varepsilon}^p}=\frac{\sqrt{\frac{2}{3}\dot{\boldsymbol{e}}^p:\dot{\boldsymbol{e}}^p}}{\dot{\varepsilon}^p}=\frac{\sqrt{\frac{2}{3}\boldsymbol{P}':\boldsymbol{P}'}}{P} \tag{3.58}$$

In the expression above $\dot{\varepsilon}_q^p=\sqrt{\frac{2}{3}\dot{\boldsymbol{e}}^p:\dot{\boldsymbol{e}}^p}$ is the incremental deviatoric strain measure.

The plastic strain tensor may be computed as the gradient of a certain surface, similar to the gradient of the plastic yield function, or it can be provided straight forward through an analytical formulation of the material current state. Assuming that the plastic potential tensor may be defined through the gradient of the plastic potential envelope (*PPE*) it needs to be convex and redefined for every stress state laying on *PYE*. In the general case, the plastic potential envelope and the plastic yield envelope

do not coincide, unless an associated flow rule is adopted (also known as normality rule). The *PPE* comprises the envelope denoted by the orthogonality of the incremental plastic strain tensors.

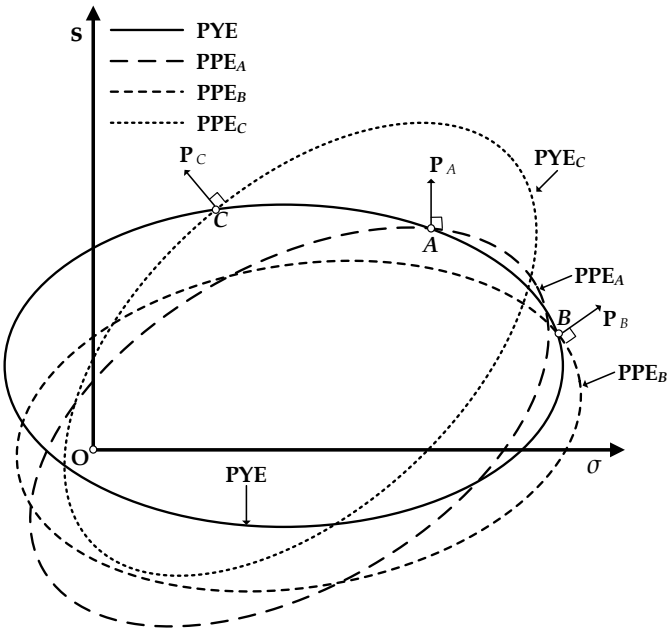

Figure 3.11: Plastic potential envelope and corresponding plastic potential tensor.

It is possible to integrate the relation associating the dilation with the stress state derived from laboratory measurements illustrated here below, analogously to expression (3.58) extended to the generalized stress hyperplane:

$$\boldsymbol{d} = \frac{\dot{\boldsymbol{e}}^{p}}{\dot{\varepsilon}^{p}} = \frac{\boldsymbol{P}'}{P} = \frac{\boldsymbol{P}'(\boldsymbol{\sigma},\boldsymbol{q})}{P(\boldsymbol{\sigma},\boldsymbol{q})} \tag{3.59}$$

The plastic potential function, depicted in equation (3.60), comprises the mathematical formulation of *PPE* and the plastic potential tensor $\boldsymbol{P} \equiv \frac{1}{3} \cdot P \cdot \boldsymbol{I} + \boldsymbol{P}'$ is its gradient:

$$g(\boldsymbol{\sigma},\boldsymbol{q}) = 0 \tag{3.60}$$

$$P \equiv \frac{\partial g(\boldsymbol{\sigma},\boldsymbol{q})}{\partial \sigma} \tag{3.61}$$

$$\boldsymbol{P}' \equiv \frac{\partial g(\boldsymbol{\sigma},\boldsymbol{q})}{\partial \boldsymbol{s}} \tag{3.62}$$

Considering, that the plastic potential tensor is the gradient of the plastic potential function it is always normal to the boundary. Hence, the flow rule may also be called as normality condition with respect to *PPE*.

On the other hand, it is possible to introduce explicitly an analytical formulation describing the plastic potential tensor as a function of the stress state and the hardening variables. Such realization allows for some flexibility in the formulation of the desired mechanical behavioral framework.

3.5.2 Associated flow rule

In most cases it is assumed that the plastic yield envelope coincides with the plastic potential envelope. Hence, the associated flow rule postulates the orthogonality of the plastic strain tensor to the plastic yield envelope (**Figure 3.12**). The formulations to describe the associated flow rule are depicted here below:

$$\boldsymbol{Q} = \boldsymbol{P} \tag{3.63}$$

$$\dot{\boldsymbol{\varepsilon}}^{p} = \dot{\Lambda} \cdot \boldsymbol{P} = \dot{\Lambda} \cdot \boldsymbol{Q} = \dot{\Lambda} \cdot \frac{\partial f(\boldsymbol{\sigma}, \boldsymbol{q})}{\partial \boldsymbol{\sigma}} \tag{3.64}$$

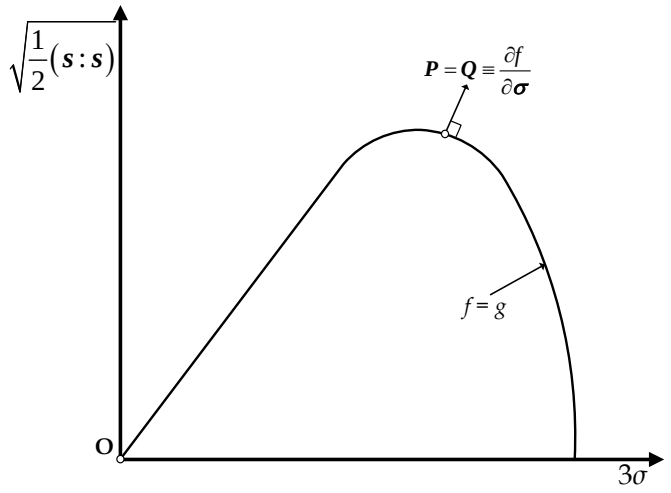

Figure 3.12: Schematic representation of associated flow rule (Desai et al., 1986).

Assuming an associated flow rule whenever the plastic hardening modulus is positive $H > 0$ the material is undergoing plastic hardening. On the other hand, negative values of the plastic hardening modulus may be representing either plastic hardening or plastic softening. Considering an elastoplastic stressing $\boldsymbol{Q} : \boldsymbol{C}^{e} : \dot{\boldsymbol{\varepsilon}} \geq 0$

the scalar measure of incremental plastic strain tensor $\dot{\Lambda}$ may be expressed by either one of equations (3.51) and (3.55):

$$\boldsymbol{Q}:\boldsymbol{C}^e:\boldsymbol{P}=\boldsymbol{Q}:\boldsymbol{C}^e:\boldsymbol{Q}>0 \tag{3.65}$$

Assuming that the plastic strain hardening is positive $H>0$ then the scalar measure is also positive $\dot{\Lambda}>0$ and consequently $\boldsymbol{Q}:\dot{\boldsymbol{\sigma}}>0$ leading to plastic hardening:

$$H>0\Rightarrow\dot{\Lambda}>0\Rightarrow\boldsymbol{Q}:\dot{\boldsymbol{\sigma}}>0\Rightarrow\text{plastic hardening} \tag{3.66}$$

On the other hand, assuming that the plastic hardening modulus is negative $H<0$ then the material exhibits either plastic hardening or plastic softening (**Figure 3.13**):

$$H<0\wedge H+\boldsymbol{Q}:\boldsymbol{C}^e:\boldsymbol{Q}>0\Rightarrow\dot{\Lambda}>0\Rightarrow\boldsymbol{Q}:\dot{\boldsymbol{\sigma}}<0\Rightarrow\text{plastic softening} \tag{3.67}$$

$$H<0\wedge H+\boldsymbol{Q}:\boldsymbol{C}^e:\boldsymbol{Q}<0\Rightarrow\dot{\Lambda}<0\Rightarrow\boldsymbol{Q}:\dot{\boldsymbol{\sigma}}>0\Rightarrow\text{plastic hardening} \tag{3.68}$$

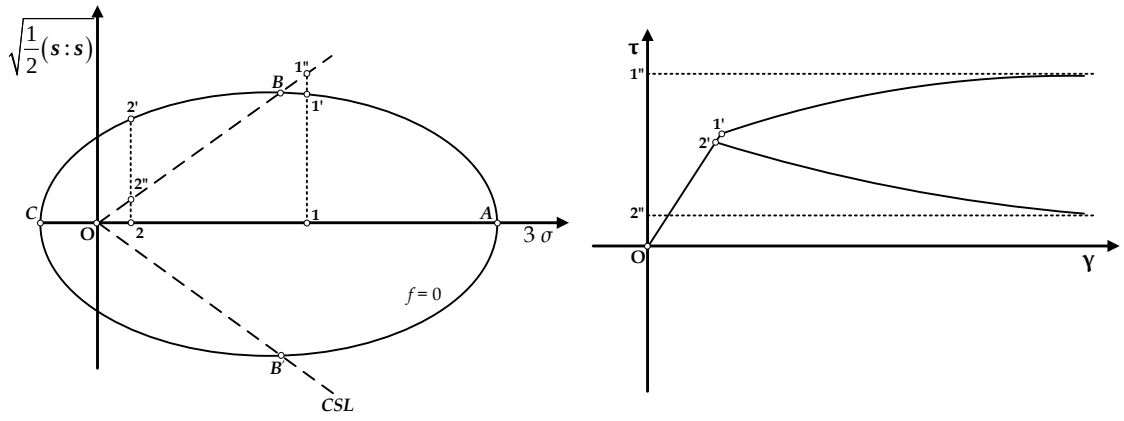

a. b.

Figure 3.13: a. Stress path 1-1'-1" denotes plastic hardening while b. stress path 2-2'-2" represents plastic softening in a formulation based on associated flow rule subjected to shear stress (from Mroz and Norris, 1982).

Drucker's stability postulate (Drucker, 1951, 1956, 1959) states that in order to ensure stability (note that the constitutive model needs also conform with the laws of thermodynamics) the following statement needs to hold true:

$$\dot{\boldsymbol{\sigma}}:\dot{\boldsymbol{\varepsilon}}^p>0 \tag{3.69}$$

The aforementioned postulate (referring to the latest form of 1959) stems from the assumption that the consumed work needs to be positive (comprises a case of

maximum entropy production according to Ziegler, 1959 and Green and Naghdi, 1965) thus leading to an associated flow rule and a convex plastic potential envelope. Once the postulate is adopted no plastic softening is allowed. The smallest value the plastic hardening modulus is allowed to undergo is $H = \boldsymbol{Q} : \boldsymbol{C}^e : \boldsymbol{Q}$ representing a purely plastic non-hardening (plastic hardening is allowed but not plastic softening) mechanical behavior.

It is noted that assuming an associated flow rule the elastoplastic stiffness matrix is symmetric.

3.5.3 Non-associated flow rule

Non-associated flow rule states that the plastic potential envelope and the plastic yield envelope are distinct and do not coincide:

$$\boldsymbol{Q} \neq \boldsymbol{P} \tag{3.70}$$

The relationship above postulates that the magnitude and the direction of the plastic potential tensor are not equal to the gradient of *PYE*. Hence, the direction of the incremental plastic strain tensor is not orthogonal to the plastic yield envelope, except possibly in some very specific cases.

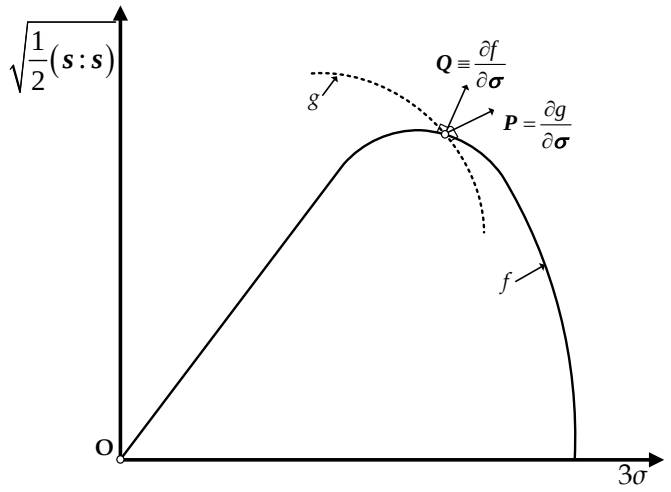

Figure 3.14: Schematic representation of non-associated flow rule (Desai et al., 1986)

Assuming a non-associated flow rule the plastic strain tensor may be computed as the gradient of *PPE* or through an explicit analytical formulation of the material current state. Assuming that the plastic potential tensor is defined through the

gradient of the plastic potential envelope (*PPE*) it needs to be convex and redefined for every state of stress laying on *PYE*. In the case of an adopted non-associated flow rule the plastic potential envelope and the plastic yield envelope do not coincide. The *PPE* comprises the envelope denoted by the orthogonality of the incremental plastic strain tensors and may be described as follows:

$$\dot{\boldsymbol{\varepsilon}}^{p} = \dot{\Lambda} \cdot \boldsymbol{P} = \dot{\Lambda} \cdot \frac{\partial g(\boldsymbol{\sigma}, \boldsymbol{q})}{\partial \boldsymbol{\sigma}} \tag{3.71}$$

Non-symmetric stiffness matrix stems from the assumption of the non-associated flow rule (Lade and Nelson, 1984). Although it may be computationally expensive in terms of numerical programming it tends to allow for a more realistic simulation of the mechanical behavior and accumulation of plastic strains. Furthermore, laboratory measurements tend to justify the assumption of the non-associative flow rule (Burghignoli et al., 1998; Callisto and Calabresi, 1998).

3.6 Hardening Rules

The hardening variables control the size, the position and even the shape of *PYE* and along with the stress state $\boldsymbol{\sigma}$ comprise the state variables employed in the definition of the plastic yield function $f(\boldsymbol{\sigma}, \boldsymbol{q})$. The hardening rules control the evolution of the hardening variables once the elastoplastic state is attained. Once the stress state enters the elastoplastic domain the stress is adjusted on *PYE* and the plastic strains accumulate. Plastic strains will cease to develop once an elastic unloading increment is sustained, thus transitioning the stress state back to elastic regime. Schematic representations of the effect governed by different hardening rules have been presented in **Figure 3.5**, **Figure 3.6** and **Figure 3.7**. The present dissertation adopts the general incremental form of the hardening rules (Kavvadas, 1982; Whittle and Kavvadas, 1994; Kavvadas and Amorosi, 1998 & 2000; Belokas and Kavvadas, 2010 & 2011; Kavvadas and Belokas, 2000) portrayed here below:

$$\dot{\boldsymbol{q}} = \dot{\Lambda} \cdot \boldsymbol{h} \tag{3.72}$$

The expression above incorporates the scalar measure of the hardening incremental hardening variables (coincides with the scalar measure of the incremental plastic strain tensor) $\dot{\Lambda}$. $\boldsymbol{h}$ determines the evolution or the direction (assuming a tensor) of

the incremental hardening variables (and to some extent the magnitude also) and it can be either a scalar quantity or represent a tensor (i.e. in anisotropic models the inclination of the bounding surface in the stress space is employed as hardening variable in a tensorial form). The hardening variables together with the stress state compose the material state and comprise the state variables. Hence, the void ratio, the total, the plastic or even the elastic (i.e. in hyperelasticity) strains, the current stress state, the size, the position and the shape of *PYE* and many other quantities may be employed as hardening variables within the constitutive framework. The mathematical formulation of the hardening rules may also introduce certain hardening parameters. Consequently, selection of $\boldsymbol{h}$ governs the form of the hardening rule and therefore the simulated mechanical behavior.

The plastic hardening modulus H, the adopted flow rule (associated or non-associated) and the hardening rules controlling the isotropic or kinematic plastic hardening or softening of the plastic yield envelope comprise the pillars of the constitutive formulation. Here follows the derivation of the plastic hardening modulus and the classification of plastic hardening/softening to isotropic and kinematic.

3.6.1 Plastic hardening modulus

The plastic hardening modulus may be defined solely for elastoplastic states and associated loading increments as it can be observed from a careful examination of expression (3.52). The plastic hardening modulus is derived by employing the consistency condition (postulating that assuming an elastoplastic increment is imposed on an elastoplastic state the new state needs to remain on the plastic yield envelope), the adopted flow and hardening rules. The mathematical representation of the consistency condition incorporates the increment of the plastic yield function $\dot{f}(\boldsymbol{\sigma},\boldsymbol{q})=0$:

$$\dot{f}(\boldsymbol{\sigma},\boldsymbol{q})=0 \Rightarrow \frac{\partial f(\boldsymbol{\sigma},\boldsymbol{q})}{\partial \boldsymbol{\sigma}}:\dot{\boldsymbol{\sigma}}+\frac{\partial f(\boldsymbol{\sigma},\boldsymbol{q})}{\partial \boldsymbol{q}}:\dot{\boldsymbol{q}}=0 \Rightarrow$$

$$\boldsymbol{Q}:\dot{\boldsymbol{\sigma}}+\frac{\partial f(\boldsymbol{\sigma},\boldsymbol{q})}{\partial \boldsymbol{q}}:\dot{\boldsymbol{q}}=0 \tag{3.73}$$

By employing the expressions (3.51) and (3.72) the aforementioned expression may be transformed as follows:

$$\boldsymbol{Q}:\dot{\boldsymbol{\sigma}}+\frac{\partial f(\boldsymbol{\sigma},\boldsymbol{q})}{\partial \boldsymbol{q}}:\dot{\boldsymbol{q}}=0\Rightarrow \dot{\Lambda}\cdot H=-\frac{\partial f(\boldsymbol{\sigma},\boldsymbol{q})}{\partial \boldsymbol{q}}:\dot{\boldsymbol{q}}=-\dot{\Lambda}\cdot\frac{\partial f(\boldsymbol{\sigma},\boldsymbol{q})}{\partial \boldsymbol{q}}:\boldsymbol{h}\Rightarrow$$

$$H=-\left(\frac{\partial f(\boldsymbol{\sigma},\boldsymbol{q})}{\partial \boldsymbol{q}}:\boldsymbol{h}\right) \tag{3.74}$$

Thus the critical state of geomaterials may be introduced through the plastic hardening modulus as the state described mathematically as follows:

$$H=0\wedge P=0\wedge\dot{\boldsymbol{q}}=\boldsymbol{0} \tag{3.75}$$

Assuming that the critical state is attained the volumetric strain component is null while at least one component of the strain deviator tends to infinity. Furthermore, the material tends to portray no plastic hardening or softening. Any elastoplastic increment originating from the critical state should satisfy $\boldsymbol{Q}:\dot{\boldsymbol{\sigma}}=0$. The critical state comprises a special case of the failure state as depicted in expression (3.54) (the concept of critical state is explained thoroughly in section 3.9.2).

3.6.2 Isotropic hardening rule

The isotropic hardening rule controls the size evolution of the plastic yield envelope during plastic straining. The visual representation of isotropic hardening is portrayed in **Figure 3.5**. Assuming that the geomaterial exhibits plastic hardening the size of the plastic yield envelope tends to grow. The stress path AB in **Figure 3.10** (and its projection on the stress space illustrated in **Figure 3.9**) is characteristic of undergoing transformations during plastic hardening. On the other hand, assuming that the material point undergoes plastic softening *PYE* has the tendency to contract (represented by stress path AC in **Figure 3.9** and **Figure 3.10**). The size of the plastic yield envelope may be described by a single parameter governing the concentric evolution of *PYE*. Assuming a spherical *PYE*, the selected size could be represented through the radius $q=r$ or in the case of an elliptical *MCC* (Modified Cam-Clay) type model through the half length of the isotropic axis denoted $q=a$ (**Figure 3.5**). Therefore the hardening rule governs the evolution of such parameters controlling the size of *PYE* during plastic straining. The isotropic hardening rule incorporating

the hardening variables $\boldsymbol{q}$ may be described through expression (3.72) or in the case of a single hardening variable q:

$$\dot{q} = \dot{\Lambda} \cdot h \tag{3.76}$$

The isotropic hardening variable describes the material state and in most cases is expressed as a function of the incremental plastic strain $\dot{\boldsymbol{\varepsilon}}^p$ or the plastic work W^p. However, the measure of the incremental hardening variables (coincides with the scalar measure of the incremental plastic strain tensor) $\dot{\Lambda}$ may be a function of further quantities such as the incremental total strain or even time assuming time-dependency is accounted for.

Historically, the first expressions of isotropic hardening addressing the mechanical behavior of geomaterials would incorporate solely the volumetric component of plastic strain (Roscoe et al., 1963). Association of the isotropic hardening with the deviatoric component of plastic strains (Mroz and Norris, 1982; Nova, 1988) or with the 2nd order plastic work (Mroz and Norris, 1982) was postulated later. In the formulation of the proposed constitutive time dependent model the plastic strain tensor and time controls the scalar measure $\dot{\Lambda}$.

3.6.3 Kinematic hardening rule

The kinematic hardening rule controls the translation, rotation and distortion of the plastic yield envelope. The translational hardening portrays the effect of homothetic rendering of *PYE* (Dafalias and Popov, 1975; Mroz et al., 1978; Prevost, 1978; Mroz and Norris, 1982; Al-Tabbaa, 1987; Al-Tabbaa and Wood, 1987; Kavvadas, 1995; Wood, 1995) as depicted in **Figure 3.6**. The rotational hardening on the other hand portrayed in **Figure 3.10** accounts for any alteration in the inclination of *PYE* (Crouch and Wolf, 1994; Hashiguchi and Chen, 1998). Distortional hardening finally accounts for any changes in the shape of the plastic yield envelope (Pender, 1978; Dafalias, 1987; Belokas, 2008). The mathematical formulation of the aforementioned hardening rules may be expressed through equation (3.72).

The two most widely known kinematic hardening rules are Prager's linear kinematic hardening law (Prager, 1955) and a modification of that undertaken by Ziegler (Ziegler, 1959). Based on Prager's kinematic hardening postulate the center of the

plastic yield envelope translates proportionally to the plastic strain increment (**Figure 3.15**). Hence, assuming that the center may be described through the stress tensor $\boldsymbol{\sigma}_K$ then the measure of the hardening incremental hardening variables is constant $\dot{\Lambda} = c$ and $\boldsymbol{h} = \dot{\boldsymbol{\varepsilon}}^p$ leading to the formulation here below:

$$\dot{\boldsymbol{\sigma}}_K = c \cdot \dot{\boldsymbol{\varepsilon}}^p \tag{3.77}$$

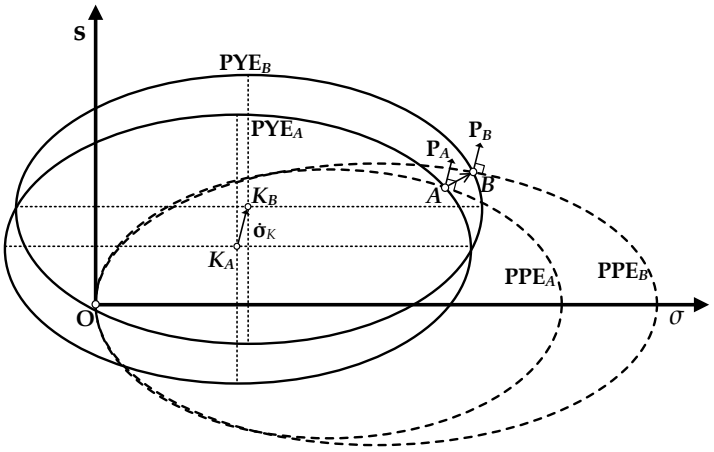

Figure 3.15: Schematic representation of Prager's linear kinematic hardening postulate.

In other words the center may be translated proportionally to the gradient of the plastic potential envelope $\boldsymbol{P}$ (the plastic potential tensor). Prager's kinematic postulate has been employed in an ensemble of constitutive formulations (i.e. Walker, 1981; Ohno, 1982; Krempl et al. 1986; Watanabe and Atluri, 1986).

Ziegler (1955) proposed a slight modification of Prager's original formulation (**Figure 3.16**), by translating the center proportionally to the back stress tensor $\boldsymbol{\sigma}_{back} = \boldsymbol{\sigma} - \boldsymbol{\sigma}_K$ and further incorporating the measure of the incremental hardening variables as $\dot{\Lambda} = \dot{\mu}$ and $\boldsymbol{h} = \boldsymbol{\sigma}_{back} = \boldsymbol{\sigma} - \boldsymbol{\sigma}_K$ leading to the following expression:

$$\dot{\boldsymbol{\sigma}}_K = \dot{\mu} \cdot \left(\boldsymbol{\sigma} - \boldsymbol{\sigma}_K \right) \tag{3.78}$$

where the employed parameter $\dot{\mu}$ may be expressed as a function of the plastic strain increment $(\dot{\mu} = b \cdot \dot{\varepsilon}^p)$ or the deviatoric stress increment $(\dot{\mu} = b \cdot \dot{q})$.

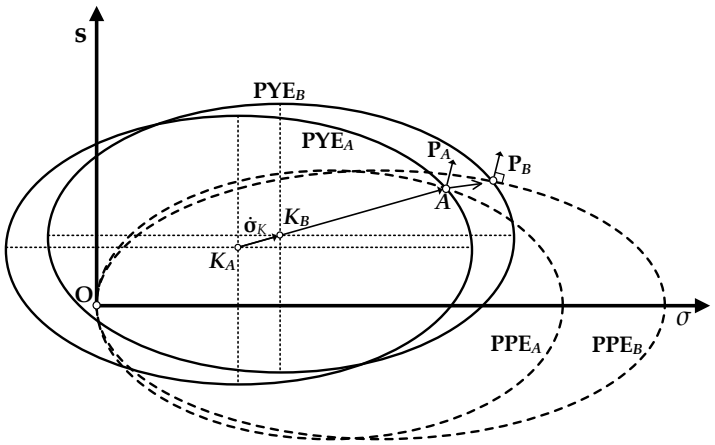

Figure 3.16: Schematic representation of Ziegler's kinematic hardening postulate.

Zieger's kinematic postulate has been employed extensively in the literature in an ensemble of constitutive formulations (i.e. Shield and Ziegler, 1958; Mroz, 1967; Nagtegaal and De Jong, 1982; Agah-Tehrani et al., 1987).

3.7 Elastoplastic stiffness modulus

The elastoplastic stiffness modulus $\boldsymbol{C}^{ep}$ associates the incremental stress with the incremental strain tensor in the case of elastoplastic stressing. The general constitutive relation connecting stress and strain can be expressed in its incremental form as follows:

$$\dot{\boldsymbol{\sigma}} = \boldsymbol{C} : \dot{\boldsymbol{\varepsilon}} \tag{3.79}$$

Assuming that the material exhibits purely elastic behavior $\boldsymbol{\varepsilon} = \boldsymbol{\varepsilon}^e$ then the total and the elastic stiffness moduli coincide $\boldsymbol{C} = \boldsymbol{C}^e$. However, assuming an elastoplastic increment is sustained, the increment of stress may be described through the following expression:

$$\dot{\boldsymbol{\sigma}} = \boldsymbol{C}^{ep} : \dot{\boldsymbol{\varepsilon}} = \boldsymbol{C}^e : \dot{\boldsymbol{\varepsilon}}^e = \boldsymbol{C}^e : \left(\dot{\boldsymbol{\varepsilon}} - \dot{\boldsymbol{\varepsilon}}^p \right) = \boldsymbol{C}^e : \left(\dot{\boldsymbol{\varepsilon}} - \dot{\Lambda} \cdot \boldsymbol{P} \right) \tag{3.80}$$

By employing expression (3.55) the elastoplastic stiffness tensor may be formulated as follows:

$$\boldsymbol{C}^{ep} : \dot{\boldsymbol{\varepsilon}} = \boldsymbol{C}^e : \left(\dot{\boldsymbol{\varepsilon}} - \dot{\Lambda} \cdot \boldsymbol{P} \right) = \boldsymbol{C}^e : \left(\dot{\boldsymbol{\varepsilon}} - \frac{\boldsymbol{Q} : \boldsymbol{C}^e : \dot{\boldsymbol{\varepsilon}}}{H + \boldsymbol{Q} : \boldsymbol{C}^e : \boldsymbol{P}} \cdot \boldsymbol{P} \right) \Rightarrow$$

$$\boldsymbol{C}^{ep}:\dot{\boldsymbol{\varepsilon}}=\boldsymbol{C}^{e}:\dot{\boldsymbol{\varepsilon}}-\frac{1}{H+\boldsymbol{Q}:\boldsymbol{C}^{e}:\boldsymbol{P}}\cdot\left(\boldsymbol{Q}:\boldsymbol{C}^{e}:\dot{\boldsymbol{\varepsilon}}\right)\cdot\left(\boldsymbol{C}^{e}:\boldsymbol{P}\right)\Rightarrow$$

$$\boldsymbol{C}^{ep}:\dot{\boldsymbol{\varepsilon}}=\boldsymbol{C}^{e}:\dot{\boldsymbol{\varepsilon}}-\frac{1}{H+\boldsymbol{Q}:\boldsymbol{C}^{e}:\boldsymbol{P}}\cdot\left[\left(\boldsymbol{C}^{e}:\boldsymbol{P}\right)\otimes\left(\boldsymbol{Q}:\boldsymbol{C}^{e}\right)\right]:\dot{\boldsymbol{\varepsilon}}\Rightarrow$$

$$\boldsymbol{C}^{ep}:\dot{\boldsymbol{\varepsilon}}=\left\{\boldsymbol{C}^{e}-\frac{1}{H+\boldsymbol{Q}:\boldsymbol{C}^{e}:\boldsymbol{P}}\cdot\left[\left(\boldsymbol{C}^{e}:\boldsymbol{P}\right)\otimes\left(\boldsymbol{Q}:\boldsymbol{C}^{e}\right)\right]\right\}:\dot{\boldsymbol{\varepsilon}}\Rightarrow$$

$$\boldsymbol{C}^{ep}=\boldsymbol{C}^{e}-\frac{1}{\Omega}\cdot\left[\left(\boldsymbol{C}^{e}:\boldsymbol{P}\right)\otimes\left(\boldsymbol{Q}:\boldsymbol{C}^{e}\right)\right] \tag{3.81}$$

and Ω may be computed through the following expression:

$$\Omega=H+\boldsymbol{Q}:\boldsymbol{C}^{e}:\boldsymbol{P} \tag{3.82}$$

In the finite element codes the initial elastoplastic stiffness matrix $\boldsymbol{C}^{ep}$ at the beginning of the loading increment is employed for the elastoplastic prediction of the forthcoming state. Assuming that equilibrium is not attained the code undergoes numerical iterations until convergence is achieved.

3.8 Hardening elastoplasticity postulates

The classical theory of elastoplasticity incorporates arbitrarily selected forms of the plastic yield and potential functions and isotropic and/or kinematic hardening rules. However, the necessity arises for certain physical aspects (Desai and Siriwardane, 1984) to be described through the aforementioned employed expressions. The basic principles (as described by Prevost and Hoeg, 1975 for the simulation of strain softening materials) are summarized here below:

- The **continuity condition** states that orthogonally to the plastic yield surface no incremental plastic strain may be accumulated. In other words during neutral loading $\boldsymbol{Q}:\dot{\boldsymbol{\sigma}}=0$ the incremental plastic strain tensor is null (Prager, 1949; Desai and Siriwardane, 1984).
- The **consistency condition** postulates that whenever elastoplastic strains are sustained the stress state needs to lay always on the plastic yield envelope. The mathematical description of the principle may be formulated through $\dot{f}(\boldsymbol{\sigma},\boldsymbol{q})=0$.

- The **irreversibility condition** states that the undergoing work during unloading followed after elastoplastic stressing is always positive $\dot{W}^p > 0$ considering the positive rate of entropy. Drucker's (1951, 1956, 1959) stability postulate would assume:

$$\Delta\boldsymbol{\sigma} : \dot{\boldsymbol{\varepsilon}}^p = \left(\boldsymbol{\sigma} - \boldsymbol{\sigma}^*\right) : \dot{\boldsymbol{\varepsilon}}^p > 0 \tag{3.83}$$

  The expression above incorporates the elastoplastic state of stress on *PYE* $\boldsymbol{\sigma}$, the elastic state $\boldsymbol{\sigma}^*$ and $\Delta\boldsymbol{\sigma}$ is the elastoplastic stress increment. Convexity of the plastic potential envelope stems from expression (3.83) (Prevost and Hoeg, 1975).

- The **uniqueness condition** dictates the existence of a unique association between the incremental state and the incremental strain response variables (Desai and Siriwardane, 1984; Darve et al., 1995). Loading is normally employed to denote any change in the state variables while alterations in the response denote transformations undergoing in the strain tensor. The alteration in a combination of certain state variables and some strain components may also be considered as loading. The remaining state variables and strain components could be classified as response variables.

The continuity and irreversibility conditions are always satisfied by the constitutive formulations founded on the elastoplasticity principles. However, special attention needs to be paid on the irreversibility and uniqueness principles in order to assure stability. The concept of irreversibility portrayed in **Figure 3.17** through the stress path AB originating from the elastic state $\boldsymbol{\sigma}^*$ (represented by point A) transitioning to an elastoplastic state $\boldsymbol{\sigma}$ (through point B) followed by a loading increment $\dot{\boldsymbol{\sigma}}$ may be described through the 2nd order plastic work required for the unloading to the original state as follows:

$$\dot{W}^p = \Delta\boldsymbol{\sigma} : \dot{\boldsymbol{\varepsilon}}^p + \dot{\boldsymbol{\sigma}} : \dot{\boldsymbol{\varepsilon}}^p = \left(\boldsymbol{\sigma} - \boldsymbol{\sigma}^*\right) : \dot{\boldsymbol{\varepsilon}}^p + \dot{\boldsymbol{\sigma}} : \dot{\boldsymbol{\varepsilon}}^p > 0 \tag{3.84}$$

Drucker's postulates may be derived from the aforementioned expression (3.84) as follows:

$$\dot{\boldsymbol{\sigma}} : \dot{\boldsymbol{\varepsilon}}^p \geq 0 \tag{3.85}$$

$$\left(\boldsymbol{\sigma}-\boldsymbol{\sigma}^{*}\right):\dot{\boldsymbol{\varepsilon}}^{p}>0 \tag{3.86}$$

Equation (3.85) dictates the use of an associated flow rule while accounting solely for plastic hardening through $\boldsymbol{Q}:\dot{\boldsymbol{\sigma}}>0$. Expression (3.86) portrays the convexity of the plastic potential envelope (coincides with *PYE*). Regardless whether Drucker's postulate does not allow simulation of plastic softening, it does conform with the uniqueness principle thus leading to a stable assumption of the constitutive behavior.

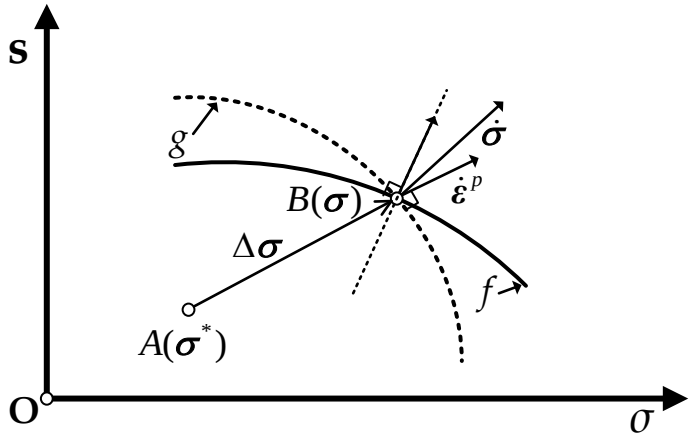

Figure 3.17: Elastoplastic loading increment originating from an elastic state.

Drucker's postulate may allow for uniqueness but still comprises an assumption and is not founded solely on the principles of thermodynamics. Instead, Prevost and Hoeg (1975) and Hueckel and Maier (1977a & 1977b) proved that it is possible for the plastic work to be negative by simulating plastic softening without any of the thermodynamic laws to be violated and even account for a non-associated flow rule. Hence, regardless whether the constitutive formulation incorporates an associated or a non-associated flow rule it is possible to conform to the uniqueness postulate for infinitesimal loading increments. Hill's stability postulate (1958) states that the second order work may be expressed as follows:

$$\forall\,\dot{\boldsymbol{\sigma}},\dot{\boldsymbol{\varepsilon}}^{p}:\dot{W}=\dot{\boldsymbol{\sigma}}:\dot{\boldsymbol{\varepsilon}}>0 \tag{3.87}$$

Hence, the second order plastic work may still become negative allowing for numerical simulation of plastic softening (Darve et al., 1985) by satisfying the condition $\dot{W}^{p}=\dot{\boldsymbol{\sigma}}:\dot{\boldsymbol{\varepsilon}}^{p}>-\dot{\boldsymbol{\sigma}}:\dot{\boldsymbol{\varepsilon}}^{e}$.

Uniqueness condition "in the large" (not accounting for infinitesimal loading increments) is impossible (based on Hueckel and Maier, 1977a & 1977b) when:

- the critical state has been attained and consequently expression (3.75) is satisfied (there is an infinite number of solutions satisfying the governing equation) or
- the conditions $H < 0$ and $\boldsymbol{Q} : \dot{\boldsymbol{\sigma}} < 0$ hold true leading to two distinct solutions for the strain tensor satisfying the same stress state. The expression leads to $-\boldsymbol{Q} : \boldsymbol{C}^e : \boldsymbol{P} < H < 0$.

The uniqueness of the solution is of crucial importance considering it is associated with the definition of the compliance matrix $\boldsymbol{D}$ ($\dot{\boldsymbol{\varepsilon}} = \boldsymbol{D} : \dot{\boldsymbol{\sigma}}$) computed through inversion of the elastoplastic modulus $\boldsymbol{D}^{ep} = \boldsymbol{C}^{ep^{-1}}$. However, the elastoplastic stiffness matrix may not always be positive definite or in simple words the following condition may not always be satisfied:

$$\left| \boldsymbol{C}^{ep} \right| \neq 0 \tag{3.88}$$

3.9 Intrinsic and structured states

In the current section we will be introducing the mechanical characteristic of structured and structureless states. The Critical State postulate is reviewed and the strength Envelopes (Intrinsic, Structure and Plastic) employed in classical elastoplasticity are summarized.

Geomaterials are characterized as structured and structureless based on their mechanical behavior (Vaughan et al., 1988; Leroueil and Vaughan, 1990). Structureless soils can only be encountered in special cases under idealized conditions. In such states the resistance attributing to the soil strength stems solely from the interlocking of the soil particles. Note, that the soil particles are considered relatively stiff and unyielding under "normal" stress levels. Structureless soils may be encountered in cases where the sedimentation and deposition results in a state that can be characterized solely by the specific volume ($v = 1 + e$) and the current effective stress field ($\boldsymbol{\sigma}$). Note that the dots have been dropped for simplicity.

3.9.1 Intrinsic strength envelope

All structureless states of a given geomaterial may be enclosed within the Intrinsic Strength Envelope (*ISE*). The *ISE* comprises the virtual boundary enclosing all structureless states at which the geomaterial falls into after the accumulation of substantial strains associated with failure. In such case the intrinsic anisotropy is null due to the chaotic distribution of the soil particle orientation at the initiation of failure. Every structureless state characterized as intrinsic can be described solely by the effective stress field and void ratio. The following expression portrays the mathematical formulation of the intrinsic strength envelope:

$$F^*\left(\boldsymbol{\sigma},\alpha^*,c\right)=\frac{1}{c^2}\cdot\boldsymbol{s}:\boldsymbol{s}+\left(\sigma-a^*\right)^2-\left(a^*\right)^2=0 \tag{3.89}$$

The star " * " superscript is employed to denote the intrinsic measures. a^* stands for the halfsize of the *ISE* oriented along the isotropic axis illustrated in **Figure 3.18**. Orientation of the intrinsic strength envelope is along the hydrostatic axis. The *ISE* is allowed to harden isotropically by associating the halfsize of the *ISE* with the alterations in the void ratio and the stress state.

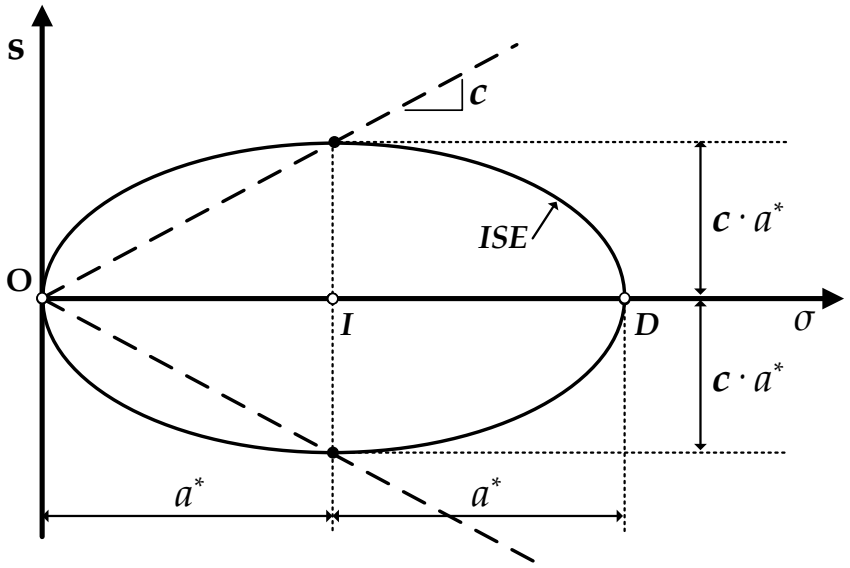

Figure 3.18: Schematic representation of the Intrinsic Strength Envelope (*ISE*).

3.9.2 Critical State

The study of structureless soils by Roscoe et al. (1963) set the foundation for the Critical State Theory along with the Critical State Soil Mechanics theory (*CSSM* by

Schofield and Wroth, 1968). The investigation of the mechanical response of structureless geomaterials contributed to the introduction of elementary empirical relations of the basic mechanical characteristics (i.e. the compressibility and strength) as a function of the index properties.

The Critical State Soil Mechanics theory comprises the foundation stone for most sophisticated constitutive formulations addressing the mechanical behavior of soils. It was originally developed to describe the response of isotropically consolidated soils. Direct simple shear and triaxial tests, emulating compression or extension, were performed on both normally loaded and preloaded specimens (Roscoe et al., 1963). The theory was founded on the observation that the structureless soils are independent of the loading history and can thus be described accurately solely from the current state $(\boldsymbol{\sigma}, v)$. The conditions at which the prior observation was based are summarized here below:

- In **Isotropic Compression** originating from a normally loaded isotropically consolidated state depicted in the *q*-*p*-*v* space through the lateral pressure coefficient $K = \sigma_3'/\sigma_1' = 1$ and the Isotropic Normal Compression Line (*I*-*NCL*) portrayed in **Figure 3.19**. The material constants N_{iso}^{*} and λ control the position and inclination of the Isotropic Normal Compression line in the *v*-ln*p* space.
- The **Critical State** at **Failure** corresponds to the accumulation of potentially infinite deviatoric strains of the soil element under constant volume assuming either drained or undrained boundary conditions. Such states are characterized as Critical and comprise the Critical State Surface (*CSS*). The projection of the *CSS* in the *v*-ln*p* space defines the Critical State Line (*CSL*). The projection of the *CSS* in the stress space *p*-*q* emulating either compression is portrayed through the inclination M_c or extension through M_e. In the *v*-ln*p* space the Critical State Line is defined through the parameters Γ and $\lambda_{cs} = \lambda$.

It is also possible to include the one-dimensional compression of normally loaded soils in the aforementioned cases justifying the Critical State Soil Mechanics postulate. In the one-dimensional compression the mechanical response in the *q*-*p*-*v* space is defined through the lateral pressure coefficient at rest denoted $K_0 = \sigma_3'/\sigma_1'$ and the K_0-Normal Compression Line (K_0-*NCL*). The material constants controlling

the mechanical behavior in this case according to the *CSSM* are the K_0 value governing the inclination in the *p*-*q* space through the stress ratio $n_0 = q/p = 3\cdot(1-K_0)/(1+2\cdot K_0)$ and the constants $N^*_{K_0}$ and λ designating the *v*-ln*p* response.

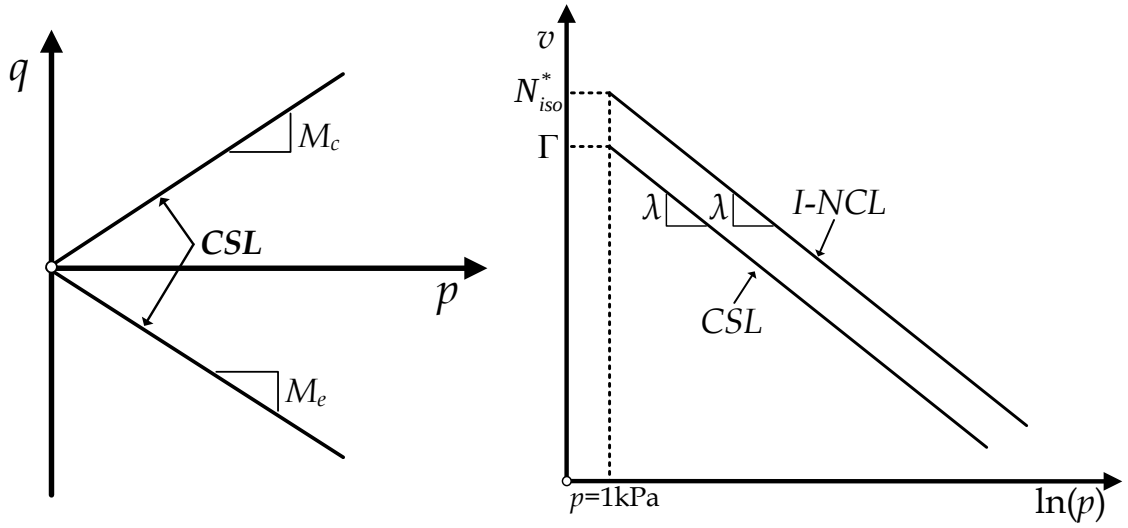

Figure 3.19: Observations on the mechanical response justifying the Critical State Soil Mechanics theory.

In the *CSSM* theory the stress history is accounted for through an equivalent isotropic pressure along the *I-NCL* (i.e. Hvorslev's equivalent stress, p_e*). Moreover, the *CSL* comprises the virtual boundary between compressive and dilative behavior. The mechanical behavior associated with volume loss under drained conditions or with the generation of positive excess water pressure assuming undrained boundary conditions will be classified as compressive. The dilative response is associated with volume increase assuming drained conditions or with the generation of negative excess porewater pressure under undrained conditions.

The projection of all stress states prescribing the transition from the compressive to the dilative mechanical response in the *v*-ln*p* space comprises the critical overconsolidation ratio line according to Roscoe et. al. (1963) (another term for the critical overconsolidation ratio line is Phase Transformation Line, *PTL*). In essence, such states lay on the phase transformation boundary. The *CSL* coincides with the critical voids ratio line by Roscoe et al. (1963). The assumption that the phase transformation line and the critical state line coincide was introduced for simplicity considering that it is a rough approximation at best as can be seen from a careful examination of **Figure 3.20**.

Finally, according to Roscoe et al. (1963) all possible states of a given soil element are defined through the Roscoe-Rendulic and Hvorslev envelopes comprising the State boundary surface (SBS) in the *CSSM* theory (**Figure 3.21**). It is emphasized that the critical state refers to the intrinsic states. Note that the inclination c in **Figure 3.18** comprises the projection of the *CSL* in the stress hyperplane.

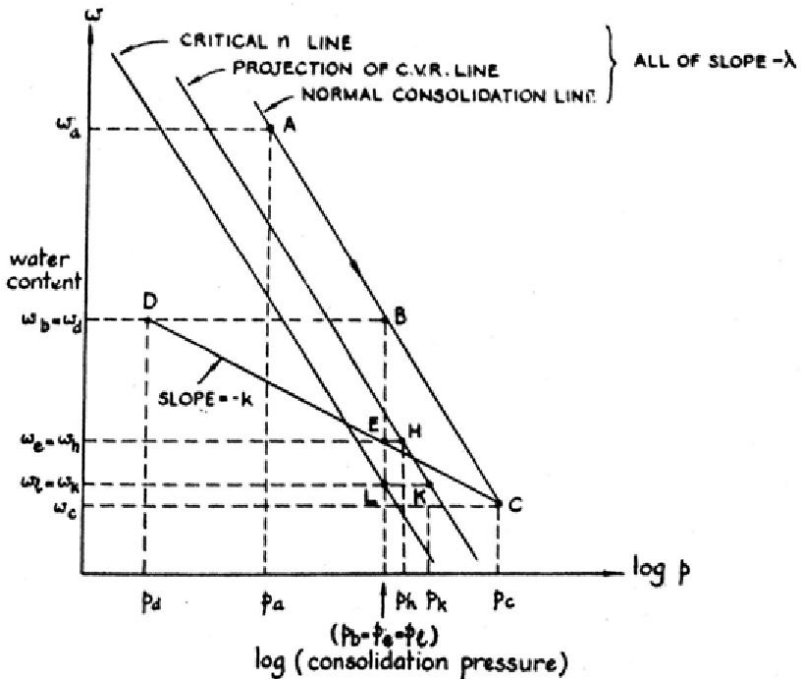

Figure 3.20: Critical State Line and Phase Transformation Line for cohesive soils (Roscoe et al., 1963).

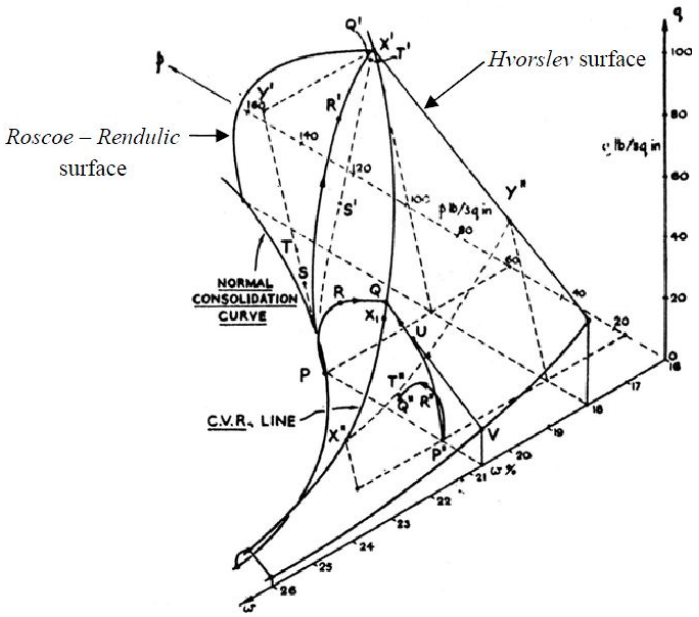

Figure 3.21: Critical State Soil Mechanics principles introduced by Roscoe et al. (from Belokas, 2008).

3.9.3 Structure strength envelope

Natural soils are often characterized as structured. In contrast with structureless media structured soils exhibit significant differences in terms of stiffness, strength, dilatancy and anisotropy influenced by structure. The two basic structure inducing mechanisms are the stress history and bonding. Structure comprises the memory of the geomaterial and governs the mechanical response of the soil. The stress history governs the memory of the geomaterial (due to the divergence of the current stress state from the structured) while bonding contributes to the interparticle resistance. Note that the stress history (i.e. Kavvadas, 1999) and the bonding process (i.e. Cotecchia and Chandler, 1998; Kavvadas, 1998) may act simultaneously.

The Structure Strength Envelope (*SSE*) portrays the effect of bonding on the soil fabric (**Figure 3.22**). It defines the available strength due to bonding formation and hence encloses the *ISE*. The shape of the *SSE* is usually considered analogous to the Intrinsic and assuming that primary anisotropy is not simulated it can be defined through equation (3.90). Considering it encloses the *ISE* its size is allowed to degrade but at no time should it cross the intrinsic surface thus justifying its limit bound on the down side.

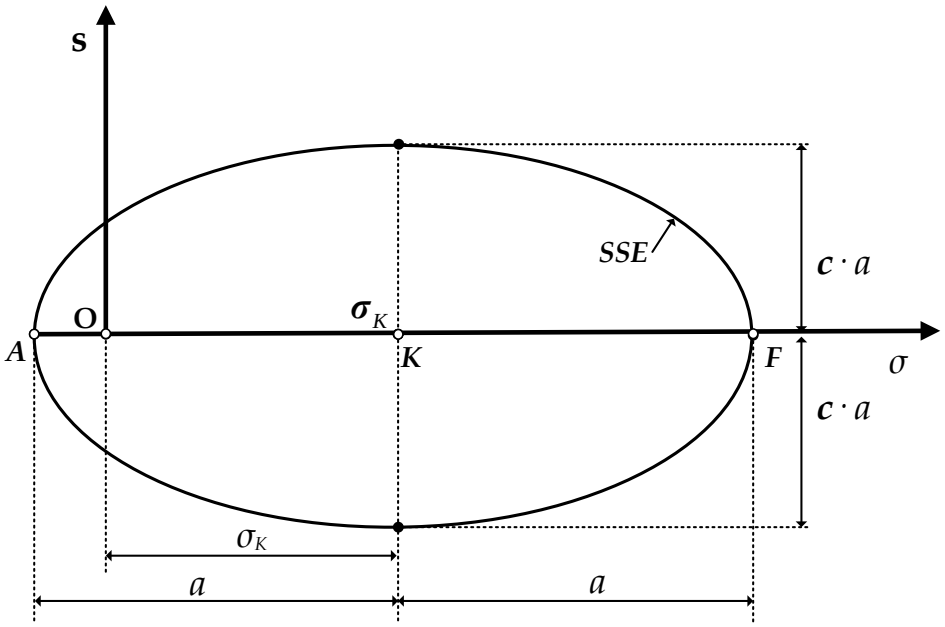

Figure 3.22: Schematic representation of the Structure Strength Envelope (*SSE*).

The expression for the Structure Strength Envelope assuming that primary anisotropy is not simulated is given below:

$$F\left(\boldsymbol{\sigma}, a, \sigma_K, c\right) = \frac{1}{c^2} \cdot \boldsymbol{s} : \boldsymbol{s} + \left(\sigma - \sigma_K\right)^2 - a^2 = 0 \tag{3.90}$$

The center of the *SSE* is translated solely along the hydrostatic axis to account for the effect of cementation and possible thixotropic bonding formed during isotropic compression responsible also for the isotropic orientation of the envelope. The halfsize of the *SSE* is denoted a and the ratio $B = \frac{a}{a^*} \geq 1$ is always greater than unity considering that the *ISE* comprises the lower bound of the Structure Strength Envelope. It is noted that at times when chemical or biological transformations have been undertaken throughout the bonding formation it is not unusual for the ratio not to reach the residual size value of the intrinsic, at least for the strain levels measured in the laboratory. Summarizing, the *SSE* comprises the bounding envelope and the *ISE* represents a characteristic surface coinciding with the *SSE* in the complete absence of structure (no primary anisotropy is considered).

3.9.4 Plastic yield Envelope

In the case of classical elastoplasticity the purely elastic domain, where the accumulated strains are recoverable upon removal of the loading increment, is infinitesimal and consequently the plastic yield surface is only but a fraction of the *SSE*. Even strains of the order of 0.01÷0.1‰ may be considered irreversible and hence inelastic (i.e. Georgiannou, 1988; Jardine, 1995; Smith et al. 1992). Hence, the Plastic Yield Envelope (*PYE*) comprises the boundary enclosing all purely elastic stress states (**Figure 3.23**). We will be assuming that the *PYE* and the *SSE* are associated through a similarity ratio denoted ξ. The similarity ratio is considered constant throughout plastic or elastic loading increments. Here follows the mathematical formulation of the *PYE* in the generalized stress space:

$$f\left(\boldsymbol{\sigma}, \boldsymbol{\sigma}_L, \alpha, c\right) = \frac{1}{c^2} \cdot \left(\boldsymbol{s} - \boldsymbol{s}_L\right) : \left(\boldsymbol{s} - \boldsymbol{s}_L\right) + \left(\sigma - \sigma_L\right)^2 - \left(\xi \cdot a\right)^2 = 0 \tag{3.91}$$

The center of the plastic yield envelope denoted $\boldsymbol{\sigma}_L$ is employed as a state variable and it may translate towards the *SSE* assuming an elastoplastic loading increment.

The proportionality ratio controls the size of the *PYE* and is assumed to be a fraction of the *SSE*, usually $\xi = 1‰ \div 5\%$. It is noted that the strain increment imposed in the

numerical analysis is not independent of the similarity ratio. Small ratios result in a small *PYE* and consequently the elastic increment to adjust the stress state on *PYE* is equally small.

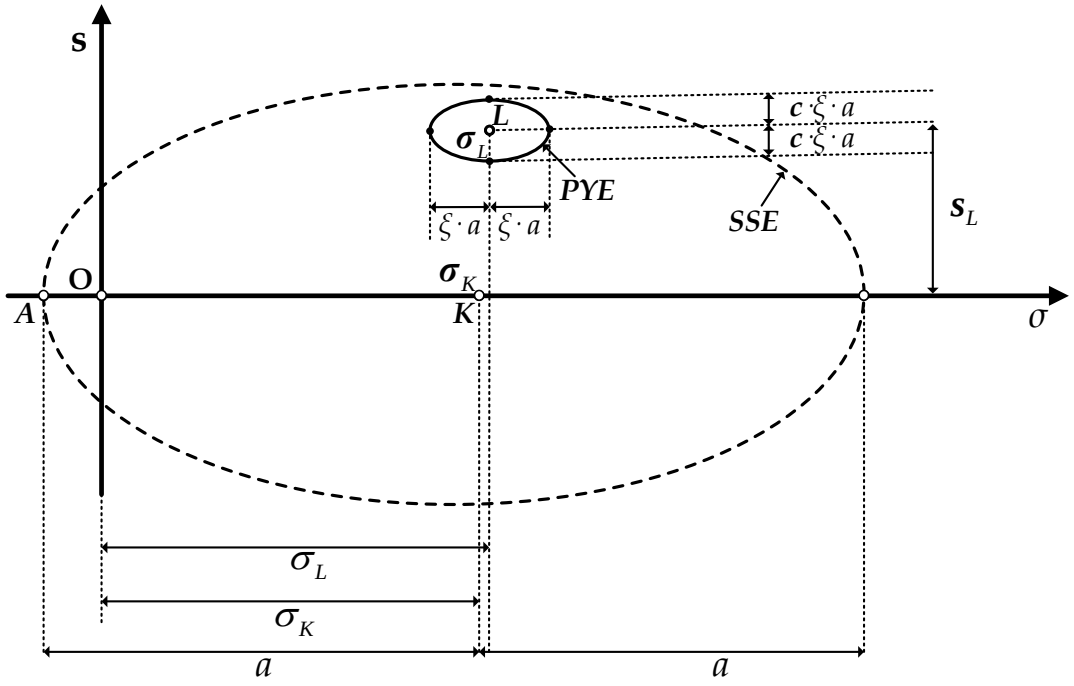

Figure 3.23: Schematic representation of the Plastic Yield Envelope (PYE).

The center of the plastic yield envelope denoted $\boldsymbol{\sigma}_L$ is controlled through a kinematic hardening law thus portraying the recent stress history through the secondary anisotropy tensor as will be shown in Chapter 5.

3.10 Concluding remarks

The present chapter summarizes the basic characteristics and principles of the classical theory of plasticity in geomaterials. The constitutive relations are employed in their incremental form and are expressed through the equations (3.11) and (3.79).

Expressions (3.11) to (3.82) portray the constitutive behavioral framework by incorporating:

a. the **elastic stiffness modulus** (through some type of elasticity-linear or nonlinear) denoted $\boldsymbol{C}^e$.

b. the **plastic yield envelope** (through the plastic yield function f) and consequently the **gradient**, $\boldsymbol{Q} = \frac{\partial f(\boldsymbol{\sigma}, \boldsymbol{q})}{\partial \boldsymbol{\sigma}}$.

c. the **plastic potential envelope** (through the plastic potential function g) or the stress-dilation relation and therefore the plastic potential tensor, $\boldsymbol{P} = \frac{\partial g(\boldsymbol{\sigma}, \boldsymbol{q})}{\partial \boldsymbol{\sigma}}$.

d. the plastic **hardening rules** of *PYE*.

e. the **plastic hardening modulus** H.

The critical state soil mechanics theory in soils was also reviewed. Soils were categorized in structured and structureless states and the critical state principle was analyzed. The Intrinsic and Structure Strength envelopes were introduced to denote the virtual boundaries enclosing all structureless and structured states respectively. Finally, the Plastic Yield Envelope was portrayed to denote the infinitesimal elastic domain.

The next chapter presents novel constitutive formulations founded on the principles of elastoplasticity further extended to account for viscous effects. Advantages and shortcomings of the most advanced constitutive formulations will be portrayed as well as the necessity for a new sophisticated framework emulating the time-dependent behavior.

4

Sophisticated time dependent constitutive models

4.1 General

The general theories describing time-dependent phenomena tend to gain more and more ground. Considering they are no longer restricted to specific boundary and loading conditions but can account for all possible undergoing stress and strain paths. Most recent time-dependent formulations allow for simulation of potentially all aspects associated with aging such as creep, stress relaxation and strain rate dependency. More advanced and sophisticated constitutive behavioral formulations are founded on the principles of elastoplasticity extended to account for time-dependency. More recent expressions of such general theories tend to allow for the plastic component to be introduced separately, through the theory of classical elastoplasticity, from the elastic and viscoplastic component.

Next, the most recent advancements in elastoviscoplastic constitutive formulations based on the overstress theory are reviewed. The proposed constitutive model to be analyzed in the forthcoming chapter incorporates the principles of the overstress postulate proposed by Perzyna (1962 & 1966). Regardless whether the viscous nucleus is given explicitly or straight forward in the proposed form to be employed in numerical modeling (it can be easily derived through experimental measurements) it satisfies and conforms to the overstress framework. Hence, here follows some basic constitutive formulations and the most recent advancements in the time-dependent overstress constitutive modeling.

4.2 Zienkiewicz's overstress constitutive framework and examples

The governing equations proposed by Zienkiewicz (Zienkiewicz and Cormeau, 1974; Zienkiewicz et al., 1975; Kanchi et al., 1978) would incorporate Perzyna's overstress principle in an elastoviscoplastic behavioral framework.

The strain tensor may be deconvolved in an elastic and a viscoplastic component as follows:

$$\boldsymbol{\varepsilon} = \boldsymbol{\varepsilon}^{e} + \boldsymbol{\varepsilon}^{vp} \tag{4.1}$$

In essence, the ideally elastic-perfectly plastic original behavior based on the classical theory of elastoplasticity was altered to account for the time effects. Hence, the plastic component of strain was replaced by the viscoplastic strain tensor.

The viscoplastic strain rate was expressed as a function of the stress state and the accumulated viscoplastic strain tensor:

$$\dot{\boldsymbol{\varepsilon}}^{vp} = \dot{\boldsymbol{\varepsilon}}^{vp}\left(\boldsymbol{\sigma}, \boldsymbol{\varepsilon}^{vp}\right) \tag{4.2}$$

Whenever the stress state exceeds the yield function F the viscoplastic component of strain tends to accumulate. The yield function may be expressed as follows:

$$F\left(\boldsymbol{\sigma}, \boldsymbol{\varepsilon}^{vp}\right) = 0 \tag{4.3}$$

In the aforementioned expression notation has not been employed randomly just to denote the difference to the plastic yield surface f. The yield function incorporated in the formulation of the governing equations coincides with the expression of overstress (the overstress principle was introduced previously in section 2.4.1). Hence, assuming that the stress state lays inside the yield surface the yield function is negative $F\left(\boldsymbol{\sigma}, \boldsymbol{\varepsilon}^{vp}\right) < 0$ and the behavior is purely elastic. When the state lays on the outer bound of the yield surface the material exhibits elastoviscoplastic behavior and the overstress function receives positive values $F\left(\boldsymbol{\sigma}, \boldsymbol{\varepsilon}^{vp}\right) > 0$.

The plastic potential tensor is computed as the gradient of the plastic potential function $g\left(\boldsymbol{\sigma}\right)$ through the following form:

$$\boldsymbol{P} = \frac{\partial g(\boldsymbol{\sigma})}{\partial \boldsymbol{\sigma}} \tag{4.4}$$

The expression above portrays the gradient of the plastic yield envelope incorporated in the governing equations to account for the viscoplastic strain rate:

$$\dot{\boldsymbol{\varepsilon}}^{vp} = \gamma \cdot \left\langle \Phi\left(F\right) \right\rangle \cdot \frac{\partial g}{\partial \boldsymbol{\sigma}} = \gamma \cdot \left\langle \Phi\left(F\right) \right\rangle \cdot \boldsymbol{P} \tag{4.5}$$

In expression (4.5) parameter γ represents a fluidity parameter, influenced by the material viscosity. Perfectly plastic behavior may be considered by employing an infinite value for the parameter $\gamma \to \infty$. The Macaulay brackets are employed for the viscous nucleus $\Phi\left(F\right)$ to account for the accumulation process of viscoplastic strains solely at instances when the overstress function takes positive values:

$$\begin{aligned} \left\langle \Phi\left(F\right) \right\rangle &= 0 \quad | \quad F < 0 \\ \left\langle \Phi\left(F\right) \right\rangle &= \Phi\left(F\right) \quad | \quad F \geq 0 \end{aligned} \tag{4.6}$$

A rather simplified linear relationship was chosen for the viscous nucleus:

$$\Phi\left(F\right) = \frac{F}{F_0} \tag{4.7}$$

In the previous expression (4.7) parameter F_0 represents some reference value of stress.

4.2.1 Non-hardening models

The plastic yield envelope and the plastic potential surface may or may not be associated. Zienkiewicz selected to describe the plastic yield function and consequently his overstress employed function through the Drucker-Prager model (degenerating to the Von Mises criterion for null value of the friction angle φ - **Figure 4.1**) and the Mohr-Coulomb failure criterion (falling into the Tresca criterion for null friction angle - **Figure 4.2**).

The mathematical formulations for the aforementioned criteria are depicted here below:

- Mohr-Coulomb:

$$F = \sigma \cdot \sin\varphi + \left(\cos a - \frac{\sin a \cdot \sin\varphi}{\sqrt{3}} \right) \cdot \sqrt{\frac{1}{2}\boldsymbol{s} : \boldsymbol{s}} - c \cdot \cos\varphi = 0 \tag{4.8}$$

- Drucker-Prager:

$$F = \frac{\sqrt{3} \cdot \sin\varphi}{\sqrt{\left(3 + \sin^2\varphi\right)}} \cdot \sigma + \sqrt{\frac{1}{2}\boldsymbol{s} : \boldsymbol{s}} - \frac{\sqrt{3} \cdot c \cdot \cos\varphi}{\sqrt{\left(3 + \cos^2\varphi\right)}} = 0 \tag{4.9}$$

Parameter a employed in equation (4.8) represents the Lode angle to be computed through the following expression:

$$-\frac{\pi}{6} < a = \frac{1}{3}\sin^{-1}\left\{ -\frac{3 \cdot \sqrt{3}}{2} \cdot \frac{\left[\frac{1}{3}\left(\boldsymbol{s} \bullet \boldsymbol{s}\right) : \boldsymbol{s}\right]}{\sqrt{\left(\frac{1}{2}\boldsymbol{s} : \boldsymbol{s}\right)^3}} \right\} \leq \frac{\pi}{6} \tag{4.10}$$

Symbol "$\bullet$" is employed to account for the product of two second order tensors.

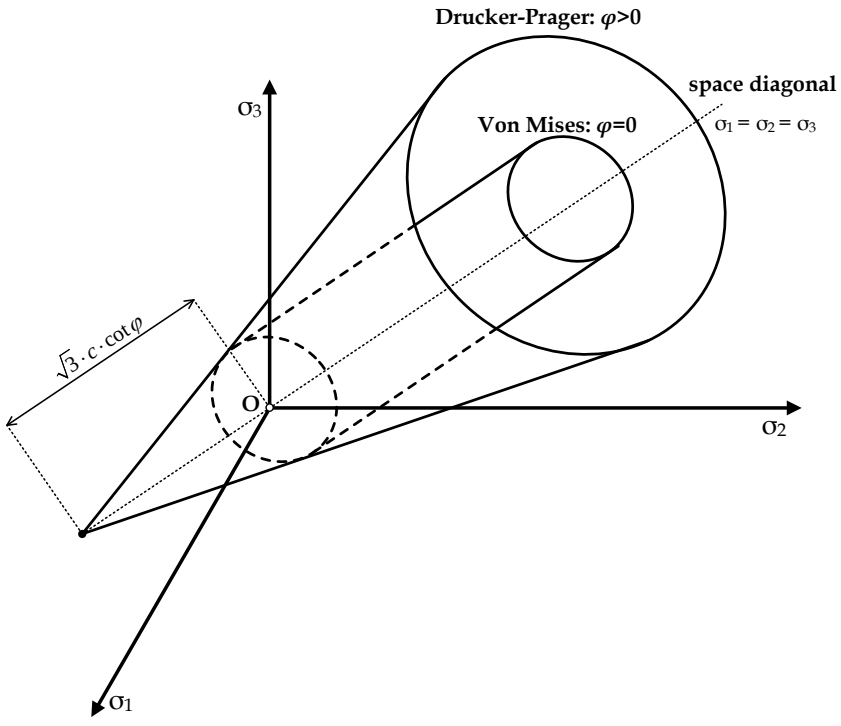

Figure 4.1: Drucker-Prager and Von-Mises failure criteria employed in Zienkiewicz's overstress viscoplastic formulation (1975).

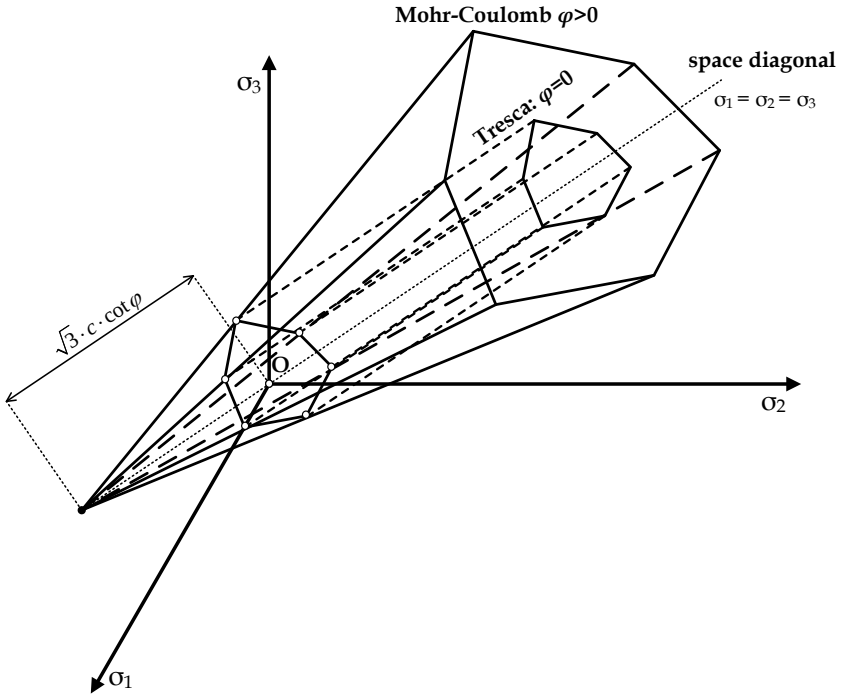

Figure 4.2: Mohr-Coulomb and Tresca failure criteria employed in Zienkiewicz's overstress viscoplastic formulation (1975).

The plastic potential function may be expressed by analogous forms:

- Mohr-Coulomb:

$$g(\boldsymbol{\sigma}) = \sigma \cdot \sin\theta + \left(\cos a - \frac{\sin a \cdot \sin\theta}{\sqrt{3}} \right) \cdot \sqrt{\frac{1}{2}\boldsymbol{s}:\boldsymbol{s}} - c^* \cdot \cos\theta \tag{4.11}$$

- Drucker-Prager:

$$g(\boldsymbol{\sigma}) = \frac{\sqrt{3} \cdot \sin\theta}{\sqrt{\left(3 + \sin^2\theta\right)}} \cdot \sigma + \sqrt{\frac{1}{2}\boldsymbol{s}:\boldsymbol{s}} - \frac{\sqrt{3} \cdot c^* \cdot \cos\theta}{\sqrt{\left(3 + \cos^2\theta\right)}} \tag{4.12}$$

The overstress function and the plastic yield function appear similar in form but different in the angle θ and c^*. The angle θ may be employed to account for any modification envisioned in the plastic potential tensor. Normality rule is justified by assuming that angle θ and the friction angle are equal. In this case, the gradient of the yield function and the plastic potential tensor coincide (the cohesion does not come into play). In any other case the flow rule is non-associated and assuming that no volume change is anticipated at elastoviscoplastic states then $\theta = 0$, thus falling into the simple Tresca (in the case of Mohr-Coulomb) or Von Mises (in the case of Drucker-Prager) failure criterion.

4.2.2 Hardening model

Another example of the elastoviscoplastic overstress framework employed by Zienkiewicz was based on the assumption of an MCC type model incorporating a Mohr-Coulomb criterion to describe the critical state line in the stress plane (**Figure 4.3**). The critical state line is represented as the line connecting points 2 and 4. Stress path 1-2 is characteristic of a strain hardening behavior while 3-4 represents plastic softening.

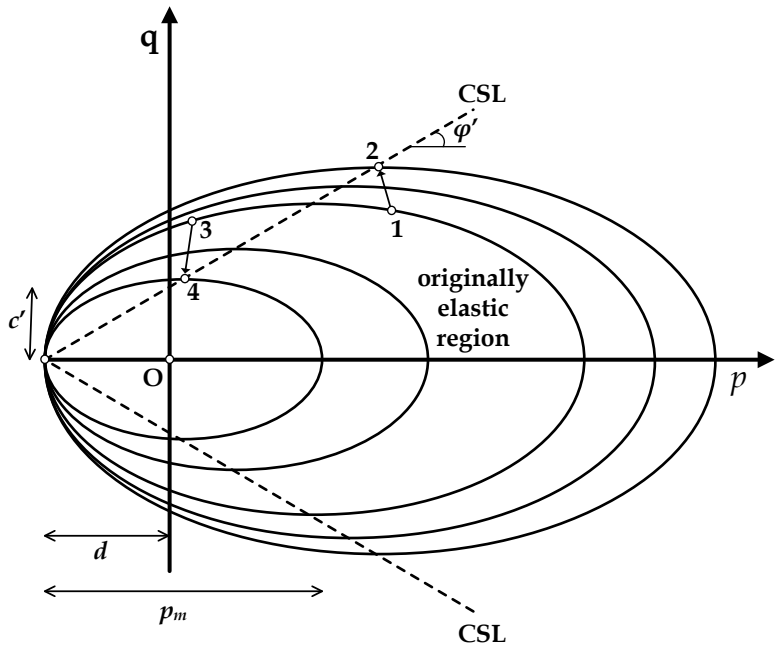

Figure 4.3: Graphical representation of the yield surface in the *p-q* space in the case of a critical strain hardening yield function (Zienkiewicz, 1975).

Parameters φ' and c' (note that $\tan(\varphi')$ resembles the *M* parameter in the *MCC*) may be expressed as a function of the friction angle φ and cohesion c as follows:

$$\tan(\varphi') = \frac{3 \cdot \sin\varphi}{\sqrt{3} \cdot \cos a - \sin a \cdot \sin\varphi}$$
$$c' = \frac{3 \cdot c \cdot \cos\varphi}{\sqrt{3} \cdot \cos a - \sin a \cdot \sin\varphi} \tag{4.13}$$

The yield function may be described through the following expression:

$$F = \frac{\left(\frac{3}{2} \cdot \boldsymbol{s} : \boldsymbol{s}\right)}{\left(p_m \cdot \tan\varphi'\right)^2} + \frac{\left(p - p_m - d\right)}{p_m^2} - 1 = 0 \tag{4.14}$$

The initial p_m is allowed to harden for a given material through evolution of the volumetric viscoplastic strain component analogously to the original law by Roscoe and Burland (1968). In this case an associated flow rule was employed $g = F$. The viscoplastic strain once again can be described through expression (4.5).

Zienkiewicz's elastoviscoplastic framework was amongst the first to employ Perzyna's overstress theory. It lacks the explicit definition of the plastic component in the classical sense of elastoplasticity and thus it cannot simulate accurately neither the plastic nor the time-dependent behavior. On the other hand, the formulation provides an insight to the elastoviscoplastic constitutive formulation and some preliminary qualitative observations on the viscous behavior may be drawn.

4.3 Adachi and Oka's overstress model

Adachi and Oka (1982) proposed a constitutive behavioral framework for the time dependent behavior of normally consolidated clays. The governing equations would incorporate Perzyna's overstress theory and the original Cam-Clay model in an elastoviscoplastic formulation. The multiparametric model would incorporate namely eight material parameters in need of calibration via experimental measurements (two undrained constant strain rate triaxial compression tests at different strain rates, simulating consolidation and swelling).

Adachi and Oka originating in a similar sense to Perzyna's overstress theory assumed the existence of a static yield function of the general form:

$$F\left(\boldsymbol{\sigma}, \boldsymbol{\varepsilon}^{vp}\right) = \frac{f\left(\boldsymbol{\sigma}, \boldsymbol{\varepsilon}^{vp}\right)}{k_s} - 1 \tag{4.15}$$

The dynamic yield function $f\left(\boldsymbol{\sigma}, \boldsymbol{\varepsilon}^{vp}\right)$ is an expression of the stress state and accumulated viscoplastic strains. Furthermore, the aforementioned formulation incorporates the work hardening parameter k_s. Perzyna's expression for the viscoplastic strains was employed:

$$\dot{\boldsymbol{\varepsilon}}^{vp} = \left\langle \Phi\left(F\right) \right\rangle \cdot \frac{\partial f}{\partial \boldsymbol{\sigma}} = \left\langle \Phi\left(F\right) \right\rangle \cdot \boldsymbol{Q} \tag{4.16}$$

Expression (4.16) portrays significant differences from equation (4.5) not simply due to the viscosity parameter γ that has been incorporated in the definition of the viscous nucleus $\Phi(F)$. By incorporating in expression (4.16) it is inherently assumed that an associated flow rule is adopted and therefore the plastic potential tensor coincides with the plastic yield gradient.

The viscous nucleus is determined experimentally and accounts for the strain rate effect upon material yielding. Hence, by manipulating equations (4.15) and (4.16) the dynamic yield function may be computed through the following expression:

$$f\left(\boldsymbol{\sigma}, \boldsymbol{\varepsilon}^{vp}\right) = k_s \cdot \left[1 + \Phi^{-1}\left(\sqrt{\frac{\dot{\boldsymbol{\varepsilon}}^{vp} : \dot{\boldsymbol{\varepsilon}}^{vp}}{\boldsymbol{Q} : \boldsymbol{Q}}}\right)\right] \tag{4.17}$$

The dynamic yield function may evolve due to isotropic viscoplastic strain rate hardening. The dynamic yield function term is employed to denote the hardening of a typical yield function (henceforth the notation for dynamic yield function assuming hardening is undertaken shall be changed to $f = f_d$). The rate sensitivity state is attained whenever the overstress $F = 0$. In such case, the $f = k_s$ and the notation shall be changed to f_s for the static situation. In this case the inelastic behavior of soils represents purely the elastoplastic state and the following postulate holds true:

$$\dot{\boldsymbol{\varepsilon}}^{p} = \dot{\Lambda} \cdot \frac{\partial f}{\partial \boldsymbol{\sigma}} = \dot{\Lambda} \cdot \boldsymbol{Q} \tag{4.18}$$

The original Cam-Clay criterion (Roscoe et al., 1963) was employed as to account for the static yield function:

$$f_s = k_s = \frac{\sqrt{\boldsymbol{s}_s : \boldsymbol{s}_s}}{M^* \cdot \sigma_s} + \ln\left(\sigma_s\right) \tag{4.19}$$

The subscript *s* is incorporated in the expressions above to denote the values at the static equilibrium state.

In the formulation of Adachi and Oka the parameter k_s is considered as a strain hardening (namely volumetric strain hardening) parameter instead of a work

hardening parameter as was envisioned by Perzyna. To put it in plain words the parameter k_s may be expressed as follows:

$$k_s = \ln\left(p_{m,s}\right) \tag{4.20}$$

The strain hardening parameter k_s may be related to the inelastic volumetric strain component (considering that the subscript *s* denotes the static equilibrium state then the inelastic and plastic components coincide - inviscid behavior) as follows:

$$\dot{\varepsilon}^p = \frac{\lambda - \kappa}{1+e} \cdot \frac{\dot{p}_{m,s}}{p_{m,s}} \tag{4.21}$$

The expression (4.21) above incorporates the compression index λ and the swelling index κ in the $e - \ln\sigma$ space. Hence, the purely elastoplastic behavior may be formulated by incorporating equations (4.18) to (4.21).

The elastoviscoplastic behavior shall be analyzed henceforth. The dynamic yield surface needs to be described by the same primal governing relation as the static yield surface (considering that the dynamic yield surface falls into the static for null values of the overstress $F = 0$):

$$f_d = k_d = \frac{\sqrt{\boldsymbol{s}:\boldsymbol{s}}}{M^* \cdot \sigma} + \ln\left(\sigma\right) \tag{4.22}$$

The parameter k_d accounts for both aspects of strain hardening and rate dependency. Analogously to the strain hardening parameter k_s the dynamic parameter k_d may be defined as follows:

$$k_d = \ln\left(p_{m,d}\right) \tag{4.23}$$

To make a long story short, the overstress function can be expressed as $F = \frac{k_d}{k_s}$. Hence the overstress portrays the effect of simultaneous contributing aspects of strain hardening and time-dependency (through the parameter k_d) over strain hardening (portrayed via parameter k_s). The schematic representation of the dynamic and static yield surfaces are depicted in **Figure 4.4**.

In the diagram $p_{d,i}$ stands for the dynamic (subscript *d*) isotropic (subscript *i*) state after a single day of creep subjected to isotropic pressure $p_{m,d,i}$. The static state $p_{s,i}$ is introduced in an exact analogy to the dynamic (characteristic of the static isotropic state after a single day of creep subjected to isotropic pressure $p_{m,s,i}$). $p_{s,i}$ represents the equivalent static state to $p_{d,i}$ with the same strain hardening, at the same inelastic (either plastic or viscoplastic) volumetric strain rate (isotropic compression is undertaken) and lays on the static isotropic consolidation line after infinite time of isotropic compression.

The path originating from $p_{d,i}$ transitioning to p_d is the graphical representation of a shear deformation being imposed leading to the accumulation of viscoplastic strains (through the viscoplastic strain rate). The path originating from $p_{d,i}$ to $p_{s,u}$ represents the porewater pressure increase when after a day of consolidation undrained conditions are established. Finally, the path from $p_{d,i}$ to $p_{s,\infty}$ is characteristic of secondary compression under constant imposed isotropic pressure.

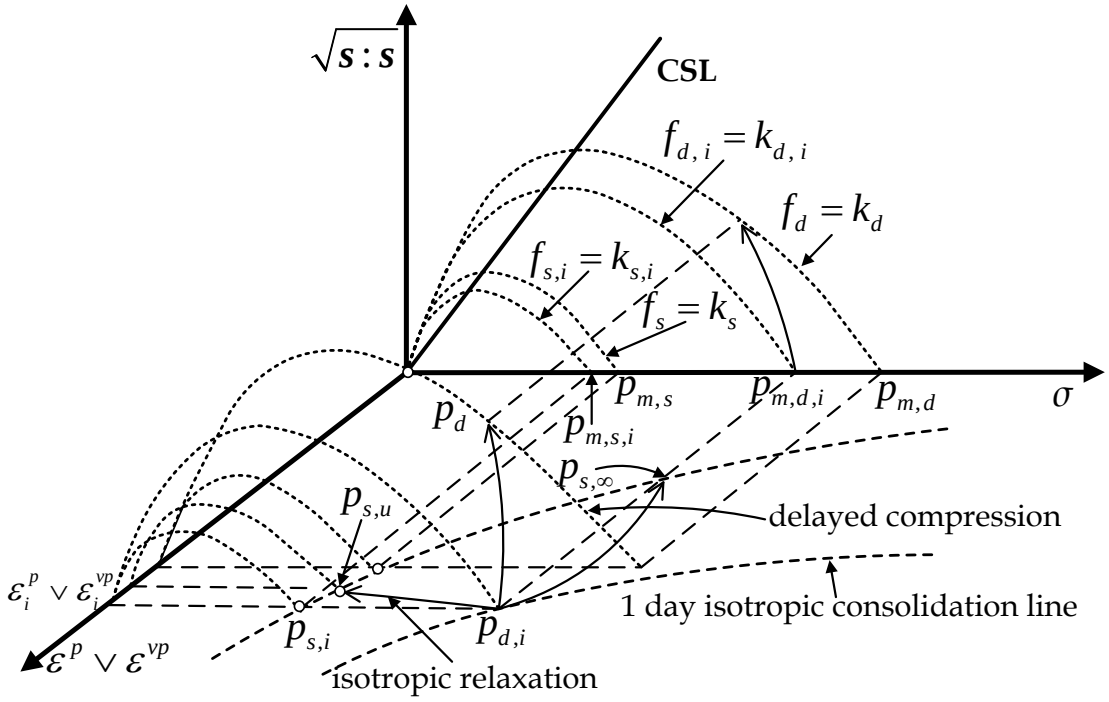

Figure 4.4: Schematic representation of both static and dynamic yield surface (Adachi and Oka, 1982).

F considering the aforementioned equations (equations (4.15), (4.19), (4.20), (4.22) and (4.23)) can thus be expressed as follows:

$$F = \frac{\ln\left(p_{m,d}\right)}{\ln\left(p_{m,s}\right)} - 1 = \frac{\ln\left(p_{m,d}\right) - \ln\left(p_{m,s}\right)}{\ln\left(p_{m,s}\right)} \tag{4.24}$$

Furthermore, by integrating equation (4.21) under the initial condition of $\varepsilon^p = \varepsilon_i^p$:

$$\varepsilon^p - \varepsilon_i^p = \frac{\lambda - \kappa}{1+e} \cdot \ln\left(\frac{p_{m,s}}{p_{m,s,i}}\right) \tag{4.25}$$

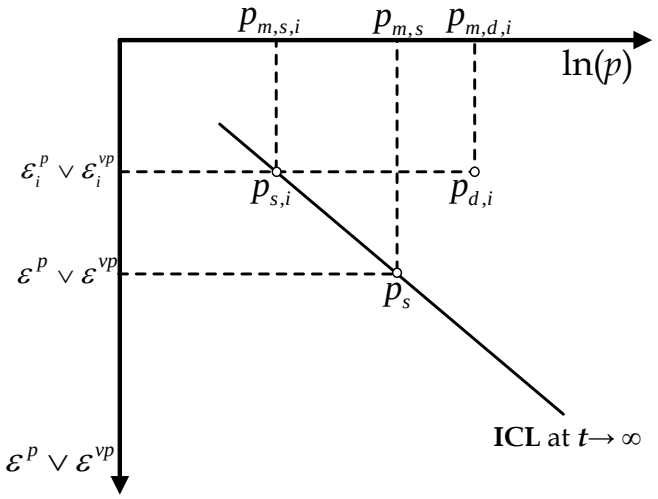

Figure 4.5: Selected strain hardening parameter as a function of inelastic (plastic or viscoplastic) volumetric strain.

The strain hardening parameter is depicted in **Figure 4.4** as a function of inelastic volumetric strain. The employed framework requires a priory selection of the $p_{m,s}$ and the volumetric inelastic strain (plastic or viscoplastic) $\varepsilon^p \vee \varepsilon^{vp}$. However, knowledge of such variables at infinite time after imposing the isotropic pressure is elusive and practically impossible. However, it may be possible to overcome such a problem by incorporating expressions (4.19) and (4.22) as will be shown here below.

The following governing equation depicts the incremental strain as a function of incremental stress for normally consolidated clays:

$$\begin{aligned} \dot{\boldsymbol{\varepsilon}} = & \frac{1}{2G} \cdot \boldsymbol{s} + \frac{\kappa}{3 \cdot (1+e)} \cdot \frac{\dot{p}}{p} \cdot \boldsymbol{I} \\ & + \frac{1}{M^* \cdot p} \cdot \Phi(F) \cdot \frac{\boldsymbol{s}}{\sqrt{\boldsymbol{s} : \boldsymbol{s}}} + \frac{1}{3 \cdot M^* \cdot p} \cdot \Phi(F) \cdot \left(M^* - \frac{\sqrt{\boldsymbol{s} : \boldsymbol{s}}}{p} \right) \cdot \boldsymbol{I} \end{aligned} \tag{4.26}$$

In the aforementioned expression G is the elastic shear modulus, κ stands for the swelling index (in the $v-\ln\sigma$ space), e portrays the void ratio and $\boldsymbol{I}$ is the identity tensor.

The selected form of viscous nucleus employed in the Adachi and Oka (1982) model is calibrated through two undrained constant strain rate compression tests in the triaxial apparatus (at different strain rates, simulating consolidation and swelling), based on the Adachi and Okano's (1974) and Oka's (1978) formulation:

$$\Phi\left(F\right)=c_0\cdot\exp\left[m'\cdot\ln\left(\frac{p_{m,d}}{p_{m,s}}\right)\right] \tag{4.27}$$

In the expression above c_0 and m' are parameters controlling the time dependent behavior of soils. In total there are eight parameters in need of calibration through experimental measurements, namely G, λ, κ, e, M^*, c_0, m' and $p_{m,s}$. By incorporating expressions (4.19) and (4.22) equation (4.27) may be rewritten in the following form:

$$\Phi\left(F\right)=c_0\cdot\exp\left\{m'\cdot\left[\frac{\sqrt{\boldsymbol{s}:\boldsymbol{s}}}{M^*\cdot\sigma}+\ln\left(\sigma\right)-\frac{\sqrt{\boldsymbol{s}_s:\boldsymbol{s}_s}}{M^*\cdot\sigma_s}-\ln\left(\sigma_s\right)\right]\right\} \tag{4.28}$$

The constitutive equations were extended to account for anisotropic behavior of soils. However, considering that the underlying principles are the same and that the proposed model will not be accounting for material primary anisotropy the formulation will not be further reviewed.

It should be noted that the Adachi and Oka's (1982) model fails to describe the undrained accelerating creep component leading to creep failure (Oka et al., 1995). Moreover it lacks the explicit definition of the plastic component in the classical sense of elastoplasticity and thus it cannot simulate accurately neither the plastic nor the time-dependent behavior.

4.4 Lemaitre's overstress model

The viscoplastic overstress model described in this section was originally proposed by Lemaitre and Chaboche (1990) to account for the time-dependent behavior of

metal alloys. The formulation was extended to the study of the time-dependency of geomaterials by Boidy (2000). Once again the model is founded on Perzyna's overstress theory.

Lemaitre's formulation states that the static yield surface is set to coincide with the principal space diagonal (hydrostatic axis) and no hardening is sustained. Therefore, the purely elastic behavior is encountered solely along the hydrostatic axis in the absence of deviatoric stress. Viscoplastic strains tend to accumulate at stress states characterized by finite (null values of the shear stress do not activate the viscoplastic component) values of the stress deviator.

The yield function f may be decomposed to a component $\overline{f}(\boldsymbol{\sigma})$, dependent solely on the stress state, and another component $k\left(\boldsymbol{\varepsilon}^{vp}\right)$, dependent only on the accumulated viscoplastic strains:

$$f = \frac{\overline{f}(\boldsymbol{\sigma})}{k\left(\boldsymbol{\varepsilon}^{vp}\right)} \tag{4.29}$$

The function $\overline{f}(\boldsymbol{\sigma})$ may be described by a Von Mises criterion:

$$\overline{f}(\boldsymbol{\sigma}) = \sqrt{\frac{3}{2}\cdot(\mathbf{s}:\mathbf{s})} \tag{4.30}$$

The function $k\left(\boldsymbol{\varepsilon}^{vp}\right)$ may be expressed as follows:

$$k\left(\boldsymbol{\varepsilon}^{vp}\right) = \left(\varepsilon_q^{vp}\right)^{-\frac{m}{n}} \tag{4.31}$$

Hence, the function $k\left(\boldsymbol{\varepsilon}^{vp}\right)$ is associated with the measure of the viscoplastic strain deviator ε_q^{vp}. Expression (4.31) incorporates two constitutive parameters m and n in need of calibration. It is noted that the constitutive parameters m and n need to conform to the following conditions:

$$n \geq 1 \tag{4.32}$$

$$1 - n < m \leq 0 \tag{4.33}$$

The measure of deviatoric strains may be computed by integrating the viscoplastic deviatoric strain rate throughout the entire time history:

$$\varepsilon_q^{vp} = \int_0^t \dot{\varepsilon}_q^{vp} \cdot d\tau \tag{4.34}$$

The viscoplastic measure of deviatoric strain rate may be expressed as follows:

$$\dot{\varepsilon}_q^{vp} = \sqrt{\frac{2}{3}\dot{\boldsymbol{e}}^{vp} : \dot{\boldsymbol{e}}^{vp}} \tag{4.35}$$

where $\dot{\boldsymbol{e}}^{vp}$ is computed through the following expression:

$$\dot{\boldsymbol{e}}^{vp} = \dot{\boldsymbol{\varepsilon}}^{vp} - \frac{1}{3} \cdot \left(\dot{\boldsymbol{\varepsilon}}^{vp} : \boldsymbol{I} \right) \cdot \boldsymbol{I} \tag{4.36}$$

The viscous nucleus incorporates a power law of the general form:

$$\Phi\left(F\right) = \left\langle F \right\rangle^n \tag{4.37}$$

As for the selected overstress function, it is set equal to the yield function f:

$$F = f = \frac{\overline{f}\left(\boldsymbol{\sigma}\right)}{k\left(\boldsymbol{\varepsilon}^{vp}\right)} \tag{4.38}$$

The viscoplastic potential function employed for the derivation of the plastic potential tensor is selected to coincide with $\overline{f}\left(\boldsymbol{\sigma}\right)$:

$$g = \overline{f}\left(\boldsymbol{\sigma}\right) = \sqrt{\frac{3}{2} \cdot \left(\boldsymbol{s} : \boldsymbol{s}\right)} \tag{4.39}$$

In other words, an associated flow rule is assumed.

By incorporating the aforementioned expressions (portrayed in equations (4.37), (4.38) and (4.39)) in Perynza's original formulation for the viscoplastic strain rate depicted in equation (2.27):

$$\dot{\boldsymbol{\varepsilon}}^{vp} = \left\{ \frac{3}{2} \cdot \gamma \cdot \left[\frac{3}{2} \cdot \left(\boldsymbol{s} : \boldsymbol{s} \right) \right]^{\frac{n-1}{2}} \cdot \left(\varepsilon_q^{vp} \right)^m \right\} \cdot \boldsymbol{s} \tag{4.40}$$

The expression above portrays the significance of the constitutive parameters m and n on the viscoplastic stress deviator and the deviatoric stress. The fluidity parameter γ controls the magnitude of the accumulated viscoplastic strains.

The aforementioned relation may be solved analytically solely in the case where the stress deviator is constant, representing creep behavior under constant stress level. In any other case numerical integration is required.

A specimen exhibiting creep behavior subjected to a constant deviatoric stress with time may be described by a power-law formulation (similar to the one given in Betten, 2005) may be described through the following expression:

$$\varepsilon_q^{vp} = a \cdot q^{\beta} \cdot t^{\delta} = a \cdot \left[\frac{3}{2} \cdot (\boldsymbol{s} : \boldsymbol{s}) \right]^{\frac{\beta}{2}} \cdot t^{\delta} \tag{4.41}$$

where the parameters a, β and δ are given here below:

$$\delta = \frac{1}{1-m} \tag{4.42}$$

$$\beta = n \cdot \delta = \frac{n}{1-m} \tag{4.43}$$

$$a = \left(\frac{\gamma}{\delta} \right)^{\delta} = \left[\gamma \cdot (1-m) \right]^{\frac{1}{1-m}} \tag{4.44}$$

For a cylindrical specimen in the triaxial apparatus subjected to axial stress σ_a and radial stress σ_r:

$$q = \sqrt{\frac{3}{2} \cdot (\boldsymbol{s} : \boldsymbol{s})} = \sigma_a - \sigma_r \tag{4.45}$$

$$\varepsilon_q^{vp} = \varepsilon_a^{vp} = -\frac{1}{2} \cdot \varepsilon_r^{vp} \tag{4.46}$$

In the aforementioned expression (4.46) the assumption of constant volume is evident. The elastic regime is set to the isotropic axis and consequently, the elastic component is null.

Once equation (4.41) undergoes derivation with respect to time it may be rewritten in logarithmic form as follows:

$$\begin{aligned}\log\left(\dot{\varepsilon}_q^{vp}\right) &= \log\left(a\cdot\delta\right)+\beta\cdot\log\left(q\right)+\left(\delta-1\right)\cdot\log\left(t\right)\\ &= \log\left(a\cdot\delta\right)+\beta\cdot\log\left[\sqrt{\frac{3}{2}\cdot\left(\boldsymbol{s}:\boldsymbol{s}\right)}\right]+\left(\delta-1\right)\cdot\log\left(t\right)\end{aligned} \tag{4.47}$$

Study of expression (4.47) reveals some interesting keypoints:

- the logarithmic viscoplastic deviatoric strain rate may be expressed as a linear function of the logarithm of time;
- the inclination of the logarithm of deviatoric strain rate as a function of the logarithm of time does not depend on the applied stress (converges with observations by Singh and Mitchell (1968) and Tavenas et al. (1978));
- the logarithm of deviatoric strain rate is a linear function of the logarithm of the stress deviator measure q (supposedly in good approximation with the expression of Mitchell and Soga (1976) - however, Mitchell's expression is linear with respect to q and not its logarithm $\log(q)$).

The expression (4.47) may be employed to derive the constitutive parameters from laboratory measurements (i.e. Debernardi, 2004; Bonini et al., 2009).

The Lemaitre's overstress viscoplastic model lacks the explicit definition of the plastic component in the classical sense of elastoplasticity and thus it cannot simulate accurately neither the plastic nor the time-dependent behavior. The elastic behavior is disregarded and the initial viscoplastic hardening modulus cannot be controlled efficiently. The model incorporates an associated flow rule. On the upside the constitutive parameters are easily extracted through experimental measurements.

4.5 Cristescu's overstress model

Cristescu's (Jin and Cristescu, 1998) formulation accounts for the time-dependent behavior of rock salt. The elastoviscoplastic model to be analyzed in this section addresses the transient behavior (primary creep) rather than focus on the stationary creep component (characterizing the secondary creep stage). The total strain rate is composed of the elastic and the inelastic component. The elastic strain rate may be computed as follows:

$$\dot{\boldsymbol{\varepsilon}}^{e} = \frac{1}{2 \cdot G} \cdot \dot{\boldsymbol{s}} + \frac{1}{3 \cdot K} \cdot \dot{\sigma} \cdot \boldsymbol{I} \tag{4.48}$$

The elastic parameters can be determined by employing the unloading procedure by Hansen and Carter (1984) and Cristescu (1989). As for the viscoplastic strain rate, it may be computed by employing the following expression:

$$\dot{\boldsymbol{\varepsilon}}^{vp} = \gamma \cdot \left\langle \Phi\left(F\right) \right\rangle \cdot \frac{\partial g}{\partial \boldsymbol{\sigma}} = \left\langle \Phi\left(F\right) \right\rangle \cdot \boldsymbol{P} \tag{4.49}$$

In Cristescu's approach, the viscous nucleus is not set equal to the overstress but it may be expressed through the following general formulation:

$$\Phi\left(F\right) = \frac{F}{1+F} \tag{4.50}$$

The overstress function incorporates the plastic work W^{p} and the yield function $f\left(\boldsymbol{\sigma}\right)$ as follows:

$$F = \frac{f\left(\boldsymbol{\sigma}\right)}{W^{p}} - 1 \tag{4.51}$$

The total plastic work may be formulated as:

$$W^{p} = \int_{0}^{t} \boldsymbol{\sigma}\left(\tau\right) : \dot{\boldsymbol{\varepsilon}}^{p}\left(\tau\right) \cdot d\tau \tag{4.52}$$

The plastic work is employed as an internal state variable or a work hardening parameter.

In the general case the flow rule is non-associated and the yield surface does not coincide with the viscoplastic potential envelope $f \neq g$. The formulation incorporates the compressibility/dilatancy boundary (Cristescu, 1989 & 1994) to derive the plastic potential and a yield surface defined as the stability boundary or relaxation boundary (Cristescu, 1967 & 1989; Lubliner, 1990). The formulations are based on curve fitting associated with laboratory measurements.

The Cristescu's overstress elastoviscoplastic model lacks the explicit definition of the plastic component. Hence, it cannot simulate accurately neither the plastic nor the time-dependent behavior. It aims solely to describe the undergoing viscous

transformations during the primary regime of creep (transient creep). Thus, at no point should it be considered to account for the stationary or tertiary creep stages comprising the essence of the deviatoric time dependency (note that the creep stages have been introduced in section 2.2.1).

The model incorporates a non-associated flow rule. The constitutive formulations are extracted through experimental measurements and can be employed solely to account for the transient viscoplastic characteristics of rock salt (for which they were derived).

4.6 Debernardi's overstress model

Debernardi's formulation or Stress Hardening ELastic VIscous Plastic model (SHELVIP) comprises an elastoviscoplastic framework addressing the time dependent mechanical behavior (mainly squeezing phenomena) of poor rock masses. Such squeezing phenomena need to be considered assuming tunnel excavation is undertaken in such rock masses (Barla, 2001 & 2005).

The constitutive formulation of this section aims to account for the mechanical behavior near failure by considering the interaction between time dependency and failure due to yielding without substantial creep deformations being reproduced (the model cannot capture delayed failure due to tertiary creep). Furthermore, the long-term behavior (aging effects) is considered as a function of the loading history and any undergoing process associated with hardening or softening.

The SHELVIP model combines the classical theory of elastoplasticity with the overstress theory developed by Perzyna. In this sense, any instantaneous irreversible alterations in the material fabric are considered. Thus, the total strain rate may be expressed as follows:

$$\dot{\boldsymbol{\varepsilon}} = \dot{\boldsymbol{\varepsilon}}^{e} + \dot{\boldsymbol{\varepsilon}}^{p} + \dot{\boldsymbol{\varepsilon}}^{vp} \tag{4.53}$$

In the aforementioned expression the superscripts *e*, *p* and *vp* are employed to denote the elastic, the plastic and viscoplastic component of the strain rate respectively.

The plastic and viscoplastic states are defined through two limit surfaces described through the Drucker - Prager criterion, portrayed in **Figure 4.6**. The plastic surface comprises the virtual boundary by which the plastic states are defined through the

classic theory of elastoplasticity. Every state laying inside is either elastic or viscoplastic (depending on its relative position with respect to the viscoplastic surface) while the stress state on the plastic surface exhibits an elastoplastic-viscoplastic behavior. The viscoplastic surface exhibits a behavior that complies with Perzyna's formulation. Hence, the viscoplastic surface denotes the lower bound for the development of viscoplastic strains.

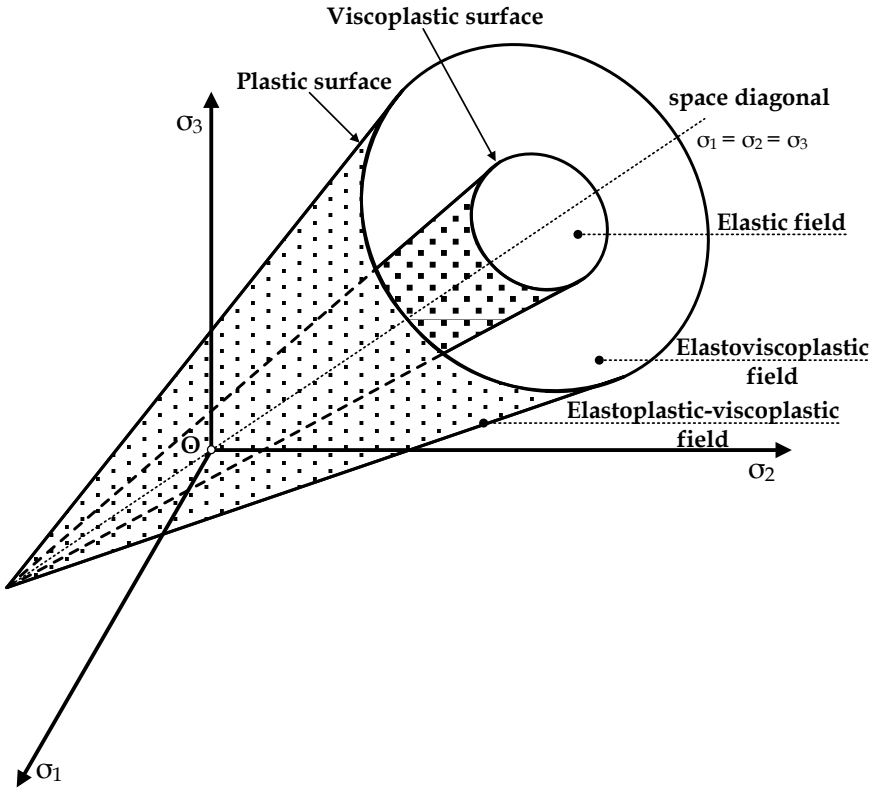

Figure 4.6: Limit surfaces and stress fields incorporated in SHELVIP formulation.

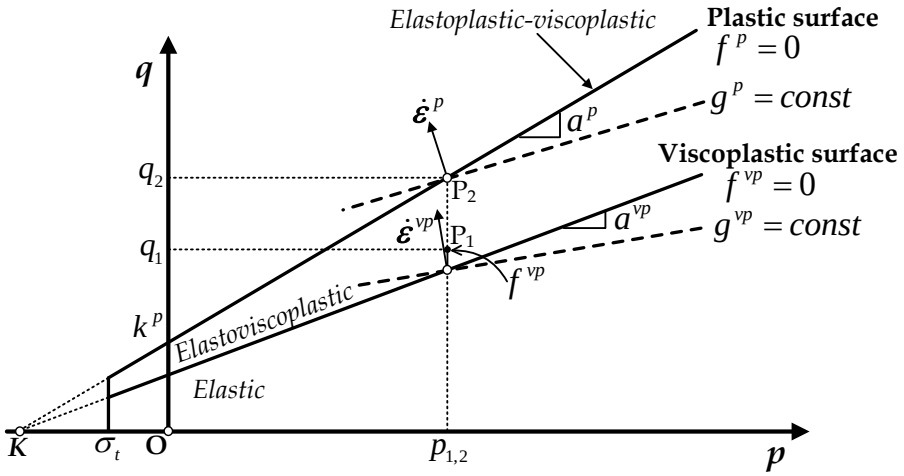

Figure 4.7: Limit surfaces and stress fields incorporated in the SHELVIP formulation portrayed in the *p-q* plane.

The plastic and viscoplastic surfaces define the following fields in the stress space:

- the **elastic field** lays inside the viscoplastic surface and the behavior is elastic:

$$\dot{\boldsymbol{\varepsilon}} = \dot{\boldsymbol{\varepsilon}}^{e} \tag{4.54}$$

- the **elastoviscoplastic field** lays between the plastic and viscoplastic surface and the geomaterial exhibits elastoviscoplastic behavior:

$$\dot{\boldsymbol{\varepsilon}} = \dot{\boldsymbol{\varepsilon}}^{e} + \dot{\boldsymbol{\varepsilon}}^{vp} \tag{4.55}$$

- the **elastoplastic-viscoplastic field** lays on the plastic surface and the geomaterial exhibits elastoplastic-viscoplastic behavior:

$$\dot{\boldsymbol{\varepsilon}} = \dot{\boldsymbol{\varepsilon}}^{e} + \dot{\boldsymbol{\varepsilon}}^{p} + \dot{\boldsymbol{\varepsilon}}^{vp} \tag{4.56}$$

The plastic yield envelope may be defined mathematically through the plastic yield function in the $p-q$ space as follows:

$$f^{p} = q - a^{p} \cdot p - k^{p} = 0 \mid \; p \geq \sigma_{t} \tag{4.57}$$

Extending the formulation to the generalized six dimensional stress space leads to the following expression:

$$f^{p} = \sqrt{\frac{3}{2} \cdot (\boldsymbol{s} : \boldsymbol{s})} - a^{p} \cdot \sigma - \sqrt{\boldsymbol{k}^{p} : \boldsymbol{k}^{p}} = 0 \mid \; p \geq \sigma_{t} \tag{4.58}$$

Parameters a^{p} and k^{p} comprise the inclination and intercept with the vertical q axis portrayed in **Figure 4.7**. The parameters may be associated to the Mohr-Coulomb friction angle and cohesion:

$$circumscribing: \begin{cases} a^{p} = \dfrac{6 \cdot \sin\varphi}{3 - \sin\varphi} \\ k^{p} = \dfrac{6 \cdot c \cdot \cos\varphi}{3 - \sin\varphi} \end{cases} \tag{4.59}$$

$$inscribing: \begin{cases} a_{p} = \dfrac{6 \cdot \sin\varphi}{3 + \sin\varphi} \\ k^{p} = \dfrac{6 \cdot c \cdot \cos\varphi}{3 + \sin\varphi} \end{cases} \tag{4.60}$$

Stress σ_t comprises the tension cut-off. The keystone of the formulation lies with the fixed plastic yield surface. The plastic yield envelope does not harden during the accumulation of either plastic or viscoplastic strains.

The viscoplastic yield surface may also be defined through the viscoplastic yield function in the $p-q$ space as follows:

$$f^{vp} = q - a^{vp} \cdot p - \left(\frac{a^{vp}}{a^{p}} \right) \cdot k^{p} = 0 \mid \; p \geq \sigma_t \tag{4.61}$$

The aforementioned expression may be rewritten in the generalized stress space as follows:

$$f^{vp} = \sqrt{\frac{3}{2} \cdot (\boldsymbol{s} : \boldsymbol{s})} - a^{vp} \cdot \sigma - \left(\frac{a^{vp}}{a^{p}} \right) \cdot \sqrt{\boldsymbol{k}^{p} : \boldsymbol{k}^{p}} = 0 \mid \; p \geq \sigma_t \tag{4.62}$$

Parameter a^{vp} comprises the inclination of the Drucker-Prager criterion in the $p-q$ plane portrayed in **Figure 4.7**.

The viscoplastic surface defines the transitional stage from the elastic to the elastoplastic-viscoplastic behavior. Considering that any transformation in the loading history alters the viscoplastic yield envelope the surface is allowed to harden through the hardening variable a^{vp}.

The elastic behavior incorporates linear elasticity through the following expression:

$$\dot{\boldsymbol{\varepsilon}}^{e} = \boldsymbol{D}^{e} : \dot{\boldsymbol{\sigma}} \tag{4.63}$$

The elastic compliance matrix is founded on Hooke's elasticity.

A non-associated plastic flow rule is assumed based on the principles of classical elastoplasticity:

$$\dot{\boldsymbol{\varepsilon}}^{p} = \dot{\Lambda} \cdot \frac{\partial g_{p}}{\partial \boldsymbol{\sigma}} \tag{4.64}$$

The plastic potential function g^{p} defines the direction of the plastic strain rate tensor and can be expressed as follows:

$$g^p = q - \omega^p \cdot p \tag{4.65}$$

$$g^p = \sqrt{\frac{3}{2} \cdot (\boldsymbol{s} : \boldsymbol{s})} - \omega^p \cdot \sigma \tag{4.66}$$

The parameter ω^p stands for the plastic dilatancy defined as the ratio of volumetric over the deviatoric incremental plastic strains.

Assuming that the stress state exceeds the viscoplastic yield surface $\left(f^{vp} > 0 \right)$ the viscoplastic strain component tends to accumulate. The viscoplastic strain rate may be computed through Perzyna's overstress theory:

$$\dot{\boldsymbol{\varepsilon}}^{vp} = \gamma \cdot \Phi\left(F\right) \cdot \frac{\partial g^{vp}}{\partial \boldsymbol{\sigma}} \tag{4.67}$$

The overstress function F represents the state of overstress with respect to the 'static' yield function, defined by the viscoplastic yield envelope. In the SHELVIP the selected expression for the overstress function coincide with the viscoplastic yield function:

$$F = f^{vp} \tag{4.68}$$

A power function was employed to define the viscous nucleus controlling the measure of viscoplastic incremental strains:

$$\Phi\left(F\right) = \left\langle F \right\rangle^n = \left\langle f^{vp} \right\rangle^n \tag{4.69}$$

The viscoplastic potential function g^{vp} may be expressed in analogous forms to equations (4.65) and (4.66):

$$g^{vp} = q - \omega^{vp} \cdot p \tag{4.70}$$

$$g^{vp} = \sqrt{\frac{3}{2} \cdot (\boldsymbol{s} : \boldsymbol{s})} - \omega^{vp} \cdot \sigma \tag{4.71}$$

The parameter ω^{vp} stands for the viscoplastic dilatancy defined as the ratio of volumetric over the incremental deviatoric viscoplastic strains, in an exact analogy as before.

By computing the derivative of the equation (4.71):

$$\frac{\partial g^{vp}}{\partial \boldsymbol{\sigma}} = \frac{3}{2} \cdot \frac{\boldsymbol{s}}{\sqrt{\frac{3}{2} \cdot (\boldsymbol{s} : \boldsymbol{s})}} - \frac{1}{3} \cdot \omega^{vp} \cdot \boldsymbol{I} \tag{4.72}$$

the viscoplastic strain rate may be expressed as follows:

$$\dot{\boldsymbol{\varepsilon}}^{vp} = \gamma \cdot \left\langle f^{vp} \right\rangle^{n} \cdot \left(\frac{3}{2} \cdot \frac{\boldsymbol{s}}{\sqrt{\frac{3}{2} \cdot (\boldsymbol{s} : \boldsymbol{s})}} - \frac{1}{3} \cdot \omega^{vp} \cdot \boldsymbol{I} \right) \tag{4.73}$$

The selected hardening variable a^{vp} is not associated with the viscoplastic work or the viscoplastic measure of deviatoric strains. Instead, the following hardening rule is adopted:

$$\dot{a}^{vp} = \frac{l}{m \cdot n} \cdot \frac{f^{vp}}{\sigma + \frac{\sqrt{\boldsymbol{k}^{p} : \boldsymbol{k}^{p}}}{a^{p}}} \cdot \left(\frac{f^{vp}}{\sqrt{\frac{3}{2} \cdot (\boldsymbol{s} : \boldsymbol{s})}} \right)^{m \cdot n} \tag{4.74}$$

In the expression above l and m are constitutive parameters (positive in nature). l is a time stretching factor that controls the scaling factor of the creep curves, while parameter m defines the shape of the strain rate curves with respect to time. Finally, n is a load factor portraying the dependency of the viscoplastic strain rate from the deviatoric stress (**Figure 4.8**).

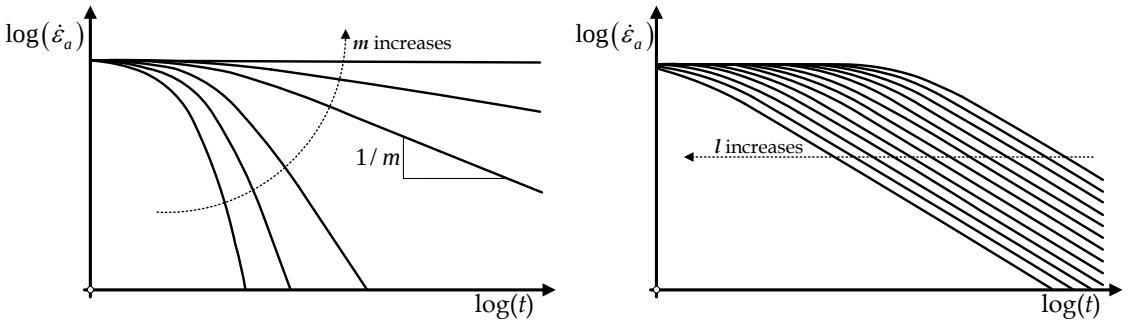

a. b.

Figure 4.8: Geometrical effect of a. parameter m and b. parameter l on the $\log(\dot{\varepsilon}_{\alpha}) - \log(t)$ space.

Assuming that the stress state remains intact, characteristic of undergoing creep, implementation of equation (4.74) depicts an alteration in the inclination of the viscoplastic surface. By doing so, the next increment will have set the new viscoplastic surface higher with respect to the original thus evolving towards the plastic yield envelope. Evolution of the viscoplastic surface will cease to develop once the stress state is adjusted on the viscoplastic yield envelope.

The SHELVIP model should be considered as a major advancement in the viscoplastic formulation of constitutive elastoviscoplastic models. It may describe the secondary compression and even simulate the primary creep conceptually accurately. However, the SHELVIP cannot represent the rapid increase of the viscoplastic strain rate at high stress levels near failure comprising the effects of tertiary creep (Debernardi, 2008). Furthermore, the model is addressing the time-dependent mechanical behavior of poor rock masses by considering a Drucker-Prager criterion and at no point should it be employed to clayey soils.

4.7 Karstunen's overstress model

Conventional overstress models may be assuming the absence of any viscoplastic strains within the static yield surface (i.e. Adachi and Oka,1982; Shahrour and Meimon, 1995; Fodil et al., 1997; Rowe and Hinchberger, 1998; Hinchberger and Rowe, 2005; Mabssout et al., 2006 Yin and Hicher; 2008) or permit the accumulation of time-dependent inelastic strains within the static yield envelope (i.e. Kutter and Sathialingam, 1992; Vermeer and Neher, 1999; Yin et al., 2002; Kimoto and Oka; 2005). Some more recent constitutive formulations may also account for anisotropy (i.e. Leoni et al., 2008; Zhou et al., 2005) by simply extending the isotropic creep models proposed formerly (i.e. Vermeer and Neher, 1999; Yin et al., 2002).

Karstunen's formulation of the governing constitutive equations is founded on Perzyna's overstress theory. Creep-SCLAY1 (Leoni et al., 2008; Yin et al., 2010; Karstunen et al., 2013; Sivasithamparam et al., 2013) is an anisotropic time dependent model incorporating an elliptical yield surface and Wheeler's rotational hardening law (Wheeler et al., 2003).

The incremental strain rate may be expressed as a function of an elastic and a viscoplastic component:

$$\dot{\boldsymbol{\varepsilon}} = \dot{\boldsymbol{\varepsilon}}^{e} + \dot{\boldsymbol{\varepsilon}}^{vp} \tag{4.75}$$

The elastic behavior is expressed by poroelasticity but is of limited interest considering that the elastic region coincides with the isotropic axis.

As for the viscoplastic strain rate it is expressed as a function of the dynamic yield function depicted below following Perzyna's formulation:

$$\dot{\boldsymbol{\varepsilon}}^{vp} = \gamma \cdot \left\langle \Phi\left(F\right) \right\rangle \cdot \frac{\partial f_d}{\partial \boldsymbol{\sigma}} \tag{4.76}$$

In the expression above γ is the fluidity parameter, $\Phi\left(F\right)$ stands for the viscous nucleus and f_d portrays the dynamic yield function. F is the overstress function controlling the distance between the dynamic and static yield envelopes. When the equilibrium is reached (the static and dynamic envelopes coincide) or the stress state lays inside the static yield surface the overstress function is $F \leq 0$ and thus the rate of viscoplastic strains is null.

The viscous nucleus is a power type expression of the ratio of dynamic over the static overstress function $\Phi\left(F\right) = \left(\frac{F_d}{F_s} \right)^N$. Conforming to Adachi and Oka's formulation, the Creep-SCLAY1 (**Figure 4.9**) incorporates the ratio of the size of the dynamic yield surface over that of the static to define the viscous nucleus:

$$\Phi\left(F\right) = \left(\frac{p_{m,d}}{p_{m,r}} \right)^N \tag{4.77}$$

Hence, the expression (4.76) may be rewritten in the following form:

$$\dot{\boldsymbol{\varepsilon}}^{vp} = \gamma \cdot \left\langle \left(\frac{p_{m,d}}{p_{m,r}} \right)^N \right\rangle \cdot \frac{\partial f_d}{\partial \boldsymbol{\sigma}} \tag{4.78}$$

In the expression above there is no need to define an overstress function F. The ratio $\frac{p_{m,d}}{p_{m,r}}$ always receives values even when the dynamic envelope crosses the static leading to ratio values lower than unity. Hence there is no restriction whatsoever for the development of viscoplastic strains considering that in this case it is possible to

account for purely linear behavior solely along the hydrostatic axis. In this sense, the static yield envelope comprises a reference surface (justifying use of subscript *r*). The reference size $p_{m,r}$ refers to a value of the apparent preconsolidation pressure computed through a selected experimental test (Yin et al., 2010).

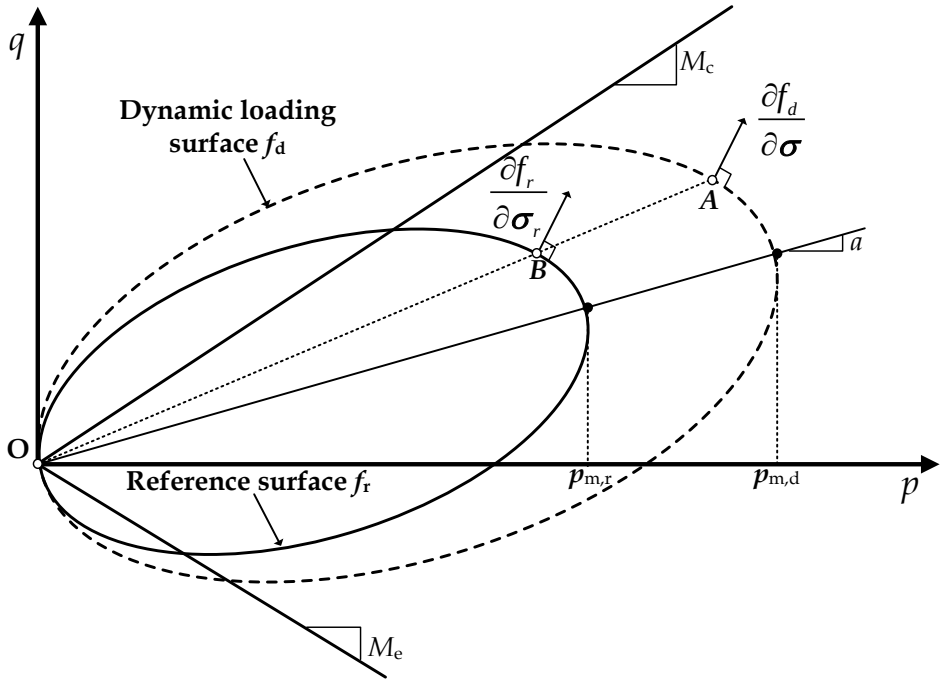

Figure 4.9: Creep-SCLAY1 graphical representation in the *p*-*q* plane.

Wheeler's elliptical (Wheeler et al., 2003) yield function is employed to account for the dynamic (and consequently the static also) yield envelope:

$$f_d = \frac{\frac{3}{2}\cdot\left(\boldsymbol{s}-\sigma\cdot\boldsymbol{a}_d\right):\left(\boldsymbol{s}-\sigma\cdot\boldsymbol{a}_d\right)}{\left(M^2-\frac{3}{2}\cdot\boldsymbol{a}_d:\boldsymbol{a}_d\right)\cdot\sigma}+\sigma-p_{m,d}=0 \tag{4.79}$$

where $\boldsymbol{a}_d$ is the deviatoric fabric tensor and M stands for the inclination of the critical state line (CSL). The inclination a in the $p-q$ space is defined as $a=\sqrt{\frac{3}{2}\cdot\left(\boldsymbol{a}_d:\boldsymbol{a}_d\right)}$ depicted in **Figure 4.9**.

The incorporated value of M tends to vary depending on the Lode angle θ (Sheng et al., 2000) between compression M_c and extension M_e:

$$M = M_c \cdot \left[\frac{2 \cdot \left(\frac{M_e}{M_c} \right)^4}{1 + \left(\frac{M_e}{M_c} \right)^4 + \left[1 - \left(\frac{M_e}{M_c} \right)^4 \right] \cdot \sin 3\theta} \right]^{\frac{1}{4}} \tag{4.80}$$

The Lode angle may be expressed as follows:

$$\theta = \frac{1}{3} \sin^{-1} \left\{ -\frac{3 \cdot \sqrt{3}}{2} \cdot \frac{\left\{ \frac{1}{3} \cdot \left[\left(\boldsymbol{s} - \sigma \cdot \boldsymbol{a}_d \right) \bullet \left(\boldsymbol{s} - \sigma \cdot \boldsymbol{a}_d \right) \right] : \left(\boldsymbol{s} - \sigma \cdot \boldsymbol{a}_d \right) \right\}}{\sqrt{\left[\frac{1}{2} \left(\boldsymbol{s} - \sigma \cdot \boldsymbol{a}_d \right) : \left(\boldsymbol{s} - \sigma \cdot \boldsymbol{a}_d \right) \right]^3}} \right\} \tag{4.81}$$

and $-\frac{\pi}{6} \le \theta \le \frac{\pi}{6}$.

As for the reference yield envelope it is allowed to harden as a function of the volumetric incremental viscoplastic strain:

$$dp_{m,r} = p_{m,r} \cdot \left(\frac{1 + e_0}{\lambda - \kappa} \right) \cdot d\varepsilon^{vp} \tag{4.82}$$

Wheeler's kinematic hardening law (Wheeler et al., 2003) is employed in the formulation of the elastoviscoplastic overstress creep model as follows:

$$d\boldsymbol{a}_d = \omega \cdot \left[\left(\frac{3 \cdot \boldsymbol{s}}{4 \cdot \sigma} - \boldsymbol{a}_d \right) \cdot \left\langle d\varepsilon^{vp} \right\rangle + \omega_d \cdot \left(\frac{3 \cdot \boldsymbol{s}}{4 \cdot \sigma} - \boldsymbol{a}_d \right) \cdot d\varepsilon_q^{vp} \right] \tag{4.83}$$

where ω is a constant controlling the rate at which the fabric tensor reorientates towards the current stress state and ω_d portrays the relative effect of the viscoplastic deviatoric strain effect over the volumetric on the rotation of the yield surface.

The volumetric viscoplastic strain rate component is depicted here below:

$$\dot{\varepsilon}^{vp} = \frac{C_{ae}}{\left(1 + e_0\right) \cdot \tau_r} \cdot \left(\frac{M_c^2 - a_{K0}^2}{M_c^2 - \eta_{K0}^2} \right) \cdot \left(\frac{p_{m,d}}{p_{m,r}} \right)^{\frac{\lambda - \kappa}{C_{ae}}} \cdot \left[\frac{M^2 - \frac{3}{2} \cdot \frac{\left(\boldsymbol{s} : \boldsymbol{s} \right)}{\sigma^2}}{M^2 - \frac{3}{2} \cdot \left(\boldsymbol{a}_d : \boldsymbol{a}_d \right)} \right] \tag{4.84}$$

where $\eta_{K0} = \frac{3 \cdot M_c}{6 - M_c}$ and $a_{K0} = \eta_{K0} - \frac{M_c^2 - \eta_{K0}^2}{3}$. The reference time τ_r depends on the duration of the loading increment in the conventional oedometer test. In general practice standard 24hr oedometer tests are conducted thus setting the reference time (to 24hr). The expression above comprises the major improvement on the ACM elastoviscoplastic model (Leoni et al., 2008). It ensures that the volumetric strain rate approaches zero as the current stress ratio approaches the critical state line inclination, by incorporating the function $\left[M^2 - \frac{3}{2} \cdot \frac{(\boldsymbol{s} : \boldsymbol{s})}{\sigma^2} \right] \Big/ \left[M^2 - \frac{3}{2} \cdot (\boldsymbol{a}_d : \boldsymbol{a}_d) \right]$.

Expression (4.84) is considerably different from Vermeer and Neher's formulation (1999):

$$\dot{\varepsilon}^{vp} = \frac{C_{ae}}{(1+e_0) \cdot \tau_r} \cdot \left(\frac{p_{m,d}}{p_{m,r}} \right)^{\frac{\lambda - \kappa}{C_{ae}}} \tag{4.85}$$

or the expression of Yin et al. (2002):

$$\dot{\varepsilon}^{vp} = \frac{C_{ae}}{(1+e_0) \cdot \tau_r} \cdot \left(1 + \frac{d\varepsilon_v}{\varepsilon_{vl}^{vp}} \right)^2 \cdot \exp \left[\frac{d\varepsilon_v}{\left(1 + \frac{d\varepsilon_v}{\varepsilon_{vl}^{vp}} \right)} \cdot \frac{1+e_0}{C_{ae}} \right] \tag{4.86}$$

where τ is the reference time and ε_{vl}^{vp} stands for the limit of viscoplastic volumetric strain.

Hence, the Creep-SCLAY1 viscoplastic strain rates may be computed as follows (Sivasithamparam et al.; 2013):

$$\dot{\boldsymbol{\varepsilon}}^{vp} = \frac{\dot{\varepsilon}^{vp}}{\left(\frac{\partial f_d}{\partial \sigma} \right)} \cdot \frac{\partial f_d}{\partial \boldsymbol{\sigma}} \tag{4.87}$$

The Creep-SCLAY1 elastoviscoplastic model comprises a major advancement in the viscoplastic formulation of constitutive models. It addresses the time-dependent mechanical response of anisotropic clayey soils by accounting for the secondary compression. However, the Creep-SCLAY1 cannot represent the rapid increase of the

viscoplastic strain rate at high stress levels near failure comprising the effects of tertiary creep or consider failure due to yielding without substantial creep deformations being accumulated.

4.8 Concluding remarks

A great number of constitutive formulations have been introduced in the literature to account for the time-dependent mechanical behavior of geomaterials. In this chapter, the most recent advancements in elastoviscoplastic constitutive formulations based on overstress theory have been presented. Some primary constitutive formulations based on overstress were reviewed followed by the most recent state of the art approaches.

Regardless whether the governing mathematical framework addresses the time dependent behavior from clayey soils to soft rocks all reviewed approaches tend to focus mainly on the stationary or even the primary creep stage and completely disregard or conveniently ignore the rapid increase of the accumulated strains exhibited at high stress levels near failure stemming from tertiary creep. Most even neglect to consider failure due to yielding without substantial creep deformations being accumulated. Regardless, whether it is the accumulation of substantial plastic or viscoplastic strains attributing to failure, a sophisticated model needs to consider both mechanisms.

Hence, the necessity arises for the formulation of a new time-dependent behavioral framework of both structured, resembling stiff soils to weak rocks, and non-structured geomaterials resembling clayey deposits. The proposed model incorporates the principles of the overstress postulate proposed by Perzyna (1962 & 1966) and is founded on the principles of classical elastoplasticity. The viscoelastoplastic formulation is based on novel empirical relations stemming from observations on laboratory measurements. Hence, the proposed formulation incorporates constitutive parameters that can be easily derived through experimental measurements. Instead, of introducing complex mathematical transformations or extending the volumetric behavior to account for all aspects of creep (even the deviatoric component) the proposed constitutive formulation employs well established empirical relations (the mathematical framework incorporates parameters associated with the physical process). Next, follows the mathematical

formulation of the proposed viscoelastoplastic constitutive model and single point results portraying the simulated time-dependent behavior.

5

The proposed model

5.1 General

The current chapter analyses the mathematical time-dependent behavioral framework to be used in the development of a new constitutive model. The time-dependent mechanical response of both structured (resembling stiff soils to weak rocks) and non-structured geomaterials (resembling normally consolidated clayey deposits) is addressed. The mathematical formulation incorporates the principles of the overstress postulate proposed by Perzyna (1962 & 1966) while at the same time is founded on the principles of classical elastoplasticity.

The proposed constitutive model accounts for structure and consequently structure degradation to a residual state that may or may not coincide with the intrinsic depending whether chemical or mechanical transformations have been undertaken. Both a Structure Strength Envelope (*SSE*) and a Plastic Yield Envelope (*PYE*) are employed, integrated within the overlying overstress behavioral framework.

The proposed model addresses the time dependent behavior associated with the stationary and tertiary creep stages leading to delayed failure while at the same time conforming with Bjerrum's postulate (1967), as mentioned in **Chapter 2**. Small strain stiffness is accounted for by employing an infinitesimal plastic yield envelope. Another key feature of the model lies with the incorporated structure degradation mechanism. The structure strength envelope is oriented along the hydrostatic axis translated towards the tensional regime to account for the bonding effect under isotropic compression. Only secondary anisotropy is incorporated in this version of the model. The critical state line projection in the stress hyperplane is allowed to transition towards a residual state through a proper kinematic hardening rule. The

kinematic hardening rule associates the inclination of the *CSL* to either the deviatoric viscous or plastic strains. The viscous component is evident even at states laying within the *PYE*. Hence, the model could be characterized as viscoelastic-viscoplastic or viscoelastoplastic; however, in this dissertation it shall be called viscoelastoplastic to denote the extension of viscoplasticity to a more robust and elegant formulation incorporating the aforementioned features.

The outline of this chapter begins with the definition of the characteristic surfaces (*SSE*, *PYE* and Intrinsic Strength Envelope-*ISE*). Next, the incremental strain will be decomposed in its primary elements and each component, elastic, plastic and viscous, will be analyzed. The isotropic and kinematic hardening rules are presented and analyzed to portray the physical meaning and gain some insight in the overall time-dependent mechanical response.

The isotropic hardening rule accounts for:

- any plastic hardening or plastic softening behavior due to plastic strains;
- structure degradation effects due to plastic strain development and
- viscous strain rate effects attributed to creep strains.

The kinematic hardening rule considers:

- the evolution of the position of the *SSE* along the isotropic axis due to the development of either plastic or viscous strain components - we shall not be denoting that as primary anisotropy considering that in the current version of this model the *SSE* is basically an *MCC* model translated solely along the hydrostatic axis towards the tensional regime;
- the evolution of solely the secondary anisotropy due to the undergoing stress path and
- the alterations in the shape of both the Structure and the Plastic Yield Envelope associated with the accumulation of either plastic or viscous strains. This is achieved by employing the inclination of the Critical State Line (*CSL*) in the stress space as a hardening variable. In the case where the plastic strains are employed in the hardening law of the *CSL* inclination, the assumption leads potentially to non-uniqueness of the critical state line thus raising a significant issue. However, it should be considered solely as a mathematical manipulation that allows for the simulation of significant

softening even in the absence of structure. On the other hand, assuming that the viscous strains are employed within formulation of the hardening rule the behavioral framework attains a physical meaning justified by experimental measurements (or by shedding light from a point of view on such).

By employing the hardening law and some interpolation rules the plastic hardening modulus may be obtained. The adopted flow rule considered is purely associated in this stage.

Following the concept by Mroz and Norris (1982), Desai et al. (1986), Pastor et al. (1990) and Gens (1995) the constitutive formulation may undergo simple transformations to fall into a simple structureless isotropic model lacking any aspects of anisotropy and even degenerate into an elastoplastic model without accounting for any undergoing time effects. Hence, the principle was extended to the time-dependent behavioral framework and a simple manipulation of certain parameters ($t_0 \to \infty$) sets the viscous component to null thus leading to a purely elastoplastic formulation.

5.2 Characteristic surfaces

The proposed time dependent constitutive model (**Figure 5.1**) incorporates the following characteristic surfaces:

- Intrinsic Strength Envelope (*ISE*)
- Structure Strength Envelope (*SSE*)
- Plastic Yield Envelope (*PYE*)

The graphical representation of the proposed model is depicted in **Figure 5.1**.

The Intrinsic Strength Envelope is employed solely as a reference surface for the destructuring mechanism. Hence, the elastoplastic underlying framework of the model is founded on the assumption of two characteristic surfaces the Structure Strength Envelope and the Plastic Yield Envelope corresponding to the two levels of yielding based on the concept of Vaughan et al. (1988) and Malandraki and Toll (1994). The *SSE* encloses all possible states for the given structure and anisotropy simulated while the *PYE* encloses all possible elastic states assuming the general elastoplastic behavioral framework. Considering that the viscoelastoplastic formulation will be founded on this framework it will have to undertake several

modifications to account for the accumulation of the viscous components even in states laying inside the plastic yield envelope. However, assuming that the model is allowed to degrade towards an elastoplastic behavioral framework the principle holds true.

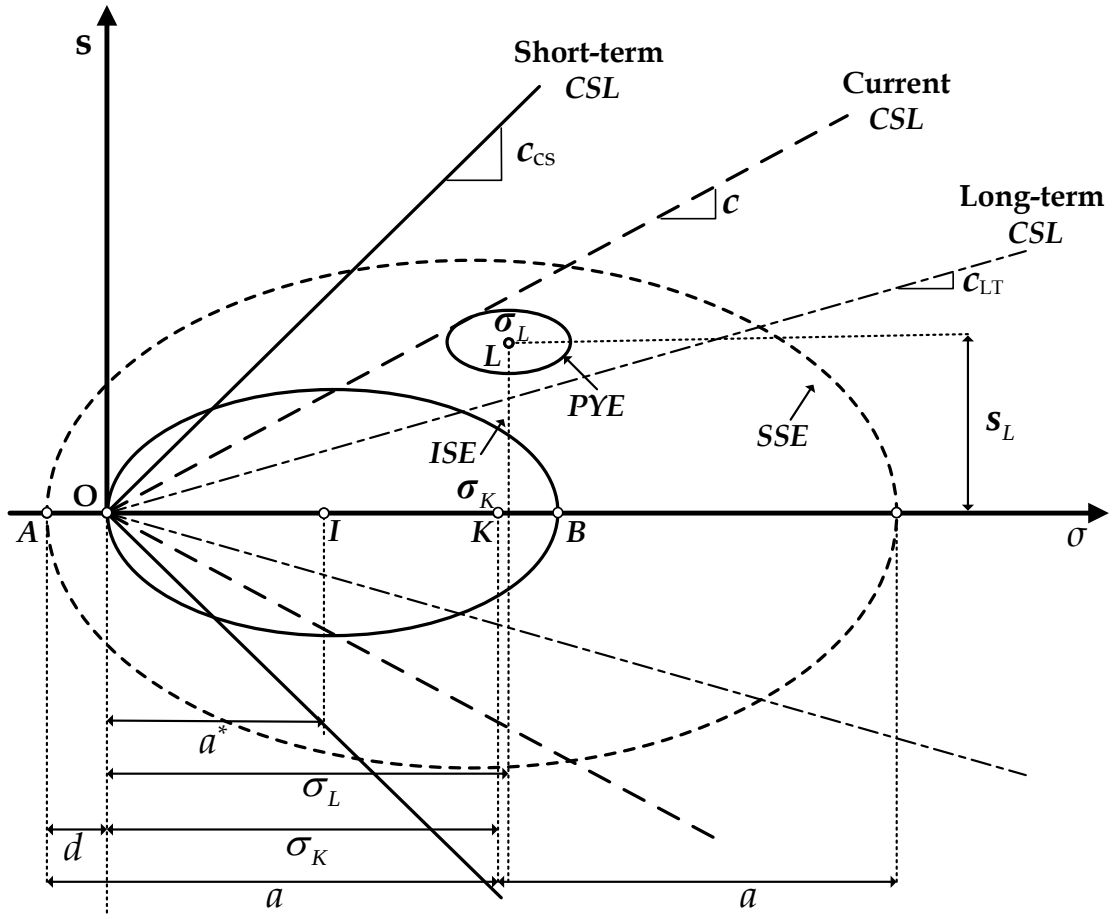

Figure 5.1: Graphical representation of the proposed model.

5.2.1 Intrinsic Strength Envelope

The Intrinsic Strength Envelope encloses all structureless states of the geomaterial. Considering that it comprises the state that the material falls into after the accumulation of substantial strains associated with critical state, the intrinsic anisotropy is null due to the chaotic distribution of the soil particle orientation at the initiation of failure. Regardless, whether a preferred orientation does occur after the shear banding forms thus leading to a macroscopic failure the proposed constitutive model will not focus on the post residual mechanical behavior of geomaterials. Every structureless state characterized as intrinsic can be described solely by the stress state

and void ratio. The following expression portrays the mathematical formulation of the intrinsic strength envelope:

$$F^*\left(\boldsymbol{\sigma},\alpha^*,c\right)=\frac{1}{c^2}\cdot\boldsymbol{s}:\boldsymbol{s}+\left(\sigma-a^*\right)^2-\left(a^*\right)^2=0 \tag{5.1}$$

The star " * " superscript is employed to denote the intrinsic measures. a^* stands for the halfsize of the *ISE* oriented along the isotropic axis illustrated in **Figure 5.2**. Orientation of the intrinsic strength envelope is along the hydrostatic axis. The *ISE* is allowed to harden isotropically by associating the halfsize of the *ISE* with undergoing alterations in the void ratio either due to creep or to the accumulation of plastic strains. The kinematic hardening of the *ISE* is of no major significance considering that the only measure of the intrinsic strength envelope required within the formulation of the constitutive model is its halfsize a^* to define the asymptote for the destructuring process of *SSE* undertaken during plastic deformation.

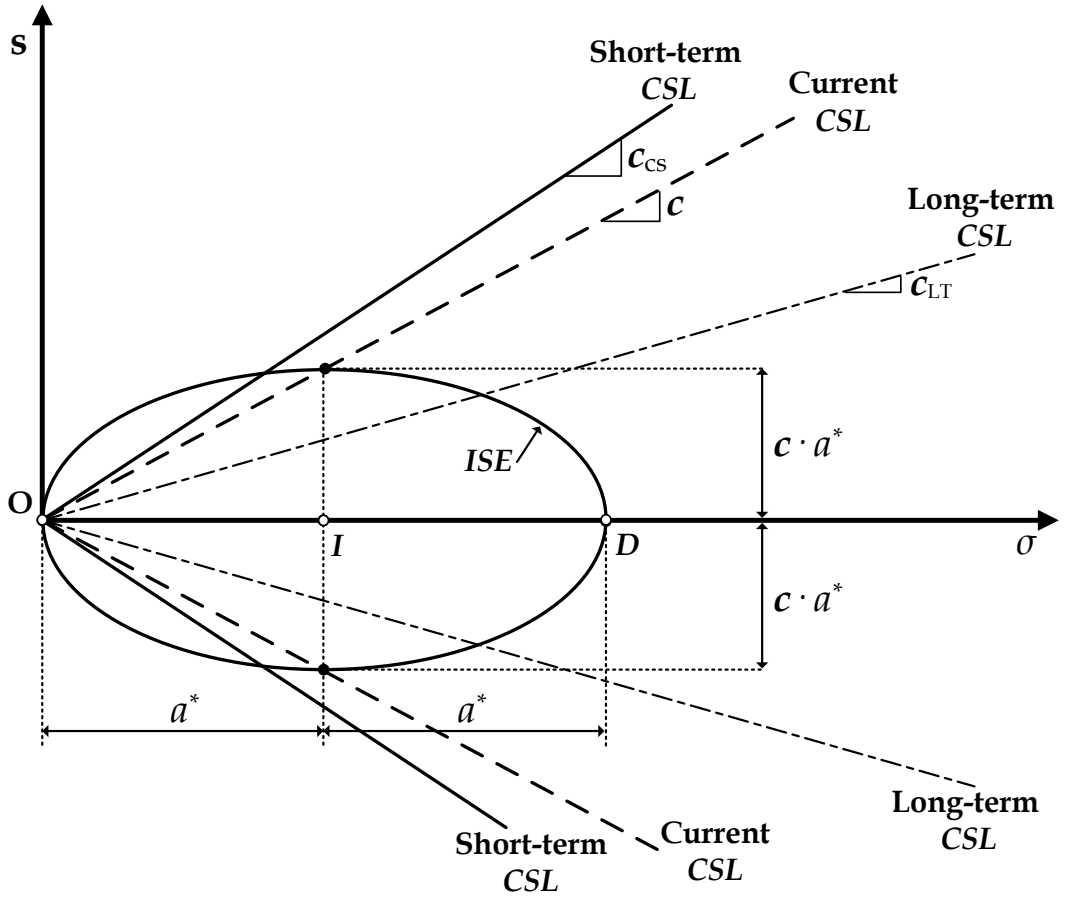

Figure 5.2: Graphical representation of the Intrinsic Strength Envelope (*ISE*) employed.

The projection of the critical state line (*CSL*) in the stress space is quantified through its inclination denoted c. The inclination of the *CSL* in the stress space is allowed to evolve from the initial c_{in} towards a residual value c_{res}. In the case when the kinematic hardening rule is associated solely to the viscous strain rate deviator the values c_{in} and c_{res} will be substituted with c_{CS} and c_{LT} respectively. Experimental measurements in the literature portray the effect of imposed strain rate on the mechanical response. Specimens subjected to rapid strain rates tend to fail at higher shear stress levels. Hence, the *CSL* is allowed to transition from the short-term Critical State Line c_{CS} (representing high speed strain rates and characteristic of the strain rates imposed in common practice in the laboratory to derive the *CSL* associated with elastoplasticity) towards the long-term *CSL* inclination c_{LT} (representing quasi static strain rates of the order $10^{-7} s^{-1}$).

5.2.2 Structure Strength Envelope

The Structure Strength Envelope portrays the effect of bonding on the soil fabric (**Figure 5.3**). It defines the available strength due to bonding formation and therefore encloses the *ISE*. The selected shape of the *SSE* is considered analogous to the Intrinsic since primary anisotropy is not simulated in this version of the model. Considering it encloses the *ISE* its size is allowed to degrade but at no time should it cross the intrinsic surface thus justifying its limit bound on the down side.

The selected expression for the Structure Strength Envelope is given below:

$$F\left(\boldsymbol{\sigma}, a, d, c\right) = \frac{1}{c^2} \cdot \boldsymbol{s} : \boldsymbol{s} + \left(\sigma - a + d\right)^2 - a^2 = 0 \tag{5.2}$$

The center of the *SSE* is translated solely along the hydrostatic axis by d to account for the effect of cementation and possible thixotropic bonding formed during isotropic compression responsible also for the isotropic orientation of the envelope. Hence, bond anisotropy is not accounted for and the sole attention will be paid to the secondary anisotropy associated with the position of the plastic yield envelope inside the *SSE*. The halfsize of the *SSE* is denoted a and the ratio $B = \frac{a}{a^*} \geq 1$ is always greater than unity considering that the *ISE* comprises the lower bound of the Structure Strength Envelope. It is noted that at times when chemical or biological

transformations have been undertaken throughout the bonding formation it is not unusual for the ratio not to reach the residual size value of the intrinsic, at least for the strain levels measured in the laboratory. Hence, conforming with the Dafalias and Popov (1975) postulate the *SSE* comprises the bounding envelope and the *ISE* represents a characteristic surface coinciding with the *SSE* in the complete absence of structure (no primary anisotropy is considered).

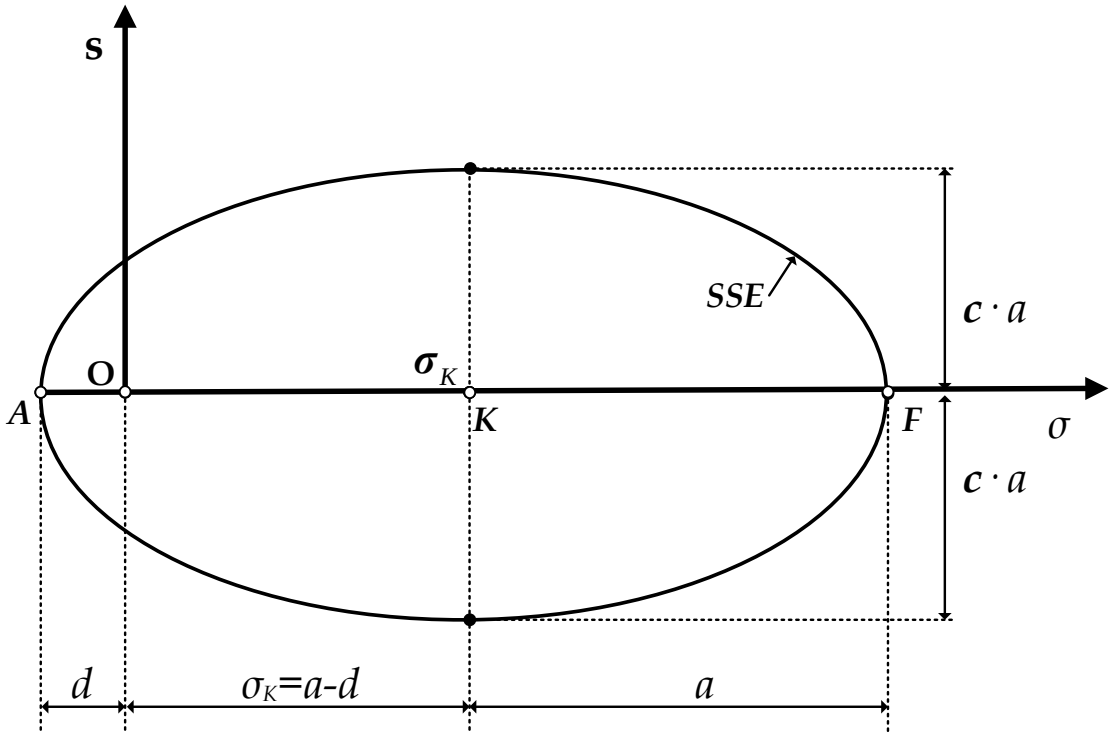

Figure 5.3: Graphical representation of the Structure Strength Envelope (*SSE*).

The *SSE* and the *PYE* employed in the formulation of the proposed viscoelastoplastic model (**Figure 5.4**) denote the following two stress fields:

- the **viscoelastic field** lays inside the plastic yield envelope and the behavior is viscoelastic:

$$d\boldsymbol{\varepsilon} = d\boldsymbol{\varepsilon}^{e} + d\boldsymbol{\varepsilon}^{v} \tag{5.3}$$

- the **viscoelastic-viscoplastic field** lays either inside or on the *SSE*, outside or on the *PYE* and the geomaterial exhibits elastoplastic-viscoplastic behavior:

$$d\boldsymbol{\varepsilon} = d\boldsymbol{\varepsilon}^{e} + d\boldsymbol{\varepsilon}^{p} + d\boldsymbol{\varepsilon}^{v} \tag{5.4}$$

The viscoelastoplastic model is allowed to degrade to a classical elastoplastic model (**Figure 5.5**) by setting the viscous strain tensor to null $\boldsymbol{\varepsilon}^{v} = \mathbf{0}$ or setting the reference time to infinity $(t_p \to \infty)$ in the numerical formulation.

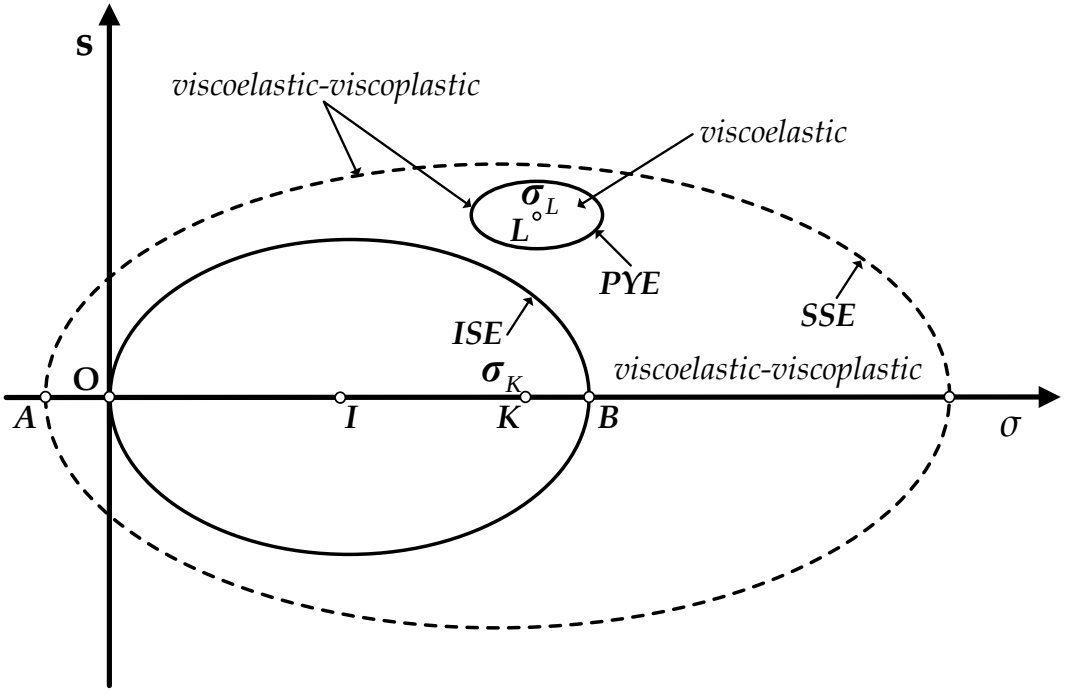

Figure 5.4: Graphical representation of the viscoelastoplastic proposed model and the employed stress fields.

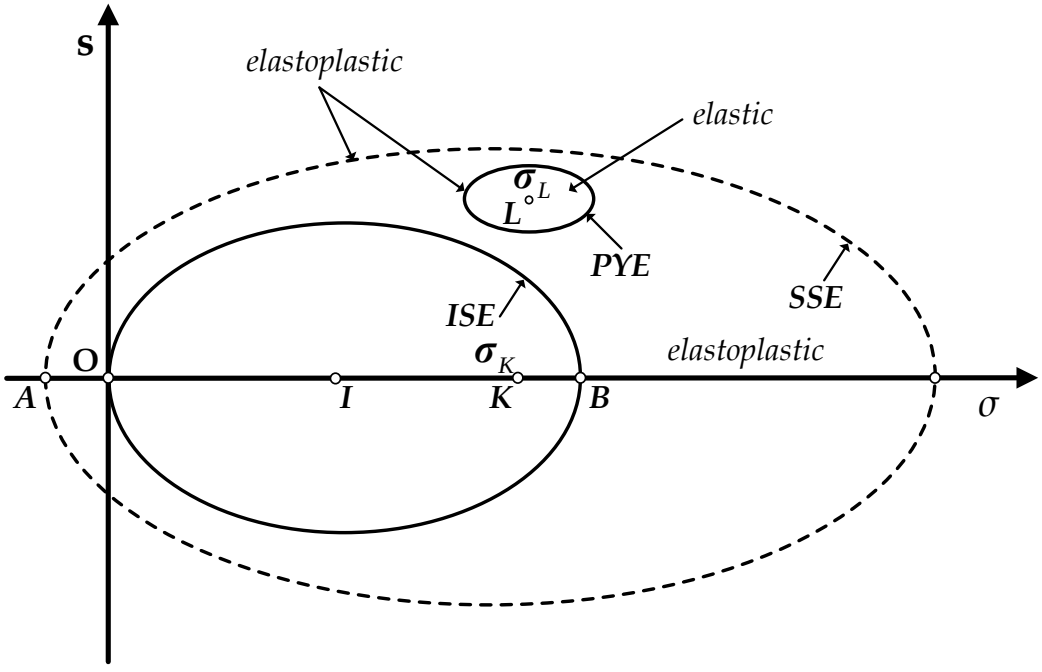

Figure 5.5: Graphical representation of the degenerated viscoelastoplastic model to a classical elastoplastic model and elastoplastic stress fields.

5.2.3 Plastic Yield Envelope

The Plastic Yield Envelope (*PYE*) defines the viscoelastic stress field (**Figure 5.6**). In the case of classical elastoplasticity the purely elastic domain, where the accumulated strains are recoverable upon removal of the loading increment, is infinitesimal and consequently the plastic yield surface is only but a fraction of the *SSE*. Even strains of the order of 0.01÷0.1‰ may be considered irreversible and thus, inelastic (i.e. Georgiannou, 1988; Jardine, 1995; Smith et al. 1992). In the formulation of the proposed model the *PYE* and the *SSE* are similar associated through a similarity ratio denoted ξ. The similarity ratio is considered constant throughout plastic, viscous or elastic loading increments undertaken. Here follows the mathematical formulation of the *PYE* in the generalized stress space:

$$f\left(\boldsymbol{\sigma},\boldsymbol{\sigma}_L,\alpha,c\right)=\frac{1}{c^2}\cdot\left(\boldsymbol{s}-\boldsymbol{s}_L\right):\left(\boldsymbol{s}-\boldsymbol{s}_L\right)+\left(\sigma-\sigma_L\right)^2-\left(\xi\cdot a\right)^2=0 \tag{5.5}$$

The center of the plastic yield envelope denoted $\boldsymbol{\sigma}_L$ is employed as a state variable and it may translate towards the *SSE* assuming a viscoelastic-viscoplastic loading increment.

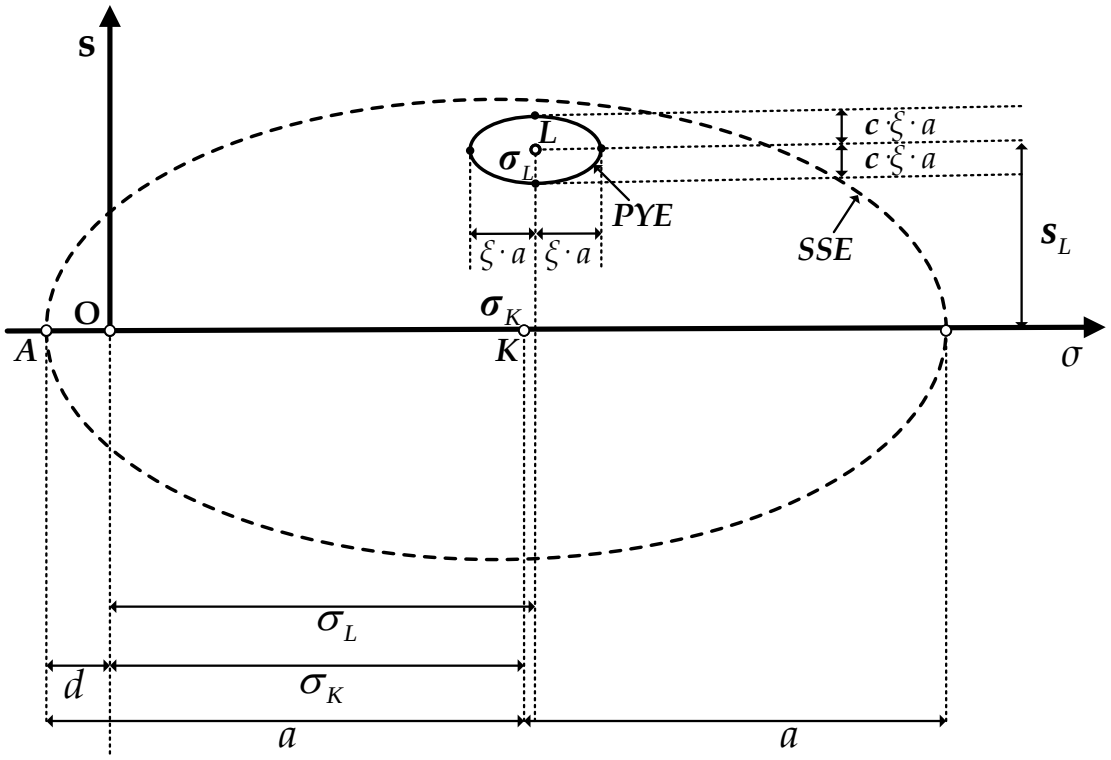

Figure 5.6: Graphical representation of the Plastic Yield Envelope (PYE) employed.

The proportionality ratio controls the size of the *PYE* and is assumed to be a fraction of the *SSE*, usually $\xi = 1‰ \div 5\%$. It is noted that the strain increment imposed in the numerical analysis is not independent of the proportionality ratio. Small similarity ratios result in a small *PYE* and consequently the elastic or viscoelastic increment to adjust the stress state on *PYE* is equally small. Hence, the similarity ratio for the numerical solution to be precise needs to be somewhere in the aforementioned range assuming that the imposed strain increment employed within the numerical programming is of the order of $10^{-6} \div 10^{-5}$.

The center of the plastic yield envelope denoted $\boldsymbol{\sigma}_L$ is controlled through a kinematic hardening law thus portraying the recent stress history through the secondary anisotropy tensor.

5.3 Elasticity

The incremental strain may be expressed as a function of its primary components as follows:

$$d\boldsymbol{\varepsilon} = d\boldsymbol{\varepsilon}^e + d\boldsymbol{\varepsilon}^p + d\boldsymbol{\varepsilon}^v = d\boldsymbol{\varepsilon}^v = d\boldsymbol{\varepsilon}^e + d\boldsymbol{\varepsilon}^p + \dot{\boldsymbol{\varepsilon}}^v \cdot dt \tag{5.6}$$

The superscripts *e*, *p* and *v* denote the elastic, plastic and viscous components. The incremental strain tensors are denoted in the differential form $d\boldsymbol{\varepsilon}$ while the viscous strain rate associated with time is expressed as $\dot{\boldsymbol{\varepsilon}}^v$. dt is the time interval employed in the integration of the constitutive equations.

This section summarizes the formulation of elastic strain component.

The elastic law in the case of classical elastoplasticity describes the mechanical behavior inside the plastic yield envelope. However, formulation of the proposed model assumes the accumulation of the volumetric viscous component within the *PYE*. Hence, there is no purely elastic domain in the formulation of the model. It is noted that solely the volumetric viscous component is accumulated within the plastic yield envelope. The reason for such assumption will be explained in the upcoming section regarding the viscous strain component.

Elasticity is incorporated within the formulation of the viscoelastoplastic stiffness matrix and by associating the incremental stress tensor with the incremental elastic strain tensor as follows:

$$d\boldsymbol{\sigma} = \boldsymbol{C}^e : d\boldsymbol{\varepsilon}^e \tag{5.7}$$

The incremental stress can be expressed also in the following form:

$$d\boldsymbol{\sigma} = \boldsymbol{C} : d\boldsymbol{\varepsilon} - d\boldsymbol{\sigma}^v \tag{5.8}$$

The stress relaxation $d\boldsymbol{\sigma}^v$ and the stiffness tensor $\boldsymbol{C}$ require knowledge of the measure of plastic strains $\dot{\Lambda}$ defined through the consistency condition of the structure strength envelope.

The poroelasticity is employed to define the elastic stiffness tensor $\boldsymbol{C}^e$.

5.3.1 Poroelasticity

The porous elastic law incorporated in the formulation of the constitutive behavioral framework is an isotropic expression of poroelasticity reviewed in a previous subchapter **3.3.2.2**. The elastic bulk modulus denoted K^e and the shear modulus G^e are pressure dependent expressions formulated as follows:

$$\dot{\sigma} = K^e \cdot \dot{\varepsilon}^e \tag{5.9}$$

$$\dot{\boldsymbol{s}} = 2G^e \cdot \dot{\boldsymbol{e}}^e \tag{5.10}$$

$$K^e = \frac{\nu}{\kappa} \cdot \sigma \tag{5.11}$$

$$G^e = \frac{1}{2} \cdot \left(\frac{2 \cdot G^e}{K^e} \right) \cdot K^e \tag{5.12}$$

The definition of the shear modulus incorporates the initial elastic ratio $\frac{2 \cdot G^e}{K^e}$ as a soil property associated with the Poisson's ratio.

5.4 Viscous component

The volumetric and deviatoric component of creep have distinctively different effect on the mechanical behavior. While the volumetric viscous component builds on strength the deviatoric component reveals its deleterious effects on soil resistance at high shear stress levels leading to delayed failure. In essence, it is postulated that the standard oedometer and triaxial tests tend to reveal a completely different fundamental behavior.

In oedometer tests it is the volumetric viscous component that is active. Following Bjerrum's approach the evolution of time is responsible for the increase of the apparent preconsolidation pressure. This is equivalent as saying that the *SSE* is allowed to increase in size stemming from undergoing transformations in the material fabric associated with thixotropic bonding attributed to the viscous volumetric component. The well established semi-logarithmic creep law has been employed widely either in its original form or in its modified expressions (i.e. Vermeer and Neher, 1999; Yin et al., 2002; Leoni et al., 2008; Yin et al., 2010). Considering it has proven to be an invaluable tool in expressing the volumetric creep strain the empirical relationship will be employed within the formulation of the viscous strain.

The deviatoric viscous component on the other hand may prove catastrophic for the overall mechanical behavior. Experimental measurements in the triaxial apparatus have revealed the deleterious effect of deviatoric creep on soil strength. Once the soil specimen is subjected to high shear stress levels the deviatoric strains tend to accumulate leading ultimately to creep failure. In the literature the Singh-Mitchell criterion has received a lot of attention and comprises to date one of the most simple and elegant empirical formulations addressing the mechanical behavior on saturated specimens subjected to undrained creep in the triaxial apparatus. The Singh-Mitchell empirical law tends to provide reasonable and accurate results for the secondary creep stage but fails to capture accurately the primary stage of creep. Hence, the well established Singh-Mitchell empirical model is employed to account for the viscous strain deviator instead of incorporating the volumetric creep component to calibrate the deviatoric (i.e. Vermeer and Neher, 1999; Yin et al., 2002; Debernardi, 2008; Leoni et al., 2008; Yin et al., 2010) by further imposing a non-associated law for the viscous plastic potential.

In order to account for the tertiary component the projection of the critical state line in the stress hyperplane is allowed to transition. Consider a triaxial drained test where the specimen is stressed and the new attained stress state lays somewhere between the short-term *CSL* and the long-term *CSL*. Assuming that the critical state envelope does not evolve then the stress state remains constantly inside the SSE and at no point should it reach the critical state. Consequently, the soil element does not exhibit failure. However, experimental measurements and in-situ slope failures reveal the deleterious effect of creep in the most pronounced way. In order for the stress state to adjust on the critical state thus leading to failure, the critical state line needs to evolve with time or plastic deformation by accounting for some sort of kinematic hardening rule.

Here follows the mathematical formulation of the viscous strain tensor in its incremental form.

5.4.1 Volumetric viscous strain

Assuming that the semi-logarithmic creep law is considered to define the volumetric viscous strain component then the void ratio may be computed as a function of time as follows:

$$e = e_i - \psi \cdot \ln\left(\frac{t}{t_0}\right) \mid t \geq t_0 \tag{5.13}$$

In the expression above the void ratio at the end of primary consolidation e_i is employed. Parameter ψ is the projection of the secondary compression coefficient $C_{\alpha e}$ in the e-ln$t$ space and therefore $\psi = \frac{C_{ae}}{\ln(10)}$.

The reference time is considered solely as an intrinsic parameter characteristic of a given soil in this formulation, as has been suggested by Leroueil et al. (1985), Bjerrum (1967) and Yin (1999). Thus, t_0 is independent of drainage conditions and thickness of the deposit.

Reference time in such sense possesses a more physical meaning. Regardless of the deposit's geological history, is strikes as odd or even ludicrous to assume that one could predict the geotechnical properties of the original deposit much more the exact

geological transformations undertaken during the last geological periods. Hence, all physical and mechanical properties extracted from the laboratory data or in-situ measurements correspond to a rather "newly" formed geomaterial. Regardless of all chemical bonding, biological alterations and mechanical transformations the soil formation is a snapshot of its geological history revealing information only for the present. Thus, the reference time of such a deposit should be considered as the time when the soil samples were extracted. In simple words, the End of Primary Consolidation (EOP) t_i and the reference time t_0 are one and the same and equal to the time measurement employed (1sec, 1min, 1 day, etc). Furthermore, creep tends to accumulate even during the process of primary compression.

By differentiating expression (5.13) with respect to time:

$$\dot{e} = \frac{\partial e}{\partial t} = -\frac{\psi}{t} \mid t \geq t_0 \tag{5.14}$$

The viscous volumetric strain rate can be expressed as:

$$\dot{\varepsilon}^v = \frac{\partial \varepsilon}{\partial t} = -\frac{\dot{e}}{1+e} = \frac{\psi}{(1+e)} \cdot \frac{1}{t} \mid t \geq t_0 \tag{5.15}$$

The expression above incorporates time within the formulation of volumetric viscous strain rate. Regardless, whether in the laboratory it is possible to measure time with a clock it is ludicrous to assume that the soil fabric may be expressed through a time scale. The soil fabric responds to stress and strains and the constitutive relation associating the two measures comprises the governing behavioral framework. In this sense constitutive equations should be solely a function of stress, strain and strain-rate rather than time. Considering that a loading increment corresponding to alterations in the stress state or hardening variables associated with behavioral characteristics (depicted through strains) it stands to reason that the viscous strain rate should be manipulated to eliminate the time scale. Hence, the expression (5.15) above may be integrated and the proper initial conditions employed $\varepsilon^v = 0\Big|_{t=t_0}$ to define the viscous strain rate as follows:

$$\varepsilon^v = \frac{\psi}{(1+e)} \cdot \ln\left(\frac{t}{t_0}\right) \mid t \geq t_0 \Rightarrow$$

$$\varepsilon^{v} = \frac{\psi}{(1+e)} \cdot \ln\left[\frac{\psi}{(1+e)\cdot t_0} \cdot \frac{1}{\dot{\varepsilon}^{v}} \right] \mid t \geq t_0 \Rightarrow$$

$$\dot{\varepsilon}^{v} = \frac{\psi}{(1+e)\cdot t_0} \cdot \exp\left[-\frac{(1+e)}{\psi} \cdot \varepsilon^{v} \right] \mid t \geq t_0 \tag{5.16}$$

The volumetric viscous component accumulates at all stress fields, regardless if the stress state is inside *PYE* on it or even at the tangent stress state by simultaneously laying on the *SSE* and the *PYE*.

5.4.2 Deviatoric viscous strain measure

The deviatoric viscous strain deviator builds on the modification of Mitchell et al. (1968) (depicted in equation (2.7)) instead of the original Singh-Mitchell criterion. Validity of the original formulation is limited to stress intensities ranging from $0.1 \leq D \leq 0.6 \div 0.9$. Thus, the modification was proposed to extend the validity in regions closer to null shear stress levels rather than to account for higher stress intensities that could potentially even lead to creep failure (Aristorenas, 1992). The model's sole aim is to predict the secondary stage of deviatoric creep.

The formulation of the Singh-Mitchell constitutive relation requires calibration through two undrained creep tests in the triaxial apparatus subjected to different shear stress levels. Hence, the axial viscous strain rate $\dot{\varepsilon}_a^{v}$ may be described through the following expression:

$$\dot{\varepsilon}_a^{v} = 2 \cdot A \cdot \sinh\left(\overline{a} \cdot D\right) \cdot \left(\frac{t_0}{t} \right)^{m} \mid t \geq t_0 \tag{5.17}$$

Considering the undrained nature of the problem at hand the radial strain rate $\dot{\varepsilon}_r^{v}$ may be expressed through the following equation:

$$\dot{\varepsilon}_r^{v} = -\nu_u \cdot \dot{\varepsilon}_a^{v} \tag{5.18}$$

where ν_u stands for the undrained Poisson ratio $\nu_u = \frac{1}{2}$. By incorporating expression (5.18) and conforming to the experimental triaxial conditions:

$$\dot{\varepsilon}_q^{v} = \frac{2}{3} \cdot \left(\dot{\varepsilon}_a^{v} - \dot{\varepsilon}_r^{v} \right) = \frac{2}{3} \cdot \left(1 + \nu_u\right) \cdot \dot{\varepsilon}_a^{v} = \frac{2}{3} \cdot \left(1 + \frac{1}{2}\right) \cdot \dot{\varepsilon}_a^{v} = \dot{\varepsilon}_a^{v} \tag{5.19}$$

Hence, the modified constitutive relation setting the basis for the upcoming introduction of the viscous strain deviator is depicted below:

$$\dot{\varepsilon}_q^v = 2 \cdot A \cdot \sinh\left(\overline{a} \cdot D\right) \cdot \left(\frac{t_0}{t}\right)^m \mid t \geq t_0 \tag{5.20}$$

The hyperbolic sinusoidal function may not always provide accurate predictions at low shear stress levels ($D \leq 0.1$) but has the advantage of providing a smooth transition towards the stationary creep stage and proves invaluable in terms of numerical programming (by eliminating the discontinuity).

In the expression above the deviatoric viscous strain rate is based on observations on undrained creep tests in the triaxial apparatus and is expressed as a function of time by incorporating three parameters A, m and $\overline{a}$. D can be defined as the ratio $D = q / q_{\text{FAIL}}$ (**Figure 2.5**). Parameter A controls the measure of the deviatoric viscous strains, parameter $\overline{a}$ portrays the stress intensity effect on creep rate while parameter m controls the tempo of strain rate increase with time.

In order to employ equation (5.20) in the time-dependent behavioral framework the time scale needs to be eliminated.

By integrating expression (5.20) we need to account for the following two cases:

- if $m \neq 1$:

$$\varepsilon_q^v = \frac{2 \cdot A \cdot \sinh\left(\overline{a} \cdot D\right)}{\left(1-m\right)} \cdot t_0 \cdot \left(\frac{t}{t_0}\right)^{1-m} + c_1 \mid t \geq t_0 \tag{5.21}$$

  By incorporating equation (5.20) into (5.21):

$$\varepsilon_q^v = \frac{2 \cdot A \cdot \sinh\left(\overline{a} \cdot D\right)}{\left(1-m\right)} \cdot t_0 \cdot \left[\frac{2 \cdot A \cdot \sinh\left(\overline{a} \cdot D\right)}{\dot{\varepsilon}_q^v}\right]^{\frac{1-m}{m}} + c_1 \mid t \geq t_0 \tag{5.22}$$

  Imposing the proper initial conditions $\varepsilon_q^v = 0\Big|_{t=t_0}$:

$$c_1 = -\frac{2 \cdot A \cdot \sinh\left(\overline{a} \cdot D\right)}{\left(1-m\right)} \cdot t_0 \tag{5.23}$$

  Incorporating expression (5.23) in equation (5.22):

$$\dot{\varepsilon}_q^v = \frac{2 \cdot A \cdot \sinh\left(\overline{a} \cdot D\right)}{\left[1 + \frac{\left(1-m\right)}{2 \cdot A \cdot \sinh\left(\overline{a} \cdot D\right) \cdot t_0} \cdot \varepsilon_q^v\right]^{\frac{m}{1-m}}} \mid t \geq t_0 \wedge \left(\boldsymbol{s} : \boldsymbol{s}\right) \neq 0 \wedge m \neq 1 \tag{5.24}$$

Assuming that the $t < t_0$ the viscous strain rate is null and therefore no viscous strains are accumulated. Furthermore whenever the stress state lays on the isotropic axis, the measure of deviatoric stress $q = \sqrt{\frac{3}{2}\left(\boldsymbol{s} : \boldsymbol{s}\right)} = 0$ equals zero, the viscous strain rate deviator is null.

- if $m = 1$ and imposing the proper initial conditions $\varepsilon_q^v = 0\Big|_{t=t_0}$:

$$\varepsilon_q^v = 2 \cdot A \cdot \sinh\left(\overline{a} \cdot D\right) \cdot t_0 \cdot \ln\left(\frac{t}{t_0}\right) \mid t \geq t_0 \tag{5.25}$$

Incorporating expression (5.25) in equation (5.22):

$$\dot{\varepsilon}_q^v = \frac{2 \cdot A \cdot \sinh\left(\overline{a} \cdot D\right)}{\exp\left[\frac{1}{2 \cdot A \cdot \sinh\left(\overline{a} \cdot D\right) \cdot t_0} \cdot \varepsilon_q^v\right]} \mid t \geq t_0 \wedge \left(\boldsymbol{s} : \boldsymbol{s}\right) \neq 0 \wedge m = 1 \tag{5.26}$$

Assuming that the $t < t_0$ the deviatoric viscous strain rate is zero and therefore no viscous strains are developed. Assuming the stress state lays on the hydrostatic axis, the measure of deviatoric stress $q = \sqrt{\frac{3}{2}\left(\boldsymbol{s} : \boldsymbol{s}\right)} = 0$ equals zero, the viscous strain rate deviator is null.

5.4.3 Derivation of the viscous strain rate tensor

The viscous strain rate tensor needs to incorporate both volumetric and deviatoric viscous components. Thus the viscous potential needs to be specified prior to composing the total viscous strain rate tensor. The adopted viscous potential denoted $\boldsymbol{R}$ may be expressed as follows:

$$\boldsymbol{R} = \frac{\boldsymbol{s}_f}{\sqrt{\boldsymbol{s}_f : \boldsymbol{s}_f}} \tag{5.27}$$

The subscript *f* denotes that the stress state needs to lay on the plastic yield envelope for the deviatoric viscous strains to develop. Assuming that the dot product of the $\boldsymbol{s}_f : \boldsymbol{s}_f$ is null the deviatoric strain rate is zero and therefore there is no evidence of the viscous strain component.

Assuming the deviatoric viscous strain rate tensor may be expressed in the following form:

$$\dot{\boldsymbol{e}}^v = \dot{M} \cdot \boldsymbol{R} \tag{5.28}$$

Then the measure of the deviatoric strain rate $\dot{\varepsilon}_q^v$ is:

$$\dot{\varepsilon}_q^v = \sqrt{\frac{2}{3}\left(\dot{\boldsymbol{e}}^v : \dot{\boldsymbol{e}}^v\right)} = \sqrt{\frac{2}{3}} \cdot \dot{M} \cdot \sqrt{\boldsymbol{R} : \boldsymbol{R}} = \sqrt{\frac{2}{3}} \cdot \dot{M} \tag{5.29}$$

Solving for the scalar measure $\dot{M}$:

$$\dot{M} = \frac{\sqrt{6}}{2} \cdot \dot{\varepsilon}_q^v \tag{5.30}$$

Hence the viscous strain rate deviator may be expressed as follows:

$$\dot{\boldsymbol{e}}^v = \frac{\sqrt{6}}{2} \cdot \dot{\varepsilon}_q^v \cdot \frac{\boldsymbol{s}_f}{\sqrt{\boldsymbol{s}_f : \boldsymbol{s}_f}} \tag{5.31}$$

Consequently, the total strain rate tensor is given through the following expression:

$$\dot{\boldsymbol{\varepsilon}}^v = \left(\frac{1}{3} \cdot \dot{\varepsilon}^v\right) \cdot \boldsymbol{I} + \dot{\boldsymbol{e}}^v = \left(\frac{1}{3} \cdot \dot{\varepsilon}^v\right) \cdot \boldsymbol{I} + \frac{\sqrt{6}}{2} \cdot \dot{\varepsilon}_q^v \cdot \frac{\boldsymbol{s}_f}{\sqrt{\boldsymbol{s}_f : \boldsymbol{s}_f}} \tag{5.32}$$

and finally the deviatoric viscous strain tensor portrayed in expression (5.6) can be computed as follows:

$$d\boldsymbol{\varepsilon}^v = \dot{\boldsymbol{\varepsilon}}^v \cdot dt = \left[\left(\frac{1}{3} \cdot \dot{\varepsilon}^v\right) \cdot \boldsymbol{I} + \frac{\sqrt{6}}{2} \cdot \dot{\varepsilon}_q^v \cdot \frac{\boldsymbol{s}_f}{\sqrt{\boldsymbol{s}_f : \boldsymbol{s}_f}}\right] \cdot dt \tag{5.33}$$

Where the volumetric strain rate is depicted through equation (5.16) while the deviatoric strain rate $\dot{\varepsilon}_q^v$ is computed by incorporating either expression (5.24) or

(5.26), depending on the value of m (derived as prescribed in the original paper by Singh and Mitchell (1968)). dt is the time interval in the integration scheme.

While the volumetric viscous component accumulates at all possible stress states (even inside *PYE*) the viscous strain deviator is evident solely at states associated with plastic deformation (on *PYE*) thus justifying the use of subscript *f* in expressions (5.31) to (5.33).

Formulation of the viscous strain rate tensor and corresponding strain tensor would be all but complete except for a small thing that has been intentionally concealed. Selection of the Singh-Mitchell parameters and the parameter ψ associated with the secondary compression index can be calculated straight forward through standard oedometer and triaxial creep tests. However, the stress ratio D needs to be fully defined for the formulation of the deviatoric viscous strain component to be complete.

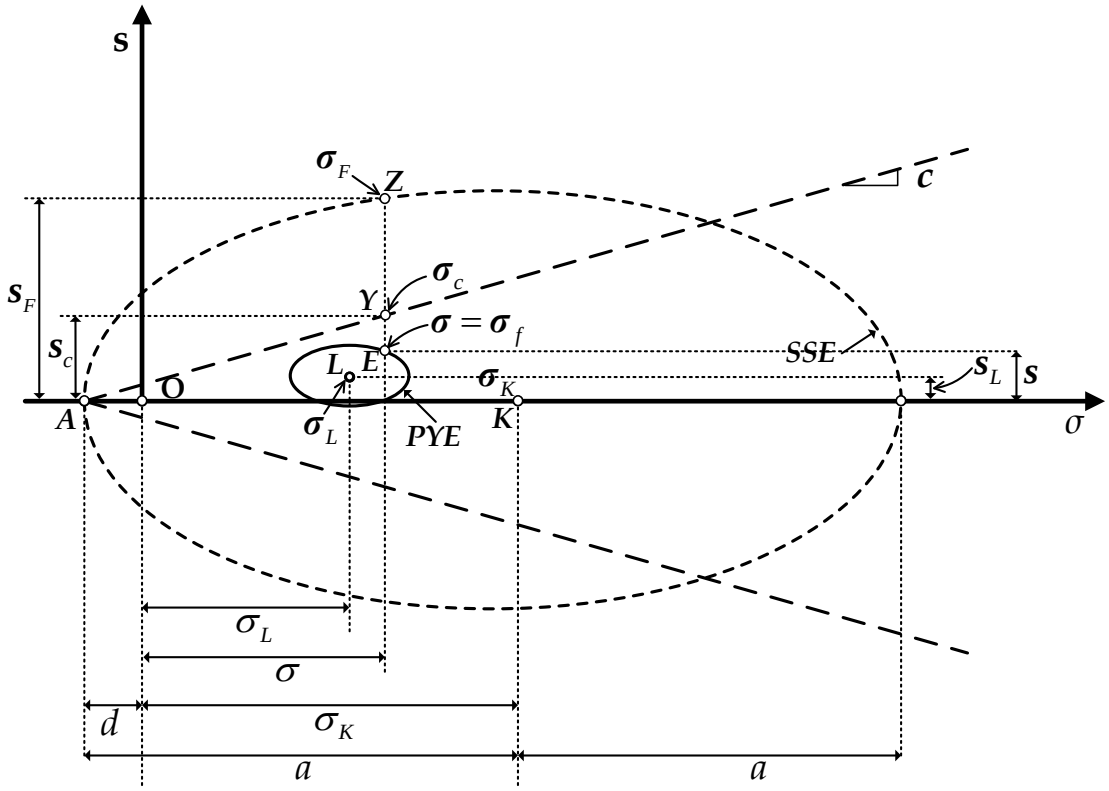

Figure 5.7: Graphical representation of the stress states employed in the definition of stress ratio *D*.

The stress ratio D is a measure of the overstress distance computed through the following expression:

$$D = \frac{q}{q_{\text{FAIL}}} = \frac{\sqrt{\frac{3}{2}\left(\boldsymbol{s}:\boldsymbol{s}\right)}}{\max\left[\sqrt{\frac{3}{2}\left(\boldsymbol{s}_F:\boldsymbol{s}_F\right)},\sqrt{\frac{3}{2}\left(\boldsymbol{s}_c:\boldsymbol{s}_c\right)}\right]} \tag{5.34}$$

The stress deviators denoted as $\boldsymbol{s}_F$ and $\boldsymbol{s}_c$ are depicted in **Figure 5.7**. The stress deviatoric tensors denote the projection of the stress state $\boldsymbol{\sigma} = \boldsymbol{\sigma}_f$ (point *E* on *PYE*) upon the *SSE* (point *Z*) and the current critical state line (point *Y*) in the stress space respectively. Consequently, stress states *E*, *Y*, and *Z* correspond to the same isotropic stress $\sigma = \sigma_f$.

In the case where the stress state *E* (on *PYE*) lays on the hydrostatic axis no viscous strains may be accumulated in the model and thus there is no reason to compute expression (5.34). In any other case, the stress deviators $\boldsymbol{s}_F$ and $\boldsymbol{s}_c$ need to be computed for equation (5.34) to be applied.

Considering that stress state *Z* lays on the *SSE* at the same isotropic stress as the original stress point $\boldsymbol{\sigma} = \boldsymbol{\sigma}_f$:

$$\boldsymbol{s}_F = \lambda_F \cdot \boldsymbol{s} \tag{5.35}$$

$$\sigma_F = \sigma \tag{5.36}$$

By satisfying expression (5.2) portraying the structure yield function:

$$F\left(\boldsymbol{\sigma}_F, a, d, c\right) = \lambda_F^2 \cdot \frac{1}{c^2} \cdot \left(\boldsymbol{s}:\boldsymbol{s}\right) + \left(\sigma - a + d\right)^2 - a^2 = 0 \Rightarrow$$

$$\left(\lambda_F^2 - 1\right) \cdot \frac{1}{c^2} \cdot \left(\boldsymbol{s}:\boldsymbol{s}\right) = F\left(\boldsymbol{\sigma}, a, d, c\right) \Rightarrow$$

$$\lambda_F = \sqrt{\left[1 - \frac{F\left(\boldsymbol{\sigma}, a, d, c\right)}{\frac{1}{c^2} \cdot \left(\boldsymbol{s}:\boldsymbol{s}\right)}\right]} \tag{5.37}$$

As for the stress state *Y* laying on the current *CSL* at the same isotropic stress as the original stress point $\boldsymbol{\sigma} = \boldsymbol{\sigma}_f$ it is possible to compute the scalar quantity requested by applying the expression for the *CSL* cone in the stress hyperplane:

$$\sqrt{\frac{3}{2}\left(\boldsymbol{s}_c : \boldsymbol{s}_c\right)} = \sqrt{\frac{3}{2}\,c^2\left(\sigma + d\right)^2} = \sqrt{\frac{3}{2}}\cdot\sqrt{c^2\left(\sigma + d\right)^2} \tag{5.38}$$

Hence the stress ratio in expression (5.34) can be computed as follows:

$$D = \frac{\sqrt{\boldsymbol{s} : \boldsymbol{s}}}{\max\left\{\left\{\sqrt{\left[1 - \frac{F\left(\boldsymbol{\sigma}, a, d, c\right)}{\frac{1}{c^2}\cdot\left(\boldsymbol{s} : \boldsymbol{s}\right)}\right]}\cdot\sqrt{\boldsymbol{s} : \boldsymbol{s}}\right\}, \sqrt{c^2\left(\sigma + d\right)^2}\right\}} \le 1 \tag{5.39}$$

In all cases the stress ratio D is lower or equal to unity.

5.5 Plastic flow rule

The adopted flow rule controls the magnitude and direction of the plastic strains. Considering the need for stability through the uniqueness postulate for infinitesimal loading increments, the incremental plastic strain may be described through the general formula below:

$$d\boldsymbol{\varepsilon}^p = d\Lambda\cdot\boldsymbol{P} \tag{5.40}$$

Expression (5.40) is similar to (3.46). $\boldsymbol{P}$ is the plastic potential tensor controlling the size (and to some extent the magnitude) of the plastic strain tensor while parameter $d\Lambda$ is the scalar quantity expressing a measure of the plastic strain tensor magnitude (depicted in expression (3.46) as $\dot{\Lambda}$). In this chapter the dot symbol " $\dot{}$ " is employed solely to denote a quantity associated with rate effects. The plastic potential tensor is a second order tensor:

$$\boldsymbol{P} = \frac{1}{3}\cdot P\cdot\boldsymbol{I} + \boldsymbol{P}' \tag{5.41}$$

where $P \equiv \boldsymbol{P} : \boldsymbol{I}$ and $\boldsymbol{P}' \equiv \boldsymbol{P} - \frac{1}{3}\cdot P\cdot\boldsymbol{I}$.

Assuming an associated flow rule:

$$\boldsymbol{Q} = \boldsymbol{P} \tag{5.42}$$

In the same notion as the plastic strain tensor the derivative of the plastic yield envelope $\boldsymbol{Q} = \partial f / \partial \boldsymbol{\sigma}$ may be decomposed in a volumetric and a deviatoric component as follows:

$$\boldsymbol{Q} = \frac{1}{3} \cdot Q \cdot \boldsymbol{I} + \boldsymbol{Q}' \tag{5.43}$$

where:

$$Q \equiv \boldsymbol{Q} : \boldsymbol{I} = \frac{\partial f}{\partial \sigma} = 2 \cdot \left(\sigma - \sigma_L \right) \tag{5.44}$$

$$\boldsymbol{Q}' \equiv \boldsymbol{Q} - \frac{1}{3} \cdot Q \cdot \boldsymbol{I} = \frac{\partial f}{\partial \boldsymbol{s}} = \frac{2}{c^2} \cdot \left(\boldsymbol{s} - \boldsymbol{s}_L \right) \tag{5.45}$$

5.6 Hardening rules

The proposed model incorporates a plastic yield envelope and a structure strength envelope. Furthermore the viscous strain component portrays its effects on the mechanical behavior even at stress states enclosed within the plastic yield envelope. The position and shape of the incorporated bounding envelopes are controlled through the hardening rules. The word plastic (hardening rules) has been removed to account for the combined effect of plastic and viscous aspects on the hardening phenomena attributing to the time-dependent mechanical response. An isotropic hardening rule controls the size a of the Structure Strength envelope and thus the plastic yield surface through the proportionality ratio ξ. The translation of the *SSE* to the tensional regime in the stress space is controlled by a kinematic hardening rule acting of the isotropic tensional translation d. Further kinematic hardening rules control the position of the plastic yield surface within the bonding strength envelope quantified through the evolution of its center $\boldsymbol{\sigma}_L$ and the shape of the *SSE* associated with the transition of the critical state line c.

5.6.1 Isotropic hardening law

The isotropic hardening rule governs the undergoing transformations associated with the size of the Structure Strength Envelope and consequently the plastic yield envelope. Hence, the proposed model incorporates the halfsize a of the *SSE* as a hardening variable. The hardening parameter a tends to evolve with the

accumulation of plastic and viscous strains. Hence, it is not necessary for the stress state to lay on the plastic yield surface for the bonding envelope to increase in size.

Assuming that structure may be quantified through the ratio B:

$$a = B \cdot a^* \tag{5.46}$$

where a is the halfsize of the Structure Strength Envelope and a^* stands for the halfsize of the *ISE* portrayed in **Figure 5.1**. During the destructuration process the bonding tends to degrade with the accumulation of the plastic strains. Hence, an initial structure $B_0 = \left(a / a^*\right)_0$ transitions towards its residual value $B_{res} = \left(a / a^*\right)_{res}$. The residual structure ratio B_{res} may be equal to unity or depending on any chemical, biological or thixotropic bonding formed during the structuration process may receive values slightly over 1.

The graphical representation of a typical stress path associated with the structure degradation process in isotropic compression is depicted in **Figure 5.8**. The kick above the Isotropic Compression Line (*ICL*) is only schematic and is employed in our constitutive model to allow for a smoother transition back to the intrinsic *ICL*.

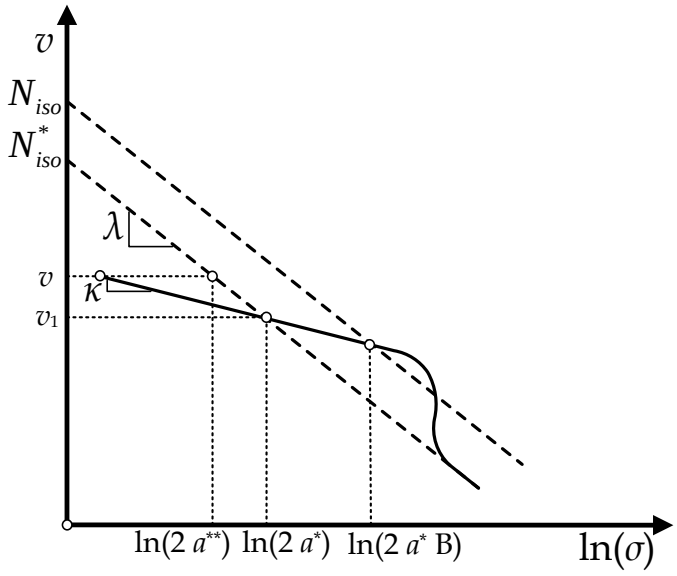

Figure 5.8: Graphical representation of the undertaken stress path in the v-lnσ space.

In the formulation for the halfsize a instead of providing a formulation in the incremental form adopt a more general approach is adopted:

$$a = a^* \cdot \left\{ \begin{array}{l} \left(B_0 - B_{res} + \zeta_v^p \cdot \left| \varepsilon^p \right| + \zeta_q^p \cdot \left| \varepsilon_q^p \right| \right) \cdot \exp\left[-\left(\eta_v^p \cdot \left| \varepsilon^p \right| + \eta_q^p \cdot \left| \varepsilon_q^p \right| \right) \right] \\ + B_{res} \end{array} \right\} \tag{5.47}$$

B_0 and B_{res} are the initial and residual structure ratios respectively $\left(B_0 \geq B_{res} \geq 1 \right)$. η_v^p, η_q^p, ζ_v^p and ζ_q^p comprise constitutive parameters in need of calibration through the destructuring process (**Figure 5.8**).

The formulation depicted through equation (5.47) is concise and robust by providing a continuous transition from the initial to the residual structure. ζ_v^p and ζ_q^p are responsible solely for the kick above the structured Isotropic Compression Line (*ICL*). They can be employed only for fine tuning assuming that a smoother transition to the residual state is of interest. In the general case the parameters can be dropped (by setting them to null) and therefore the parameters controlling the structure degradation process are η_v^p and η_q^p. The first controls the degradation of bonding attributed to the volumetric plastic strain component calibrated through oedometer test results. η_q^p requires the activation of the deviatoric plastic component and can be derived through triaxial experimental data. The principle is similar to Belokas and Kavvadas (2010). Assuming that the reader or a practitioner would like to incorporate parameters ζ_v^p and ζ_q^p a general guideline is to adopt a value within the range of $1\% \div 5\%$ of η_v^p and η_q^p respectively.

Next, the increment of the halfsize a is defined as follows:

$$da = \frac{\partial a}{\partial \boldsymbol{\varepsilon}^p} : d\boldsymbol{\varepsilon}^p + \frac{\partial a}{\partial t} \cdot dt \tag{5.48}$$

The component associated with the plastic strain increment is depicted here below:

$$\frac{\partial a}{\partial \boldsymbol{\varepsilon}^p} : d\boldsymbol{\varepsilon}^p = \left\{ \begin{array}{l} \dfrac{1+e}{\lambda - \kappa} \cdot a^* \cdot d\varepsilon^p \cdot \left(\text{PART} \cdot \text{EXPONENT} + B_{res} \right) \\ + a^* \cdot \left(\zeta_v^p \cdot \left| d\varepsilon^p \right| + \zeta_q^p \cdot \left| d\varepsilon_q^p \right| \right) \cdot \text{EXPONENT} \\ - a^* \cdot \left(\text{PART} \cdot \text{EXPONENT} \right) \cdot \left(\eta_v^p \cdot \left| d\varepsilon^p \right| + \eta_q^p \cdot \left| d\varepsilon_q^p \right| \right) \end{array} \right\} \tag{5.49}$$

where:

$$\begin{aligned}&\text{PART} = \left(B_0 - B_{res} + \zeta_v^p \cdot \left|\varepsilon^p\right| + \zeta_q^p \cdot \left|\varepsilon_q^p\right|\right)\\&\text{EXPONENT} = \exp\left[-\left(\eta_v^p \cdot \left|\varepsilon^p\right| + \eta_q^p \cdot \left|\varepsilon_q^p\right|\right)\right]\end{aligned} \tag{5.50}$$

Assuming that the incremental plastic strain can be expressed in the following form:

$$d\boldsymbol{\varepsilon}^p = \left(d\Lambda\right) \cdot \boldsymbol{P} \tag{5.51}$$

The plastic hardening rule $(\frac{\partial q}{\partial \boldsymbol{\varepsilon}^p} : d\boldsymbol{\varepsilon}^p = \frac{\partial a}{\partial \boldsymbol{\varepsilon}^p} : d\boldsymbol{\varepsilon}^p = \left(d\Lambda\right) \cdot h_a = \left(d\Lambda\right) \cdot \left(\frac{\partial a}{\partial \boldsymbol{\varepsilon}^p} : \boldsymbol{P}\right))$ may undertake the following form:

$$h_a = \left\{\begin{array}{l}\frac{1+e}{\lambda-\kappa} \cdot a^* \cdot P \cdot \left(\text{PART} \cdot \text{EXPONENT} + B_{res}\right)\\ +a^* \cdot \left(\zeta_v^p \cdot \left|P\right| + \zeta_q^p \cdot \sqrt{\frac{2}{3} \cdot \left(\boldsymbol{P}' : \boldsymbol{P}'\right)}\right) \cdot \text{EXPONENT}\\ -a^* \cdot \left(\text{PART} \cdot \text{EXPONENT}\right) \cdot \left(\eta_v^p \cdot \left|P\right| + \eta_q^p \cdot \sqrt{\frac{2}{3} \cdot \left(\boldsymbol{P}' : \boldsymbol{P}'\right)}\right)\end{array}\right\} \tag{5.52}$$

As for the component in expression (5.48) associated with time:

$$\frac{\partial a}{\partial t} \cdot dt = \frac{\partial a^*}{\partial t} \cdot dt \cdot \left[\left(\text{PART} \cdot \text{EXPONENT}\right) + B_{res}\right] \tag{5.53}$$

Computation of the incremental halfsize a requires the definition of the halfsize a^* of the intrinsic strength envelope. In the literature it is typical to use the size of the intrinsic strength envelope denoted a^{**} depicted in **Figure 5.8** (i.e. Kavvadas and Amorosi, 1998 & 2000; Belokas and Kavvadas, 2010 & 2011). Halfsize a^{**} is usually calculated through the expression below:

$$a^{**} = \frac{1}{2} \cdot \exp\left(\frac{N_{iso}^* - v}{\lambda}\right) \tag{5.54}$$

The proposed time-dependent mechanical framework however, builds on the assumption that the *ISE* can be described through the size a^* denoting its halfsize:

$$a^* = \frac{1}{2} \cdot \exp\left(\frac{N_{iso}^* - v - \kappa \cdot \ln\sigma}{\lambda - \kappa}\right) \tag{5.55}$$

The reason for the above implementation lies on the fact that the size a^* is directly associated to the plastic strain increment thus it can be manipulated to extract the hardening modulus and furthermore the size of the Intrinsic Strength Envelope does not change assuming that the stress state returns at states enclosed by the *ISE*.

Similar to classical elastoplasticity the assumption is made that the increment of the *ISE* halfsize may be expressed as follows:

$$da^* = \frac{1+e}{\lambda-\kappa}\cdot a^* \cdot d\varepsilon^p \tag{5.56}$$

The word assumption has not been considered lightly in the aforementioned statement. It stems from the definition of the incremental void ratio:

$$\left.\begin{aligned} e = e_0 - \lambda\cdot\ln\left(\frac{\sigma}{\sigma_0}\right) \Rightarrow de = -\lambda\cdot\frac{d\sigma}{\sigma} \\ e^e = e_0 - \kappa\cdot\ln\left(\frac{\sigma}{\sigma_0}\right) \Rightarrow de^e = -\kappa\cdot\frac{d\sigma}{\sigma} \end{aligned}\right\} \Rightarrow de^p = -\left(\lambda-\kappa\right)\cdot\frac{d\sigma}{\sigma} \tag{5.57}$$

Although the expression above holds in the case of classical elastoplasticity it is an approximation in the case where the creep strain needs to be considered. The argument could be made that the λ accounts solely for the elastic and plastic strain component but it is rather impossible to distinguish them from the plastic (Kaliakin and Dafalias, 1990a). However, the viscous component is evident both in the definition of κ and λ. Hence, regardless whether the expression (5.57) is not an accurate condition it comprises the best possible approximation for the formulation of the constitutive equations.

The volumetric plastic strain increment is given below:

$$d\varepsilon^p = -\frac{de^p}{1+e} = \frac{\left(\lambda-\kappa\right)}{1+e}\cdot\frac{d\sigma}{\sigma} \tag{5.58}$$

Equation (5.56) may be derived from expression (5.58) by imposing $\sigma = 2\cdot a^*$ and $d\sigma = 2\cdot da^*$.

By having fully defined the *ISE* it is now possible to compute the time derivative of the a^* through the underlying expression:

$$\frac{\partial a^*}{\partial t}\cdot dt = -a^*\cdot\frac{1}{\lambda-\kappa}\cdot\frac{\partial e}{\partial t}\cdot dt = \frac{1+e}{\lambda-\kappa}\cdot a^*\cdot\dot{\varepsilon}^v\cdot dt = \frac{1+e}{\lambda-\kappa}\cdot a^*\cdot d\varepsilon^v \tag{5.59}$$

The viscous strain rate may be computed by employing expression (5.16).

5.6.2 Kinematic hardening rules

The kinematic hardening rules control the evolution of the secondary anisotropy through the center of the *PYE* associated with the undergoing stress path. The translation of the tensional shift along the hydrostatic axis (it is not classified as primary anisotropy) is also controlled through a kinematic hardening law. The shape of the *SSE* may transition to a rather elongated state by employing the inclination of the *CSL* projection in the stress space as a hardening variable controlled through a final kinematic hardening rule.

5.6.2.1 Kinematic hardening of the *CSL* projection in the stress space

Aiming to capture failure associated with viscous phenomena the inclination of the critical state line (*CSL*) in the stress space has been employed as a hardening variable. The principle is rather elementary in its conception. Consider a triaxial drained stress path where the specimen is loaded until a deviatoric stress q_0 is attained and then it is allowed to creep (**Figure 5.9**).

The stress state is set constant to point *E* with time evolving. Assuming that the volumetric component was evident the Structure Strength Envelope would increase until the stress state would lay within the *SSE*. Hence, no plastic strains would accumulate transitioning the state towards the critical state. One could state that the isotropic hardening would increase the size a of the *SSE* considerably so that the stress point would adjust again on the plastic yield surface but on the diagonal side. Even in this case however the stress state would be constant and the critical state would not be attained.

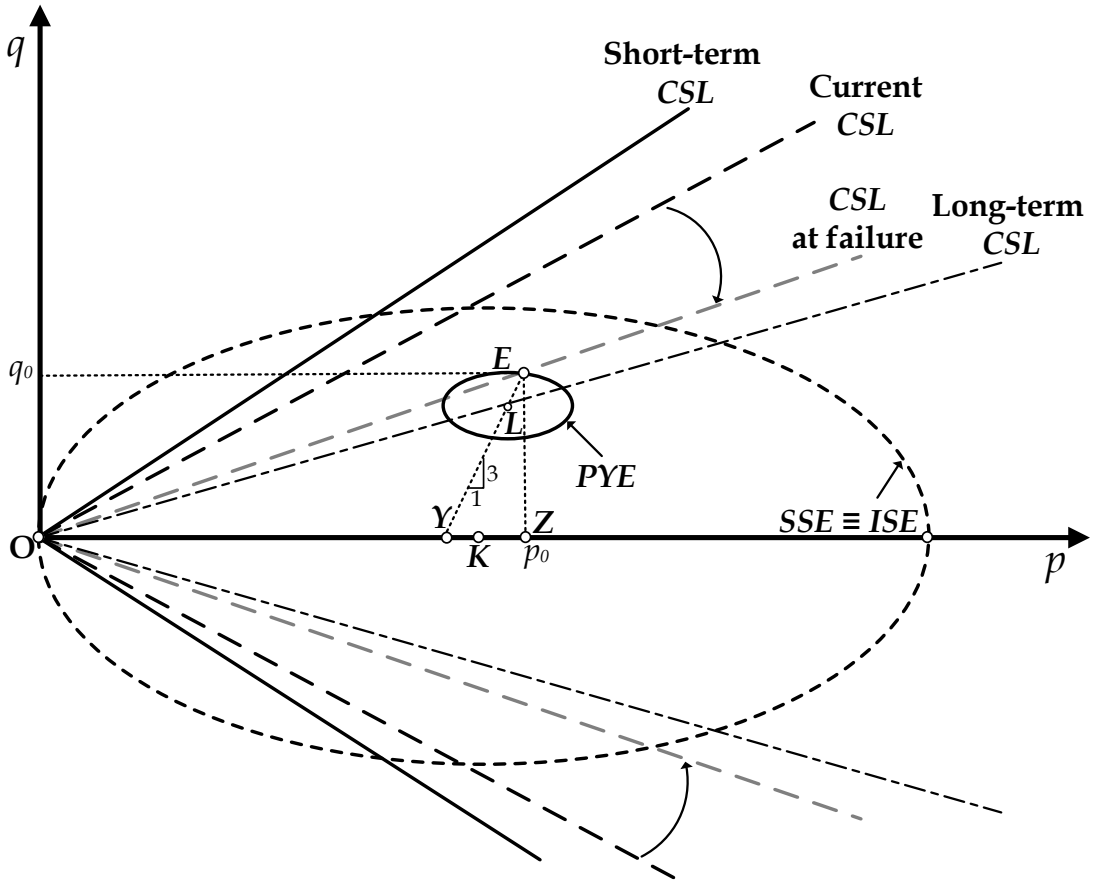

Figure 5.9: Schematic representation of the kinematic hardening of the *CSL* projection in the *p*-*q* space assuming drained triaxial conditions.

So the question arises of how to account for the delayed behavior revealed through triaxial testing portraying its catastrophic effects in slope stability problems. The sole certainty lies in the necessity for another approach that accounts for the delayed characteristics of failure. In plain words, for the specimen to fail it is undeniable that the stress state needs to lay on the current *CSL* projection in the stress space while at the same time laying at the tangent point of *PYE* and *SSE*. Hence, the *CSL* needs to transition until the stress state is adjusted on it.

Expressing the current inclination of the *CSL* in the stress space as a function of deviatoric plastic and viscous strain:

$$c = \left(c_{in} - c_{fin}\right) \cdot \exp\left[-\left(a_1^v \cdot \left|\varepsilon_q^v\right| + \theta_q^p \cdot \left|\varepsilon_q^p\right|\right)\right] + c_{fin} \tag{5.60}$$

In the expression above c_{in} and c_{fin} are the initial and residual values of the inclination of the *CSL*. a_1^v and θ_q^p are constitutive parameters associated with the

CSL degradation with evolving deviatoric viscous strain ε_q^v and deviatoric plastic strain ε_q^p respectively. Assuming that the *CSL* is allowed to transition with respect to the deviatoric plastic strain ε_q^p uniqueness of the critical state line is not justified. Associating the *CSL* should be seen from the prism of predicted mechanical behavior. In order to simulate significant strain softening even for structureless states a purely fictitious initial value c_{in} may transition to the residual critical state line inclination measured in the laboratory. The aforementioned principle portrays a resemblance to the soil hardening model principle (Schanz et al., 1999). In the case where the deviatoric viscous strain ε_q^v is employed to control the transition towards the long-term *CSL* then the process tends to reveal its physical interpretation considering that specimens subjected to rapid strain rates fail at higher shear stress levels.

The behavioral framework is founded on such principle. Henceforth the initial value of the *CSL* inclination c_{in} will be replaced with the short-term inclination c_{cs}. Analogously the residual value of the *CSL* inclination c_{fin} will be substituted from the long-term inclination c_{LT}. The *CSL* is allowed to degrade from the short-term Critical State Line (representing high speed strain rates and characteristic of the strain rates imposed in common practice in the laboratory to derive the CSL associated with elastoplasticity) towards the long-term CSL (representing quasi static strain rates of the order $10^{-7}\,s^{-1}$). The degrading process is controlled through the constitutive parameter a_1^v. Parameter a_1^v can be computed through a drained creep test in the triaxial apparatus leading to delayed failure.

In this end equation (5.60) may be transformed as follows:

$$c = \left(c_{cs} - c_{LT}\right) \cdot \exp\left[-\left(a_1^v \cdot \left|\varepsilon_q^v\right| + \theta_q^p \cdot \left|\varepsilon_q^p\right|\right)\right] + c_{LT} \tag{5.61}$$

Considering that the incremental description is required for the computation of the plastic hardening modulus:

$$dc = \frac{\partial c}{\partial \boldsymbol{\varepsilon}^p} : d\boldsymbol{\varepsilon}^p + \frac{\partial c}{\partial t} \cdot dt \tag{5.62}$$

where the components associated with plastic and viscous degradation are depicted here below:

$$\frac{\partial c}{\partial \boldsymbol{\varepsilon}^p} : d\boldsymbol{\varepsilon}^p = -\left(c - c_{LT}\right) \cdot \theta_q^p \cdot \left| d\varepsilon_q^p \right| \tag{5.63}$$

$$\frac{\partial c}{\partial t} \cdot dt = -\left(c - c_{LT}\right) \cdot a_1^v \cdot \left| d\varepsilon_q^v \right| = -\left(c - c_{LT}\right) \cdot a_1^v \cdot \left| \dot{\varepsilon}_q^v \right| \cdot dt \tag{5.64}$$

The plastic hardening rule $\left(\frac{\partial q}{\partial \boldsymbol{\varepsilon}^p} : d\boldsymbol{\varepsilon}^p = \frac{\partial c}{\partial \boldsymbol{\varepsilon}^p} : d\boldsymbol{\varepsilon}^p = \left(d\Lambda\right) \cdot h_c = \left(d\Lambda\right) \cdot \left(\frac{\partial c}{\partial \boldsymbol{\varepsilon}^p} : \boldsymbol{P} \right)\right)$ may undertake the following form:

$$h_c = \frac{\partial c}{\partial \boldsymbol{\varepsilon}^p} : d\boldsymbol{P} = -\left(c - c_{LT}\right) \cdot \theta_q^p \cdot \sqrt{\frac{2}{3} \cdot \left(\boldsymbol{P}' : \boldsymbol{P}'\right)} \tag{5.65}$$

It is possible to account for different stress ratio inclinations depending on the stress axis. Hence, instead of employing a sole value for the short-term and the long-term Critical State Line inclination c it is possible to construct a tensor and employ that as hardening variables associated with the viscous and plastic measures of the stress tensor deviators through expression (5.62). The capability is incorporated within the formulation of the model following Belokas (2008) principle.

Finally, it should be noted and emphasized at the most pronounced way possible that the proposed model should not be employing both the a_1^v and θ_q^p parameters simultaneously. The reason does not lay on some computational deficiency but rather on the lack of physical meaning.

Regardless of the complication involved in the aforementioned expressions or in the overall time dependent behavioral framework the keypoint lies on the assumption that the viscous strains (assuming that the viscous strain is responsible for the degradation of the CSL towards the long term state) tend to inflate plastic straining. Assuming that the stress state lays on PYE somewhere between c_{cs} and c_{LT} the geomaterial will creep but eventually it will exhibit delayed failure due to plastic deformation. The viscous component comprises the trigger while the plastic strain component is the bullet thus leading to the unavoidable outcome of delayed failure. Hence, the tertiary creep stage is indeed induced by the creep strains but attributed

to the plastic strain component. After all, the soil fabric cannot distinguish between elastic, plastic or viscous strains. It is solely an assumption made in the constitutive formulation of the governing equations.

5.6.2.2 Kinematic hardening of the SSE's tensional shift d

The effect of bonding associated with isotropic compression is quantified through the parameter d depicted in **Figure 5.1**. Assuming that the material undergoes alterations in its material fabric associated with plastic straining or time-dependent phenomena then that tensional transpose tends to shift towards the null, thus comprising a perfect MCC bounding surface.

Expressing the tensional transpose of the Structure Strength Envelope as a function of deviatoric plastic and viscous strain analogously to the *CSL* inclination:

$$d = d_{in} \cdot \exp\left[-\left(a_2^v \cdot \left|\varepsilon_q^v\right| + \vartheta_q^p \cdot \left|\varepsilon_q^p\right|\right)\right] \tag{5.66}$$

where d_{in} represent the initial value of the Structure Strength Envelope translation to the tensional regime. a_2^v and ϑ_q^p are constitutive parameters associated with the tensional transpose d with evolving deviatoric viscous strain ε_q^v and deviatoric plastic strain ε_q^p respectively. Expression (5.66) reveals that the residual value for the tensional translation of the bonding strength envelope is the null origin of the hydrostatic axis.

Considering that the incremental description is required for the computation of the plastic hardening modulus:

$$d\left(d\right) = \frac{\partial d}{\partial \boldsymbol{\varepsilon}^p} : d\boldsymbol{\varepsilon}^p + \frac{\partial d}{\partial t} \cdot dt \tag{5.67}$$

where the components associated with plastic and viscous degradation are portrayed here below:

$$\frac{\partial d}{\partial \boldsymbol{\varepsilon}^p} : d\boldsymbol{\varepsilon}^p = -d \cdot \vartheta_q^p \cdot \left|d\varepsilon_q^p\right| \tag{5.68}$$

$$\frac{\partial d}{\partial t} \cdot dt = -d \cdot a_2^v \cdot \left|d\varepsilon_q^v\right| = -d \cdot a_2^v \cdot \left|\dot{\varepsilon}_q^v\right| \cdot dt \tag{5.69}$$

The plastic hardening rule $(\frac{\partial d}{\partial \boldsymbol{\varepsilon}^p} : d\boldsymbol{\varepsilon}^p = \frac{\partial d}{\partial \boldsymbol{\varepsilon}^p} : d\boldsymbol{\varepsilon}^p = (d\Lambda) \cdot h_d = (d\Lambda) \cdot \left(\frac{\partial d}{\partial \boldsymbol{\varepsilon}^p} : \boldsymbol{P} \right))$ may undertake the following form:

$$h_d = \frac{\partial d}{\partial \boldsymbol{\varepsilon}^p} : d\boldsymbol{P} = -d \cdot \vartheta_q^p \cdot \sqrt{\frac{2}{3} \cdot (\boldsymbol{P}' : \boldsymbol{P}')} \tag{5.70}$$

It is noted that the proposed model should not be employing both the a_2^v and ϑ_q^p parameters simultaneously. The reason does not lay on some computational deficiency but rather on the lack of physical meaning. It is advised that assuming that the viscous component is employed in the degradation of the critical state line, towards the long-term inclination, the same component to be activated in the degradation of the tensional translation of the bounding envelope since the same phenomena are attributing to the shift. The principle is not bounding. The parameters may be derived through an isotropic extension test by reducing the hydrostatic pressure. As a general guideline the parameters ϑ_q^p and a_2^v should be 1.5÷2 times higher than the constitutive parameters θ_q^p and a_1^v considering that it is desirable for the tensional shift to reach the null of hydrostatic axis much earlier than the long term inclination of the *CSL* is attained.

5.6.2.3 Kinematic hardening of the secondary anisotropy tensor σ_L

Depending on whether the stress state lays on the bonding strength envelope or inside, it is necessary to account for two distinct loading cases. The Structure Strength Envelope and the position of the *PYE* evolve due to plastic straining and transformations attributed to viscous effects. Both envelopes tend to translate and elongate. Thus, the position of the *PYE* needs to conform with the new state by transitioning to the conjugate point with time evolving and plastic straining.

Prior however to providing the framework for the kinematic hardening of the plastic yield center denoted $\boldsymbol{\sigma}_L$ it is necessary to define the conjugate point M' depicted in **Figure 5.10**.

The conjugate point *M*' may be derived by assuming that:

$$\boldsymbol{KM}' = \lambda_f \cdot \boldsymbol{LM} \Rightarrow$$

$$\boldsymbol{\sigma}_{M'} - (a-d)\cdot \boldsymbol{I} = \lambda_f \cdot (\boldsymbol{\sigma} - \boldsymbol{\sigma}_L) \Rightarrow$$

$$\boldsymbol{\sigma}_{M'} = \lambda_f \cdot (\boldsymbol{\sigma} - \boldsymbol{\sigma}_L) + (a-d)\cdot \boldsymbol{I} \tag{5.71}$$

Considering that the stress state *M*' lays on the *SSE*:

$$F(\boldsymbol{\sigma}_{M'}, a, d, c) = 0 \Rightarrow$$
$$\lambda_f^2 \cdot \left[\frac{1}{c^2} \cdot (\boldsymbol{s} - \boldsymbol{s}_L) : (\boldsymbol{s} - \boldsymbol{s}_L) + (\sigma - \sigma_L)^2 \right] - a^2 = 0 \Rightarrow$$
$$\lambda_f^2 \cdot \left[f(\boldsymbol{\sigma}, a, d, c) + (\xi \cdot a)^2 \right] - a^2 = 0$$

Considering that the stress state $\boldsymbol{\sigma}$ lays on PYE:

$$\lambda_f^2 \cdot \left[f(\boldsymbol{\sigma}, a, d, c) + (\xi \cdot a)^2 \right] - a^2 = 0 \Rightarrow$$
$$\lambda_f^2 \cdot \left[(\xi \cdot a)^2 \right] - a^2 = 0 \Rightarrow$$
$$a^2 \cdot \left[(\lambda_f \cdot \xi)^2 - 1 \right] = 0 \Rightarrow$$

$$\lambda_f = \frac{1}{\xi} \tag{5.72}$$

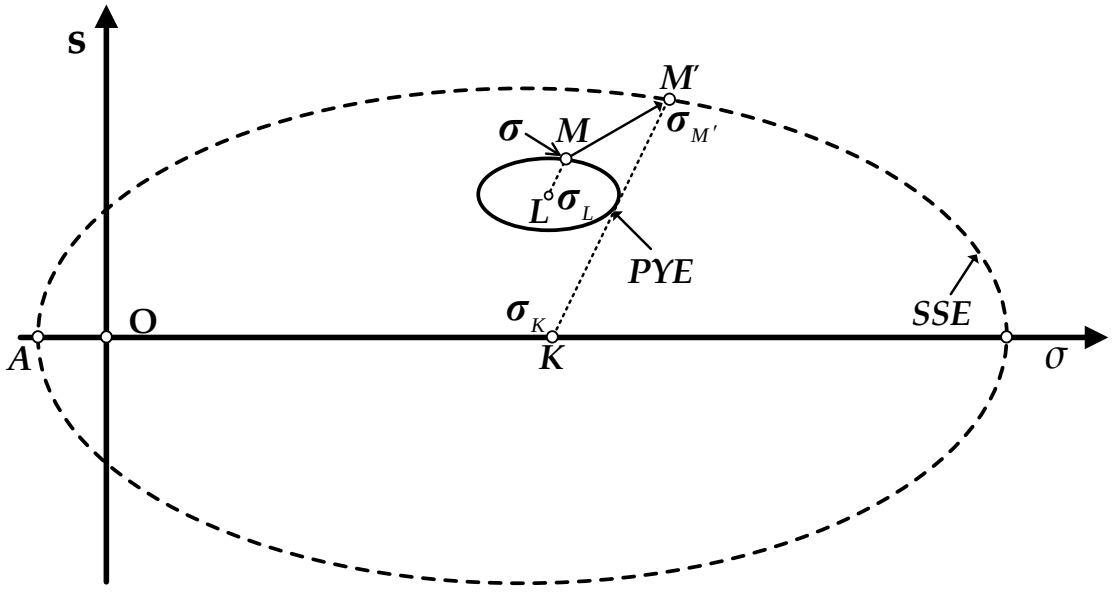

Figure 5.10: Definition of the conjugate point *M*'.

Hence, the conjugate point *M*' can be computed through the following expression:

$$\boldsymbol{\sigma}_{M'} = \left(a - d\right) \cdot \boldsymbol{I} + \frac{1}{\xi} \cdot \left(\boldsymbol{\sigma} - \boldsymbol{\sigma}_L\right) \tag{5.73}$$

Two general cases need to be stated and examined separately concerning the evolution of the secondary anisotropy tensor depicted through $\boldsymbol{\sigma}_L$. The first scenario describes the stress states on the structure strength envelope while the other accounts for the states laying on *PYE* transitioning towards the conjugate point. It is noted that stress states laying inside the plastic yield surface are not responsible for any alteration in the secondary anisotropy tensor. The translation is associated to either plastic strains or deviatoric viscous deformations that are accumulated solely on states laying on *PYE* and *SSE*.

- **For states laying on the SSE**:

  The material states laying on the *SSE* are adjusted on the unique point of intersection between the bonding strength envelope and the plastic yield surface (**Figure 5.11**).

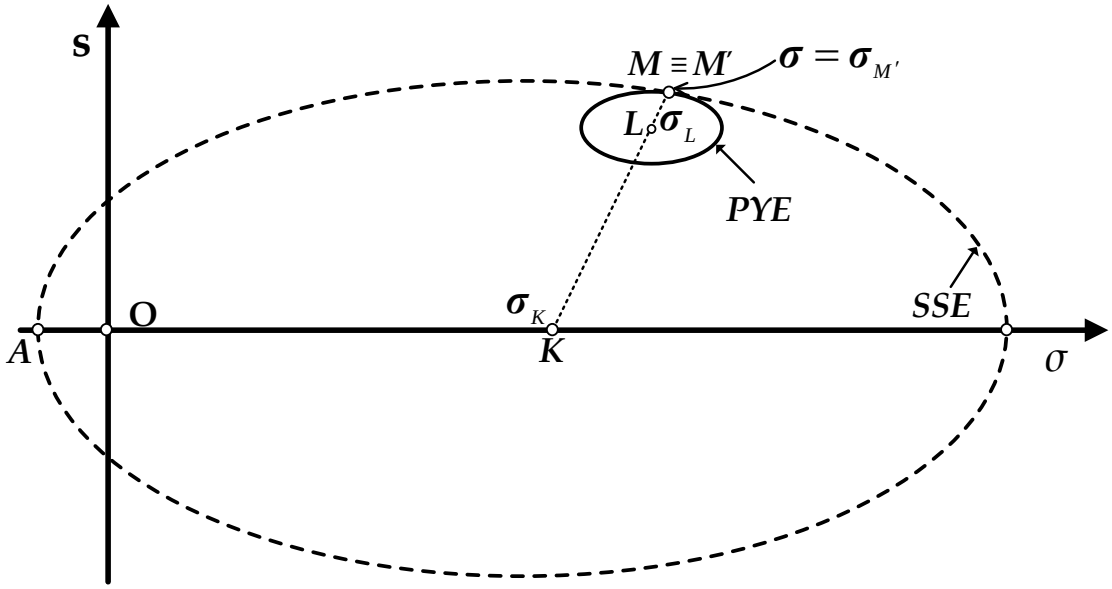

Figure 5.11: Graphical representation of the conjugate point for material states laying on PYE.

Accounting for the similarity between the *PYE* and *SSE*, the two bounding surfaces are tangent along the axis defined through their centers:

$$\frac{\boldsymbol{\sigma}-\boldsymbol{\sigma}_L}{\xi\cdot a}=\frac{\boldsymbol{\sigma}-\boldsymbol{\sigma}_K}{a}\Rightarrow$$
$$\frac{\boldsymbol{\sigma}-\boldsymbol{\sigma}_L}{\xi\cdot a}=\frac{\boldsymbol{\sigma}-(a-d)\cdot\boldsymbol{I}}{a}\Rightarrow$$

$$\boldsymbol{\sigma}_L=(1-\xi)\cdot\boldsymbol{\sigma}+\xi\cdot(a-d)\cdot\boldsymbol{I} \tag{5.74}$$

Hence, assuming that the conjugate point *M*' and the stress point *M* coincide the stress anisotropy portrayed through the center of the plastic yield envelope can be computed through expression (5.74).

- **For states enclosed in the SSE but on PYE**:
  Assuming that the stress state lays on *PYE* and transitions towards the conjugate point (**Figure 5.10**) then the secondary anisotropy tends to evolve. Assuming that a non-radial stress path is undertaken then the stress state tends to evolve even on *PYE* thus altering slightly the target conjugate point. For the material states laying on *PYE* it is assumed that the evolution of the plastic yield envelope center $\boldsymbol{\sigma}_L$ is a function of the isotropic hardening due to a and further associated with the evolution of the stress state towards the conjugate point $\boldsymbol{\beta}=\boldsymbol{MM'}$. Note, that the adopted kinematic hardening rule is proposed by Kavvadas and Amorosi (1998 & 2000):

$$d\boldsymbol{\sigma}_L=\frac{da}{a}\cdot\boldsymbol{\sigma}_L+(d\mu)\cdot\boldsymbol{\beta} \tag{5.75}$$

where the tensor $\boldsymbol{\beta}$ can be expressed as follows:

$$\boldsymbol{\beta}=\boldsymbol{MM'}=\boldsymbol{\sigma}_M-\boldsymbol{\sigma}=\frac{1}{\xi}\cdot(\boldsymbol{\sigma}-\boldsymbol{\sigma}_L)-\left[\boldsymbol{\sigma}-(a-d)\cdot\boldsymbol{I}\right] \tag{5.76}$$

The isotropic hardening da and the measure of the stress state translation along the direction $\boldsymbol{\beta}$ are functions of both plastic and viscous strain components.

The kinematic hardening of the plastic yield envelope center incorporates two distinct features (**Figure 5.12**):

- ✓ The component $\frac{da}{a}\cdot\boldsymbol{\sigma}_L$ comprises the translation along the direction $\boldsymbol{OL}$ transposed by $\frac{da}{a}\cdot\boldsymbol{\sigma}_L$. This portion accounts for the isotropic evolution of the size associated with the structure yield envelope and through the proportionality ratio with the plastic yield surface.
- ✓ The component $(d\mu)\cdot\boldsymbol{\beta}$ represents the translation along the direction $\boldsymbol{\beta}$. The magnitude is controlled through the measure $d\mu$ (on the most part considering that to some extent $\boldsymbol{\beta}$ has already a measure and therefore $\sqrt{\boldsymbol{\beta}:\boldsymbol{\beta}}\neq 1$). By employing the direction $\boldsymbol{\beta}$ in the expression of the kinematic hardening rule of the *PYE* it is assumed that the stress state will be adjusted on the conjugate point and not intersect the bounding surface (i.e. Mroz, 1978) at some random point for finite increments of the da and $d\mu$ (Kavvadas, 1995).

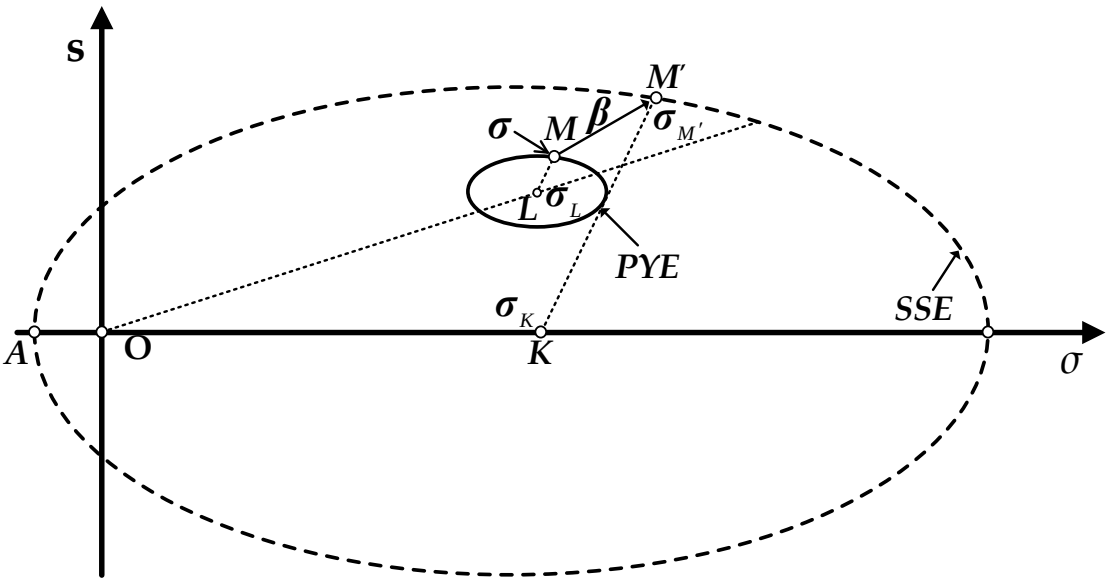

Figure 5.12: Graphical representation of parameters employed in the kinematic hardening of *PYE*.

For the expression (5.75) to be fully defined, the measure $d\mu$ needs to be computed through the consistency condition of the plastic yield envelope. Assuming that the original stress state lays on the *PYE* undergoing a viscoelastoplastic increment then the new stress state should also lay on the surface:

$$df\left(\boldsymbol{\sigma},\boldsymbol{\sigma}_L,a,c\right)=0\Rightarrow\frac{\partial f}{\partial\boldsymbol{\sigma}}:d\boldsymbol{\sigma}+\frac{\partial f}{\partial\boldsymbol{\sigma}_L}:d\boldsymbol{\sigma}_L+\frac{\partial f}{\partial a}\cdot da+\frac{\partial f}{\partial c}\cdot dc=0 \tag{5.77}$$

By accounting for the following conditions:

$$\boldsymbol{Q}=\frac{\partial f}{\partial\boldsymbol{\sigma}}=\frac{1}{3}\cdot Q\cdot\boldsymbol{I}+\boldsymbol{Q}' \tag{5.78}$$

$$Q=2\cdot\left(\sigma-\sigma_L\right) \tag{5.79}$$

$$\boldsymbol{Q}'=\frac{2}{c^2}\cdot\left(\boldsymbol{s}-\boldsymbol{s}_L\right) \tag{5.80}$$

$$\frac{\partial f}{\partial\boldsymbol{\sigma}_L}=-\frac{1}{3}\cdot2\cdot\left(\sigma-\sigma_L\right)\cdot\boldsymbol{I}-\frac{2}{c^2}\cdot\left(\boldsymbol{s}-\boldsymbol{s}_L\right)=-\boldsymbol{Q} \tag{5.81}$$

$$\frac{\partial f}{\partial a}=-2\cdot\xi^2\cdot\alpha \tag{5.82}$$

$$\frac{\partial f}{\partial c}=-\frac{2}{c}\cdot\left[\frac{1}{c^2}\cdot\left(\boldsymbol{s}-\boldsymbol{s}_L\right):\left(\boldsymbol{s}-\boldsymbol{s}_L\right)\right] \tag{5.83}$$

the measure $d\mu$ may be given trough the following expression:

$$d\mu=\frac{\boldsymbol{Q}:d\boldsymbol{\sigma}-\frac{da}{a}\cdot\left[\boldsymbol{Q}:\boldsymbol{\sigma}_L+2\cdot\left(\xi\cdot\alpha\right)^2\right]-\left[\frac{2}{c^2}\cdot\left(\boldsymbol{s}-\boldsymbol{s}_L\right):\left(\boldsymbol{s}-\boldsymbol{s}_L\right)\right]\cdot\left(\frac{1}{c}\cdot dc\right)}{\boldsymbol{Q}:\boldsymbol{\beta}} \tag{5.84}$$

In order to compute the aforementioned expression each individual component needs to be analyzed individually and expression (5.84) needs to be recomposed in its computational form employed within the numerical integration scheme:

$$\boldsymbol{Q}:\boldsymbol{\sigma}_L+2\cdot\left(\xi\cdot\alpha\right)^2=2\cdot\left(\sigma-\sigma_L\right)\cdot\sigma_L+\frac{2}{c^2}\cdot\left(\boldsymbol{s}-\boldsymbol{s}_L\right):\boldsymbol{s}_L+2\cdot\left(\sigma-\sigma_L\right)^2$$
$$+\frac{2}{c^2}\cdot\left(\boldsymbol{s}-\boldsymbol{s}_L\right):\left(\boldsymbol{s}-\boldsymbol{s}_L\right)\Rightarrow$$

$$\boldsymbol{Q}:\boldsymbol{\sigma}_L+2\cdot\left(\xi\cdot\alpha\right)^2=\boldsymbol{Q}:\boldsymbol{\sigma}_L+\boldsymbol{Q}:\left(\boldsymbol{\sigma}-\boldsymbol{\sigma}_L\right)=\boldsymbol{Q}:\boldsymbol{\sigma} \tag{5.85}$$

$$\boldsymbol{Q}:d\boldsymbol{\sigma}=2\cdot\left(\sigma-\sigma_L\right)\cdot d\sigma+\frac{2}{c^2}\cdot\left(\boldsymbol{s}-\boldsymbol{s}_L\right):d\boldsymbol{s} \tag{5.86}$$

$$\boldsymbol{Q}:d\boldsymbol{\sigma}_L = 2\cdot\left(\sigma-\sigma_L\right)\cdot d\sigma_L + \frac{2}{c^2}\cdot\left(\boldsymbol{s}-\boldsymbol{s}_L\right):d\boldsymbol{s}_L \tag{5.87}$$

As for the denominator denoted $\boldsymbol{Q}:\boldsymbol{\beta}$ it may be computed as follows:

$$\boldsymbol{Q}:\boldsymbol{\beta} = \frac{2}{\xi}\cdot\left(\sigma-\sigma_L\right)^2 - 2\cdot\left(\sigma-\sigma_L\right)\cdot\left(\sigma-a+d\right) + \frac{1}{\xi}\cdot\frac{2}{c^2}\cdot\left(\boldsymbol{s}-\boldsymbol{s}_L\right):\left(\boldsymbol{s}-\boldsymbol{s}_L\right)$$
$$-\frac{2}{c^2}\cdot\left(\boldsymbol{s}-\boldsymbol{s}_L\right):\boldsymbol{s} \Rightarrow$$

$$\boldsymbol{Q}:\boldsymbol{\beta} = \frac{2}{\xi}\cdot\left\{\begin{array}{l}\left[\frac{1}{c^2}\cdot\left(\boldsymbol{s}-\boldsymbol{s}_L\right):\left(\boldsymbol{s}-\boldsymbol{s}_L\right)+\left(\sigma-\sigma_L\right)^2\right] \\ -\left[\frac{1}{c^2}\cdot\left(\boldsymbol{s}-\boldsymbol{s}_L\right):\boldsymbol{s}+\left(\sigma-\sigma_L\right)\cdot\left(\sigma-a+d\right)\right]\end{array}\right\} \Rightarrow$$

$$\boldsymbol{Q}:\boldsymbol{\beta} = \frac{2}{\xi}\cdot\left\{\left(\xi\cdot a\right)^2 - \left[\frac{1}{c^2}\cdot\left(\boldsymbol{s}-\boldsymbol{s}_L\right):\boldsymbol{s}+\left(\sigma-\sigma_L\right)\cdot\left(\sigma-a+d\right)\right]\right\} \Rightarrow$$

$$\boldsymbol{Q}:\boldsymbol{\beta} = 2\cdot\left\{\xi\cdot a^2 - \left[\frac{1}{c^2}\cdot\left(\boldsymbol{s}-\boldsymbol{s}_L\right):\boldsymbol{s}+\left(\sigma-\sigma_L\right)\cdot\left(\sigma-a+d\right)\right]\right\} \tag{5.88}$$

Hence, the expression (5.84) can be computed through the following formulation:

$$d\mu = \frac{\text{PART1}-\text{PART2}}{\xi\cdot a^2 - \left[\frac{1}{c^2}\cdot\left(\boldsymbol{s}-\boldsymbol{s}_L\right):\boldsymbol{s}+\left(\sigma-\sigma_L\right)\cdot\left(\sigma-a+d\right)\right]} \tag{5.89}$$

where:

$$\text{PART1} = \frac{1}{c^2}\cdot\left(\boldsymbol{s}-\boldsymbol{s}_L\right):\left(d\boldsymbol{s}-\frac{da}{a}\cdot\boldsymbol{s}\right)+\left(\sigma-\sigma_L\right)\cdot\left(d\sigma-\frac{da}{a}\cdot\sigma\right) \tag{5.90}$$

$$\text{PART2} = \left[\frac{1}{c^2}\cdot\left(\boldsymbol{s}-\boldsymbol{s}_L\right):\left(\boldsymbol{s}-\boldsymbol{s}_L\right)\right]\cdot\left(\frac{1}{c}\cdot dc\right) \tag{5.91}$$

Noted that dc and da comprise functions of the plastic incremental strains and time, computed by applying expressions (5.62) and (5.48).

5.7 Plastic hardening modulus

The plastic hardening modulus can be specified accurately solely on stress states laying on the Structure Strength Envelope. For all other plastic states enclosed by the

bonding surface but adjusted on the plastic yield envelope an interpolation rule needs to be considered; interpolation between an initial infinite value at the moment of first plastic yielding to the value of the hardening modulus at the conjugate point laying on the *SSE*.

In classical elastoplasticity the measure of plastic strains denoted $\dot{\Lambda}$ is associated with the hardening modulus through the expression (3.55). In the proposed model the measure of the plastic strains denoted $d\Lambda$ portrayed in expression (5.40) is altered to account for alterations in the nominator attributed to the time associated transformations in the material fabric.

Measure $d\Lambda$ may be computed through the consistency condition of the Structure Strength Envelope. Assuming that a stress point laying on the *SSE* undergoes a viscoelastoplastic increment then the new stress state needs to remain adjusted on the envelope:

$$dF\left(\boldsymbol{\sigma},a,d,c\right)=0\Rightarrow\frac{\partial F}{\partial\boldsymbol{\sigma}}:d\boldsymbol{\sigma}+\frac{\partial F}{\partial a}\cdot da+\frac{\partial F}{\partial d}\cdot d\left(d\right)+\frac{\partial F}{\partial c}\cdot dc=0 \tag{5.92}$$

Considering that $d\boldsymbol{\sigma}=\boldsymbol{C}^{e}:d\boldsymbol{\varepsilon}^{e}$ and at the tangent point of the *SSE* and *PYE* $\boldsymbol{Q}=\xi\cdot\frac{\partial F}{\partial\boldsymbol{\sigma}}$ attributed to the similarity of the two bounding surfaces quantified through the proportionality ratio ξ the expression (5.92) may be manipulated as follows:

$$\begin{aligned}
&\frac{\partial F}{\partial\boldsymbol{\sigma}}:d\boldsymbol{\sigma}+\frac{\partial F}{\partial a}\cdot da+\frac{\partial F}{\partial d}\cdot d\left(d\right)+\frac{\partial F}{\partial c}\cdot dc=0\Rightarrow\\
&\frac{1}{\xi}\cdot\boldsymbol{Q}:d\boldsymbol{\sigma}+\frac{\partial F}{\partial a}\cdot da+\frac{\partial F}{\partial d}\cdot d\left(d\right)+\frac{\partial F}{\partial c}\cdot dc=0\Rightarrow\\
&\frac{1}{\xi}\cdot\left(\boldsymbol{Q}:\boldsymbol{C}^{e}:d\boldsymbol{\varepsilon}^{e}\right)+\frac{\partial F}{\partial a}\cdot da+\frac{\partial F}{\partial d}\cdot d\left(d\right)+\frac{\partial F}{\partial c}\cdot dc=0\Rightarrow\\
&\boldsymbol{Q}:\boldsymbol{C}^{e}:\left(d\boldsymbol{\varepsilon}-d\boldsymbol{\varepsilon}^{p}-\dot{\boldsymbol{\varepsilon}}^{v}\cdot dt\right)=-\xi\cdot\left(\frac{\partial F}{\partial a}\cdot da+\frac{\partial F}{\partial d}\cdot d\left(d\right)+\frac{\partial F}{\partial c}\cdot dc\right)\Rightarrow
\end{aligned}$$

$$\begin{aligned}
\boldsymbol{Q}:\boldsymbol{C}^{e}:\left(d\boldsymbol{\varepsilon}-d\boldsymbol{\varepsilon}^{p}-\dot{\boldsymbol{\varepsilon}}^{v}\cdot dt\right)&=-\xi\cdot\left(\frac{\partial F}{\partial a}\cdot\frac{\partial a}{\partial t}\cdot dt+\frac{\partial F}{\partial d}\cdot\frac{\partial d}{\partial t}\cdot dt+\frac{\partial F}{\partial c}\cdot\frac{\partial c}{\partial t}\cdot dt\right)\\
&-\xi\cdot\left(\frac{\partial F}{\partial a}\cdot\frac{\partial a}{\partial\boldsymbol{\varepsilon}^{p}}:d\boldsymbol{\varepsilon}^{p}+\frac{\partial F}{\partial d}\cdot\frac{\partial d}{\partial\boldsymbol{\varepsilon}^{p}}:d\boldsymbol{\varepsilon}^{p}+\frac{\partial F}{\partial c}\cdot\frac{\partial c}{\partial\boldsymbol{\varepsilon}^{p}}:d\boldsymbol{\varepsilon}^{p}\right)\Rightarrow
\end{aligned}$$

By further incorporating expressions (5.40) and $\frac{\partial \boldsymbol{q}}{\partial \boldsymbol{\varepsilon}^p} : d\boldsymbol{\varepsilon}^p = (d\Lambda)\cdot \boldsymbol{h}$:

$$(d\Lambda)\cdot\left[\boldsymbol{Q}:\boldsymbol{C}^e:\boldsymbol{P}-\xi\cdot\left(\frac{\partial F}{\partial a}\cdot h_a+\frac{\partial F}{\partial d}\cdot h_d+\frac{\partial F}{\partial c}\cdot h_c\right)\right]=$$
$$=\boldsymbol{Q}:\boldsymbol{C}^e:\left(d\boldsymbol{\varepsilon}-\dot{\boldsymbol{\varepsilon}}^v\cdot dt\right)+\xi\cdot\left(\frac{\partial F}{\partial a}\cdot\frac{\partial a}{\partial t}+\frac{\partial F}{\partial d}\cdot\frac{\partial d}{\partial t}+\frac{\partial F}{\partial c}\cdot\frac{\partial c}{\partial t}\right)\cdot dt \Rightarrow$$

$$d\Lambda=\frac{\boldsymbol{Q}:\boldsymbol{C}^e:\left(d\boldsymbol{\varepsilon}-\dot{\boldsymbol{\varepsilon}}^v\cdot dt\right)+\xi\cdot\left(\frac{\partial F}{\partial a}\cdot\frac{\partial a}{\partial t}+\frac{\partial F}{\partial d}\cdot\frac{\partial d}{\partial t}+\frac{\partial F}{\partial c}\cdot\frac{\partial c}{\partial t}\right)\cdot dt}{\boldsymbol{Q}:\boldsymbol{C}^e:\boldsymbol{P}-\xi\cdot\left(\frac{\partial F}{\partial a}\cdot h_a+\frac{\partial F}{\partial d}\cdot h_d+\frac{\partial F}{\partial c}\cdot h_c\right)} \tag{5.93}$$

In the general case:

$$d\Lambda=\frac{\boldsymbol{Q}:\boldsymbol{C}^e:\left(d\boldsymbol{\varepsilon}-\dot{\boldsymbol{\varepsilon}}^v\cdot dt\right)+\xi\cdot\left(\frac{\partial F}{\partial a}\cdot\frac{\partial a}{\partial t}+\frac{\partial F}{\partial d}\cdot\frac{\partial d}{\partial t}+\frac{\partial F}{\partial c}\cdot\frac{\partial c}{\partial t}\right)\cdot dt}{H+\boldsymbol{Q}:\boldsymbol{C}^e:\boldsymbol{P}} \tag{5.94}$$

- **For states laying on the *SSE*** the plastic hardening modulus H_0 may be computed through the following expression:

$$H_0=-\xi\cdot\left(\frac{\partial F}{\partial a}\cdot h_a+\frac{\partial F}{\partial d}\cdot h_d+\frac{\partial F}{\partial c}\cdot h_c\right) \tag{5.95}$$

The partial derivatives of F with respect to size a, tensional isotropic translation d and *CSL* inclination transition c are portrayed here below:

$$\frac{\partial F}{\partial a}=-2\cdot(\sigma-d) \tag{5.96}$$

$$\frac{\partial F}{\partial d}=2\cdot(\sigma-a+d) \tag{5.97}$$

$$\frac{\partial F}{\partial c}=-\frac{2}{c}\cdot\left[\frac{1}{c^2}\cdot(\boldsymbol{s}:\boldsymbol{s})\right] \tag{5.98}$$

The plastic hardening rules denoted h_a, h_d and h_c may be computed through (5.52), (5.70) and (5.65) respectively.

- **For states enclosed within the *SSE* laying on *PYE*** an interpolation rule is required. Instead of adopting interpolation formulae similar to Mroz et al. (1978) depicted below:

$$H = H_0 + h \cdot \left(\frac{\delta/\delta_0}{1-\delta/\delta_0} \right)^m \tag{5.99}$$

$$H = H_0 + h \cdot \ln\left(\frac{1+\delta/\delta_0}{1-\delta/\delta_0} \right) \tag{5.100}$$

it is necessary for the interpolation rule to be pressure dependent and associated with the phase transformation line (in the current model coincides with the critical state). Hence, it should be expressed as a function of stress and state variables similar to the principle of Dafalias and Herrmann (1982):

$$H = H_0 + h(\boldsymbol{\sigma}, \boldsymbol{q}) \cdot \ln\left(\frac{1+\delta/\delta_0}{1-\delta/\delta_0} \right) \tag{5.101}$$

In the expressions (5.99) to (5.101) the parameter h is measured in units [kPa]^3 and assuming a realization similar to Mroz et al. (1978) it is pressure independent and constant. In the expression by Dafalias and Herrmann (1982) parameter h is a function of $(\boldsymbol{Q}:\boldsymbol{Q}) \cdot p_{atm}$.

In the proposed constitutive formulation, an expression that is pressure dependent and further associated to the critical state is introduced without employing the atmospheric pressure p_{atm} (simply to set the units straight while at the same time dropping the physical meaning). Furthermore, a rather different measure of the distance δ/δ_0 is proposed (where δ_0 is the initial distance from the conjugate point at the time of first yielding while the current distance is expressed through δ). The proposed formulation considers the ellipsoidal shape of the Structure Strength envelope as follows:

$$H = H_{M'} + (\boldsymbol{Q}:\boldsymbol{C}^e:\boldsymbol{P}) \cdot \lambda^* \cdot \left[\frac{\frac{1}{c^2} \cdot (\boldsymbol{s}_{M'} - \boldsymbol{s}) : (\boldsymbol{s}_{M'} - \boldsymbol{s}) + (\sigma_{M'} - \sigma)^2}{\frac{1}{c^2} \cdot (\boldsymbol{s} - \boldsymbol{s}_0) : (\boldsymbol{s} - \boldsymbol{s}_0) + (\sigma - \sigma_0)^2} \right]^\gamma \tag{5.102}$$

In the expression above, the plastic modulus of the conjugate point *M'* is denoted as $H_{M'}$ instead of H_0. The plastic hardening modulus prior to computation of $H_{M'}$ through expression (5.95) requires the definition of the conjugate point *M'* through equation (5.73). Expression (5.73) holds for states on the *SSE* solely and thus, it is employed on *M'* and not *M*. $\boldsymbol{\sigma}_{M'}$ is the target conjugate point that is allowed to evolve considering that the stress state may evolve on PYE thus transforming its corresponding target. $\boldsymbol{\sigma}_0$ is the stress state at the time of first yielding. λ^* and γ comprise constant constitutive soil parameters in need of calibration through experimental tests (at intrinsic geomaterial conditions to be portrayed in the following chapter).

Formulations similar to Kavvadas and Amorosi (1998 & 2000) and Belokas (2008) have been disregarded considering that they prove erroneous results on the dry side considering that the stress state cannot exceed the critical state cone for states laying within the Structure Strength Envelope corresponding to highly overconsolidated soil conditions.

In the expression (5.102) the interpolation rule is a pressure dependent function of the phase transformation line. Considering, that in this version of the model an associated flow rule in assumed $\boldsymbol{Q}=\boldsymbol{P}$ the dot product $\boldsymbol{Q}:\boldsymbol{C}^e:\boldsymbol{P}$ is equal to $\boldsymbol{Q}:\boldsymbol{C}^e:\boldsymbol{Q}$.

At the time of first yielding $\boldsymbol{\sigma}=\boldsymbol{\sigma}_0$ the denominator is set to null and thus, the limit of the ratio (in expression (5.102)) tends to infinity $H\to\infty$. Once the stress state has been adjusted on the *SSE* $\boldsymbol{\sigma}=\boldsymbol{\sigma}_{M'}$ the nominator is set to zero and consequently the plastic hardening modulus is $H=H_{M'}=H_0$.

Employing expression (5.102) into (5.94):

$$d\Lambda=\frac{\boldsymbol{Q}:\boldsymbol{C}^e:\left(d\boldsymbol{\varepsilon}-\dot{\boldsymbol{\varepsilon}}^v\cdot dt\right)+\xi\cdot\left(\frac{\partial F}{\partial a}\cdot\frac{\partial a}{\partial t}+\frac{\partial F}{\partial d}\cdot\frac{\partial d}{\partial t}+\frac{\partial F}{\partial c}\cdot\frac{\partial c}{\partial t}\right)\cdot dt}{H_{M'}+\boldsymbol{Q}:\boldsymbol{C}^e:\boldsymbol{P}\cdot\left\{1+\lambda^*\cdot\left[\frac{\frac{1}{c^2}\cdot\left(\boldsymbol{s}_{M'}-\boldsymbol{s}\right):\left(\boldsymbol{s}_{M'}-\boldsymbol{s}\right)+\left(\sigma_{M'}-\sigma\right)^2}{\frac{1}{c^2}\cdot\left(\boldsymbol{s}-\boldsymbol{s}_0\right):\left(\boldsymbol{s}-\boldsymbol{s}_0\right)+\left(\sigma-\sigma_0\right)^2}\right]^{\gamma}\right\}} \quad (5.103)$$

5.8 Concluding remarks

In the present chapter the mathematical time-dependent behavioral framework was established and analyzed. The time-dependent mechanical behavior of both structured (resembling stiff soils to weak rocks) and non-structured geomaterials (resembling normally consolidated clayey deposits) is addressed. The mathematical formulation incorporates the principles of the overstress postulate proposed by Perzyna (1962 & 1966) while at the same time is founded on the principles of classical elastoplasticity.

The proposed time-dependent constitutive model accounts for bonding and portrays the effect of structure degradation attributed to plastic or time related phenomena. The Structure Strength envelope is allowed to degrade towards the intrinsic state due to plastic straining thus comprising its limiting bound on the down side.

The viscoelastoplastic (or viscoelastic-viscoplastic) model incorporates the following characteristic surfaces:

- an Intrinsic Strength Envelope (*ISE*) employed solely as a reference state;
- a Structure Strength Envelope (*SSE*) to account for the effect of preexisting structure and
- a plastic yield envelope (*PYE*) to denote the infinitesimal viscoelastic domain.

Following the concept by Mroz and Norris (1982), Desai et al. (1986), Pastor et al. (1990) and Gens (1995) the formulation may undergo simple transformations to degrade into a simple structureless isotropic model lacking any aspects of anisotropy and even degenerate into an intrinsic elastoplastic model disregarding any undergoing viscous effects.

The major characteristics of the proposed time dependent formulation are summarized here below:

- Both the stationary viscous behavior and the tertiary stage can be simulated by means of the governing equations. Delayed failure can be simulated by employing the critical state line inclination as hardening variable. The deviatoric viscous strain deviator proves the fuse that inflates the transition towards failure. Hence, it is not a creep failure but rather plastic straining triggered by viscous phenomena.

- The critical state line projection in the stress hyperplane is allowed to transition towards a residual state also due to the accumulation of significant plastic strains. This situation comprises a mathematical trick-manipulation of the governing constitutive equations allowing for the simulation of significant softening even in cases without structure. In this case, the residual *CSL* inclination comprises the critical state line projection measured through laboratory testing while the initial state is a purely fictitious situation to be calibrated with respect to the simulated behavior (the amount of softening).
- The volumetric viscous strain is assumed to be existent within the plastic yield surface. This leads to the increase of strength thus conforming to Bjerrum's postulate (1967). The viscous deviatoric component develops solely at states laying on *PYE* associated with plastic straining.
- Small strain stiffness is accounted for by employing an infinitesimal plastic yield envelope. The Structure Strength Envelope and the Plastic Yield surface are similar associated through a proportionality ratio ξ. The plastic yield envelope transitions towards the conjugate point on the *SSE* due to plastic or deviatoric viscous straining by thus altering the plastic hardening modulus. The proposed expression for the interpolation rule is pressure dependent associated with the phase transformation line projection in the stress hyperplane. In this version of the model an associated flow rule is assumed and therefore the derivative of the plastic yield surface and the plastic potential tensor coincide.
- The Structure Strength Envelope is adjusted along the hydrostatic axis translated towards the tensional regime to account for the effects of bonding under isotropic compression. Only secondary anisotropy is incorporated in the model.
- Finally, it is noted that the elastic stiffness tensor is controlled by assuming an isotropic poroelastic law.

6

Evaluation of proposed model

6.1 General

The proposed constitutive model addresses the time dependent mechanical behavior of geomaterials. The mathematical framework introduced in the previous chapter aims to describe the time-dependency of both structured and non-structured deposits. The governing equations of classical elastoplasticity have been manipulated to incorporate the overstress postulate by Perzyna (1962 & 1966).

This chapter evaluates the proposed model through a parametric study of the proposed constitutive parameters. The effects of initial and small strain stiffness as well as the structure degradation process due to plastic straining are examined in the degenerated elastoplastic basis model. Single point or element based (in Finite Element Code SIMULIA ABAQUS) results illustrate the effect of each individual parameter in the overall elastoplastic mechanical behavior. The time-dependent effects on long-term strength will be portrayed separately in wet conditions through element based results (in ABAQUS). The reason for not portraying results referring to the dry, characteristic of highly overconsolidated states, lies on the negligible effect of viscous phenomena in such regions. Delayed failure is associated solely with states or loadings setting the stress state on the wet domain. It is noted that the stress state is required to be "sufficiently" close to the failure envelope for the deleterious creep effects on soil strength to be dominant. This means that the stress state needs to lay on the intermediate boundary of short and long-term *CSL*.

The proposed model is evaluated by investigating the employed constitutive parameters associated with each individual behavioral characteristic. The governing equations are solved numerically in the general effective transformed space (Prevost,

1978; Kavvadas and Amorosi, 2000). The transformed stress and strain measures are energy conjugate and portray an advancement in terms of computational efficiency and memory requirement. The stresses and strains are depicted in the original Cartesian or cylindrical (in the case of triaxial testing) stress and strain hyperspace instead of the transformed. Hence, the transformed stress space is employed solely within the formulation for the integration of the constitutive equations.

6.2 Structure degradation

The governing constitutive equations incorporate an ensemble of material constants comprising the constitutive parameters. The elastoplastic degenerated model comprises an extension of the Modified Cam-Clay model incorporating an infinitesimal elastic region. Depending on the simulated structure it is translated towards the tensional regime to allow for a rather accurate simulation of bonding effects. The tensional translation degrades with plastic or viscous strain towards the null of the hydrostatic axis.

What becomes evident however from a brief review of the governing equations is the substantial amount of constitutive parameters in need of calibration. Depending on their physical meaning the material constants can either be derived straight forward from laboratory measurements or may be computed through trial and error analyses.

The current chapter focuses on the simulated behavior and investigates the relative effect of each material constant individually. In such sense, the reader shall gain an insight into the predicted mechanical behavior along with a range of magnitude associated with each parameter.

6.2.1 Degradation of size a

The isotropic hardening rule governs the undergoing transformations associated with the size of the Structure Strength Envelope and consequently the plastic yield envelope. The hardening parameter a, denoting the halfsize of the *SSE*, tends to evolve with the accumulation of plastic and viscous strains.

a is the halfsize of the Structure Strength Envelope and a^* stands for the halfsize of the *ISE*. During the destructuration process the bonding tends to degrade with the

accumulation of plastic strains. Hence, an initial structure $B_0 = \left(a / a^*\right)_0$ transitions towards its residual value $B_{res} = \left(a / a^*\right)_{res}$. The residual structure ratio B_{res} may be equal to unity or depending on any chemical, biological or thixotropic bonding formed during the structuration process may receive values slightly over 1.

λ represents the inclination of the Isotropic Compression Line for isotropic loading increments of normally consolidated soil deposits depicted in the *v*-ln*σ* diagram. It can be associated to the virgin compression index C_c through the following expression:

$$\lambda = \frac{C_c}{\ln(10)} \approx 0.434 \cdot C_c \tag{6.1}$$

The compression index is a well established quantity in the literature associated with different material types ranging from organic materials and peats to stiff clays (Bowles , 1996). It is noted that the compression indices in the literature especially for peats and organic clays may be including a substantial portion of inelastic strains associated with viscous phenomena. However, the rapid rate of loading associated with failure, setting the stress state on the *CSL*, justifies the use of the novel values for the compression index C_c and consequently the compressibility parameter λ.

The (poroelastic) material constant κ controls the slope of the Isotropic Compression Line for isotropic rebound tests on overconsolidated soil deposits depicted in the *v*-ln*σ* diagram. Parameter κ is associated to the swelling index C_r through the following expression:

$$\kappa = \frac{C_r}{\ln(10)} \approx 0.434 \cdot C_r \tag{6.2}$$

The poroelastic compressibility parameter κ can be selected as a portion of the compressibility coefficient λ somewhere in the range between $\lambda/\kappa = 4 \div 10$.

The N^*_{iso} represents the void ratio along the Intrinsic Isotropic Compression Curve for a mean effective isotropic stress equal to 1kPa (Burland , 1990). An isotropic stress of such low intensity is unfeasible to attain without completely failing the specimen.

This approach is established solely for the mathematical formulation of the poroelastic law.

The similarity ratio ξ controls the size of the *PYE* and is assumed to be a fraction of the *SSE*, usually $\xi = 1‰ \div 5\%$. Strains of the order of $10^{-5} \div 10^{-4}$ may be considered irreversible and thus, inelastic (i.e. Georgiannou, 1988; Jardine, 1995; Smith et al. 1992). The strain increment imposed in the numerical analysis is not independent of the similarity ratio. Small similarity ratios result in a small *PYE* and consequently the elastic or viscoelastic increment to adjust the stress state on the Plastic Yield Envelope is equally small. Hence, the similarity ratio for the numerical solution to be precise needs to be somewhere in the aforementioned range assuming that the imposed strain increment employed within the numerical programming is of the order of $10^{-6} \div 10^{-5}$.

The material constants η_v^p and ζ_v^p can be computed through an isotropic compression test on a structured geomaterial. η_v^p controls the tempo of bonding degradation attributed to the volumetric plastic strain component. It is involved within the exponentially decaying assumed law transitioning the size of the Structure Strength Envelope towards the Intrinsic state. The constitutive parameter ζ_v^p on the other hand is employed for fine tuning assuming that a smoother transition to the residual state is of interest (**Figure 6.1**). In the general case the parameter can be dropped (by setting it to null). The effect of the destructuring parameters is depicted in **Figure 6.1** revealing that the stress state transitions and is ultimately adjusted along the Intrinsic Isotropic Compression Line in the v-lnσ diagram. The constitutive parameters associated with **Figure 6.1** are portrayed in **Table 6.1**. The significance of the remaining material factors is discussed hereafter.

Note that the soil element was isotropically consolidated to 25kPa. Originally it was assumed that the halfsize of the Intrinsic Strength Envelope was equal to $a^* = 50kPa$ and the halfsize of the Structure Strength Envelope $a = 150kPa$ thus attributing to a high initial imposed structure $B_0 = a/a^* = 3$ and an equally high overconsolidation ratio. The element was isotropically stressed to an isotropic strain of 0.2. The reference time was assumed infinite to isolate the elastoplastic response.

Table 6.1: Constitutive parameters associated with **Figure 6.1**.

N_{iso}*	B_0	B_{res}	a* (kPa)	c	c_{in}	c_{fin}	σ (kPa)	$2\cdot\left(G/K\right)^{e}$
2.08053	3	1	50	0.9798	0.9798	0.9798	25	0.75
λ	κ	λ*	γ	d_{in}	η_q^p	ζ_q^p	θ_q^p	ϑ_q^p
0.08686	0.008686	5	1	0	75	0	0	0
t_0	a_1^v	a_2^v	ψ	A	m	$\bar{a}$	DLIMIT	ξ
∞	0	0	0.002	0.016	0.8	2.5	10^{-6}	0.02

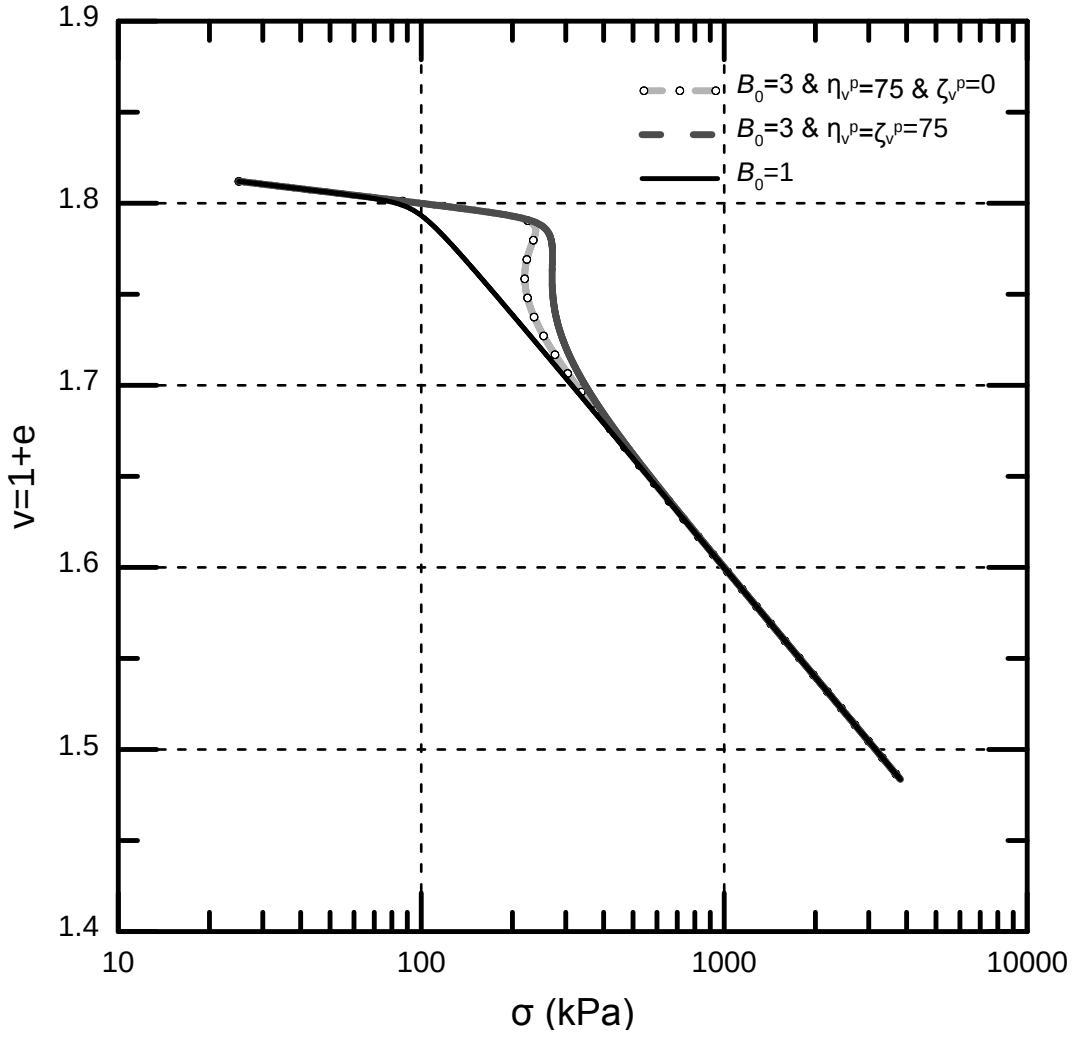

Figure 6.1: Structure degradation in isotropic compression.

The ensemble of material parameters are portrayed In **Table 6.1** associated with the elastoplastic mechanical behavior depicted in **Figure 6.1**. It is noted that the selection of the intrinsic state size denoted a^* was established to account for a void ratio around the proximity of 0.7. The N_{iso}^* was computed conforming to Burland (2000) suggestions for the intrinsic properties of clayey soils. A significant initial structure

was established $B_0 = 3$ transitioning towards the residual value of $B_{res} = 1$ once the stress point was adjusted upon the Intrinsic Isotropic Compression Line in the *v*-ln*σ* diagram. The *CSL* inclination in the stress space c was not allowed to transition (hence, $c = c_{in} = c_{fin}$ and $a_1^v = 0$).

The inclination of the *CSL* in the stress space denoted c can be computed through shear tests activating different deviatoric stress components. In the general case, three direct simple shear and another two triaxial tests may be employed to establish the *CSL* inclination c. Note that in the mathematical formulation and computational programming of the proposed model the hardening parameter c is expressed not as a single variable but rather as an ensemble of deviatoric hardening variables $\{c\} = [c_1, c_2, c_3, c_4, c_5]^T$. Consequently, the initial $\{c_{in}\} = [c_{in-1}, c_{in-2}, c_{in-3}, c_{in-4}, c_{in-5}]^T$ and residual values $\{c_{fin}\} = [c_{fin-1}, c_{fin-2}, c_{fin-3}, c_{fin-4}, c_{fin-5}]^T$ can be expressed in analogous forms. In the upcoming results portraying the capabilities and shortcomings of the proposed model a single value will be selected to denote the inclination of the *CSL* in all directions in the deviatoric stress hyperplane:

$$\begin{aligned} \{c\} &= c \cdot [1,1,1,1,1]^T \\ \{c_{in}\} &= c_{in} \cdot [1,1,1,1,1]^T \\ \{c_{fin}\} &= c_{fin} \cdot [1,1,1,1,1]^T \end{aligned} \tag{6.3}$$

The aforementioned expressions assume the use of a single variable a_1^v and θ_q^p controlling the evolution of the *CSL* inclination to the long-term or the residual state respectively depending on whether c is associated with the viscous or plastic strains. The inclination c is proportional to the Cam-Clay parameter M:

$$c = \sqrt{\frac{2}{3}} \cdot M \tag{6.4}$$

The inclination c may also be associated to the effective friction angle φ of the Coulomb failure criterion through the following expression:

$$c = \sqrt{\frac{2}{3}} \cdot \frac{6 \cdot \sin\varphi}{3 - \sin\varphi} \tag{6.5}$$

The above expression reveals that the inclination c is calibrated solely for compression considering that the *CSL* inclination in the stress space c should be transformed to account for extension as $c = \sqrt{\frac{2}{3}} \cdot \frac{6 \cdot \sin\varphi}{3 + \sin\varphi}$ (the minus has been disregarded considering that the expression of SSE involves the square of c). In our formulation the exact same value c is employed to control both compression and extension. This might raise an issue considering that the argument could be made that a constant value of c does not conform to the experimental data. However, it is noted that our assumption proves higher values for extension compared to compression conforming at least qualitatively to the measurements. Furthermore, considering the fact that extension measurements are rather cumbersome to impose in the laboratory, results should be treated with caution and skepticism. Regardless of all possible discrepancies involved in the determination of the material constants c associated with extension the proposed model considers solely the values for compression thus revealing a limitation of the model. Note that the Lode angle is not employed in the definition c in expression (6.4) and (6.5). It comprises a constant associated to the deviatoric loading stress path independent of the Lode angle in the π-plane. In the analyses to be portrayed hereafter a value of 0.9798 has been selected for the c leading to a rather elevated friction angle of 30°. An upcoming section focuses on the transition to the residual state due to plastic yielding.

The material constant $2 \cdot (G/K)^e$ is introduced to impose the stress dependency of the shear modulus. The bulk modulus can be computed by employing the expression (5.11) accounting for the stress state and the poroelastic compressibility κ. As for the current shear modulus, the expression (5.12) employs the initial parameter $2 \cdot (G/K)^e$ and the current bulk modulus for scaling purposes, as to set the isotropic stress on the current state. The material constant $2 \cdot (G/K)^e$ is characteristic of the soil material and can be associated with the Poisson's ratio υ (stemming from the isotropic linear elasticity):

$$\frac{2 \cdot G^e}{K^e} = 3 - \frac{9 \cdot \upsilon}{1 + \upsilon} \tag{6.6}$$

Hence, the selected value for the analyses presented in **Figure 6.1** is 0.75 to justify the use of a Poisson's ratio of 0.333.

The intrinsic compressibility λ was associated to a virgin compression index $C_c = 0.2$ and the poroelastic compressibility parameter κ was selected as a portion (10%) of λ.

Next, the triaxial drained and undrained response is examined through single point and element test results to illustrate the effect of structure degradation portrayed in the size a of the *SSE*. The behavioral characteristics associated with parameter η_q^p are investigated next, after clarifying the effect of the material constants η_v^p and ζ_v^p on the mechanical response in isotropic compression. The effect of ζ_q^p is of similar significance as the ζ_v^p and will not be investigated any further considering it is employed solely for a smooth transition towards the residual state and can be dropped (by setting it to null) at any time. As a general guideline it is suggested ζ_v^p and ζ_q^p to be selected as a portion (5%÷10%) of the exponential associated parameters η_v^p and η_q^p.

Numerical results at drained conditions associated with triaxial testing are portrayed in **Figure 6.2**. The projection of the undergoing stress path is depicted in the *p*-*q* space following an inclination of 1:3. The *q*-ε_q diagram reveals the effects of the deviatoric exponentially decaying parameter η_q^p (it is a combined effect of the isotropic and deviatoric component acting through η_v^p and η_q^p but the former has already been computed through the isotropic compression test). Higher values of the η_q^p result in a steeper descent in the *q*-ε_q diagram and a lower maximum value attributed to the destructuring process undergoing even at states laying within the *SSE* but on *PYE*. In order to clarify the effect of the exponentially decaying associated parameters the material constants ζ_v^p and ζ_q^p have been dropped. The material parameters associated to **Figure 6.2** are depicted in **Table 6.2**. It is noted that the results address the mechanical elastoplastic behavior of highly overconsolidated soil deposits.

The soil element was initially isotropically consolidated to 25kPa (Point A). Originally it was assumed that the halfsize of the Intrinsic Strength Envelope was

equal to $a^* = 50kPa$ and the halfsize of the Structure Strength Envelope $a = 150kPa$ thus attributing to a high initial imposed structure $B_0 = a/a^* = 3$ and an equally high overconsolidation ratio. The confining pressure was kept constant to 25kPa while the axial strain was increased until failure (from Point A to B and ultimately C). The reference time was assumed infinite to isolate the elastoplastic response.

Table 6.2: Constitutive parameters associated with **Figure 6.2** and **Figure 6.3**.

N_{iso}*	B_0	B_{res}	a* (kPa)	c	c_{in}	c_{fin}	σ (kPa)	$2\cdot(G/K)^e$
2.08053	3	1	50	0.9798	0.9798	0.9798	25	0.75
λ	κ	λ*	γ	d_{in}	ζ_v^p	ζ_q^p	θ_q^p	ϑ_q^p
0.08686	0.008686	5	1	0	0	0	0	0
t_0	a_1^v	a_2^v	ψ	A	m	$\bar{a}$	DLIMIT	ξ
∞	0	0	0.002	0.016	0.8	2.5	10^{-6}	0.02

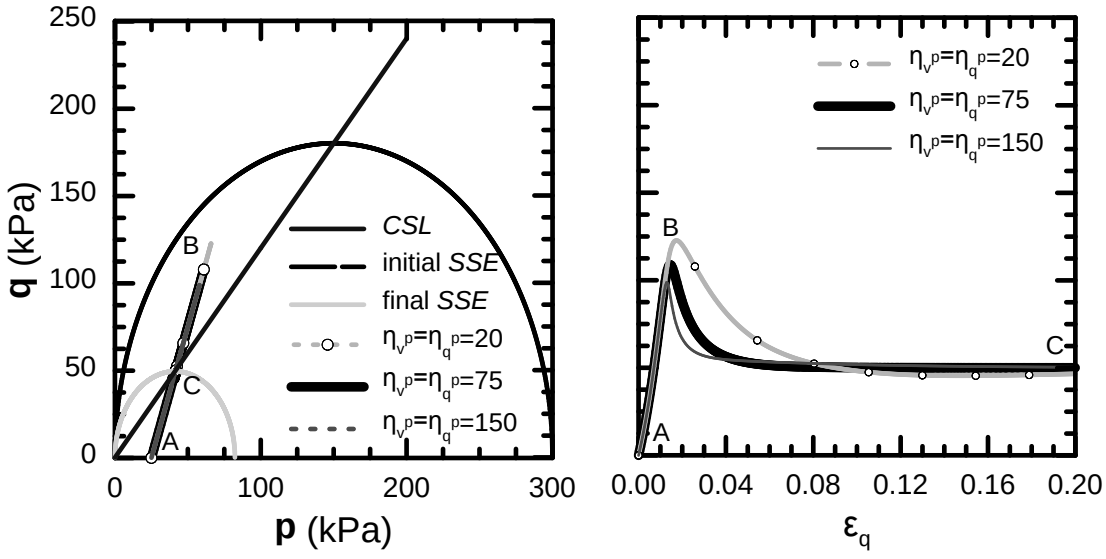

a. b.

Figure 6.2: Structure degradation in triaxial drained testing on the dry side depicted in a. the p-q space and b. q-ε_q diagram.

Assuming that the drainage conditions were changed to account for no flow at the boundaries the undrained mechanical behavior is depicted in **Figure 6.3**. The soil element was once again consolidated isotropically initially to 25kPa (Point A). The halfsize of the Intrinsic Strength Envelope was assumed originally equal to $a^* = 50kPa$ and the halfsize of the Structure Strength Envelope $a = 150kPa$ thus

attributing to a high initial imposed structure $B_0 = a/a^* = 3$ and an equally high overconsolidation ratio. The axial strain was increased until failure (from Point A to peak B and ultimately to failure C) while at the same time the volumetric strain was set to null. The reference time was assumed infinite to isolate the elastoplastic response.

The hook type behavior in the p-q space is characteristic of the structure degradation process. Considering that the degradation process is slow the stress state increases thus converging to the *SSE* and attributing to the accumulation of plastic strains by approaching the intersection point of the *CSL* while the *SSE* shifts to the right. Once the accumulated plastic strains increase significantly the stress state drops resulting in significant softening.

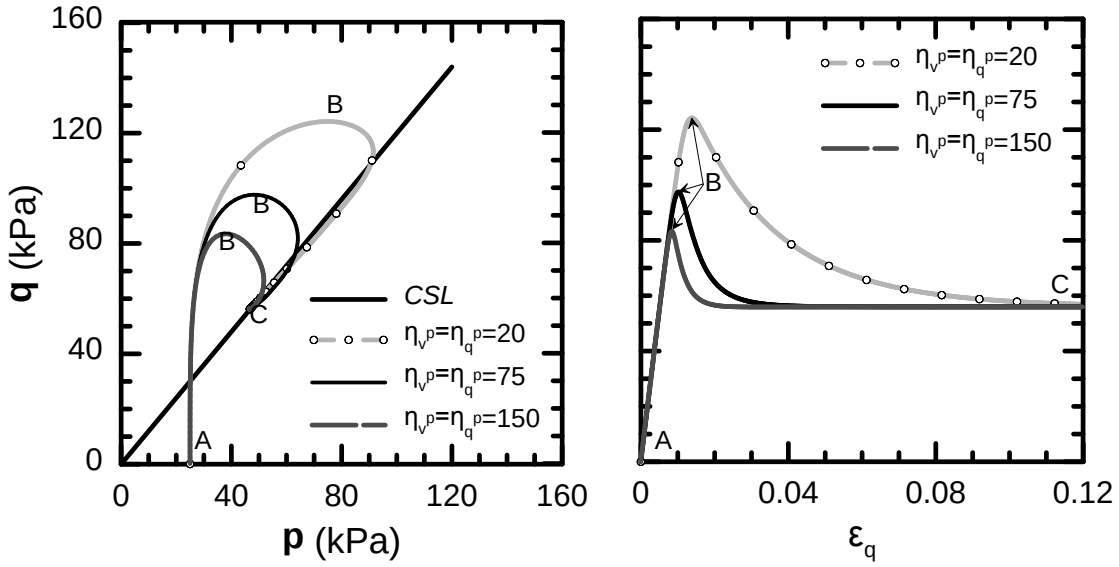

Figure 6.3: Structure degradation in triaxial undrained testing on the dry side depicted in a. the *p*-*q* space and b. q-ε_q diagram.

The q-ε_q diagram (**Figure 6.3**) reveals the effects of the deviatoric exponentially decaying parameter η_q^p. Higher values of the η_q^p result in a steeper descent and a lower maximum value.

Assuming that the stress state originates on the wet domain, characteristic of slightly overconsolidated samples with an overconsolidation ratio $OCR < 2$, the elastoplastic behavior associated with the constitutive parameters of **Table 6.3** is portrayed in **Figure 6.4**. The soil element was consolidated initially isotropically to 96kPa (Point

A). The halfsize of the Intrinsic Strength Envelope was assumed originally equal to $a^* = 50kPa$ and the halfsize of the Structure Strength Envelope $a = 60kPa$ thus attributing to a low initial structure $B_0 = a/a^* = 1.2$ and an equally low overconsolidation ratio. Considering the undrained nature of the problem, the axial strain was increased until failure (from Point A to peak B and ultimately to failure C) while at the same time the volumetric strain was set to null. The reference time was assumed infinite to isolate the elastoplastic response.

It is evident that failure occurs at the exact same point (Point C) on the *CSL* at different shear strain levels depending on the material constants controlling the bonding degradation. Low values of the parameters lead to a higher increase of strength thus shifting the residual state at higher deviatoric strains.

Table 6.3: Constitutive parameters associated with **Figure 6.4**.

N_{iso}*	B_0	B_{res}	a* (kPa)	c	c_{in}	c_{fin}	σ (kPa)	$2\cdot(G/K)^e$
2.08053	1.2	1	50	0.9798	0.9798	0.9798	96	0.75
λ	κ	λ*	γ	d_{in}	ζ_v^p	ζ_q^p	θ_q^p	ϑ_q^p
0.08686	0.008686	5	1	0	0	0	0	0
t_0	a_1^v	a_2^v	ψ	A	m	$\bar{a}$	DLIMIT	ξ
∞	0	0	0.002	0.016	0.8	2.5	10^{-6}	0.02

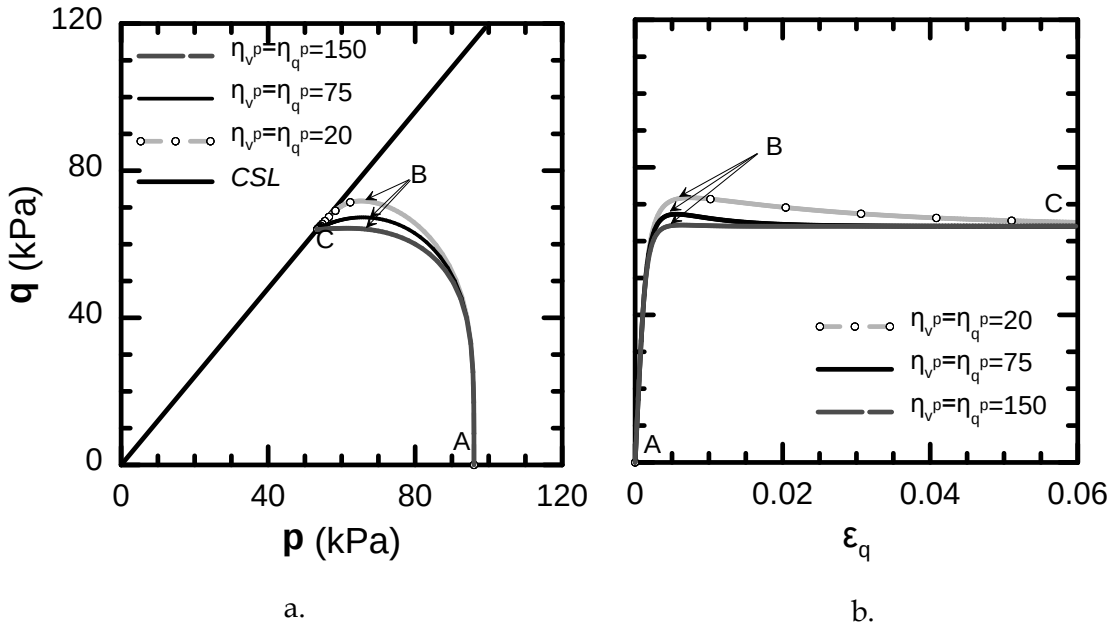

Figure 6.4: Structure degradation in triaxial undrained testing on the wet side depicted in a. the *p*-*q* space and b. *q*-ε_q diagram.

Results are shown solely for undrained conditions on slightly overconsolidated states. Assuming drained conditions the mechanical behavior in the p-q space would once again reveal a slope of 1:3 and depending on the material constants controlling the structure degradation (namely η_v^p and η_q^p) a softening behavior in the q-ε_q diagram. However, failure would be attained at the exact same point thus providing no further information for the mechanical behavior.

6.2.2 Strength envelope evolution due to plastic straining

The Critical State Line in the stress space is allowed to transition towards the residual state. In the case where the transition is associated with the strain rate dependency it portrays the physical meaning straight forward. However, the strength envelope evolution due to plastic straining may appear as arbitrary and even erroneous. The argument could be made that it does not lead to the uniqueness of the critical state line.

The transition of the *CSL* projection in the stress space towards the residual state associated with plastic yielding should be considered solely as a mathematical manipulation to simulate significant softening even in the absence of structure. Consider a structureless soil specimen subjected to loading in the triaxial apparatus under undrained conditions. Assuming a highly overconsolidated soil sample the stress rebound would be evident. However, without accounting for stress and structure anisotropy and by further neglecting bonding it is impossible to simulate significant softening. Hence, another approach needs to be established.

In the case where the strength envelope evolution is associated with the accumulation of plastic strains the original *CSL* is a fictitious state imposed solely to account for the amount of softening measured in the triaxial experiments under undrained conditions. The measured values of the critical state line inclinations in the stress hyperplane measured through triaxial and direct simple shear test coincide with the residual values $\{c_{res}\}$.

Figure 6.5 portrays the undergoing stress path, conforming to the material constants portrayed in **Table 6.4**, assuming a highly overconsolidated structureless soil specimen is subjected to loading in the triaxial apparatus under undrained conditions. The soil element was once again consolidated isotropically initially to

25kPa (Point A). The halfsize of the Intrinsic Strength Envelope was assumed originally equal to $a^* = 50kPa$ and the halfsize of the Structure Strength Envelope $a = 50kPa$, characteristic of a structureless state where $B_0 = a/a^* = 1$. The axial strain was increased until failure (from Point A to peak B and ultimately to failure C) while at the same time the volumetric strain was set to null. The reference time was assumed infinite to isolate the elastoplastic response. The *CSL* is allowed to transition towards the residual state corresponding to an effective friction angle of 22° (note that the initial inclination of the *CSL* projection in the stress space corresponds to a friction angle of 30°). Even in this case when no structure is simulated it is possible to account for significant softening (consider the difference in the soil response between the lines $\theta_q^p = 0$, where the strength envelope does not degrade, and $\theta_q^p = 75$).

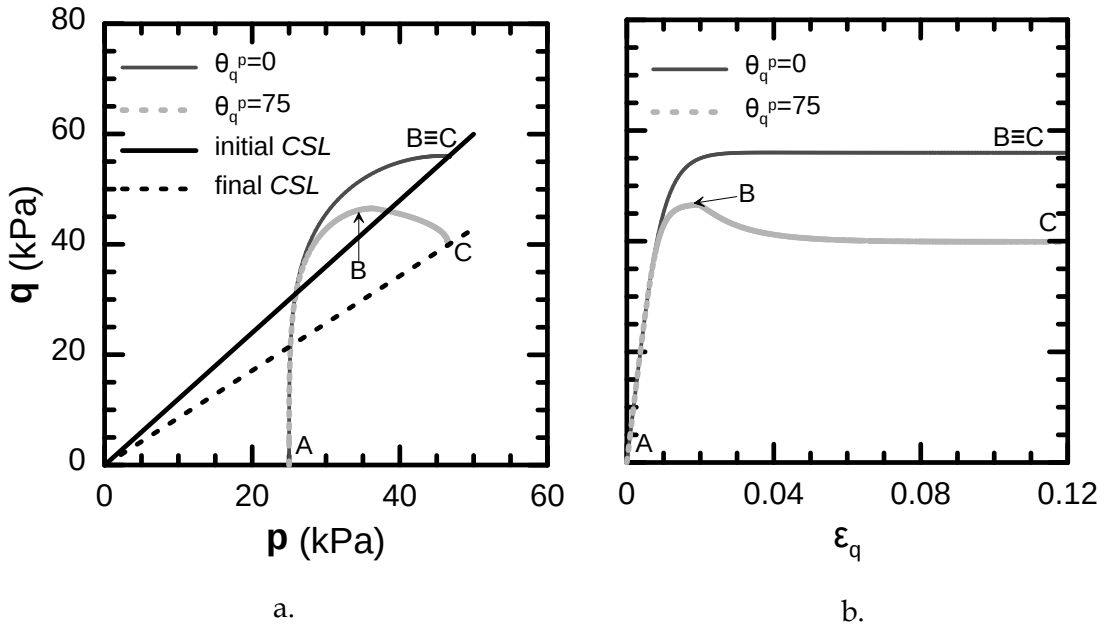

Figure 6.5: Strength envelope evolution due to plastic straining in triaxial undrained testing of a structureless soil specimen on the dry side depicted in a. the *p*-*q* space and b. q-ε_q diagram.

Table 6.4: Constitutive parameters associated with **Figure 6.5**.

N_{iso}*	B_0	B_{res}	a* (kPa)	c_{in}	c_{fin}	σ (kPa)	$2\cdot(G/K)^e$	λ
2.08053	1	1	50	0.9798	0.7	25	0.75	0.08686
κ	λ*	γ	d_{in}	η_v^p	η_q^p	ζ_v^p	ζ_q^p	ϑ_q^p
0.008686	5	1	0	75	75	0	0	0
t_0	a_1^v	a_2^v	ψ	A	m	$\bar{a}$	DLIMIT	ξ
∞	0	0	0.002	0.016	0.8	2.5	10^{-6}	0.02

In the case where a slightly overconsolidated specimen is subjected to triaxial undrained loading conforming to the material constants of **Table 6.5** the undergoing stress paths are illustrated in **Figure 6.6.** The soil element was consolidated isotropically initially to 96kPa (Point A). The halfsize of the Intrinsic Strength Envelope was assumed originally equal to $a^* = 50kPa$ and the halfsize of the Structure Strength Envelope $a = 50kPa$, characteristic of a structureless state where $B_0 = a/a^* = 1$. Considering the undrained nature of the problem, the axial strain was increased until failure (from Point A to peak B and ultimately to failure C) while at the same time the volumetric strain was set to null. The reference time was assumed infinite to isolate the elastoplastic response. The *CSL* is allowed to transition towards the final state of an effective friction angle of 22° (note that the initial inclination of the *CSL* projection in the stress space corresponds to a friction angle of 30°). Even for slightly overconsolidated states it is possible to account for softening without accounting for structure. Hence the initial *CSL* is a fictitious envelope to be calibrated depending on the stress rebound desired in the mechanical behavior. Softening might appear a bit stretched when considering such a slight overconsolidated structureless soil specimen but results are shown solely to illustrate the capability of the model.

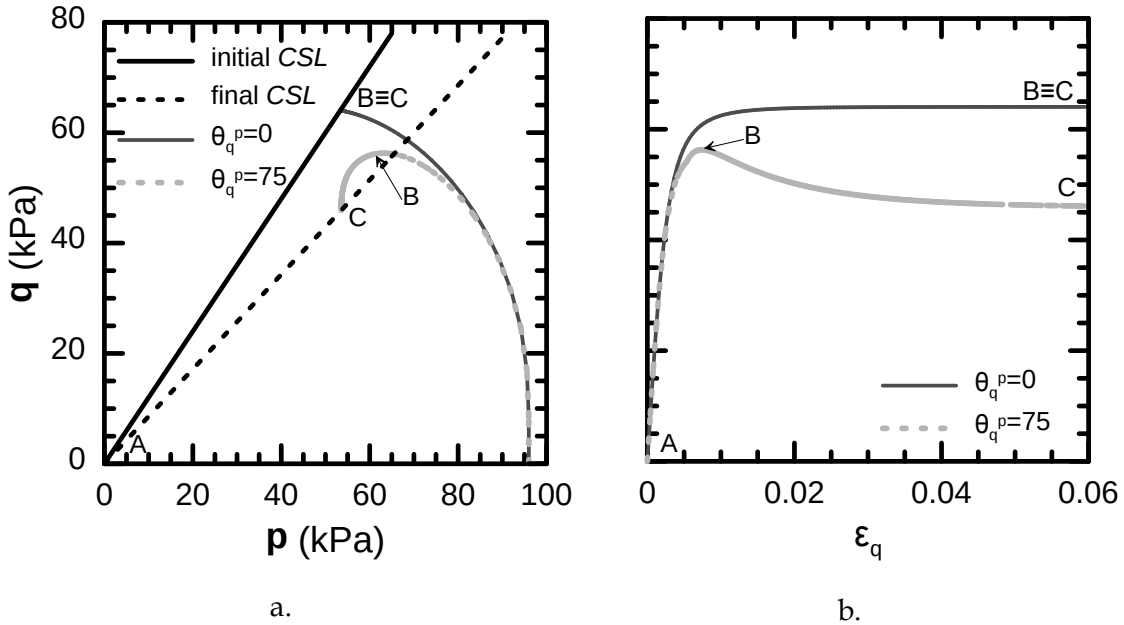

a. b.

Figure 6.6: Strength envelope evolution due to plastic straining in triaxial undrained testing of a structureless soil specimen on the wet side depicted in a. the *p*-*q* space and b. q-ε_q diagram.

Table 6.5: Constitutive parameters associated with **Figure 6.6**.

N_{iso}*	B_0	B_{res}	a* (kPa)	c_{in}	c_{fin}	σ (kPa)	$2\cdot(G/K)^e$	λ
2.08053	1	1	50	0.9798	0.7	96	0.75	0.08686
κ	λ*	γ	d_{in}	η_v^p	η_q^p	ζ_v^p	ζ_q^p	ϑ_q^p
0.008686	5	1	0	75	75	0	0	0
t_0	a_1^v	a_2^v	ψ	A	m	$\bar{a}$	DLIMIT	ξ
∞	0	0	0.002	0.016	0.8	2.5	10^{-6}	0.02

In the diagrams above we have selected to portray the effect of the strength envelope evolution towards the residual state due to plastic straining on a structureless geomaterial. The effect was crystallized through the difference in the simulated response between the lines $\theta_q^p = 0$, characteristic of no degradation in the strength envelope, and $\theta_q^p = 75$. The combined effect of structure degradation and strength envelope evolution would portray a softening effect that could not be easily attributed to the one or the other mechanism. However, it is of major importance to investigate the combined effect in terms of the overall elastoplastic mechanical behavior. Aiming to clarify the relative effect of one mechanism on top of the other results are depicted in **Figure 6.7** and **Figure 6.8**.

Figure 6.7 portrays the inviscid mechanical response of a highly overconsolidated structured soil subjected to undrained triaxial loading conforming to the material constants depicted in **Table 6.6**. The soil element was once again consolidated isotropically initially to 25kPa (Point A). The halfsize of the Intrinsic Strength Envelope was assumed originally equal to $a^* = 50kPa$ and the halfsize of the Structure Strength Envelope $a = 150kPa$ thus attributing to a high initial imposed structure $B_0 = a/a^* = 3$ and an equally high overconsolidation ratio. Considering the undrained nature of the problem, the axial strain was increased until failure (from Point A to peak B and ultimately to failure C) while at the same time the volumetric strain was set to null. The reference time was assumed infinite to isolate the elastoplastic response. The *CSL* was allowed to transition towards the residual state corresponding to an effective friction angle of 22° (note that the initial inclination of the *CSL* projection in the stress space corresponds to a friction angle of 30°). Moreover, the structure degradation constitutive parameters were set equal to

$\eta_v^p = \eta_q^p = 75$. The preexistent structure is high enough to result in significant softening (line $\theta_q^p = 0$). However, the combined effect of structure degradation and strength enveloped evolution due to plastic straining results in even greater softening of more than 50% of the peak deviatoric stress (line $\theta_q^p = 75$). Furthermore, it is evident that the specimen tends to fail at approximately the same mean effective pressure but at different shear stress levels.

Table 6.6: Constitutive parameters associated with **Figure 6.7**.

N_{iso}*	B_0	B_{res}	a* (kPa)	c_{in}	c_{fin}	σ (kPa)	$2\cdot(G/K)^e$	λ
2.08053	3	1	50	0.9798	0.7	25	0.75	0.08686
κ	λ*	γ	d_{in}	η_v^p	η_q^p	ζ_v^p	ζ_q^p	ϑ_q^p
0.008686	5	1	0	75	75	0	0	0
t_0	a_1^v	a_2^v	ψ	A	m	$\bar{a}$	DLIMIT	ξ
∞	0	0	0.002	0.016	0.8	2.5	10^{-6}	0.02

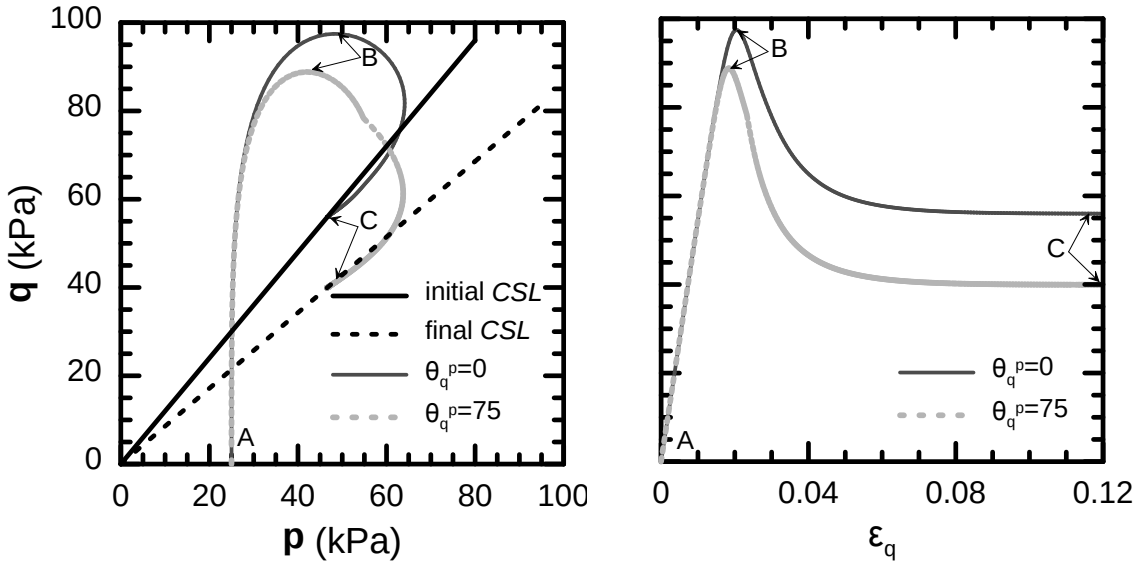

a. b.

Figure 6.7: Strength envelope evolution due to plastic straining in triaxial undrained testing of a structured soil specimen on the dry side depicted in a. the p-q space and b. q-ε_q diagram.

Figure 6.8 illustrates the time-invariant mechanical response of a slightly overconsolidated structured soil subjected to undrained triaxial loading conforming to the material constants depicted in **Table 6.7**. The soil element was consolidated initially isotropically to 96kPa (Point A). The halfsize of the Intrinsic Strength

Envelope was assumed originally equal to $a^* = 50kPa$ and the halfsize of the Structure Strength Envelope $a = 60kPa$ thus attributing to a low initial structure $B_0 = a/a^* = 1.2$ and an equally low overconsolidation ratio. Considering the undrained nature of the problem, the axial strain was increased until failure (from Point A to peak B and ultimately to failure C) while at the same time the volumetric strain was set to null. The reference time was assumed infinite to isolate the elastoplastic response. The *CSL* was allowed to transition towards the residual state corresponding to an effective friction angle of 22o (note that the initial inclination of the *CSL* projection in the stress space corresponds to a friction angle of 30o). Furthermore, the structure degradation constitutive parameters were set equal to $\eta_v^p = \eta_q^p = 75$. The initial structure is negligible thus resulting in unnoticeable plastic softening (line $\theta_q^p = 0$). However, the combined effect of structured degradation and strength enveloped evolution due to plastic straining results in significant softening even in the case when the stress state lays on the wet domain (line $\theta_q^p = 75$). Once again, it is clear that the specimen fails at approximately the same mean effective stress.

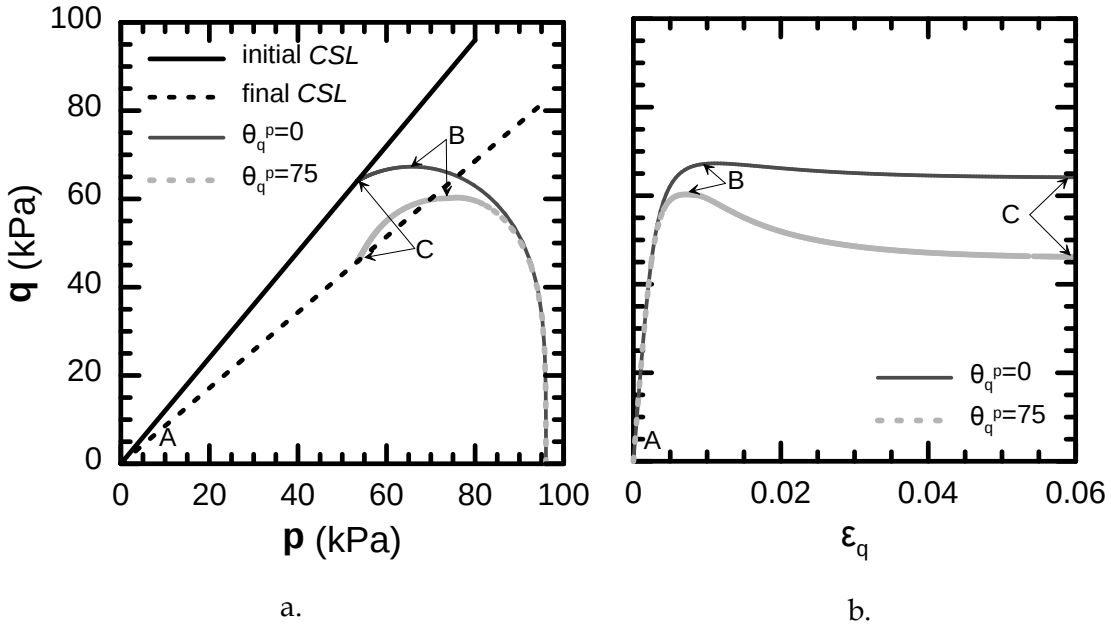

Figure 6.8: Strength envelope evolution due to plastic straining in triaxial undrained testing of a structured soil specimen on the wet side depicted in a. the *p*-*q* space and b. *q*-ε_q diagram.

Table 6.7: Constitutive parameters associated with **Figure 6.8**.

N_{iso}*	B_0	B_{res}	a* (kPa)	c_{in}	c_{fin}	σ (kPa)	$2\cdot(G/K)^e$	λ
2.08053	1.2	1	50	0.9798	0.7	96	0.75	0.08686
κ	λ*	γ	d_{in}	η_v^p	η_q^p	ζ_v^p	ζ_q^p	ϑ_q^p
0.008686	5	1	0	75	75	0	0	0
t_0	a_1^v	a_2^v	ψ	A	m	$\bar{a}$	DLIMIT	ξ
∞	0	0	0.002	0.016	0.8	2.5	10^{-6}	0.02

6.2.3 Degradation of tensional translation *d*

The translation d to the tensional regime can only be estimated by accounting for the undergoing stress path in the *p*-*q* space. In structured soils it is not uncommon for the material to withstand tensional stresses undergoing on the soil skeleton. Chemical alterations in the material fabric, cementation and thixotropic bonding may result in the tensional translation. Regardless, whether the proposed model aims to capture the mechanical behavior in such low stresses the capability is incorporated within the formulation.

The original tensional shift is allowed to transition to the null along the hydrostatic axis with plastic yielding (and with viscous strains). The hardening variable d was incorporated mainly to account for some sort of equivalent cohesion without altering any other behavioral characteristic of the geomaterial (i.e. the *CSL* inclination $\{c\}$ or the size of *SSE* a that could potentially lead to discrepancies in terms of the predicted mechanical response). In inviscid elastoplasticity the proposed model is allowed to degrade its tensional shift due to the deviatoric plastic strains. The argument could be made that isotropic extension would at some point lead to a predicament considering that the *PYE* would adjust on the *SSE* in the tensional regime without transitioning to the isotropic null with evolving isotropic plastic deformation. However, tensional stresses in soils are considered extremely rare possibly associated with some sort of failure (i.e. in tunneling face stability or in retrogressive slope instability problems at the toe) and are usually linked to the compatibility condition.

To exaggerate a bit, even a fly would create enough stress to shift the stress to compression. Hence, it is ludicrous to assume that tensional stressing is no more than

a fictitious state in soils at least for monotonic loading. What's more, the poroelastic expression involves the natural logarithm of stress that provides erroneous results in regions below 1kPa. In the formulation of the constitutive model a tension cutoff has been introduced to assure that the stress state will not undergo such tensional stresses, thus attributing to the inherent limitations of the model.

Next, the effect of the degradation of the tensional translation is investigated in undrained triaxial loading. The results refer to the same experimental loading conditions as in the previous section to allow for a comparative review of the simulated mechanical behavior. The combined effect of structure degradation in size a, translation d and the strength envelope transition due to plastic straining are portrayed in **Figure 6.9** (conforming with the material constants depicted in **Table 6.8**). The soil element was consolidated isotropically initially to 25kPa (Point A). The halfsize of the Intrinsic Strength Envelope was assumed originally equal to $a^* = 50kPa$ and the halfsize of the Structure Strength Envelope $a = 150kPa$ thus attributing to a high initial imposed structure $B_0 = a/a^* = 3$ and an equally high overconsolidation ratio. The initial tensional transpose of the *SSE* was assumed a fraction of the size of the Structure Strength Envelope equal to $d_{in}/2 \cdot a = 5\%$. Considering the undrained nature of the problem, the axial strain was increased until failure (from Point A to peak B and ultimately to failure C) while at the same time the volumetric strain was set to null. The reference time was assumed infinite to isolate the elastoplastic response. The *CSL* was allowed to transition towards the residual state corresponding to an effective friction angle of 22^o (note that the initial inclination of the *CSL* projection in the stress space corresponds to a friction angle of 30^o). Moreover, the structure degradation constitutive parameters were set equal to $\eta_v^p = \eta_q^p = 75$.

While the effect of structure degradation in terms of softening is evident on its own accord (consider line $\vartheta_q^p = \theta_q^p = 0$), incorporating the strength envelope evolution and the tensional shift as hardening variables reveals a higher stress rebound (line $\vartheta_q^p = \theta_q^p = 75$). The relative increase is attributed mainly to the strength envelope evolution considering that the effect of tensional translation d is minor compared to the former mechanism. One last keypoint to be noted is that the two lines tend to fail at the exact same deviatoric stress while being translated along the isotropic axis.

Table 6.8: Constitutive parameters associated with **Figure 6.9**.

N_{iso}*	B_0	B_{res}	a* (kPa)	c_{in}	c_{fin}	σ (kPa)	$2\cdot(G/K)^e$	λ
2.08053	3	1	50	0.9798	0.7	25	0.75	0.08686
κ	λ*	γ	$d_{in}/2\cdot a$	η_v^p	η_q^p	ζ_v^p	ζ_q^p	t_0
0.008686	5	1	0.05	75	75	0	0	∞
a_1^v	a_2^v	ψ	A	m	$\bar{a}$	DLIMIT	ξ	
0	0	0.002	0.016	0.8	2.5	10^{-6}	0.02	

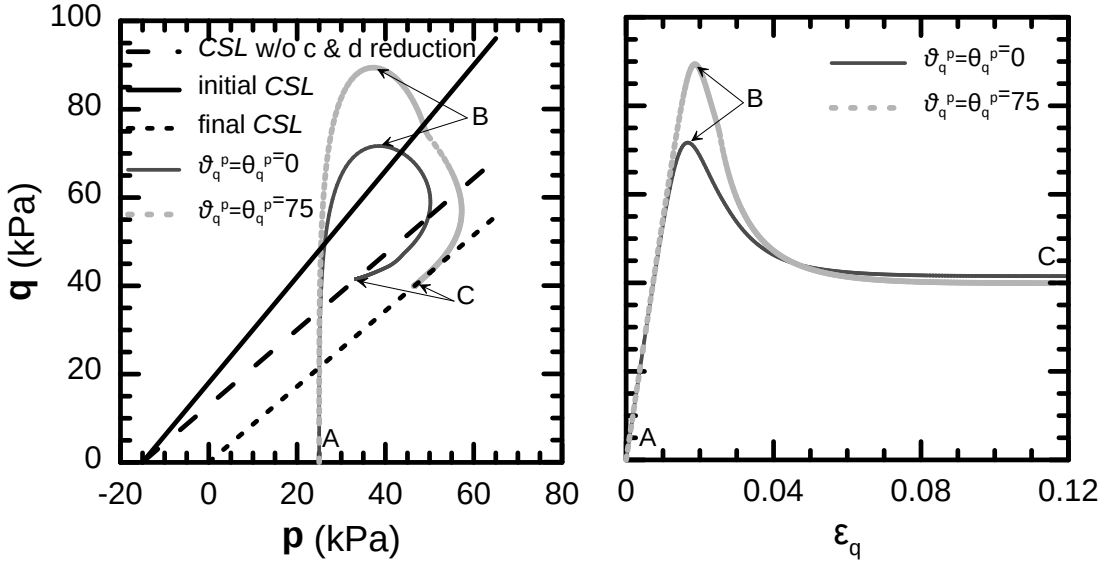

a. b.

Figure 6.9: Combined effect of structure degradation of size a, tensional translation d and strength envelope evolution due to plastic straining in triaxial undrained testing of a structured soil specimen on the dry side depicted in a. the p-q space and b. q-ε_q diagram.

Figure 6.10 illustrates the inviscid mechanical response of a slightly overconsolidated structured soil subjected to undrained triaxial loading conforming to the material constants depicted in **Table 6.9**. The soil element was consolidated initially isotropically to 96kPa (Point A). The halfsize of the Intrinsic Strength Envelope was assumed originally equal to $a^* = 50kPa$ and the halfsize of the Structure Strength Envelope $a = 60kPa$ thus attributing to a low initial structure $B_0 = a/a^* = 1.2$ and an equally low overconsolidation ratio. Considering the undrained nature of the problem, the axial strain was increased until failure (from Point A to peak B and ultimately to failure C) while at the same time the volumetric strain was set to null. The reference time was assumed infinite to isolate the elastoplastic response. The

CSL was allowed to transition towards the residual state corresponding to an effective friction angle of 22° (note that the initial inclination of the *CSL* projection in the stress space corresponds to a friction angle of 30°). Furthermore, the structure degradation constitutive parameters were set equal to $\eta_v^p = \eta_q^p = 75$.

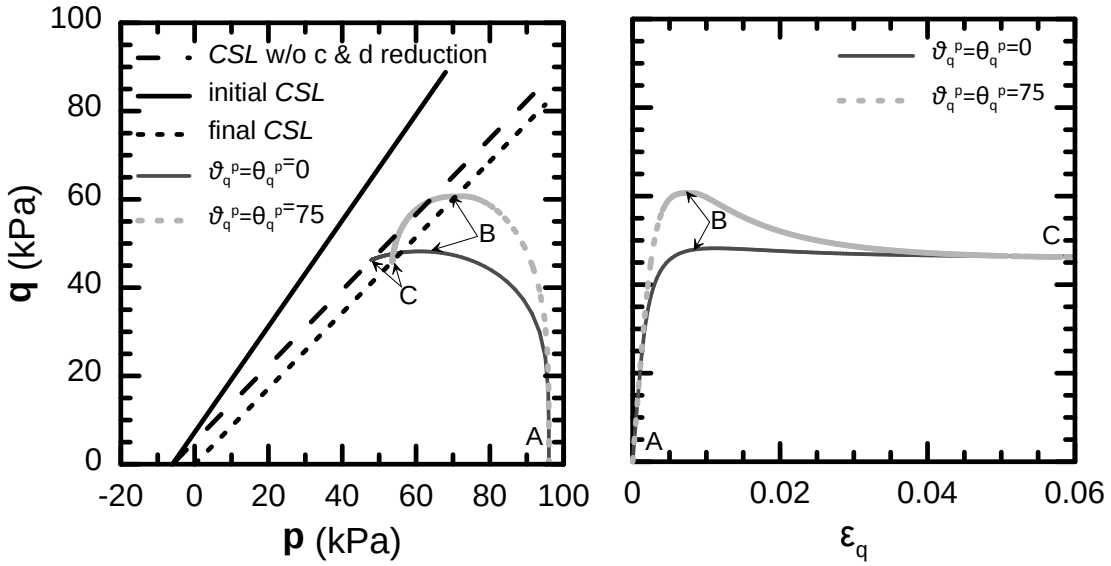

a. b.

Figure 6.10: Combined effect of structure degradation of size a, tensional translation d and strength envelope evolution due to plastic straining in triaxial undrained testing of a structured soil specimen on the wet side depicted in a. the p-q space and b. q-ε_q diagram.

Table 6.9: Constitutive parameters associated with **Figure 6.10**.

N_{iso}*	B_0	B_{res}	a* (kPa)	c_{in}	c_{fin}	σ (kPa)	$2\cdot(G/K)^e$	λ
2.08053	1.2	1	50	0.9798	0.7	96	0.75	0.08686
κ	λ*	γ	$d_{in}/2\cdot a$	η_v^p	η_q^p	ζ_v^p	ζ_q^p	t_0
0.008686	5	1	0.05	75	75	0	0	∞
a_1^v	a_2^v	ψ	A	m	$\bar{a}$	DLIMIT	ξ	
0	0	0.002	0.016	0.8	2.5	10^{-6}	0.02	

The preexistent structure is negligible thus resulting in unnoticeable plastic softening on its own accord (line $\vartheta_q^p = \theta_q^p = 0$) as has been observed previously from **Figure 6.8**. However, the combined effect of structure degradation in size a, translation d and the strength envelope transition due to plastic yielding (line $\vartheta_q^p = \theta_q^p = 75$) results in significant softening even in the case where the stress state lays on the wet

side. It is evident that incorporating the strength envelope evolution and the tensional shift as hardening variables results in a higher stress rebound. The relative increase is attributed mainly to the strength envelope evolution considering that the effect of tensional translation d is minor compared to the former mechanism. One final keypoint noted is that the two lines tend to fail at approximately the same shear stress level while being translated along the hydrostatic axis.

This section summarizes results (based on numerical analyses) revealing the overall mechanical response of combined effects associated with structure degradation of size a, tensional translation d and strength envelope evolution due to plastic straining. The tensional translation is evident solely in the case of structured soils; consequently, the effects of structure degradation of size a and tensional shift d are investigated in conjunction. Considering that the effect of degradation associated with the translation d is negligible (only 5% of the size of the *SSE* was selected), the strength envelope was incorporated in the analyses to denote the capability for significant softening as well as reveal possible undesired simulated mechanical behavioral aspects.

6.3 Initial stiffness

This section investigates the capability of the model to control the initial stiffness through the initial value of $2\cdot\left(G/K\right)^{e}$ and the poroelastic compressibility κ. A careful examination of the diagrams above reveals a rather steep initial portion until the peak strength is attained. The question arises whether it is possible to control the initial stiffness and even smoothen the elastoplastic behavior. As for the second part it will be investigated in the next section addressing the small strain stiffness. The initial stiffness however is controlled by namely two parameters.

The material constant $2\cdot\left(G/K\right)^{e}$ is introduced to account for the stress dependency of the shear modulus. The bulk modulus can be computed by employing the expression (5.11) accounting for the current stress state and the poroelastic compressibility κ. As for the current shear modulus, the expression (5.12) employs the initial parameter $2\cdot\left(G/K\right)^{e}$ and the current bulk modulus for scaling purposes, as to set the isotropic stress on the current state. The material constant $2\cdot\left(G/K\right)^{e}$ is

characteristic of the soil material and can be associated with the Poisson's ratio υ through equation (6.6). Expression (6.6) builds on the assumption of isotropic linear elasticity. However, the assumption is adopted in this dissertation primarily to induce some physical meaning in the constitutive parameter $2\cdot\left(G/K\right)^{e}$ and secondarily to investigate the effect of the material constant on the simulated response by accounting for an ensemble of Poisson's ratio values.

The effect of the $2\cdot\left(G/K\right)^{e}$ will be portrayed in undrained triaxial compression tests to illustrate the effect in both the *p*-*q* space and in the *q*-ε_q diagram (drained triaxial would result again in a slope of 1:3 and the stress path would be set). **Figure 6.11** portrays the undergoing stress paths assuming a structureless soil specimen (conforming to the material constants in **Table 6.10**) is subjected to loading in the triaxial apparatus under undrained conditions. The soil element was consolidated isotropically initially to 25kPa (Point A). The halfsize of the Intrinsic Strength Envelope was assumed originally equal to $a^{*}=50kPa$ and the halfsize of the Structure Strength Envelope $a=50kPa$, characteristic of a structureless state where $B_0=a/a^{*}=1$. The axial strain was increased until failure (from Point A to failure C) while at the same time the volumetric strain was set to null. The reference time was assumed infinite to isolate the elastoplastic response. The *CSL* was not allowed to transition towards the residual state considering that the employed constitutive parameter was set to zero $\theta_q^{p}=0$. The tensional translation was also considered as null $d_{in}=0$.

It is evident that regardless of the Poisson's ratio values the specimen always fails at the exact same stress state on the *CSL* (Point C). However, the mechanical behavior tends to portray significant ductility with increasing $2\cdot\left(G/K\right)^{e}$ values (characterized by lower Poisson's ratio values) thus shifting the stress paths lower and resulting in a smoother curve in the *q*-ε_q diagram reaching the residual state at higher deviatoric strain values ε_q (note that in triaxial loading $\varepsilon_q=\frac{2}{3}\cdot\left(\varepsilon_a-\varepsilon_r\right)$, where ε_a is the axial strain and ε_r stands for the radial).

Table 6.10: Constitutive parameters associated with **Figure 6.11**.

N_{iso}*	B_0	B_{res}	a* (kPa)	c_{in}	c_{fin}	σ (kPa)	λ	κ
2.08053	1	1	50	0.9798	0.7	25	0.08686	0.008686
λ*	γ	d_{in}	η_v^p	η_q^p	ζ_v^p	ζ_q^p	θ_q^p	ϑ_q^p
5	1	0	75	75	0	0	0	0
t_0	a_1^v	a_2^v	ψ	A	m	$\bar{a}$	DLIMIT	ξ
∞	0	0	0.002	0.016	0.8	2.5	10^{-6}	0.02

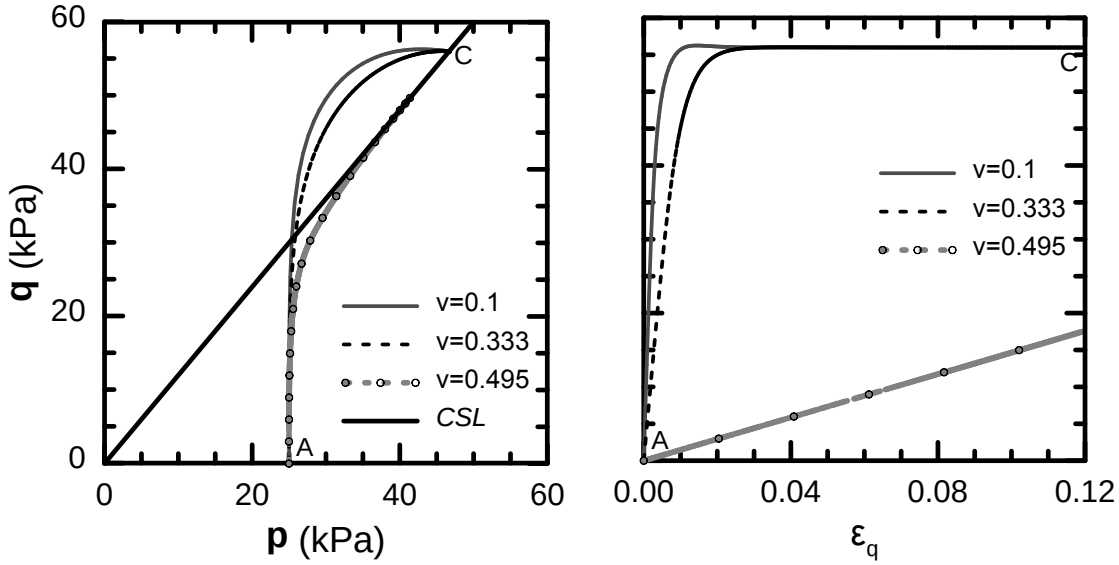

a. b.

Figure 6.11: Investigation of the Poisson's ratio effect in the initial stiffness in triaxial undrained testing of a structureless soil specimen on the dry side depicted in a. the *p*-*q* space and b. q-ε_q diagram.

Figure 6.12 illustrates the undergoing stress path assuming a structureless slightly overconsolidated soil specimen (conforming to the material constants in **Table 6.11**) is subjected to loading in the triaxial apparatus under undrained conditions. The soil element was consolidated isotropically initially to 80kPa (Point A). The halfsize of the Intrinsic Strength Envelope was assumed originally equal to $a^* = 50kPa$ and the halfsize of the Structure Strength Envelope $a = 50kPa$, characteristic of a structureless state where $B_0 = a/a^* = 1$. The axial strain was increased until failure (from Point A to failure C) while at the same time the volumetric strain was set to null. The reference time was assumed infinite to isolate the elastoplastic response. The *CSL* was not allowed to transition towards the residual state considering that the

employed constitutive parameter was set to zero $\theta_q^p = 0$. The tensional translation was also considered as null $d_{in} = 0$.

Regardless of the Poisson's ratio value the specimen always fails at the exact same stress state on the *CSL* (Point C). The inviscid mechanical response tends to portray significant ductility with increasing $2 \cdot (G/K)^e$ values thus shifting the lines lower and resulting once again in a smoother curve in the q-ε_q diagram by reaching the residual state at higher shear strain levels ε_q.

Table 6.11: Constitutive parameters associated with **Figure 6.12**.

N_{iso}*	B_0	B_{res}	a* (kPa)	c_{in}	c_{fin}	σ (kPa)	λ	κ
2.08053	1	1	50	0.9798	0.7	80	0.08686	0.008686
λ*	γ	d_{in}	η_v^p	η_q^p	ζ_v^p	ζ_q^p	θ_q^p	ϑ_q^p
5	1	0	75	75	0	0	0	0
t_0	a_1^v	a_2^v	ψ	A	m	$\bar{a}$	DLIMIT	ξ
∞	0	0	0.002	0.016	0.8	2.5	10^{-6}	0.02

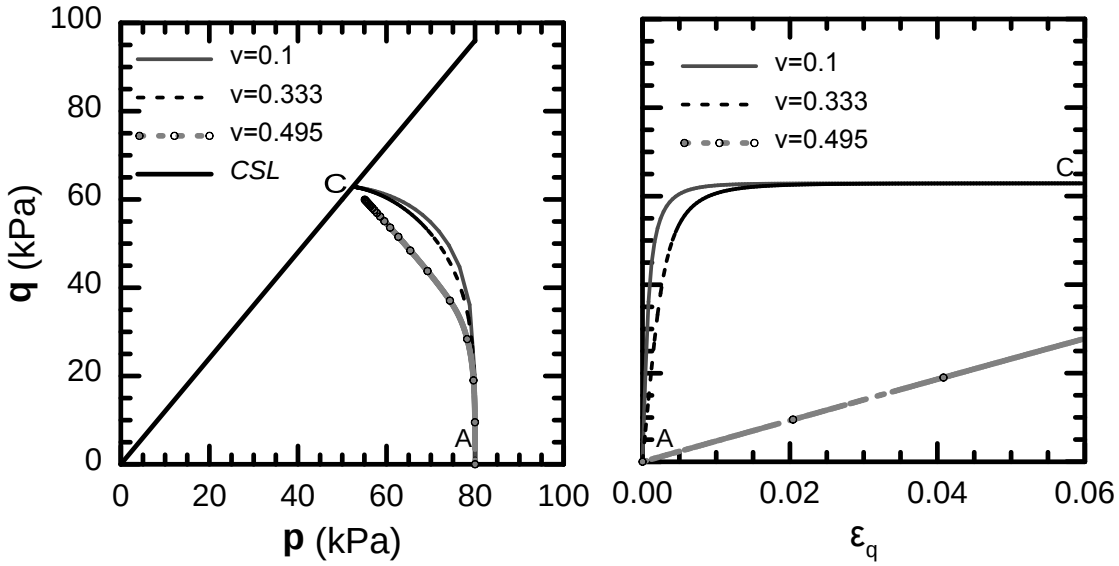

a. b.

Figure 6.12: Investigation of the Poisson's ratio effect in the initial stiffness in triaxial undrained testing of a structureless soil specimen on the wet side depicted in a. the p-q space and b. q-ε_q diagram.

While the effect of the material constant $2 \cdot (G/K)^e$ controls the initial stiffness, it is undeniable that the bulk modulus (scaled for the current stress state) dominates the

overall mechanical behavior. Considering, equations (5.11) and (5.12) the poroelastic compressibility portrays a significant role in the inviscid mechanical behavior. Next, the effect of the poroelastic compressibility parameter κ is investigated assuming a constant Poisson's ratio equal to $\nu = 0.333$. Once again, the results will be addressing the undrained inviscid soil behavior namely for two reasons. The first is attributed to the necessity of providing comparable diagrams with the previous plots investigating the effect of Poisson's ratio in the initial stiffness. The second concerns the undergoing stress paths in drained triaxial conditions that reveal no real information in the *p*-*q* space.

Table 6.12: Constitutive parameters associated with **Figure 6.13**.

N_{iso}*	B_0	B_{res}	a* (kPa)	c_{in}	c_{fin}	σ (kPa)	$2\cdot(G/K)^e$	λ
2.08053	1	1	50	0.9798	0.7	25	0.75	0.08686
λ*	γ	d_{in}	η_v^p	η_q^p	ζ_v^p	ζ_q^p	θ_q^p	ϑ_q^p
5	1	0	75	75	0	0	0	0
t_0	a_1^v	a_2^v	ψ	A	m	$\bar{a}$	DLIMIT	ξ
∞	0	0	0.002	0.016	0.8	2.5	10^{-6}	0.02

The mechanical behavior of a highly overconsolidated soil specimen (conforming to the constitutive parameters depicted in **Table 6.12**) subjected to loading in the triaxial apparatus under undrained conditions is portrayed in **Figure 6.13**. The soil element was consolidated isotropically initially to 25kPa (Point A). The halfsize of the Intrinsic Strength Envelope was assumed originally equal to $a^* = 50kPa$ and the halfsize of the Structure Strength Envelope $a = 50kPa$, characteristic of a structureless state where $B_0 = a/a^* = 1$. The axial strain was increased until failure (from Point A to peak B and ultimately to failure C) while at the same time the volumetric strain was set to null. The reference time was assumed infinite to isolate the elastoplastic response. The *CSL* was not allowed to transition towards the residual state considering that the employed constitutive parameter was set to zero $\theta_q^p = 0$. The tensional translation was also considered as null $d_{in} = 0$.

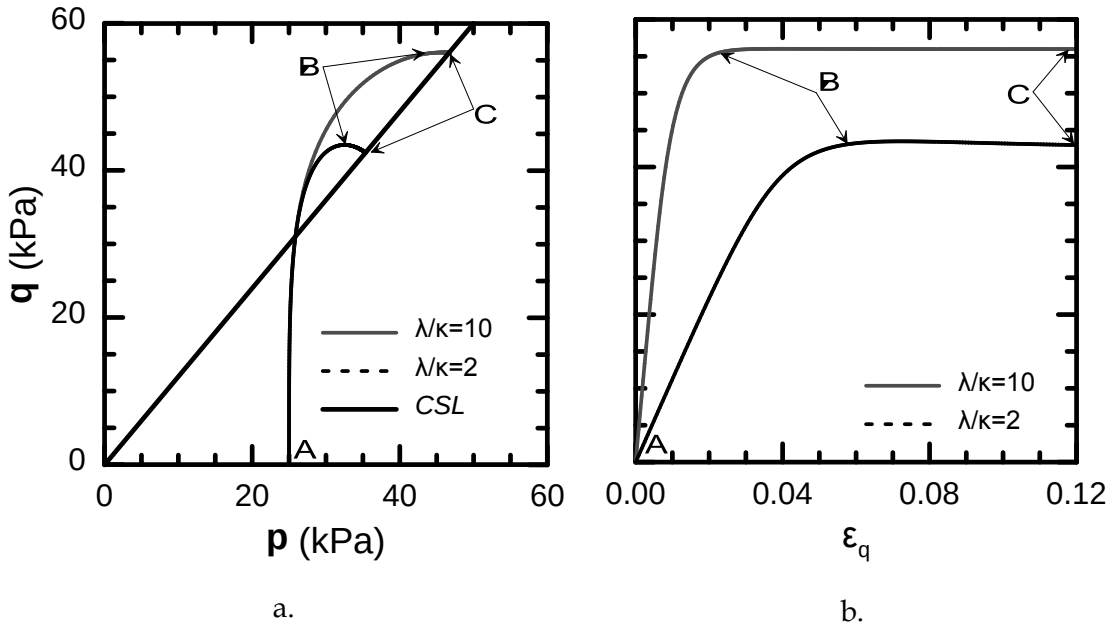

a. b.

Figure 6.13: Investigation of the poroelastic compressibility parameter κ effect in the initial stiffness in triaxial undrained testing of a structureless soil specimen on the dry side depicted in a. the p-q space and b. q-ε_q diagram.

It is evident that the specimen fails at a different stress state on the *CSL* (Point C). Neither the isotropic nor the deviatoric failure stresses are the same. A higher value of the poroelastic compressibility tends to produce significant plastic strains. Considering that the stress state lays on the dry side the size of the *SSE* decreases while the stress point laying on *PYE* transitions towards failure on the *CSL*. Hence, failure is attained at a lower stress state at the intersection of the *SSE* and *CSL*. The initial stiffness is further affected revealing a more ductile behavior for higher κ values thus shifting the inclination to the right in the q-ε_q diagram.

Figure 6.14 reveals the inviscid constitutive response (by assuming the material constants depicted in **Table 6.13**) of a slightly overconsolidated structureless soil specimen subjected to loading in the triaxial apparatus under undrained conditions. The soil element was consolidated isotropically initially to 80kPa (Point A). The halfsize of the Intrinsic Strength Envelope was assumed originally equal to $a^* = 50kPa$ and the halfsize of the Structure Strength Envelope $a = 50kPa$, characteristic of a structureless state where $B_0 = a/a^* = 1$. The axial strain was increased until failure (from Point A to failure C) while at the same time the volumetric strain was set to null. The reference time was assumed infinite to isolate the elastoplastic response. The *CSL* was not allowed to transition towards the

residual state considering that the employed constitutive parameter was set to zero $\theta_q^p = 0$. The tensional translation was also considered as null $d_{in} = 0$.

Table 6.13: Constitutive parameters associated with **Figure 6.14**.

N_{iso}*	B_0	B_{res}	a* (kPa)	c_{in}	c_{fin}	σ (kPa)	$2\cdot(G/K)^e$	λ
2.08053	1	1	50	0.9798	0.7	80	0.75	0.08686
λ*	γ	d_{in}	η_v^p	η_q^p	ζ_v^p	ζ_q^p	θ_q^p	ϑ_q^p
5	1	0	75	75	0	0	0	0
t_0	a_1^v	a_2^v	ψ	A	m	$\bar{a}$	DLIMIT	ξ
∞	0	0	0.002	0.016	0.8	2.5	10^{-6}	0.02

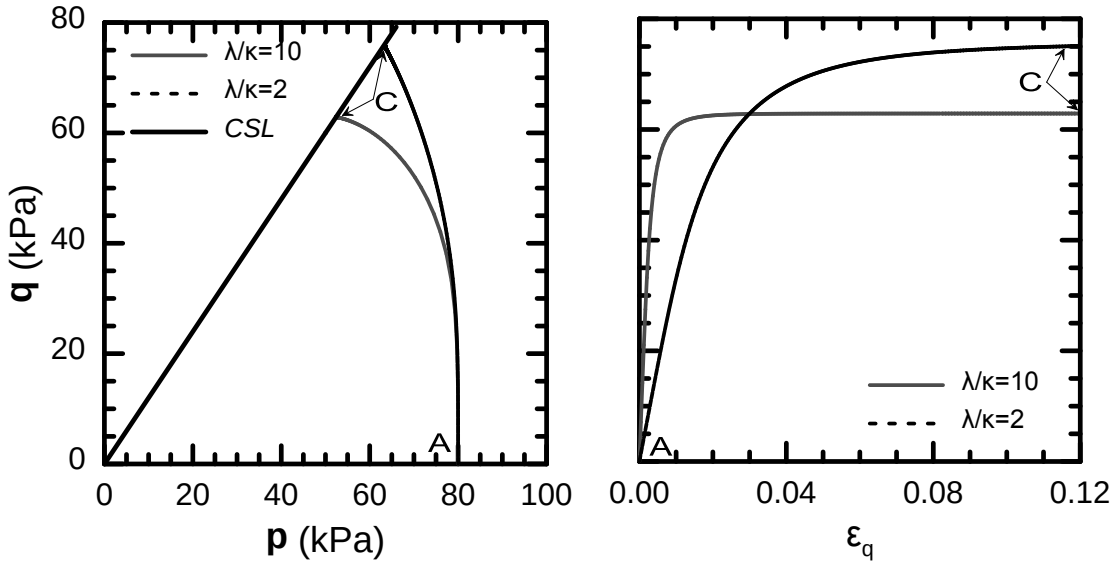

Figure 6.14: Investigation of the poroelastic compressibility parameter κ effect in the initial stiffness in triaxial undrained testing of a structureless soil specimen on the wet side depicted in a. the p-q space and b. q-ε_q diagram.

Once again, the specimen fails at a different stress state on the *CSL*. The higher value of the poroelastic compressibility κ tends to produce significant plastic strains. Considering that the stress state lays on the wet side, the size of the *SSE* increases significantly while the stress point laying on *PYE* transitions towards failure on the *CSL*. Hence, failure occurs at a higher stress state at the intersection of the *SSE* and *CSL*. The initial stiffness is further affected revealing a more ductile behavior for higher κ values thus shifting the inclination to the right in the q-ε_q diagram.

6.4 Small strain stiffness

The small strain stiffness controls the transition towards the Structure Strength Envelope. Considering that the proposed model incorporates an infinitesimal elastic region in its inviscid form every loading increment has a good chance of setting the stress state on the plastic yield surface thus transitioning the *PYE* towards the *SSE* through the kinematic hardening law controlling the secondary anisotropy. This transition dominates the plastic hardening modulus and consequently the time-invariant soil response until the stress is adjusted on the *SSE*.

In this section the constitutive parameters λ^* and γ are investigated in terms of the simulated mechanical response. For the same reason as above the undrained triaxial response of a structureless specimen will be examined both in the wet and the dry regimes. The reason for choosing to investigate the mechanical response in undrained triaxial conditions lies on the undergoing stress path revealing aspects in the simulated response both in the *p*-*q* plane and the *q*-ε_q space.

The effect of superscript γ (incorporated in the expression (5.102)) in the simulated inviscid elastoplastic response is investigated next be assuming a constant value for the material constant $\lambda^* = 5$. Assuming that a highly overconsolidated structureless soil specimen is stressed in the triaxial apparatus under undrained conditions the simulated mechanical response is portrayed in **Figure 6.15** (the material constants involved are depicted in **Table 6.14**). The soil specimen was consolidated isotropically initially to 25kPa (Point A). The halfsize of the Intrinsic Strength Envelope was assumed originally equal to $a^* = 50kPa$ and the halfsize of the Structure Strength Envelope $a = 50kPa$, characteristic of a structureless state where $B_0 = a/a^* = 1$. The axial strain was increased until failure (from Point A to failure C) while at the same time the volumetric strain was set to null. The reference time was assumed infinite to isolate the elastoplastic response. The *CSL* was not allowed to transition towards the residual state considering that the employed constitutive parameter was set to zero $\theta_q^p = 0$. The tensional translation was also considered as null $d_{in} = 0$.

It is obvious that the soil specimen tends to fail at the exact same stress state (Point C). Any discrepancies are attributed to the large strain increment imposed and the

response associated with the highest value of γ has not yet reached the *CSL*. It gradually freezes in convergence speed until the failure state is attained, at an extremely high value of deviatoric strain ε_q. The sudden change in the slope associated with the smallest value of γ occurs at the point where the *PYE* and the *SSE* coincide thus acting as a simple MCC model (not exactly considering that there is a complete set of hardening variables involved but the principle is the same). It is evident that high values of the constant γ produce a brittle behavior (compared to smaller ones) thus leading to a more ductile response. The initial slope may appear a bit steep but the behavioral characteristics of the initial stiffness are not controlled through the constant parameter γ.

Table 6.14: Constitutive parameters associated with **Figure 6.15**.

N_{iso}*	B_0	B_{res}	a* (kPa)	c_{in}	c_{fin}	σ (kPa)	$2\cdot(G/K)^e$	λ
2.08053	1	1	50	0.9798	0.7	25	0.75	0.08686
κ	λ*	d_{in}	η_v^p	η_q^p	ζ_v^p	ζ_q^p	θ_q^p	ϑ_q^p
0.008686	5	0	75	75	0	0	0	0
t_0	a_1^v	a_2^v	ψ	A	m	$\bar{a}$	DLIMIT	ξ
∞	0	0	0.002	0.016	0.8	2.5	10^{-6}	0.02

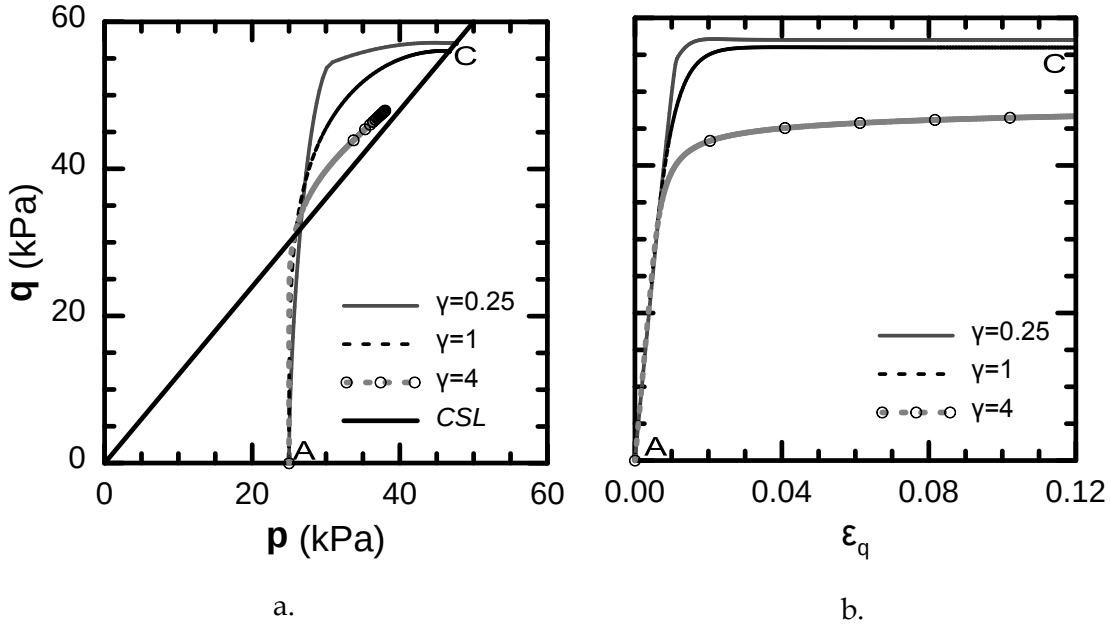

Figure 6.15: Investigation of the material constant γ on the small strain stiffness in triaxial undrained testing of a structureless soil specimen on the dry side depicted in a. the p-q space and b. q-ε_q diagram.

Table 6.15: Constitutive parameters associated with **Figure 6.16**.

N_{iso}*	B_0	B_{res}	a^* (kPa)	c_{in}	c_{fin}	σ (kPa)	$2\cdot(G/K)^e$	λ
2.08053	1	1	50	0.9798	0.7	80	0.75	0.08686
κ	λ*	d_{in}	η_v^p	η_q^p	ζ_v^p	ζ_q^p	θ_q^p	ϑ_q^p
0.008686	5	0	75	75	0	0	0	0
t_0	a_1^v	a_2^v	ψ	A	m	$\bar{a}$	DLIMIT	ξ
∞	0	0	0.002	0.016	0.8	2.5	10^{-6}	0.02

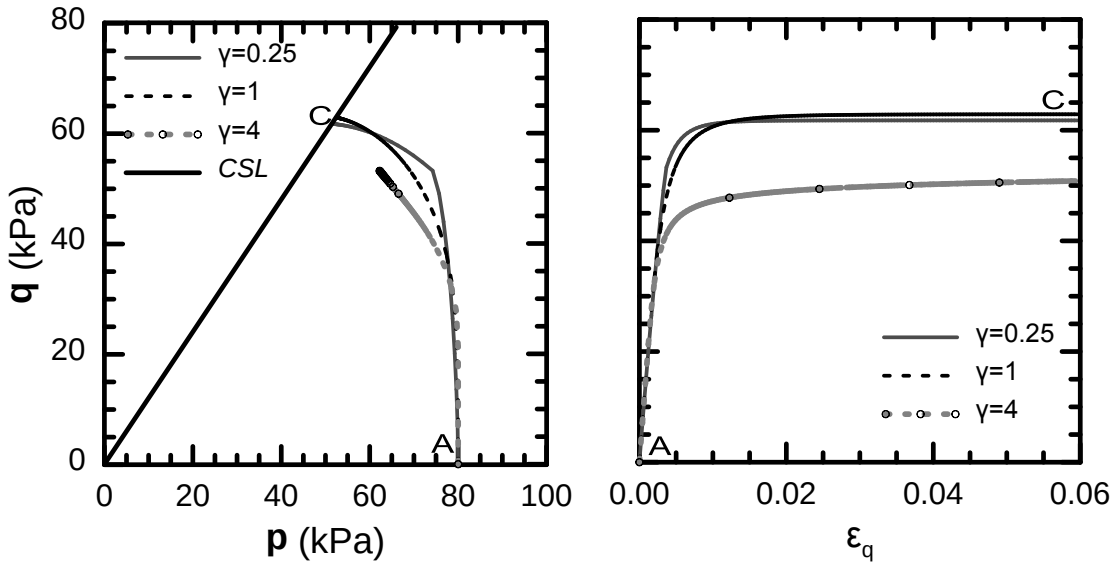

a. b.

Figure 6.16: Investigation of the material constant γ on the small strain stiffness in triaxial undrained testing of a structureless soil specimen on the wet side depicted in a. the *p*-*q* space and b. q-ε_q diagram.

Figure 6.16 portrays the elastoplastic response of a slightly overconsolidated structureless specimen subjected to triaxial undrained compression (the material constants associated with **Figure 6.16** are depicted in **Table 6.15**). The soil specimen was consolidated isotropically initially to 80kPa (Point A). The halfsize of the Intrinsic Strength Envelope was assumed originally equal to $a^* = 50kPa$ and the halfsize of the Structure Strength Envelope $a = 50kPa$, characteristic of a structureless state where $B_0 = a/a^* = 1$. The axial strain was increased until failure (from Point A to failure C) while at the same time the volumetric strain was set to null. The reference time was assumed infinite to isolate the elastoplastic response. The *CSL* was not allowed to transition towards the residual state considering that the

employed constitutive parameter was set to zero $\theta_q^p = 0$. The tensional translation was also considered as null $d_{in} = 0$.

Note that the soil specimen fails at the exact same stress state (Point C) regardless of any discrepancies attributed to the large imposed strain increment. The response associated with the highest value of γ has not yet reached the *CSL*. It gradually slows the convergence rate until the failure state is attained at an extremely high value of shear strain ε_q level. The rapid change in the stress path associated with the smallest value of γ in the *p*-*q* space lays once again at the point where the *PYE* and the *SSE* coincide. It is evident that high values of the constant γ produce a brittle behavior (compared to smaller ones) thus leading to ductile response. The initial slope appears a bit steep, it could also be mistaken for purely elastic, but the behavioral characteristics of the initial stiffness are not controlled through the constitutive parameter γ.

The material constant λ^* holds the most important role in the transition of the plastic hardening modulus towards the states laying on the *SSE*. Stress states laying on the *SSE* are defined explicitly in terms of the plastic hardening modulus through the consistency condition of the Structure Strength Envelope. However, elastoplastic states on *PYE* transitioning towards the bounding surface may be described solely by assuming some sort of interpolation rule portrayed in equation (5.102). While the exponent γ may have some influence on the predicted soil response, the dominant effect lies with λ^*. Next, results are presented on structureless triaxial undrained compression aiming to clarify the effect of the material constant λ^* on the small strain stiffness mainly in the q-ε_q diagram.

The multiplier λ^* incorporated in the expression (5.102) will be investigated parametrically to portray its dominating effect on the small strain stiffness assuming a constant value for the material constant $\gamma = 1$. The value for the superscript material constant γ was selected to lay somewhere between the examined extreme values above, simulating neither brittle nor ductile behavior. Hence, the selected value of $\gamma = 1$ was assumed appropriate to be employed as a starting point for the upcoming study.

Assuming a highly overconsolidated structureless soil specimen is stressed in the triaxial apparatus under undrained conditions, the simulated constitutive response is portrayed in **Figure 6.17** (the material constants involved are depicted in **Table 6.16**). The soil specimen was consolidated isotropically initially to 25kPa (Point A). The halfsize of the Intrinsic Strength Envelope was assumed originally equal to $a^* = 50kPa$ and the halfsize of the Structure Strength Envelope $a = 50kPa$, characteristic of a structureless state where $B_0 = a/a^* = 1$. The axial strain was increased until failure (from Point A to peak B to failure C) while at the same time the volumetric strain was set to null. The reference time was assumed infinite to isolate the elastoplastic response. The *CSL* was not allowed to transition towards the residual state considering that the employed constitutive parameter was set to zero $\theta_q^p = 0$. The tensional translation was also considered as null $d_{in} = 0$.

It is evident that the soil specimen fails at the exact same stress state. In this case, the lowest value of λ^* has not yet reached the *CSL*. What becomes clear from a careful examination of **Figure 6.17** is that for values higher than $\lambda^* = 5$ the behavior can be characterized as brittle. On the other hand, the effect of the other extreme at $\lambda^* = 0.1$ depicts a purely ductile inviscid mechanical response. Hence, the selected range should be considered somewhere between $\lambda^* \in [0.1, 5]$. To make a long story short the constitutive parameter to be calibrated correctly dominating the small strain stiffness is λ^*. The exponential material constant γ has been employed solely for fine tuning assuming that the experimental data can support calibration of another less significant parameter and can be dropped at any time by setting it to unity $(\gamma = 1)$.

Table 6.16: Constitutive parameters associated with **Figure 6.17**.

N_{iso}*	B_0	B_{res}	a* (kPa)	c_{in}	c_{fin}	σ (kPa)	$2\cdot(G/K)^e$	λ
2.08053	1	1	50	0.9798	0.7	25	0.75	0.08686
κ	γ	d_{in}	η_v^p	η_q^p	ζ_v^p	ζ_q^p	θ_q^p	ϑ_q^p
0.008686	1	0	75	75	0	0	0	0
t_0	a_1^v	a_2^v	ψ	A	m	$\bar{a}$	DLIMIT	ξ
∞	0	0	0.002	0.016	0.8	2.5	10^{-6}	0.02

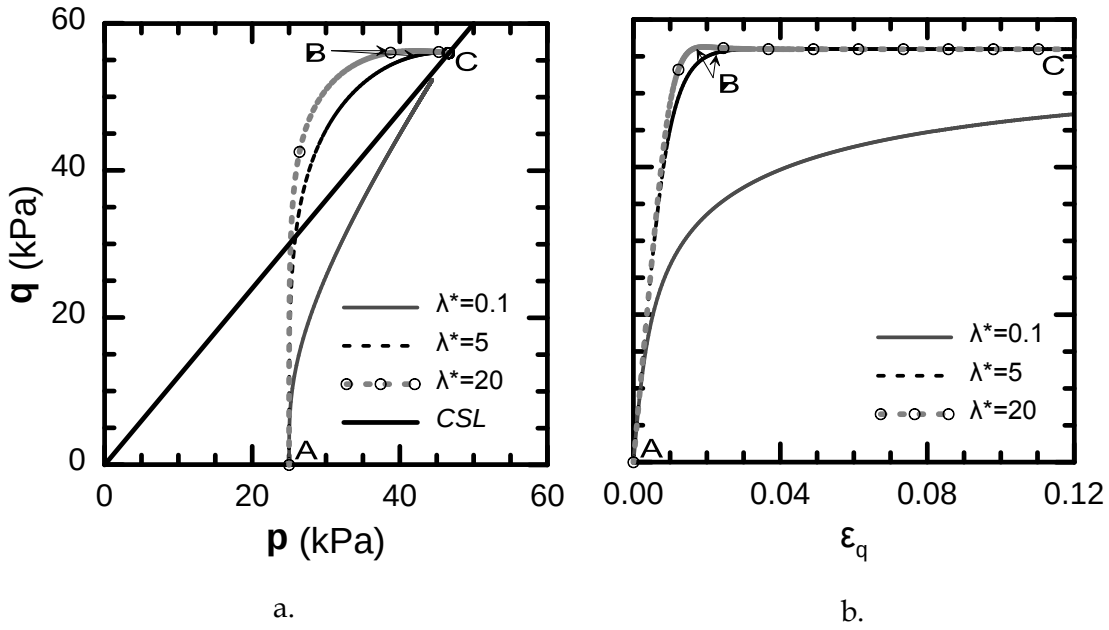

a. b.

Figure 6.17: Investigation of the material constant λ^* on the small strain stiffness in triaxial undrained testing of a structureless soil specimen on the dry side depicted in a. the *p*-*q* space and b. *q*-ε_q diagram.

In the case of a slightly overconsolidated structureless soil specimen stressed in the triaxial apparatus under undrained conditions the predicted constitutive response is depicted in **Figure 6.18** (the material constants involved are summarized in **Table 6.17**). The soil specimen was consolidated isotropically initially to 80kPa (Point A). The halfsize of the Intrinsic Strength Envelope was assumed originally equal to $a^* = 50kPa$ and the halfsize of the Structure Strength Envelope $a = 50kPa$, characteristic of a structureless state where $B_0 = a/a^* = 1$. The axial strain was increased until failure (from Point A to failure C) while at the same time the volumetric strain was set to null. The reference time was assumed infinite to isolate the elastoplastic response. The *CSL* was not allowed to transition towards the residual state considering that the employed constitutive parameter was set to zero $\theta_q^p = 0$. The tensional translation was also considered as null $d_{in} = 0$.

Again the lowest value of λ^* has not yet reached the *CSL*. What becomes crystal clear is that values of λ^* higher than $\lambda^* = 5$ lead to a rather brittle behavior. However, values as low as $\lambda^* = 0.1$ are characteristic of a purely ductile time-invariant mechanical response. Summarizing, the selected range should be considered somewhere between $\lambda^* \in [0.1, 5]$.

Table 6.17: Constitutive parameters associated with **Figure 6.18**.

N_{iso}*	B_0	B_{res}	a^* (kPa)	c_{in}	c_{fin}	σ (kPa)	$2\cdot(G/K)^e$	λ
2.08053	1	1	50	0.9798	0.7	80	0.75	0.08686
κ	γ	d_{in}	η_v^p	η_q^p	ζ_v^p	ζ_q^p	θ_q^p	ϑ_q^p
0.008686	1	0	75	75	0	0	0	0
t_0	a_1^v	a_2^v	ψ	A	m	$\bar{a}$	DLIMIT	ξ
∞	0	0	0.002	0.016	0.8	2.5	10^{-6}	0.02

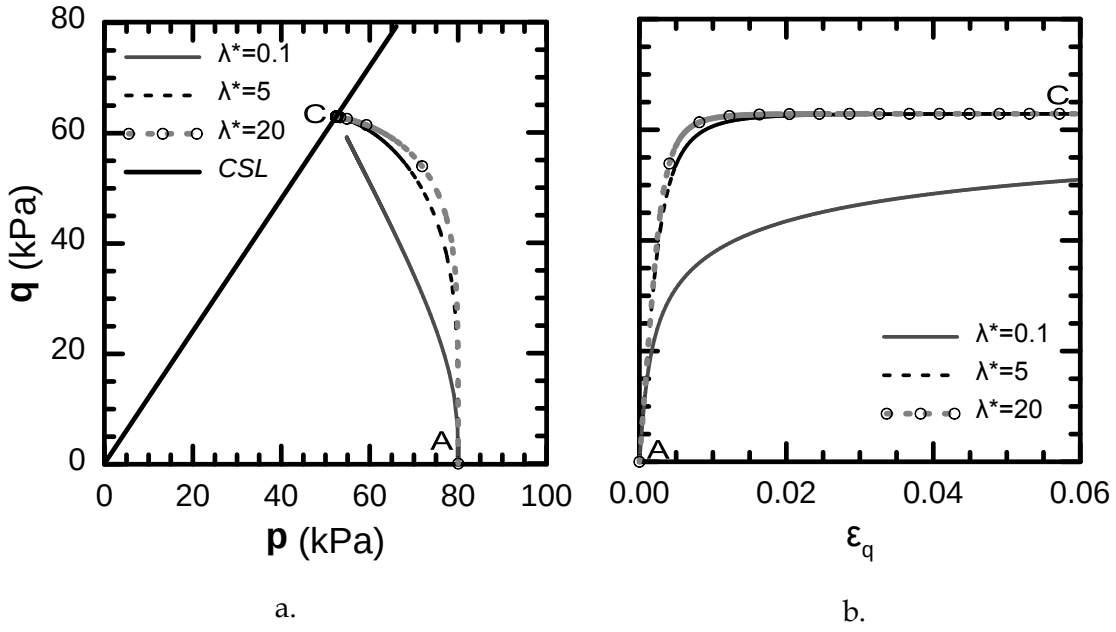

a. b.

Figure 6.18: Investigation of the material constant λ^* on the small strain stiffness in triaxial undrained testing of a structureless soil specimen on the wet side depicted in a. the p-q space and b. q-ε_q diagram.

6.5 Time dependent behavior

This current section examines the time-dependent characteristics of the proposed behavioral framework. The time-dependent associated behavior acts in a rather tricky way. On the one hand, the volumetric creep strain component builds on strength by increasing the size of the bounding surface. The evolution of time results in the increase of the preconsolidation pressure attributed to the volumetric creep component (the principle conforms to the Bjerrum's postulate). On the other hand, the deviatoric creep strain component reveals its deleterious effects on soil strength whenever the deviatoric stress is evident. It appears as if the deviatoric creep

component desires to reset the stress state back to the isotropic thus achieving stability through a state of lesser enthalpy.

Hence, nature always attempts to find a stable state associated with lesser enthalpy compared to the previous state. The volumetric viscous component acts on that principle by increasing the soil strength while the deviatoric creep strain reveals its catastrophic effects associated with failure by transitioning the stress state to a more stable equilibrium.

It is to the author's belief that there exists a common misconception concerning the time-dependent mechanical behavior of clayey soils associated with creep. Every experiment tends to shed light from a point of view on some aspect of creep. Focusing on a single one while neglecting the others will result in erroneous results. Hence, each experimental setup is addressed individually while attempting to clarify certain aspects of the viscous mechanical soil response. The investigation focuses on slightly overconsolidated soil samples subjected to stress controlled tests (with the sole exception of the stress relaxation oedometer test to be examined last). The reason for focusing on structureless states and at states laying on the wet side is that plastic softening in such cases causes the numerical analysis to suspend once the peak strength is attained. Furthermore, in highly overconsolidated specimens the undergoing stress path reaches the *CSL* after the peak strength has been attained without accounting for the creep effects but solely due to the inviscid behavior. The effect might be a bit different in the loading of overconsolidated specimens under undrained situations but considering that pure creep refers to drained conditions it would be redundant to even go into that conversation.

6.5.1 Time dependent behavior in triaxial loading

This section investigates the effect of creep in shearing mode in the triaxial apparatus under drained conditions. Laboratory measurements on creep associated with triaxial compression reveals namely three stages of time dependent behavior: a. the primary or transient, b. the secondary or stationary and finally c. the tertiary or acceleration creep stage. The creep stages depend on the imposed shear stress level. While low shear stress levels activate solely the primary stage significantly higher stress intensities lead to delayed failure.

Hence, the current chapter investigates the capability of the model to account for failure associated with the devastating effects of deviatoric creep strain. The essence of this section lays in the aforementioned statement. The triaxial specimen is ABAQUS originally consolidated isotropically is loaded until the stress state is set somewhere between the short-term and the long-term *CSL* regardless whether the stress state is adjusted on the *SSE* (in the results portrayed herein the *PYE* and the *SSE* are not tangent). Then the specimen is allowed to creep and depending on the material constant a_1^v associated with the strength envelope evolution (due to the viscous effects) delayed failure occurs sooner or later. It is noted that in the laboratory not all stress states laying between the short-term and the long-term *CSL* fail at times that can be measured (creep failure may require several years). For one, the time for the delayed failure to occur may be so long that there is no point in keeping the apparatus occupied for that kind of period. For example if the specimen fails after a year of viscous acting phenomena, the soil skeleton will have sustained so many alterations in its chemical composition that would not truly be characteristic of the original sample. The formation of fungous in the interparticle space, considering that the water is stationary, will result in bonding thus transforming the material properties and in essence the soil itself.

The loading steps are portrayed here below:

- **Geostatic step**: The soil element is originally consolidated isotropically to 80kPa (Point A). The initial step is undertaken to establish equilibrium between the initial values and the calculated stress state. The time period of this step is fixed and equal to 1day.
- **Loading step**: The axial stress was increased from 80kPa to 180kPa while the confining pressure was kept constant to 80kPa. Hence, the specimen is loaded until the stress state lays on *PYE* at a state between the short-term and the long-term Critical State Line inclination. In order to disregard any viscous effects this loading increment was undertaken at $\Delta t = 0.05$ days.
- **Creep step**: The stress field is kept constant while the specimen is allowed to creep. Failure (at point C) is attained once the stress state is adjusted on the *CSL*. It is noted that it is not necessary for the *CSL* to reach the long-term inclination for the soil specimen to fail.

What is important to remember is that failure is triggered by the viscous effects. However, it is the plastic deformation that accumulates faster leading to failure. Hence, the tertiary or acceleration creep stage may not be suitable to describe the phenomenon of delayed failure. After all in the laboratory measurements refer to the axial strain during creep and are attributed to the viscous effects (it is just an assumption). The term tertiary creep is nothing else but our limited insight of the phenomenon. The soil fails to distinguish between the elastic, plastic or viscous strain components. Separating the behavior in fields and regimes stems from our lack of understanding of the underlying mechanisms attributing to the overall mechanical response. The focal point is to provide the stress-strain-strain rate soil response simulating the mechanical behavior measured in the experimental tests. It is of no consequence whether it is the plastic or the viscous strain that leads to failure, as long the predicted behavior is justified through the experimental measurements. In this end, the term tertiary creep will not be used henceforth in this dissertation to denote failure due to creep but failure attributed to plastic strains triggered by viscous phenomena.

A structureless slightly overconsolidated soil specimen conforming to the material constants displayed in **Table 6.18** is subjected to creep once loaded to a stress state between the short and the long-term *CSL* on the wet domain. The halfsize of the Intrinsic Strength Envelope was assumed originally equal to $a^* = 50kPa$ and the halfsize of the Structure Strength Envelope $a = 50kPa$, characteristic of a structureless state where $B_0 = a/a^* = 1$. The axial strain was increased until failure (from Point A to point B and then it was left to creep until failure C) while at the same time the volumetric strain was set to null. The tensional translation was also considered as null $d_{in} = 0$.

The mechanical response assuming different material constants a_1^v is depicted in **Figure 6.19**. Once again regardless of the assumed material constant value a_1^v the stress path portrays an inclination of 1:3 in the *p-q* diagram reaching the exact same shear stress (the problem is stress controlled). Then the specimen is allowed to creep thus transitioning the strength envelope towards the long-term state. For the two higher assumed values of the material constant a_1^v the soil sample fails. For the lowest examined value of $a_1^v = 1$ the *CSL* continues translate towards the stress state

but requires significantly more time to attain it. Note that the value of $\varepsilon_q \approx 0.34$ refers to 300 days of undergoing creep for the $a_1^v = 1$ curve.

The volumetric and deviatoric creep strain components associated with the creep testing in the triaxial apparatus are depicted in **Figure 6.20**. It is evident that the volumetric creep strain component is minimal while the shear viscous strain is significant and approximately two orders of magnitude higher.

Table 6.18: Constitutive parameters involved in the investigation of delayed failure in the triaxial apparatus.

N_{iso}*	B_0	B_{res}	a* (kPa)	c_{in}	c_{fin}	σ (kPa)	$2\cdot(G/K)^e$	λ
2.08053	1	1	50	0.9798	0.7	80	0.75	0.08686
κ	λ^*	γ	d_{in}	η_v^p	η_q^p	ζ_v^p	ζ_q^p	θ_q^p
0.008686	5	1	0	75	75	0	0	0
ϑ_q^p	t_0 (days)	a_2^v	ψ	A	m	$\bar{a}$	DLIMIT	ξ
0	1	0	0.002	0.016	0.8	2.5	10^{-6}	0.02

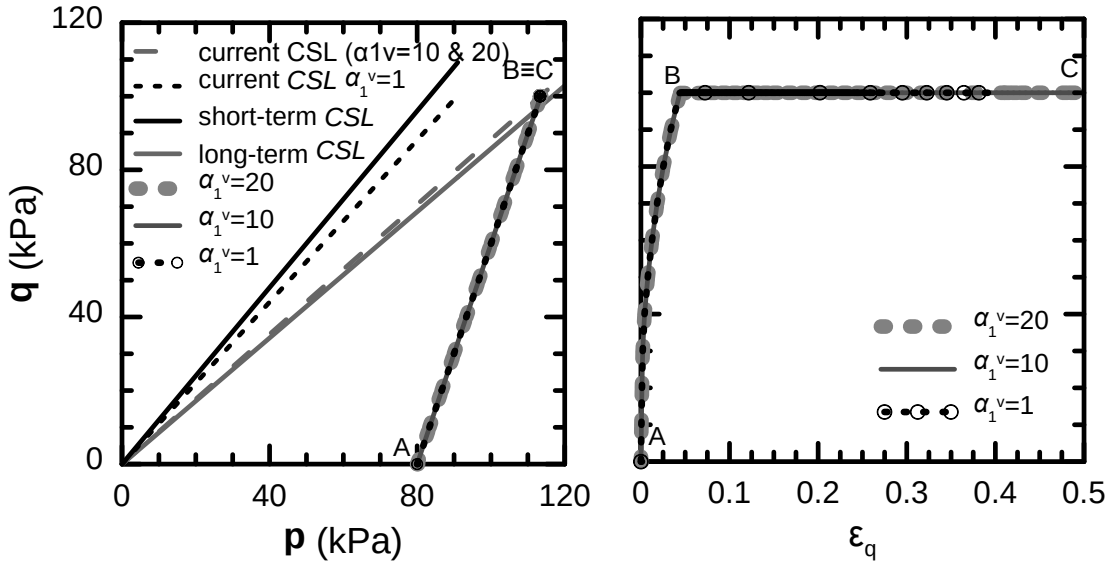

a. b.

Figure 6.19: Investigation of strength envelope evolution in triaxial drained creep testing of a structureless soil specimen on the wet side depicted in a. the p-q space and b. q-ε_q diagram.

While all the curves concerning the volumetric creep strain component are aligned following the exact same curve for all material constant values a_1^v the deviatoric

viscous behavior portrays some differences in terms of the simulated response. The reason for this is relatively simple. The volumetric creep strain component acts on the current stress state that lays intact throughout time. Hence, there is no reason for the curves to follow a different inclination whatsoever. The curves appear simply to stop once the failure state is attained. On the other hand, the deviatoric viscous response involves the relative distance from the strength envelope (or the peak strength assuming a highly overconsolidated sample). While the stress state does not change the strength envelope evolves thus increasing the shear stress ratio D. Hence, different material constants a_1^v result in distinctly different paths.

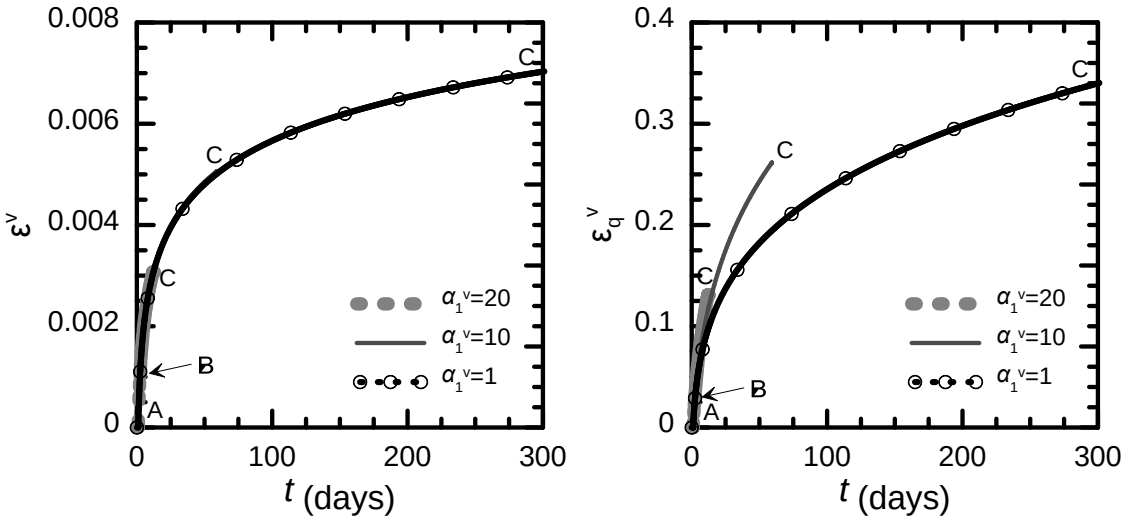

a. b.

Figure 6.20: a. Volumetric and b. deviatoric viscous strain components expressed as a function of time in triaxial drained creep testing.

The most important however plot revealing delayed failure has been left for last. **Figure 6.21** portrayed the shear strain as a function of time. The sole thing to be extracted from this diagram lies on the capability of the model to simulate the delayed failure, not through the rapid increase of the viscous strains but due to the accumulation of plastic deformations. Smaller values of the material constant a_1^v shift failure to considerable longer time periods. One might assume that the lowest value assumed $a_1^v = 1$ portrays the secondary compression stage but a careful examination of **Figure 6.20** reveals that the viscous deviatoric strains continues to increase with time thus resetting the strength envelope closer to the stress state until failure occurs.

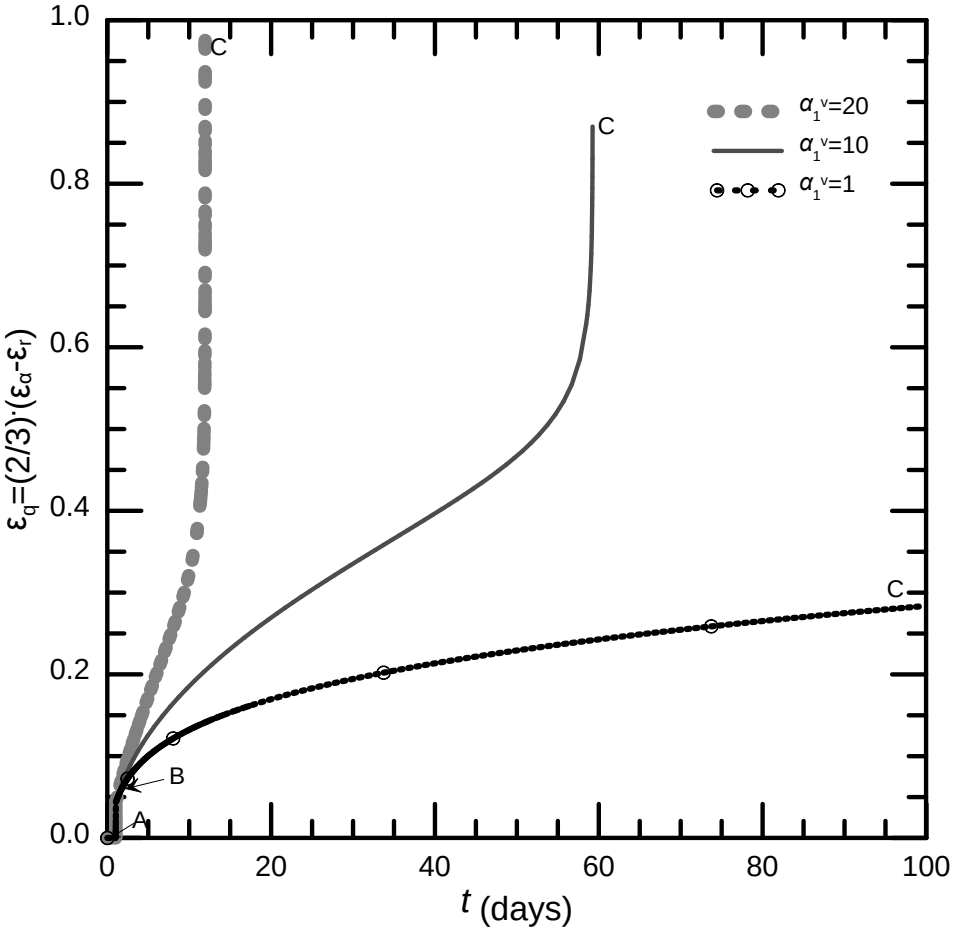

Figure 6.21: Investigation of strength envelope evolution in triaxial drained creep testing of a structureless soil specimen on the wet side depicted in ε_q-t diagram.

6.5.2 Time dependent behavior in plane strain loading

The effect of creep in plane strain compression is investigated in this section under drained conditions. The creep response in this case appears similar to the previous. Low shear stress levels activate solely the primary stage while significantly higher stress intensities lead to failure.

The current subsection investigates the deleterious effects of deviatoric creep strain on soil strength at plane strain shearing modes. The plane strain element is ABAQUS is originally consolidated isotropically at 80kPa (Point A). After equilibrium is attained the element the vertical stress increases from 80kPa to 355kPa while the confining pressure is kept constant and equal to 80kPa (Point B). The soil element is allowed to freely deform in the horizontal direction (the cross sectional displacement is null considering plane strain conditions). The axial loading sets the stress state

somewhere between the short-term and the long-term *CSL* regardless whether the stress state is adjusted on the *SSE*. The element is allowed to creep and depending on the material constant a_1^v delayed failure occurs sooner or later (Point C).

The loading steps involved are portrayed below (similar to the previous case):

- **Geostatic step**: The soil element is originally consolidated isotropically to 80kPa (Point A). The initial step is undertaken to establish equilibrium between the initial values and the calculated stress state. The time period of this step is fixed and equal to 1day.
- **Loading step**: The vertical stress increases from 80kPa to 355kPa while the confining pressure is kept constant and equal to 80kPa (Point B). The element is allowed to freely deform in the horizontal direction (the cross sectional displacement is null considering plane strain conditions). Loading sets the stress state somewhere between the short-term and the long-term *CSL* regardless whether the stress state is adjusted on the *SSE*. In order to disregard any viscous effects this loading increment was concluded after $\Delta t = 0.05$ days.
- **Creep step**: The stress field is kept constant while the element is allowed to creep. Failure (at point C) is attained once the stress state is adjusted on the *CSL*. It is noted that it is not necessary for the *CSL* to reach the long-term inclination for the soil element to fail.

The same structureless slightly overconsolidated soil specimen as before (conforming to the material constants displayed in **Table 6.18**) is subjected to creep once loaded to a stress state between the short-term and the long-term *CSL* on the wet domain. The halfsize of the Intrinsic Strength Envelope was assumed originally equal to $a^* = 50kPa$ and the halfsize of the Structure Strength Envelope $a = 50kPa$, characteristic of a structureless state where $B_0 = a/a^* = 1$. The tensional translation was set to null $d_{in} = 0$.

The constitutive time dependent response assuming different material constants a_1^v is depicted in **Figure 6.22**. Regardless of the assumed material constant value a_1^v the stress path in the *p-q* diagram reaches the exact same shear stress state (the problem is stress controlled). The element is allowed to creep thus transitioning the strength

envelope towards the long-term state. For the two higher assumed values of the material constant a_1^v the soil element fails. For the lowest examined value of $a_1^v = 5$ the *CSL* continues to transpose towards the stress state but requires significantly more time to attain it. Note that the value of $\varepsilon_q \approx 0.31$ refers to 300 days of undergoing creep for the $a_1^v = 5$ curve.

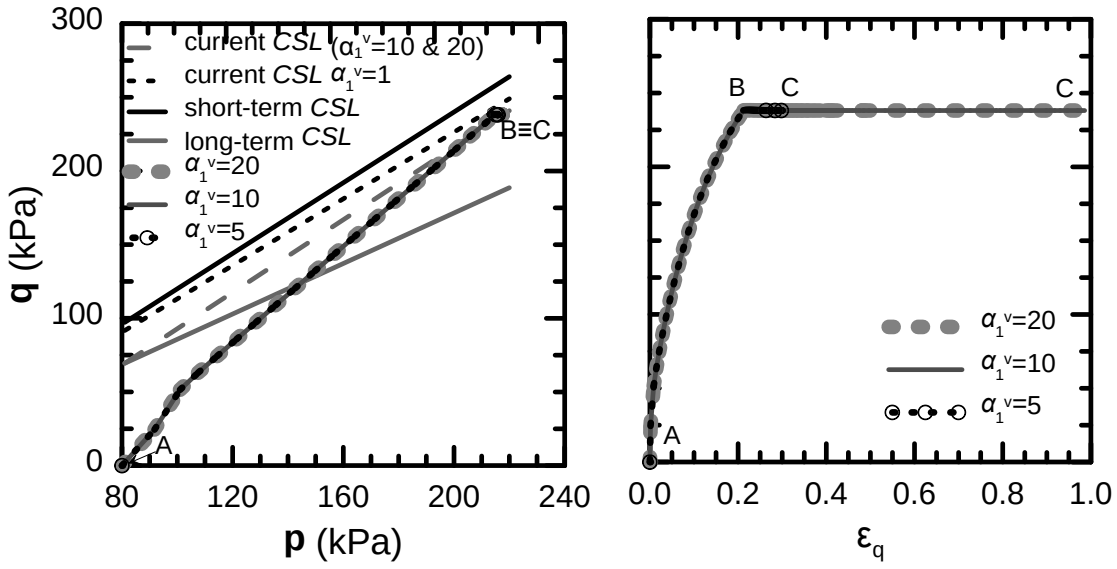

a. b.

Figure 6.22: Investigation of strength envelope evolution in plane strain drained creep testing of a structureless soil specimen on the wet side depicted in a. the *p*-*q* space and b. *q*-ε_q diagram.

The volumetric and deviatoric creep strain components associated with the creep testing under plane strain conditions are depicted in **Figure 6.23**. It is observed that the volumetric creep strain component is minimal while the shear viscous strain is approximately two orders of magnitude higher. The argument could be made that the selection of the parameters was a bit crude concerning the volumetric component. However, the effect of volumetric component will be examined later on oedometer creep and stress relaxation tests revealing that the selected values are more than accurate and conforming with the selected inviscid parameters according to Mesri and Gholamreza (1977).

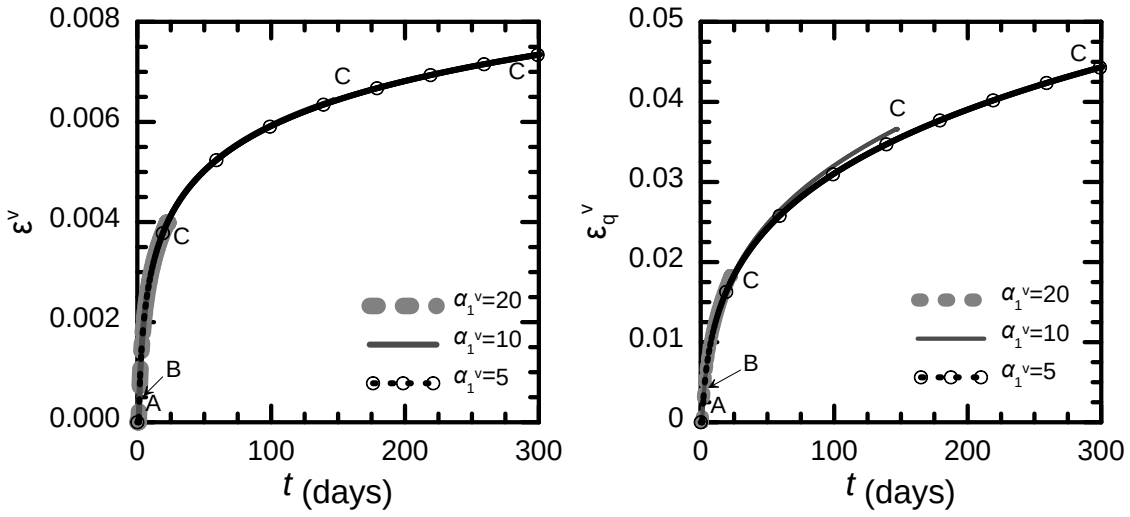

a. b.

Figure 6.23: a. Volumetric and b. deviatoric viscous strain components expressed as a function of time in plane strain drained creep testing.

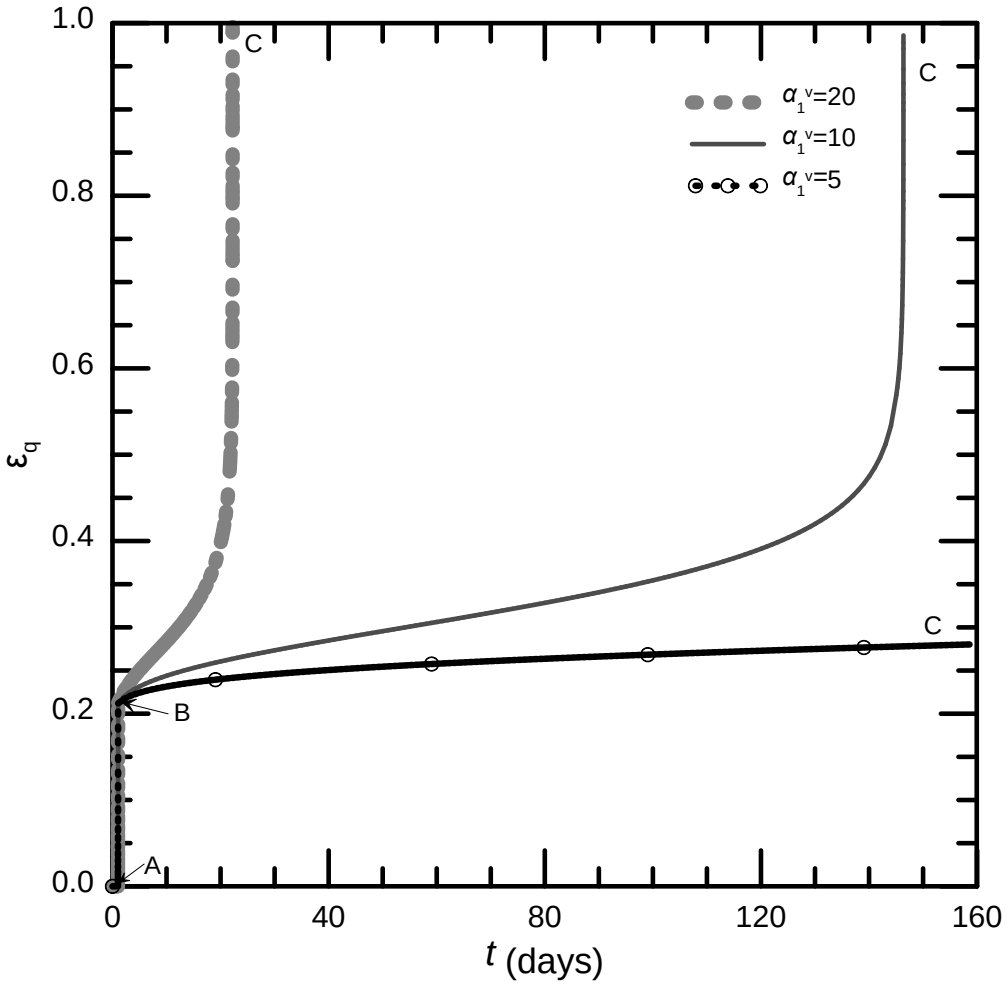

Figure 6.24: Investigation of strength envelope evolution in plane strain drained creep testing of a structureless soil specimen on the wet side depicted in ε_q-t diagram.

All volumetric creep strain component curves are aligned regardless of the selected material constant values a_1^v. The deviatoric viscous component however reveals the same differences as before in terms of the simulated response. The volumetric creep strain component acts on the current stress state that lays intact throughout time. Hence, there is no reason for the curves to follow a different inclination whatsoever. The curves simply cease to evolve once the failure state is attained. On the other hand, the deviatoric viscous strain component involves the relative distance from the strength envelope. While the stress state does not change the strength envelope evolves thus increasing the shear stress ratio D. Hence, different material constants a_1^v result in distinctly different paths.

However, the most important plot revealing delayed failure is **Figure 6.24** portraying the shear strain as a function of time. Note that the proposed model can capture the delayed failure response. Once again, smaller values of the material constant a_1^v translate failure to considerable longer time periods. The soil response for the lowest value of $a_1^v = 5$ does not really depict the secondary compression stage (at point C). A thorough examination of **Figure 6.23** reveals that the viscous deviatoric strain continues to increase with time thus resetting the strength envelope closer to the stress state until failure occurs. The material reveals its stationary creep stage at the time scale selected to depict the simulated response.

6.5.3 Time dependent behavior in direct simple shear testing

A structureless slightly overconsolidated soil sample subjected to direct simple shear testing is examined in terms of the mechanical behavior associated with time dependent phenomena. Although direct simple shear testing may appear redundant at first glance, the main reason lays with the retrogressive slope instability problem activating the exact same shearing mode. Hence, it is of interest to investigate the mechanical behavior under direst simple shear testing.

The effect of viscous shear strain on the mechanical behavior is examined in a direct simple shear test. The inviscid elastoplasticity cannot account for the post yielding failure of the soil associated with time. Assuming that a soil specimen is subjected to direct simple shear without failing, the classical elastoplasticity theory cannot account for the time dependent behavior which leads to delayed failure.

A single element is subjected to direct simple shearing in the Finite Element Code ABAQUS. The objective is to stress the element far enough as to set the stress state at the intermediate space defined through the intersection of the short-term and long-term *CSL* in the stress hyperplane. This step is assumed to be concluded very rapidly to minimize the time-dependent effects on the overall mechanical behavior during the initial loading step. Afterwards the element is allowed to creep until failure. What is of great interest is to investigate the effect of the material constant a_1^v in the failure time period.

The loading steps involved are summarized here below:

- **Geostatic step**: The soil element is originally consolidated isotropically to 80kPa (Point A). The initial step is undertaken to establish equilibrium between the initial values and the calculated stress state. The time period of this step is fixed and equal to 1day.
- **Loading step**: The element was sheared by imposing the same nodal force (lateral 6.5kN) in each node defining the upper surface of the element (note that the nodes defining the bottom surface were pinned). The applied shear stress was equal to 26kPa in total, thus setting the stress state on *PYE* somewhere between the short-term and the long-term *CSL* (Point B). In order to disregard any viscous effects this loading increment was concluded after $\Delta t = 0.05$ days.
- **Creep step**: The stress field is kept intact while the specimen is allowed to creep. Failure (at point C) is attained once the stress state is adjusted on the *CSL*. It is noted that it is not necessary for the *CSL* to reach the long-term inclination for the soil specimen to fail.

A structureless slightly overconsolidated soil element (the associated material constants are depicted in **Table 6.18**) is subjected to creep once loaded to a stress state laying at the intersection of the short-term and long-term *CSL* on the wet domain. The halfsize of the Intrinsic Strength Envelope was assumed originally equal to $a^* = 50kPa$ and the halfsize of the Structure Strength Envelope $a = 50kPa$, characteristic of a structureless state where $B_0 = a/a^* = 1$. The tensional translation was set to null $d_{in} = 0$. The predicted time-dependent mechanical behavior assuming different material constants a_1^v is depicted in

Figure 6.24. Regardless of the assumed material constant value a_1^v the stress path in the *p*-*q* diagram reaches the exact same shear stress state (the problem is stress controlled). Then the specimen is allowed to creep thus transitioning the strength envelope towards the long-term state. All assumed values of the material constant a_1^v result in delayed failure. Elevated values of the constitutive parameter a_1^v result in a more rapid failure.

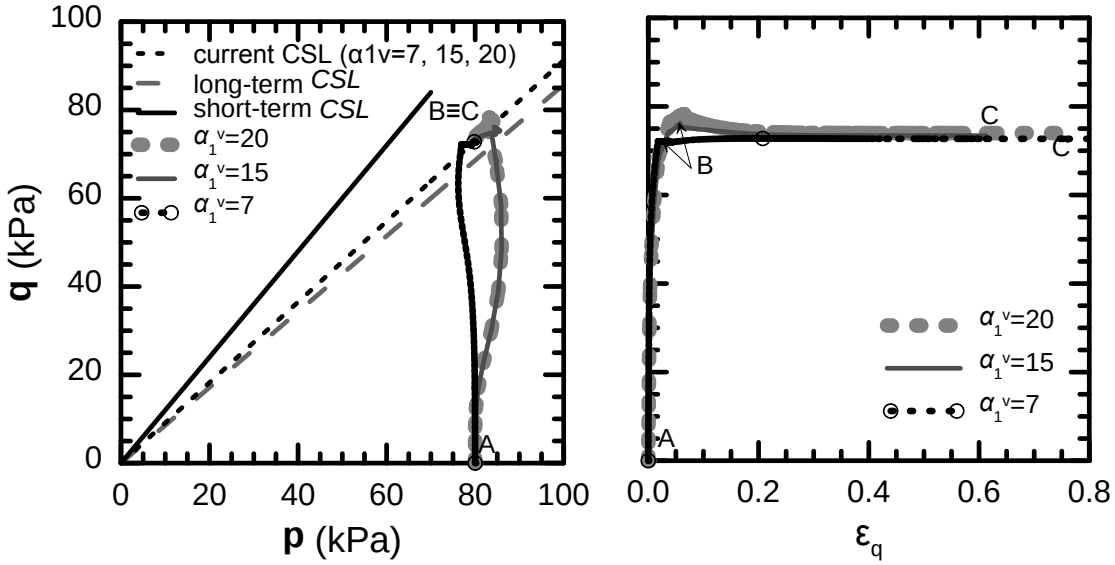

Figure 6.25: Investigation of strength envelope evolution in direct simple shear creep testing of a structureless soil specimen on the wet side depicted in a. the *p*-*q* space and b. q-ε_q diagram.

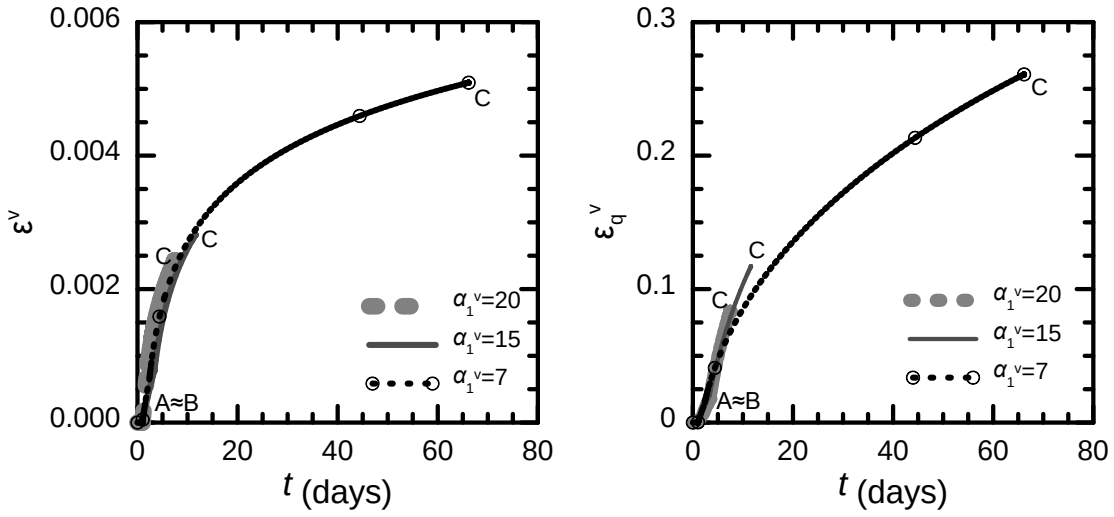

Figure 6.26: a. Volumetric and b. deviatoric viscous strain components expressed as a function of time in direct simple shear creep testing.

The volumetric and deviatoric creep strain components associated with the creep testing in direct simple shear are depicted in **Figure 6.26**. It is evident that the volumetric creep strain component is minimal while the shear viscous strain is approximately two orders of magnitude higher. A brief examination of the diagram reveals that it is not the viscous component that builds up for failure to occur. It is simply the trigger shifting the strength envelope towards the current stress state. Note that all volumetric creep strain curves are aligned regardless of the selected material constant values a_1^v.

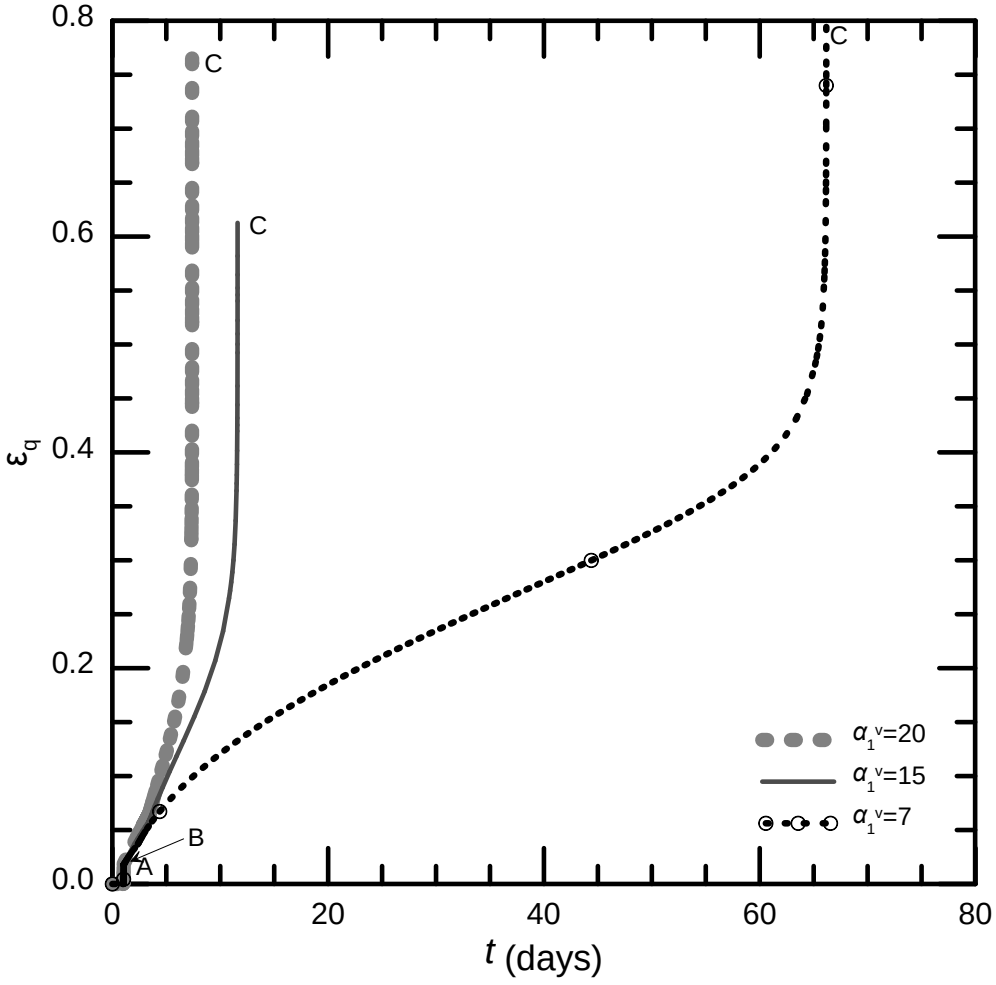

Figure 6.27: Investigation of strength envelope evolution in direct simple shear creep testing of a structureless soil specimen on the wet side depicted in ε_q-t diagram.

The deviatoric viscous component however diverges in terms of the simulated response. On the one hand, the volumetric creep strain component acts on the current stress state (hence, laying intact considering that the stress state does not change) and on the other the deviatoric viscous strain component involves the

relative distance from the strength envelope. While the stress state does not change the strength envelope evolves thus increasing the shear stress ratio D. Hence, different material constants a_1^v result in distinctly different paths.

Figure 6.27 portrays the shear strain as a function of time. Note that the proposed model can capture the delayed failure response. Once again, smaller values of the material constant a_1^v translate failure towards considerable longer time periods.

6.5.4 Time dependent behavior in standard oedometer creep tests

While the plane strain and direct simple shear tests have been incorporated within the current chapter to illustrate the deleterious effect of viscous deviatoric strain on the material strength they offer no new insight in the time-dependent mechanical behavior of geomaterials. What is of major importance however, is to investigate the combined effect of volumetric and deviatoric viscous strains in both standard oedometer and stress relaxation tests (to be analyzed next).

To make a long story short, numerical analyses referring to a structureless slightly overconsolidated soil sample (the associated material constants are summarized in **Table 6.18**) are performed in order to illustrate the combined effect of the volumetric and the deviatoric viscous strain. The halfsize of the Intrinsic Strength Envelope was assumed originally equal to $a^* = 50kPa$ and the halfsize of the Structure Strength Envelope $a = 50kPa$, characteristic of a structureless state where $B_0 = a/a^* = 1$. The tensional translation was set to null $d_{in} = 0$.

This section focuses on a single value of the material constant $a_1^v = 20$, in order to clarify the overall mechanical behavior considering that there is no failure involved in the system. Hence, an isotropically original consolidated state is assumed equal to 80kPa. The element is stressed vertically from 80kPa to 3636kPa corresponding to a vertical strain of approximately 0.2. Then the element is allowed to creep while the vertical stress is kept intact.

The loading steps involved are analyzed here below in further detail:

- **Geostatic step**: The soil element is originally consolidated isotropically to 80kPa (Point A). The initial step is undertaken to establish equilibrium

between the initial values and the calculated stress state. The time period of this step is fixed and equal to 1day.

- **Loading step**: The element is compressed vertically. The vertical pressure increases from 80kPa to 3,636kPa (corresponding to a vertical strain of approximately 0.2-Point B). In order to disregard any viscous effects this loading increment was concluded after $\Delta t = 0.05$ days.
- **Creep step**: The vertical imposed stress is kept constant while the specimen is allowed to creep for 1,000 days (point C).

Figure 6.28 summarized the mechanical response of the system both in the stress space and in terms of the shear stress-strain behavior. It is evident that the stress state does not lay in the intersection of the short and long-term *CSL* (hence, it is impossible for the element to fail). The sudden drops in both the *p*-*q* space and the *q*-ε_q diagram are associated with the effect of viscous strains.

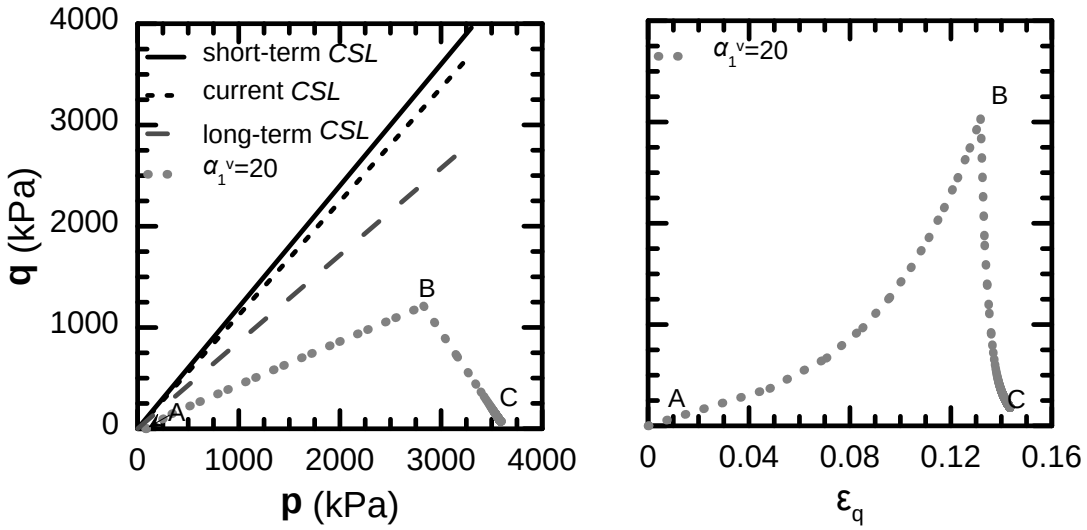

a. b.

Figure 6.28: Investigation of time dependent soil response in standard oedometer creep testing of a structureless soil specimen on the wet side depicted in a. the *p*-*q* space and b. *q*-ε_q diagram.

What is to be expected from the standard oedometer creep test is summarized in **Figure 6.29**. During creep the void ratio decreases with evolving time while the vertical effective stress is kept constant. This results in the drop in the v-ln(σ_v) diagram. Hence, it is the volumetric creep strain that contributes to this simulated behavior. The effect of the deviatoric viscous deformation is depicted through the sudden drop in **Figure 6.28** and can be associated with the increase of the horizontal effective stress depicted in **Figure 6.30**. The deviatoric creep strain component

accumulates at a considerably faster rate than the volumetric. Considering that the total strain equals the vertical and that the volumetric creep component is approximately two orders of magnitude smaller than the deviatoric creep viscous deformation the element tends to undergo a stress rebound by resetting the stress state towards the isotropic state.

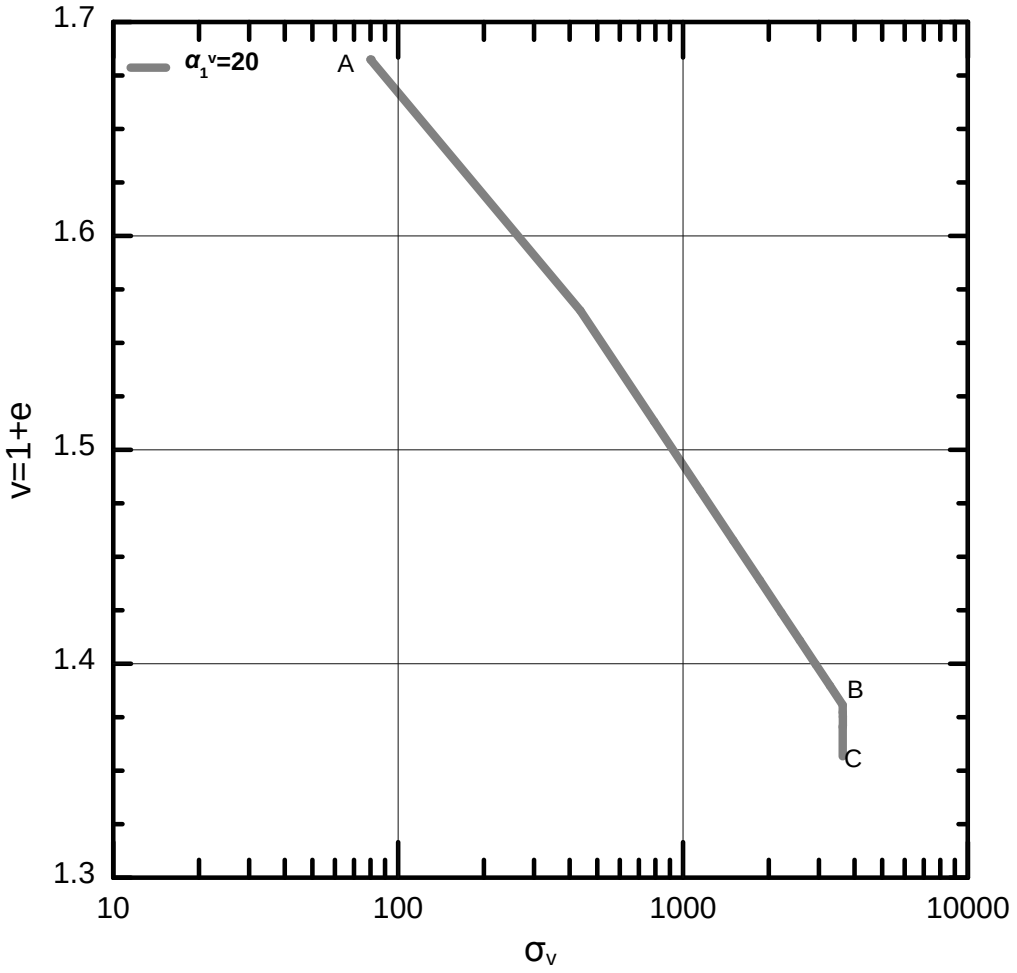

Figure 6.29: Investigation of time dependent soil response in standard oedometer creep testing of a structureless soil specimen on the wet side depicted in the v-ln(σ_v) space.

In this sense, the vertical stress is fixed considering it is externally applied and equilibrium needs to be satisfied while the horizontal stress is allowed to increase. The deviatoric stress is small enough to change the inclination of the *CSL* in the stress space rapidly (consider **Figure 6.28**). Hence, the deviatoric plastic strain component during creep is negligible. This means that approximately the horizontal viscous equals the elastic strain component in magnitude causing the lateral pressure to

increase. Hence, the lateral pressure coefficient *K* tends to evolve towards unity with time.

Summarizing, it is the combined effect of volumetric and shear creep that is revealed in the standard oedometer test. The volumetric builds on strength resulting in the drop depicted in the v-ln(σ_v) diagram while the deviatoric strain is responsible for transitioning the stress state towards isotropic pressures.

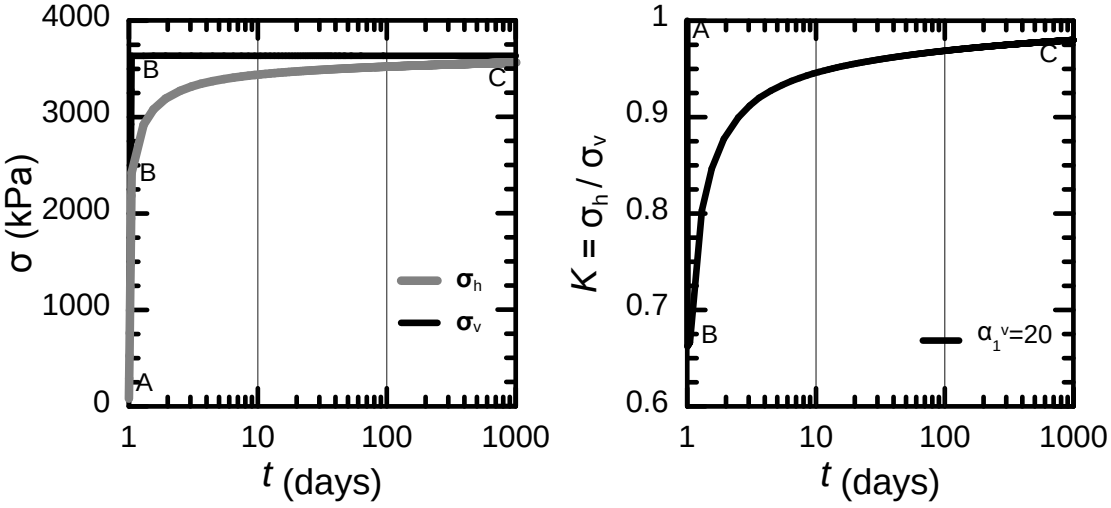

Figure 6.30: Investigation of a. the principal stress components and b. the lateral earth pressure coefficient *K* as a function of time in a standard oedometer creep test.

6.5.5 Time dependent behavior in stress relaxation tests

This subsection investigates the predicted mechanical response of a slightly overconsolidated soil element subjected to stress relaxation. Next, the research focuses on results based on numerical analyses in the F.E.M. Code Simulia ABAQUS assuming the material constants depicted in **Table 6.18**. The halfsize of the Intrinsic Strength Envelope was assumed originally equal to $a^* = 50kPa$ and the halfsize of the Structure Strength Envelope $a = 50kPa$, characteristic of a structureless state where $B_0 = a/a^* = 1$. The tensional translation was set to null $d_{in} = 0$. An original isotropically consolidated state is assumed equal to 80kPa. In the stress relaxation test simulated in this section a given soil element was compressed by prescribing a vertical displacement equal to 0.2. The loading increment did not set the stress state at the intersection of the short and long-term *CSL* considering that it is a K_0 situation and therefore the element does not fail.

Following the compression the element is allowed to creep but the displacement field is kept intact. This results in the stress relaxation as can be seen from **Figure 6.31**. This section focuses on a single value of the material constant $a_1^v = 20$, in order to clarify the overall mechanical behavior (considering that there is no failure involved in the system).

The loading steps involved are analyzed here below in further detail:

- **Geostatic step**: The soil element is originally consolidated isotropically to 80kPa (Point A). The initial step is undertaken to establish equilibrium between the initial values and the calculated stress state. The time period of this step is fixed and equal to 1day.
- **Loading step**: The element is compressed vertically until the imposed strain reaches 0.2 (Point B). In order to disregard any viscous effects the current loading increment was concluded after $\Delta t = 1\,\text{day}$.
- **Creep step**: The vertical imposed stress is kept constant while the specimen is allowed to creep for 1,000 days (point C).

The stress path in the *p*-*q* space reveals a peculiar behavior at first glance. Once the loading ceases to act on the soil element the viscous phenomena force the stress state to decrease and tend to set it back to null isotropic stresses. The phenomenon is also visible in the shear stress-strain diagram. The drop in the shear stress is attributed to the deviatoric viscous strain acting to set the horizontal and the vertical stresses aligned (**Figure 6.33**).

Figure 6.32 portrays the decrease of isotropic pressure at a constant void ratio. The mechanism is rather simple in its essence. The vertical stress is allowed to decrease thus slowly aligning with the lateral. At the mean time the volumetric creep component acting on the element forces the isotropic pressure to decrease and assuming that the stress relaxation was allowed to undergo infinitely it would set the stress state at null hydrostatic pressure.

Summarizing, what is important to store in mind is that the deviatoric creep strain causes the vertical stress to decrease thus setting the lateral pressure coefficient to unity (Figure 6.33). This sums up the difference from the standard oedometer creep test where the viscous shear deformation would increase the lateral stress to adjust with the vertical. In terms of the volumetric viscous strain in stress relaxation testing

it causes the isotropic pressure to transgress to null hydrostatic pressure while in the standard oedometer test it has the exact opposite effect.

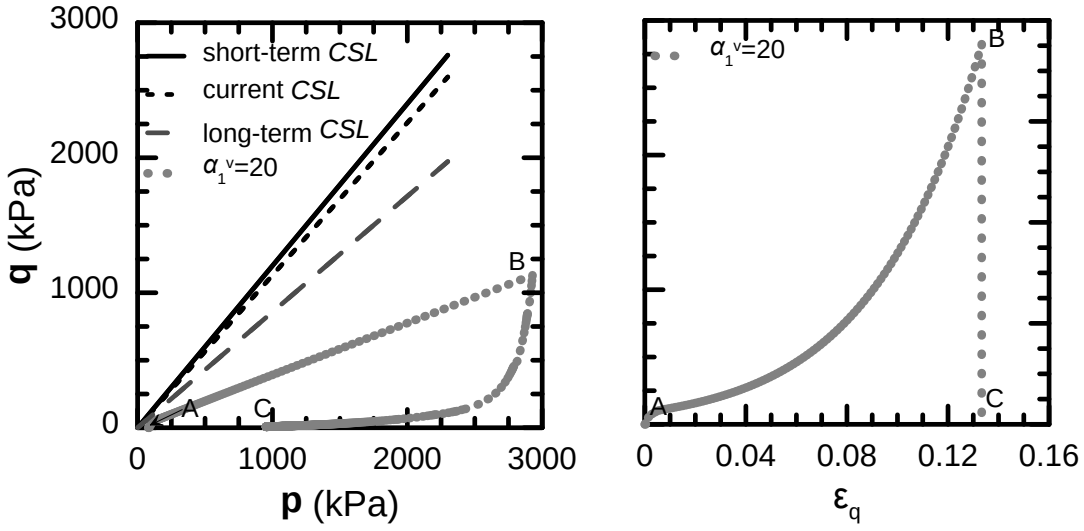

a. b.

Figure 6.31: Investigation of time dependent soil response in stress relaxation testing of a structureless soil specimen on the wet side depicted in a. the *p*-*q* space and b. q-ε_q diagram.

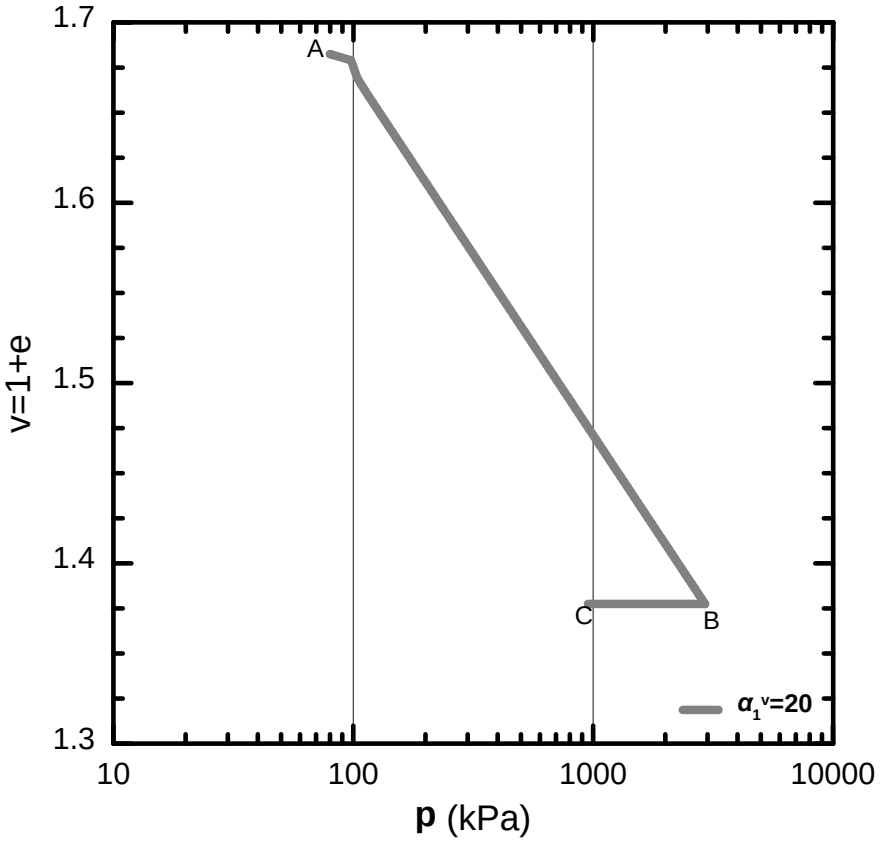

Figure 6.32: Investigation of time dependent soil response in stress relaxation testing of a structureless soil specimen on the wet side depicted in the v-ln(p) space.

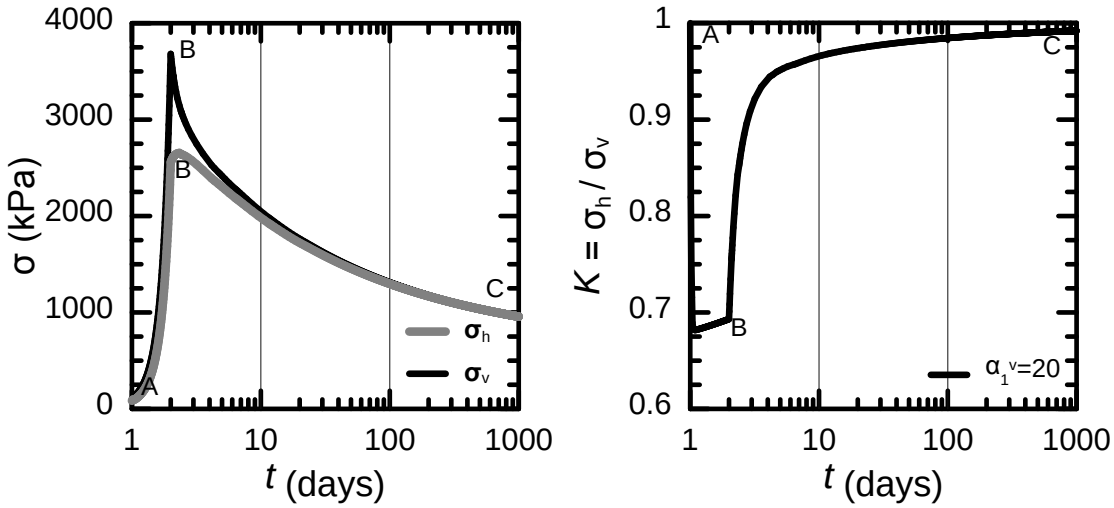

a. b.

Figure 6.33: Investigation of a. the principal stress components and b. the lateral earth pressure coefficient *K* as a function of time in a stress relaxation test.

6.6 Concluding remarks

In this chapter the predicted constitutive behavior of the proposed model was investigated on both structured and non-structured deposits. The proposed model was evaluated through a parametric study investigating different aspects of the simulated behavior.

The effects of initial and small strain stiffness as well as the structure degradation process due to plastic straining were examined in the degenerated elastoplastic basis model. In this end, an ensemble of single point or element based (in Finite Element Code SIMULIA ABAQUS) numerical analyses were conducted. All elastoplastic material constants were analyzed and the associated behavior was examined in the elastoplastic model thus providing a range of magnitude for future selection.

As for the time dependent soil response the strength envelope was examined through further numerical analyses incorporating the viscous phenomena within the constitutive governing equations. Results were presented in drained triaxial, plane strain and direct simple shear testing on a slightly overconsolidated soil specimen. The deviatoric component revealed its devastating effect on soil strength leading ultimately to delayed failure. The reason for imposing drained conditions lies with the definition of creep postulating drained boundary conditions for the stress state to remain intact. The reason for not including results referring to the dry side

(characteristic of highly overconsolidated states) lies on the negligible effect of viscous phenomena in such regions. In these cases the softening effect would cause the stress imposed problem to rebound thus not revealing any significant information about the true time-dependent soil behavior. It is noted that the stress state is required to be "sufficiently" close to the failure envelope for the deleterious creep effects on soil strength to be dominant. This means that the stress state needs to lay on the intermediate boundary of the short and long-term *CSL*.

The effect of time dependency was further evaluated in standard oedometer creep and in stress relaxation tests. While both experimental setups result in the lateral pressure coefficient to become unity the trigger mechanism is considerably different. In the case of the standard oedometer test the shear viscous strain causes the lateral stress to increase thus aligning ultimately (with time evolving) with the vertical. In the meantime, the volumetric creep component builds on strength thus increasing the size of the *SSE*, decreasing the void ratio and increasing the isotropic pressure (only the vertical pressure is constant - the horizontal increases with time). In the stress relaxation tests the deviatoric viscous strain results in the vertical pressure to decrease and align with the lateral. The volumetric viscous component on the other hand results in the drop of the isotropic pressure at a constant void ratio, thus translating to null isotropic values at infinite time.

7

Comparison with experimental measurements

7.1 General

The current chapter addresses the necessity for the evaluation of the proposed model against laboratory measurements both in the oedometer and in the triaxial apparatus. The constitutive parameters will be quantified in an attempt to simulate the mechanical time-dependent response of a soil sample. Considering that the oedometer viscous response of soils has been extensively covered in the literature (i.e. Terzaghi, 1996; Leoni et al., 2008; Yin et al., 2010; Sivasithamparam, 2013) estimation of the secondary compression index is well established and requires no further investigation. The oedometer viscous response of a very soft clay (resembling peat) is addressed to investigate the capabilities and limitations of the proposed model.

Attention will be paid to the deleterious effects on the soil strength revealed in triaxial loading. Considering that the elastoplastic basis model is an extension of the Modified Cam Clay (MCC) criterion the governing equations can simulate accurately the mechanical response of clayey structured and non-structured soils. However, purely drained triaxial results on clays are rather difficult to attain. The time period to reveal the deleterious effects of the shear viscous strain may be of the order of 200 to 1,000 days. Thus, it is evident that such tests cannot be easily found in novel data. A very limited amount of published studies address the drained time-dependent mechanical behavior of clays in the triaxial apparatus, namely by Bishop (1966) and Ter-Stepanian (1975). Bishop conducted drained triaxial creep tests on brown London clay from Hendon (delayed failure occurred after 200 days) while Ter-Stepanian presented results on sensitive clay (failure occurred after 1,000 days).

Most researchers tend to address the time-dependent behavior of clays by focusing on the undrained response. Bjerrum et al. (1958) performed undrained triaxial tests on Fernubu clay originating from an isotropic consolidation state. Similar experiments were undertaken by Richardson and Whitman (1963) on a Mississippi Valley alluvial clay, by Ladd (1972) on Atchafalaya clay, by Alberro and Santoyo (1973) on Mexican clay, by Vaid and Campanella (1977) on undisturbed Haney Clay, by Mayne and Kulhawy (1990) on Marine clay and Zhu and Yin (2000) on re-consolidated Hong-Kong Marine clay deposits. Undrained triaxial creep tests have also been performed by originating from anisotropic consolidation states either at K_0 conditions or at different shear stress ratios.

Berre (1975) presented undrained triaxial results on Drammen clay assuming an original anisotropic state of consolidation. Hight (1983) performed similar experiments on Lower cays. Graham et al. (1983) conducted undrained step range strain rate creep tests in the triaxial apparatus on Belfast and Mastemyr clay (similar to Karstunen et al., 2013; Sivasithamparam et al., 2013; Yin et al., 2010). Lefebre and Leboeuf (1987) and Marques et al. (2004) examined the time-dependent response of various clays assuming undrained boundary conditions originating from either isotropic or anisotropic consolidation states. Sheahan et al. (1996) and Yin and Cheng (2006) investigated the strain-rate dependent behavior of K_0 consolidated specimens in the triaxial apparatus assuming undrained conditions. By further accounting for the Mitchell et al.' (1968) experiments addressing the undrained time-dependent behavior of remolded illite, remolded San Francisco Bay Mud and a Kaolinite-Sand mixture in the triaxial apparatus it becomes evident that the majority of experimental results on clays refer to undrained boundary conditions. Many researchers (i.e. Mitchell et al., 1968; Vaid and Campanella, 1977; Karstunen et al., 2013; Sivasithamparam et al., 2013; Yin et al., 2010) imposed Constant Strain Rate loading regarding such process as characteristic of creep behavior. Regardless, whether the effect of constant strain rate loading affects the soil strength it is not characteristic of pure creep and should not be employed to clarify the elemental mechanisms associated with the time-dependent mechanical behavior.

Note that during undrained loading the shear viscous strains tend to increase while the total volumetric strain is fixed. Hence, the specimen is on the one hand, allowed to relax and on the other the shear viscous strain leads to failure. By further taking

into account, that the very definition of creep accounts for constant effective stress it becomes evident why drained conditions are required to portray the total response of the system. Hence, the current dissertation needs to investigate the effect of viscous shear strain in another geomaterial (other than clay that is) under drained conditions in the triaxial apparatus.

Di Prisco and Imposimato (1996) conducted both dry and saturated drained and undrained experiments on loose Houston sand of relative density $D_r = 20\%$ in the triaxial apparatus. The mechanical response of sand does not appear suitable for application considering that the proposed constitutive model addresses the time-dependent behavior of clayey deposits and structured materials resembling cohesive media. Furthermore delayed failure which is the major keypoint to be considered is portrayed solely in an undrained experiment. Heap et al. (2009) and Ventura et al. (2010) performed constant shear stress triaxial experiments on sandstone. Yang and Jiang (2010) further conducted triaxial experiments on sandstone leading to tertiary failure. However, slices were included in the sandstone specimens to examine the overwhelming time-dependent effect of coal on the associated failure.

An ensemble of researchers have focused on the time-dependent behavior of rock salt considering possible applications in radioactive waste disposal systems (i.e. Yang et al., 1999; Hunsche and Hampel, 1999; Slizowski and Lankof, 2003; Zhang et al., 2012). An extensive survey of such efforts and experimental measurements reveals that at extremely high shear stress levels the strain increases rapidly leading to high axial measured values but soon recovers. Hence, no delayed failure occurs in the specimens at least at the strain levels that can be measured in the laboratory. This justifies also its use in the radioactive waste disposal systems to heal potential cracking.

Shao et al. (2003) and Gasc-Barbier et al. (2004) focused on the time-dependent response of hard argillites. Granite (i.e. Fujii et al., 1999; Maranini and Yamaguchi, 2001; Brantut et al., 2012), tuffs (i.e. Martin et al., 1997; Ma and Daemen, 2006; Shibata et al., 2007; Okubo et al., 2008) and basalt (i.e. Heap et al., 2011) has also been the focal point of numerous publications addressing the time-dependent mechanical response of geomaterials. Further experimental surveys investigate the time-

dependent response in triaxial tests addressing limestone (i.e. Maranini and Brignoli, 1999) and even Recycled Asphalt Pavements (RAP) (i.e. Juarez-Badillo, 2011).

What is however astonishing is that very few researchers tend to focus on the mechanical response of the system subjected to a loading stress path (to the inviscid behavioral characteristics). Instead, attention is given solely on the strain-strain rate-time plots and completely neglect to examine any loading path. An elastic modulus and possibly a friction angle are to be expected at best. If a picture speaks louder than a thousand words consider having solely the strain-strain rate-time diagram as a single word to extract the entire mechanical response of the geomaterial. It is ludicrous if not impossible to do so. In this end, the capability of the proposed model to simulate the delayed failure mechanism is examined in a well documented case of coal by Debernardi (2008).

7.2 Evaluation of the proposed model in oedometer tests

The proposed constitutive model incorporates the secondary compression index for the estimation of the volumetric creep strain component. Considering that the secondary compression index is a well established quantity in the literature (usually expressed as a fraction of the virgin compression index) the research focuses on simulating the time-dependent response solely in an oedometer test on a very soft natural clay resembling peat (Yin et al., 2010).

The original consolidation state corresponds to K_0 conditions thus not conforming probably to the constant orientation of the bounding surface along the hydrostatic axis. The proposed elastoplastic basis model employed does not allow for simulation of the primary anisotropy of the material fabric. Regardless, however of any possible shortcomings of the proposed model in that respect the predicted mechanical behavior will be investigate regardless.

Figure 7.1 portrays the simulated mechanical response in terms of the volumetric strain as a function of time. The constitutive parameters associated with the predicted soil response are depicted in **Table 7.1**. Originally the specimen was stressed until the vertical effective pressure reached 132kPa and then it was allowed to creep. The simulated mechanical response portrayed in **Figure 7.1** coincides with the measured experimental line of Yin et al. (2010). Note that the simulated line

corresponds to a significant value of ψ to capture the experimental measurements, which is characteristic of peat rather than clay. However, considering the extremely elevated compressibility parameter λ and the minimal poroelastic parameter κ (the measured ratio $\lambda/\kappa \approx 12.63$ which is extremely low) the aforementioned statement is justified. Based on the experimental measurements of λ and κ and the physical properties of the soil sample as portrayed in **Table 7.1** the value of the constitutive parameter ψ adopted is 0.028. Note that the authors suggest use of $C_a = 0.022$ which corresponds to a value of $\psi = 0.026$. Considering that there are no available data to simulate the shear viscous strain and that the model results in a different K_0 value (0.6548) than the experimental 0.48 the target was set solely to predict the simulated response.

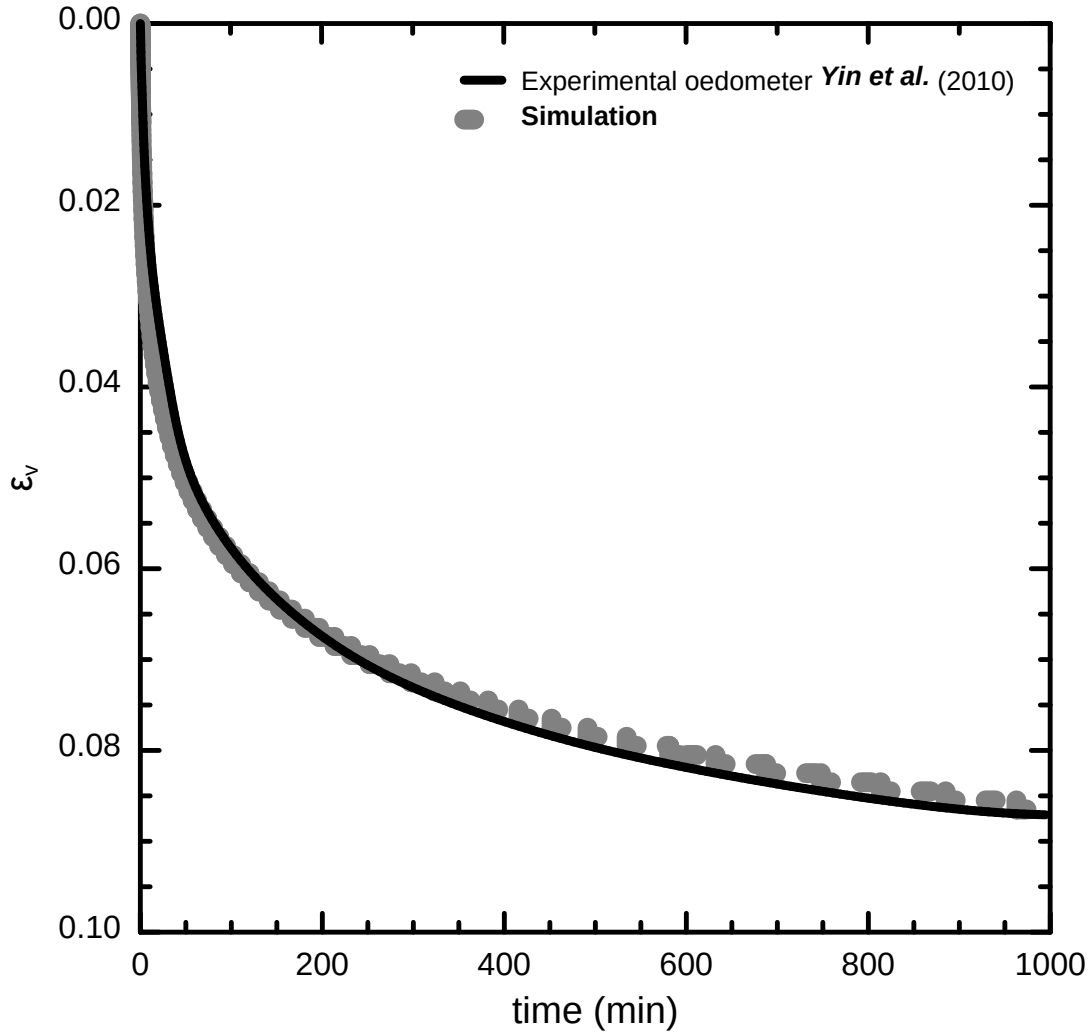

Figure 7.1: Comparison of the simulated time-dependent soft natural clay response (dotted line) with the experimental measurements (solid line) by Yin et al. (2010) in an oedometer test.

Table 7.1: Constitutive parameters associated with Yin et al. (2010).

N_{iso}*	B_0	B_{res}	a* (kPa)	c_{in}	c_{fin}	OCR	$2\cdot(G/K)^e$	λ
4.8793	1	1	36.225	0.9798	0.9798	1.05	0.75	0.48
κ	λ^*	γ	d_{in}	η_v^p	η_q^p	ζ_v^p	ζ_q^p	θ_q^p
0.038	5	1	0	75	75	0	0	0
ϑ_q^p	t_0 (days)	$a_1^v = a_2^v$	ψ	A	m	$\bar{a}$	DLIMIT	ξ
0	1	0	0.028	0.016	0.8	2.5	10^{-6}	0.02

It is noted that for such high values of the secondary compression index corresponding to peat rather than clay the appropriate and accurate definition of the stiffness matrix becomes significant. Hence, the simulation above was conducted in a single point analysis rather than ABAQUS considering that the finite element code employed does not allow for a definition of a separate relaxation matrix but solely for an individual stiffness tensor. Values for the secondary compression index are easily accessible in the literature and have been the focal point of many researchers. Hence, the oedometer time-dependent response will not be discussed any further.

7.3 Evaluation of the proposed model in triaxial tests

This section investigates the deleterious effect of viscous shear strain on the soil strength. Drained conditions will be assumed corresponding to a constant effective stress field characteristic of pure creep. The capability of the proposed model to simulate the delayed failure mechanism is examined in a well documented case of coal by Debernardi (2008).

The mechanical behavior of coal is considerably different from clay. Considering that several MPa of stress need to be applied for the soil specimen to fail, Debernardi (2008) conducted shearing tests resembling triaxial conditions in a High Pressure Triaxial Apparatus (HPTA) of Polytechnico di Torino depicted in **Figure 7.2**. The apparatus is characterized by a maximum vertical load capacity of 250kN. The specimens tested are cylindrical of either 50mm, 70mm or 100mm in diameter and of height up to 200mm. This means that for the case of the highest diameter of 100mm the maximum vertical pressure that can be applied is 31.83MPa. The HPTA can apply a confining pressure up to 64MPa and interstitial water pressure up to 32MPa.

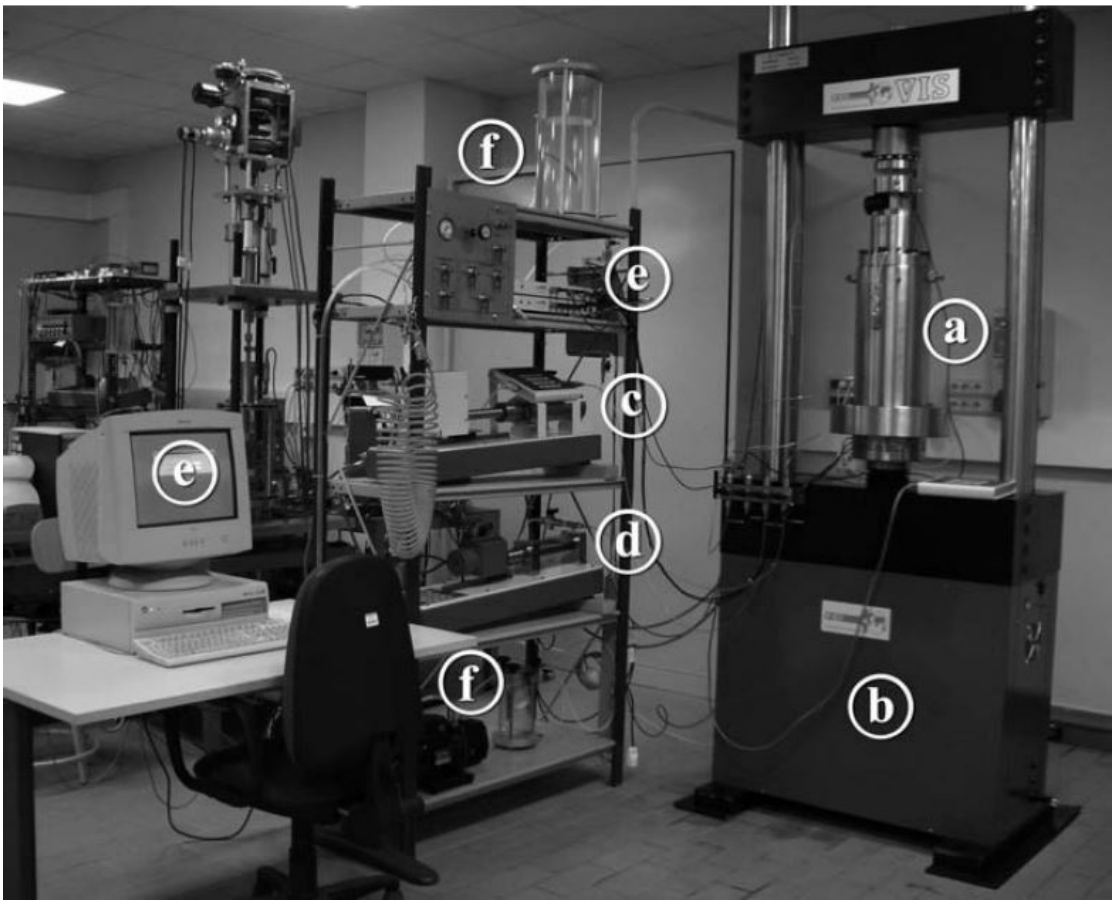

Figure 7.2: High Pressure Triaxial Apparatus employed by Debernardi (2008) (a. triaxial cell; b. load frame; c. cell pressure actuator; d. back pressure hydraulic actuator; e. acquisition and control system; f. hydraulic tank system).

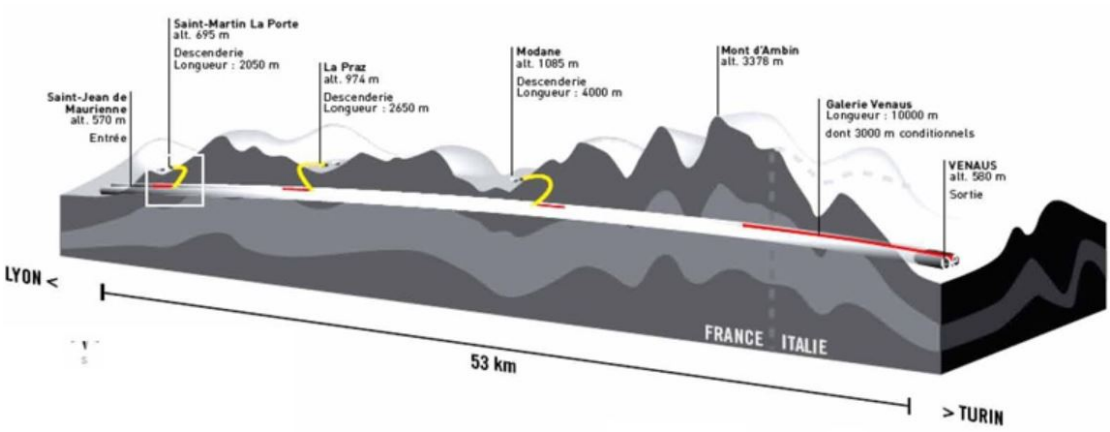

Figure 7.3: General layout of the high speed railway tunnel Torino-Lyon (from Debernardi, 2008).

The rock samples investigated by Debernardi (2008) were extracted from the Saint Martin La Porte access adit along the Torino-Lyon Base tunnel. The Saint Martin La Porte access edit (80m^2 cross section and 2050m in length) comprises one of the three

access adits, on the French side portrayed in **Figure 7.3**. Intact coal samples were extracted from a borehole adjacent to tunnel face. The sample depth is portrayed in **Table 7.2** to clarify the fact that the samples were extracted at significant depths ranging from 400m to 500m and therefore the confining pressure is extremely high.

Table 7.2: Core samples of intact coal extracted (Debernardi, 2008).

Sample	Box	Depth from (m)	Depth to (m)	Length (mm)	Diameter (mm)
A10	178	394.20	394.40	200	85
A11	179	397.40	397.70	300	65
A12	-	398.50	399.00	500	65
A13	-	399.50	400.00	500	65
A15	208	507.40	507.65	250	65
A16	208	508.40	508.80	400	65
A17	208	509.40	510.20	700	65

Table 7.3: Physical and index properties of coal (Debernardi, 2008).

Unit weight	γ	17.29	kN/m^3
Specific weight	G_s	1.99	kg/m^3
Porosity	n	15.94	%
Void ratio	e	0.19	
Water content	w	3.36	%
Degree of saturation	S_r	35.26	%
Liquidity limit	LL	36.21	
Plasticity limit	PL	25.71	
Plasticity index	PI	10.55	
$CaCO_3$ content		0.70	%

The natural properties associated with coal are depicted in **Table 7.3**. Note that the porosity is extremely high resembling a soil rather than rock. Regardless, whether coal cannot be characterized as a conventional soil geomaterial similar to clay the index properties have been determined. They provide no information whatsoever but are simply incorporated for completeness. An elastic Young's modulus of $E = 5GPa$ was selected by Debernardi.

In this section, two multi-stage creep tests are addressed. Experiments A17b and A17a will be examined and the time-dependent response will be simulated. The

creep test A17a in the triaxial apparatus leads ultimately to delayed failure. Hence, it will be a good case study to validate the proposed model.

7.3.1 Creep triaxial experiment A17b

In the experimental study A17b a cylindrical coal specimen of 50.1mm in diameter and 100mm in height is subjected to a multi-stage creep test. Note that in the experimental study the specimen was originally consolidated isotropically at 5MPa and it was left to creep after 3 days (the experiment was stopped due to certain problems with the triaxial apparatus). Afterwards the specimen was compressed isotropically at 10MPa and was left to creep for 21 days experiencing an axial strain of $2*10^{-5}$. The creep strains measured are negligible and tend to a constant value after the first 5days. Thus, solely the subsequent loading steps activating the shear viscous strain will be investigated henceforth.

In the current investigation (it is assumed that) the original state corresponds to the isotropic consolidation state at 10MPa (Point B). The specimen is then loaded until the mean effective pressure reaches p=8.33MPa and the deviatoric stress increases to q=10MPa (Point C). In other words the axial pressure increases while the confining pressure is reduced. The stress path in the s-t diagram (according to the MIT convention) follows a straight line by keeping the s $\left(s=\frac{1}{2}\cdot\left(\sigma_1+\sigma_3\right)\right)$ constant and changing the shear stress t $\left(t=\frac{1}{2}\cdot\left(\sigma_1-\sigma_3\right)\right)$. The specimen is left to creep for 13 days by keeping the stress field constant and afterwards loading is resumed. The final state sets the mean effective pressure to p=7.67MPa and the deviatoric stress to q=14MPa (Point D). A creep stage of 18days follows the loading step to Point D. The simulated loading increments are depicted in **Table 7.4**.

Figure 7.4 portrays the graphical representation of the undergoing stress path along with the simulated response in terms of the axial strain as a function of time. What becomes evident from a careful examination of the predicted mechanical response is the fact that the model fails to represent accurately the primary compression. This is an inherent assumption of the Singh-Mitchell expression focusing solely on the secondary stage.

Table 7.4: Stress path associated with experiment A17b (Debernardi, 2008).

Stress states	p (MPa)	q (MPa)
Point B	10.00	0.00
Point C	8.33	10.00
Point D	7.67	14.00

Stress state C and D lay far from the strength envelope. Hence, the shear stress level denoted D is minimal and therefore the viscous strains do not accumulate in a rapid rate. Consequently, no failure occurs in the specimen associated with time-dependent phenomena. Furthermore, each loading increment is concluded within 36min to minimize any time-dependent effects during the loading phase. Note that while for the lower deviatoric stress C (q=10MPa) the exponential Singh-Mitchell parameter is $m = 0.81$ it shows the tendency to increase to $m = 1.07$ which is characteristic of solely primary compression (**Figure 7.5**). Regardless, whether the experimental values should result in the same exponential parameter m one would assume that higher values of m should be anticipated for the smaller deviatoric stress level, rather than the other way around.

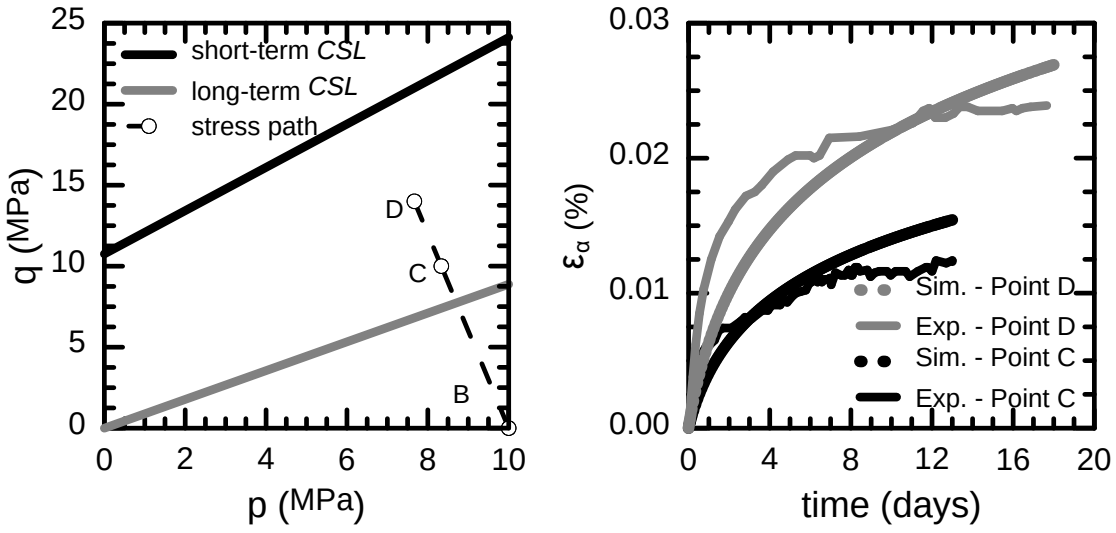

a. b.

Figure 7.4: a. Stress path associated with triaxial experiment A17b and b. simulated response (Sim.) vs. experimental measurements (Exp.) in a diagram of axial strain expressed as a function of time.

Regardless however, of any discrepancies and inconsistencies involved in the experimental data the proposed model performs adequately in this case even though

the primary creep stage cannot be simulated accurately. The constitutive parameters involved in the simulations are portrayed in **Table 7.5**.

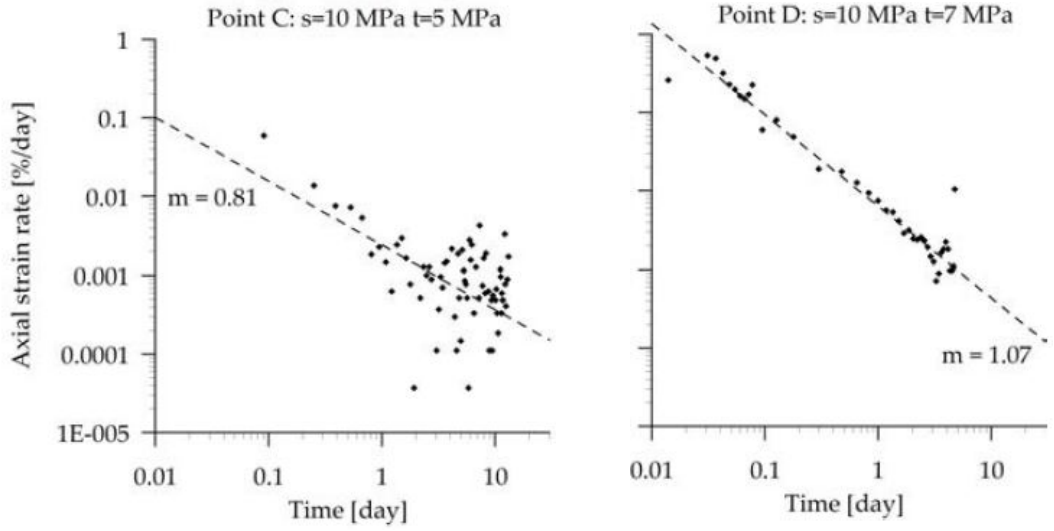

a. b.

Figure 7.5: Strain rate computed for the experiment A17b for the creep phase a. at stress state C (p=8.33MPa & q=10MPa) and b. at stress state D (p=7.67MPa & q=14MPa) (from Debernardi, 2008).

Table 7.5: Constitutive parameters associated with experiment A17b (Debernardi, 2008).

B_0	B_{res}	a^* (MPa)	v	c_{in}	c_{fin}	$2\cdot(G/K)^e$	λ	κ
1	1	12.53	1.19	1.099	0.8736	0.923	0.0042	0.00289
λ^*	γ	d_{in} (MPa)	η_v^p	η_q^p	ζ_v^p	ζ_q^p	θ_q^p	ϑ_q^p
5	1	8.05	75	75	0	0	0	0
t_0 (days)	a_1^v	a_2^v	ψ	A	m	$\bar{a}$	DLIMIT	ξ
1	0	0	2.7E-5	2.7E-5	0.994	4	10^{-6}	0.02

7.3.2 Creep triaxial experiment A17a

In the experimental study A17a a cylindrical coal specimen of 50.1mm in diameter and 100mm in height was subjected to a multi-stage creep test. In the experimental study the specimen was originally consolidated at 20MPa. After 4 days of creep negligible deformations were measured in the specimen. The specimen was then loaded until the mean effective pressure reached p=17.67MPa and the deviatoric stress increased to q=14MPa. In other words the axial pressure increased while the

confining pressure was reduced. The stress path in the *s*-*t* diagram (according to the MIT convention) follows a straight line once again by keeping the *s* constant and changing the shear stress *t*. The specimen was left to creep for 16 days by keeping the stress field constant and afterwards loading was resumed. The following loading increment set the mean effective pressure to p=16.67MPa and the deviatoric stress to q=20MPa. After 50 days of keeping the stress field constant and allowing the specimen to creep the measured strains were negligible (the axial creep strain measured was approximately $2*10^{-5}$-the axial creep strain was even smaller in the previous creep stage of 16 days at a lower shear stress level). Loading was resumed once more thus setting the stress state to a mean effective pressure of p=15.67MPa and the shear stress to q=26MPa. At this point the specimen was allowed to relax for 13 days. The shear stress rebound was 1MPa thus setting the new state to p=15.33MPa and the shear stress to q=25MPa (Point F). Note that the stress drop was experienced rapidly. The stress drop was characterized negligible and consequently the loading was further continued (Debernardi, 2008).

This study assumes that the stress state of origin lays on Point F. In the subsequent loading increments the confining pressure is kept constant at 7MPa while the axial stress increases. The compression is interrupted at stress states G, H, I, J and K and the specimen is left to creep for 3, 3.5, 15 and 13 days respectively. The stress states corresponding to the aforementioned loading steps are portrayed in **Table 7.6**. Note that the specimen exhibits failure attributed to viscous phenomena during the last stage of loading at Point K.

Table 7.6: Stress path associated with experiment A17a (Debernardi, 2008).

Stress states	p (MPa)	q (MPa)
Point F	15.33	25.00
Point G	16.33	28.00
Point H	17.00	30.00
Point I	17.67	32.00
Point J	18.33	34.00
Point K	19.00	36.00

The graphical representation of the undergoing stress path is depicted in **Figure 7.6**. What is also visible in **Figure 7.6** are the experimental measurements expressing the

axial strain ε_a as a function of time. The measurements for the final stage at Point K portraying creep failure will be examined separately considering that the order of magnitude is different. Note that in the experiment there was some technical problem encountered during the first creep stages at Point G and H and the creep stages were stopped after approximately 3 days. Moreover, the fluctuations portrayed in the experimental measurements are attributed to the variation of the temperature inside the laboratory, spiking during the weekend (Debernardi, 2008).

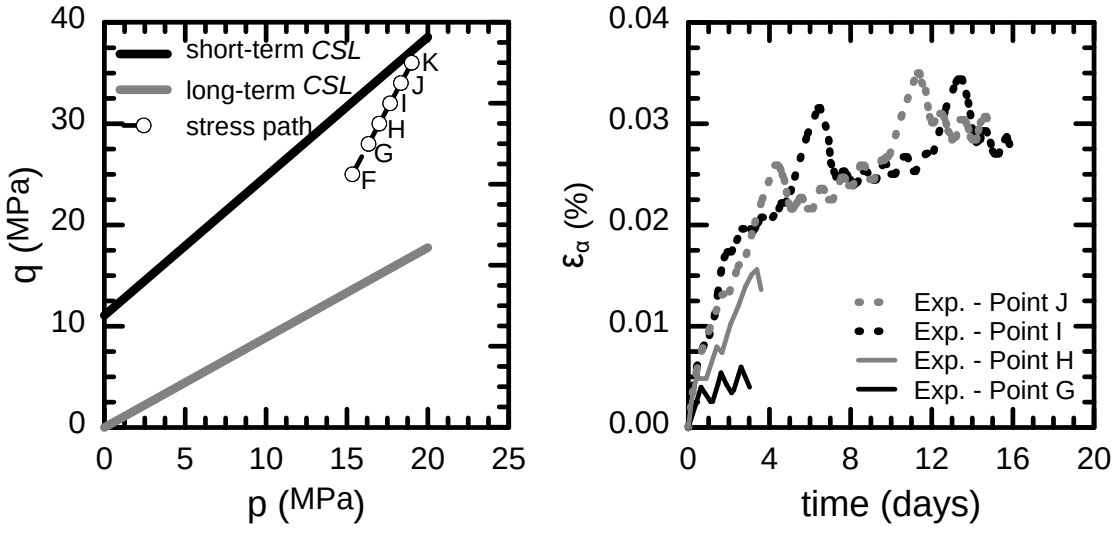

a. b.

Figure 7.6: a. Stress path associated with triaxial experiment A17a and b. experimental measurements (Exp.) in a diagram of axial strain expressed as a function of time at the stress states F, G, I and J.

The simulated response associated with the constitutive parameters portrayed in **Table 7.7** is depicted in **Figure 7.7**. It is obvious that for the lowest value of shear stress level corresponding to state G there is a considerable difference between the predicted and the experimental response in terms of the axial strain (expressed as a function of time). This is attributed to two major factors. There was some technical problem during the first stages and foremost the Singh-Mitchell basis model employed does not aim to simulate the accurately the primary creep stage. The low intensity of the shear stress justifies the statement that the geomaterial experiences solely the primary creep stage since $m = 1.18$ (**Figure 7.8**). In our simulation a mean value $m = 0.994$ of the exponential parameter was selected. Note that each loading increment is concluded within 36min to minimize any time-dependent effect during the loading phase.

For higher shear stress levels **Figure 7.7** reveals a rather elegant convergence between the experimental measurements and the simulated time-dependent mechanical response. Any comparative difference between the experimental data and the simulated response is attributed to the fluctuations due to the increase or decrease of the laboratory temperature.

Table 7.7: Constitutive parameters associated with experiment A17a (Debernardi, 2008).

B_0	B_{res}	a^* (MPa)	υ	c_{in}	c_{fin}	$2\cdot(G/K)^e$	λ	κ
1	1	22.03	1.19	1.099	0.8736	0.923	0.0042	0.00289
λ^*	γ	d_{in} (MPa)	η_v^p	η_q^p	ζ_v^p	ζ_q^p	θ_q^p	ϑ_q^p
5	1	8.05	75	75	0	0	0	0
t_0 (days)	a_1^v	a_2^v	ψ	A	m	$\bar{a}$	DLIMIT	ξ
1	50	2	2.3E-5	4.8E-6	0.994	7	10^{-6}	0.02

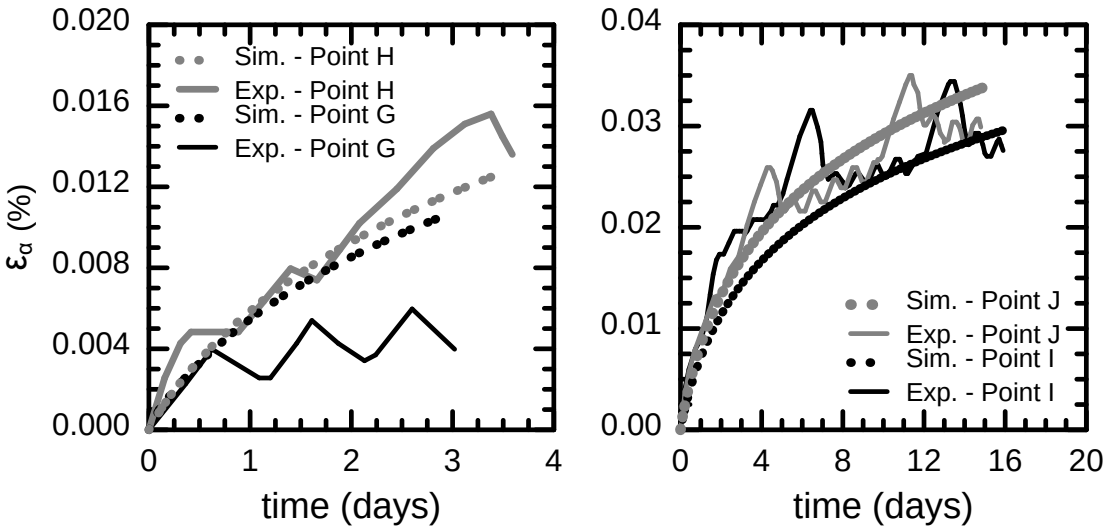

a. b.

Figure 7.7: Simulated response (Sim.) of the axial strain as a function of time compared to the experimental measurements (Exp.) in multi-stage creep test A17a a. at stress states G and H and b. I and J.

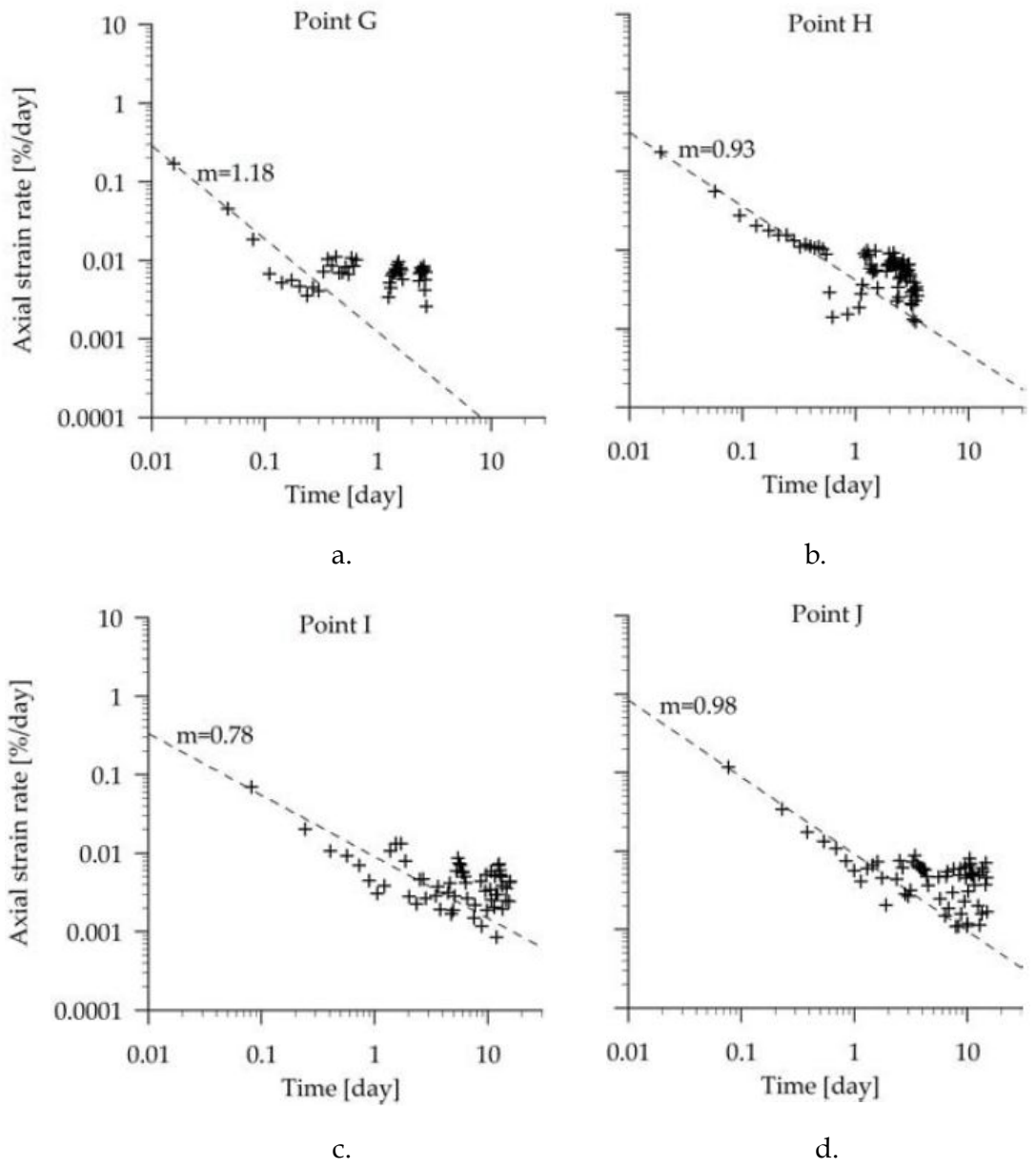

Figure 7.8: Strain rate computed for the experiment A17a for the creep phase at stress state G (p=16.33MPa & q=28MPa), H (p=17MPa & q=30MPa), I (p=17.67MPa & q=32MPa) and J (p=18.33MPa & q=34MPa) (from Debernardi, 2008).

Next, the tertiary creep stage will be investigated associated with stress state K. **Figure 7.9** portrays the simulated response compared to the experimental measurements. What becomes clear from a careful examination of the failure based on the triaxial data is that the coal specimen tends to exhibit brittle failure due to the propagation of the micro-cracking in the sample associated with the undergoing viscous phenomena. The predicted mechanical behavior reveals a rather "ductile" response attributed to the deficiency of the Singh-Mitchell empirical model that fails to simulate accurately the primary creep stage. Considering that it is very difficult to

isolate the primary portion the simulated mechanical behavior, **Figure 7.9** portrays the maximum potential performance of the proposed model in the multi-stage experiment A17a. What is however important to note is that the proposed model can indeed capture delayed failure encountered during the tertiary creep stage. The measured exponential Singh-Mitchell parameter *m* is portrayed in **Figure 7.10**.

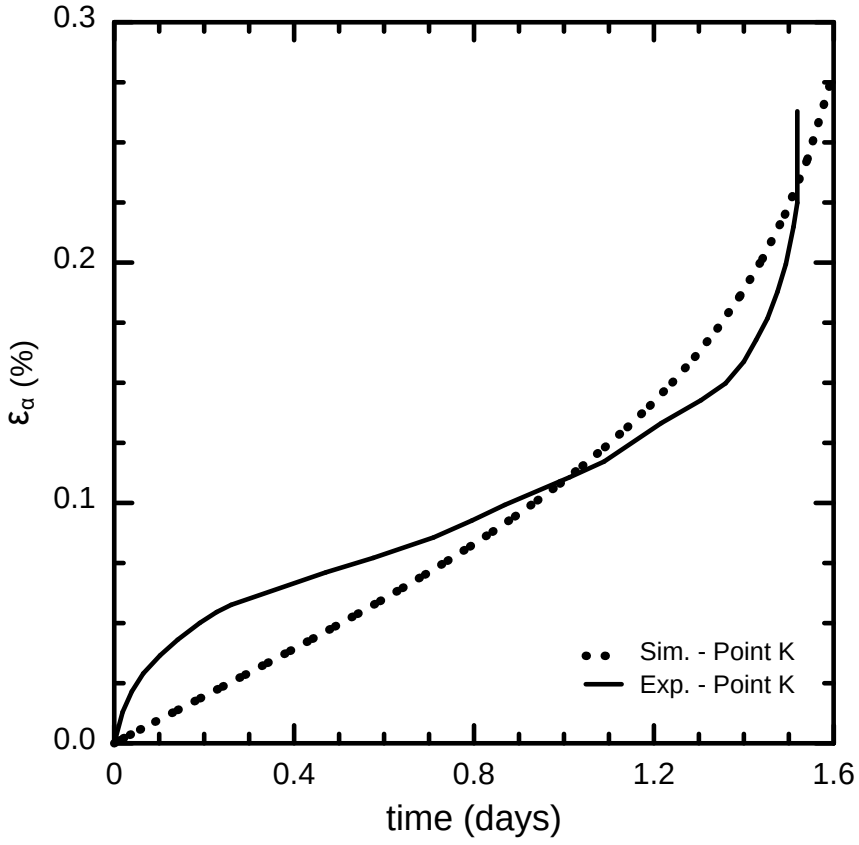

Figure 7.9: Simulated response (dotted line) of the axial strain as a function of time compared to the experimental measurements (solid line) in multi-stage creep test A17a at stress state K portraying delayed failure. The difference portrayed in the beginning of the test is attributed to the significant portion of strain due to loading.

To sum up, the proposed model can capture the elementary mechanisms attributing to delayed failure regardless of any approximations made in the simulated mechanical response. It is noted that the primary creep stage (as was introduced in **Chapter 2**) eludes the purpose of this dissertation. This is an inherent assumption of the Singh-Mitchell and assuming that at some point in the future the need arises for a rather more robust approximation of the creep process the need for a more elegant empirical relation is evident. However, any new empirical formulation needs to be founded on the abundance of experimental measurements and a good understanding of the physical process during creep.

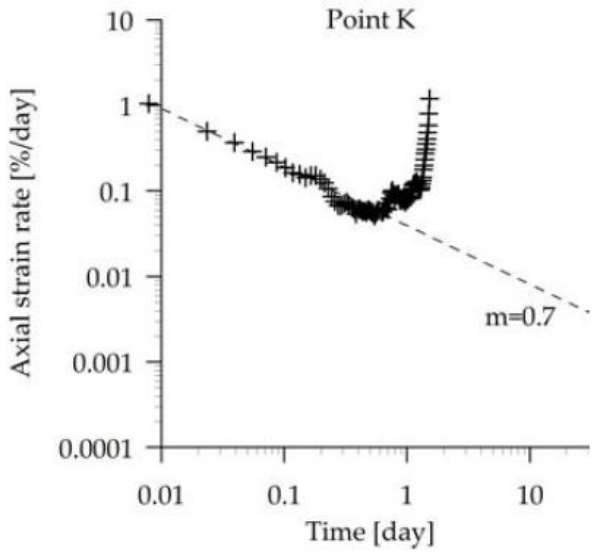

Figure 7.10: Strain rate computed for the experiment A17a for the creep phase at stress state K (p=19MPa & q=36MPa) portraying delayed failure (from Debernardi, 2008).

7.4 Investigation of the Singh-Mitchell parameters

The effect of the Singh-Mitchell constitutive parameters has not been considered this far within the context of the current dissertation. The effect of the Singh-Mitchell parameters is investigated next, in the aforementioned experimental study in order to use the computed parameters simulating the experimental data as a common denominator for the parametric investigation. The time-dependent mechanical response at stress point J (in the multi-stage test A17a) will be examined henceforth.

7.4.1 Effect of Singh-Mitchell parameter *A*

The Singh-Mitchell parameter A does not solely control the initial slope but shifts the secondary creep stage at higher axial strain levels, as depicted in **Figure 7.11** . Hence, elevated values of the parameter A result in the axial strain to transition higher in the axial strain vs. time diagram. Note that, all the remaining parameters involved remain constant.

Consequently, the deviatoric creep strains tend to accumulate rapidly thus resulting in a faster transition of the current *CSL* towards its residual state. It is noted that the strains are very small and the constitutive parameter employed is equally low (depicted in **Table 7.7**) for the specimen to portray delayed failure at the current shear stress ratio.

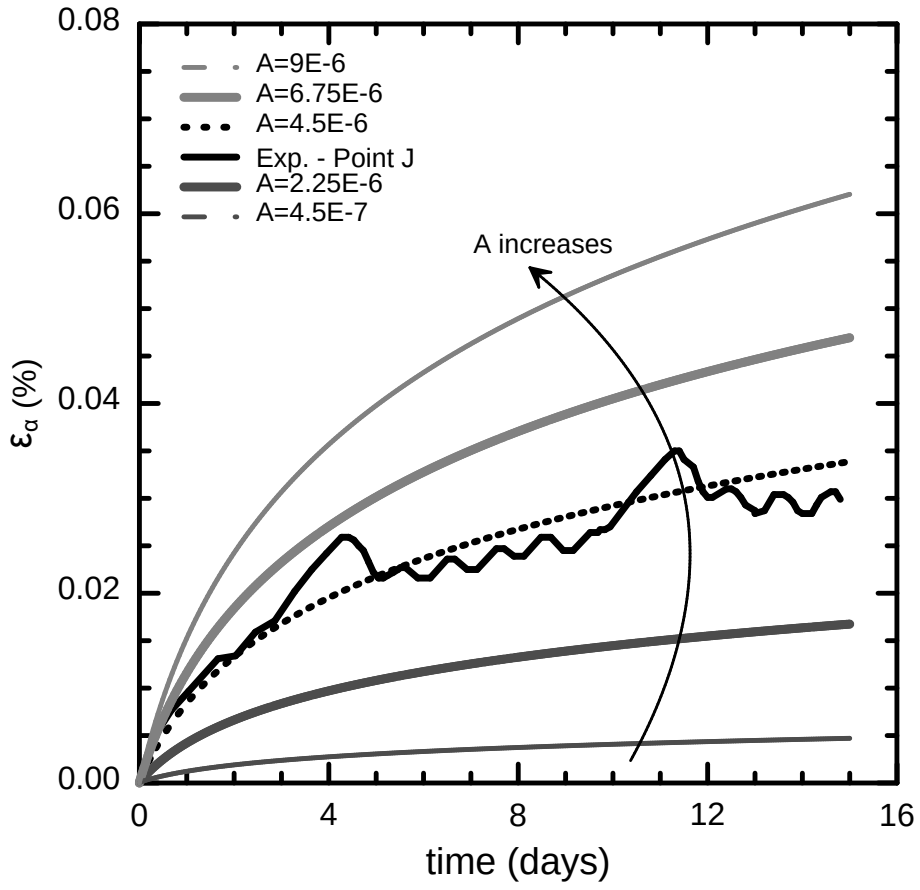

Figure 7.11: Parametric investigation of the Singh-Mitchell parameter A in the experiment A17a for the creep phase at stress state J (the experimental measurements are portrayed through the solid black line).

7.4.2 Effect of the Singh-Mitchell parameter $\bar{a}$

The constitutive parameter $\bar{a}$ involved in expression (5.20) is investigated in the same experimental study as before at the stress point J (experiment A17a). Once again all the other constitutive parameters remain intact in order to investigate the effect of $\bar{a}$. The exponential parameter appears to control both the initial slope and the strain level at which secondary creep stage occurs. Elevated values of the parameter $\bar{a}$ shift the strain response in the ε_a - t diagram higher (**Figure 7.12**).

Consequently, the deviatoric creep strains accumulate at a faster pace resulting in a more rapid transition of the current *CSL* towards the long-term *CSL*. Note, that the strains are minimal and the constitutive parameter employed is equally low (depicted in **Table 7.7**) for the specimen to exhibit delayed failure at the current shear stress ratio D.

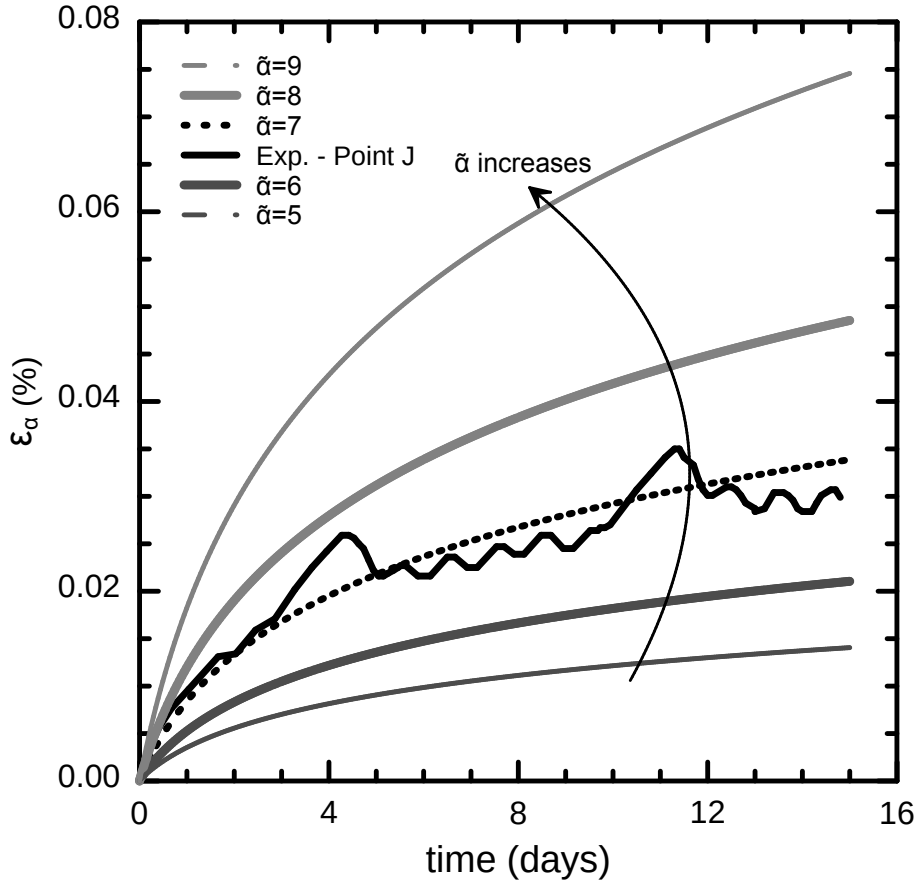

Figure 7.12: Parametric investigation of the Singh-Mitchell parameter $\tilde{a}$ in the experiment A17a for the creep phase at stress state J (the experimental measurements are portrayed through the solid black line).

7.4.3 Effect of the Singh-Mitchell parameter *m*

The effect of the constitutive parameter *m* involved in expression (5.20) is studied in the same experimental study at the stress point J (experiment A17a). All the remaining constitutive parameters remain constant in order to investigate solely the effect of *m*. The parameter *m* appears to control the strain level at which secondary creep stage occurs. Lower values of the parameter *m* transposes the strain response in the ε_a - *t* diagram higher (**Figure 7.13**).

Note that all values investigated are smaller than unity. A careful examination of the expression (5.21) reveals that the denominator involves $(1-m)$ which becomes negative once the parameter *m* becomes greater than 1. The physical meaning lies on the inherent assumption of the Singh-Mitchell parameter simulating solely the secondary creep stage. This summarizes the reason for the Singh-Mitchell guideline for the selection of parameter *m* to lay somewhere within the region of $m \in [0.75,1]$.

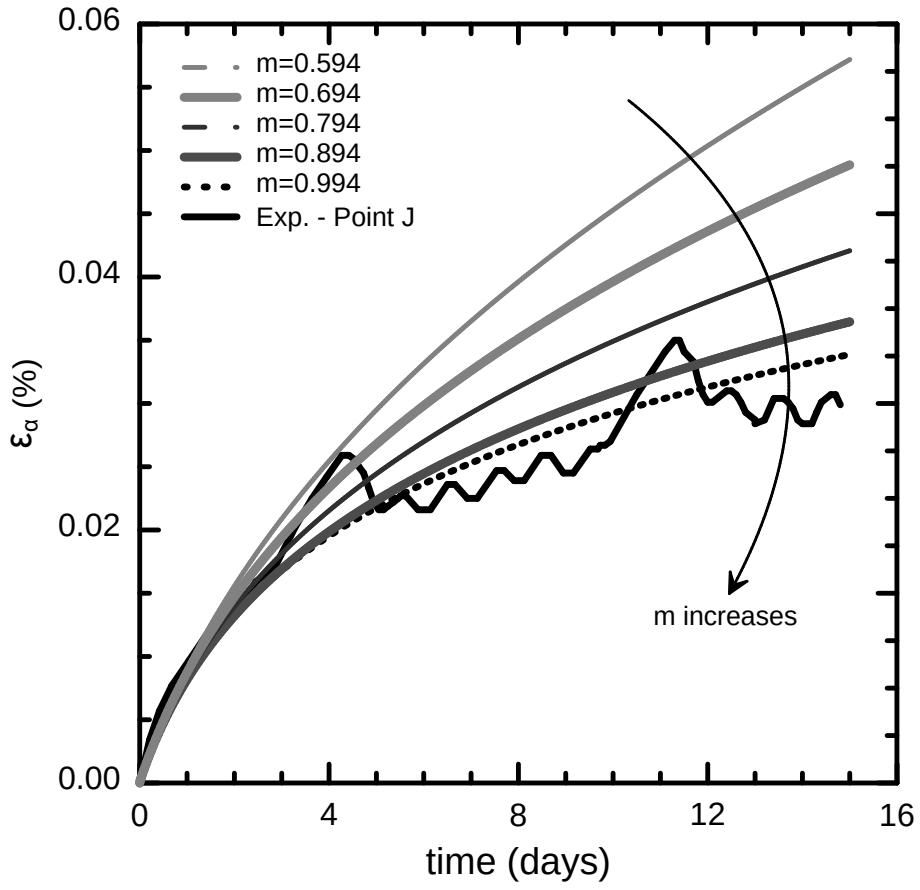

Figure 7.13: Parametric investigation of the Singh-Mitchell parameter *m* in the experiment A17a for the creep phase at stress state J (the experimental measurements are portrayed through the solid black line).

7.5 Concluding remarks

The current chapter evaluates the proposed model against experimental measurements both in the oedometer and in the triaxial apparatus. The secondary compression coefficient comprises a well established quantity in the literature and has long been the focal point of numerous studies. Hence, the time-dependent response in an oedometer test was portrayed in a natural soft clay specimen resembling the mechanical response of a peat. It was shown that the proposed model converges to the exact same mechanical response with the experimental measurements. Selection of the case study was not random considering that the highest discrepancy that could be potentially encountered would prove at such a soft geomaterial.

Next, the mechanical response was examined in an experimental study of coal in the triaxial apparatus. A thorough literature review revealed only a limited number of

publications addressing the drained time-dependent response of clay with the last one dating back to 1975 (Bishop, 1966; Ter-Stepanian, 1975). The reason lies with the considerable time period required for the specimen to fail in creep. The time interval required for failure to occur may exceed 200 days and even reach 1,000days. It is evident, that such experiments are very difficult to conduct with so many potential parameters that could potentially affect the soil response. Simply consider the fluctuations involved in Debernardi's measurements with just a slight increase of temperature of no more than a few degrees Celsius, not considering any chemical or biological transformations that could potentially affect the soil specimen by transforming the soil fabric (i.e. considering the static nature of the interparticle water fungus might develop thus resulting in the formation of chemical bonding).

Therefore it was necessary to examine the time-dependent response of another geomaterial. The research focused in the investigation of the mechanical response on coal in a well documented case where the multi-stage creep tests permit simulation of the time-dependent response at different shear stress levels. Delayed failure was portrayed in a specimen subjected to a high stress level and was simulated by incorporating the proper constitutive parameters.

Regardless of any logical approximations made in the definition of the governing equations of the proposed model or some discrepancy involved in the experimental measurements the proposed model performs relatively well. It is noted, that the proposed model fails to capture the primary creep stage by focusing on the secondary creep stage. This is an inherent approximation of the Singh-Mitchell empirical relations comprising the foundation stone of the model.

8

Application in slope stability analysis

8.1 General

This Chapter applies the proposed model in a 2D slope stability analysis via the finite element method (using the computer program ABAQUS). The proposed model is used to describe the time-dependent soil response in a slope that can potentially lead to delayed failure by activating the deleterious effects of viscous shear strain on soil strength.

The analysis starts by exhibiting the deficiency of time-independent elastoplastic constitutive models for structured soils to simulate slope instability (e.g. the models proposed by Kavvadas and Amorosi; 2000; Belokas; 2008). Such models attempt to capture the slope instability mechanism through plastic softening, either due to structure degradation or via strength envelope evolution associated with plastic strains. Considering that time-independent models have no control on the magnitude of the plastic strains (which can trigger the above failure mechanisms) it was proven difficult to capture failure in such a way. On the contrary, time-dependent behavior permits the temporal accumulation of inelastic strains (plastic and creep) in highly stressed zones and thus permits the description of progressive failure in the analyzed slope. The analyses show that the proposed model has the capabilities to predict delayed failure of a slope by triggering tertiary creep and a retrogressive slope instability mechanism.

As mentioned above, it was first attempted to investigate the onset of slope instability without invoking the time-dependent characteristics of the model, i.e., by using only the plastic-strain induced structure degradation characteristics of the model. Following that, this chapter focuses on creep induced slope instability by

examining three cases (all under fully-saturated conditions: a first case where the incorporated parameters lead to immediate failure; a second case where the slope reaches initial equilibrium but fails with evolving time and finally a third case where the slope continuously creeps comprising a characteristic case study of the secondary creep stage). Finally, the difference in the mechanical response assuming saturated and dry conditions is outlined.

8.2 Deficiency of the inviscid elastoplastic approach

This section studies the shortcoming of the elastoplastic approach in predicting delayed failure by consolidation even using models including inviscid structure degradation. The proposed model incorporates several features to simulate significant strain softening in the measured mechanical response. Structure degradation and strength envelope evolution may be employed independently or simultaneously to introduce plastic softening. The current subchapter focuses on the simulated response associated with strength envelope evolution due to plastic strains.

The geometrical characteristics of the selected ideal slope are depicted in **Figure 8.1**. An original slope $40m$ in height is assumed at an inclination of approximately 20˚. Afterwards the toe is excavated and the slope is either left to creep (assuming that the viscous characteristics of the model are activated) or it is simply allowed to consolidate (thus plastic strains develop that could potentially lead to failure). The excavation of the final cut assumes an inclination of 45˚. Regardless, whether there are confinement issues stemming from the close proximity of the selected boundaries the problem is employed solely to examine qualitatively the mechanical response. Assuming that a back analysis is undertaken in the future the boundaries might need to be further translated to the far field.

8 node plane strain elements (either CPE8 or CPE8P to account for pore pressures) are employed in the numerical analyses. The total number of elements is 7,876 and the associated number of nodes is 24,029. The Commercial Finite Element Code Simulia Abaqus is employed to solve the numerical problem at hand.

Next follow the initial state and following excavation stages portrayed in **Figure 8.2**:

- **Geostatic step** (Figure 8.2a.): The structureless soil elements are originally consolidated isotropically, considering that the selected coefficient of lateral pressure is $K_0 = 1$ (the selected OCR=3). In the case where the elements are assumed to be fully saturated, the water table coincides with the soil surface (at all times). The initial step is undertaken to establish equilibrium between the initial values and the calculated stress state. The time period of this step is fixed and equal to 1day (note that the geostatic step is followed by a consolidation step of 80 days to assure steady state conditions assuming water is present).
- **Excavation of the initial slope** (Figure 8.2b.): The elements are removed to construct the initial slope. The excavation is concluded within $\Delta t = 10$ days (note that the excavation of the initial slope is followed by a consolidation step of 140 days to assure steady state conditions assuming water is present).
- **Excavation of the final cut** (Figure 8.2c.): The toe is removed to construct the final slope. The excavation is concluded within $\Delta t = 0.5$ days (note that the excavation of the toe is followed by a consolidation step until steady state or failure assuming water is achieved).

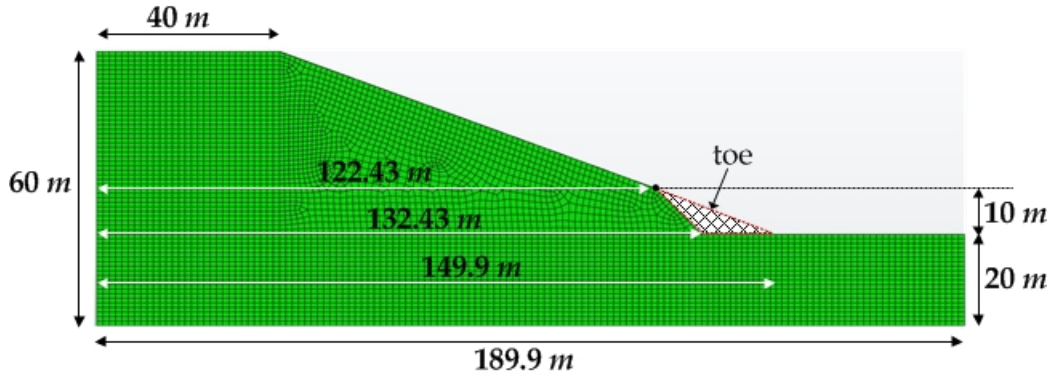

Figure 8.1: Geometrical characteristics of the investigated slope.

Assuming dry conditions and no creep involved in the mechanical response then the duration of the excavation steps is irrelevant considering the inviscid nature of the problem. The constitutive parameters associated with the elastoplastic response of this section are depicted in **Table 8.1**.

Note that the selected saturated unit weight $\gamma_{sat} = 20\,kN/m^3$ is constant leading to a variable ρ_s with depth. The compressibility coefficient λ was set equal to $\lambda = 0.0869$ characteristic of a virgin compressibility index $C_c = 0.2$. The poroelastic

coefficient κ was selected as a fraction of λ (10%). Finally, the inclination of the *CSL* projection in the stress space transitions from $c_{in} = 0.9798$ (characteristic of an effective friction angle $\varphi' \approx 30^{\circ}$) to $c_{res} = 0.3068$ (characteristic of an effective friction angle $\varphi' \approx 10^{\circ}$). In this section, in order to disregard any time-dependent associated response the reference time t_0 was set equal to 100,000days.

Table 8.1: Constitutive parameters associated with elastoplastic response of the proposed model.

B_0	B_{res}	OCR	N^*_{iso}	c_{in}	c_{fin}	$2\cdot(G/K)^e$	λ	κ
1	1	3	2.2	0.9798	0.3068	0.75	0.0869	0.00869
λ^*	γ	d_{in}	η^p_v	η^p_q	ζ^p_v	ζ^p_q	θ^p_q	ϑ^p_q
5	1	0	50	50	0	0	12	12
t_0 (days)	$a^v_1 = a^v_2$	ψ	A	m	$\bar{a}$	γ_{sat} (kN/m^3)	ξ	k (m/s)
10^5	0	1.E-9	5. E-6	0.8	2.5	20	0.02	10^{-8}

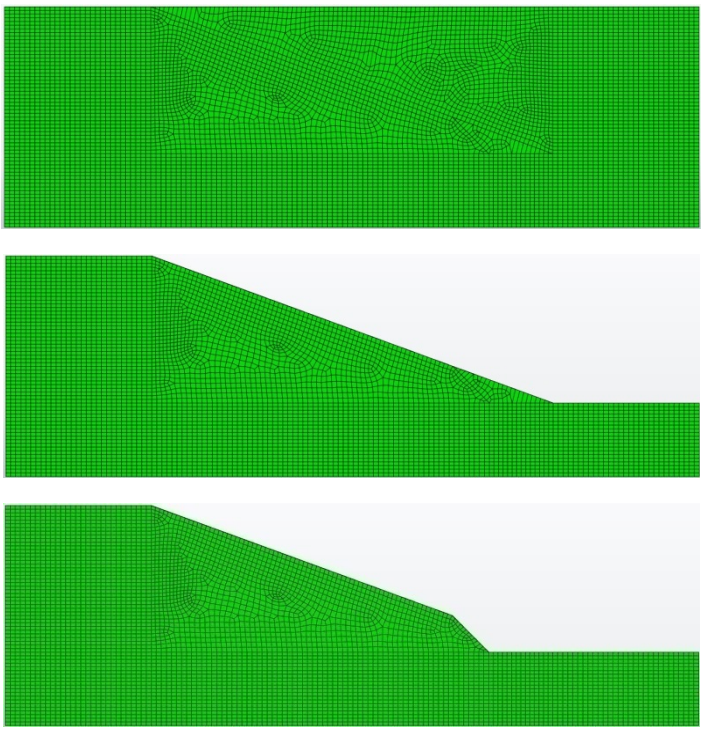

a.

b.

c.

Figure 8.2: Schematic representation of the initial state and the following excavation steps: a. geostatic step; b. excavation of the initial slope and c. excavation of the final cut.

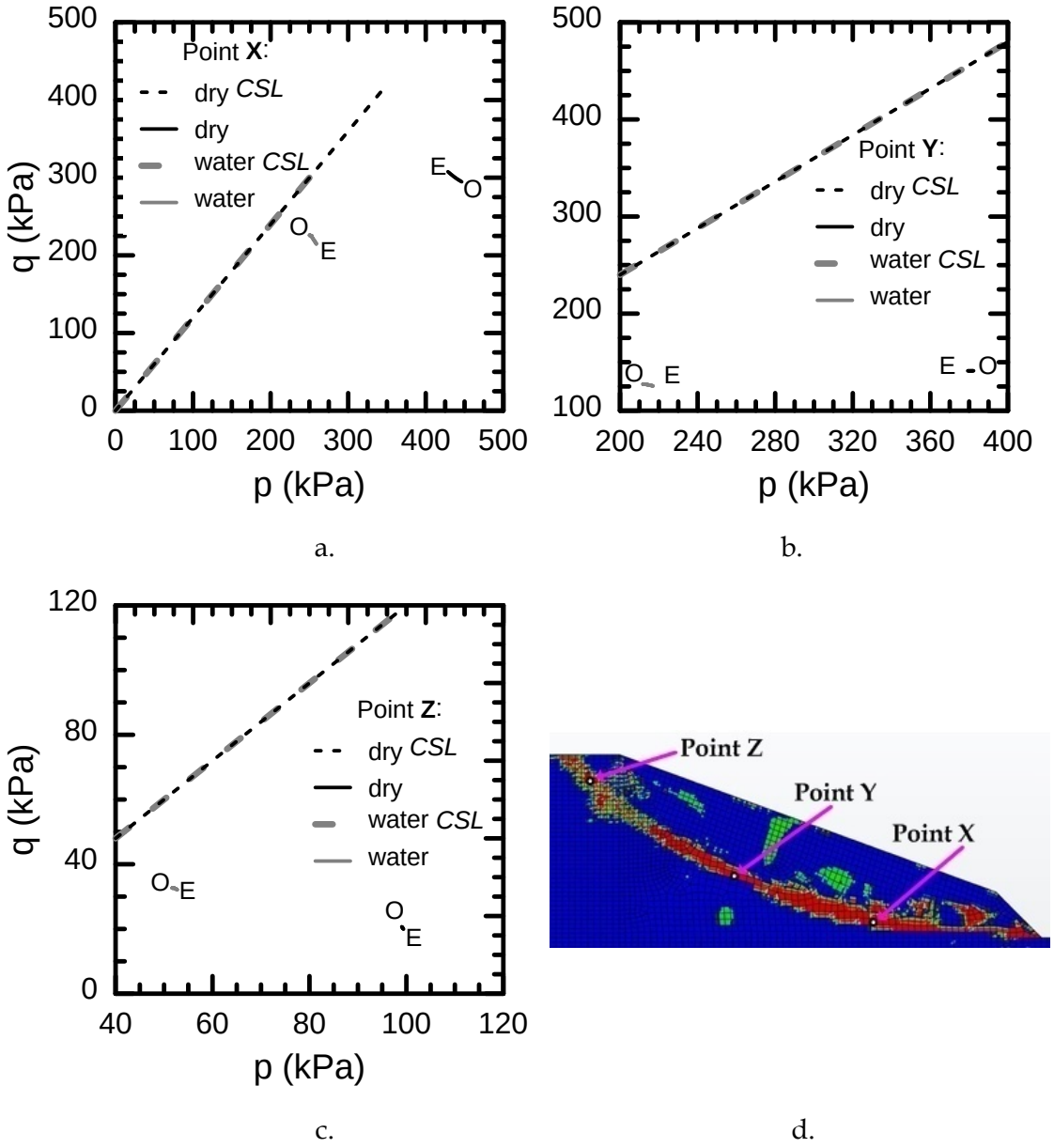

a. b. c. d.

Figure 8.3: Stress paths depicted in the *p-q* space and associated *CSL* lines assuming that the strength envelope evolves due to plastic strains (Points X, Y and Z portrayed in Figure 8.3d refer to a creep analysis to be summarized in an upcoming section 8.3.2 – aiming to provide comparable results at the same stress points): a. saturated (water) and dry soil response at point X; b. saturated and dry response at point Y and c. saturated and dry response at point Z (from O to E).

Figure 8.3 compares the saturated and dry response of the slope characterized by the constitutive parameters depicted in **Table 8.1**. Results are depicted at the centroid of three elements represented by Points X, Y and Z in **Figure 8.3d**. Note that **Figure 8.3d** does not refer to the elastoplastic response examined in this section but is characteristic of a creep induced failure to be portrayed below. However, results are portrayed referring to the exact same points to allow for a comparative examination

of the simulated behavior. The stress paths in the **Figure 8.3** originate from O (denoting the Origin) and transition to E (denoting the End - portraying either failure or steady state). The stress path corresponding to the dry situation originates at the beginning of the excavation of the final slope (Point O). As for the saturated case results are shown both on the excavation step of the toe (0.5 days) and for the subsequent consolidation step (39days).

A rather brief glance at the results above reveals that the inclination of the *CSL* is almost equal to the initial. This means that the analysis either does not exhibit significant plastic strains or that elements close to the surface fail, thus leading to unconverged increments in the Finite Element analysis. Note that, the selection of a constitutive parameter $\theta_q^p > 12$ would lead to failure at the excavation step of the toe and not during the subsequent consolidation step as it was envisioned. However, the increase of maximum displacement of 3.5cm in the case of the saturated slope examined (**Figure 8.4**) and 1cm assuming dry conditions (**Figure 8.5**) cannot be characterized as failure. The excess porewater pressures generated in the case of the saturated slope is less that 5% of the original and thus will not be portrayed.

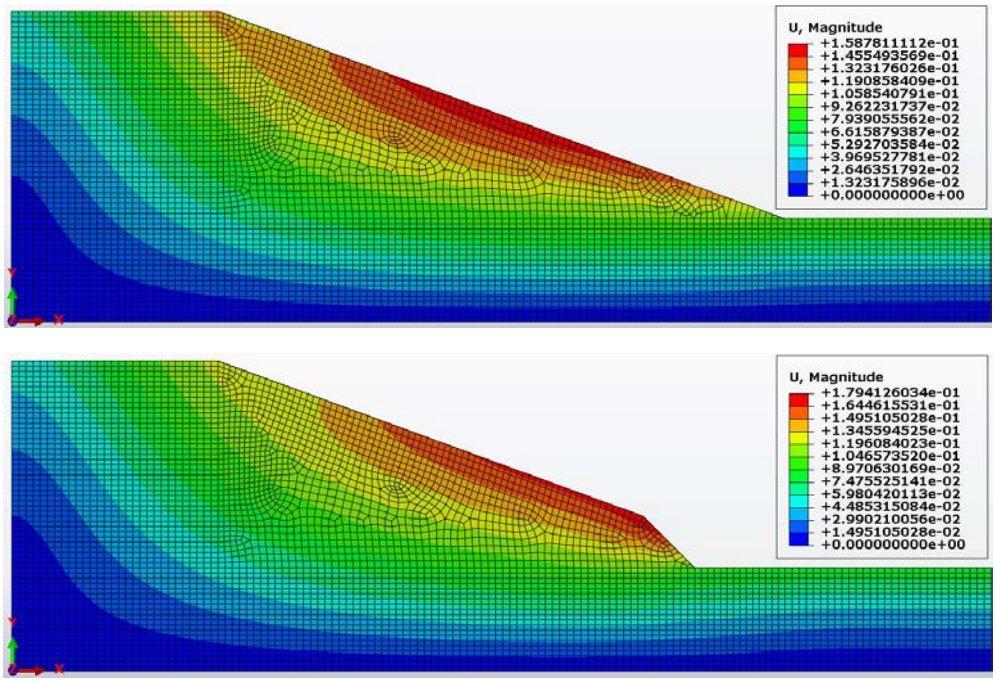

Figure 8.4: Displacement magnitude U (*m*) at saturated conditions (water) (assuming strength envelope evolution occurs solely due plastic strains): a. before the excavation of the toe and b. after the excavation of the final cut and the subsequent consolidation step for 39 days.

What is to be concluded from the investigation of the elastoplastic mechanical response of the proposed mode lies with the difficulty to control the strength envelope evolution due to the accumulation of plastic strains. The plastic strains are associated to the stress field. Considering however that the stress field is more or less fixed (certainly for the initial and the excavation of the final slope - but not during the consolidation process) this means that the plastic strains are imposed by the physical problem. Here lies the fundamental problem associated with the deficiency of the elastoplastic response of the proposed model in the slope instability problem at hand.

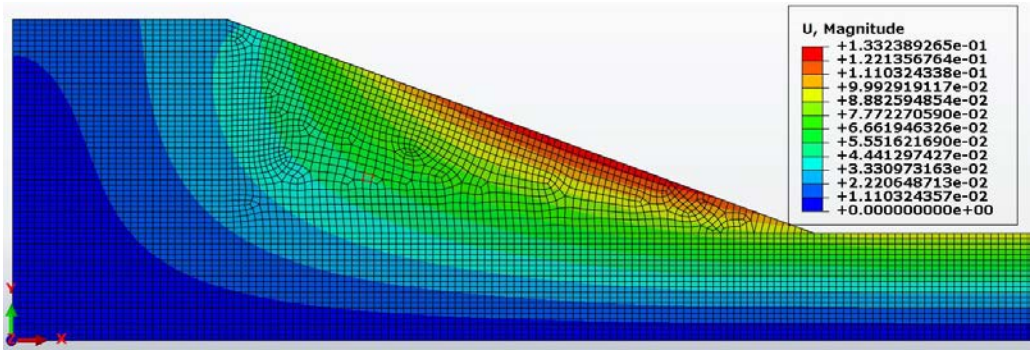

a.

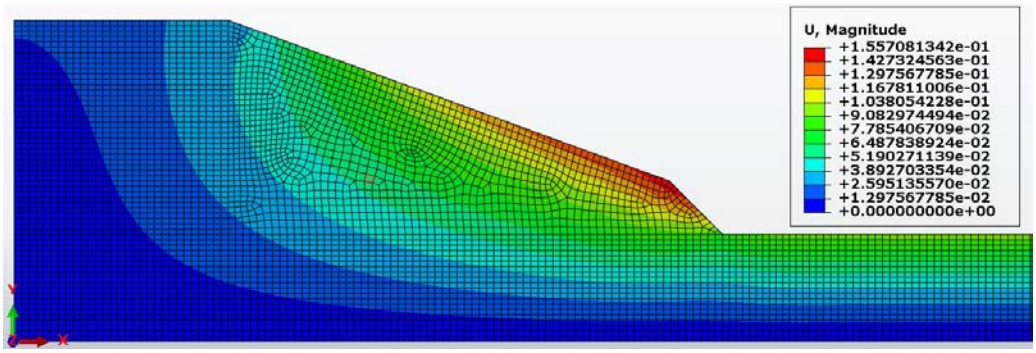

b.

Figure 8.5: Displacement magnitude U (m) at dry conditions (assuming strength envelope evolution occurs solely due plastic strains): a. before the excavation of the toe and b. after the excavation of the final cut.

8.3 Creep induced slope instability

This section addresses the time-dependent mechanical response leading to slope instability. The elastoplastic characteristics of the model could not reveal the deleterious effects on soil strength associated with softening. The plastic strains cannot be controlled and therefore it is impossible to trigger retrogressive slope instability propagating from the toe to the crest (note that the process of retrogressive slope instability will be examined here below) without changing the initial geometric

configuration (or accordingly transform the initial and residual inclinations of the *CSL* in the stress space).

Next, slope stability is investigated in namely three individual cases. A situation where the excess porewater pressures dissipate is assumed followed by the accumulation of viscous strains leading ultimately to delayed failure under saturated conditions. This example will serve as a common denominator for the current chapter. All results will be portrayed with respect to the aforementioned case study. The other two cases reveal either the stationary component of creep after approximately 5,500days (approximately 15years) or failure at very short consolidation times. Hence, the current subchapter focuses on the capability of the model to accurately simulate the retrogressive slope instability mechanism and on the versatility of the constitutive framework to account for media that tend to fail after considerable times.

Finally, saturated conditions prove to be the key activating the retrogressive instability mechanism. Saturated conditions do not simply attribute to failure; they dominate the overall mechanical response. It is noted that in the current chapter the term saturated is employed to denote the presence of water while dry conditions refer to the complete absence of such. The reason for not incorporating the term "drained" lies with the formation of shear banding at failure forming the distinct slip line, designating undrained conditions along the failure surface.

The saturated inviscid mechanical response of the excavated cut needs to be examined prior to investigating the comparative effect of creep on the simulated soil response. Hence, it is essential to establish that the consolidation following the excavation of the toe reaches the steady state and the associated displacements are relatively small.

8.3.1 Saturated inviscid elastoplastic slope response

The inviscid elastoplastic response of the slope after the excavation of the toe is examined in this section. The strength envelope is not allowed to evolve towards the residual state and is thus kept constant to $c = c_{in} = 0.9798$ (characteristic of an effective friction angle of $\varphi' = 30^{\circ}$).

Here follow the simulated excavation stages and consolidation steps:

- **Geostatic step** (Figure 8.2a.): The structureless soil elements are originally consolidated isotropically, considering that the selected coefficient of lateral pressure is $K_0 = 1$ (the selected OCR=3). The water table coincides with the soil surface (at all times). The initial step is undertaken to establish equilibrium between the initial values and the calculated stress state. The time period of this step is fixed and equal to 1 day.
- **Consolidation step**: A consolidation step of 80 days is sustained to assure steady state conditions (note that the permeability is equal to $k = 10^{-8} m/s$).
- **Excavation of the initial slope** (Figure 8.2b.): The elements are removed to construct the initial slope. The excavation is assumed to be concluded within $\Delta t = 10$ days.
- **Consolidation step**: A consolidation step of 140 days is imposed to assure steady state conditions.
- **Excavation of the final cut** (Figure 8.2c.): The toe is removed to construct the final slope. The excavation is assumed to be concluded within $\Delta t = 0.5$ days.
- **Consolidation step**: A consolidation step is undertaken until steady state is attained after $\Delta t = 27.25$ days (note that the steady state was attained until the rate of porewater change in all nodes was lower than 0.4kPa/day when the maximum porewater pressure sustained in the model is 600kPa).

The associated stress paths are depicted in **Figure 8.6** in the *p-q* space. The stress paths originate from O (designating the origin-characteristic of the initial slope) transition to A (denoting the excavation of the toe after 0.5days) and consolidate to E (designating the end of the consolidation process following the excavation of the final cut (the toe). Note that the stress paths always lay beneath the *CSL* projection in the stress space. The selected elements portraying the simulated behavior refer to highly overconsolidated states (note that solely the elements along the slope may lay on the wet side) and thus, it is evident that no failure occurs. Once again results are depicted at the exact same points (X, Y and Z) as before. The stress paths appear similar as in the previous case (considering that the *CSL* at such points hadn't evolved in the previous case and that the elements lay relatively far from the slope to be affected through the continuity condition).

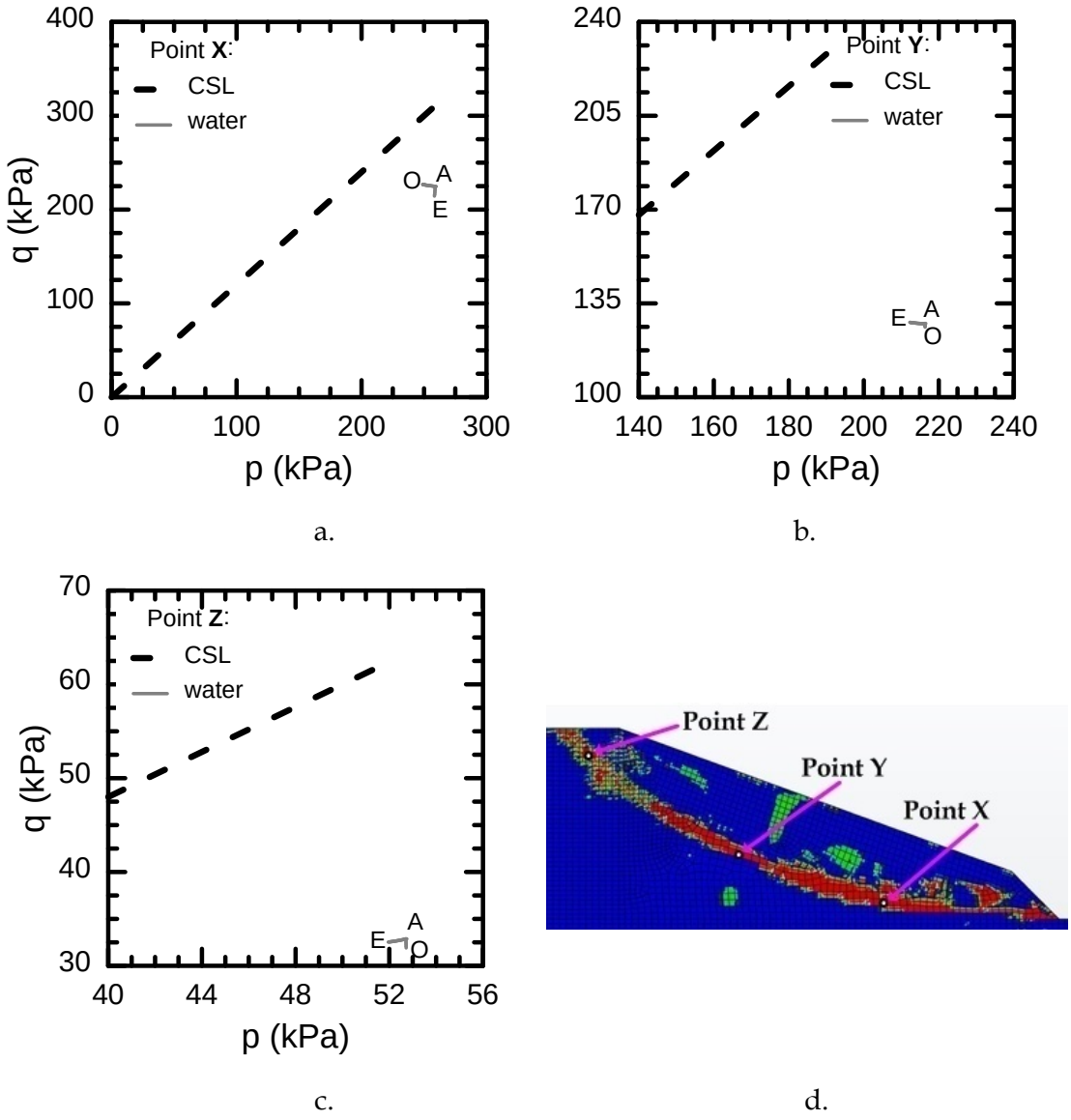

Figure 8.6: Saturated (water) soil response depicted through stress paths in the *p-q* space and associated *CSL* lines assuming that the strength envelope does not evolve (Points X, Y and Z portrayed in Figure 8.6d refer to a creep analysis to be summarized in an upcoming section 8.3.2): a. at point X7; b. at point Y and c. at point Z (from O to A and finally to E).

The associated displacement fields before the excavation and after the consolidation step reaching steady state are summarized in **Figure 8.7**. Note that the highest displacement magnitude increase is measured at the intersection point of the initial slope and the final cut (3.46cm). **Figure 8.8** portrays the pore pressure contour plots before the excavation of the final slope and after the steady state has been attained. It is evident that equilibrium was reached and the pore pressures have consolidated. It is emphasized that proper porewater pressure boundaries have been placed in the far field emulating hydrostatic conditions. Considering that the change in pore pressures is negligible at points X, Y and Z, the associated pore pressure diagrams

are not included. Concluding, considering how the pore pressures reach steady state and the displacement field is relatively low there is no evidence to support failure.

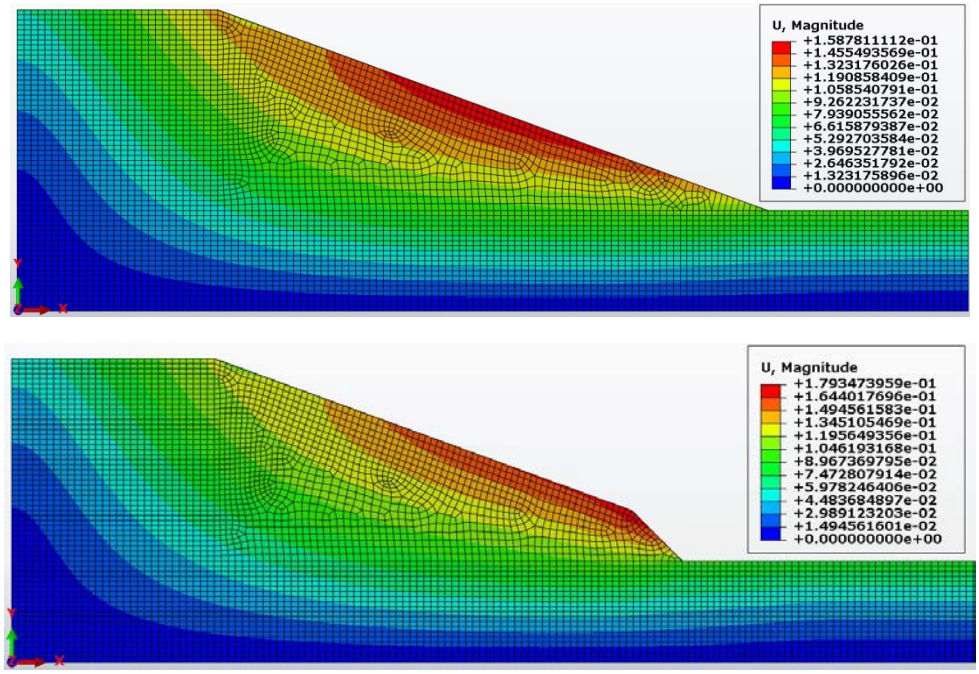

Figure 8.7: Displacement magnitude U (*m*) at saturated conditions (water) (assuming that the strength envelope does not evolve): a. before the excavation of the toe and b. after the excavation of the final cut and the subsequent consolidation step for 27.25 days.

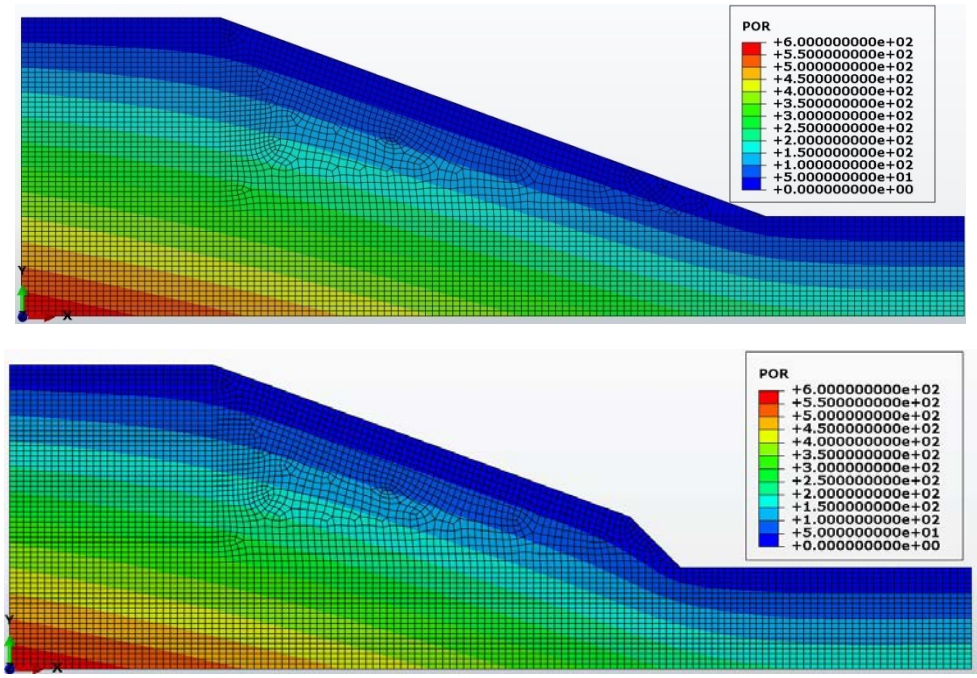

Figure 8.8: Porewater pressures POR (kPa) at saturated conditions (water) (assuming that the strength envelope does not evolve): a. before the excavation of the toe and b. after the excavation of the final cut and the subsequent consolidation step for 27.25 days.

8.3.2 Creep induced slope instability

The time-dependent response leading to delayed failure after the excavation of the toe is investigated in this section. The strength envelope is allowed to evolve from the short-term ($c_{cs} = 0.9798$ characteristic of an effective friction angle of $\varphi' = 30^{\circ}$) to the long-term *CSL* inclination ($c_{LT} = 0.3068$ characteristic of an effective friction angle of $\varphi' \approx 10^{\circ}$). The associated constitutive parameters are portrayed in **Table 8.2**.

Table 8.2: Constitutive parameters associated with the creep induced slope instability (paragraph 8.3.2).

B_0	B_{res}	OCR	N^*_{iso}	c_{in}	c_{fin}	$2\cdot(G/K)^e$	λ	κ
1	1	3	2.2	0.9798	0.3068	0.75	0.0869	0.00869
λ^*	γ	d_{in}	η^p_v	η^p_q	ζ^p_v	ζ^p_q	θ^p_q	ϑ^p_q
5	1	0	50	50	0	0	0	0
t_0 (days)	$a^v_1 = a^v_2$	ψ	A	m	$\bar{a}$	γ_{sat} (kN/m^3)	ξ	k (m/s)
231.5	10^3	1.E-9	5. E-6	0.8	2.5	20	0.02	10^{-8}

Here follow the simulated excavation stages and consolidation steps:

- **Geostatic step** (Figure 8.2a.): The structureless soil elements are originally consolidated isotropically, considering that the selected coefficient of lateral pressure is $K_0 = 1$ (the selected OCR=3). The water table coincides with the soil surface (at all times). The initial step is undertaken to establish equilibrium between the initial values and the calculated stress state. The time period of this step is fixed and equal to 1 day.
- **Consolidation step**: A consolidation step of 80 days is sustained to assure steady state conditions.
- **Excavation of the initial slope** (Figure 8.2b.): The elements are removed to construct the initial slope. The excavation concluded within $\Delta t = 10$ days.
- **Consolidation step**: A consolidation step of 140 days is assumed to assure steady state conditions.
- **Excavation of the final cut** (Figure 8.2c.): The toe is removed to construct the final cut. The excavation concluded within $\Delta t = 0.5$ days.

- **Consolidation step**: A consolidation step is undertaken until failure. The reference time was selected equal to $t_0 = 231.5$ days as to kick in at the initiation of this step. Hence, consolidation and creep are sustained simultaneously. Failure occurs after approximately $\Delta t \approx 106$ days.

The consolidation and creep act simultaneously on the soil response. Hence, on the one side, consolidation is responsible for the dissipation of the excess porewater pressures while creep is responsible for the accumulation of the viscous strains. The cumulative viscous strains are associated with the evolution of the *CSL* projection in the stress space towards the long-term *CSL* thus increasing the developed plastic deformations. Assuming that the proper set of constitutive parameters is employed then the slope should theoretically (at least) fail. However, selecting proper parameters is not the sole problem of the approach. Considering that creep failure develops over substantial times consolidation needs to have reached a pseudo-steady state. The term "pseudo-steady" state is introduced to denote the dissipation of the excess porewater pressures attributed to the excavation of the toe (and not the final state of equilibrium). The pseudo-steady state does not represent the final state of equilibrium considering that the generation of creep strains results in transient conditions. The problem at hand is no longer stationary but transitions to failure at an accelerating pace.

The aforementioned statement postulates what is theoretically to be expected by incorporating the proposed time-dependent behavioral framework. However, theory needs to be proved in practice. **Figure 8.9** summarizes the pore pressure contour plots at several stages of the excavation. The initial stage is introduced to denote the state before the excavation of the final cut while **Figure 8.9b** is characteristic of the aforementioned pseudo-steady state after 13.13 days of creep and consolidation phenomena acting in parallel. Note how the difference with **Figure 8.8b** (referring to the pore pressure plot assuming that the strength envelope is stationary) is negligible. The final state at failure is illustrated in **Figure 8.8c**. It is evident that negative pore pressures have developed in the model along the failure surface (it is proved here below that the maximum negative pore pressures occur along the slip line). It is not simply that the excess porewater pressure tends to be negative. Considering the highly overconsolidated state of the elements, the porewater

pressure becomes negative thus shifting the stress point to failure (the associated stress paths will be examined here below).

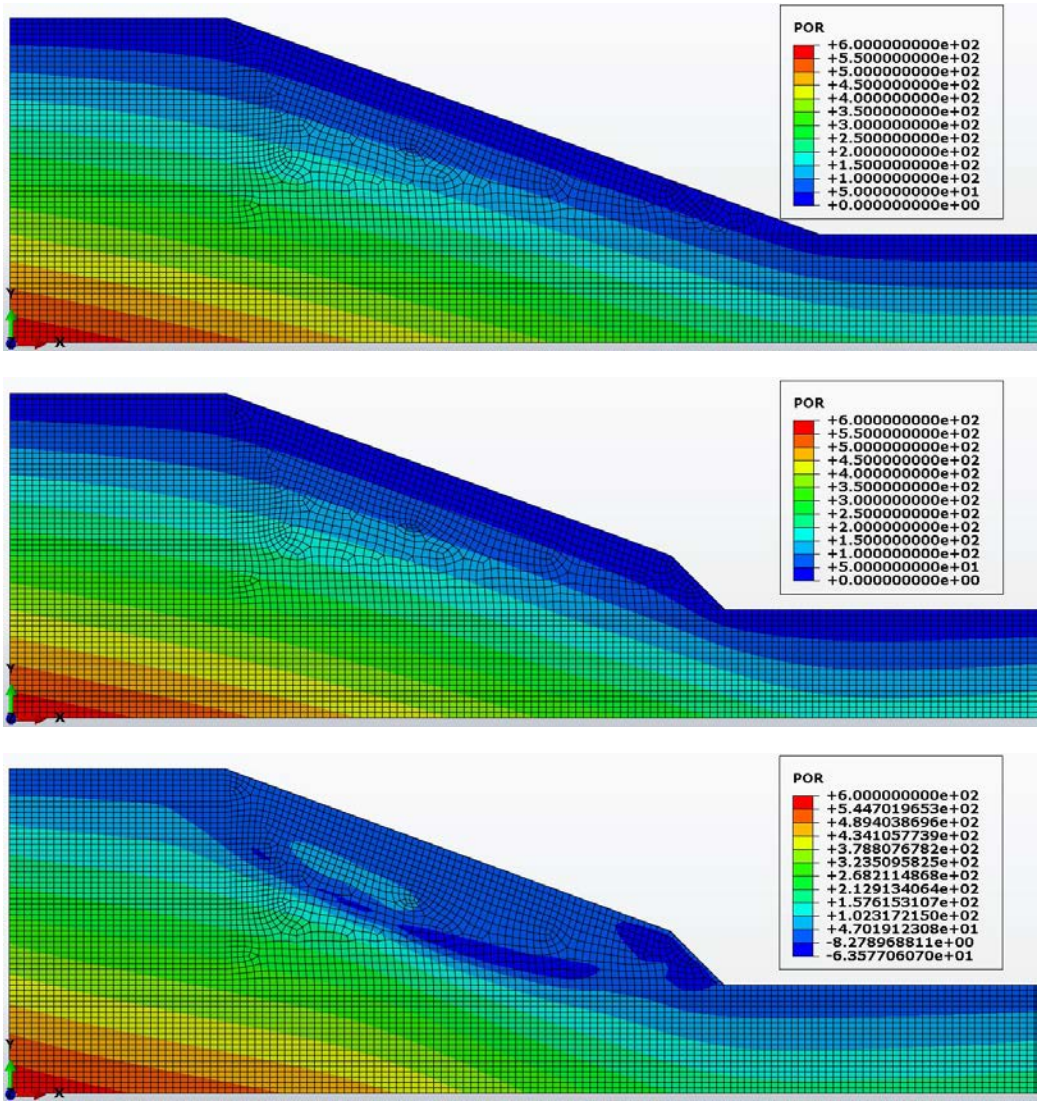

Figure 8.9: Pore pressures POR (kPa) at saturated conditions (water) assuming that the strength envelope evolves with time (conforming with the constitutive parameters of **Table 8.2**): a. before the excavation of the toe and b. 13.13 days after the excavation of the final cut (consolidation and creep act in parallel) and c. at failure after 106 days.

The displacement fields follow a similar trend. **Figure 8.10** portrays the displacement magnitude associated with the initial slope, the pseudo-steady state condition after the excavation of the final cut and the moment of failure. What becomes crystal clear from observing the aforementioned contour plots lies with the insignificant increase of the displacement field until the pseudo-steady state is achieved after 13.13 days of creep and consolidation sustained simultaneously. The maximum displacement (at the pseudo-steady state) may be approximately 1cm higher than the case portrayed

in **Figure 8.7b** (after 27.25days) but still follows the same behavioral trend and has not increased rapidly to even imply failure.

The displacement field at failure portrays a maximum of 1.4m at the toe. However, considering that some surficial elements may have failed along the final cut by thus ruining the contour plot (the contour plot does not allow for a comparative study of the space fields associated with the contour intervals), the maximum displacement magnitude was set equal to 75cm. Note how there is still a substantial portion exceeding the maximum set value (of 75cm). It is obvious that the elements close to the cut exhibit higher displacement values than those laying on the crest.

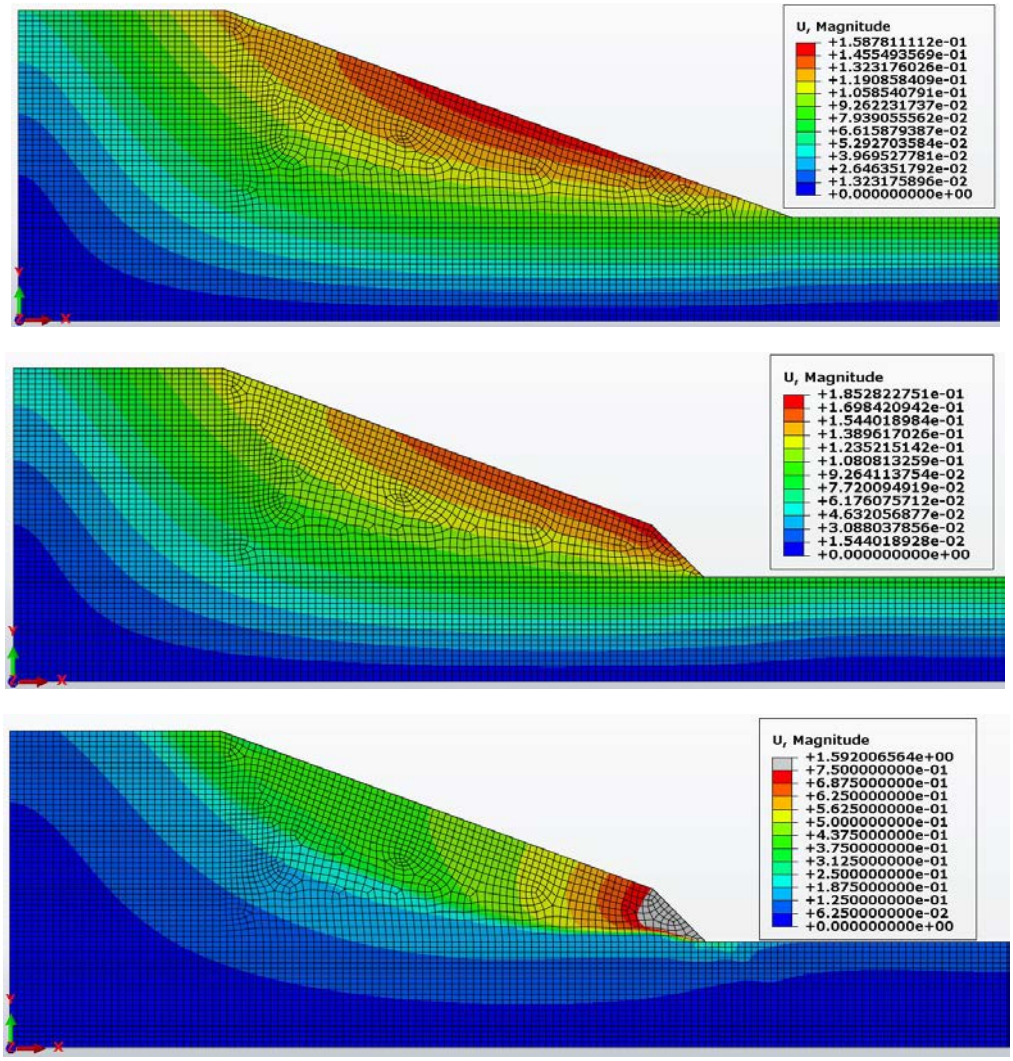

Figure 8.10: Displacement magnitude U (*m*) at saturated conditions (water) assuming that the strength envelope evolves with time (conforming to the constitutive parameters of **Table 8.2**): a. before the excavation of the toe and b. 13.13 days after the excavation of the final cut (while consolidation and creep act in parallel) and c. at failure after 106 days.

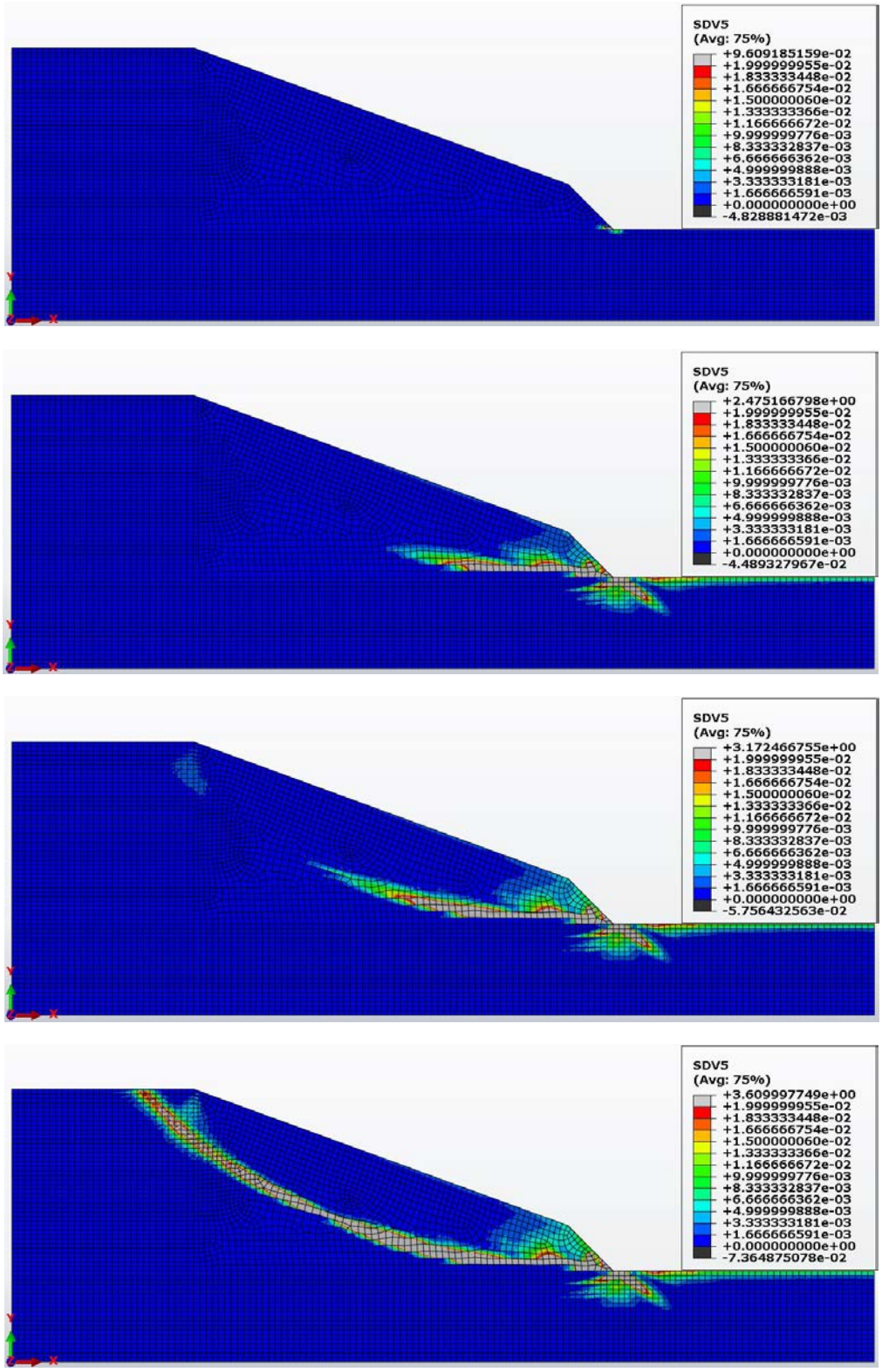

Figure 8.11: Activation of the retrogressive slope instability mechanism portrayed through the evolution of the deviatoric plastic strains ε_q^p (SDV5) at saturated conditions (water) assuming that the strength envelope degrades with time (conforming with **Table 8.2**) at: a. 13.13 days; b. 91.56 days; c. 102 days and d. failure (106 days) after the excavation of the final cut (while consolidation and creep act in parallel).

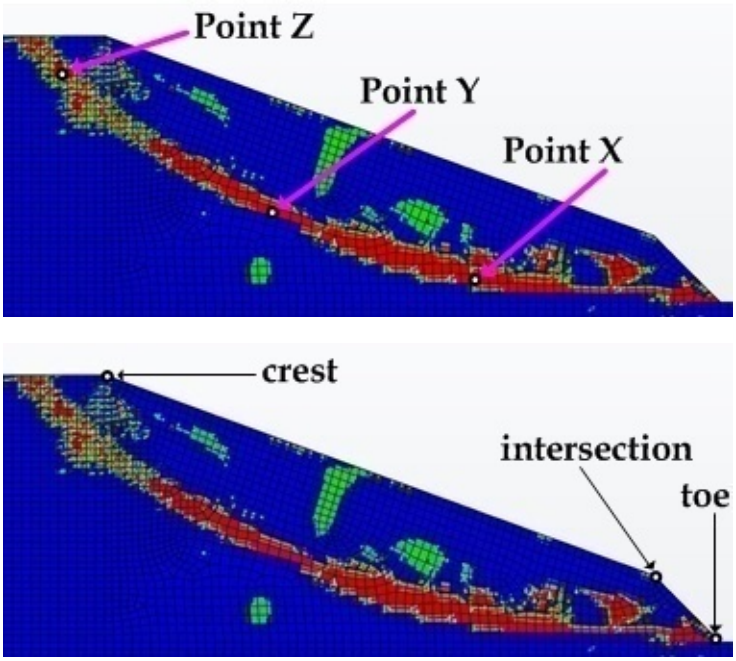

Figure 8.12: a. Declaration of the Points X, Y and Z (elements painted red denote failure while blue denote plastic state and green designate viscoelastic response) and b. declaration of the crest, the intersection (of the initial slope and the final cut) and the toe (we are referring to nodes to be used henceforth to portray the displacement as a function of time) in the creep induced slope instability case of section 8.3.2 (conforming with **Table 8.2**).

To make a long story short, the maximum displacement increased from 18cm to 1.5m at approximately 92.7 days of creep and consolidation (from 13.13 days to failure at 106 days). It is evident that a phenomenon has been triggered in those 92.7 days leading to slope instability. Considering that the critical state is associated with infinite deviatoric plastic strains. Hence, the deviatoric plastic strain contour plots are studied at multiple consolidation states along the time frame of 92.7 days (depicted in **Figure 8.11**). While initially (after 13.13 days - **Figure 8.11a**) there are significant deviatoric strains solely along the toe (the minimum was mixed to null and the maximum to 2% to allow for the comparative study) the failure surface tends to propagate backwards with evolving time originating from the toe (at 91.56days - **Figure 8.11b**). At some point while the slip line continues to propagate backwards and upslope significant deviatoric strains begin to accumulate near the crest and transition downwards (at 102 days - **Figure 8.11c**). It is as if the slope starts creeping more or less as a rigid block. Shortly after the slip line originating from the top transitioning downwards and the failure surface propagating backwards and uphill

(from the toe) unite thus leading to failure (at 106days - **Figure 8.11d**). This justifies the triggered retrogressive slope instability mechanism.

Points X, Y and Z portrayed previously in the diagrams refer to the current case and are portrayed thoroughly in **Figure 8.12**. Points X, Y and Z comprise elements laying along the failure surface. Note that the elements painted red lay mostly along the failure surface. They denote that the stress state lays simultaneously on the *SSE* and *PYE*. Elements portrayed with blue are characteristic of plastic states (the stress state lays on *PYE* but not on the *SSE*) while elements depicted in green exhibit purely viscoelastic response.

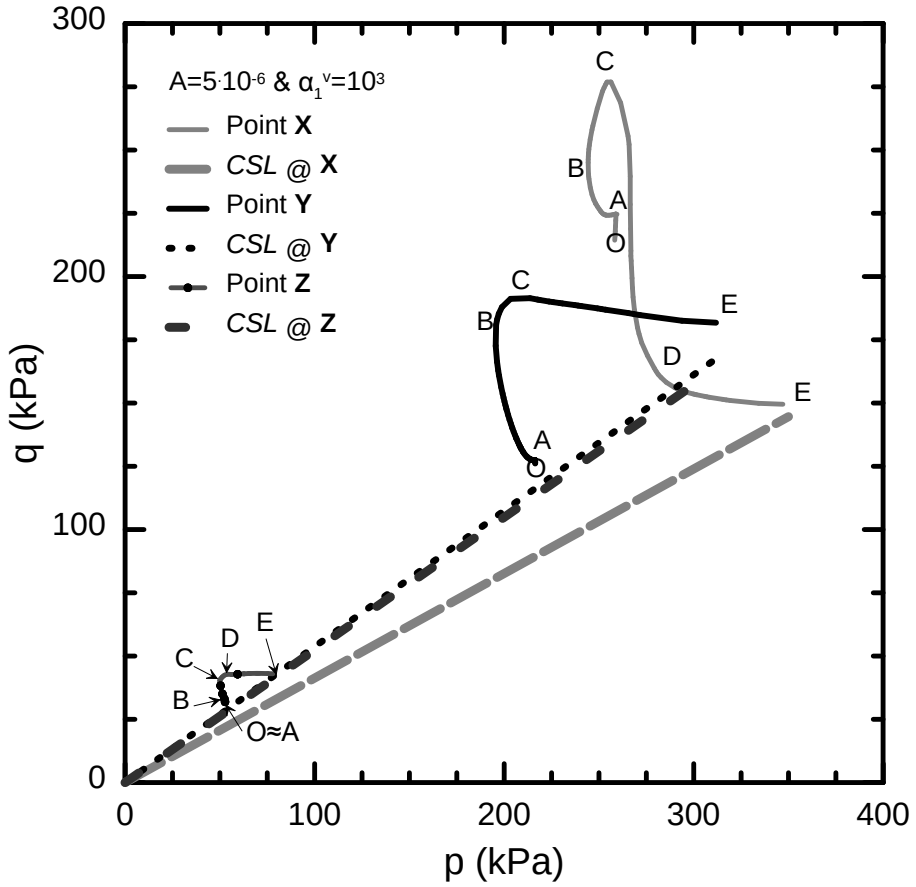

Figure 8.13: Saturated (water) soil response depicted through stress paths in the *p-q* space and associated *CSL* lines assuming that the strength envelope evolves with time (conforming with **Table 8.2**) at points X, Y and Z (from O to E through intermediate states A, B, C and D consecutively).

The undergoing stress path at Points X, Y and Z are portrayed in **Figure 8.13**. It is evident that the stress paths lay higher that the associated *CSL* lines characteristic of highly overconsolidated stress states. The stress path originates from point O (for origin) and transitions to E (for end denoting failure) through some intermediate

points (A, B, C and D) employed to denote certain behavioral characteristics portrayed also in **Figure 8.14**. **Figure 8.14** illustrates the excess porewater pressure in kPa during the excavation of the final cut ($\Delta u = u - u_0$, where u is the current porewater pressure and u_0 the pore pressure before the excavation of the toe). Note how each point is mapped from one diagram to the other. State A is characteristic of the excavation step of 0.5days (the excavation of the final cut is assumed to be concluded within 0.5days). It is evident that state E lays either on or close to the *CSL* projection in the stress space while the excess porewater pressures have significantly increased at that time. Stress state E shifts the stress path to the right of the isotropic axis and it looks as if the evolution of the *CSL* is "chasing" the stress as to set it upon the *CSL*. It is characteristic of the undrained nature of a highly overconsolidated stress state.

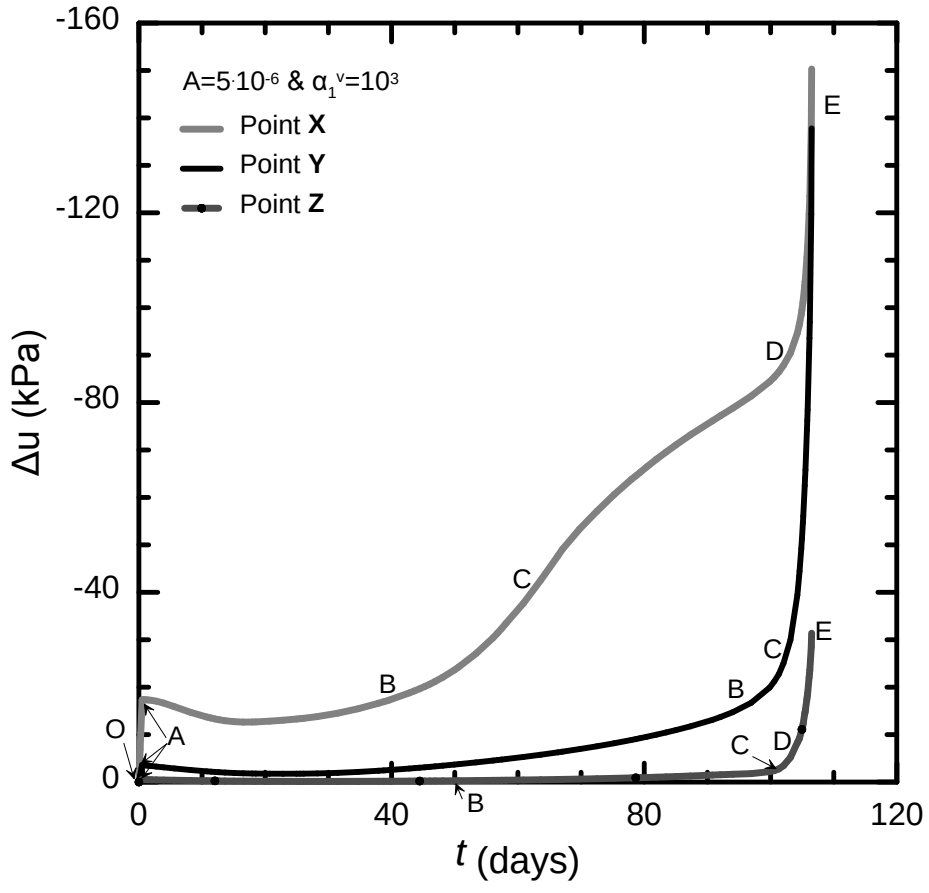

Figure 8.14: Saturated (water) soil response depicted through the excess porewater paths assuming that the strength envelope evolves with time (conforming to **Table 8.2**) at points X, Y and Z (from O to E through intermediate states A, B, C and D consecutively).

Figure 8.12b introduces the node set of the crest, the intersection (of the initial slope and the final cut) and the toe. The node set is used here below to examine results on the displacement expressed as a function of time (**Figure 8.15**). The time origin is set to the time of the final cut excavation (Point O). It is evident that the delayed failure occurs after approximately 3.5 months. The toe reveals extremely high displacements characteristic of failure on the surficial element. What is however of the greatest significance is that the Crest proves relatively smaller displacement values. This is characteristic of the slope flowing downwards.

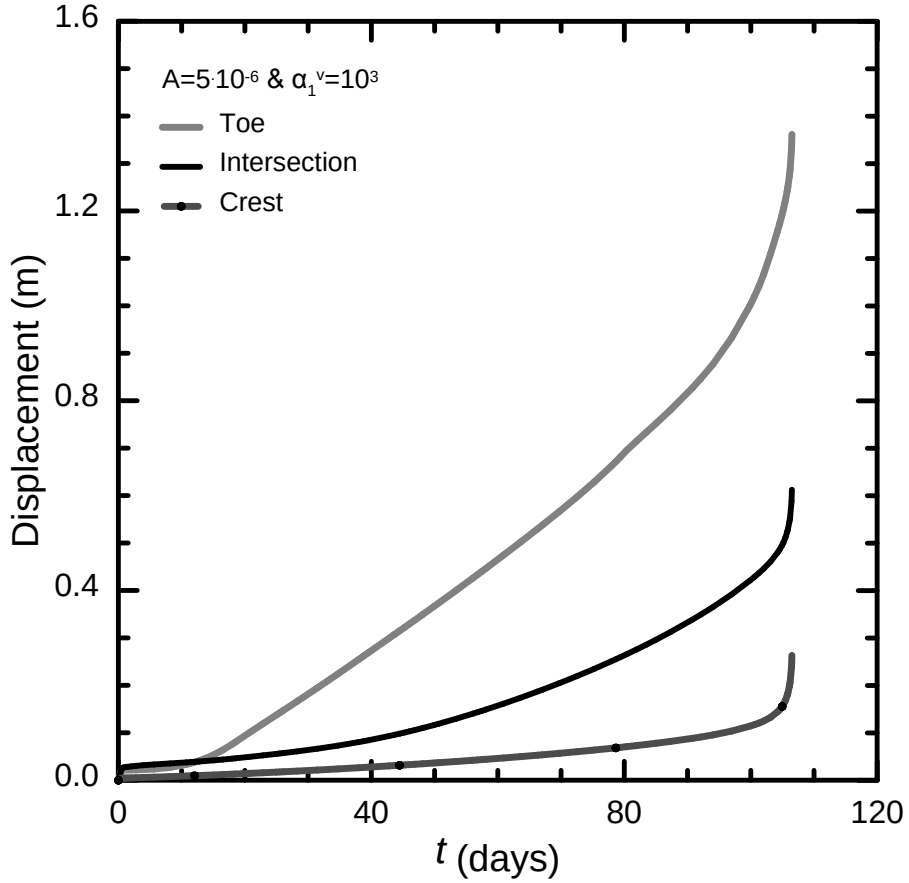

Figure 8.15: Displacement expressed as function of time at saturated (water) soil conditions assuming that the strength envelope evolves with time (conforming to **Table 8.2**) at the Crest, the Intersection and the Toe (depicted in **Figure 8.12**).

8.3.3 Rapid induced slope instability associated with viscous phenomena

This section focuses on a very rapid pace of induced slope instability. In other words the employed constitutive parameters do not allow for the pseudo-steady state (introduced earlier) to be attained. Instead, the combined effect of creep and consolidation leads rapidly to failure (note that the term delayed failure will be

avoided). This can be achieved by either setting the magnitude of the deviatoric creep strains significantly high or by increasing the constitutive parameter controlling the strength envelope degradation. The rapid induced slope instability was encountered by accident when a poor selection of the Singh-Mitchell parameter A led to failure without the consolidation playing any role whatsoever.

The strength envelope is allowed to evolve from the short-term ($c_{cs} = 0.9798$ characteristic of an effective friction angle of $\varphi' = 30^\circ$) to the long-term *CSL* inclination ($c_{LT} = 0.3068$ characteristic of an effective friction angle of $\varphi' \approx 10^\circ$). The associated constitutive parameters are summarized in **Table 8.3**.

Table 8.3: Constitutive parameters associated with the rapid induced slope instability due to viscous phenomena (paragraph 8.3.3).

B_0	B_{res}	OCR	N^*_{iso}	c_{in}	c_{fin}	$2\cdot(G/K)^e$	λ	κ
1	1	3	2.2	0.9798	0.3068	0.75	0.0869	0.00869
λ^*	γ	d_{in}	η_v^p	η_q^p	ζ_v^p	ζ_q^p	θ_q^p	ϑ_q^p
5	1	0	50	50	0	0	0	0
t_0 (days)	$a_1^v = a_2^v$	ψ	A	m	$\bar{a}$	γ_{sat} (kN/m^3)	ξ	k (m/s)
231.5	10^2	1.E-9	1.6 E-4	0.8	2.5	20	0.02	10^{-8}

Here follow the simulated excavation stages and consolidation steps:

- **Geostatic step** (Figure 8.2a.): The structureless soil elements are originally consolidated isotropically, considering that the selected coefficient of lateral pressure is $K_0 = 1$ (the selected OCR=3). The water table coincides with the soil surface (at all times). The initial step is undertaken to establish equilibrium between the initial values and the calculated stress state. The time period of this step is fixed and equal to 1 day.
- **Consolidation step**: A consolidation step of 80 days is sustained to assure steady state conditions.
- **Excavation of the initial slope** (Figure 8.2b.): The elements are removed to construct the initial slope. The excavation is concluded within $\Delta t = 10$ days.
- **Consolidation step**: A consolidation step of 140 days is sustained to assure steady state conditions.

- **Excavation of the final cut** (Figure 8.2c.): The toe is removed to construct the final cut. The excavation is assumed to be concluded within $\Delta t = 0.5$ days.
- **Consolidation step**: A consolidation step is undertaken until failure. The reference time was selected equal to $t_0 = 231.5$ days as to kick in at the initiation of this step. Hence, consolidation and creep are sustained simultaneously. It is assumed that failure occurs after approximately $\Delta t \approx 72$ days (note that failure in terms of displacements has occurred much sooner).

Figure 8.16 portrays the porewater pressure contour plot at failure. The initial stage before the excavation of the toe is the same as **Figure 8.9a**. It can be observed that substantial negative pore pressures develop along the failure surface. Considering the highly overconsolidated stress state of the elements, the porewater pressure becomes negative thus shifting the stress points to failure. As for the associated displacements portrayed in **Figure 8.17** they reach a maximum of 7.8m at the crest. While formerly (referring to paragraph 8.3.2) the retrogressive slope instability mechanism revealed higher displacements along the toe, the current case offers a rather different behavior at first glance. However, this is not the case. The toe does originally produce higher displacements. Once the slip surface has formed displacements tend to develop thus shifting the maximum point uphill to the crest. The aforementioned statement is justified through **Figure 8.18**.

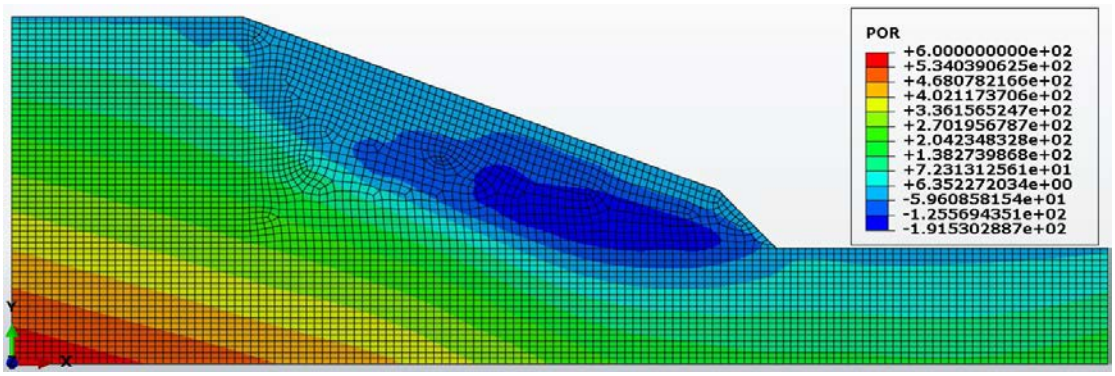

Figure 8.16: Pore pressures POR (kPa) at saturated conditions (water) assuming that the strength envelope evolves with time (conforming to the constitutive parameters of **Table 8.3**) depicted at failure after 72 days.

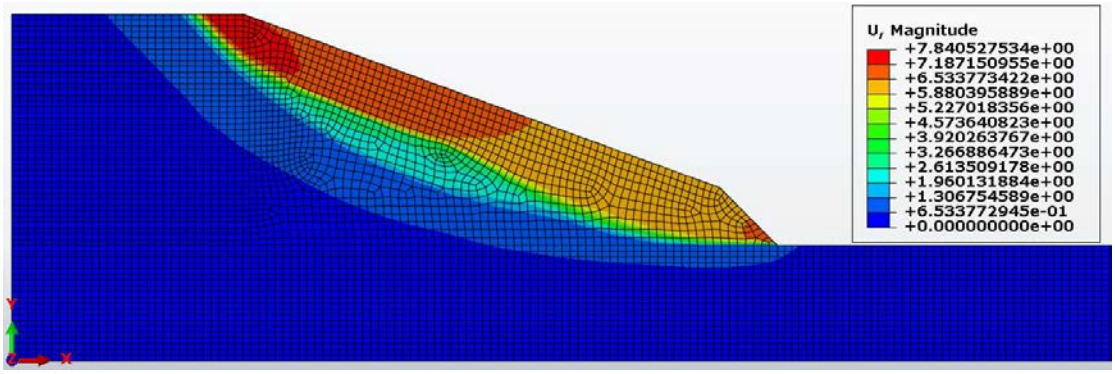

Figure 8.17: Displacement magnitude U (*m*) at saturated conditions (water) assuming that the strength envelope evolves with time (conforming to the constitutive parameters of **Table 8.3**) depicted at failure after 72 days.

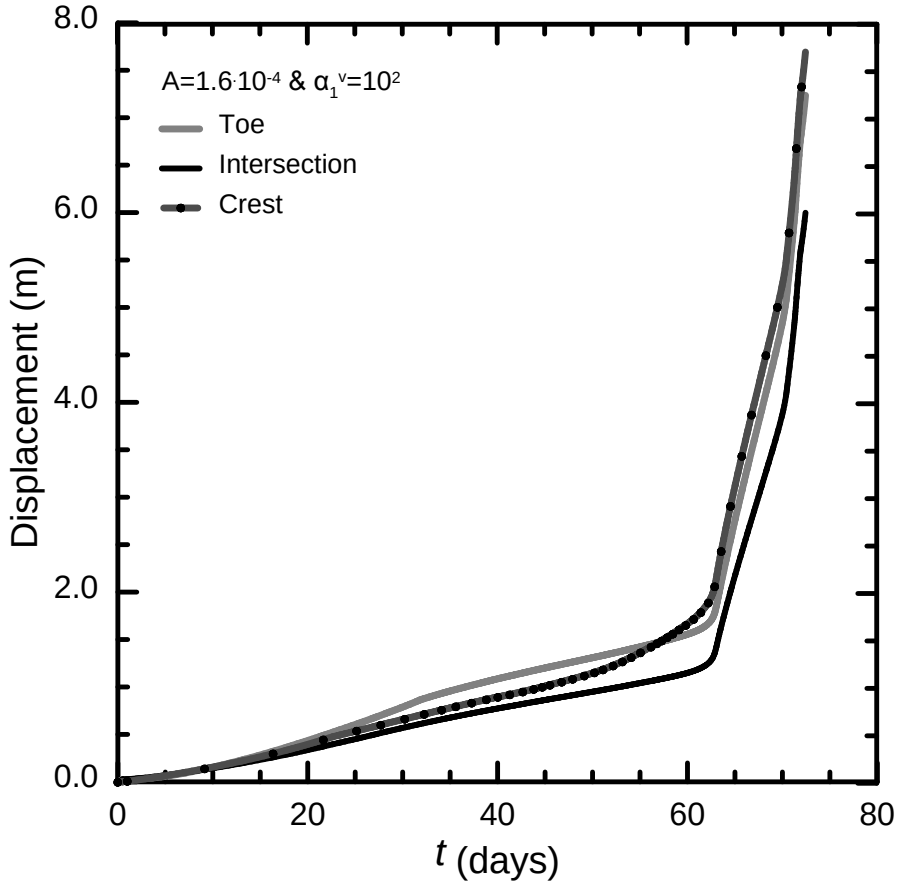

Figure 8.18: Displacement expressed as function of time at saturated (water) soil conditions assuming that the strength envelope evolves with time (conforming to **Table 8.3**) at the Crest, the Intersection and the Toe (depicted in **Figure 8.12**).

It is also emphasized that substantial displacement around 0.5m develops equally at all selected nodes (Crest, Intersection and Toe) around 20days of consolidation time (creep is acting in parallel). This justifies the original statement that the selection of

the Sing-Mitchell parameter A controlling the magnitude of the shear viscous strains was considerably high. It further proves that there is no quasi-steady state attained in this situation considering that the displacement tends to build up continuously at the same pace until 65 days (at 65 days the displacements accumulate at an accelerating rate leading to failure after 72 days).

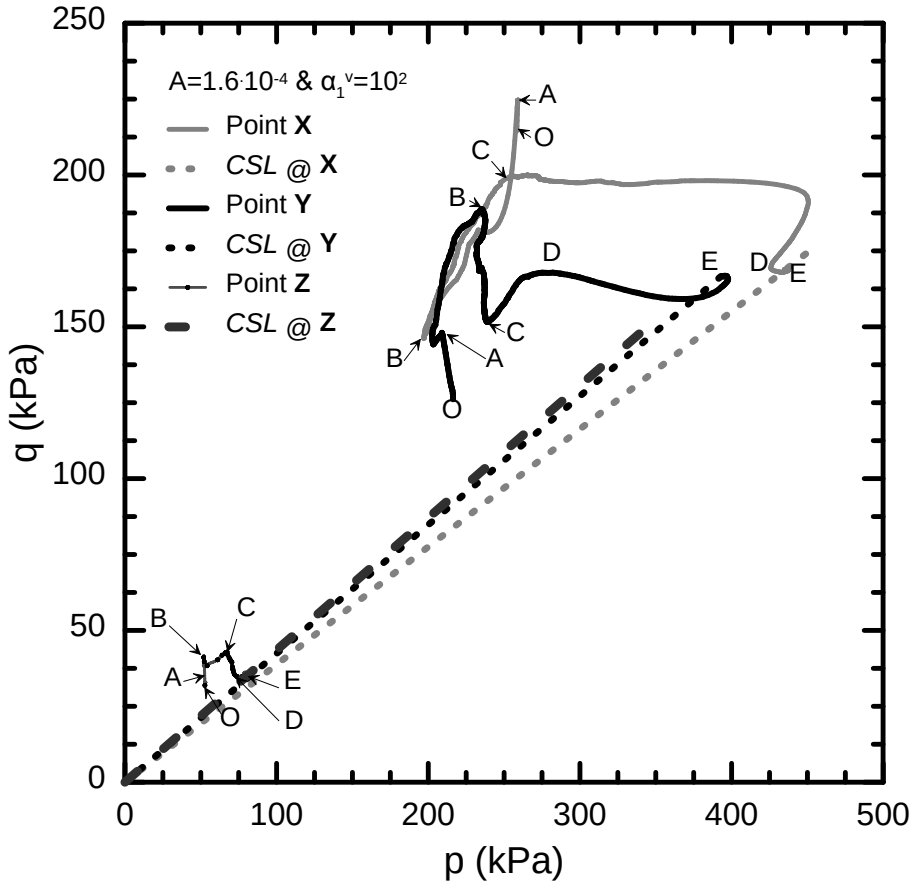

Figure 8.19: Saturated (water) soil response depicted through stress paths in the *p-q* space and associated *CSL* lines assuming that the strength envelope evolves with time (conforming with **Table 8.3**) at points X, Y and Z (from O to E through intermediate states A, B, C and D consecutively).

The undergoing stress paths at points X, Y and Z (depicted in Figure 8.12) are illustrated in **Figure 8.19**. Once again, the undergoing stress path originates from O (stating the origin of the excavation) and transitions through A (after final cut at 0.5days) to failure E (denoting the end). Intermediate points from B to D are incorporated to denote mechanical transformations undergoing until failure. Note that the same stress states are depicted in **Figure 8.20** to allow for a thorough and elaborate observation of the simulated soil response. Once again the stress paths are characteristic of highly overconsolidated geomaterial stress states. The stress state

transitions to the right representative of the undrained nature of the problem at hand. State E is adjusted on the current *CSL* projection in the stress space at all points (X, Y and Z). Note how the excess porewater pressure tends to portray almost a stationary response. However, this is not the case considering that point Z rests close to the surface (the pore pressures are relatively small and therefore the excess porewater pressure is equally low).

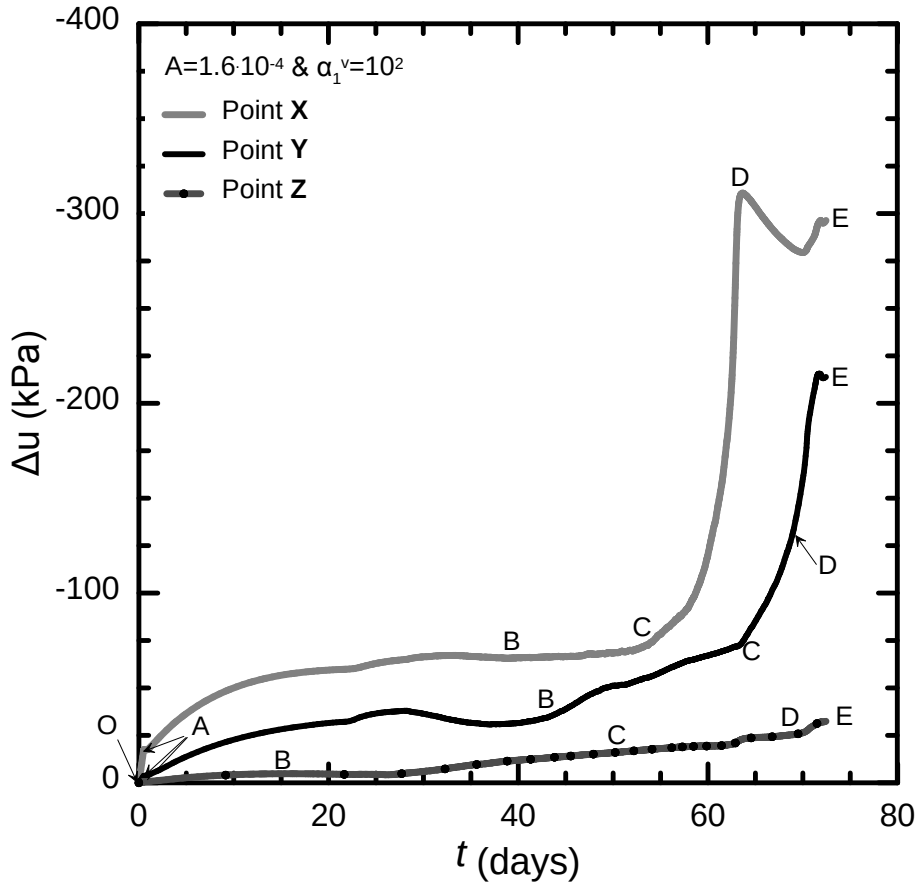

Figure 8.20: Saturated (water) soil response depicted through the excess porewater paths assuming that the strength envelope evolves with time (conforming to **Table 8.3**) at points X, Y and Z (from O to E through intermediate states A, B, C and D consecutively).

8.3.4 Stationary creep slope stability

This section investigates a very slow rate of strength envelope evolution. Hence, solely the secondary creep stage will be activated for the time frame of interest (we have selected to show results for 15years). To this end, the Singh-Mitchell parameter was selected equal to $A = 10^{-5}$ (similar to that incorporated in paragraph 8.3.2 - the value used in that section was equal to $A = 5 \cdot 10^{-6}$).

The strength envelope is allowed to evolve from the short-term ($c_{cs} = 0.9798$ characteristic of an effective friction angle of $\varphi' = 30^{\circ}$) to the long-term *CSL* inclination ($c_{LT} = 0.3068$ characteristic of an effective friction angle of $\varphi' \approx 10^{\circ}$). The associated constitutive parameters are summarized in **Table 8.4**.

Table 8.4: Constitutive parameters associated with the stationary creep slope stability of paragraph 8.3.4.

B_0	B_{res}	OCR	N^*_{iso}	c_{in}	c_{fin}	$2\cdot(G/K)^e$	λ	κ
1	1	3	2.2	0.9798	0.3068	0.75	0.0869	0.00869
λ^*	γ	d_{in}	η^p_v	η^p_q	ζ^p_v	ζ^p_q	θ^p_q	ϑ^p_q
5	1	0	50	50	0	0	0	0
t_0 (days)	$a^v_1 = a^v_2$	ψ	A	m	$\bar{a}$	γ_{sat} (kN/m^3)	ξ	k (m/s)
231.5	20	1.E-9	1.E-5	0.8	2.5	20	0.02	10^{-8}

Here follow the simulated excavation stages and consolidation steps:

- **Geostatic step** (Figure 8.2a.): The structureless soil elements are originally consolidated isotropically, considering that the selected coefficient of lateral pressure is $K_0 = 1$ (the selected OCR=3). The water table coincides with the soil surface (at all times). The initial step is undertaken to establish equilibrium between the initial values and the calculated stress state. The time period of this step is fixed and equal to 1 day.
- **Consolidation step**: A consolidation step of 80 days is sustained to assure steady state conditions.
- **Excavation of the initial slope** (Figure 8.2b.): The elements are removed to construct the initial slope. The excavation is concluded within $\Delta t = 10$ days.
- **Consolidation step**: A consolidation step of 140 days is assumed to assure steady state conditions.
- **Excavation of the final cut** (Figure 8.2c.): The toe is removed to construct the final cut. The excavation is concluded within $\Delta t = 0.5$ days.
- **Consolidation step**: A consolidation step is undertaken. The reference time was selected equal to $t_0 = 231.5$ days as to kick in at the initiation of this step.

Hence, consolidation and creep act in parallel. The slope is allowed to creep for 5,614 days (15.3 years).

Figure 8.21 depicts the porewater pressure contour plot at the end of 15.3 years of creep acting in conjunction with the consolidation process. The initial stage before the excavation of the toe is the same as **Figure 8.9a**. Note that the pore pressures are the exact same as the ones portrayed in **Figure 8.9b** (in the case where the strength envelope is not allowed to evolve). Hence, solely from the porewater pressure contour plot it is evident that no failure occurs or more accurately no failure surface forms in the slope. As for the associated displacements illustrated in **Figure 8.22** they reach a maximum of 1.2m at the crest. Note that 1.2m is not negligible to say the least regardless of the considerable time frame of 15.3 years imposed.

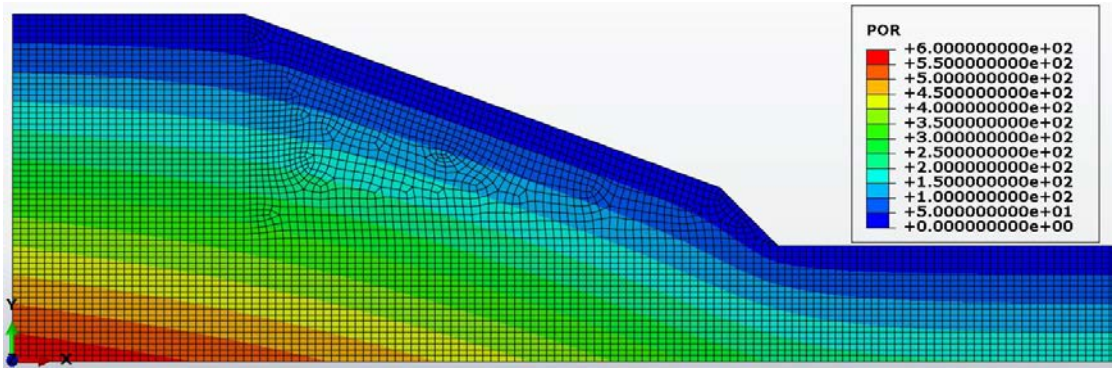

Figure 8.21: Porewater pressure POR (kPa) at saturated conditions (water) assuming that the strength envelope evolves with time (conforming to **Table 8.4**) after 5,614 days denoting the stationary creep stage.

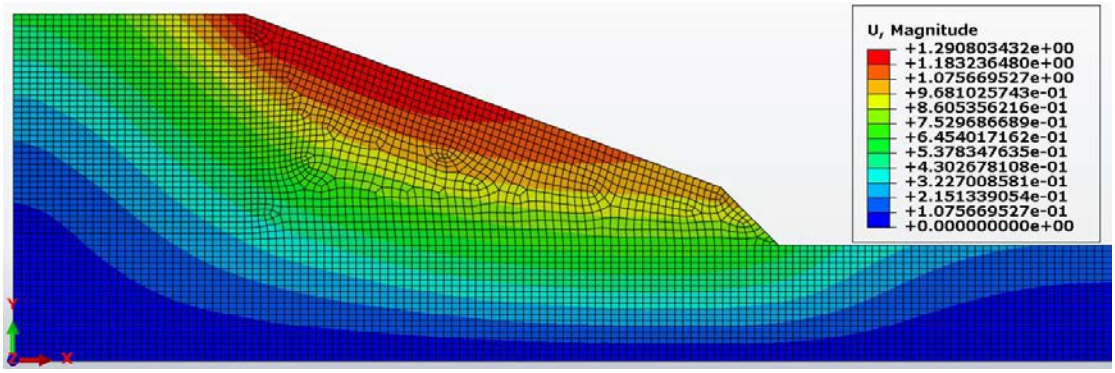

Figure 8.22: Displacement magnitude U (*m*) at saturated conditions (water) assuming that the strength envelope evolves with time (conforming to **Table 8.4**) after 5,614 days portraying the stationary creep stage.

A structure founded in the close proximity of that slope would sustain significant deformation and potential failure. The examined case study reveals that regardless

whether a distinct slip surface has formed it is possible to exhibit considerable displacements over time assuming that the creep potential of the soil is elevated. **Figure 8.23** further justifies the stationary designation of the sustained creep process. The argument could be made that the slope does not fail in a traditional fashion by producing a distinct failure surface but creeps as a viscous fluid. It continues to creep and deforms until after considerable time it shall fail (as it was revealed in section 8.3.2).

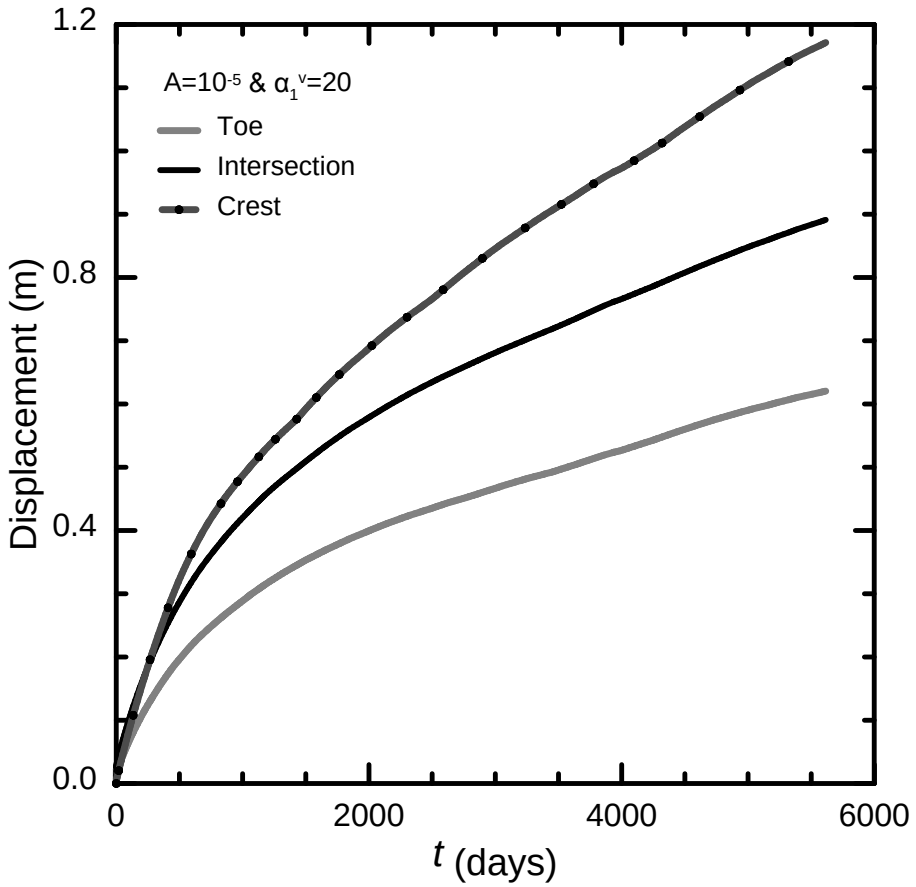

Figure 8.23: Displacement expressed as function of time at saturated (water) soil conditions revealing the stationary creep process (conforming to **Table 8.4**) at the Crest, the Intersection and the Toe (depicted in **Figure 8.12**).

Figure 8.24 portrays the undergoing stress paths in the *p-q* space. It is characteristic of transformations associated with the continuity condition and consequently no significant observation can be concluded (it was incorporated for completeness). The stress path originates from the stress state O (for origin) and transitions towards E (denoting the end of the 5,614 days time period). Stress state A designates the end of the final cut excavation (concluded in 0.5 days) while intermediate points from B to

D have been employed to denote mechanical transformations undergoing in the slope.

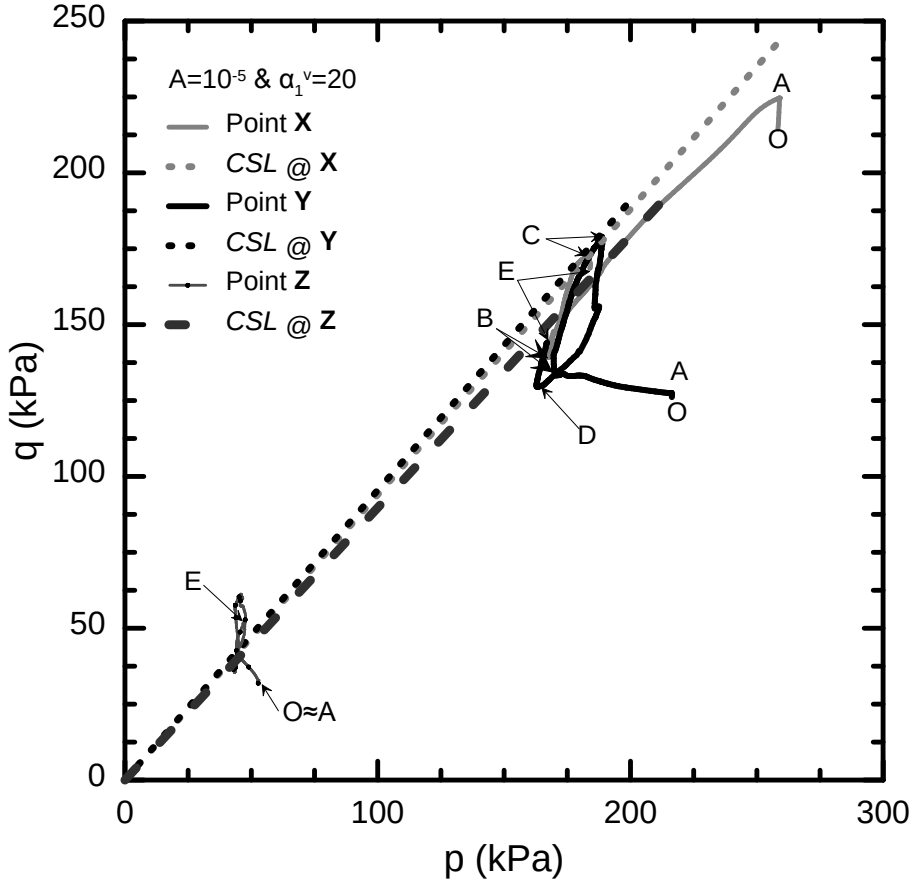

Figure 8.24: Saturated (water) soil response depicted through stress paths in the *p*-*q* space and associated *CSL* lines revealing the stationary creep process (conforming to **Table 8.4**) at points X, Y and Z (from O to E through intermediate states A, B, C and D consecutively).

The excess porewater pressure is expressed as a function of time in **Figure 8.25**. Note how the stress states of **Figure 8.24** are depicted in **Figure 8.25**. It is obvious that the continuity condition governs the overall time-dependent soil response. The deformation of one element influences the adjacent elements thus transforming the soil response. Consequently, no observation can be made in the excess porewater diagram other than the fact that porewater pressures reach an equilibrium in time regardless whether the deformations continue to accumulate. It is evident that the slope is stable in the classical sense that no failure surface occurs. However, the predicted displacements are considered extremely high for any structure to sustain.

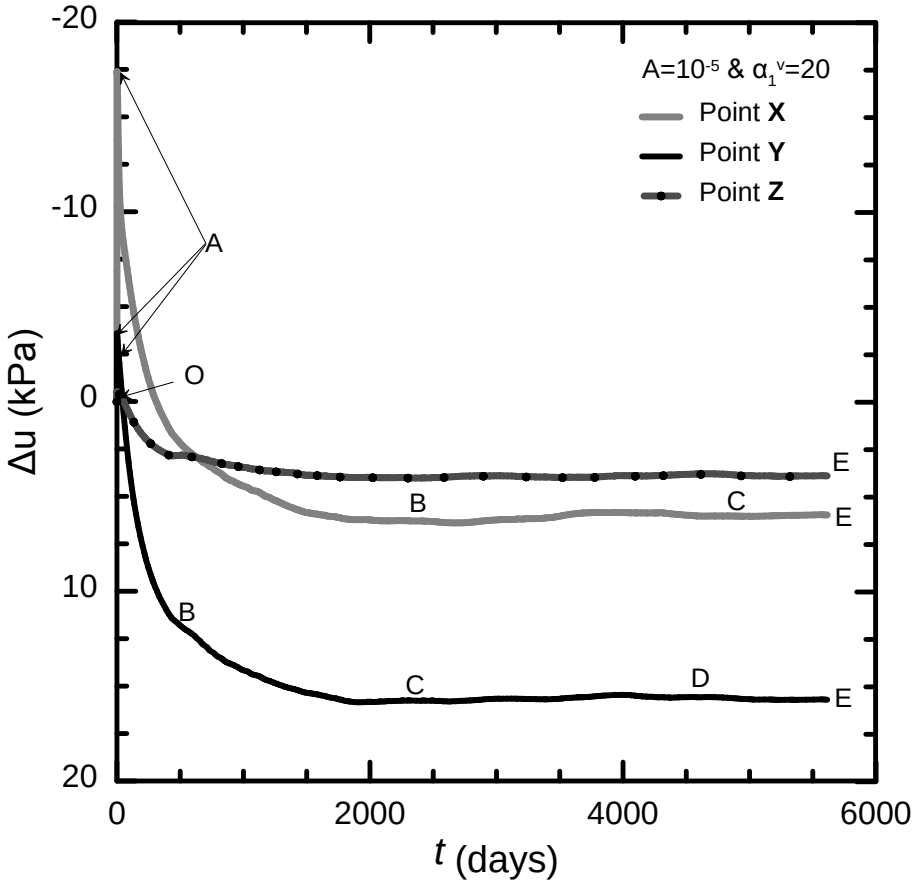

Figure 8.25: Saturated (water) soil response depicted through the excess porewater paths revealing the stationary creep process (conforming to **Table 8.4**) at points X, Y and Z (from O to E through intermediate states A, B, C and D consecutively).

8.3.5 Importance of water in triggering retrogressive slope instability

This section evaluates the importance of water in the retrogressive slope instability process. **Figure 8.11** revealed the manner at which the failure mechanism originates from the toe and propagates backwards and uphill while at some time another part is activated on the crest transitioning downwards. When the two segments unite and the failure surface is formed the slope fails. This summarizes the triggering of the retrogressive slope instability mechanism associated not as much with saturated conditions as it is with the presence of water to be shown here below.

Hence, this section investigates the exact same case study as the one summarized in paragraph 8.3.2 but in this case dry conditions will be assumed instead. The unit weight is kept constant and equal to 20kN/m^3 while every other material constant remains intact (the constitutive parameters are depicted in **Table 8.2**). The strength

envelope is allowed to evolve from the short-term ($c_{cs} = 0.9798$ characteristic of an effective friction angle of $\varphi' = 30^{\circ}$) to the long-term *CSL* inclination ($c_{LT} = 0.3068$ characteristic of an effective friction angle of $\varphi' \approx 10^{\circ}$).

However, the simulation raised two arguments associated with the reference time. The simulation of the dry slope is independent of time assuming that creep is not present in the original steps (of the excavation of the initial slope and that of the final cut). Creep is sustained solely after the excavation of the final cut. Hence, it would be possible to excavate the initial slope or the final slope in considerable less time periods than 10 days or 0.5 days (as it was assumed in the case where water was present). Furthermore the consolidation process requires substantial time periods considering that the imposed permeability was set equal to $10^{-8}\,\mathrm{m/s}$. Theoretically, assuming that the reference time t_0 changes the Singh-Mitchell parameter would also need to be transformed, in order to introduce comparable viscous characteristics. Simply consider equation (5.21). For the shear viscous strains to remain intact the quantity $A \cdot t_0$ needs to be constant. Furthermore the time period needs to be scaled considering the ratio t/t_0. In order to avoid such manipulations, the excavation steps were "adjusted" as to result in the same reference time as before ($t_0 = 231.5 days$).

Here follow the simulated excavation stages in detail:

- **Geostatic step** (Figure 8.2a.): The structureless soil elements are originally consolidated isotropically, considering that the selected coefficient of lateral pressure is $K_0 = 1$ (the selected OCR=3). The initial step is undertaken to establish equilibrium between the initial values and the calculated stress state. The time period of this step is fixed and equal to 1 day.
- **Excavation of the initial slope** (Figure 8.2b.): The elements are removed to construct the initial slope. The excavation is concluded within $\Delta t = 120$ days.
- **Excavation of the final cut** (Figure 8.2c.): The toe is removed to construct the final cut. The excavation is concluded within $\Delta t = 110.5$ days.
- **Creep step**: The slope is left to creep. The reference time was selected equal to $t_0 = 231.5$ days as to kick in at the initiation of this step. The simulation stopped converging after 171 days.

The displacement fields immediately after the excavation of the final cut and at the time when the simulation stopped converging (after 171 days) are depicted in **Figure 8.26**. Note how the maximum displacement increases from 15.7cm to 78.7cm after 171 days of creep. Regardless whether the displacement appears to be elevated around the toe, it is evident that the increase of displacement is negligible at all other fields.

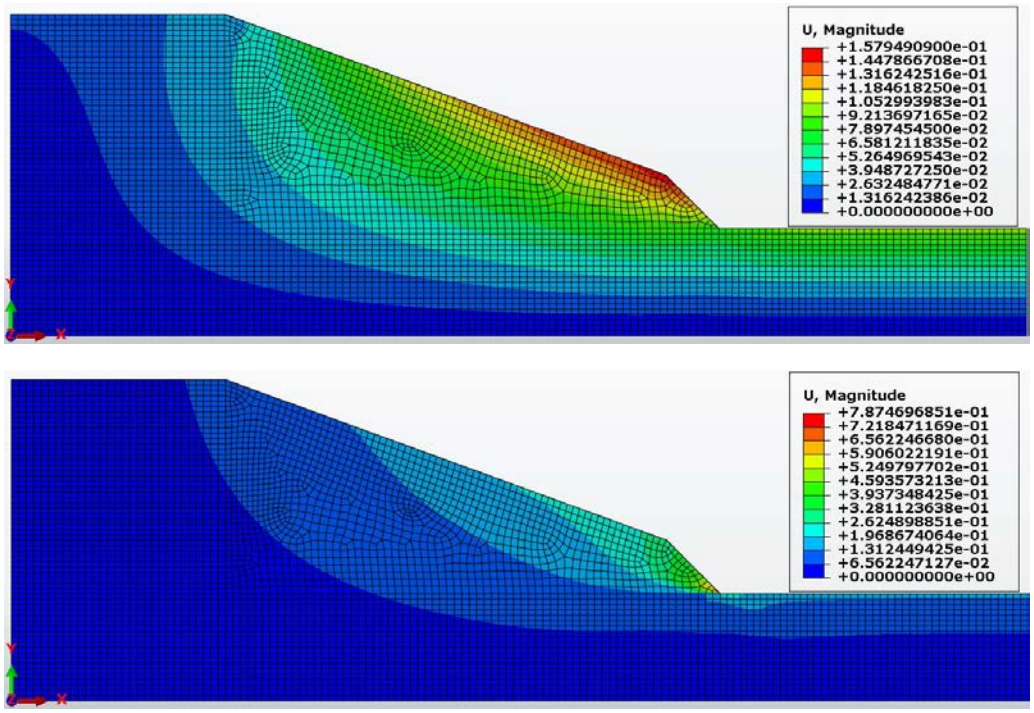

Figure 8.26: Displacement magnitude U (*m*) at dry conditions assuming that the strength envelope evolves with time (conforming to the constitutive parameters of **Table 8.2**): a. right after the excavation of the toe and b. 171 days of creep.

Consequently, the analysis stopped converging due to localized failure at the toe and possible at some surficial elements as can be observed from **Figure 8.27**. It is clear that the deviatoric plastic strains develop solely at the toe and at the surficial elements. However, there is no evidence to justify the triggering of a retrogressive slope instability mechanism. The model ceased to converge simply because the toe failed. However, all other regions of the model appear to be intact without considerable displacements or plastic deformations visible. The displacements at the Crest, at the Toe and at the Intersection point (of the initial slope and the final cut) are depicted in **Figure 8.28**.

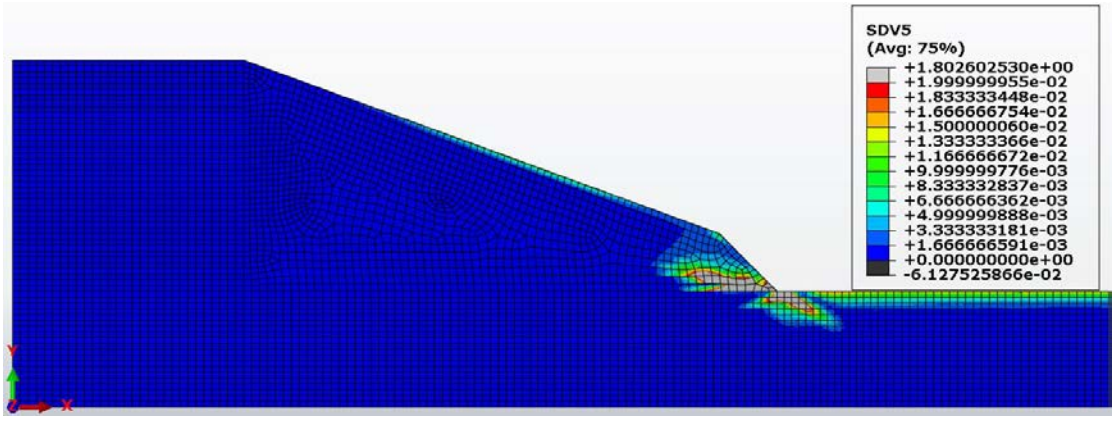

Figure 8.27: Deviatoric plastic strain ε_q^p (SDV5) at dry conditions assuming that the strength envelope evolves with time (conforming To the constitutive parameters of **Table 8.4**) after 171 days of creep.

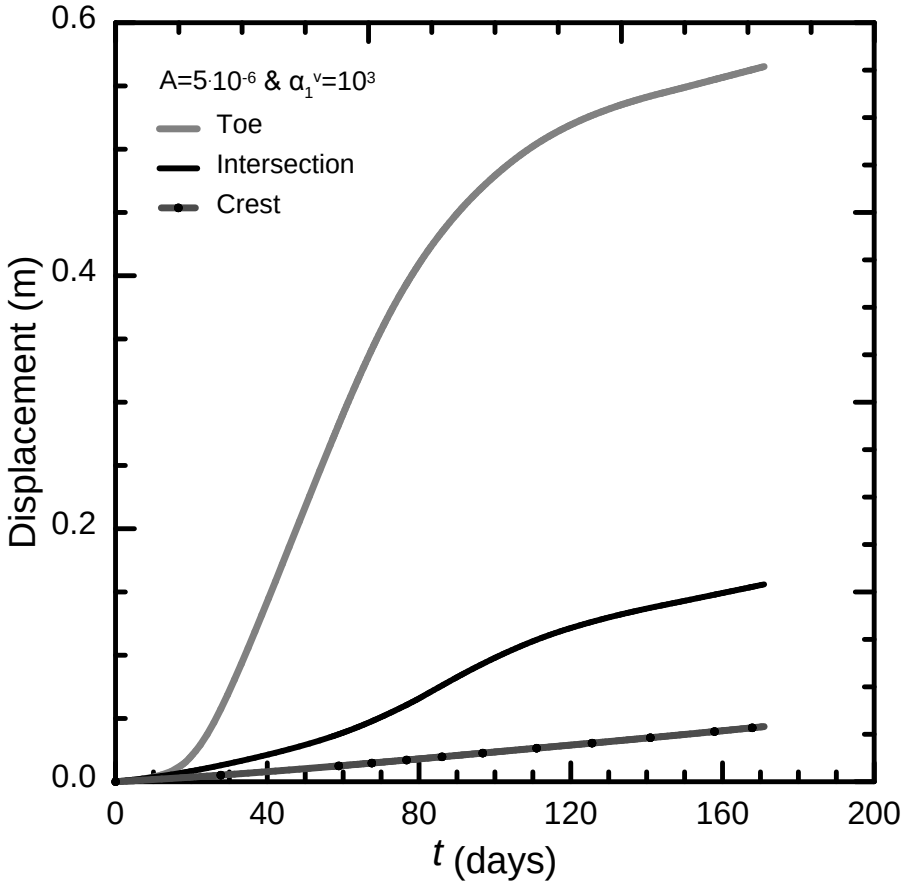

Figure 8.28: Displacement expressed as function of time at dry conditions assuming that the strength envelope evolves (conforming to **Table 8.2**) at the Crest, the Intersection and the Toe (depicted in **Figure 8.12**).

Note how the displacement at the toe tends to increase rapidly in the initial 20 days of creep. However, after the initial 100 days the displacement recovers gradually leading to a response resembling the stationary creep stage. What happens is that the toe has failed but the continuity condition redistributes the stress. In reality however

the toe should have collapsed thus resulting in the progressive failure mechanism. Hence, it is the presence of water that activates the triggering of the retrogressive slope instability mechanism.

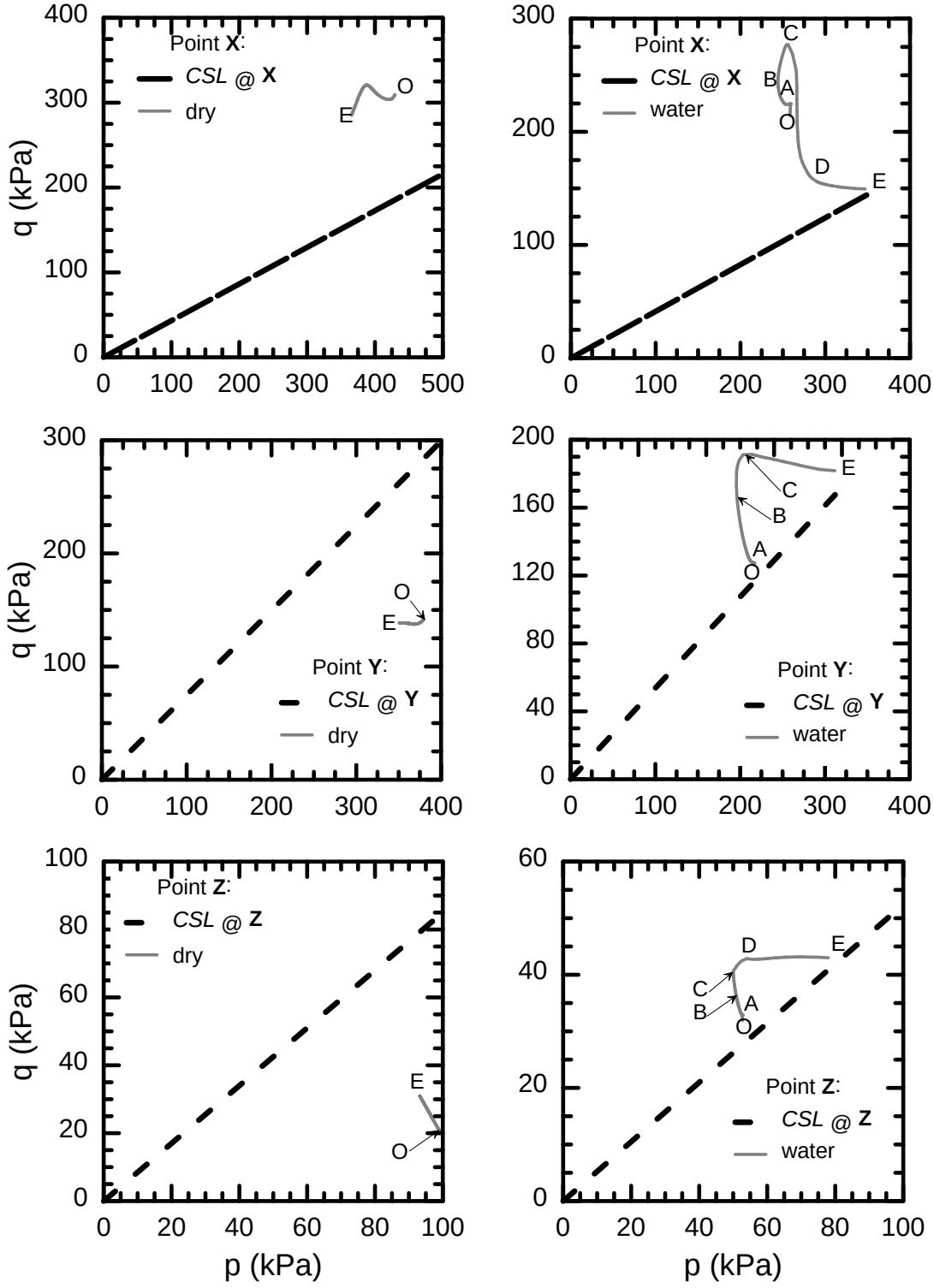

Figure 8.29: Saturated (water) vs. dry soil response depicted through stress paths in the *p-q* space and associated *CSL* lines assuming that the strength envelope evolution degrades (conforming to **Table 8.2**) at Points X, Y and Z.

Figure 8.29 portrays the undergoing stress paths originating from stress state O (designating the origin of the creep step) to E (denoting the end of the creep state after 171 days). The saturated soil response is also incorporated in the figure to emphasize the difference in the simulated response. It is evident that the soil elements X, Y and Z portray no failure considering how far the stress state E is from the *CSL* projection in the stress space. Note that the case study assuming the presence of water failed after 107 days. The dry slope incorporating the exact same constitutive parameters revealed failure solely at the toe after 171 days.

8.4 Concluding remarks

The current chapter investigates the stability of a saturated slope using the proposed model. A slope of mild inclination (20˚ degrees) subjected to an undrained excavation at the toe was modeled. It is shown that the inviscid elastoplastic response, even with strength envelope evolution as a kinematic hardening rule does not lead to failure because this model cannot control the strength envelope evolution due to the accumulation of plastic strains. The plastic strains are associated to the stress field. Considering that the stress field is more or less fixed, the model cannot control the generation of plastic strains of sufficient magnitude to initiate slope instability along a failure surface.

At first, the mechanical behavior of the excavated cut was examined assuming the presence of water. It was established that the excavation was stable (assuming that the strength envelope would not degrade) and the toe reached the steady state while at the same time the associated displacements were relatively small.

Next, the creep induced slope failure was investigated in namely three individual cases. A situation where the excess porewater pressures would dissipate was assumed followed by the accumulation of viscous strains leading ultimately to delayed failure under saturated conditions. This example served as a common denominator for the current chapter. The creep parameters selected were chosen carefully to portray that a pseudo-steady state was attained (the pseudo-steady state is a term established to denote the dissipation of the excess porewater pressures associated with the excavation of the final cut regardless whether it is not truly a steady state but rather a transient situation). After the pseudo-state was attained deviatoric creep gradually revealed its deleterious effect on soil strength. The failure

surface started propagating from the toe backwards and uphill while at some time another slip line originated from the crest and transitioned downwards to unite with the former segment. Once the failure line was complete bifurcation began. This statement summarizes the progressive failure mechanism.

The other two cases revealed either the stationary component of creep after approximately 5,614 days (approximately 15.3 years) or failure at very short consolidation times. The current chapter revealed the capability of the model to accurately simulate the retrogressive slope instability mechanism and the versatility of the constitutive framework to account for media that tend to fail after considerable times.

Finally, it was clarified that the retrogressive slope instability mechanism is associated to the presence of water in the slope without which failure is located solely along the toe.

9

Conclusions

9.1 Summary of main points

The present dissertation develops a constitutive model for structured soils with time dependent characteristics. The model builds on previously developed models for structured soils (Kavvadas and Amorosi, 2000; Belokas, 2008) and includes additional structural features (e.g. a strength envelope degradation with plastic strains) and, mainly, a complete set of time-dependent characteristics.

The need for the development of this model was based on finite element analyses of slope stability which indicated that structure degradation effects could not model the onset of slope instability by a mechanism of strength reduction due to plastic strains. This deficiency was attributed to the fact that classical inviscid elastoplastic models for structured soils cannot control the magnitude of plastic strains (and thus cannot generate large-enough plastic strains to cause failure), as plastic strains are imposed by the physical problem. The new idea stems from the fact that the addition of time-dependent characteristics can solve this problem, as accumulation of "creep" strains can be independently controlled and reach large-enough values to cause failure. Thus, the combination of time-dependent characteristics and classical structure degradation can lead to the solution of "delayed" failures is slopes (but also in other geotechnical problems). The developed model was used in the analysis of slope stability and the above features were successfully modeled by predicting a retrogressive slope instability mechanism triggering failure in a saturated slope.

The proposed model combines features of structured soils and time-dependent characteristics. Specifically :

a. The proposed model is founded on the principles of classical elastoplasticity for structured soils and the time-dependent overstress theory by Perzyna (1962, 1966). The model includes structure degradation attributed to both plastic-strain and creep-strain related phenomena. The Structure Strength envelope is allowed to degrade towards the intrinsic state due to plastic straining thus comprising its limiting bound on the down side.

   The viscoelastoplastic formulation incorporates an Intrinsic Strength Envelope (*ISE*) to designate the reference state, a Structure Strength Envelope (*SSE*) to account for the effect of preexisting structure and a plastic yield envelope (*PYE*) to denote the infinitesimal viscoelastic domain.

   The Structure Strength Envelope is adjusted along the hydrostatic axis translated towards the tensional regime to account for the effects of bonding under isotropic compression. Only secondary anisotropy is incorporated in the model. Small strain stiffness is accounted for by employing an infinitesimal plastic yield envelope. The *PYE* transitions towards the conjugate point on the *SSE* due to plastic or deviatoric viscous straining by thus altering the plastic hardening modulus. The proposed expression for the interpolation rule is pressure dependent associated with the phase transformation line projection in the stress hyperplane (it addresses the deficiency of Kavvadas and Amorosi (2000) and Belokas (2008) at stress states laying on the dry side).

   Following the concept by Mroz and Norris (1982), Desai et al. (1986), Pastor et al. (1990) and Gens (1995) the formulation may degrade into a simple structureless isotropic model lacking any aspect of anisotropy and it can even degenerate into an intrinsic elastoplastic model disregarding any undergoing viscous effects.

b. The volumetric viscous strain is assumed to be existent within the plastic yield surface. This leads to the increase of strength thus conforming to Bjerrum's postulate (1967). The viscous deviatoric component develops solely at states laying on *PYE* associated with plastic straining. Note that the volumetric viscous strain definition incorporates the secondary compression coefficient while the shear viscous strain component is founded on the Singh-Mitchell (1968) empirical formulation.

Both the stationary viscous behavior and the tertiary creep stage are simulated by means of the governing equations. Delayed failure is predicted by employing the critical state line inclination as hardening variable. The viscous shear strain deviator proves the fuse that inflates the transition towards failure. The primary creep stage cannot be captured accurately considering the deficiency of the Sing-Mitchell expression comprising the foundation stone for the definition of the deviatoric shear viscous strain deviator.

The critical state line projection in the stress hyperplane is associated also to the accumulation of deviatoric plastic strains. This situation comprises a mathematical manipulation of the governing constitutive equations allowing for the simulation of significant softening even in cases lacking structure.

The proposed model was evaluated through a parametric study investigating different aspects of the simulated behavior. An ensemble of single point or element based (in Finite Element Code SIMULIA ABAQUS) numerical analyses were conducted to investigate the elastoplastic and time-dependent simulated response. Results were presented in drained triaxial, plane strain and direct simple shear testing on a slightly overconsolidated structureless soil specimen. The deviatoric component revealed its devastating effect on soil strength leading ultimately to delayed failure. Drained conditions were applied to account for pure creep postulating drained boundary conditions for the stress state to remain intact. The effect of time-dependency was further evaluated in standard oedometer creep and stress relaxation tests. Both experimental setups resulted in the lateral pressure coefficient increasing to unity.

c. The proposed model was further evaluated against experimental measurements both in the oedometer and in the triaxial apparatus. The time-dependent response in an oedometer test was depicted in a natural soft clay specimen resembling peat. It was shown that the proposed model converged to the exact same mechanical response with the experimental measurements. Selection of the case study was not random considering that the highest discrepancy would prove at such a soft geomaterial.

A thorough literature review revealed only a limited number of publications addressing the drained time-dependent response of clay in the triaxial

apparatus with the last one dating back to 1975 (Bishop, 1966; Ter-Stepanian, 1975). The reason lies with the considerable time period required for the specimen to fail in creep (time to failure may exceed 200 days and even reach 1000 days). Hence, the mechanical response was examined in an experimental study of coal in the triaxial apparatus. Delayed failure was portrayed in a specimen subjected to a high stress level and was simulated by incorporating the proper constitutive parameters.

Regardless of any logical approximations made in the definition of the governing equations the proposed model performed relatively well. It was concluded that the model fails to capture the primary creep stage by focusing on the secondary creep stage. This was attributed to the inherent approximation of the Singh-Mitchell empirical relation comprising the foundation stone of the model.

d. The proposed model was applied in a 2D slope stability analysis via the finite element method (using the computer program ABAQUS). The analysis revealed the deficiency of time-independent elastoplastic constitutive models for structured soils to simulate slope instability (e.g. the models proposed by Kavvadas and Amorosi; 2000; Belokas; 2008). Such models attempt to capture the slope instability mechanism through plastic softening, either due to structure degradation or via strength envelope evolution associated with plastic strains. Considering that time-independent models have no control on the magnitude of the plastic strains (which can trigger the above failure mechanisms) it was proven difficult to capture failure in such a way. On the contrary, time-dependent behavior permits the temporal accumulation of inelastic strains (plastic and creep) in highly stressed zones and thus permits the description of progressive failure in the analyzed slope. The analyses show that the proposed model has the capabilities to predict delayed failure of a slope by triggering tertiary creep and a retrogressive slope instability mechanism.

e. The retrogressive slope instability mechanism was triggered in a creep induced slope failure. The failure surface would propagate from the toe backwards and uphill while at same time another slip line originating from the crest would transition downwards to unite with the primal segment. Once the two sections would unite to form the final slip surface the slope

would fail. The progressive failure mechanism is inextricably linked to the presence of water in the slope without which failure is located solely along the toe.

9.2 Recommendations for future research

The current Thesis introduces a time-dependent mechanical framework emulating delayed failure by incorporating a complete set of time-dependent characteristics. Based on observations on experimental measurements and further numerical analyses it was concluded that the proposed model can qualitatively at least emulate correctly the underlying mechanisms leading to failure (by accounting for the temporal accumulation of inelastic strains).

It is worth to continue in the same direction by improving on the proposed time-dependent mechanical framework and further investigate the practical implications of the time-dependent characteristics of the proposed model. Hence, the following topics are proposed to elaborate on both the constitutive response and the practical implications of the model:

a. Primary anisotropy needs to be considered. At the current version of the model, the Structure Strength Envelope is oriented along the hydrostatic axis and solely the secondary anisotropy is accounted for. Consequently the center of the *SSE* needs to be deflected off the isotropic axis and follow a kinematic rule similar to the one presented in Sitarenios et al. (2013). Furthermore, incorporating a non-associative flow rule will result in a more realistic simulation of the experimental measurements.
b. The experimental data revealed the shortcoming of the Singh-Mitchell approach. Hence, another empirical formulation emulating the primary and secondary creep stage needs to be established based on published experimental measurements and possible new data sets. Note that the experiments need to address drained conditions thus resulting in considerable times especially in the case where the time-dependent clayey response is of interest.
c. The retrogressive slope instability mechanism was established by propagating from the toe backwards and uphill to unite with another section

originating from the crest. The phenomenon needs to be further investigated and evaluated possibly through back analyses in well documented cases where creep induced slope failures have occurred.

d. The practical implication associated with introducing a set of possible mitigation measures and techniques needs to be investigated. It would be of great practical significance assuming that certain "surgical" interventions would prevent the retrogressive slope instability mechanism to form. The proposed formulation should be primarily employed in the original design of a project to prevent potential failure. Cost and time-effective mitigation measures could be introduced based on the time-dependent characteristics of the model, assuming that the failure has already occurred (attributed to viscous phenomena).

e. The time-dependent soil response around the tunnel final lining dictates a pressure increase attributed to viscous phenomena. The sustained increase in the final load can result in potential cracking and thus prove catastrophic for the structure. The time-dependent constitutive framework could be employed to designate the percentage of pressure increase in the design.

f. Time-dependent behavior permits the temporal accumulation of inelastic strains (plastic and creep) in highly stressed zones and thus permits the description of progressive failure in the analyzed slope. It fails however, to account for the soil collapse attributed to the alterations in suction. Hence, the time-dependent behavioral framework needs to incorporate unsaturated soil mechanics principles in the future.

10

References

Abuzeid, O. M., Al-Rabadi, A. N., & Alkhaldi, H. S. (2010). Fractal geometry-based hypergeometric time series solution to the hereditary thermal creep model for the contact of rough surfaces using the Kelvin-Voigt medium. *Mathematical Problems in Engineering, 2010*.

Adachi, T., & Oka, F. (1982). Constitutive Equations for Normally Consolidated Clay Based on Elasto-Viscoplasticity. *Soils and Foundations, 22*(4), 57-70.

Adachi, T., Oka, F., & Mimura, M. (1987). MATHEMATICAL STRUCTURE OF AN OVERSTRESS ELASTO-VISCOPLASTIC MODEL FOR CLAY. *Soils and Foundations, 27*(3), 31-42.

Adachi, T., & Okano, M. (1974). A CONSTITUTIVE EQUATION FOR NORMALLY CONSOLIDATED CLAY. *Soils and Foundations, 14*(4), 55-73.

Agah-Tehrani, A., Lee, E., Mallett, R., & Onat, E. (1987). The theory of elastic-plastic deformation at finite strain with induced anisotropy modeled as combined isotropic-kinematic hardening. *Journal of the Mechanics and Physics of Solids, 35*(5), 519-539.

Al-Tabbaa, A. (1987). *Permeability and stress-strain response of speswhite kaolin.* University of Cambridge.

Al-Tabbaa, A., & Wood, D. M. (1987). Some measurements of the permeability of kaolin. *Geotechnique, 37*(4), 499-514.

Alberro, J., & Santoyo, E. (1973). Long term behaviour of Mexico city clay.

Allman, M., & Atkinson, J. (1992). Mechanical properties of reconstituted Bothkennar soil. *Geotechnique, 42*(2), 289-301.

Aristorenas, G. V. (1992). *Time-dependent behavior of tunnels excavated in shale.* Massachusetts Institute of Technology.

Barla, G. B. (2001). Tunnelling under squeezing rock conditions. *Tunnelling Mechanics (Eurosummerschool, Innsbruck)*.

Barla, G. B. (2005). *Design analysis for tunnels in squeezing rock.* Paper presented at the Proc. of the 11th International Conference of the International Association of Computer Methods and Advances in Geomechanics (IACMAG), Torino, Italy.

Barré de Saint Venant, A. (1855). Mémoire sur la Torsion des Prismes, Mém. Divers Savants. *CR Math. Acad. Sci. Paris, 14*, 233-560.

Belokas, G. (2008). *Modelling of the mechanical behaviour of bonded and anisotropic soils.* (PhD), National Technical University of Athens (NTUA), Athens, Greece.

Belokas, G., & Kavvadas, M. (2010). An anisotropic Model for Structured Soils: Part I: Theory. *Computers and Geotechnics, 37*(6), 737-747.

Belokas, G., & Kavvadas, M. (2011). An intrinsic compressibility framework for clayey soils. *Geotechnical and Geological Engineering, 29*(5), 855-871.

Berre, T. (1973). *Shear strength of normally consolidated clays.* Paper presented at the Proc. of 8th Int. Conf. on SMFE.

Betten, J. (2005). *Creep mechanics*: Springer.

Bingham, E. C. (1922). *Fluidity and plasticity* (Vol. 1): McGraw-Hill New York.

Bishop, A. W. (1966). The Strength of Soils as Engineering Materials. *Geotechnique, 16*(02), 91-130. http://www.icevirtuallibrary.com/content/article/10.1680/geot.1966.16.2.91

Bjerrum, L. (1967). Engineering geology of Norwegian normally-consolidated marine clays as related to settlements of buildings. *Geotechnique, 17*(2), 83-118.

Bjerrum, L., Simons, N., & Torblaa, I. (1958). *The effect of time on the shear strength of a soft marine clay.* Paper presented at the Proc., Brussels Conf. on Earth Pressure Problems.

Bodner, S., & Partom, Y. (1975). Constitutive Equations for Elastic-Viscoplastic Strain-Hardening Materials. *Journal of Applied Mechanics, 42*, 385.

Boidy, E. (2002). *Modélisation numérique du comportement différé des cavités souterraines.* Université Joseph-Fourier-Grenoble I.

Bonini, M., Debernardi, D., Barla, M., & Barla, G. (2009). The mechanical behaviour of clay shales and implications on the design of tunnels. *Rock mechanics and rock engineering, 42*(2), 361-388.

Bowles Joseph, E. (1996). Foundation analysis and design: Mc. Graw Hill Companies.

Brantut, N., Baud, P., Heap, M., & Meredith, P. (2012). Micromechanics of brittle creep in rocks. *Journal of Geophysical Research: Solid Earth (1978–2012), 117*(B8).

Burgers, J. M. (1948). A mathematical model illustrating the theory of turbulence. *Advances in applied mechanics, 1*, 171-199.

Burghignoli, A., Miliziano, S., & Soccodato, F. (1998). *The effect of bond degradation in cemented clayey soils.* Paper presented at the Proceedings of the symposium on geotechnical engineering of hard soils–soft rocks, Balkema.

Burland, J. (1989). Small is Beautiful, Ninth Laurits Bjerrum Memorial Lecture. *Canadian Geotechnical Journal, 26*(4), 499-516.

Burland, J. (1990). On the compressibility and shear strength of natural clays. *Geotechnique, 40*(3), 329-378.

Callisto, L., & Calabresi, G. (1998). Mechanical behaviour of a natural soft clay. *Geotechnique, 48*(4), 495-513.

Christensen, R. W., Wu, T. H., & Mencl, V. (1964). Analysis of clay deformation as a rate process. *Journal of Soil Mechanics & Foundations Div, 90*(6411).

Cotecchia, F., & Chandler, R. (1998). *One-dimensional compression of a natural clay: structural changes and mechanical effects.* Paper presented at the Proceedings of the 2nd International Symposium on Hard Soils-Soft Rocks, Napoli.

Cristescu, N. (1967). *Dynamic plasticity* (Vol. 4).

Cristescu, N. (1989). *Rock rheology*: Kluwer Academic Publishers.

Cristescu, N. (1994). *Viscoplasticity of geomaterials*: Springer Verlag, New York.

Crouch, R., & Wolf, J. (1994). Unified 3D critical state bounding-surface plasticity model for soil incorporating continuous plastic loading under cyclic paths. I: Constitutive relations. *International Journal for Numerical and Analytical Methods in Geomechanics, 18*(11), 735-758.

d'Onofrio, A., de Magistris, F. S., & Olivares, L. (1998). *Influence of soil structure on the behavior of two natural stiff clays in the prefailure range.* Paper presented at the Proc. 2nd Intern. Symp. on the Geotechnics of Hard Soils - Soft Rocks, Naples.

Dafalias, Y., & Popov, E. (1975). A model of nonlinearly hardening materials for complex loading. *Acta Mechanica, 21*(3), 173-192.

Dafalias, Y. F. (1987). *An anisotropic critical state clay plasticity model.* Paper presented at the Proc. of 2nd International Conference on Constitutive Laws for Engineering Materials, Tucson-Arizona.

Darve, F., Flavigny, E., & Meghachou, M. (1995). Constitutive modelling and instabilities of soil behaviour. *Computers and Geotechnics, 17*(2), 203-224. doi: http://dx.doi.org/10.1016/0266-352X(95)93869-K

Debernardi, D. (2004). *Prove specialistiche e analisi numeriche a ritroso riguardanti lo scavo di gallerie profonde in Argille Scagliose tenendo conto della dipendenza dal tempo (Specialistic tests and back analyses regarding the excavation of deep tunnels in Clay Shales taking into account the time dependency).* (Master of Science in Civil Engineering, Structural Eng. specialization), Politecnico di Torino, Torino.

Debernardi, D. (2008). *Viscoplastic behaviour and design of tunnels.* Ph. D. Thesis, Politecnico di Torino, Department of Structural and Geotechnical Engineering, Italy.

Debernardi, D., & Barla, G. (2009). New viscoplastic model for design analysis of tunnels in squeezing conditions. *Rock mechanics and rock engineering, 42*(2), 259-288.

Desai, C., Somasundaram, S., & Frantziskonis, G. (1986). A hierarchical approach for constitutive modelling of geologic materials. *International Journal for Numerical and Analytical Methods in Geomechanics, 10*(3), 225-257.

Desai, C., & Zhang, D. (1987). Viscoplastic model for geologic materials with generalized flow rule. *International Journal for Numerical and Analytical Methods in Geomechanics, 11*(6), 603-620.

Desai, C. S., & Siriwardane, H. J. (1984). *Constitutive laws for engineering materials, with emphasis on geologic materials* (Vol. 11): Prentice-Hall Englewood Cliffs, NJ.

di Prisco, C., & Imposimato, S. (1996). Time dependent mechanical behaviour of loose sands. *Mechanics of Cohesive-frictional Materials*, *1*(1), 45-73.

Drucker, D. C. (1951). *A more fundamental approach to plastic stress-strain relations*: Division of Applied Mathematics, Brown University.

Drucker, D. C. (1956). On uniqueness in the theory of plasticity. *Quarterly of Applied Mathematics, 14*, 35-42.

Drucker, D. C. (1959). A definition of stable inelastic material. *Journal of Applied Mechanics, 26*, 101–195.

Drucker, D. C., Gibson, R. E., & Henkel, D. J. (1959). Soil mechanics and work hardening theories of plasticity. *Transactions of the American Society of Civil Engineers, 122*.

Duncan, J. M., & Chang, C.-Y. (1970). Nonlinear analysis of stress and strain in soils. *Journal of the Soil Mechanics and Foundations Division, 96*(5), 1629-1653.

Feda, J. (1992). *Creep of Soils and Related Phenomena*: Access Online via Elsevier.

Fodil, A., Aloulou, W., & Hicher, P. (1997). Viscoplastic behaviour of soft clay??? *Geotechnique, 47*(3), 581-591.

Fortsakis, P. (2012). *Investigation of the static interaction of the surrounding soil/rock with the tunnel final lining.* (PhD), Technical University of Athens (NTUA), Athens (in Greek).

Fujii, Y., Kiyama, T., Ishijima, Y., & Kodama, J. (1999). Circumferential strain behavior during creep tests of brittle rocks. *International Journal of Rock Mechanics and Mining Sciences, 36*(3), 323-337. doi: http://dx.doi.org/10.1016/S0148-9062(99)00024-8

Garlanger, J. E. (1972). The consolidation of soils exhibiting creep under constant effective stress. *Geotechnique, 22*(1), 71-78.

Gasc-Barbier, M., Chanchole, S., & Bérest, P. (2004). Creep behavior of Bure clayey rock. *Applied Clay Science, 26*(1), 449-458.

Gens, A. (1995). *General report: Prediction, performance and design.* Paper presented at the of: Int. Symp. on pre-failure deformation charact. of geomaterials.

Georgiannou, V. N. (1988). *The behaviour of clayey sands under monotonic and cyclic loading.* Imperial College London (University of London).

Graham, J., Crooks, J., & Bell, A. (1983). Time effects on the stress-strain behaviour of natural soft clays. *Geotechnique, 33*(3), 327-340.

Green, A. E., & Naghdi, P. M. (1965). A general theory of an elastic-plastic continuum. *Archive for rational mechanics and analysis, 18*(4), 251-281.

Hansen, F. D., & Carter, N. L. (1984). *Creep of avery island rocksalt.* Paper presented at the Proceedings of the First Conference on Mechanical Behaviour of Salt, Trans. Tech. Publ., Causthal-Zellerfield, Germany.

Hansen, J. B. (1963). Discussion of Hyperbolic stress-strain response: cohesive soils. *Journal of the Soil Mechanics and Foundations Division, ASCE, 89*(1), 241-242.

Hashiguchi, K., & Chen, Z. P. (1998). Elastoplastic constitutive equation of soils with the subloading surface and the rotational hardening. *International Journal for Numerical and Analytical Methods in Geomechanics, 22*(3), 197-227.

Hashiguchi, K., & Okayasu, T. (2000). Time-dependent elastoplastic constitutive equation based on the subloading surface model and its application to soils. *Soils and Foundations, 40*(4), 19-36.

Havel, F. (2004). *Creep in soft soils.* Norwegian University of Science and Technology.

Heap, M., Baud, P., Meredith, P., Bell, A., & Main, I. (2009). Time-dependent brittle creep in Darley Dale sandstone. *Journal of Geophysical Research: Solid Earth (1978–2012), 114*(B7).

Heap, M., Baud, P., Meredith, P., Vinciguerra, S., Bell, A., & Main, I. (2011). Brittle creep in basalt and its application to time-dependent volcano deformation. *Earth and Planetary Science Letters, 307*(1), 71-82.

Hight, D. W. (1983). *Laboratory investigations of sea-bed clays.* Imperial College London (University of London).

Hill, R. (1958). A general theory of uniqueness and stability in elastic-plastic solids. *Journal of the Mechanics and Physics of Solids, 6*(3), 236-249.

Hinchberger, S. D., & Rowe, R. K. (2005). Evaluation of the predictive ability of two elastic-viscoplastic constitutive models. *Canadian Geotechnical Journal, 42*(6), 1675-1694.

Hooke, R., Waller, R., Smith, S., & Walford, B. (1705). *The Posthumous Works of Robert Hooke, MDSRS Geom. Prof. Gresh. &c: Containing His Cutlerian Lectures, and Other Discourses, Read at the Meetings of the Illustrious Royal Society: in which... Illustrated with Sculptures: to These Discourses is Prefixt the Author's Life, Giving an Account of His Studies and Employments, with an Enumeration of the Many Experiments, Instruments, Contrivances and Inventions, by Him Made and Produc'd as Curator of Experiments to the Royal Society*: Sam Smith and Benj. Walford,(printers to the Royal Society) at the Princes Arms in St. Paul's Church-yard.

Houlsby, G. (1985). The use of a variable shear modulus in elastic-plastic models for clays. *Computers and Geotechnics, 1*(1), 3-13.

Hsieh, H., Kavazanjian Jr, E., & Borja, R. (1990). Double-yield-surface Cam-clay plasticity model. I: theory. *Journal of Geotechnical Engineering, 116*(9), 1381-1401.

Hueckel, T., & Maier, G. (1977a). Incremental boundary value problems in the presence of coupling of elastic and plastic deformations: a rock mechanics oriented theory. *International Journal of Solids and Structures, 13*(1), 1-15.

Hueckel, T., & Maier, G. (1977b). *Non-associated and coupled flow rules of elastoplasticity for geotechnical media.* Paper presented at the Proceedings of the 9th International Conference on Soil Mechanics and Foundation Engineering (JCSFE).

Hunsche, U., & Hampel, A. (1999). Rock salt — the mechanical properties of the host rock material for a radioactive waste repository. *Engineering Geology, 52*(3–4), 271-291. doi: http://dx.doi.org/10.1016/S0013-7952(99)00011-3

Jamiolkowski, M., Lancellotta, R., & Lo Presti, D. (1995). *Remarks on the stiffness at small strains of six Italian clays.* Paper presented at the PRE-FAILURE DEFORMATION OF GEOMATERIALS. PROCEEDINGS OF THE INTERNATIONAL SYMPOSIUM, 12-14 SEPTEMBER 1994, SAPPORO, JAPAN. 2 VOLS.

Jardine, R. (1992). Some observations on the kinematic nature of soil stiffness. *Soils and Foundations, 32*(2), 111-124.

Jardine, R. (1995). *One perspective of the pre-failure deformation characteristics of some geomaterials.* Paper presented at the PRE-FAILURE DEFORMATION OF GEOMATERIALS. PROCEEDINGS OF THE INTERNATIONAL SYMPOSIUM, 12-14 SEPTEMBER 1994, SAPPORO, JAPAN. 2 VOLS.

Jin, J., & Cristescu, N. (1998). An elastic/viscoplastic model for transient creep of rock salt. *International Journal of Plasticity, 14*(1), 85-107.

Juárez-Badillo, E. (2011). The Principle of Natural Proportionality applied to the creep of compacted recycled asphalt pavement.

Kaliakin, V. N., & Dafalias, Y. F. (1990a). Theoretical aspects of the elastoplastic-viscoplastic bounding surface model for cohesive soils. *Soils and Foundations, 30*(3), 11-24.

Kaliakin, V. N., & Dafalias, Y. F. (1990b). Verification of the Elastoplastic-Viscoplastic Bounding Surface Model for Cohesive Soils. *Soils and Foundations, 30*(3), 25-36.

Kanchi, M., Zienkiewicz, O., & Owen, D. (1978). The visco-plastic approach to problems of plasticity and creep involving geometric non-linear effects. *International Journal for Numerical Methods in Engineering, 12*(1), 169-181.

Karstunen, M., Sivasithamparam, N., Brinkgreve, R., & Bonnier, P. (2013). *Modelling rate-dependent behaviour of structured natural clays.* Paper presented at the Proc. International Conference on Installation Effects in Geotechnical Engineering, Rotterdam, NL, 23-27 March 2013.

Kavazanjian, E., & Mitchell, J. K. (1977). *A general stress-strain-time formulation for soils.* Paper presented at the Proceedings of 9th International Conference on Soil Mechanics and Foundation Engineering. Tokyo: Japanese Society of Soil Mechanics and Foundation Engineering.

Kavazanjian, E. J., & Mitchell, J. K. (1980). Time-dependent deformation behavior of clays. *Journal of Geotechnical and Geoenvironmental Engineering, 106*(ASCE 15488).

Kavvadas, M. (1982). *Non-linear consolidation around driven piles in clays.* Massachusetts Institute of Technology.

Kavvadas, M. (1995). *A plasticity approach to the mechanical behaviour of bonded soils.* Paper presented at the Proceedings of 4th international conference on computational plasticity (COMPLAS IV), Barcelona.

Kavvadas, M., & Amorosi, A. (2000). A constitutive model for structured soils. *Geotechnique, 50*(3), 263-273.

Kavvadas, M., & Belokas, G. (2000). *An anisotropic elastoplastic constitutive model for natural soils.* Paper presented at the Computer Methods and Advances in Geomechanics: Proceedings of the Kenth International Conference, Tuscon, AZ, USA, 7-12 January 2001.

Kavvadas, M. J. (1998). *General report: Modelling the soil behaviour-Selection of soil parameters.* Paper presented at the Proc. 2nd Int. Conf. Geotech. Hard Soils-Soft Rocks, Naples.

Kavvadas, M. J., & Amorosi, A. (1998). A plasticity approach for the mechanical behaviour of structured soils. *The geotechnics of hard soils±soft rocks (eds Evangelista and Picarelly)*, 603-612.

Kavvadas, M. J., & Anagnostopoulos, A. (1998). *A framework for the mechanical behaviour of structured soils.* Paper presented at the Proceedings 2nd Int Symp on the Geotechnics of Hard Soils-Soft Rocks, Naples.

Kimoto, S., & Oka, F. (2005). An elasto-viscoplastic model for clay considering destructuralization and consolidation analysis of unstable behavior. *Soils and Foundations, 45*(2), 29-42.

Kondner, R. L. (1963). Hyperbolic stress-strain response: cohesive soils. *Journal of the Soil Mechanics and Foundations Division, ASCE, 89*(1), 115-143.

Kramer, S. L. (1996). *Geotechnical earthquake engineering*: Pearson Education India.

Krempl, E., McMahon, J., & Yao, D. (1986). Viscoplasticity based on overstress with a differential growth law for the equilibrium stress. *Mechanics of materials, 5*(1), 35-48.

Kulhawy, F. H., Duncan, J. M., & Seed, H. B. (1969). Finite Element Analyses of Stresses and Movements in Embankments During Construction: DTIC Document.

Kutter, B., & Sathialingam, N. (1992). Elastic-viscoplastic modelling of the rate-dependent behaviour of clays. *Geotechnique, 42*(3), 427-441.

Lacerda, W. A., & Houston, W. N. (1973). *Stress relaxation in soils.* Paper presented at the 8th ICSMFE.

Ladd, C. C. (1972). *Engineering Properties of Soft Foundation Clays at Two South Louisiana Levees Sites*: Massachusetts Institute of Technology.

Lade, P. V., & Nelson, R. B. (1984). Incrementalization procedure for elasto-plastic constitutive model with multiple, intersecting yield surfaces. *International Journal for Numerical and Analytical Methods in Geomechanics, 8*(4), 311-323.

Lefebvre, G., & Leboeuf, D. (1987). Rate effects and cyclic loading of sensitive clays. *Journal of Geotechnical Engineering, 113*(5), 476-489.

Lemaitre, J., & Chaboche, J. (1990). Mechanics of solid materials: Cambridge University Press, Cambridge.

Leoni, M., Karstunen, M., & Vermeer, P. (2008). Anisotropic creep model for soft soils. *Geotechnique, 58*(3), 215-226.

Leroueil, S., Kabbaj, M., Tavenas, F., & Bouchard, R. (1985). Stress–strain–strain rate relation for the compressibility of sensitive natural clays. *Geotechnique, 35*(2), 159-180.

Leroueil, S., & Vaughan, P. (1990). The general and congruent effects of structure in natural soils and weak rocks. *Geotechnique, 40*(3), 467-488.

Lubliner, J. (1990). *Plasticity theory*: Courier Dover Publications.

Ma, L., & Daemen, J. J. K. (2006). An experimental study on creep of welded tuff. *International Journal of Rock Mechanics and Mining Sciences, 43*(2), 282-291. doi: http://dx.doi.org/10.1016/j.ijrmms.2005.07.002

Mabssout, M., Herreros, M., & Pastor, M. (2006). Wave propagation and localization problems in saturated viscoplastic geomaterials. *International Journal for Numerical Methods in Engineering, 68*(4), 425-447.

Malandraki, V., & Toll, D. (1994). *Yielding of a weakly bonded artificial soil.* Paper presented at the Proceedings of the International Symposium on Pre-Failure Deformation Characteristics of Geomaterials, Hokkaido, Japan.

Maranini, E., & Brignoli, M. (1999). Creep behaviour of a weak rock: experimental characterization. *International Journal of Rock Mechanics and Mining Sciences, 36*(1), 127-138. doi: http://dx.doi.org/10.1016/S0148-9062(98)00171-5

Maranini, E., & Yamaguchi, T. (2001). A non-associated viscoplastic model for the behaviour of granite in triaxial compression. *Mechanics of materials, 33*(5), 283-293. doi: http://dx.doi.org/10.1016/S0167-6636(01)00052-7

Marques, M. E. S., Leroueil, S., & Soares de Almeida, M. d. S. (2004). Viscous behaviour of St-Roch-de-l'Achigan clay, Quebec. *Canadian Geotechnical Journal, 41*(1), 25-38.

Martin, R. J., Noel, J. S., Boyd, P. J., & Price, R. H. (1997). Creep and static fatigue of welded tuff from Yucca Mountain, Nevada. *International Journal of Rock Mechanics and Mining Sciences, 34*(3–4), 190.e191-190.e117. doi: http://dx.doi.org/10.1016/S1365-1609(97)00179-2

Matsui, T., & Abe, N. (1985). *Elasto/viscoplastic constitutive equation of normally consolidated clays based on flow surface theory.* Paper presented at the International conference on numerical methods in geomechanics.

Maxwell, J. C. (1868). On governors. *Proceedings of the Royal Society of London, 16*, 270-283.

Mayne, P. W., & Kulhawy, F. H. (1990). Direct and indirect determination of in situ Ko in clays. *Transportation Research Record*(1278).

Mesri, G., & Choi, Y. (1985). Settlement analysis of embankments on soft clays. *Journal of Geotechnical Engineering, 111*(4), 441-464.

Mesri, G., & Godlewski, P. M. (1977). Time and stress-compressibility interrelationship. *Journal of the Geotechnical Engineering Division, 103*(5), 417-430.

Mitchell, J. K., Campanella, R. G., & Singh, A. (1968). Soil creep as a rate process. *Journal of Soil Mechanics & Foundations Division*.

Mitchell, J. K., & Soga, K. (1976). *Fundamentals of soil behavior*: Wiley New York.

Mroz, Z. (1967). On the description of anisotropic work hardening. *Journal of the Mechanics and Physics of Solids, 15*(3), 163-175.

Mroz, Z., & Norris, V. (1982). Elastoplastic and viscoplastic constitutive models for soils with application to cyclic loading. *Soil mechanics-transient and cyclic loads, 173*.

Mrŏz, Z., Norris, V. A., & Zienkiewicz, O. C. (1978). An anisotropic hardening model for soils and its application to cyclic loading. *International Journal for Numerical and Analytical Methods in Geomechanics, 2*(3), 203-221. doi: 10.1002/nag.1610020303

Murad, M. A., Guerreiro, J. N., & Loula, A. F. (2001). Micromechanical computational modeling of secondary consolidation and hereditary creep in soils. *Computer methods in applied mechanics and engineering, 190*(15), 1985-2016.

Murayama, S., & Shibata, T. (1966). Flow and stress relaxation of clays *Rheology and Soil Mechanics/Rhéologie et Mécanique des Sols* (pp. 99-129): Springer.

Naghdi, P. M., & Murch, S. A. (1963). On the Mechanical Behavior of Viscoelastic/Plastic Solids. *Journal of Applied Mechanics, 30*(3), 321-328. doi: 10.1115/1.3636556

Nagtegaal, J., & De Jong, J. (1982). Some aspects of non-isotropic work-hardening in finite strain plasticity. *Plasticity of metals at finite strain: theory, experiment and computation, 65*.

Newton, I. (1687). Philosophiae Naturalis Principia Mathematica (mathematical principles of natural philosophy). *London (1687)*.

Nguyen-Minh, D. (1986). Modèles rhéologiques pour l 'analyse du comportement différé des galeries profondes. *Proceedings of the Int. Cong. On Large Underground Openings, 2*, 659-666.

Nova, R. (1982). *A viscoplastic constitutive model for normally consolidated clay.* Paper presented at the Proceedings IUTAM Conf. Deformation and Failure of Granular Materials.

Nova, R. (1988). Sinfonietta classica: an exercise on classical soil modelling. *Constitutive Equations for Granular Non-Cohesive Soils. Rotterdam: Balkema*, 501-519.

Ohno, N. (1982). A Constitutive Model of Cyclic Plasticity With a Nonhardening Strain Region. *Journal of Applied Mechanics, 49*(4), 721-727. doi: 10.1115/1.3162603

Oka, F. (1978). *Constitutive Theory for Solid-Fluid Mixture and Its Application to Stress Wave Propagation through Cohesive Soil.* Paper presented at the Proc. JSCE.

Oka, F., Adachi, T., & Yashima, A. (1994). Instability of an elasto-viscoplastic constitutive model for clay and strain localization. *Mechanics of materials, 18*(2), 119-129.

Oka, F., Adachi, T., & Yashima, A. (1995). A strain localization analysis using a viscoplastic softening model for clay. *International Journal of Plasticity, 11*(5), 523-545.

Okubo, S., Fukui, K., & Hashiba, K. (2008). Development of a transparent triaxial cell and observation of rock deformation in compression and creep tests. *International Journal of Rock Mechanics and Mining Sciences, 45*(3), 351-361.

Olszak, W., & Perzyna, P. (1966). *The constitutive equations of the flow theory for a nonstationary yield condition.* Paper presented at the Applied mechanics. Proceedings of the 11th international congress.

Papadimitriou, A. (1999). *Elastoplastic modeling of monotonic and dynamic behavior of soils.* Doctorate Thesis, Department of Geotechnical Engineering, Faculty of Civil Engineering, National Technical University of Athens.

Pastor, M., Zienkiewicz, O., & Chan, A. (1990). Generalized plasticity and the modelling of soil behaviour. *International Journal for Numerical and Analytical Methods in Geomechanics, 14*(3), 151-190.

Pender, M. (1978). A model for the behaviour of overconsolidated soil. *Geotechnique, 28*(1), 1-25.

Perzyna, P. (1962). The constitutive equations for rate sensitive plastic materials: DTIC Document.

Perzyna, P. (1966). Fundamental problems in viscoplasticity. *Advances in applied mechanics, 9*(2), 243-377.

Pestana, J. (1994). A unified constitutive model for clays and sands. *ScD thesis, Massachusetts Institute of Technology, Cambridge, Mass*.

Prager, W. (1949). Recent developments in the mathematical theory of plasticity. *Journal of Applied Physics, 20*(3), 235-241.

Prager, W. (1955). The theory of plasticity: a survey of recent achievements. *Proceedings of the Institution of Mechanical Engineers, 169*(1), 41-57.

Prevost, J.-H. (1978). Plasticity theory for soil stress-strain behavior. *Journal of the Engineering Mechanics Division, 104*(5), 1177-1194.

Prevost, J.-H., & Höeg, K. (1975). Soil mechanics and plasticity analysis of strain softening. *Geotechnique, 25*(2), 279-297.

Rampello, S., Silvestri, F., & Viggiani, G. (1994). *The dependence of small strain stiffness on stress state and history for fine grained soils: The example of Vallericca clay.* Paper presented at the Proc 1st Int Symp on Pre-Failure Defomation of Geomaterials, Sapporo.

Rampello, S., Viggiani, G., & Amorosi, A. (1997). Small-strain stiffness of reconstituted clay compressed along constant triaxial effective stress ratio paths. *Geotechnique, 47*(3), 475-489.

Richardson, A. M., & Whitman, R. V. (1963). Effect of strain-rate upon undrained shear resistance of a saturated remoulded fat clay. *Geotechnique, 13*(4), 310-324.

Roscoe, K., Schofield, A., & Thurairajah, A. (1963). Yielding of clays in states wetter than critical. *Geotechnique, 13*(3), 211-240.

Roscoe, K. H., & Burland, J. (1968). On the generalized stress-strain behaviour of wet clay.

Rowe, R. K., & Hinchberger, S. D. (1998). The significance of rate effects in modelling the Sackville test embankment. *Canadian Geotechnical Journal, 35*(3), 500-516.

Saleeb, A., Arnold, S., Castelli, M., Wilt, T., & Graf, W. (2001). A general hereditary multimechanism-based deformation model with application to the viscoelastoplastic response of titanium alloys. *International Journal of Plasticity, 17*(10), 1305-1350.

Schanz, T., Vermeer, P., & Bonnier, P. (1999). *The hardening soil model: formulation and verification*. Paper presented at the Beyond 2000 in computational geotechnics: 10 years of PLAXIS International; proceedings of the International Symposium beyond 2000 in Computational Geotechnics, Amsterdam, The Netherlands, 18-20 March 1999.

Schofield, A. N., & Wroth, P. (1968). Critical state soil mechanics.

Sekiguchi, H. (1984). Theory of undrained creep rupture of normally consolidated clay based on elasto-viscoplasticity. *Soils and Foundations, 24*(1), 129-147.

Sekiguchi, H. (1985). Constitutive laws of soils. Macrometric approaches—static-intrinsically time dependent. *Discussion session. Proceedings of the 11th ICSMFE, San Francisco, USA*.

Shahrour, I., & Meimon, Y. (1995). Calculation of marine foundations subjected to repeated loads by means of the homogenization method. *Computers and Geotechnics, 17*(1), 93-106.

Shao, J.-F., Zhu, Q., & Su, K. (2003). Modeling of creep in rock materials in terms of material degradation. *Computers and Geotechnics, 30*(7), 549-555.

Sheahan, T. C., Ladd, C. C., & Germaine, J. T. (1996). Rate-dependent undrained shear behavior of saturated clay. *Journal of Geotechnical Engineering, 122*(2), 99-108.

Sheng, D., Sloan, S., & Yu, H. (2000). Aspects of finite element implementation of critical state models. *Computational mechanics, 26*(2), 185-196.

Shibata, K., Tani, K., & Okada, T. (2007). CREEP BEHAVIOR OF TUFFACEOUS ROCK AT HIGH TEMPERATURE OBSERVED IN UNCONFINED COMPRESSION TEST. *Soils and Foundations, 47*(1), 1-10.

Shield, R. T., & Ziegler, H. (1958). On Prager's hardening rule. *Zeitschrift für angewandte Mathematik und Physik ZAMP, 9*(3), 260-276.

Singh, A., & Mitchell, J. (1968). General stress-strain-time function for soils. *Journal of Soil Mechanics & Foundations Division*(94), 21-46.

Sitarenios, P., Belokas, G., & Kavvadas, M. (2013). *The Incorporation of new Isotropic and Kinematic hardening rules in an Anisotropic Constituitve Model.* Paper presented at the Proc. of the 3rd International Symposium in Computational Geomechanichs (ComGeo III), Krakow, Poland.

Sivasithamparam, N., Karstunen, M., Brinkgreve, R., & Bonnier, P. (2013). *Comparison of two anisotropic rate dependent models at element level.* Paper presented at the Proc. International Conference on Installation Effects in Geotechnical Engineering, Rotterdam, NL, 23-27 March 2013.

Ślizowski, J., & Lankof, L. (2003). Salt-mudstones and rock-salt suitabilities for radioactive-waste storage systems: rheological properties. *Applied Energy, 75*(1–2), 137-144. doi: http://dx.doi.org/10.1016/S0306-2619(03)00026-6

Smith, P., Jardine, R., & Hight, D. (1992). The yielding of Bothkennar clay. *Geotechnique, 42*(2), 257-274.

Tavenas, F., Leroueil, S., Rochelle, P. L., & Roy, M. (1978). Creep behaviour of an undisturbed lightly overconsolidated clay. *Canadian Geotechnical Journal, 15*(3), 402-423.

Ter-Stepanian, G. (1975). Creep of a clay during shear and its rheological model. *Geotechnique, 25*, 299-320. http://www.icevirtuallibrary.com/content/article/10.1680/geot.1975.25.2.299

Terzaghi, K. (1996). *Soil mechanics in engineering practice*: John Wiley & Sons.

Terzaghi, v. K. (1936). *The shearing resistance of saturated soils and the angle between the planes of shear.* Paper presented at the Proceedings of the 1st International Conference on Soil Mechanics and Foundation Engineering.

Vaid, Y. P., & Campanella, R. G. (1977). Time-dependent behavior of undisturbed clay. *Journal of the Geotechnical Engineering Division, 103*(7), 693-709.

Vaughan, P., Maccarini, M., & Mokhtar, S. (1988). Indexing the engineering properties of residual soil. *Quarterly Journal of Engineering Geology and Hydrogeology, 21*(1), 69-84.

Ventura, G., Vinciguerra, S., Moretti, S., Meredith, P., Heap, M., Baud, P., . . . Kummerow, J. (2010). Understanding slow deformation before dynamic failure *Geophysical Hazards* (pp. 229-247): Springer.

Vermeer, P., & Neher, H. (1999). *A soft soil model that accounts for creep.* Paper presented at the Proceedings of the International Symposium "Beyond 2000 in Computational Geotechnics.

Walker, K. P. (1981). Research and development program for non-linear structural modeling with advanced time-temperature dependent constitutive relationships[Final Report].

Watanabe, O., & Atluri, S. (1986). Constitutive modeling of cyclic plasticity and creep, using an internal time concept. *International Journal of Plasticity, 2*(2), 107-134.

Wesley, L. D. (1990). Influence of structure and composition on residual soils. *Journal of Geotechnical Engineering, 116*(4), 589-603.

Wheeler, S. J., Näätänen, A., Karstunen, M., & Lojander, M. (2003). An anisotropic elastoplastic model for soft clays. *Canadian Geotechnical Journal, 40*(2), 403-418. doi: 10.1139/t02-119

Whittle, A. J., & Kavvadas, M. J. (1994). Formulation of MIT-E3 constitutive model for overconsolidated clays. *Journal of Geotechnical Engineering, 120*(1), 173-198.

Wood, M. D. (1995). *Kinematic hardening model for structured soil.* Paper presented at the Proc. of Int. Symp. on Numerical Models in Geomechanics (NUMOG V), Davos.

Yang, C., Daemen, J. J. K., & Yin, J.-H. (1999). Experimental investigation of creep behavior of salt rock. *International Journal of Rock Mechanics and Mining Sciences, 36*(2), 233-242. doi: http://dx.doi.org/10.1016/S0148-9062(98)00187-9

Yang, S., & Jiang, Y. (2010). Triaxial mechanical creep behavior of sandstone. *Mining Science and Technology (China), 20*(3), 339-349.

Yin, J.-H. (1999). Non-linear creep of soils in oedometer tests. *Geotechnique, 49*(5), 699-707.

Yin, J.-H., & Cheng, C.-M. (2006). Comparison of Strain-rate Dependent Stress-Strain Behavior from K o-consolidated Compression and Extension Tests on Natural Hong Kong Marine Deposits. *Marine Georesources and Geotechnology, 24*(2), 119-147.

Yin, J.-H., & Graham, J. (1996). Elastic visco-plastic modelling of one-dimensional consolidation. *Geotechnique, 46*(3), 515-527.

Yin, J.-H., Zhu, J.-G., & Graham, J. (2002). A new elastic viscoplastic model for time-dependent behaviour of normally and overconsolidated clays: theory and verification. *Canadian Geotechnical Journal, 39*(1), 157-173. doi: 10.1139/t01-074

Yin, Z.-Y., Chang, C. S., Karstunen, M., & Hicher, P.-Y. (2010). An anisotropic elastic–viscoplastic model for soft clays. *International Journal of Solids and Structures, 47*(5), 665-677.

Yin, Z. Y., & Hicher, P. Y. (2008). Identifying parameters controlling soil delayed behaviour from laboratory and in situ pressuremeter testing. *International Journal for Numerical and Analytical Methods in Geomechanics, 32*(12), 1515-1535.

Zhang, H., Wang, Z., Zheng, Y., Duan, P., & Ding, S. (2012). Study on tri-axial creep experiment and constitutive relation of different rock salt. *Safety Science, 50*(4), 801-805.

Zhou, C., Yin, J.-H., Zhu, J.-G., & Cheng, C.-M. (2005). Elastic anisotropic viscoplastic modeling of the strain-rate-dependent stress–strain behavior of K 0-consolidated natural marine clays in triaxial shear tests. *International Journal of Geomechanics, 5*(3), 218-232.

Zhu, J.-G., & Yin, J.-H. (2000). Strain-rate-dependent stress-strain behavior of overconsolidated Hong Kong marine clay. *Canadian Geotechnical Journal, 37*(6), 1272-1282.

Ziegler, H. (1959). A modification of Prager's hardening rule. *Quart. Appl. Math, 17*(1), 55.

Zienkiewicz, O., & Cormeau, I. (1974). Visco-plasticity—plasticity and creep in elastic solids—a unified numerical solution approach. *International Journal for Numerical Methods in Engineering, 8*(4), 821-845.

Zienkiewicz, O., Humpheson, C., & Lewis, R. (1975). Associated and non-associated visco-plasticity and plasticity in soil mechanics. *Geotechnique, 25*(4), 671-689.